frontiers | Research Topics

Offshore aquacultural engineering and its interaction with the marine environment

Edited by
Zhao Yunpeng, Fukun Gui and Igor Tsukrov

Coordinated by
Gang Wang

Published in
Frontiers in Marine Science

ISSN 1664-8714
ISBN 978-2-8325-3460-1
DOI 10.3389/978-2-8325-3460-1

About Frontiers

Frontiers is more than just an open access publisher of scholarly articles: it is a pioneering approach to the world of academia, radically improving the way scholarly research is managed. The grand vision of Frontiers is a world where all people have an equal opportunity to seek, share and generate knowledge. Frontiers provides immediate and permanent online open access to all its publications, but this alone is not enough to realize our grand goals.

Frontiers journal series

The Frontiers journal series is a multi-tier and interdisciplinary set of open-access, online journals, promising a paradigm shift from the current review, selection and dissemination processes in academic publishing. All Frontiers journals are driven by researchers for researchers; therefore, they constitute a service to the scholarly community. At the same time, the *Frontiers journal series* operates on a revolutionary invention, the tiered publishing system, initially addressing specific communities of scholars, and gradually climbing up to broader public understanding, thus serving the interests of the lay society, too.

Dedication to quality

Each Frontiers article is a landmark of the highest quality, thanks to genuinely collaborative interactions between authors and review editors, who include some of the world's best academicians. Research must be certified by peers before entering a stream of knowledge that may eventually reach the public - and shape society; therefore, Frontiers only applies the most rigorous and unbiased reviews. Frontiers revolutionizes research publishing by freely delivering the most outstanding research, evaluated with no bias from both the academic and social point of view. By applying the most advanced information technologies, Frontiers is catapulting scholarly publishing into a new generation.

What are Frontiers Research Topics?

Frontiers Research Topics are very popular trademarks of the *Frontiers journals series*: they are collections of at least ten articles, all centered on a particular subject. With their unique mix of varied contributions from Original Research to Review Articles, Frontiers Research Topics unify the most influential researchers, the latest key findings and historical advances in a hot research area.

Find out more on how to host your own Frontiers Research Topic or contribute to one as an author by contacting the Frontiers editorial office: frontiersin.org/about/contact

Offshore aquacultural engineering and its interaction with the marine environment

Topic editors
Zhao Yunpeng — Dalian University of Technology, China
Fukun Gui — Zhejiang Ocean University, China
Igor Tsukrov — University of New Hampshire, United States

Topic coordinator
Gang Wang — Yellow Sea Fisheries Research Institute, Chinese Academy of Fishery Sciences (CAFS), China

Citation
Yunpeng, Z., Gui, F., Tsukrov, I., Wang, G., eds. (2023). *Offshore aquacultural engineering and its interaction with the marine environment*. Lausanne: Frontiers Media SA. doi: 10.3389/978-2-8325-3460-1

Table of contents

frontiers | Frontiers in Marine Science

TYPE Original Research
PUBLISHED 28 October 2022
DOI 10.3389/fmars.2022.1049769

EDITED BY
Morten Omholt Alver,
Norwegian University of Science and Technology, Norway

REVIEWED BY
Aichun Feng,
Shanghai Jiao Tong University, China
Junliang Gao,
Jiangsu University of Science and Technology, China

*CORRESPONDENCE
Chao Ma
dlutmc37@mail.dlut.edu.cn

SPECIALTY SECTION
This article was submitted to Marine Fisheries, Aquaculture and Living Resources, a section of the journal Frontiers in Marine Science

RECEIVED 21 September 2022
ACCEPTED 13 October 2022
PUBLISHED 28 October 2022

CITATION
Zhao Y, Xie S and Ma C (2022) Experimental investigations on the hydrodynamics of a multi-body floating aquaculture platform exposed to sloping seabed environment. *Front. Mar. Sci.* 9:1049769. doi: 10.3389/fmars.2022.1049769

Experimental investigations on the hydrodynamics of a multi-body floating aquaculture platform exposed to sloping seabed environment

Yunpeng Zhao[1,2], Sida Xie[1] and Chao Ma[1*]

[1]State Key Laboratory of Coastal and Offshore Engineering, Dalian University of Technology, Dalian, China, [2]Ningbo Institute of Dalian University of Technology, Ningbo, China

The coastal area near islands has become a key area for aquaculture because of the long offshore distance and suitable wave conditions. There is a topographic change near the islands, and the reflected waves generated by the topography modify the wave field in the aquaculture area, which may cause structural damage to the offshore net cage. Most studies on the hydrodynamic characteristics of aquaculture structures do not consider the effects of topography. Therefore, we investigated the hydrodynamic characteristics and wave field of a multi-body floating aquaculture platform under the influence of sloping seabed by leveraging a physical model approach. The results show that the low-frequency component of the surge motion of the cage on the weather side increases significantly under the influence of sloping seabed. However, the heave and pitch motions change slightly. Considering the presence of the sloping seabed, the wave elevations inside cages have been changed too., The wave breaking inside the cage on the weather side becomes more evident when the incident wavelength is equal to the width of the cage. And its wave response gradually shifts from wave frequency to high frequency. Regarding the cage on the lee side, the wave response inside it is positively correlated with the incident wavelength. The results of this study provide a reference for the design and optimization of aquaculture structures anchored near islands.

KEYWORDS
multi-body floating aquaculture platform, physical model approach, seabed topography, wave-structure interaction, regular wave

1 Introduction

Aquaculture is a sustainable industry that secures the global food supply. In addition to traditional agriculture and animal husbandry, it is a crucial source of protein and essential trace elements for balanced nutrition and good health. According to a report by the Food and Agriculture Organization of the United Nations, by 2030, seafood demand can reach approximately 180 million tons owing to the increasing world population (FAO, 2018). Expansion of aquaculture to open oceans with larger structures is a solution to increase seafood production. However, severe environmental conditions in the open ocean pose challenges to the design of aquaculture structures. Alternatively, inshore aquaculture practices are particularly favored because the coastline and islands provide a natural shelter that avoids severe conditions. Nevertheless, the wave mechanisms affected by the complicated seabed topography in shelter water (e.g., Figures 1A, B) and the subsequent effects on aquaculture platforms have received insignificant attention. Therefore, studying the wave mechanisms and hydrodynamic performance of aquaculture platforms in sheltered environments is the aim of this study.

Previously, there was a considerable number of studies focused on hydrodynamic characteristics of aquaculture structures (Gao et al., 2020; Gao et al., 2021). Tsukrov et al. (2003) proposed a consistent net element to predict the hydrodynamic forces on aquaculture net panels. Lader and Fredheim (2006) utilized a screen model to analyze the dynamic properties of a flexible net sheet exposed to waves and currents. Gui et al. (2006) proposed a method based on the CCD image technique for analyzing the motion responses of moving objects. And the validity of the method was verified through a specific experiment. Zhao et al. (2008) used a lumped-mass model to simulate net panels under current and waves. Lee et al. (2008) established a mass–spring model to approximate a net cage. The dynamic response was calculated by solving the dynamic equilibrium equation and comparing the results with experimental results. Bi et al. (2014) proposed a numerical approach to simulate the hydrodynamic characteristics of an offshore net cage at a steady current. The numerical approach was based on the joint use of the porous-media fluid model and lumped-mass mechanical model. Chen and Christensen (2016) proposed a new approach to calculate the porous resistance coefficients based on the transformation of Morison type load model. Bi et al.(2017) analyzed the wave attenuation by a square array of biofouled net cages through numerical simulation. Bai et al. (2018) proposed a fatigue life assessment procedure for a float collar under random waves, and then analyzed the probability density function to estimate the floating system fatigue life. Qin et al. (2020) analyzed the nonlinear vertical acceleration and mooring loads of cages under extreme loads. Liu et al. (2020) applied a new method that combined the boundary element method with the Morison equation to investigate the hydrodynamic responses of a semi-submersible aquaculture facility. Knysh et al. (2021) investigated the significance of a protective barrier through physical testing, numerical simulations and field deployment. Shen et al. (2021) compared the motion responses and interior waves of closed and semi-enclosed fish cages. Yang et al. (2022) proposed a one-way fluid–structure coupling model to examine the flow interaction with pile-net structures. Regarding the cage array, Fredriksson et al. (2004) used standard chain catenary equations and

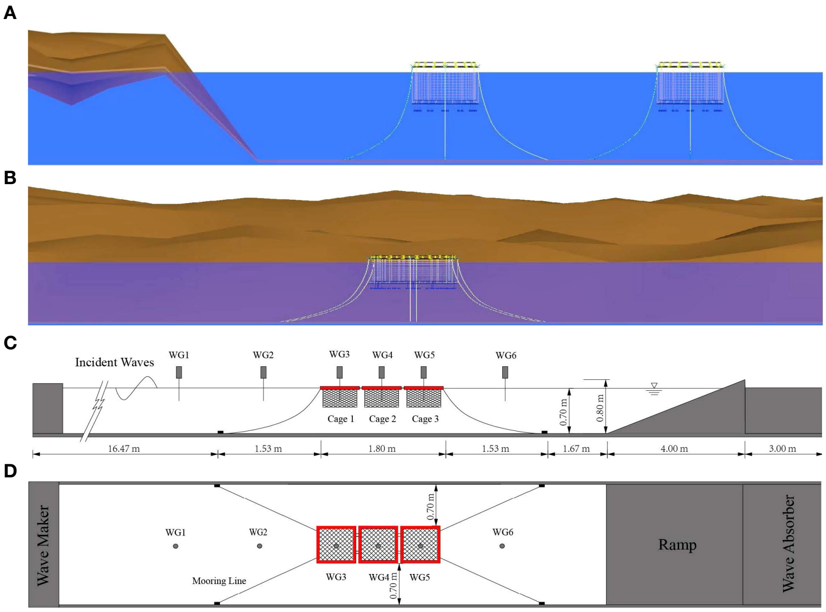

FIGURE 1
Net cages anchored near the island and specifications of the experimental setups: **(A)** perpendicular to the coastline, **(B)** parallel to the coastline, **(C)** elevation view, **(D)** plan view.

equilibrium analysis to study the dynamics of a submerged, four-cage grid mooring system. Xu et al. (2012) developed a numerical model based on the lumped mass method and the principle of rigid body kinematics to investigate the hydrodynamic responses of multiple offshore net cages and mooring grid systems in regular waves. Bi et al. (2021) studied the hydrodynamic characteristics of a multi-body floating aquaculture platform and measured the horizontal stiffness of a platform's mooring system. Ma et al. (2022a) compared the effects of floating aquaculture cages in single and tandem arrangements on the wave field. The relationship between the wavelength and wave-dissipation performance was analyzed. The impact of a changing seabed on floating bodies is an important issue to be considered. Buchner (2006); Ferreira and Newman (2009) and De Hauteclocque et al. (2009) developed second body model to describe the sloping seabed profile and found a sloping seabed significantly influenced the magnitudes of the cross coupling hydrodynamic coefficients. Kim and Kim (2013) proposed two models involving the Rankine source method and a unified method coupled to the Boussinesq equation. They found that the peak frequency of the exciting forces and motion responses shifted due to the influence of the sloping seabed. Feng and Price (2018); Feng et al. (2019) used a boundary element model to examine the influences of wave and current on the hydrodynamic responses of a floating or fixed body in the presence of a flat or sloping seabed. Yang et al. (2019) claimed that the wave statistics experienced a change when propagating and approaching the sloping seabed. Ding et al. (2020) established a direct coupling analysis method based on the Boussinesq equation and Rankine source method to investigate the wave propagation near the island. Furthermore, the motions and connector load of a very large floating structure (VLFS) deployed on a typical island were examined. When the water depth was assumed to be constant by ignoring the influence of seabed topography, the load of connectors between modules was underestimated (Yang et al, 2019). Feng et al. (2017); Feng et al. (2021) adopted a continuous Rankine source method to investigate two-dimensional or three-dimensional water wave problems in an environment with a flat or sloping rigid seabed. To study the effect of the complicated seabed topography on the performance of aquaculture cages, we conduct physical model experiments in a wave flume. A ramp is used to simplify the sloping seabed. Subsequently, the influence of the ramp on the structural hydrodynamic and wave field characteristics is investigated. The dynamic response, mooring force, and wave performance under different wave conditions are analyzed.

The remainder of this paper is organized as follows. We first report the laboratory experiments, including the physical model, experimental setup, test conditions, and data processing in Section 2. The dependence of the dynamic response and mooring loads of the weather-side cage on the wave steepness and wavelength is analyzed in Section 3. The wave elevations inside different cages are also considered. Thereafter, the hydrodynamic characteristics and free surface effect of the cage are analyzed in the frequency domain using a fast Fourier transform (FFT). Finally, the conclusions of this study are presented in Section 4.

2 Experiment

Selecting an appropriate model scale and the environmental loads to minimize the influence of the flume walls on the measurements is vitally important. Three major factors that affect the scale selection should be considered: (1) model characteristics; (2) wave/tow basin dimensions; and (3) wave generation (Qin et al., 2020).

Physical model tests of the aquaculture platform under regular waves are conducted in a wave flume at the Ningbo Institute of Dalian University of Technology, Ningbo, China. This wave flume is 30 m long, 2 m wide, and 1.2 m in height. The wave flume is equipped with a servo motor-driven piston-type wave-maker to generate regular and irregular waves. Wave absorbers are installed at the end of the flume to mitigate wave reflection.

2.1 Physical model

The multi-body floating aquaculture platform consists of three net cages connected by hinges and a mooring system. Compared with other connection methods, the hinge-connected structures can effectively eliminate the influence of the longitudinal bending moment (Ma et al., 2022b). Each cage includes a floating frame, netting, and bottom weight. The platform is moored to the bottom of the flume using four cables, as illustrated in Figures 1C, D. The physical model we utilize has a 1:60 scale, which is within the range of scales typically used in wave flumes, from 1:10 to 1:100 (Chakrabarti, 1994). Froude similarity criterion is used for the components of the physical model and wave conditions, except for the nets.

The floating frame is the primary component of a floating aquaculture cage that is subjected to environmental loads. Two floating frames are connected by hinge joints with zero rotational stiffness, which restrict the relative translational motion between the two frames, as shown in Figure 2A. Owing to the large stiffness of Plexiglas, the model is not considered to be deformed, and the elasticity of the frame is ignored in the experiment. Detailed parameters of the floating frames are listed in Table 1.

In the experiment, a smaller model scale of 1/5 is adopted to determine the mesh size and twine diameter of the model owing

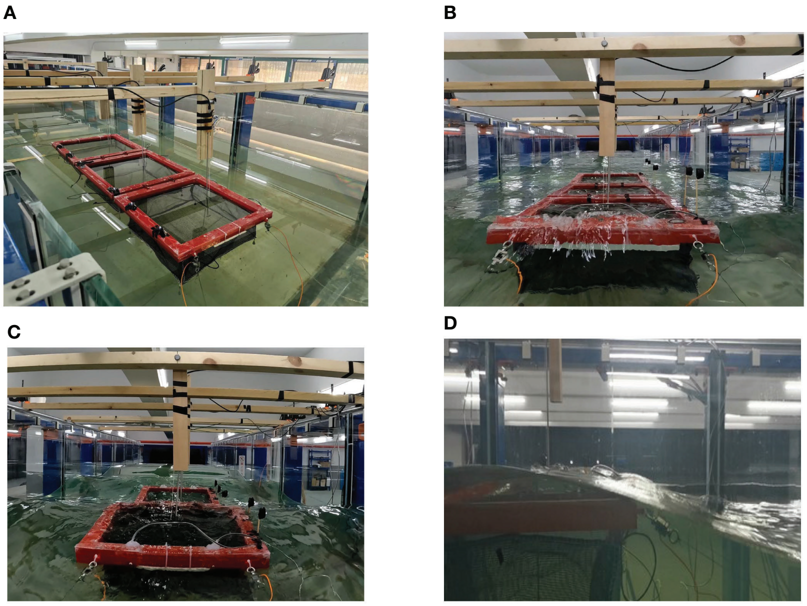

FIGURE 2
Physical model of the floating aquaculture platform: **(A)** model in the calm water, **(B)** wave slamming of the net cage, **(C)** wave reflection inside cage, **(D)** completely submerged net cage.

to material limitations. If the scale of the twine diameter is the same as that of the floating frame, it would be 0.03 mm in the physical model, which is too small to be acquired. The main hydrodynamic force acting on the nets is the drag force, which is related to the projected area of the net per unit area in the normal direction of the current. In our experiment, an equivalent net is used to ensure that the equivalent and prototype nets have the same projected area. The geometric similarity criterion for the nets is satisfied provided that the ratio of mesh size to net diameter of the model nets is consistent with the ratio of mesh size to net diameter of the prototype nets (Zhao et al, 2007). The geometric similarity of the nets is defined as $a_1 / d_1 = a_2 / d_2 = 5.0$, where a_1 and d_1 are the prototype mesh size and net diameter, respectively, and a_2 and d_2 are model values.

Owing to the change in scale, the weight of the equivalent model net must not satisfy Froude's similarity criterion. Therefore, the weight of the equivalent model net has to be corrected. The formula for calculating the modified mass is as follows:

$$\Delta W = \left(\frac{1}{\Lambda 2} - \frac{1}{\Lambda 1}\right) \times \left(\frac{\pi d_1^2}{4 a_1 \mu_1 \mu_2} \times 10^4\right) \times (\rho_n - \rho) \times S_n \times S_{net} \quad (1)$$

where ΔW is the corrected weight of the model nets; Λ2 is the small scale of the nets that can be calculated by d_1 / d_2; Λ1 is the geometric scale; μ1 and μ2 are the horizontal and vertical hanging ratios, respectively; ρ_n is the net material density; S_n is the solidity ratio of the nets; S_{net} is the contour area of the model nets. The weight of the equivalent nets should be increased by 9.7 g after the calculation to meet the similarity principle. The mass of the sinker in the air of a single net cage is 228 g, which includes the weight of the equivalent nets that should be increased. The structural parameters of the nets used in this study are listed in Table 2.

The platform is held in place by four mooring lines that are designed based on the Froude similarity criterion. All mooring

TABLE 1 **Structural parameters of the floating frame.**

Components	Parameters	Model scale	Full scale
Width	D_{frame}	0.60 m	36 m
Depth	H_{frame}	0.05 m	3.0 m
Width of the cross-section	B_{frame}	50 mm	3.0 m
Mass	M_{frame}	2.925 kg	631.8 t
Draft	H_{draft}	0.03 m	1.8 m
Material	—	Plexiglass	Steel

lines exhibit the same properties. And a single mooring line consists of two parts: one made of a steel chain at the bottom and the other of nylon rope at the top. Such multicomponent lines provide an optimal combination of stiffness and total weight (Journée et al., 2000). The details of the mooring system are listed in Table 3.

2.2 Experimental setup

A ramp is used to simplify the depth-varying seabed, as illustrated in Figure 1. Considering the reality of the island, the vertical height of the ramp needs to be greater than the water depth to ensure that the ramp can be exposed to the water. So, we set the height of the ramp to 0.8m. But the length of the wave flume is limited, too small a slope will result in insufficient space for cage mooring. Therefore, referring to Ning's research (Ning et al., 2022), we set the slope of the ramp to be 1/5 and the corresponding horizontal length of the ramp to be 4m. Plexiglass panels of 0.6 cm are used for the ramp surface. Before the experiment, we design a reasonable frame structure to support the Plexiglas plates and limit their deformation, which is proven to be effective. Simultaneously, five weights of 25 kg are placed at the bottom of the frame to ensure that the ramp remains stable in the flume under the effect of the wave.

The configuration of the experimental setup is shown in Figure 1. Six wave gauges (WG1, WG2, WG3, WG4, WG5, and WG6) are used to measure wave-induced variations in water surface elevation. The measurement range is 60 cm with an accuracy of ±1 mm.WG1 is used to measure the incident wave height, and is placed 10 m from the wave-making plate. WG2 and WG6 are placed 1 m away from the net cages. Other wave gauges are placed at the center of the cage. We choose a suitable position for them to avoid the cages touching the wave gauges. A sampling frequency of 100 Hz is used to record the time history of the wave height. Three CCD cameras are placed directly in front of each cage to record its motion response. The frame rate of the camera was 25. The mooring force of the cage was measured using four water-resistant load cells with a range of 50 N. A camera running at a frame rate of 60 fps and a resolution of 3840×2160 pixels was placed in front of the cage on the weather side to record the general behavior of the platform.

2.3 Test conditions

The wave field near the floating net cages is closely related to the ratio of the wavelength to the structural span. Longer wavelengths correspond to lower wave frequencies, which is more likely to cause larger surge motion and greater mooring force of the cages. (Bi et al., 2021; Ma et al., 2022a). However, considering the working ability of water flume, the wavelength is too long to ensure that enough of the reflected wave is absorbed by the dissipating material. Therefore, regular waves with

TABLE 2 Structural parameters of the nets.

Components	Parameters	Model scale	Full scale
Mesh size	a	5 mm	25 mm
Twine diameter	d	1 mm	5 mm
Shape	—	Square	Square
Net solidity ratio	S_n	0.42	0.42
Horizontal hanging ratio	μ_1	0.707	0.707
Vertical hanging ratio	μ_2	0.707	0.707
Contour area	S_{net}	0.5 m^2	1800 m^2
Height	H_{net}	0.25 m	15 m
Material	—	Polyethylene	Polyethylene

TABLE 3 Parameters of the mooring system.

Components	Parameters	Model scale	Full scale
Length of the nylon rope	L_{nylon}	0.40 m	24 m
Length of the steel chain	L_{steel}	1.35 m	81 m
Diameter of the nylon rope	D_{nylon}	0.56 mm	33.6 mm
Diameter of the steel chain	D_{steel}	1.5 mm	90 mm
Minimum breaking load of the nylon rope	F_{nylon}	176.5 N	635.4 kN
Weight per unit of the steel chain	M_{steel}	0.041 kg/m	147.6 kg/m

periods in the range 0.62–1.08 s are used in the experiment. The ratio of the wavelength to the structural span varies in the range 1–3. Because wave steepness is closely related to wave nonlinearity, the influence of different wave steepnesses on the structure should be considered. Referring to Qin's experiment (Qin et al., 2020) and the working ability of the wave maker, three wave steepness values (H/λ = 1/15, 1/30, and 1/60) are used in the experiment. The water depth of the experiment is 0.7 m. And the corresponding prototype water depth is 42 m. The parameters of the regular wave are listed in Table 4, where T is the wave period, H is the wave height, and λ is the wavelength.

Because of the voltage fluctuations and interference from other electronic equipment, it is difficult for wave makers to produce waves exactly in accordance with the prescribed wave height. Through several tests, we obtained an empirical coefficient that describes the proportional relationship between the prescribed and measured values; this reduces the influence of the aforementioned error caused by wave makers. In addition, we waited 5–10 min before the next test to prevent interference between the tests. Each test was repeated three times to ensure reproducibility. Comparisons between the prescribed and measured wave heights in the absence of the models are presented in Table 5. $H^{(p)}$ and $H^{(m)}$ are the prescribed and measured wave heights in meters, respectively.

Filtering the experimental data is important as it helps (1) eliminate noise, (2) isolate low- and high-frequency data, (3) prepare the data for spectral analysis, and (4) remove the transition data (Qin et al., 2020). The Savitzky–Golay filter, designed based on the least-squares method, was used in the experiment (Savitzky and Golay, 1964). We can remove high-frequency noise or separate low-frequency noise because of its low-pass characteristics.

3 Results and discussion

To understand the influence of ramp on the hydrodynamic characteristics and wave field of the aquaculture platform, we regard regular waves as environmental loads. We employ different wave length that are equally divided into five groups spanning from λ = 0.6 m to λ = 1.8 m in the experiment. In addition, the effect of the wave steepness is considered. Three wave steepnesses are used in the experiment: 1/15, 1/30, and 1/60. The cage on the weather side is most likely to suffer structural damage due to direct wave slamming without shelter. Therefore, we select this cage as an example to analyze the effect of ramp on structure.

3.1 Time domain analysis

3.1.1 Dynamic response of cage array

Figure 3 shows the time histories of the surge motion, trajectories of the cage and dependence of the amplitude of the surge motion on wavelength under different wave steepness. The maximum wavelength L = 1.8 m (λ/L = 3) was chosen as the representative owing to the low-frequency characteristics of the surge motion (Bi et al., 2021). As can be seen in Figure 3, the equilibrium position of the surge of the cage is further away from the initial position with an increase in wave steepness. In

TABLE 4 Wave parameters used in the experiments.

Wave period T (s)	Wavelength λ (m)	λ/L	Wave height H (m)	Wave steepness H/λ
0.62	0.60	1.0	0.010-0.040	1/60-1/15
0.76	0.90	1.5	0.015-0.060	
0.88	1.20	2.0	0.020-0.080	
0.98	1.50	2.5	0.025-0.100	
1.08	1.80	3.0	0.030-0.120	

TABLE 5 Comparisons of prescribed and measured wave heights.

	Wave Steepness, H/λ								
Periods (s)	1/60			1/30			1/15		
T	$H^{(p)}$	$H^{(m)}$	Error	$H^{(p)}$	$H^{(m)}$	Error	$H^{(p)}$	$H^{(m)}$	Error
0.62	0.010	0.0101	1.00%	0.020	0.0199	0.50%	0.040	0.0399	0.25%
0.76	0.015	0.0151	0.67%	0.030	0.0305	1.67%	0.060	0.0602	0.33%
0.88	0.020	0.0199	0.50%	0.040	0.0394	1.50%	0.080	0.0804	0.50%
0.98	0.025	0.0249	0.40%	0.050	0.0495	1.00%	0.100	0.0993	0.70%
1.08	0.030	0.0299	0.33%	0.060	0.0599	0.17%	0.120	0.1201	0.08%

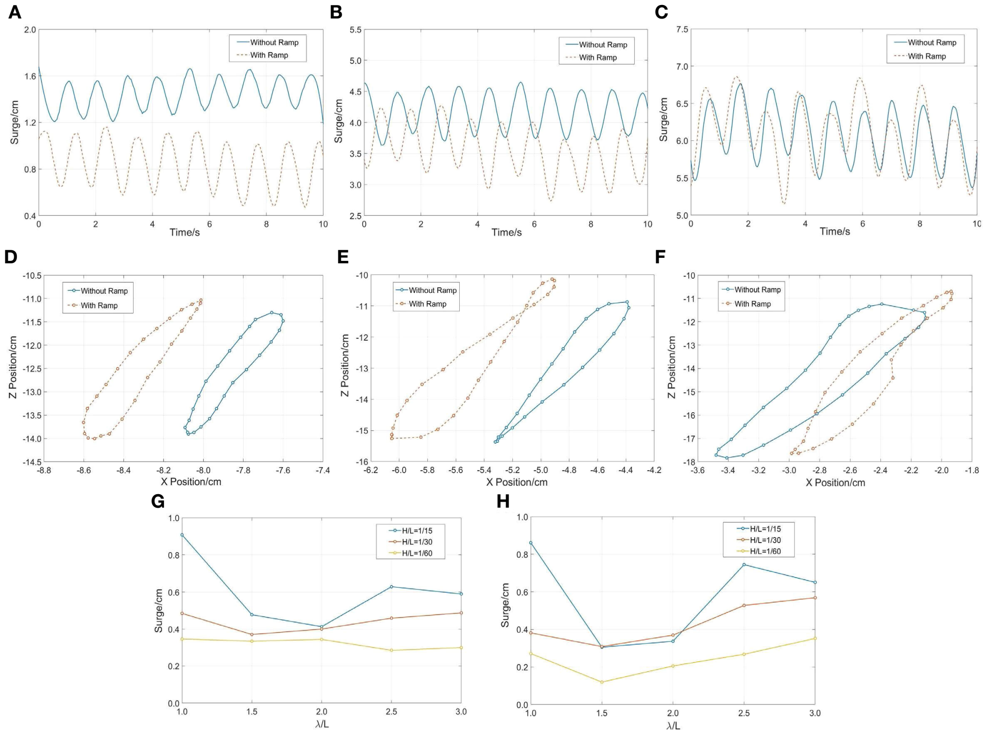

FIGURE 3
Time histories of the surge motion, trajectories of the cage and dependence of the amplitude of the surge motion on wavelength under different wave steepness: **(A, D)** H/λ=1/60, λ/L=3; **(B, E)** H/λ=1/30, λ/L=3; **(C, F)** H/λ=1/15, λ/L=3, **(G)** without ramp, **(H)** with ramp.

other words, the drift distance of the cage gradually increased. This is because the drift distance depends on the average wave force, which is proportional to the square of the wave height. When the wavelength was constant, the wave height increased with an increase in wave steepness. Larger wave heights resulted in greater average wave forces and drift distances. In addition, the trajectories of the cage were not as elliptical as the water particle trajectories for wave motion near the free surface owing to the nonlinear characteristics of the mooring lines. Notably, the trajectory became irregular with the effect of the ramp. This trend became increasingly significant as the wave steepness increased, which can be attributed to wave reflection caused by the ramp, resulting in more intense wave slamming and breaking near the cage on the weather side. The water particle trajectories became more random with the influence of these phenomena.

As shown in the Figure 3, we compare the amplitudes of the surge motion under different wave conditions. It can be observed that the surge motion has evident nonlinearity when the effect of the ramp is not considered, which is caused by the material nonlinearity of the nylon cable. The nonlinear stretching mooring strength members develop a permanent, nonelastic length increase under the first loading and respond with nonlinear elastic stretching to applied tensions with a considerably higher elastic modulus at their second and subsequent load cycles (Walther and Gibson, 2000). This trend became increasingly significant as the wave steepness increased.

Figure 4 exhibits the time histories of the heave and the dependence of the heave amplitude on wavelength under different wave steepnesses. The amplitude of the heave motion response is positively correlated with the wave length. It reaches the maximum value of 3.70 cm when the wave steepness is 1/15 and wavelength is 1.8 m (λ/L = 3). In addition, the motion response is significantly affected by the wave steepness. When the wave steepness is 1/30, the maximum value is 2.62 cm. When the wave steepness is 1/60, the maximum value is 1.42 cm. In a word, when the wave steepness increases from 1/60 to 1/15, the motion responses of the cage are increased by 84.6% and 41.2%. This is because when the wavelength is fixed, the increase of the wave steepness causes a rise in the wave height. Considering the effect of ramp, the heave motion response of the cage shows the slightly decreasing trend. However, the phase changes significantly.

As can be seen in Figure 5, the time histories and amplitudes of the pitch motion under different wave conditions were considered in the experiment. The motion characteristics of pitch are similar to those of heave, owing

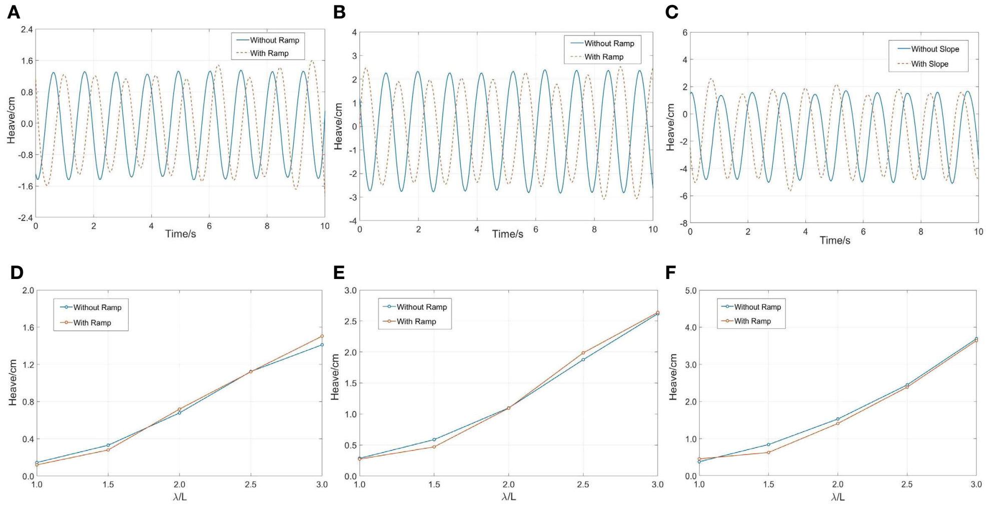

FIGURE 4
Time histories and dependence of the amplitude of the heave motion on wavelength under different wave steepness: **(A, D)** H/λ=1/60, λ/L=3; **(B, E)** H/λ=1/30, λ/L=3; **(C, F)** H/λ=1/15, λ/L=3.

to their coupling. Considering the constant wave steepness, longer wavelengths cause greater motion response. When the wavelength is 1.8 m (λ/L = 3), the motion response reaches the maximum value of 8.19°. The influence of wave steepness on pitch motion cannot be ignored. Taking the maximum wavelength of 1.8 m as an example, the pitch motion of the cage has increased by 66.6% and 42.9% when the wave steepness increases from 1/60 to 1/15. Similar to the conclusion of heave motion, there is a slight decrease in the pitch amplitude because of the ramp.

In conclusion, surge and pitch motion responses are positively correlated with wavelength. A large pitch motion challenges the strength of the hinges connecting the floating frame. In addition, the initial drift distance in the horizontal direction and motion amplitude in the vertical direction of the cage increased as the wave steepness increased. Considering the influence of ramp on structure, the motion trajectory of the cage becomes more random, and the amplitude of heave and pitch motion decreases slightly.

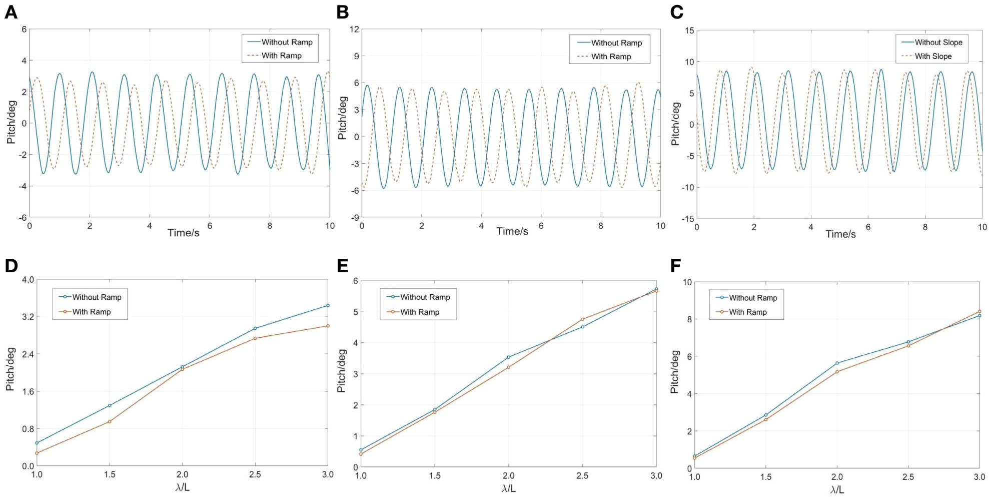

FIGURE 5
Time histories and the dependence of the amplitude of the pitch motion on wavelength under different wave steepness: **(A, D)** H/λ=1/60, λ/L=3; **(B, E)** H/λ=1/30, λ/L=3; **(C, F)** H/λ=1/15, λ/L=3.

3.1.2 Mooring loads

Figure 6 depicts the time histories and maximum value of the mooring force under different wave conditions. The peak value of the cable force is positively correlated with the incident wavelength. When the wave steepness was 1/15, and the wavelength was 1.8 m (λ/L = 3), the maximum cable force was 9.43 N. When the wave steepness was 1/30, the maximum value was 0.94 N. When the wave steepness was 1/60, the maximum value was 0.17 N. It can be concluded that large motion response caused by great wave steepness can lead to large cable force. Considering the influence of the ramp, the cable force of the cage was significantly increased. Taking the maximum wave steepness of 1/15 as an example, the cable force has increased by 74.5%, 45.6%, 25.5%, 20.0%, 15.1% with the wavelength growth. Therefore, the more reasonable design of the mooring system and the more reliable material of cable should be required for the cages anchored near the islands.

3.1.3 Wave elevations

The change in the wave surface is closely related to the safety of the cage. The change in the wave surface causes nonlinear motion of the cage, particularly for wave breaking. And the wave slamming occurring on the floating frame becomes more obvious under extreme wave conditions, which poses a challenge to the safety of the cage, as shown in Figure 2B.

Figures 7A–C shows time histories of the free-surface elevations in different net cages when the wavelength is 0.6 m (λ/L = 1) and the wave steepness is 1/15. The cage on the weather side is defined as Cage 1. The one on the lee side is called Cage 3. The middle one is called Cage 2. The wave response in the cage gradually decreases along the wave propagation direction. Compared with the other two cages, the wave surface in Cage 1 has stronger nonlinearity. This is because there is more significant wave reflection and breaking inside the cage when the incident wavelength is equal to the cage width, as shown in Figure 2C. In addition, the draft of the floating frame is much less than its width ($H_{draft}/L = 0.02$). The wave energy gradually decreases along the wave propagation direction under the influence of turbulence. With the effect of the reflected waves generated by the ramp, the wave elevations have increased by 10.6% in Cage 1, 40.2% in Cage 2 and 38.4% in Cage 3. Compared with other positions, the wave response inside Cage 2 is the largest. And the wave surface inside Cage 1 exhibits stronger nonlinearity because of the ramp.

Time histories of the free-surface elevations in different net cages when the wavelength is 1.2 m (λ/L = 2) and the wave steepness is 1/15, as shown in Figures 7D–F. The wave response in Cage 1 is similar to Cage 2. The maximum difference of wave response between the two cages is 5.6%. There is smaller wave response in Cage 3. Considering the effect of the ramp, there are lower wave responses inside Cage 1 and Cage 2. Note that the opposite conclusion is obtained inside Cage 3. Compared to other positions, the wave response in Cage 1 is the largest.

Figures 7G-I depict time histories of the free-surface elevations in different net cages when the wavelength is 1.8 m (λ/L = 3) and the wave steepness is 1/15. As shown in the figure, the wave responses inside different cages are close, and the maximum difference in wave amplitudes is only 3.4% when ramp is not considered. The nonlinearity of the wave surface inside the cages is weak. Considering the effect of the ramp, the

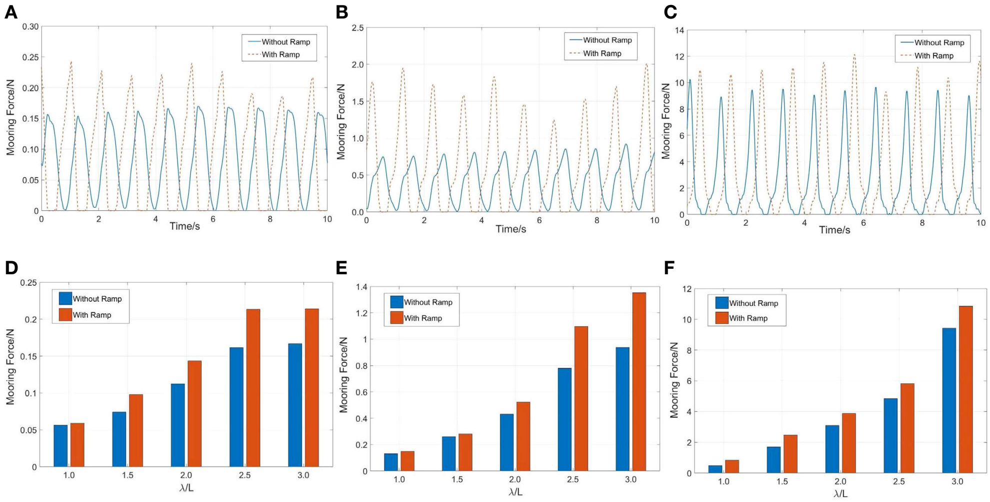

FIGURE 6
Time histories and the dependence of the peak value of the weather-side cable force on wavelength under different wave steepness:**(A, D)** H/λ=1/60, λ/L=3; **(B, E)** H/λ=1/30, λ/L=3; **(C, F)** H/λ=1/15, λ/L=3.

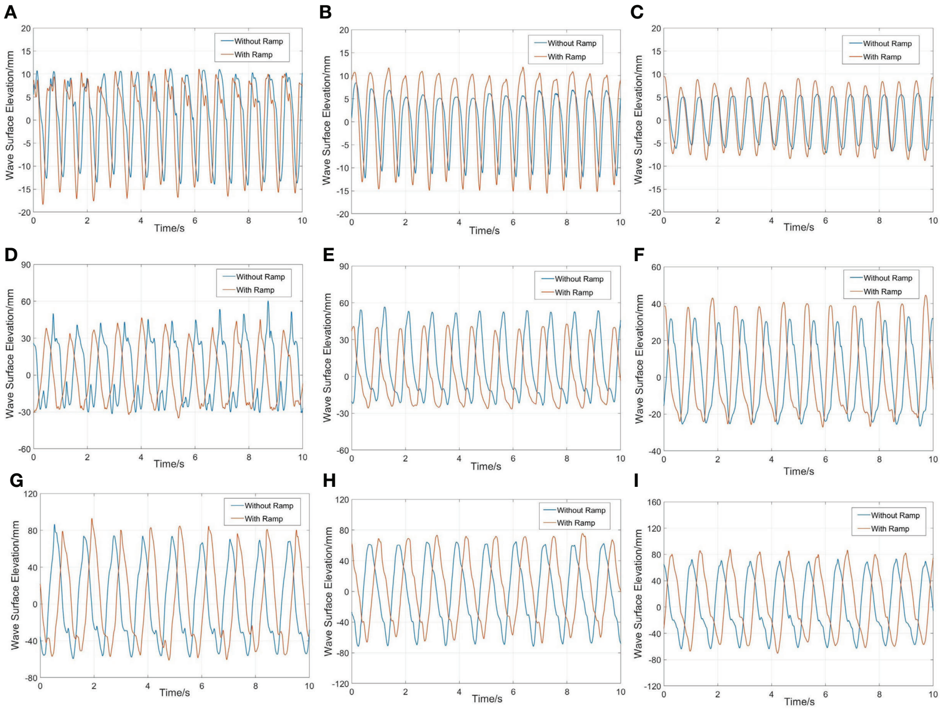

FIGURE 7
Time histories of the free-surface elevations in different net cages when the wave steepness is 1/15:**(A)** Cage 1, λ/L=1; **(B)** Cage 2, λ/L=1; **(C)** Cage 3, λ/L=1; **(D)** Cage 1, λ/L=2; **(E)** Cage 2, λ/L=2; **(F)** Cage 3, λ/L=2; **(G)** Cage 1, λ/L=3; **(H)** Cage 2, λ/L=3; **(I)** Cage 3, λ/L=3.

wave surface elevations inside three cages are increased. There is the largest wave response in Cage 3, and the wave response inside Cage 2 is the weakest.

3.2 Frequency domain analysis

In the last part, the data, including motion response, cable force, and wave response, are analyzed in the time domain. However, it cannot attain the characteristics of these data in the frequency domain Therefore, in this section, the fast Fourier transform (FFT) is used to conduct the frequency-domain analysis.

3.2.1 Spectrum analysis

Figures 8A–C depict the amplitude spectrum of the surge motion of the cage with different wavelengths. The wave steepness we considered in the figures is 1/15. Although high- and low-frequency components are involved, the surge motion response of the cage is dominated by the wave-frequency component. This is because the regular wave has a single frequency, and the wave load is concentrated on it. Regardless of the effect of the ramp, the high frequency motion accounts for 63.6% of the wave frequency motion when the wavelength is 1.2 m (λ/L = 2). Considering the effect of the ramp, the amplitude of low-frequency motion of the cage increases significantly. When the wavelength is 1.2 m (λ/L = 2), the amplitude of the low-frequency motion response of the cage with the ramp is three times higher than that without the ramp, and the wave frequency motion decreased by 20%. Low-frequency motion accounted for 54% of the wave frequency motion. The reason is that the low-frequency wave load of the cage is increased because of the superposition of the incident and reflected waves generated by the ramp. The natural frequency of the surge of the cage is low, and it easily resonates with the low-frequency wave load.

Figures 8D–F depict the amplitude spectrum of the heave motion of the cage with different wavelength. The wave steepness we consider is 1/15. From Figures 8D–F motion response of the cage is dominated by the wave response component. The high frequency motion of the cage only accounts for 20% of the wave frequency motion at most when the wavelength is 1.2 m (λ/L = 2). Considering the effect of the ramp, the motion response of cage on wave frequency is reduced, which becomes less obvious with the

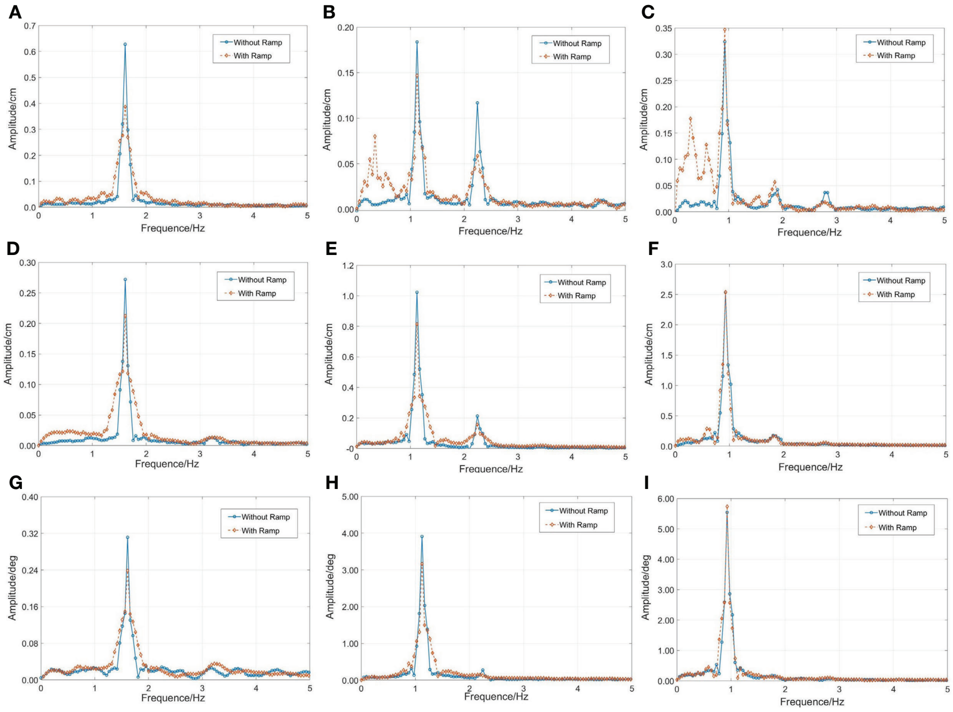

FIGURE 8
Amplitude spectra of the motion response of the cage with different wavelength when the wave steepness is 1/15: **(A)** λ/L=1, surge motion; **(B)** λ/L=2, surge motion **(C)** λ/L=3, surge motion; **(D)** λ/L=1, heave motion; **(E)** λ/L=2, heave motion **(F)** λ/L=3, heave motion; **(G)** λ/L=1, pitch motion; **(H)** λ/L=2, pitch motion **(I)** λ/L=3, pitch motion;.

increase of the wavelength. This is because the restoring force of the heave motion of the offshore platform is usually produced by the change in the drainage volume caused by the draught change of the platform. When the wavelength is short (λ/L = 1,2), the superposition of incident and reflected waves increases the draft of the floating frame. When the wavelength is long (λ/L = 3), the heave motion amplitude is 3.7 cm without the effect of the ramp and the draft depth of the floating frame water is 3 cm. The cage is placed completely underwater, as shown in Figure 2D. The motion response hardly changes because of the constant drainage volume.

Figures 8G–I depict the amplitude spectrum of the pitch motion of the cage with different wavelength. The wave steepness we consider is 1/15. Because of the coupling of the heave motion and pitch motion, the motion characteristic of pitch is similar to the heave.

Figure 9 shows the power spectrum of the mooring force at different wavelengths. The wave steepness we considered was 1/15. Although high and low components are involved, the mooring force of the cage is dominated by the wave frequency component. The effect of ramp on the wave frequency cable force is significantly greater than that it in other components. And the cable force in the low-frequency region increases because of the rise of motion amplitude in this part, as shown in the Figure 8. But the proportion of the low-frequency cable force to total cable force is significantly less than that of the wave frequency.

3.2.2 Free surface effects

In this section, we compare the energy spectra of wave response inside cages with different wavelengths. The wave steepness we consider is 1/15.Although higher-frequency components are involved, the wave responses inside frames are dominated by the wave-frequency component. The wave response is positively correlated with wavelength regardless of the effect of ramp. When the wave wavelength is equal to the span of the cage, the energy spectra of the wave response inside cages are shown in the Figures 10A, B. The presence of the ramp significantly increases the wave frequency component of wave response inside Cage 2 and Cage 3, but has slight effect on Cage 1. The wave response in Cage 1 increases by only 1.6%. Note that the wave response of the high-frequency components inside Cage 1 increases significantly, which is different from other cages. Wave reflection generated by ramp prompts wave breaking inside

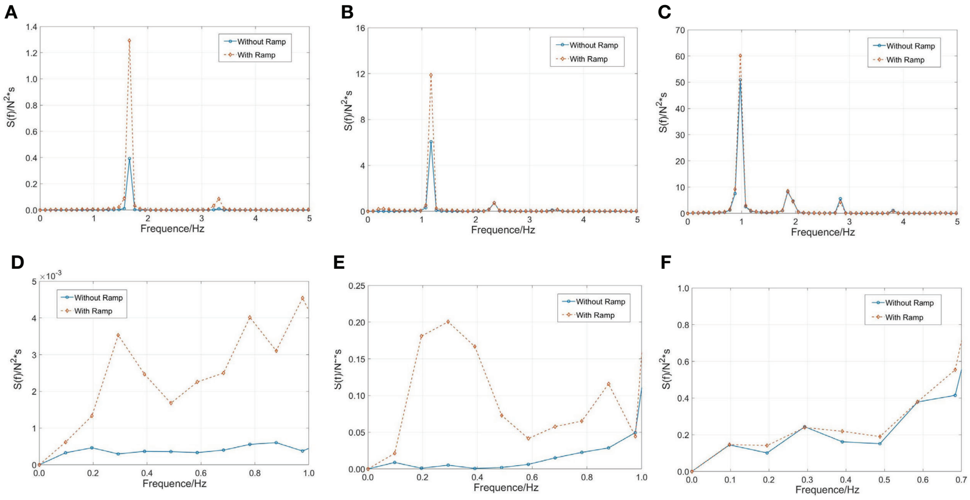

FIGURE 9
Power spectra of the mooring force with different wavelength:**(A, D)** λ/L=1, H/λ=1/15; **(B, E)** λ/L=2, H/λ=1/15; **(C, F)** λ/L=3, H/λ=1/15.

Cage 1, and the wave response is transferred from the wave frequency to the high frequency components.

The wavelength we consider in the Figures 10C, D is 1.2m(λ/L=2). Considering the effect of the ramp, the wave responses of Cage 1 and Cage 2 are reduced by 8.9%. The wave responses of Cage 3 increased by 28.8%.

The wavelength we considered in Figures 10 E, F is 1.8 m (λ/L = 3). The effect of the ramp on Cage 3 is greater than that on Cage 1 and Cage 2. The wave response of the wave frequency component of Cage 3 has increased by 48.4%. As for other cages, it has only increased by 2.49% and 0.82%.

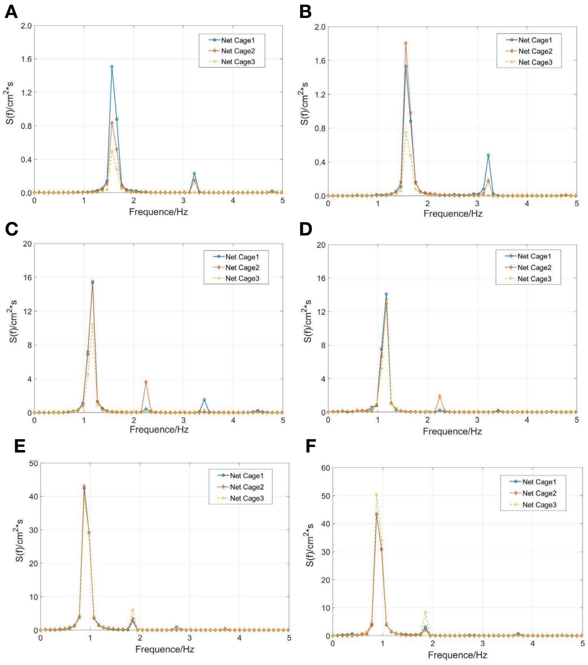

FIGURE 10
Energy spectra of wave elevations in the net cages when the wave steepness is 1/15: **(A)** λ/L=1, without ramp; **(B)** λ/L=1, with ramp; **(C** λ/L=2, without ramp; **(D)** λ/L=2, with ramp; **(E)** λ/L=3, without ramp; **(F)** λ/L=3, with ramp.

4 Conclusion

In this study, we analyze the hydrodynamic and wave field characteristics of a multi-body floating aquaculture platform under the influence of a ramp *via* physical model experiments. Dependence of motion response, cable force, as well as wave elevation on wave steepness, wavelength, and ramp influence is also analyzed. The innovation of this paper is to consider the influence of the sloping seabed on aquaculture facilities, which has been ignored in previous studies. The research results of this paper can provide a reference for the structure optimization and mooring system design of aquaculture facilities near islands.

(1) The motion response and cable force of the cage gradually increase with increasing wavelength and wave steepness. The wave response inside the cage is significantly correlated with the ratio of wavelength to cage width. Longer wavelengths generally result in larger wave responses.

(2) The effect of ramp on the surge motion response of the cage is greater than that of the heave and pitch motion. The low-frequency components of the surge motion response and mooring force become greater. As for the heave and pitch motion response, the amplitude has decreased on account of the growth of the structure draft. However, the effect of the ramp is limited owing to the low freeboard height of the structure.

(3) The cable force is significantly increased because of the presence of the ramp. Although the low-frequency components have risen with the increase of the surge response motion at low-frequency components, the wave frequency components are still the main part of the cable force.

(4) The presence of the ramp does not always increase the wave response inside the cage. When the wavelength is equal to the span of the cage, the wave breaking inside Cage 1 is promoted because of the ramp, and the wave response at high-frequency is increased. With a rise in the incident wave wavelength, the wave response inside Cage 3 is increased significantly.

Data availability statement

The raw data supporting the conclusions of this article will be made available by the authors, without undue reservation.

Author contributions

YZ: Conceptualization, Supervision, Project administration, Funding acquisition, Writing - review & editing. SX: Investigation, Data curation, Writing - original draft. CM: Conceptualization, Supervision, Writing - review & editing. All authors contributed to the article and approved the submitted version.

Funding

This work was financially supported by the National Key R&D Program of China (No. 2019YFD0900902); National Natural Science Foundation of China (Nos. 31972843); LiaoNing Revitalization Talents Program (Nos. XLYC907139); Dalian Technology Talents Program, projects No. 2020RQ107.

Conflict of interest

The authors declare that the research was conducted in the absence of any commercial or financial relationships that could be construed as a potential conflict of interest.

Publisher's note

References

Bai, X., Zhao, Y., Dong, G., and Bi, C. (2018). Probabilistic analysis and fatigue life assessment of floating collar of fish cage due to random wave loads. *Appl. Ocean Res.* 81, 93–105. doi: 10.1016/j.apor.2018.09.018

Bi, C.-W., Ma, C., Zhao, Y.-P., and Xin, L.-X. (2021). Physical model experimental study on the motion responses of a multi-module aquaculture platform. *Ocean Eng.* 239, 109862. doi: 10.1016/j.oceaneng.2021.109862

Bi, C.-W., Zhao, Y.-P., Dong, G.-H., Xu, T.-J., and Gui, F.-K. (2017). Numerical study on wave attenuation inside and around a square array of biofouled net cages. *Aquacultural Eng.* 78, 180–189. doi: 10.1016/j.aquaeng.2017.07.006

Bi, C.-W., Zhao, Y.-P., Dong, G.-H., Zheng, Y.-N., and Gui, F.-K. (2014). A numerical analysis on the hydrodynamic characteristics of net cages using coupled fluid–structure interaction model. *Aquacultural Eng.* 59, 1–12. doi: 10.1016/j.aquaeng.2014.01.002

Buchner, B. (2006). The motions of a ship on a sloped seabed. *International Conference on Offshore Mechanics and Arctic Engineering*, 47462, 339–347. doi: 10.1115/OMAE2006-92321

Chakrabarti, S. K. (1994). *Offshore structure modeling* (Singapore World Scientific).

Chen, H., and Christensen, E. D. (2016). Investigations on the porous resistance coefficients for fishing net structures. *J. Fluids Structures* 65, 76–107. doi: 10.1016/j.jfluidstructs.2016.05.005

De Hauteclocque, G., Rezende, F. V., Giorgiutti, Y., and Chen, X.-B. (2009). "Wave kinematics and seakeeping calculation with varying bathymetry," in *ASME 2009 28th International Conference on Ocean, Offshore and Arctic Engineering.* (Honolulu, Hawaii, USA.) 515–523.

Ding, J., Xie, Z., Wu, Y., Xu, S., Qiu, G., Wang, Y., et al. (2020). Numerical and experimental investigation on hydroelastic responses of an 8-module VLFS near a typical island. *Ocean Eng.* 214, 107841. doi: 10.1016/j.oceaneng.2020.107841

FAO (2018). *The state of world fisheries and aquaculture 2018-meeting the sustainable development goals* (Rome, Italy: Food and Agriculture Organization of the United Nations).

Feng, A., Bai, W., and Price, W. G. (2017). Two-dimensional wave radiation and diffraction problems in a flat or sloping seabed environment. *J. Fluids Structures* 75, 193–212. doi: 10.1016/j.jfluidstructs.2017.09.001

Feng, A., Cai, H., and You, Y. (2019). Freely floating body motion responses induced by wave and current in seabed conditions. *Ocean Eng.* 172, 396–406. doi: 10.1016/j.oceaneng.2018.12.002

Feng, A., Chen, K., You, Y., and Jiang, S.-C. (2021). Three dimensional numerical modelling for wave radiation problem under arbitrary seabed condition. *Ocean Eng.* 230, 108885. doi: 10.1016/j.oceaneng.2021.108885

Feng, A., and Price, W. G. (2018). Numerical simulations of the hydrodynamic responses of a body interacting with wave and current over a sloping seabed. *Appl. Ocean Res.* 79, 184–196. doi: 10.1016/j.apor.2018.08.004

Ferreira, M. D., and Newman, J. N. (2009). Diffraction effects and ship motions on an artificial seabed. *Proc. 24th Int. Workshop Water Waves Floating Bodies, Zelenogorsk, Russia.*

Fredriksson, D. W., Decew, J., Swift, M. R., Tsukrov, I., Chambers, M. D., and Celikkol, B. (2004). The design and analysis of a four-cage grid mooring for open ocean aquaculture. *Aquacultural Eng.* 32, 77–94. doi: 10.1016/j.aquaeng.2004.05.001

Gao, J., Ma, X., Dong, G., Chen, H., Liu, Q., and Zang, J. (2021). Investigation on the effects of Bragg reflection on harbor oscillations. *Coast. Eng.* 170, 103977. doi: 10.1016/j.coastaleng.2021.103977

Gao, J., Ma, X., Zang, J., Dong, G., Ma, X., Zhu, Y., et al. (2020). Numerical investigation of harbor oscillations induced by focused transient wave groups. *Coast. Eng.* 158 103670. doi: 10.1016/j.coastaleng.2020.103670

Gui, F., Li, Y., Dong, G., and Guan, C. (2006). Application of CCD image scanning to sea-cage motion response analysis. *Aquacultural Eng.* 35, 179–190. doi: 10.1016/j.aquaeng.2006.01.003

Journee, J. M. J., Massie, W. W.Delft University of Technology, F. O. C. E., Geosciences, Huijsmans, R. H. M, Delft University Of Technology, F. O. M and Maritime & Engineering M (2000). *Offshore hydromechanics* (Netherlands: TU Delft).

Kim, Y. (2013). Numerical analysis on floating-body motion responses in arbitrary bathymetry. *Ocean Eng.* 62, 123–139. doi: 10.1016/j.oceaneng.2013.01.012

Knysh, A., Coyle, J., Decew, J., Drach, A., Swift, M. R., and Tsukrov, I. (2021). Floating protective barriers: Evaluation of seaworthiness through physical testing, numerical simulations and field deployment. *Ocean Eng.* 227, 108707. doi: 10.1016/j.oceaneng.2021.108707

Lader, P. F., and Fredheim, A. (2006). Dynamic properties of a flexible net sheet in waves and current–a numerical approach. *Aquacultural Eng.* 35, 228–238. doi: 10.1016/j.aquaeng.2006.02.002

Lee, C.-W., Kim, Y.-B., Lee, G.-H., Choe, M.-Y., Lee, M.-K., and Koo, K.-Y. (2008). Dynamic simulation of a fish cage system subjected to currents and waves. *Ocean Eng.* 35, 1521–1532. doi: 10.1016/j.oceaneng.2008.06.009

Liu, H.-F., Bi, C.-W., and Zhao, Y.-P. (2020). Experimental and numerical study of the hydrodynamic characteristics of a semisubmersible aquaculture facility in waves. *Ocean Eng.* 214 107714. doi: 10.1016/j.oceaneng.2020.107714

Ma, C., Bi, C.-W., Xu, Z., and Zhao, Y.-P. (2022a). Dynamic behaviors of a hinged multi-body floating aquaculture platform under regular waves. *Ocean Eng.* 243, 110278. doi: 10.1016/j.oceaneng.2021.110278

Ma, C., Zhao, Y.-P., Xu, Z., and Bi, C.-W. (2022b). Experimental investigation on the wave performance with the interference of floating aquaculture cages in single and tandem arrangements. *Ocean Eng.* 262, 112255. doi: 10.1016/j.oceaneng.2022.112255

Ning, D., Liang, C., Chen, L., and Zhang, C. (2022). Numerical investigation on the propagation and evolution of focused waves over a sloping bed. *Ocean Eng.* 250, 111035. doi: 10.1016/j.oceaneng.2022.111035

Qin, H., Xu, Z., Li, P., and Yu, S. (2020). A physical model approach to nonlinear vertical accelerations and mooring loads of an offshore aquaculture cage induced by wave-structure interactions. *Ocean Eng.* 197, 106904. doi: 10.1016/j.oceaneng.2019.106904

Savitzky, A., and Golay, M. J. E. (1964). Smoothing and differentiation of data by simplified least squares procedures. *Analytical Chem.* 36, 1627–1639. doi: 10.1021/ac60214a047

Shen, Y., Firoozkoohi, R., Greco, M., and Faltinsen, O. M. (2021). Experimental investigation of a closed vertical cylinder-shaped fish cage in waves. *Ocean Eng.* 236, 109444. doi: 10.1016/j.oceaneng.2021.109444

Tsukrov, I., Eroshkin, O., Fredriksson, D., Swift, M. R., and Celikkol, B. (2003). Finite element modeling of net panels using a consistent net element. *Ocean Eng.* 30, 251–270. doi: 10.1016/S0029-8018(02)00021-5

Walther, J. A., and Gibson, P. T. (2000). *Final report on testing of stretch rubber hoses* (Huntington Beach, CA: Tension Member Technol.).

Xu, T.-J., Dong, G.-H., Zhao, Y.-P., Li, Y.-C., and Gui, F.-K. (2012). Numerical investigation of the hydrodynamic behaviors of multiple net cages in waves. *Aquacultural Eng.* 48, 6–18. doi: 10.1016/j.aquaeng.2011.12.003

Yang, P., Liu, X., Wang, Z., Zong, Z., Tian, C., and Wu, Y. (2019). Hydroelastic responses of a 3-module VLFS in the waves influenced by complicated geographic environment. *Ocean Eng.* 184, 121–133. doi: 10.1016/j.oceaneng.2019.05.020

Yang, H., Xu, Z., Bi, C., and Zhao, Y.-P. (2022). Numerical modeling of interaction between steady flow and pile-net structures using a one-way coupling model. *Ocean Eng.* 254, 111362. doi: 10.1016/j.oceaneng.2022.111362

Zhao, Y.-P., Li, Y.-C., Dong, G.-H., Gui, F.-K., and Teng, B. (2007). A numerical study on dynamic properties of the gravity cage in combined wave-current flow. *Ocean Eng.* 34, 2350–2363. doi: 10.1016/j.oceaneng.2007.05.003

Zhao, Y.-P., Li, Y.-C., Dong, G.-H., Gui, F.-K., and Wu, H. (2008). An experimental and numerical study of hydrodynamic characteristics of submerged flexible plane nets. *Aquacultural Engineering*, 38, 16–25. doi: 10.1016/j.aquaeng.2007.10.004

frontiers | Frontiers in Marine Science

TYPE Original Research
PUBLISHED 21 November 2022
DOI 10.3389/fmars.2022.1070638

OPEN ACCESS

EDITED BY
Zhao Yunpeng,
Dalian University of Technology, China

REVIEWED BY
Houjie Li,
Dalian Minzu University, China
Jianchang Liu,
Northeastern University, China
Ning Wang,
Dalian Maritime University, China

*CORRESPONDENCE
Yuan Cheng
cheny_nbi@dlut.edu.cn

SPECIALTY SECTION
This article was submitted to
Marine Fisheries, Aquaculture and
Living Resources,
a section of the journal
Frontiers in Marine Science

RECEIVED 15 October 2022
ACCEPTED 02 November 2022
PUBLISHED 21 November 2022

CITATION
Liu D, Wang P, Cheng Y and Bi H
(2022) An improved algae-YOLO
model based on deep learning for
object detection of ocean
microalgae considering aquacultural
lightweight deployment.
Front. Mar. Sci. 9:1070638.
doi: 10.3389/fmars.2022.1070638

An improved algae-YOLO model based on deep learning for object detection of ocean microalgae considering aquacultural lightweight deployment

Dan Liu[1,2], Pengqi Wang[3], Yuan Cheng[4]* and Hai Bi[5]

[1]College of Information Engineering, Dalian Ocean University, Dalian, China, [2]Key Laboratory of Environment Controlled Aquaculture (Dalian Ocean University) Ministry of Education, Dalian, China, [3]College of Mechanical and Power Engineering, Dalian Ocean University, Dalian, China, [4]Ningbo Institute of Dalian University of Technology, Ningbo, China, [5]Research and Development (R&D) Department, Hangzhou Yunxi Smart Vision Technology Co., LTD, Dalian, China

Algae are widely distributed and have a considerable impact on water quality. Harmful algae can degrade water quality and be detrimental to aquaculture, while beneficial algae are widely used. The accuracy and speed of existing intelligent algae detection methods are available, but the size of parameters of models is large, the equipment requirements are high, the deployment costs are high, and there is still little research on lightweight detection methods in the area of algae detection. In this paper, we propose an improved Algae-YOLO object detection approach, which is based on ShuffleNetV2 as the YOLO backbone network to reduce the parameter space, adapting the ECA attention mechanism to improve detection accuracy, and redesigning the neck structure replacing the neck structure with ghost convolution module for reducing the size of parameters, finally the method achieved the comparable accuracy. Experiments showed that the Algal-YOLO approach in this paper reduces the size of parameters by 82.3%, and the computation (FLOPs) is decreased from 16G to 2.9G with less loss of accuracy, and mAP by only 0.007 when compared to the original YOLOv5s. With high accuracy, the smaller model size are achieved, which reduces the equipment cost during actual deployment and helps to promote the practical application of algae detection.

KEYWORDS

object detection, lightweight, ShuffleNetV2, ECA attention, algae

Introduction

Algae are large and intricate biomes found in the ocean and rivers, and they have a substantial impact on the natural environment and water quality. Harmful algal blooms (HABs) can wreak in the water environment, affecting water quality and biological survival, as well as easily resulting in the loss or death of organisms in aquaculture zones. HABs can cover a large area of the water surface in a short time, blocking sunlight and thus affecting plant photosynthesis. In addition, algal blooms consume a large amount of oxygen in the water body, releasing undesirable gases and toxic substances and damaging the seawater and river water environment, which is not conducive to aquatic organism survival. Microalgae can also act as clean energy sources and purify wastewater, and some algae can be used as food for humans. The various uses of microalgae contribute significantly to reducing the greenhouse effect, saving energy and protecting the environment. Therefore, deploying algae monitoring systems to manage the abundance and types of algal populations in the water environment is necessary for aquaculture and the water environment.

One of the most frequent conventional techniques for detecting algal cells is manual microscopy using a microscope, which is not only time-consuming but also requires specialized knowledge of algae. As processing power has increased, computer vision has evolved, and support vector machines (SVMs) are increasingly employed for algal detection. For example, Xu Y (Xu et al., 2014), Babu M J (Babu et al., 2016) and Shan S (Shan et al., 2020) investigated the use of SVM in forecasting red tide, while Tao J (Tao et al., 2010) and Göröcs Z (Göröcs et al., 2018) combined a support vector machine with flow cytometry, and its accuracy reached 90%. Artificial neural networks (ANNs) have a better solution to this problem with significantly less manual involvement and generally higher accuracy. Mosleh M A A (Mosleh et al., 2012) and Park J (Park et al., 2019) used artificial neural networks for algal feature extraction with 93% accuracy, while Medina E (Medina et al., 2017) and Schaap A (Schaap et al., 2012) compared convolutional neural networks with MLP and discriminant analysis classification methods in artificial neural networks and found that convolutional neural networks possess greater performance.

Deep learning research has advanced with the development of computer image processing technology. Ning Wang et.al (Wang et al., 2022) also prove that deep learning can solve a series of marine problems. In these years, Two-stage object detection approaches have swiftly progressed from R-CNN (Girshick et al., 2014) to FastRCNN (Girshick, 2015) and FasterRCNN (Ren et al., 2015), with advances in model design and additional increases in detection speed and accuracy, although their speed is not yet sufficient for real-time detection. In algae research, Samantaray A (Samantaray et al., 2018) proposed a computer vision system based on deep learning for algae monitoring with a wide range of applicable platforms but only 82% accuracy. Cho S (Cho et al., 2021) and Deglint J L (Deglint et al., 2019) explored the potential application of deep learning on algae in conjunction with 3D printing and other devices with sufficient accuracy, but its cost is high. Hayashi K (Hayashi et al., 2018) investigated the detection of cell division in algae and separated mitosis from interphase division with a 92% degree of accuracy. The mean average precision (mAP) was between 74% and 81% in the deep learning framework proposed by Qian P (Qian et al., 2020). Ruiz-Santaquiteria J (Ruiz-Santaquiteria et al., 2020) compared instance segmentation with semantic segmentation for diatoms versus nondiatoms and found instance segmentation to be more accurate by 85%. The preceding study is significantly weak in detection speed and detection accuracy, as well as identification that is quick and accurate.

One-stage object detection approaches emphasize the speed of recognition. YOLO (Redmon et al., 2016) was the first one-stage object detection method, which is quicker than the two-stage approach but with the loss of precision and has undergone iterative development with several variants. Using YOLOv3 for algae detection, Park J (Park et al., 2021) obtained a mAP of 81 for five algal species. Tingkai Chen et.al (Chen et al., 2021) proposed one-stage CNN detector-based benthonic organisms detection scheme, which used the generalized intersection over union (GIoU) for localizing benthonic organisms easily. Cao M (Cao et al., 2021) used MobileNet to enhance the backbone network of YOLOv3, hence reducing the weight of the model. Ali S (Ali et al., 2022) investigated YOLOv3, YOLOv4, and YOLOv5 and demonstrated that YOLOv5 produced the best outcomes. Park J (Park et al., 2022) studied YOLOv3, YOLOv3-small, YOLOv4 and YOLOv4-tiny, and the findings showed that the micro (tiny) model was superior in terms of detection speed and precision. Based on the algae detection advancements for YOLOv3, YOLOv4, and YOLOv5, the YOLO framework may possibly be used for algae detection, and the tiny model is enhanced with YOLOv5; however, there is a dearth of study on the improved approaches for algae identification in lightweight YOLOv5.

Based on the current status of the research literature, the research on algae has been constantly developing. From the improvement in traditional manual detection methods to the application of traditional computer vision, it can be seen that research on algae detection is constantly increasing. After the emergence of artificial intelligence technology, a large number of deep learning approaches have been used for algae detection, which is enough to prove the importance of microalgae detection. However, the aforementioned neural network technique for detecting algae has complex deep neural network architecture and a large number of parameters, which require high computational power and high deployment costs in a realistic setting, and there are no lightweight solutions for YOLOv5 algae identification. From the standpoint of research images, the majority of study objects are high-magnification microscopic images of algae, and there is a dearth of research on low-magnification microscopic photographs of algae. Although the pictures of algae at high magnification are clear, the number of cells in the field of view is much smaller than that of low-magnification microscopy. Furthermore, the high-magnification microscope is more costly. In the low-magnification micrographs of algae, the cells are closely packed and difficult to identify with the naked eye, and low-magnification microscopes is cheaper.

Due to the high cost of high magnification microscopy acquisition, we used low magnification microscopy to acquire algae microscopic images to reduce the cost in the data collection. For the practical deployment of algae detection, we propose a lightweight algae object detection network, named Algae-YOLO, based on YOLOv5, by replacing original backbone network with lightweight module of ShuffleNetV2, thereby significantly reducing the model size and computation, and by adding an ECA attention mechanism to ShuffleNetV2, the detection accuracy significantly improves without increasing computational cost. In the neck structure, a lightweight structure combined with ghost convolution is designed, and the depth of the network and the width of the feature layer input are increased to ensure the balance between model accuracy and computational effort, allowing for low-cost deployment while achieving accuracy comparable to that of YOLOv5s.

Related work

Low-magnification microscopic image acquisition of algae

Microalgae strains (laboratory grown) of *Chlorella* sp. and *Isochrysis* sp. samples were photographed in full color using a Leica DM4 B digital microscope with a low-magnification. Sixty images of each of the two kinds of low-magnification algae were gathered, the number of algae in each sample photograph was between 100-200, and local pictures of the samples are shown in Figure 1.

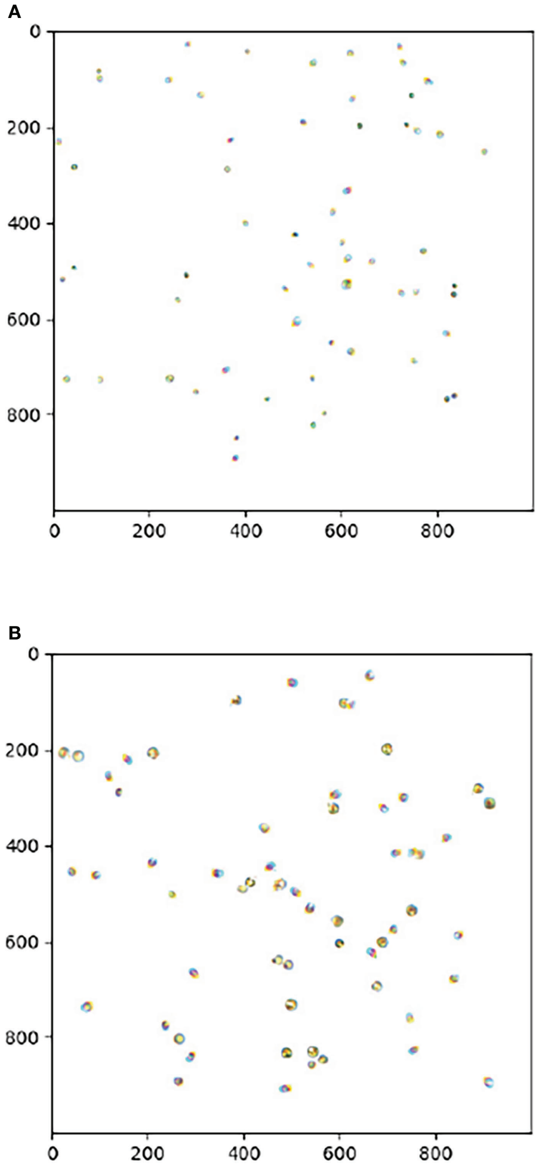

FIGURE 1
(A) *Chlorella sp* **(B)** *Isochrysis sp.*Image of the local microscopic digital sample.

Data preprocessing

The original algal microscopic photos were few, their data were in TIF format with 1920*1200 resolution, and the algal dispersion was dense and abundant. To minimize the difficulty of time-consuming manual annotation, data preprocessing was performed to obtain algal independent cells, and then the dataset was automatically constructed utilizing independent cells.

In the original image preprocessing, the image was read by OpenCV and then threshold and grayed out using a binarization method. The image was then stretched and eroded to complete the algae morphology, contour detection was conducted, and the set of algae border coordinates was located and saved as a distinct cell image.

After obtaining the independent cells, they were randomly pasted into blank pictures, and the location data were processed according to the YOLO dataset format. Figure 2 depicts the resulting photos of *Chlorella* sp., *Isochrysis* sp., and a mixture of both. Some portions of the illustration are exhibited with local magnification for observational ease.

Data enhancement

Considering the issue of algal cell occlusion in microscopic images, this study employs the mask technique to produce a training dataset of algal occlusion images. The previous work created distinct photographs of *Chlorella* sp. and *Isochrysis* sp.; therefore, the masking technique may be utilized to generate

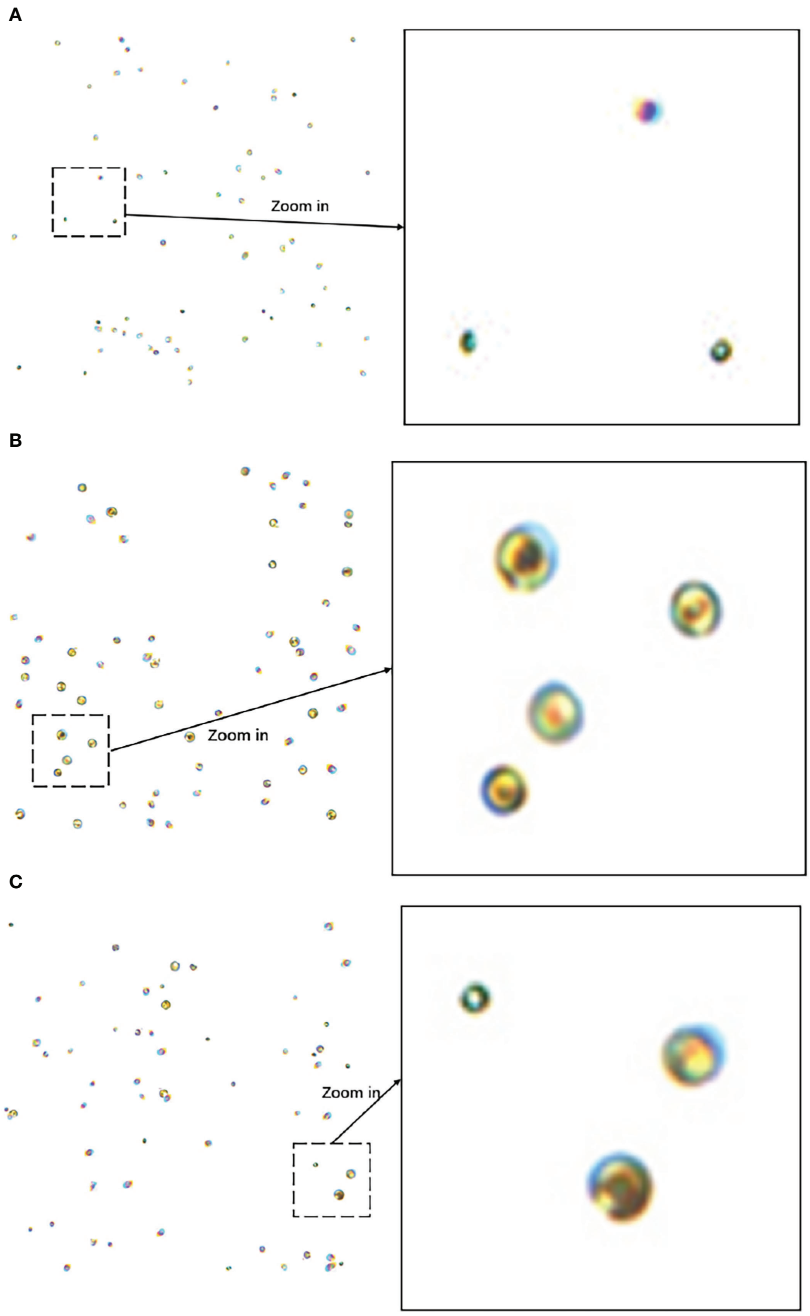

FIGURE 2
(A) *Image of Chlorella sp.* **(B)** *Isochrysis sp*. image **(C)** Mixed image of *Chlorella sp. and Isochrysis sp*. Example images of the algae dataset.

masked data images during the production of dataset images. The main process is to paste the first algal cell at random onto a blank image and then superimpose the second algal cell on top of the first, with the overlap area between the two set at 20%. An illustration of masked image data is shown in Figure 3.

To improve the generalization performance of the dataset, this research darkens the processed algae dataset photos and uses them to replicate algae microscopic images in low-light circumstances. Its darkened image is shown in Figure 4.

2,000 photographs of *Chlorella* sp., 2,000 images of *Isochrysis* sp., 3,000 images of mixed algae, and 3,000 images of masked images were generated for this study. The dataset contains a total of 10,000 images, and the ratio of the training set, validation set, and test set is 8:1:1. In the process of the picture input model,

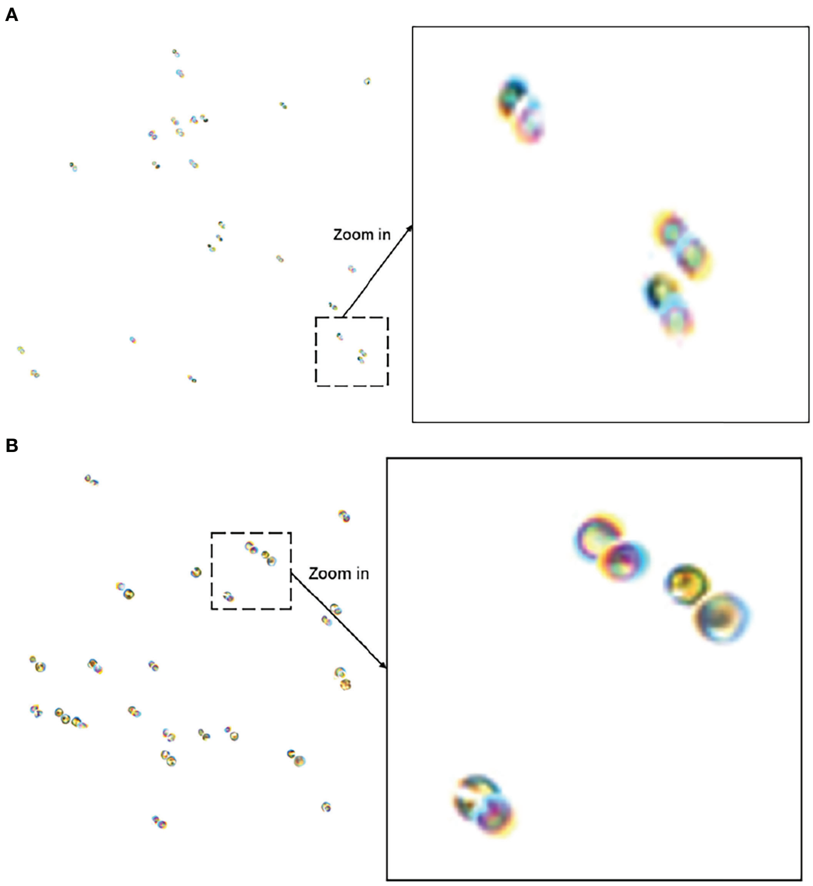

FIGURE 3
(A) *Inter-Chlorella occlusion* images **(B)** *Inter-Isochrysis* occlusion image. Masked image example.

mosaic data enhancement is also activated, and four images are stitched together by random cropping and scaling so that the actual number of images involved in training is increased and the sample set is more diverse.

Method introduction

YOLOv5

Since its release in 2020, YOLOv5 has been one of the most popular object detection approaches by combining the latest research in a variety of fields with other approaches to make YOLO lighter and more efficient. YOLOv5 is composed of a backbone network (Backbone), a neck structure (Neck) and a prediction head (Head). Figure 5 depicts the backbone network structural diagram, which comprises focus, CSP1, CSP2, SPPF, and other structures.

After focus segmentation, the input image data are sent to the backbone network for feature extraction, processed by spatial pyramid pooling-fast (SPPF), sent to the neck structure for the feature fusion operation, and finally predicted and output in the prediction head. Figure 6 illustrates the overall YOLOv5 flowchart.

Attention Module

Efficient channel attention (ECA) is a novel lightweight attention mechanism (Hayashi et al., 2018). Compared to SE attention, ECA is effective at modifying feature weights while avoiding frequent dimensionality reduction operations. ECA acquires the interaction information of each channel and its k neighbors with a fast 1D convolution with convolution kernel k after global average pooling, where the convolution kernel k is proportionate to the number of channel dimensions to adaptive acquisition, the relationship between k and c is as follows:

$$\mathrm{k} = \varphi(\mathrm{C}) = \left| \frac{\log_2(\mathrm{C})}{\gamma} + \frac{b}{\gamma} \right|_{odd} \tag{1}$$

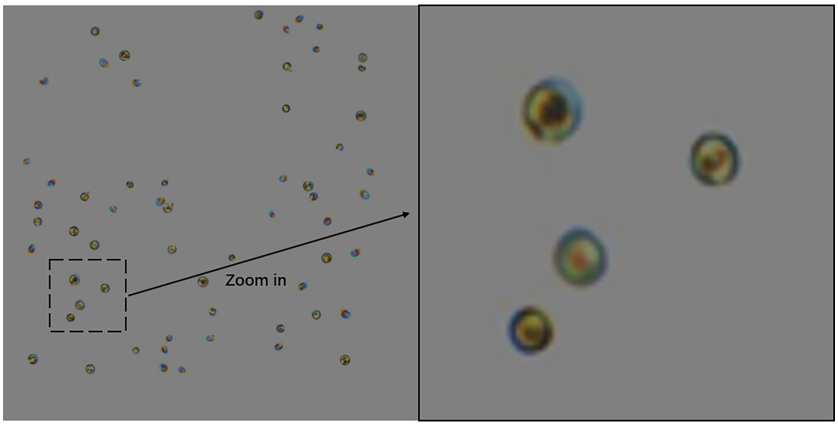

FIGURE 4
Example of darkened *Isochrysis* sp. image.

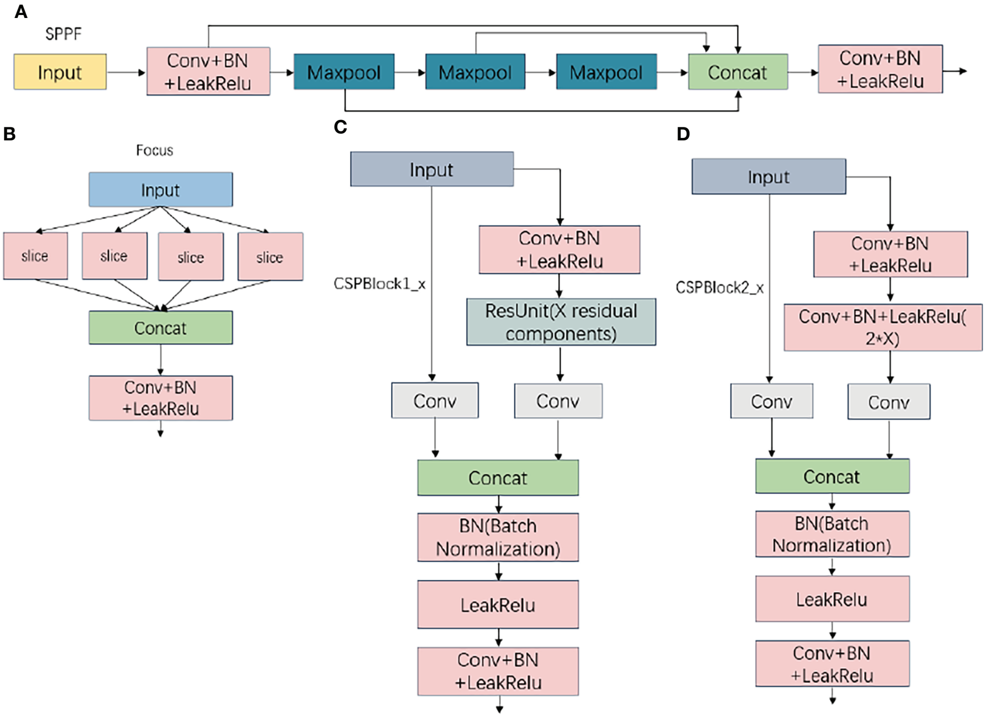

FIGURE 5
(A) SPPF Structure **(B)** Focus structure **(C)** CSPBlock1_x Structure **(D)** CSPBlock2_x StructureImages of Focus, CSP1, CSP2, and SPPF structures.

where γ and b are taken to be 2 and 1 respectively, and $|t|_{odd}$ means the oddest number closest to $|t|$. To achieve the parameter complexity of tillage, the weights of all channels are shared. In this calculation, the w_k array containing K*C parameters is utilized to learn the attention, and the weight ω_i of channel y_i is calculated by considering only the interaction information between y_i and its k neighbors, which is expressed as:

$$\omega_i = \sigma\left(\sum_{j=1}^{k} w_i^j y_i^j\right), y_i^j \in \Omega_i^k \qquad (2)$$

where Ω_i^k denotes the set of k neighboring channels of y_i and σ is the sigmoid activation function. The information interaction is

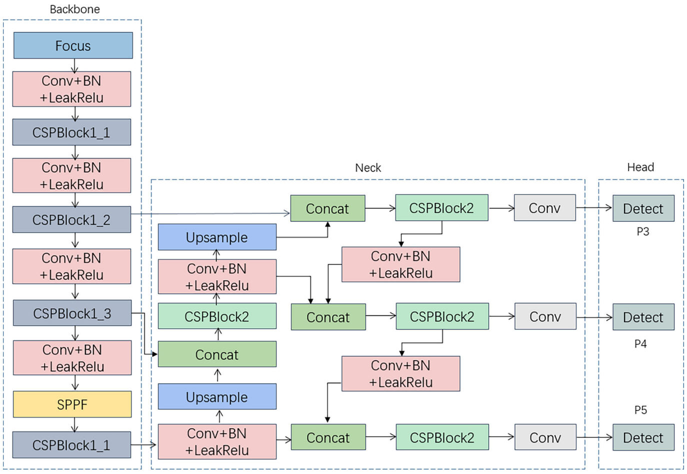

FIGURE 6
YOLOv5 Structure.

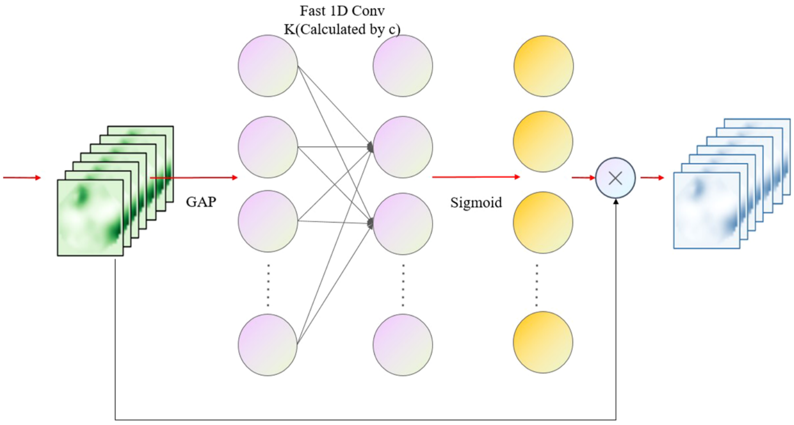

FIGURE 7
ECA overall structure diagram.

followed by weight sharing, which is given by:

$$\omega_i = \sigma\left(\sum_{j=1}^{k} w^j y_i^j\right), y_i^j \in \Omega_i^k \tag{3}$$

The entire calculation procedure is dependent on the fast 1D convolution with k convolution kernels (adaptive size of k) in the ECA structure, which is denoted by:

$$\omega = \sigma(C1D_k(y)) \tag{4}$$

where $C1D$ is the fast 1D convolution. This cross-channel information interaction attention may effectively increase the effectiveness of attention without introducing additional computing factors. The overall structure of ECA is shown in Figure 7.

ShuffleNetV2

The ShuffleNetV2 network is based on the ShuffleNet network, and the network building blocks of V1 are modified in accordance with the four guidelines for designing efficient networks to reduce the memory access cost (MemoryAccessCost, MAC) of the network convolution process. Figure 8 depicts the structures of the two new ShuffleNetV2 units. In ShuffleNetV2 cell 1, the feature map of the input C-channel number is divided into two copies, C1 and C2, and

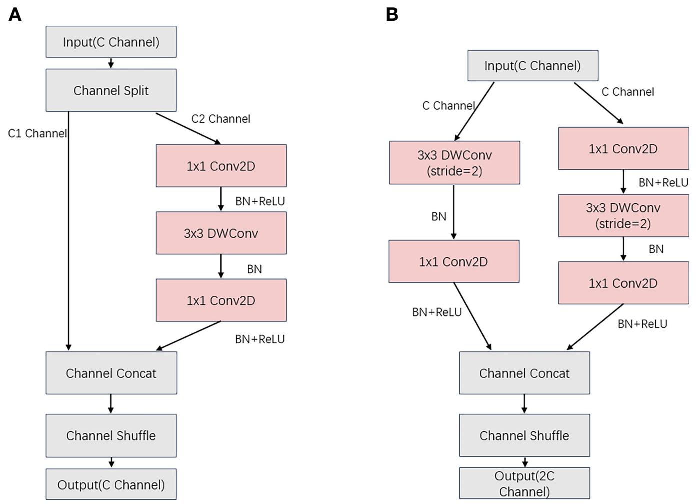

FIGURE 8
(A) ShuffleNetV2 Unit1 **(B)** ShuffleNetV2 Unit2.

the feature map of the C1 channel number is not modified, while the feature map of the C2 channel number is passed through three convolution layers with the same input and output channels, including two 1X1 ordinary convolutions (Conv2D) and one 3X3 depth-separate convolution (DWConv). After the two branches are completed, the Concat operation is executed to concatenate the channels, which are fused into an initial C-channel feature map, and interact with the information data *via* channel blending. In ShuffleNetV2 cell 2, the input C-channel count feature map is no longer subjected to the channel division operation and is instead divided into two separate convolution operations. The same Concat operation is used after the convolution operation, and the 2C-channel count feature map is output after channel blending so that the network width is increased with fewer parameters added.

GhostConv module

GhostConv is a type of convolution proposed by the GhostNet neural network that employs fewer parameters to obtain more target features during computation. GhostConv is separated into two portions of normal convolution at the beginning of the convolution procedure. To build a portion of the feature map, the first step is a small amount of convolution using a convolution kernel with fewer channels than standard convolution. The objective of this convolution is to integrate the features, generalize and condense the input feature map, and generate a new feature map. The second step is to execute a reduced computational operation on the feature map obtained in the first stage using deep separable convolution to build further feature maps. The two created feature maps are then stitched together using the Concat technique to create the ghost feature map. An example of the ghost convolution process is shown in Figure 9.

Improvement

ShuffleNetV2-ECA backbone network

The original backbone network (Backbone) component of YOLOv5 employs CSPDarknet53, which offers excellent feature extraction capabilities but cannot be implemented in a lightweight and cost-effective way due to its complicated network design. Therefore, this study chooses the lightweight network structure ShuffleNetV2 and enhances it based on its design principles, and all improvements in the paper are based on YOLOv5s.

In this study, ShuffleNet modules are constructed utilizing ShuffleNetV2 units 1 and 2 as a lightweight ShuffleNet backbone network for YOLOv5. To improve the feature extraction capability of the backbone network, ECA attention is combined with ShuffleNetV2 unit 1 and unit 2 to form ShuffleECA module 1 and module 2, respectively, which further improves the cross-channel capability and feature extraction capability with only a small number of parameters involved. ShuffleECA module 1 and module 2 are shown in Figure 10.

Using the ShuffleECA module, the ShuffleNetV2-ECA backbone network is then established. Table 1 displays the network structure of its upgraded backbone. ShuffleECA module_1 indicates that the layer is ShuffleECA module 1, whereas ShuffleECA module_2 indicates that ShuffleECA module 2 is in use. The three parameters in the argument

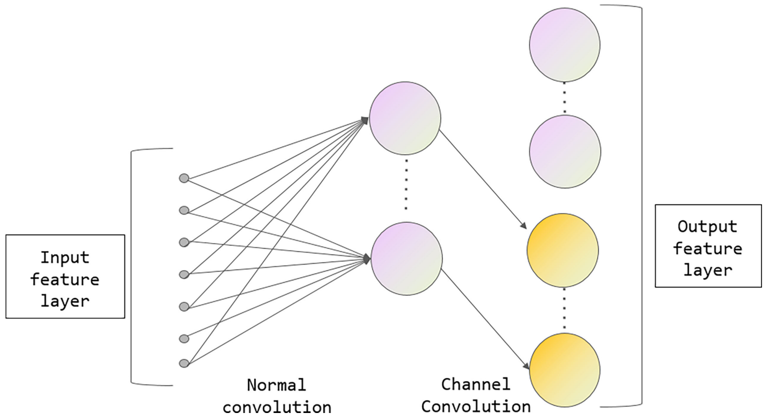

FIGURE 9
Ghost convolution process.

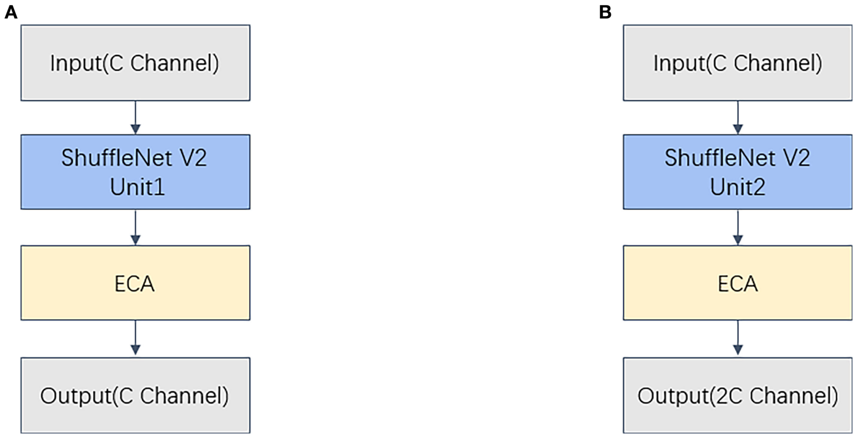

FIGURE 10
(A) ShuffleECA Module 1 **(B)** ShuffleECA Module 2. ShuffleECA Module.

represent the number of input channels, the number of output channels, and the step size. Parameters indicate the number of layer structure parameters.

After the feature map is input to the backbone network, the original YOLOv5 first performs the focus module, and after multiple slicing together in the way of channel expansion, which creates more memory overhead and violates the ShuffleNetV2 design principle, the focus is replaced with a convolutional kernel of 3*3 ordinary convolution with a BN layer, activation function, and maximum pooling convolutional combination, i.e., Conv_BN_Relu_Maxpool in Table 1, to keep the network light and efficient while reducing the degree of network fragmentation. In addition, the primary function of the SPPF structure at the end of the original backbone network is to expand the network perceptual field through the use of multiple maximum pooling operations for enhanced feature extraction. However, since the algal object targets studied in this paper are tiny, such operations not only create a greater computational burden but also increase the possibility of losing algal targets, so it was decided to remove the SPPF structure from the improved ShuffleNetV2-ECA backbone network.

Lightweight YOLOv5Neck

To further lower the computing needs of the model deployment, a lighter GhostBottleneck module is built in the neck section by adapting the GhostNet architecture. GhostBottleneck comprises two types of GhostConv and residual structures: GhostConv1 comprises GhostConv and

TABLE 1 ShuffleNetV2-ECA Backbone Network Structure Table.

Serial Number	N	Module	Parameters	Argument
0	1	Conv_BN_Relu_Maxpool	464	[3, 16, 2]
1	1	ShuffleECA Module_2	2,768	[16, 64, 2]
2	3	ShuffleECA Module_1	2,528	[64, 64, 1]
3	1	ShuffleECA Module_2	14,080	[64, 128, 2]
4	7	ShuffleECA Module_1	18,304	[128, 128, 1]
5	1	ShuffleECA Module_2	52,736	[128, 256, 2]
6	3	ShuffleECA Module_1	34,688	[256, 256, 1]

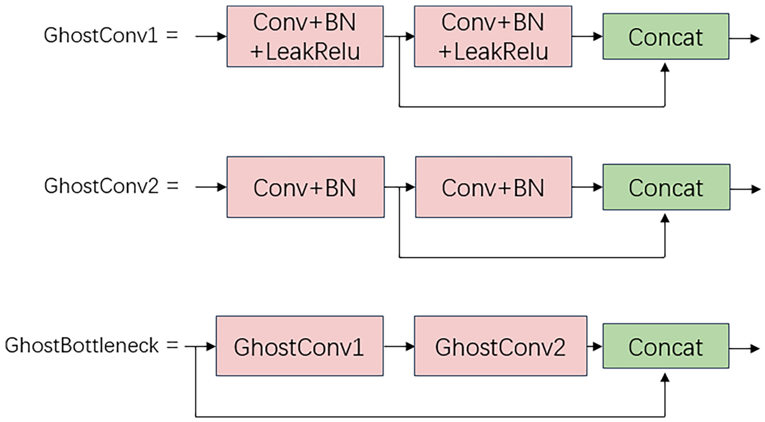

FIGURE 11
GhostBottleneck module.

BN layers and activation functions, whereas GhostConv2 consists of only GhostConv and BN layers and can successfully extract image feature information in a lighter structure. The structure diagram of the three is shown in Figure 11. The CSPBlock2 structure of the whole neck component is replaced with GhostBottleneck, and the conventional convolutional CBL (Conv+BN+LeakRelu) is replaced with GhostConv1, resulting in a network with increased feature fusion that is lightweight and efficient.

Improved lightweight algae-YOLO

YOLOv5 is divided into five models: n, s, m, l and x. The structure remains the same while the model depth and channel width increase in order, with YOLOv5m corresponding to values of 0.67 and 0.75. In the YAML file, the ratio of the input model depth to the channel width of the feature layer is changed from 0.33 vs. 0.5 to 0.67 vs. 0.75, which increases the number of runtime parameters but improves operational precision. The total network architecture is shown in Figure 12.

The algae target images are input from the ShuffleECA backbone network after one convolutional kernel size of 3*3 ordinary convolution, BN layer normalization, activation function and maximum pooling and thus sent into the two stacked ShuffleECA modules, where N in the figure represents the number of ShuffleECA module repetitions on the right side, which are required to pass into the neck. Greater repetitions of the three ShuffleECA modules are present in the improved feature network. In the neck structure, GhostBottleneck substitutes the original CSPBlock_2, and GhostConv_1 replaces the original regular convolution process.

Experiment and evaluation

Evaluation metrics

To evaluate the model, research compares a variety of assessment measures. The mAP is the most commonly used evaluation metric in the field of object detection and is calculated from P (Precision) and R (Recall), with P and R being calculated as:

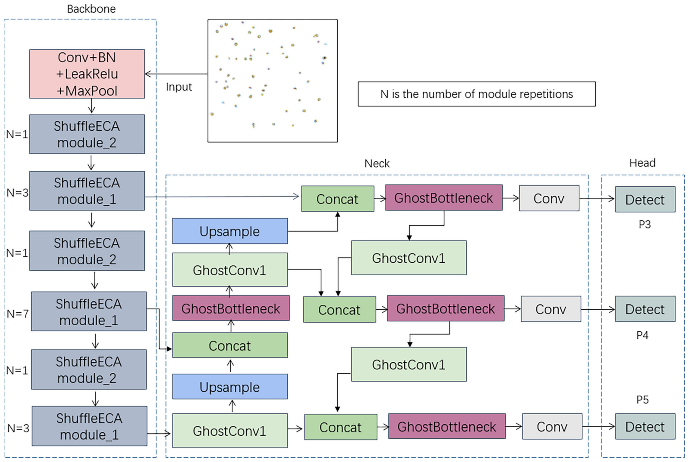

FIGURE 12
Algae-YOLO overall network structure.

$$\mathrm{P} = \frac{\mathrm{TP}}{TP + FP} \times 100\,\% \tag{5}$$

$$R = \frac{\mathrm{TP}}{TP + FN} \times 100\,\% \tag{6}$$

where TP is the number of algal targets accurately recognized, FP represents the number of erroneous detections, and FN represents the number of targets that went unnoticed. The mAP is calculated using Equations (7) and (8), where n is the number of algal categories. The mAP is derived from P and R after computing the AP (average precision) of each category.

$$AP = \int_0^1 P(R)dR \tag{7}$$

$$mAP = \frac{1}{n}\sum_{i=1}^{n} AP_i \tag{8}$$

Data comparison

Multiple object detection models are selected for comparison to confirm the benefits of the approaches described in this study. MobileNetV3 and GhostNet are both classic lightweight networks that have been frequently used in lightweight improvements and are good objects for comparison; therefore, this paper implements the backbone network replacement improvement of MobileNetV3 and GhostNet based on YOLOv5s, namely, MobileNet-YOLOv5s and GhostNet-YOLOv5s, respectively. In addition, the traditional approaches YOLOv4 and SSD are also chosen, and then the improved Algae-YOLO is added for training comparison, with all other hyper parameters remaining unaltered throughout the training process.

In this paper, the approach runs on Windows 10, the CPU is an Intel i5-12600KF, the GPU is GTX3060, the training framework is PyTorch version 1.7.1, the BatchSize is 16, and each approach is trained with 150 epochs. The Binary Cross-Entropy loss function is used to calculate the loss of category probabilities and target confidence scores during the training process, and CIOU Loss is used as the loss of the bounding box regression. After training completed, the data-enhanced test set is used to test and assess each model in turn. After training, each model is tested and assessed using the data-enhanced test set, and then the key evaluation parameters for each model are created, as shown in Table 2.

In Table 2, the model size is displayed. The mAP0.5 is the mAP size when the threshold is set to 0.5, whereas mAP0.5:0.95 is the average of all threshold values between 0.5 and 0.95. GPU Memory specifies the size of the video memory necessary to run the model. The deployment cost of a graphics card is proportional to the video memory size. Weigh shows the size of the model-generated parameter file. FLOPs represent the number of floating point operations per second, while the lower the value is, the less computations are performed per second and the fewer resources are used. FPS (frames per second) is the detection speed of the model. In this paper, we investigate FPS on CPU devices.

In Table 2, the indices of SSD and YOLOv4 are not dominant, and the sizes of MobileNet-YOLOv5s and GhostNet-YOLOv5s, which are improved and compared, have decreased by approximately half compared with the original YOLOv5s. However, the size in the improved Algae-YOLO approach in this paper has decreased by 82.3% compared with YOLOv5s, which is the lowest among all approaches. In terms of GPU Memory utilization during training runs, Algae-YOLO is only 0.37 G higher than

TABLE 2 Comparison of the parameters of the improved approach with other approachs.

Network	Parameters (M)	mAP 0.5	mAP 0.5:0.95	GPU Memory	Weight	FLOPs	FPS On CPU
YOLO5s	7.01	0.988	0.859	6.73G	14.3MB	16.0G	14.49
MobileNetYOLOv5s	3.54	0.982	0.799	4.83G	7.4MB	6.3G	20
GhostNetYOLOv5s	3.67	0.986	0.84	3.55G	7.7MB	8.0G	15.15
YOLOv4	64.36	0.955	0.738	9.6G	244MB	30.17G	5.64
SSD	26.15	0.856	0.631	6.6G	91.1MB	31.39G	3.92
Algae_ YOLO	**1.23**	0.981	0.79	3.92G	**2.8MB**	**2.9G**	19.61

The bold values i indicates that some performance of AlgaeYOLO is better.

TABLE 3 Datasheet of ablation experiment results.

Network	Parameters (M)	mAP 0.5	mAP 0.5:0.95	GPUMemory	Weight	FLOPs	FPS On CPU
Model 0	7,01	0.988	0.859	6.73G	14.3 MB	16.0 G	14.49
Model 1	0.84	0.970	0.743	2.43G	1.9 MB	1.8 G	29.41
Model 2	0.84	0.977	0.768	2.55G	2.0MB	1.8 G	27.77
Model 3	0.49	0.975	0.756	2.43G	1.3 MB	1.2 G	27.02
Model 4	3.00	0.982	0.80	4.22G	6.3MB	5.2G	19.80
Model 5	1,23	0.981	0.79	3.92G	2.8 MB	2.9 G	19.61

GhostNet-YOLOv5s and 2.81 G lower than YOLOv5s; hence, the dependence of Algae-YOLO on memory capacity is significantly smaller than that of the original YOLOv5s. On FLOPs, the improved approach Algae-YOLO is just 2.9G, making it the most efficient of all models and requiring the fewest calculations per second. Finally, in terms of FPS metrics, Algae-YOLO performs second best.

Ablation study

Ablation experiments are required to demonstrate the efficacy of the approach improvements. The original version of YOLOv5s is labeled as Model 0, YOLOv5s with ShuffleNetV2 as the backbone network labelled as Model 1, ShuffleNetV2-ECA-YOLOv5s with improved ECA attention labelled as Model 2, replaced the neck network on top of ShuffleNetV2-ECA labelled as Model 3, adjusted the depth and width of the model directly on top of ShuffleNetV2-ECA labelled as Model 4, and adjusted the network depth and feature layer channel width on top of Model 3 labelled as Model 5.Table 3 reveals the results of the ablation trials.

In Table 3, after replacing the backbone network with ShuffleNetV2 in Model 1, the model size of the network decreased significantly, from seven million to eighty-four million, and after adding the ECA attention mechanism, the sizes increased by only 30 from Model 1 to Model 2, which is almost negligible, but its mAP0.5 increased by 0.007 and the mAP0.5:0.95 increased by 0.025. It is demonstrated that ECA attention has a positive effect on increasing the network's precision. Model 3 employs a lighter neck structure based on Model 2, and the FLOPs are lowered by an additional 0.6 G; however, it also results in a 0.002 accuracy loss. The network model is light, but its accuracy is too low, which impairs the detection results. The mAP value of Model 5(Algae-YOLO) is 0.981, which is closer to Model 0 and has 2.9 GFLOPs, which means that the number of operations per second is much smaller than that of Model 0, i.e., with less computational overhead than Model 0 and Model 5 has a closer operational accuracy, indicating that the model proposed in this paper has good performance in terms of computation. The Algae-YOLO approach investigated is proven to have an optimal balance between computational overhead and precision. Based on the comparison between Model 4 and Model 5, it can be deduced that an increase in network depth and breadth as a result of improvements to ShuffleNet and ECA will result in a considerable increase in size of network parameters, as well as FLOPs, memory utilization, and weight file size. However, the mAP of Model 4 is enhanced by 0.1 compared to Model 5. Because of the dramatic increase in parameters, carrying out such a procedure is completely unnecessary. It also illustrates the need for making the neck section lightweight before expanding the network depth and channel width. In the model improvement, the FPS of Model 5 (AlgaeYOLO) decreased compared to Model 1, but it was still higher than that of Model 0 (YOLOv5s).

Conclusion

In this research, to address the current algae detection problems, we propose a lightweight Algae-YOLO object detection network employing low-magnification microscopy images. The approach exhibits comparable detection accuracy while drastically decreasing computational overhead, reduces the computational cost, and serves as a benchmark for algal lightweight detection and deployment. The improved Algae-YOLO object detection approach reduces the detection accuracy in low-magnification microscopic images by 0.007 compared to the original YOLOv5s, assuming that parameter size is decreased by 82.3%, the GPU memory footprint is reduced by 2.81G, and the FLOPs are decreased by 13.1 GFLOPs. Ablation experiments demonstrate that the introduction of ECA attention considerably increases the network accuracy while essentially little increase in network size and improves detection accuracy. Some parameters increased due to the modified model depth and channel width, but they are significantly smaller than size of YOLOv5, and its mAP also increased. Overall, the improved model provides a tradeoff between parameters size and detection accuracy and can achieve good performance when deployed in low-cost devices, which is advantageous for mobile and embedded system platform deployment in aquatic work, as well as for reducing the incidence of harmful algae in aquaculture.

There is a wide variety of algal species, and the current study does not cover a broad enough sample, requiring further expansion of the training data. In future research, the species of single-celled algae might be enlarged even more, which will help improve the classification of different phyla and orders of algae.

Data availability statement

The original contributions presented in the study are included in the article/supplementary material. Further inquiries can be directed to the corresponding author.

Author contributions

DL, PW, YC conceived and designed the research. PW conducted the experiment. HB and YC analysed the data. DL and PW wrote the paper. All authors contributed to the article and approved the submitted version.

Funding

Key Laboratory of Environment Controlled Aquaculture (Dalian Ocean University) Ministry of Education (202213); Dalian Program on Key Science and Technology R&D Project (2021YF16SN013); Basic Scientific Research Projects for Higher Education Institutions of the Education Department of Liaoning Province.

Conflict of interest

Author HB is employed by Hangzhou Yunxi Smart Vision Technology Co., LTD.

The remaining authors declare that the research was conducted in the absence of any commercial or financial relationships that could be construed as a potential conflict of interest.

The handling editor ZY declared a shared parent affiliation with the author CY at the time of review.

Publisher's note

References

Ali, S., Khan, Z., Hussain, A., Athar, A., and Kim, H.-C. (2022). Computer vision based deep learning approach for the detection and classification of algae species using microscopic images. *Water* 14 (14), 2219. doi: 10.3390/w14142219

Babu, M. J., Geetha, P., and Soman, K. P. (2016). Classification of remotely sensed algae blooms along the coast of india using support vector machines and regularized least squares. *Ind. J. Sci. Technol.* 9, 30. doi: 10.17485/ijst/2016/v9i30/99001

Cao, M., Wang, J., Chen, Y., and Wang, Y. (2021). Detection of microalgae objects based on the improved YOLOv3 model. *Environ. Sci.: Proc. Impacts* 23 (10), 1516–1530. doi: 10.1039/D1EM00159K

Chen, T., Wang, N., Wang, R., Zhao, H., and Zhang, G. (2021). One-stage CNN detector-based benthonic organisms detection with limited training dataset. *Neural Networks* 144, 247–259. doi: 10.1016/j.neunet.2021.08.014

Cho, S., Shin, S., Sim, J., and Lee, J. (2021). Development of microfluidic green algae cell counter based on deep learning. *J. Korean Soc. Visualization* 19 (2), 41–47. doi: 10.5407/jksv.2021.19.2.041

Deglint, J. L., Jin, C., and Wong, A. (2019). Investigating the automatic classification of algae using the spectral and morphological characteristics via deep residual learning. *International Conference on Image Analysis and Recognition*. 269–280. (Cham: Springer).

Göröcs, Z., Tamamitsu, M., Bianco, V., Wolf, P., Roy, S., Shindo, K., et al. (2018). A deep learning-enabled portable imaging flow cytometer for cost-effective, high-throughput, and label-free analysis of natural water samples. *Light: Sci. Appl.* 7 (1), 1–12. doi: 10.1038/s41377-018-0067-0

Girshick, R. (2015). Fast R-CNN. *In Proceedings of the IEEE International Conference on Computer Vision*. 1440–1448. (Washington, DC, USA: IEEE).

Girshick, R., Donahue, J., Darrell, T., and Malik, J. (2014). Rich feature hierarchies for accurate object detection and semantic segmentation. In *Proceedings of the IEEE Conference on Computer Vision and Pattern Recognition*. 580–587. (Washington, DC, USA: IEEE).

Hayashi, K., Kato, S., and Matsunaga, S. (2018). Convolutional neural network-based automatic classification for algae morphogenesis. *Cytologia* 83 (3), 301–305. doi: 10.1508/cytologia.83.301

Medina, E., Petraglia, M. R., Gomes, J. G. R., and Petraglia, A. (2017). Comparison of CNN and MLP classifiers for algae detection in underwater pipelines. In *2017 seventh international conference on image processing theory, tools and applications (IPTA)*. 1–6 (Washington, DC, USA: IEEE).

Mosleh, M. A. A., Manssor, H., Malek, S., Milow, P., and Salleh, A. (2012). A preliminary study on automated freshwater algae recognition and classification system[C]//BMC bioinformatics. *BioMed. Cent.* 13 (17), 1–13. doi: 10.1186/1471-2105-13-S17-S25

Park, J., Baek, J., Kim, J., You, K., and Kim, K. (2022). Deep learning-based algae detection model development considering field application. *Water* 14 (8), 1275. doi: 10.3390/w14081275

Park, J., Baek, J., You, K., Nam, S. W., and Kim, J. (2021). Microalgae detection using a deep learning object detection algorithm, YOLOv3. *J. Korean Soc. Water Environ.* 37 (4), 275–285. doi: 10.15681/KSWE.2021.37.4.275

Park, J., Lee, H., Park, C. Y., Hasan, S., Heo, T. Y., and Lee, W. H. (2019). Algae morphological identification in watersheds for drinking water supply using neural architecture search for convolutional neural network. *Water* 11 (7), 1338. doi: 10.3390/w11071338

Qian, P., Zhao, Z., Liu, H., Wang, Y., Peng, Y., Hu, S., et al. (2020). Multi-target deep learning for algae detection and classification. In *2020 42nd annual international conference of the IEEE engineering in medicine & biology society (EMBC)*. 1954–1957 (Washington, DC, USA: IEEE).

Redmon, J., Divvala, S., Girshick, R., and Farhadi, A. (2016). You only look once: Unified, real-time object detection. *In Proceedings of the IEEE Conference on Computer Vision and Pattern Recognition*. 779–788 (Las V egas, NV , USA: IEEE).

Ren, S., He, K., Girshick, R., and Sun, J. (2015). Faster R-CNN: Towards real-time object detection with region proposal networks. In *Adv. Neural Inf. Process. Syst*, 28. 91–99. Available at: https://proceedings.neurips.cc/paper/2015/file/14bfa6bb14875e45bba028a21ed38046-Paper.pdf (accessed on 2 May 2022).

Ruiz-Santaquiteria, J., Bueno, G., Deniz, O., et al. (2020). Semantic versus instance segmentation in microscopic algae detection. *Eng. Appl. Artif. Intell.* 87, 103271. doi: 10.1016/j.engappai.2019.103271

Samantaray, A., Yang, B., Dietz, J. E., and Min, B. C. (2018). *Algae detection using computer vision and deep learning* (Ithaca, NY, USA: arXiv).

Schaap, A., Rohrlack, T., and Bellouard, Y. (2012). Optofluidic microdevice for algae classification: a comparison of results from discriminant analysis and neural network pattern recognition. In *Microfluidics, BioMEMS, and Medical Microsystems X. SPIE*, (San Francisco, California, United States: Microfluidics, BioMEMS, and Medical Microsystems X. SPIE) 8251. 31–40.

Shan, S., Zhang, W., Wang, X., and Tong, M. (2020). Automated red tide algae recognition by the color microscopic image. in *2020 13th International Congress on Image and Signal Processing, BioMedical Engineering and Informatics (CISP-BMEI)*. 852–861 (Washington, DC, USA: IEEE).

Tao, J., Cheng, W., Boliang, W., Jiezhen, X., Nianzhi, J., and Tingwei, L. (2010). Real-time red tide algae recognition using SVM and SVDD. In *2010 IEEE international conference on intelligent computing and intelligent systems*, 1. 602–606 (Washington, DC, USA: IEEE).

Wang, N., Wang, Y., and Er, M. J. (2022). Review on deep learning techniques for marine object recognition: Architectures and algorithms. *Control Eng. Pract.* 118, 104458. doi: 10.1016/j.conengprac.2020.104458

Xu, Y., Cheng, C., Zhang, Y., and Zhang, D. (2014). Identification of algae blooms based on support vector machine classification in haizhou bay, East China Sea. *Environ. Earth Sci.* 71 (1), 475–482. doi: 10.1007/s12665-013-2455-3

frontiers | Frontiers in Marine Science

TYPE Original Research
PUBLISHED 29 November 2022
DOI 10.3389/fmars.2022.1069711

Application of transcriptome analysis to investigate the effects of long-term low temperature stress on liver function in the tiger puffer (*Takifugu rubripes*)

Zhifeng Liu[1,2†], Liguang Zhu[1,2,3†], Xinan Wang[1,2], Shiying Liu[1,2], Aijun Ma[1,2*], Haowen Chang[1,2,4], Zhibin Sun[1,2], Fei Xu[1,2] and Haichi Zhao[1,2,4]

[1]Yellow Sea Fisheries Research Institute, Chinese Academy of Fishery Sciences, Qingdao, China, [2]Laboratory for Marine Biology and Biotechnology, Pilot National Laboratory for Marine Science and Technology (Qingdao), Qingdao, China, [3]College of Fisheries and Life Science, Dalian Ocean University, Dalian, China, [4]College of Fisheries and Life Science, Shanghai Ocean University, Ministry of Education, Shanghai, China

The tiger puffer (*Takifugu rubripes*) is an important economic fish species in northern China. However, it is a warm-temperature species, and low winter temperatures can result in high mortality in aquaculture. Understanding the mechanisms of cold resistance in tiger puffers will thus provide critical information to help cope with winter cold. In this study, we performed transcriptome analysis of livers from puffer fish kept at different temperatures (18°C, 13°C, and 8°C) to identify the key pathways and genes involved in the response to low-temperature stress. We also detected serum levels of proteases, arginine, and proline to obtain further information on the response to cold adaption. Totals of 51, 942, and 195 differentially expressed genes were identified in the 18°C vs 13°C, 18°C vs 8°C, and 13°C vs 8°C groups, respectively. Pathway analysis showed that significantly enriched pathways were mainly related to digestion, metabolism, and environmental adaptation. Most genes in the pathways related to digestion and metabolism were down-regulated, while most genes in the pathways related to environmental adaptation were up-regulated. Serum levels of proteases were significantly lower in the low-temperature groups (13°C and 8°C) compared with the control group (18°C), while arginine and proline levels were significantly higher in the 8°C group compared with the other two groups. These results suggest that low temperature caused digestive and metabolic disorders, as well as adaptive changes to low temperature in tiger puffers. On this premise, we found that some up-regulated genes in the pancreatic secretion pathway, arginine and proline metabolism pathway, and circadian rhythm pathway played important roles in the survival, growth, and development of tiger

OPEN ACCESS

EDITED BY
Zhao Yunpeng,
Dalian University of Technology, China

REVIEWED BY
Rui Jia,
Freshwater Fisheries Research Center (CAFS), China
Huanhuan Huo,
Jiangxi Agricultural University, China

*CORRESPONDENCE
Aijun Ma
maaj@ysfri.ac.cn

†These authors have contributed equally to this work

SPECIALTY SECTION
This article was submitted to Marine Fisheries, Aquaculture and Living Resources, a section of the journal Frontiers in Marine Science

RECEIVED 14 October 2022
ACCEPTED 09 November 2022
PUBLISHED 29 November 2022

CITATION
Liu Z, Zhu L, Wang X, Liu S, Ma A, Chang H, Sun Z, Xu F and Zhao H (2022) Application of transcriptome analysis to investigate the effects of long-term low temperature stress on liver function in the tiger puffer (*Takifugu rubripes*).
Front. Mar. Sci. 9:1069711.
doi: 10.3389/fmars.2022.1069711

puffers under low-temperature stress. The accumulation of arginine and proline can maintain metabolism and circulation and resist cold stress. The circadian rhythm is closely related to digestion and metabolism, which is an adaptive change and plays a positive role in the resistance to low temperature. The results of this study provide new insights and a theoretical basis for the study of cold tolerance in tiger puffers.

KEYWORDS

Takifugu rubripes, low temperature, liver, transcriptome, qPCR

Introduction

Water temperature plays an important role in the survival of fish by directly affecting their physiology, biochemical state, and behavior (Beitinger et al., 2000; Zhou L.Y et al., 2019). The tiger puffer (*Takifugu rubripes*) is a eurythermal, euryhaline carnivorous fish that is suitable for cage culture in northern China, with a growth-temperature range of 16–25°C. However, lower water temperatures in winter may result in reduced growth performance or even death. Tiger puffers cultivated in northern China inevitably experience the process of the land-sea relay breeding method and the overwintering process, due to the decrease of winter temperature, which requires heating to raise the water temperature, which will increase the cost and pressure of environmental-protection pressures. Economic losses caused by low temperatures can be reduced by breeding lines with cold-tolerant traits, and understanding the regulatory mechanisms at low temperature can provide a strong foundation for related research.

Recent advancements in sequencing technology mean that Illumina RNA-seq technology has played an increasingly important role in analyzing the regulation of economic traits, including the study of fish under environmental stress. For example, both low salinity and high temperature were shown to disrupt lipid metabolism in the liver of turbot (*Scophthalmus maximus*), and the corresponding key genes were screened using transcriptomics technology (Liu et al., 2021; Zhao et al., 2021). Low temperature also affected renal immune function-related pathways in Nile tilapia (*Oreochromis niloticus*) (Zhou T et al., 2019) and amino acid metabolism-related pathways in European perch (*Dicentrarchus labrax*) (Zhang et al., 2021). In addition, high temperature resulted in immune disorders and metabolic imbalance in crayfish (*Procambarus clarkii*) (Luo et al., 2021). These studies demonstrate the important effects of temperature on the metabolic responses of fish. The liver is an important metabolic organ in fish and plays an important role in environmental adaptation, coping with environmental disturbance, and homeostasis of the internal environment (Ibarz et al., 2010; Jiao et al., 2020). The liver is thus a suitable organ in which to analyze the metabolic adaptability of fish to changes in temperature.

Considering the importance of cold tolerance in tiger puffers in aquaculture, we studied the transcriptomic changes in livers from tiger puffers subjected to cold stress. We carried out RNA sequencing of livers from puffer fish kept at normal temperature (18°C) and low temperatures (13°C and 8°C) using Illumina sequencing technology, followed by Gene Ontology (GO) and Kyoto Encyclopedia of Genes and Genomes (KEGG) analyses to determine the key pathways. We also examined the physiological responses in the blood to clarify the metabolic effects of temperature. This study aimed to investigate the adaptive molecular regulatory mechanisms in tiger puffers maintained in a long-term low-temperature environment, and identify key signaling pathways and genes. The results further our understanding of the molecular consequences of low-temperature exposure in puffer fish, and lay the foundation for selective breeding programs aimed at improving cold tolerance in puffer fish.

Materials and methods

Ethics statement

The study protocol was approved and supervised by the Institutional Animal Care and Use Committee of the Yellow Sea Fisheries Research Institute (Qingdao, China).

Experimental design and sample collection

Tiger puffers were maintained by our research group at an aquatic farm in Tangshan, China. The fish had no surface damage and showed active swimming. Fish used in the experiment was 8 months with a body weight of 106.6 ± 4.9

(M ± SD) g and body length of 15.0 ± 0.2 (M ± SD) cm. We set up three groups of fish in constant-temperature recirculating aquaculture systems, with three experimental barrels (1000 L) per group. Each experimental barrel included 30 randomly selected fish, and was kept at 18°C for 1 week before the experiment. Barrels in the three groups were then set at temperatures of 18°C (group A), 13°C (group B), and 8°C (group C), respectively, with 18°C used as the control group and 13°C and 8°C used as the low-temperature groups. Three parallel groups were set for each temperature. At the beginning of the experiment, the water temperatures in the two low-temperature groups were adjusted to 8°C and 13°C within 12 h, respectively, and the control group was kept at 18°C. The fish were then stocked at a constant water temperature under natural light for 4 weeks, with salinity 30 ppt, dissolved oxygen > 8 mg/L and ammonia nitrogen < 0.2 mg/L. Three fish were randomly selected from each barrel at the fourth week, anesthetized in 200 mg/L MS-222 (Sigma-Aldrich Corporation, St. Louis, MO, USA), and immediately dissected on ice. Blood samples were collected from the caudal vein, transferred into RNase-free tubes, and stored at 4°C for 6 h. Afterward, the supernatant was collected by centrifugation at 2000×g for 10 min at 4°C. The liver was removed from each fish and immediately placed in a microtube, flash frozen in liquid nitrogen, and then stored at −80°C prior to RNA extraction.

RNA extraction, cDNA library construction, and sequencing

RNA from 3 fish in the same barrel was combined into one sample. Each temperature group had three biological replicates. Total RNA was extracted from the liver using the TRIzol (Invitrogen, Carlsbad, CA, USA) method, and its concentration and purity were detected using a Nanodrop2000 (NanoDrop Technologies, LLC, Wilmington, DE, USA). RNA integrity was detected by 1% agarose gel electrophoresis. Each sample was prepared using 1 µg total RNA (Concentration ≥ 35ng/µL, OD260/280 ≥ 1.8, OD260/230 ≥ 1.0) for library construction using an Illumina Truseq^{TM} RNA Sample Prep Kit. The mRNA was then enriched by the oligo(dT) method, followed by adding fragmentation buffer, and the RNA was randomly fractured into small fragments of about 300 bp. First and second strands of cDNA were synthesized using reverse transcriptase, random primers, and mRNA templates. The viscous ends of double-stranded cDNA were filled using End Repair Mix and an A base was added to the 3' end. The product was purified and sorted. Polymerase chain reaction (PCR) amplification was performed using the sorted product and the library was obtained after purification. After QuantiFluor$^{®}$ dsDNA System quantification, sequencing was performed using the Illumina platform.

Analysis of differentially expressed genes and functional enrichment analysis

Expression levels of genes and transcripts were analyzed quantitatively using the RSEM method (Li and Dewey, 2011) (fragments per kilobase of exon per million mapped reads). Differences in expression levels between samples were analyzed using EdgeR software (Love et al., 2014). Genes with a false discovery rate < 0.05 and log2 fold-change ≥ 1 were considered as DEGs. DEGs were further examined for gene function enrichment using GO (http://www.geneo-ntology.org/) and KEGG (http://www.genome.jp/kegg/) analyses. DEGs were significantly enriched when the adjusted *P* value was ≤ 0.05.

Real-time PCR verification of Illumina sequencing data

We selected 15 DEGs with roles in pancreatic secretion, circadian rhythm, and arginine and proline metabolism pathways for verification by quantitative PCR (qPCR). Primers were designed using Primer 5 based on the obtained sequences (Table 1). β-actin was used as an internal reference gene. All RNA samples were reverse-transcribed to cDNA using a FastKing RT Kit and the obtained cDNA was subjected to qPCR using an Applied Biosystems StepOnePlus PCR instrument. The reaction was performed using the TOROGreen qPCR Master Mix kit, with a 20 µL reaction containing Master Mix (10.0 µL), RNase-free water (6.4 µL), forward and reverse primer (0.8 µL), and first-strand cDNA (2 µL). The reaction procedure included a pre-denaturation at 95°C for 60 s, followed by 40 cycles of denaturation at 95°C for 10 s and annealing at 60°C for 30 s in a 20 µL reaction mixture. Relative gene quantification was calculated by the $2^{-\Delta\Delta Ct}$ method (Livak and Schmittgen, 2001). Two-way ANOVA was used to detect the statistical differences between the groups. Differences were considered statistically significant at $P < 0.05$. The consistency between the RNA-seq and qPCR results was analyzed by correlation scatterplots using GraphPad Prism 6.0.

Detection the proteases, arginine and proline of serum

Serum levels of proteases, arginine, and proline were detected at different temperatures using protease enzyme-

TABLE 1 List of primers used for this study.

Gene name	Forward primer (5′-3′)	Reverse primer (5′-3′)
nos1	CGTCCATAGCGGAGTTCACCATTC	GGTAATGTAAGGCAAGAGGCAGAGG
odc1	TTCGGCTTACACGCTGGTTGTC	TTGGTCCTCTCATCCTCCTCATCAG
prodha	CCGCAGTTCCTCCTCCAGTTTTC	CCAGCAGCATCATCTCAGACTTCC
arntl1a	GAAGACACTGAGAGGTGCTGCTAAC	TCACAACCGACCACAAACAGGAAC
clocka	GCTGATGCTGGAGGCTTTAGATGG	TCAACAGGTTCTGGTCAACAAGGTC
arntl2	TAGAGTGGAAGGTGAGTGGCTGAC	GAAGGACAAGAATCGGCAACAAACG
npas2	TGATTGCCACCGTGCGATTAGTC	GTATCCGATGATTGGTGAGGCTCTG
atp2a2	TCAAGGAGTACGAGCCCGAGATG	TCCAACGGCGACTTCCACAATG
rhoab	AATGATGAGCACACACGCAGAGAG	CACTTCCCGCACACCATCCTTG
gamt	TGACCTACTGTAACCTGACCTCCTG	AACCTGCGTCTCCTCAAACATCTTC
cry5	TGAGGAGACTGGAGGAGCACATG	CTGGGACTTAGCGAGTTTGGAGATG
cpa5	GCAGAGCCAGGACATCCAACAC	GAAACGAGCAGCCGACTCCATC
per2	CGTCAGAGGTCAGAGGTCAGAGG	CCGAGTCAGGATTGTGGTGATGC
ela2	GGTGGTCGGTGGAGAGGATGTC	GCCGCAGGTGTGGTAGAAGTTG
cpb1	GGAGCAGAGTGGCATGGAATACG	TGGAGGTGGAGATGGAGGCAATC
β-actin	GAGACCTTCAACACCCCTGC	AGAGCGTAGCCCTCGTAGATG

linked immunosorbent assay (ELISA), FISH proline ELISA, and FISH Arg ELISA kits (Shanghai Enzyme-linked Biotechnology Co., Ltd.). The kit numbers are YJ722032, YJ712912, and YJ729390, respectively.

Results

Sequencing results and analysis

Nine libraries were sequenced using the Illumina sequencing platform, and 400,970,296 raw reads were obtained, including 133,649,204 in group A, 124,086,566 in group B, and 143,234,526 in group C. A total of 398,272,128 clean reads were obtained, including 132,791,888 in group A, 123,305,596 in group B, and 142,174,644 in group C. The Q30 base percentage was 91.84%– 92.91% and the GC content was 51.36%–53.64%. After mapping with the tiger puffer reference genome, a total of 376,359,666 mapped reads were obtained, including 338,645,140 multiple mapped reads (Table 2).

Analysis of DEGs

EdgeR identified DEGs between the control group (A: 18°C) and low-temperature groups (B: 13°C, C: 8°C). Comparative analysis identified 51 DEGs in the 13°C group compared with the control group (A vs B), including 33 up-regulated genes and 18 down-regulated genes; 942 DEGs were identified in the 8°C group compared with the control group (A vs C), including 384 up-

TABLE 2 Results of sequencing data statistics and comparison with the reference genome.

	A			B			C		
	T18_1	T18_2	T18_3	T13_1	T13_2	T13_3	T8_1	T8_2	T8_3
Raw reads	44516934	44923096	44209174	41413044	43480164	39193358	53768280	44366732	45099514
Total clean reads	44228190	44614704	43948994	41178452	43202774	38924370	53360042	44030338	44784264
Mapped reads	42253525 (95.54%)	42183960 (94.55%)	41801122 (95.11%)	39040497 (94.81%)	40931629 (94.74%)	36896856 (94.79%)	50137719 (93.96%)	41557179 (94.38%)	41557179 (94.38%)
Uniquely mapped	37618901 (85.06%)	37697973 (84.5%)	36760820 (83.64%)	34440495 (83.64%)	35709967 (82.66%)	33019953 (84.83%)	45729970 (85.7%)	38586540 (87.64%)	39080521 (87.26%)
Multiple mapped	4634624 (10.48%)	4485987 (10.05%)	5040302 (11.47%)	4600002 (11.17%)	5221662 (12.09%)	3876903 (9.96%)	4407749 (8.26%)	2970639 (6.75%)	3231891 (7.22%)
GC content (%)	53.51	52.21	53.64	52.76	53.6	52.91	52.35	51.44	51.36
Q30 (%)	92.79	92.82	92.91	92.79	92.51	92.4	91.84	92.35	92.6

regulated and 558 down-regulated genes; and 195 DEGs were identified in the 8°C group compared with the 13°C group (B vs C), including 54 up-regulated and 141 down-regulated genes (Figure 1).

GO annotation analysis

GO terms can be categorized by biological process (BP), molecular function (MF), and cellular component (CC). The most obvious subclassification terms between different comparison groups are basically the same (Figure 2). DEGs between the 18°C and 13°C groups were mainly enriched in membrane part (12 genes), membrane (10 genes), and cell part (8 genes) in CC, cellular process (17 genes), biological regulation (15 genes), and metabolic process (13 genes) in BP, and binding (21 genes) and catalytic activity (17 genes) in MF. Comparing the 18°C and 8°C groups, DEGs were mainly enriched in membrane part (277 genes), membrane (251 genes), and cell part (213 genes) in CC, cellular process (326 genes), metabolic process (298 genes), and biological regulation (208 genes) in BP, and binding (450 genes), catalytic activity (362 genes), and transporter activity (48 genes) in MF. DEGs between the 13°C and 8°C groups were mainly enriched in membrane part (49 genes), membrane (42 genes), and cell part (36 genes) in CC, cellular process (76 genes), biological regulation (58 genes), and metabolic process (36 genes) in BP, and binding (84 genes), catalytic activity (83 genes), and transporter activity (16 genes) in MF.

KEGG enrichment analysis

We further elucidated the functions of the DEGs in signaling pathways by detecting significantly abundant pathways in the

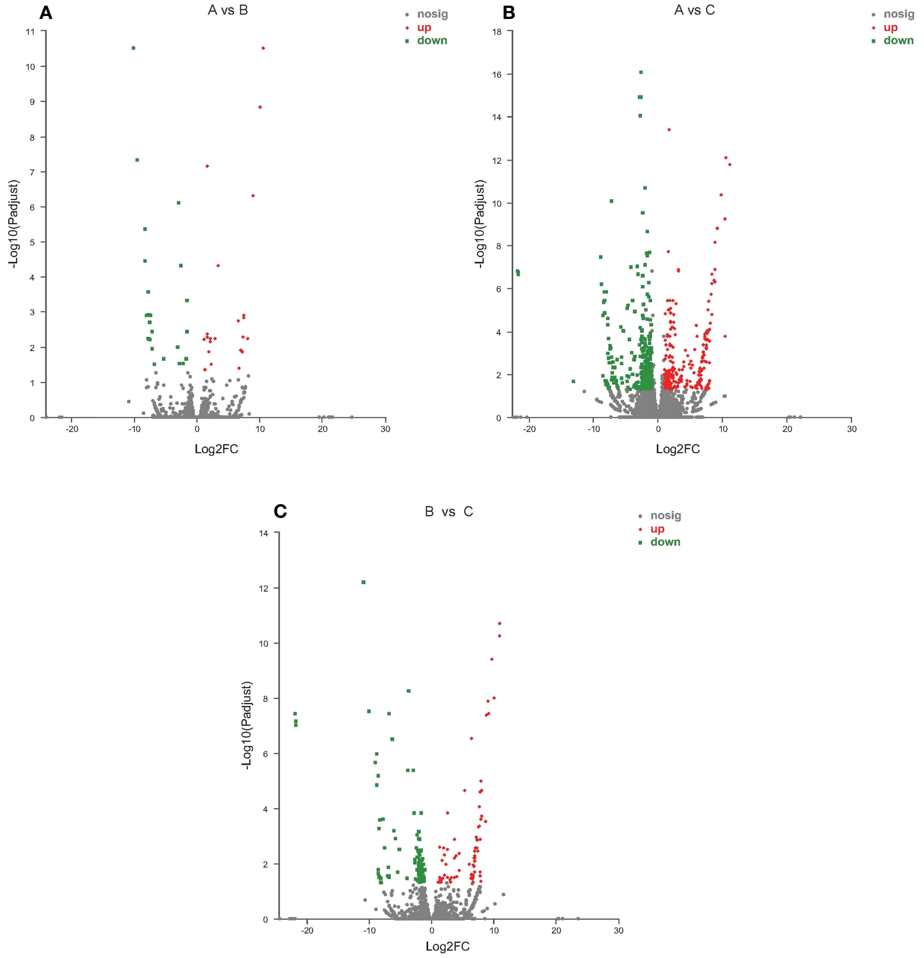

FIGURE 1
Volcano plot of differentially expressed genes identified from different temperature groups. **(A)** 13°C group compared with 18°C group; **(B)** 8°C group compared with 18°C group; **(C)** 8°C group compared with 13°C group. Each dot represents a gene, blue dots representing significantly down regulated genes, red dots representing significantly up regulated genes, and gray dots representing not significantly different genes.

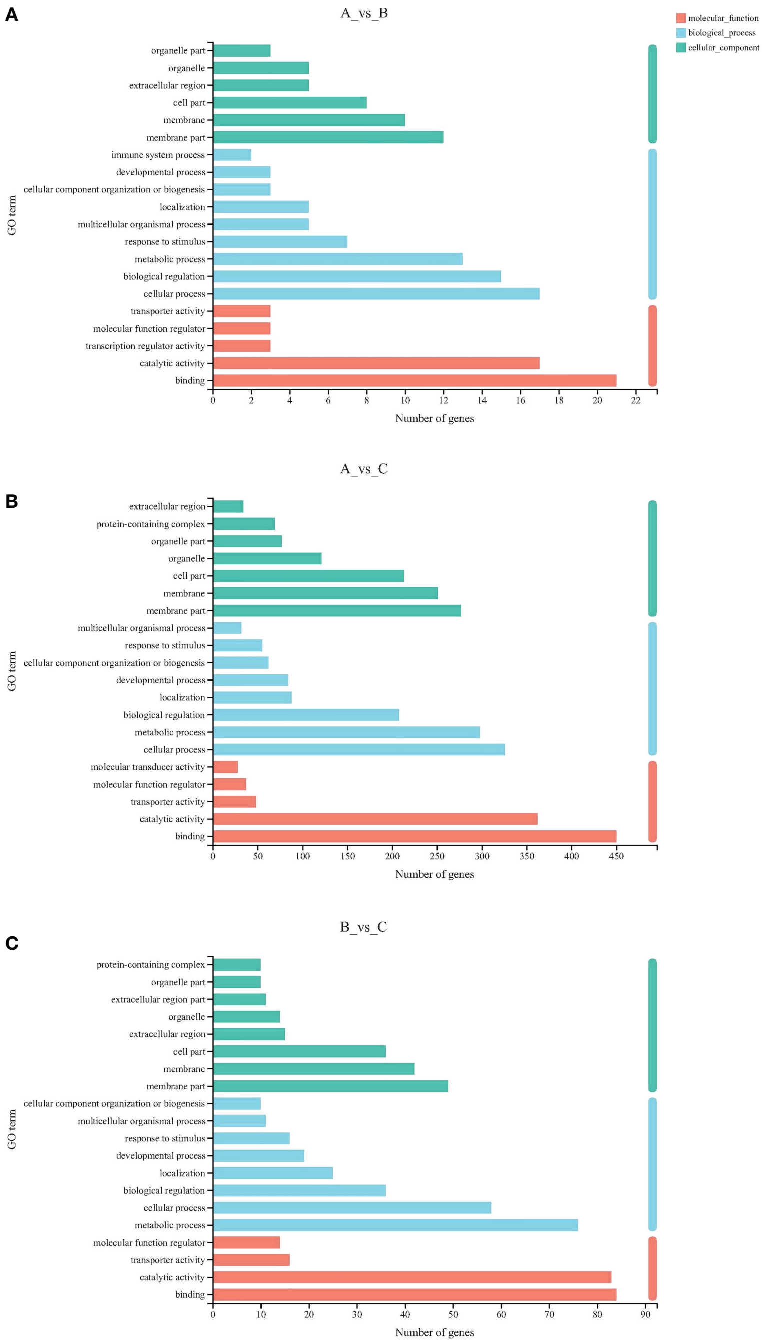

FIGURE 2
GO classification statistical histogram. **(A)** 13°C group compared with 18°C group; **(B)** 8°C group compared with 18°C group; **(C)** 8°C group compared with 13°C group. The Y-axis represents the secondary classification term for GO. The X-axis represents the number of genes. Three colors represent three categories.

KEGG database (Figures 3, 4; Table 3). Six pathways were significantly enriched in the 13°C group compared with the 18°C group, including circadian rhythm-fly, circadian rhythm, peroxisome proliferator-activated receptor signaling pathway, fatty acid biosynthesis, adipocytokine signaling pathway, and transcriptional misregulation in cancer. There were 19 genes in these pathways, including 11 up-regulated genes and 8 down-regulated genes. The top three significantly enriched pathways were circadian rhythm-fly (3 up-regulated genes, 0 down-regulated genes), circadian rhythm (2 up-regulated genes, 1

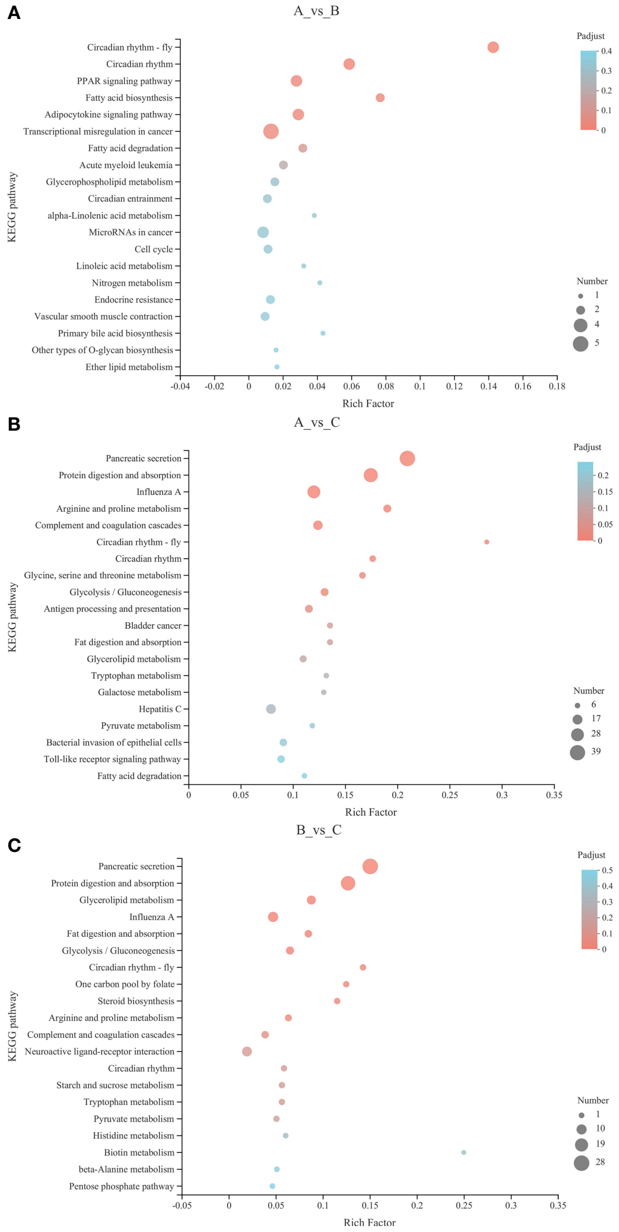

FIGURE 3
KEGG enrichment analysis bubble diagram. **(A)** 13°C group compared with 18°C group; **(B)** 8°C group compared with 18°C group; **(C)** 8°C group compared with 13°C group. The Y-axis represents the pathway name. The X-axis represents the number of genes. The size of the points represents the number of genes in the pathway. The colors of the points correspond to different Padjust ranges.

down-regulated gene), and fatty acid biosynthesis (2 up-regulated genes, 0 down-regulated genes). Ten pathways were significantly enriched in the 8°C group compared with the 18°C group, including pancreatic secretion, protein digestion and absorption, influenza A, arginine and proline metabolism, complement and coagulation cascades, circadian rhythm-fly, circadian rhythm, glycine, serine and threonine metabolism, glycolysis/gluconeogenesis, and antigen processing and presentation. There were 176 genes in these pathways, including 33 up-regulated genes and 143 down-regulated genes. The top three significantly enriched pathways were circadian rhythm-fly (5 genes up-regulated, 1 down-regulated), pancreatic secretion (3 genes up-regulated, 36 down-regulated), and arginine and proline metabolism (3 genes up-regulated, 9 down-regulated). Ten pathways were significantly enriched in the 8°C group compared with the 13°C group, including

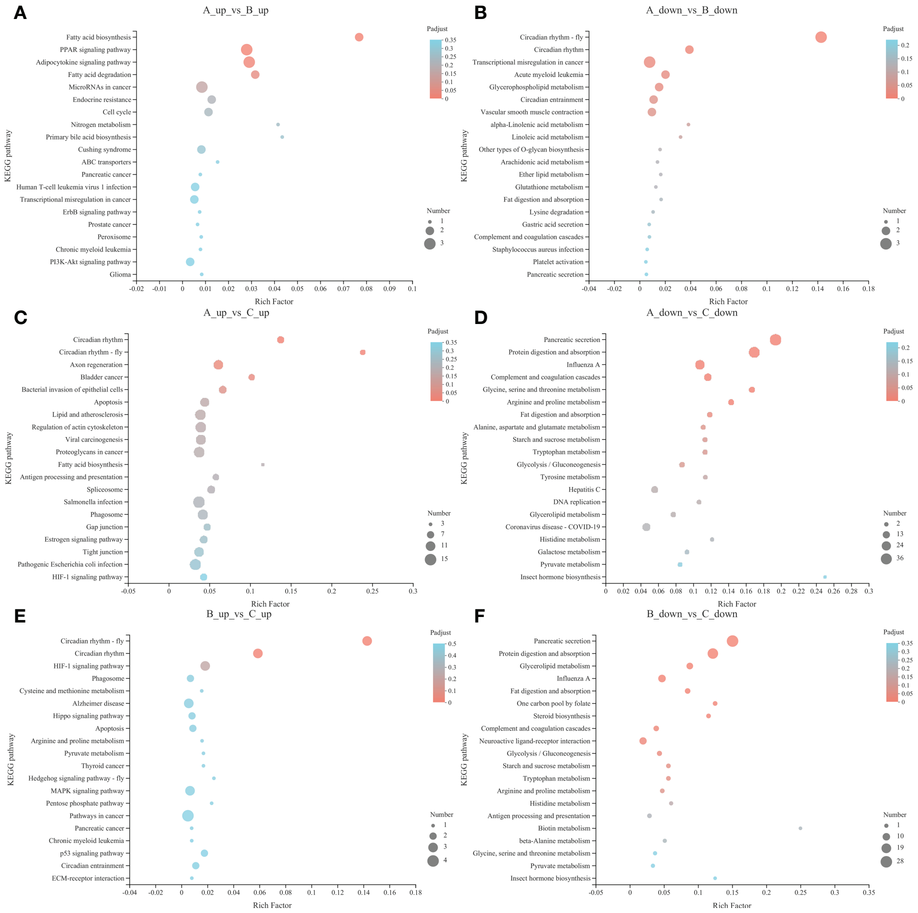

FIGURE 4
Up-regulated pathways KEGG enrichment analysis bubble diagram of 13°C group compared with 18°C group **(A)**, 8°C group compared with 18°C group **(C)** and 8°C group compared with 13°C group **(E)**. Down-regulated pathways KEGG enrichment analysis bubble diagram of 13°C group compared with 18°C group **(B)**, 8°C group compared with 18°C group **(D)** and 8°C group compared with 13°C group **(F)**. The Y-axis represents the pathway name. The X-axis represents the number of genes. The size of the points represents the number of genes in the pathway. The colors of the points correspond to different Padjust ranges.

pancreatic secretion, protein digestion and absorption, glycerolipid metabolism, influenza A, fat digestion and absorption, glycolysis/gluconeogenesis, circadian rhythm-fly, one-carbon pool by folate, steroid biosynthesis, and arginine and proline metabolism. There were 95 genes in these pathways, including 6 up-regulated genes and 89 down-regulated genes. The top three significantly enriched pathways were pancreatic secretion (0 up-regulated genes, 28 down-regulated genes), circadian rhythm-fly (3 up-regulated genes, 0 down-regulated genes), and protein digestion and absorption (1 up-regulated gene, 23 down-regulated genes). These pathways were mainly related to digestion, metabolism, the immune system, environmental adaptation, and the endocrine system, and the top three significantly enriched pathways were mainly related to digestion, metabolism, and environmental adaptation.

qPCR analysis

The pathways that were significantly enriched in this study mainly involved digestion, metabolism, and environmental adaptation. We selected 15 genes with roles in pancreatic secretion, arginine and proline metabolism, and circadian rhythm for verification by qPCR. The RNA-seq results indicated that low temperature resulted in up-regulation of nitric oxide synthase 1 (*nos1*), ornithine decarboxylase 1 (*odc1*), proline dehydrogenase 1 (*prodha*), aryl hydrocarbon receptor nuclear translocator-like 1a (*arntl1a*), clock circadian regulator a (*clocka*), aryl hydrocarbon receptor nuclear translocator-like 2 (*arntl2*), neuronal PAS domain protein 2 (*npas2*), ATPase sarcoplasmic/endoplasmic reticulum Ca^{2+} transporting 2 (*atp2a2*), ras homolog gene family, member Ab

TABLE 3 The number of up-regulated and down-regulated genes in the top three significantly enriched pathways.

group	Pathway	Number of genes	
		up-regulated	down-regulated
A vs B	Circadian rhythm-fly	3	0
	Circadian rhythm	2	1
	Fatty acid biosynthesis	2	0
A vs C	Circadian rhythm-fly	5	1
	Pancreatic secretion	3	36
	Arginine and proline metabolism	3	9
B vs C	Pancreatic secretion	0	28
	Circadian rhythm-fly	3	0
	Protein digestion and absorption	1	23

(*rhoab*), and period circadian protein homolog 2-like (*per2*), and down-regulation of guanidinoacetate N-methyltransferase (*gamt*), cryptochrome circadian regulator 5 (*cry5*), carboxypeptidase A5 (*cpa5*), elastase 2 (*ela2*), and carboxypeptidase B1 (*cpb1*). We created a histogram of expression levels based on the qPCR results and combined these with the RNA-seq results to produce a correlation scatter plot. The results showed that the expression levels determined by qPCR were consistent with the RNA-seq results, with a significant positive correlation ($0.7705 \leq r \leq 0.9985$, $P<0.05$). This suggested that the RNA-seq results were credible (Figures 5, 6).

Serum levels of proteases, arginine and proline

The protease content was significantly higher in the control group compared to the low-temperature groups ($P<0.05$), and increased with increasing temperature. Serum levels of arginine and proline were significantly higher in the 8°C group compared to the other two groups ($P<0.05$), and decreased with increasing temperature (Figure 7).

Discussion

Water temperature is one of the most common abiotic stress factors (Long et al., 2013) and has been extensively investigated in aquatic organisms such as turbot (Ma et al., 2018), Nile tilapia (Qiang et al., 2013), yellow drum (*Nibea albiflora*) (Jiao et al., 2020), and pacific white shrimp (*Litopenaeus vannamei*) (Wen et al., 2017). Temperature is also an important factor limiting the survival, growth, and development of tiger puffers in culture (Kikuchi et al., 2006; Liu et al., 2022). However, most studies of the effects of low temperature on tiger puffers to date have focused on short-term low-temperature stress (Liu et al., 2022), and a lack of understanding of the molecular mechanisms involved in long-term stress has limited progress in breeding tiger puffers for cold tolerance. In the present study, we carried out liver transcriptome analysis at different temperatures to analyze the molecular mechanisms of adaptation under chronic low-temperature stress. GO functional annotation and KEGG enrichment were used to analyze the functions and pathways of DEGs. Fifty-one and 942 DEGs were found in the 13°C and 8°C groups compared with the control group, respectively, and 195 DEGs were found in the 8°C group compared with the 13°C group. These results indicated that a fall in temperature to 13°C had little effect on tiger puffers, while a temperature of 8°C had a greater impact. KEGG analysis produced similar results. Ten were significantly enriched in 8°C group compared with other two groups, while six pathways were significantly enriched in the 13°C group compared with the control group. The significantly enriched signaling pathways in the three comparison groups were related to digestion, metabolism, and environmental adaptation. Four pathways were significantly enriched in the 8°C group compared with the other two groups, including circadian rhythm, pancreatic secretion, protein digestion and absorption, and arginine and proline metabolism, while only circadian rhythm was significantly enriched in the 13°C group compared with the control group.

Previous studies found that extreme temperature conditions affected fish metabolism and digestion, while low temperatures reduced fish growth and metabolic rates (Chang et al., 2006; Teodósio et al., 2021). And the digestive rate of fish is also affected at non-adaptive temperature (Yúfera et al., 2019; Xing et al., 2022). Similarly, change in temperature also affected the circadian rhythm in fish (Liu et al., 2020; Bernal et al., 2022). In the present study, most genes in the enriched pathways related to digestion, metabolism, and environmental adaptation were down-regulated at low temperature and only a few genes were up-regulated, suggesting that low temperature inhibited normal digestion and metabolism in tiger puffers, and changed their

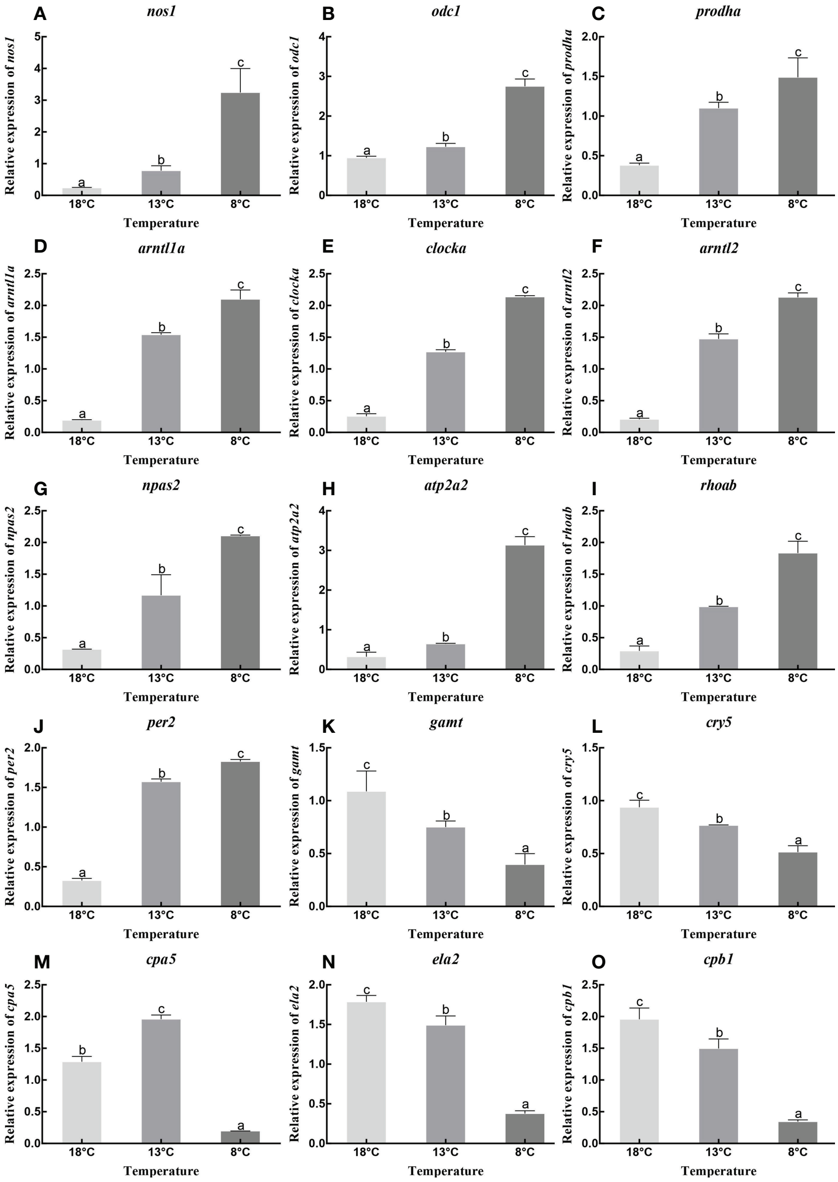

FIGURE 5
Relative expression of *nos1* **(A)**, *odc1* **(B)**, *prodha* **(C)**, *arntl1a* **(D)**, *clocka* **(E)**, *arntl2* **(F)**, *npas2* **(G)**, *atp2a2* **(H)**, *rhoab* **(I)**, *per2* **(J)**, *gamt* **(K)**, *cry5* **(L)**, *cpa5* **(M)**, *ela2* **(N)** and *cpb1* **(O)** under different temperature. Data were presented as the mean ± SEM. Different letters indicate significant differences between groups ($P<0.05$).

circadian rhythm. These up-regulated genes may play an important role in response to low-temperature stress.

Genes in the pancreatic secretion pathway were mostly down-regulated, including *cpa1*, *cpb1*, and *ela2*, which are associated with proteolysis. *cpa1* and *cpb1* are biomarkers related to proteolysis, and their content in plasma were shown to be higher under normal proteolysis conditions compared with proteolysis inhibition (Dieden et al., 2021). Deletion of *ela2* resulted in the destruction of proteolytic activity (Salipante et al., 2007). Genes enriched in the protein digestion and absorption pathway were mainly down-regulated with decreased temperature, suggesting that low temperature may inhibit the expression of genes related to proteolysis in pancreatic secretion, leading to disruption of protein digestion and absorption. In addition, serum protease levels were significantly lower in the low-temperature groups compared with the control group, thus confirming the reliability of the study conclusion. Furthermore, the expression levels of genes related to ATP hydrolysis and cell processes, including *atp2a2* and *rhoab*, increased at low temperature. The *atp2a2* gene encodes SERCA Ca^{2+}-ATPases,

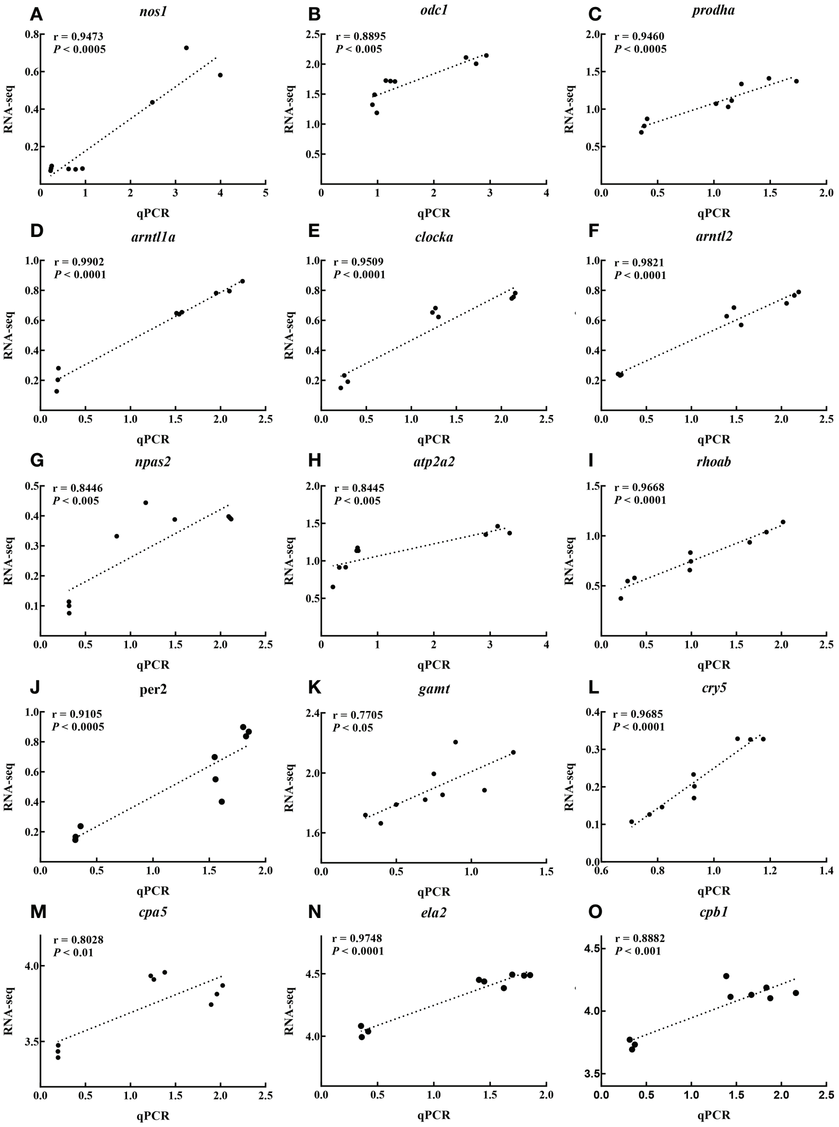

FIGURE 6
Scatter plot of correlation between RNA-seq and qPCR results of *nos1* **(A)**, *odc1* **(B)**, *prodha* **(C)**, *arntl1a* **(D)**, *clocka* **(E)**, *arntl2* **(F)**, *npas2* **(G)**, *atp2a2* **(H)**, *rhoab* **(I)**, *per2* **(J)**, *gamt* **(K)**, *cry5* **(L)**, *cpa5* **(M)**, *ela2* **(N)** and *cpb1* **(O)** under different temperature.

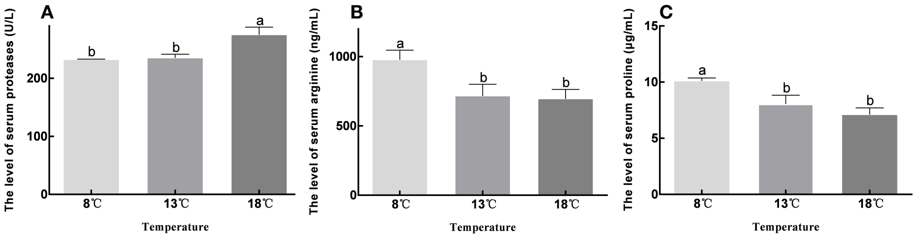

FIGURE 7
Contents of proteases, arginine and proline in serum at different temperature groups. Data were presented as the mean ± SEM. Different letters indicate significant differences between groups (P<0.05).

which catalyze the hydrolysis of ATP and the transport of calcium ions from the cytoplasm to the sarcoplasmic reticulum lumen (Kabashima et al., 2020; Muslimova et al., 2020). The *rhoab* gene was shown to enable Rho GTPase activity in zebrafish (Salas-Vidal et al., 2007), which plays an important role in a series of cellular processes, including proliferation, apoptosis, cell migration, cell polarization, membrane trafficking, cytoskeleton rearrangements, and transcriptional regulation. All known Rho GTPases are involved in normal development in animals (Salas-Vidal et al., 2005). Low temperature disrupts pancreatic secretion, and normal metabolism will be affected by inhibition of protein digestion and absorption (Hou et al., 2015). However, the up-regulation of genes related to energy expenditure and cell function at low temperature may be important for improving the survival, growth, and development of tiger puffers.

Arginine and proline metabolism was significantly enriched in many metabolomics studies of temperature tolerance in fish (Jiao et al., 2020; Zhang et al., 2021). Arginine and proline have been shown to have a protective effect against temperature changes in some fish species (Zhao et al., 2015; Cheng et al., 2021). In addition, arginine and proline were shown to improve the cold resistance of crops and reduce damage caused by freezing (Zhang et al., 2010; Alvarez et al., 2022). These results suggest that arginine and proline metabolism may play an important role in the response of tiger puffers to low temperature. In the present study, genes involved in the arginine and proline metabolism, and glycine, serine, and threonine metabolism pathways were generally down-regulated at low temperatures, suggesting that low temperature can inhibit amino acid metabolism. However, *prodha*, *odc1*, and *nos1* genes involved in arginine and proline metabolism were up-regulated at low temperature. Proline was previously shown to accumulate in plants in response to environmental stress, and was rapidly oxidized by proline dehydrogenase (ProDH) when the stress was relieved (Cabassa-Hourton et al., 2016). Not only the accumulation of proline, but also continuous proline metabolism or turnover was required to cope with drought in arabidopsis (*Arabidopsis thaliana*) (Sharma et al., 2011). This explains why *prodha* expression increases in response to cold stress: during cold tolerance, both the continuous accumulation of proline and the continuous oxidation of proline by *prodha* is required to maintain normal metabolism and turnover in tiger puffers during cold tolerance. Under the action of arginase, arginine was decomposed into ornithine, and then ornithine was catalyzed by ornithine decarboxylase to synthesize putrescine, which has been shown to alleviate cold damage (Kovács et al., 2010; Zuo et al., 2021). Nitric oxide synthase is a key enzyme in arginine catabolism, and decomposes nitric oxide (NO) from arginine (Martínez, 1995), while low temperature makes plants accumulate more NO to reduce cold damage (Plohovska et al., 2019). This also indicates that increased arginine accumulation is required to supply ornithine and NO production at low temperatures. Moreover, serum levels of arginine and proline were significantly higher at 8°C than at the higher temperatures, and increased with decreasing temperature, further confirming that *prodha*, *odc1*, and *nos1* in arginine and proline metabolism were essential components of the response to cold stress in tiger puffers, even though low temperatures results in metabolic disorders.

Our current understanding of the molecular mechanism of the circadian system in fish is mainly based on zebrafish, in which the interaction of clock gene products is similar to that in mammals (Cahill, 2002). In the present study, several genes, including *arntl1a*, *clocka*, *arntl2*, *per2*, and *cry5*, were involved in the circadian rhythm pathway, and all except *cry5* increased as the temperature decreased. Studies of circadian rhythms in mammals and fish found that these genes formed a transcription–translation feedback loop: heterodimeric interactions of clock transcription factors (CLOCK (orthologous to fish *clocka*) and BMAL1 (ARNTL)) drive the transcription and translation of PERIOD1-3 (*PER1-3*) and CRYPTO-CHROME 1-2 (*CRY1-2*), which are translated into proteins and form heterodimers themselves, and are recycled from the cytoplasm back to the nucleus to inhibit BMAL1 and CLOCK (Cahill, 2002; Zhdanova and Reebs, 2006; Anea et al., 2018). Global loss of the *BMAL1* or *PER* genes in this conserved transcription–translation feedback loop impairs vascular endothelial cell layer function, and has acute and chronic adverse effects on vascular system adaptation (Viswambharan et al., 2007; Somanath et al., 2011). Overexpression of clock components can also prevent the generation of deleterious vascular phenotypes (Qin and Deng, 2015). Circadian rhythms also regulate metabolism and digestion primarily *via* through this feedback loop (Zhong et al., 2018; Segers and Depoortere, 2021), which controls and drives metabolism, mainly including neurotransmitters, hormones, amino acids, and lipids (Han et al., 2022). Meanwhile, the circadian rhythm and metabolism interact with each other to maintain normal physiological activities (Reinke and Asher, 2019; Takahashi, 2019; Sinturel et al., 2020). Previous studies showed that circadian clock genes caused diurnal fluctuations in the digestive system by altering the activities of various digestive enzymes (Maouyo et al., 1993; Espinosa-Chaurand et al., 2017). Therefore, the circadian rhythm has a complex relationship with digestion and metabolism, and the regulation of circadian rhythm can alleviate the damage caused by digestive and metabolic disorders, which is an adaptive change and plays a positive role in the resistance to low temperature.

Conclusions

In the present study, we analyzed the effects of long-term cold stress on the liver transcriptome in tiger puffers. Totals of 942 and 195 DEGs were identified in the 8°C group compared with the 18°C and 13°C groups, respectively. Further characterization showed that most DEGs were enriched in pathways related to digestion, metabolism, and environmental adaptation, in which arginine and proline metabolism, pancreatic secretion, and circadian rhythm were considered to be the primary signaling pathways. Regarding the effects of low temperature on metabolic and digestive disorders, genes involved in arginine and proline metabolism and pancreatic secretion were up-regulated at low temperatures, which may help to improve cold resistance in tiger puffers. Serum tests confirmed protease inhibition and the accumulation of arginine and proline at low temperatures. In addition, low temperature induced adaptive changes in the circadian rhythm in tiger puffers, which may also improve their low-temperature tolerance. To the best of our knowledge, this was the first study to expose tiger puffers to long-term cold stress, and the results provide new insights into the mechanism of cold tolerance in this species. The selected key genes may provide potential biomarkers for cold response in tiger puffers, to allow the screening of populations with cold tolerance.

Data availability statement

The datasets presented in this study can be found in online repositories. The names of the repository/repositories and accession number(s) can be found in the article/Supplementary Material.

Ethics statement

The animal study was reviewed and approved by Institutional Animal Care and Use Committee of the Yellow Sea Fisheries Research Institute.

Author contributions

All authors certify that they have participated sufficiently in the work to take public responsibility for the content, including participation in the concept, design, analysis, writing, or revision of the manuscript. Furthermore, each author certifies that this material or similar material will not be submitted to or published in any other publication before its appearance in the Frontiers in Marine Science. ZL and LZ participated in the experimental design, data processing and manuscript writing of this research. AM participated in the discussion of experimental results. XW, SL, HC, ZS, FX and HZ helped to perform the low temperature stress experiment and carried out sample preparation. All authors contributed to the article and approved the submitted version.

Funding

This work was supported by the Key Research and Development Plan of Nation (Grant No. 2018YFD0900301-12); National Nature Science Foundation of China (Grant No. 32002362); Key Research and Development Plan of Nation (Grant No. 2018YFD0900102); Shandong Provincial Natural Science Foundation, China (Grant No. ZR2019BC089); Central Public-interest Scientific Institution Basal Research Fund, CAFS (Grant No. 2020TD25).

Conflict of interest

The authors declare that the research was conducted in the absence of any commercial or financial relationships that could be construed as a potential conflict of interest.

Publisher's note

References

Alvarez, M. E., Savouré, A., and Szabados, L. (2022). Proline metabolism as regulatory hub. *Trends Plant Sci.* 27, 39–55. doi: 10.1016/j.tplants.2021.07.009

Anea, C. B., Merloiu, A. M., Fulton, D. J. R., Patel, V., and Rudic, R. D. (2018). Immunohistochemistry of the circadian clock in mouse and human vascular tissues. *Vessel Plus* 2, 16. doi: 10.20517/2574-1209.2018.46

Beitinger, T. L., Bennett, W. A., and McCauley, R. W. (2000). Temperature tolerances of north American freshwater fishes exposed to dynamic changes in temperature. *Environ. Biol. Fishes* 58, 237–275. doi: 10.1023/A:1007676325825

Bernal, M. A., Schmidt, E., Donelson, J. M., Munday, P. L., Ravasi, T., and Ravasi, T. (2022). Molecular response of the brain to cross-generational warming in a coral reef fish. *Front. Mar. Sci.* 9 doi: 10.3389/fmars.2022.784418

Cabassa-Hourton, C., Schertl, P., Bordenave-Jacquemin, M., Saadallah, K., Guivarc'h, A., Lebreton, S., et al. (2016). Proteomic and functional analysis of proline dehydrogenase 1 link proline catabolism to mitochondrial electron transport in Arabidopsis thaliana.. *Biochem. J.* 473:2623–2634. doi: 10.1042/BCJ20160314

Cahill, G. M. (2002). Clock mechanisms in zebrafish. *Cell Tissue Res.* 309, 27–34. doi: 10.1007/s00441-002-0570-7

Chang, Y. M., Kuang, Y. Y., Cao, D. C., Liang, L., Sun, X. W., and Lei, Q. Q. (2006). Effects of cooling temperature stress on hematology and serum chemistry values of. *J. Fisheries China* 30, 701–706. doi: 10.1360/aps050066

Cheng, Y., Li, X., Wang, L., Lu, K., Song, K., Ai, Q., et al. (2021). Effects of dietary arginine levels on growth, immune function of physical barriers and serum parameters of spotted seabass (Lateolabrax maculatus) reared at different water temperatures. *Aquaculture* 541, 736812. doi: 10.1016/j.aquaculture.2021.736812

Dieden, A., Malan, L., Mels, C., Lammertyn, L., Wentzel, A., Nilsson, P., et al. (2021). Exploring biomarkers associated with deteriorating vascular health using a targeted proteomics chip: The SABPA study. *Medicine* 100:e25936. doi: 10.1097/MD.0000000000025936

Espinosa-Chaurand, D., Vega-Villasante, F., Carrillo-Farnés, O., and Nolasco-Soria, H. (2017). Effect of circadian rhythm, photoperiod, and molt cycle on digestive enzymatic activity of macrobrachium tenellum juveniles. *Aquaculture* 479, 225–232. doi: 10.1016/j.aquaculture.2017.05.029

Han, H., Dou, J. M., Hou, Q. Q., and Wang, H. J. (2022). Role of circadian rhythm and impact of circadian rhythm disturbance on the metabolism and disease. *J. Cardiovasc. Pharmacol.* 79, 254–263. doi: 10.1097/FJC.0000000000001178

Hou, Y., Yin, Y., and Wu, G. (2015). Dietary essentiality of "nutritionally non-essential amino acids" for animals and humans. *Exp. Biol. Med. (Maywood N.J.)* 240, 997–1007. doi: 10.1177/1535370215587913

Ibarz, A., Martín-Pérez, M., Blasco, J., Bellido, D., de Oliveira, E., and Fernández-Borràs, J. (2010). Gilthead sea bream liver proteome altered at low temperatures by oxidative stress. *PROTEOMICS* 10, 963–975. doi: 10.1002/pmic.200900528

Jiao, S., Nie, M., Song, H., Xu, D., and You, F. (2020). Physiological responses to cold and starvation stresses in the liver of yellow drum (Nibea albiflora) revealed by LC-MS metabolomics. *Sci. Total Environ.* 715, 136940. doi: 10.1016/j.scitotenv.2020.136940

Kabashima, Y., Ogawa, H., Nakajima, R., and Toyoshima, C. (2020). What ATP binding does to the Ca 2+ pump and how nonproductive phosphoryl transfer is prevented in the absence of Ca 2+. *Proc. Natl. Acad. Sci.* 117, 18448–18458. doi: 10.1073/pnas.2006027117

Kikuchi, K., Iwata, N., Kawabata, T., and Yanagawa, T. (2006). Effect of feeding frequency, water temperature, and stocking density on the growth of tiger puffer, takifugu rubripes. *J. World Aquaculture Soc.* 37, 12–20. doi: 10.1111/j.1749-7345.2006.00002.x

Kovács, Z., Simon-Sarkadi, L., Szűcs, A., and Kocsy, G. (2010). Differential effects of cold, osmotic stress and abscisic acid on polyamine accumulation in wheat. *Amino Acids* 38, 623–631. doi: 10.1007/s00726-009-0423-8

Li, B., and Dewey, C. N. (2011). RSEM: accurate transcript quantification from RNA-seq data with or without a reference genome. *BMC Bioinf.* 12, 323. doi: 10.1186/1471-2105-12-323

Liu, Z. F., Ma, A. J., Yuan, C. H., Zhao, T. T., Chang, H. W., and Zhang, J. S. (2021). Transcriptome analysis of liver lipid metabolism disorders of the turbot scophthalmus maximus in response to low salinity stress. *Aquaculture* 534, 736273. doi: 10.1016/j.aquaculture.2020.736273

Liu, Z. F., Ma, A., Yuan, C. H., Zhu, L., Chang, H. W., Yu, L. L., et al. (2022). Kidney transcriptome analysis of tiger puffer (Takifugu rubripes) uncovers key pathways and genes in response to low-temperature stress. *Aquaculture Rep.* 26, 101287. doi: 10.1016/j.aqrep.2022.101287

Liu, L., Zhang, R., Wang, X., Zhu, H., and Tian, Z. (2020). Transcriptome analysis reveals molecular mechanisms responsive to acute cold stress in the tropical stenothermal fish tiger barb (Puntius tetrazona). *BMC Genomics* 21, 737. doi: 10.1186/s12864-020-07139-z

Livak, K. J., and Schmittgen, T. (2001). Analysis of relative gene expression data using real-time quantitative PCR and the 2-DDCt method. *Methods* 25, 402–408. doi: 10.1006/meth.2001.1262

Long, Y., Song, G., Yan, J., He, X., Li, Q., and Cui, Z. (2013). Transcriptomic characterization of cold acclimation in larval zebrafish. *BMC Genomics* 14, 612. doi: 10.1186/1471-2164-14-612

Love, M. I., Huber, W., and Anders, S. (2014). Moderated estimation of fold change and dispersion for RNA-seq data with DESeq2. *Genome Biol.* 15, 550. doi: 10.1186/s13059-014-0550-8

Luo, L., Huang, J. H., Liu, D. L., Jiang, S. G., Zhou, F. L., Jiang, S., et al. (2021). Transcriptome reveals the important role of metabolic imbalances, immune disorders and apoptosis in the treatment of procambarus clarkii at super high temperature. *Comp. Biochem. Physiol. Part D: Genomics Proteomics* 37, 100781. doi: 10.1016/j.cbd.2020.100781

Maouyo, D., Sarfati, P., Guan, D., Morisset, J., and Adelson, J. W. (1993). Circadian rhythm of exocrine pancreatic secretion in rats: major and minor cycles. *Am. J. Physiol.* 264, G792–G800. doi: 10.1152/ajpgi.1993.264.4.g792

Martínez, A. (1995). Nitric oxide synthase in invertebrates. *Histochemical J.* 27, 770–776. doi: 10.1007/BF02388302

Ma, A. J., Wang, X. A., Huang, Z. H., Liu, Z. F., Cui, W. X., and Qu, J. B. (2018). Estimation of genetic parameters for upper thermal tolerance and growth-related traits in turbot scophthalmus maximus using the Bayesian method based on Gibbs sampling. *Acta Oceanologica Sin.* 37, 40–46. doi: 10.1007/s13131-018-1185-5

Muslimova, E. F., Rebrova, T. Y., Kondratieva, D. S., Akhmedov, S. D., and Afanasiev, S. A. (2020). Expression of the Ca2+-ATPase SERCA2a (ATP2A2) gene and the ryanodine receptor (RYR2) gene in patients with chronic heart failure. *Russian J. Genet.* 56, 843–848. doi: 10.1134/S1022795420070108

Plohovska, S. H., Krasylenko, Y. A., and Yemets, A. I. (2019). Nitric oxide modulates actin filament organization in arabidopsis thaliana primary root cells at low temperatures. *Cell Biol. Int.* 43, 1020–1030. doi: 10.1002/cbin.10931

Qiang, J., Yang, H., Wang, H., Kpundeh, M. D., and Xu, P. (2013). Interacting effects of water temperature and dietary protein level on hematological parameters in Nile tilapia juveniles, oreochromis niloticus (L.) and mortality under streptococcus iniae infection. *Fish Shellfish Immunol.* 34, 8–16. doi: 10.1016/j.fsi.2012.09.003

Qin, B., and Deng, Y. (2015). Overexpression of circadian clock protein cryptochrome (CRY) 1 alleviates sleep deprivation-induced vascular inflammation in a mouse model. *Immunol. Lett.* 163, 76–83. doi: 10.1016/j.imlet.2014.11.014

Reinke, H., and Asher, G. (2019). Crosstalk between metabolism and circadian clocks. *Nat. Rev. Mol. Cell Biol.* 20, 227–241. doi: 10.1038/s41580-018-0096-9

Salas-Vidal, E., Cheng, X., Cui, C., Li, X., Schnabel, D., Meijer, A. H., et al. (2007). Functional genomics of zebrafish rhoab, cdc42c and rac1a rho small GTPases. *Dev. Biol.* 306, 380. doi: 10.1016/j.ydbio.2007.03.353

Salas-Vidal, E., Meijer, A. H., Cheng, X., and Spaink, H. P. (2005). Genomic annotation and expression analysis of the zebrafish rho small GTPase family during development and bacterial infection. *Genomics* 86, 25–37. doi: 10.1016/j.ygeno.2005.03.010

Salipante, S. J., Benson, K. F., Luty, J., Hadavi, V., Kariminejad, R., Kariminejad, M. H., et al. (2007). Double *de novo* mutations of ELA2 in cyclic and severe congenital neutropenia. *Hum. Mutat.* 28, 874–881. doi: 10.1002/humu.20529

Segers, A., and Depoortere, I. (2021). Circadian clocks in the digestive system. *Nat. Rev. Gastroenterol. Hepatol.* 18, 239–251. doi: 10.1038/s41575-020-00401-5

Sharma, S., Villamor, J., and Verslues, P. (2011). Essential role of tissue-specific proline synthesis and catabolism in growth and redox balance at low water potential. *Plant Physiol.* 157, 292–304. doi: 10.1104/pp.111.183210

Sinturel, F., Petrenko, V., and Dibner, C. (2020). Circadian clocks make metabolism run. *J. Mol. Biol.* 432, 3680–3699. doi: 10.1016/j.jmb.2020.01.018

Somanath, P. R., Podrez, E. A., Chen, J., Ma, Y., Marchant, K., Antoch, M., et al. (2011). Deficiency in core circadian protein Bmal1 is associated with a prothrombotic and vascular phenotype. *J. Cell. Physiol.* 226, 132–140. doi: 10.1002/jcp.22314

Takahashi, J. S. (2019). Circadian clock genes and the transcriptional architecture of the clock mechanism. *IBRO Rep.* 6, S2–S3. doi: 10.1016/j.ibror.2019.07.171

Teodósio, R., Aragão, C., Colen, R., Carrilho, R., Dias, J., and Engrola, S. (2021). A nutritional strategy to promote gilthead seabream performance under low temperatures. *Aquaculture* 537, 736494. doi: 10.1016/j.aquaculture.2021.736494

Viswambharan, H., Carvas, J. M., Antic, V., Marecic, A., Jud, C., Zaugg, C. E., et al. (2007). Mutation of the circadian clock gene Per2 alters vascular endothelial function. *Circulation* 115, 2188–2195. doi: 10.1161/CIRCULATIONAHA.106.653303

Wen, H., Ren, C., Li, H., Da, H., Wang, Y., Jiang, X., et al. (2017). Transcriptomic analyses on muscle tissues of litopenaeus vannamei provide the first profile insight into the response to low temperature stress. *PLoS One* 12, 1–21. doi: 10.1371/journal.pone.0178604

Xing, Q., Tu, H., Yang, M., Chen, G., Tang, Q., Yi, S., et al. (2022). Evaluation of cold tolerance and gene expression patterns associated with low-temperature stress in giant freshwater prawn macrobrachium rosenbergii. *Aquaculture Rep.* 24, 101172. doi: 10.1016/j.aqrep.2022.101172

Yúfera, M., Nguyen, M. V., Navarro-Guillén, C., Moyano, F. J., Jordal, A. E. O., Espe, M., et al. (2019). Effect of increased rearing temperature on digestive function in cobia early juvenile. *Comp. Biochem. Physiol. Part A: Mol. Integr. Physiol.* 230, 71–80. doi: 10.1016/j.cbpa.2019.01.007

Zhang, X., Shen, L., Li, F., Zhang, Y., Meng, D., and Sheng, J. (2010). Up-regulating arginase contributes to amelioration of chilling stress and the antioxidant system in cherry tomato fruits. *J. Sci. Food Agric.* 90, 2195–2202. doi: 10.1002/jsfa.4070

Zhang, Z. Q., Zhou, C., Fan, K. P., Zhang, L., Liu, Y., and Liu, P. F. (2021). Metabolomics analysis of the effects of temperature on the growth and development of juvenile European seabass (Dicentrarchus labrax). *Sci. Total Environ.* 769, 145155. doi: 10.1016/j.scitotenv.2021.145155

Zhao, X.-l., Han, Y., Ren, S.-T., Ma, Y.-M., Li, H., and Peng, X.-X. (2015). L-proline increases survival of tilapias infected by streptococcus agalactiae in higher water temperature. *Fish Shellfish Immunol.* 44, 33–42. doi: 10.1016/j.fsi.2015.01.025

Zhao, T. T., Ma, A. J., Huang, Z. H., Liu, Z. F., Sun, Z. B., Zhu, C. Y., et al. (2021). Transcriptome analysis reveals that high temperatures alter modes of lipid metabolism in juvenile turbot (Scophthalmus maximus) liver. *Comp. Biochem. Physiol. Part D: Genomics Proteomics* 40, 100887. doi: 10.1016/j.cbd.2021.100887

Zhdanova, I., and Reebs, S. (2006). Circadian rhythms in fish. *Fish Physiol.* 24, 197–238. doi: 10.1016/S1546-5098(05)24006-2

Zhong, X., Yu, J., Frazier, K., Weng, X., Li, Y., Cham, C. M., et al. (2018). Circadian clock regulation of hepatic lipid metabolism by modulation of m6A mRNA methylation. *Cell Rep.* 25, 1816–1828. doi: 10.1016/j.celrep.2018.10.068

Zhou, L. Y., Fu, S. J., Fu, C., Ling, H., and Li, X. M. (2019). Effects of acclimation temperature on the thermal tolerance, hypoxia tolerance and swimming performance of two endangered fish species in China. *J. Comp. Physiol. B* 189, 237–247. doi: 10.1007/s00360-018-01201-9

Zhou, T., Gui, L., Liu, M. L., Li, W. H., Hu, P., Duarte, D. F. C., et al. (2019). Transcriptomic responses to low temperature stress in the Nile tilapia, oreochromis niloticus. *Fish Shellfish Immunol.* 84, 1145–1156. doi: 10.1016/j.fsi.2018.10.023

Zuo, X., Cao, S., Zhang, M., Cheng, Z., Cao, T., Jin, P., et al. (2021). High relative humidity (HRH) storage alleviates chilling injury of zucchini fruit by promoting the accumulation of proline and ABA. *Postharvest Biol. Technol.* 171, 111344. doi: 10.1016/j.postharvbio.2020.111344

frontiers | Frontiers in Marine Science

TYPE Original Research
PUBLISHED 08 December 2022
DOI 10.3389/fmars.2022.1055873

Numerical studies on wake and turbulence characteristics of aquaculture nets

Lingyun Xu[1,2], Peng Li[3,4,5]*, Hongde Qin[3] and Zhijing Xu[6]

[1]China Ship Science Research Center, Wuxi, China, [2]Taihu Laboratory of Deepsea Technological Science, Wuxi, China, [3]College of Shipbuilding Engineering, Harbin Engineering University, Harbin, China, [4]Yantai Research Institute of Harbin Engineering University, Yantai, China, [5]Science and Technology on Underwater Vehicle Laboratory, Harbin Engineering University, Harbin, China, [6]Ningbo Institute of Dalian University of Technology, Ningbo, China

OPEN ACCESS

EDITED BY
Igor Tsukrov,
University of New Hampshire,
United States

REVIEWED BY
Alexander Knysh,
University of New Hampshire,
United States
Are Johan Berstad,
Aquastructures, Norway

*CORRESPONDENCE
Peng Li
peng.li@hrbeu.edu.cn

SPECIALTY SECTION
This article was submitted to
Marine Fisheries, Aquaculture
and Living Resources,
a section of the journal
Frontiers in Marine Science

RECEIVED 28 September 2022
ACCEPTED 24 November 2022
PUBLISHED 08 December 2022

CITATION
Xu L, Li P, Qin H and Xu Z (2022)
Numerical studies on wake and
turbulence characteristics of
aquaculture nets.
Front. Mar. Sci. 9:1055873.
doi: 10.3389/fmars.2022.1055873

This paper aims to understand the drag coefficient discrepancy between the equivalent-twine and twisted-twine nets based on their wake and turbulence characteristics. To that end, we conduct unsteady Reynolds-averaged Navier-Stokes (URANS) and the second-moment (Reynolds stress, RSM) simulations at a Reynolds number, Re=4.5×10^3, based on the effective diameter of the net twine, which corresponds to the subcritical flow regime. Then, the vortex structures and the turbulence statistics are assessed at AOA=90°. The results highlight that the wake interactions for the twisted-twine net are relatively strong compared to the equivalent-twine net, due to the disturbance of the helixes on the twisted twines. In comparison to the classical Karman vortex, the overall vortex shedding of these two nets is well organized. Symmetric vortices form behind the equivalent-twine net, while single vortices form behind the twisted-twine net. Moreover, the Reynolds normal and shear stresses show symmetric and anti-symmetric profiles. The addition of helixes to smooth circular cylinders changes the flow development, leading to a decrease of turbulence kinetic energy. With this understanding, engineers need to be carefully select the net type for preliminary design of marine aquaculture cages to avoid over- or underestimation of the drag forces.

KEYWORDS
aquaculture nets, wake, turbulence, URANS, RSM

Introduction

Aquaculture farming is a sustainable method that provides food to the increasing world population. Aquaculture farms are growing in size and open-ocean farming is becoming more favorable. However, the harsh oceanic conditions in the open ocean place significant demands on the farming-system designs. Aquaculture cages must be designed to withstand harsh conditions and to provide a dependable habitat for the farmed fish. As such, it is vital to understand the hydrodynamic interactions between ocean environmental loads, for this will help improve the design of aquaculture nets/systems.

According to (Xu and Qin, 2020), physical model tests and field measurements have been conducted to understand hydrodynamic behaviors of net panels and aquaculture systems in steady flow (Bi et al., 2013; DeCew et al., 2013; Klebert and Su, 2020; Tang et al., 2021), oscillating flow (Liu et al., 2012) and waves (Fredriksson et al., 2003; Fredriksson et al., 2004; Lader et al., 2007; Zhao et al., 2008; Park et al., 2021). Many experimental tests examined the biofouling effects on net panels (Swift et al., 2006; Bi et al., 2018; Bi et al., 2020). These experimental studies evaluate hydrodynamic behaviors of net panels based on the angle of attack, α, the solidity ratio, S_n, and the Reynolds number, *Re*. The physical model approach requires wave basins, instruments and certain similarity principles. The opposing numerical approach was used to analyze the hydrodynamic performances of net panels and aquaculture cages in current and waves. These include the finite element method (Tsukrov et al., 2000; Tsukrov et al., 2003; Tsukrov et al., 2005; Fredriksson et al., 2007; Fredriksson et al., 2014; Cheng et al., 2021; Su et al., 2021), the computational fluid dynamics method (Patursson et al., 2010; Zhao et al., 2013a; Zhao et al., 2013b; Chen and Christensen, 2016; Bi et al., 2018) and the coupled fluid-structure interactions (FSI) method (Bi et al., 2014a; Chen and Christensen, 2017; Martin et al., 2020).

In the finite element method (FEM) framework, the net is modeled with triangular/truss elements or mass-spring systems. Priour (2003) developed a triangular element model to calculate the fluid forces acting on net panels. The results revealed that the triangular element model presented a reasonable representation for the net deformation. Tsukrov et al. (2003) modeled the net panel using an equivalent truss element method. When applied to a tension-leg cage, the extreme environmental loading caused large deformations but moderate tensions. Lader and Fredheim (2006) studied the dynamic properties of a flexible net panel when exposed to waves and current using a screen model. Their results highlighted that the slack caused by floater motion led to large dynamic forces in the bottom of the net structure. Zhao et al. (2008) used a lumped-mass model to approximate the net panels under current and waves. The results showed that the lumped-mass model could accurately predict the hydrodynamic behavior of the net panels in waves. The FEM-based models are computationally efficient, because they use a grouping mesh method. However, due to the absent interference of the flow field these FEM models overestimated the drag force of the net.

In order to examine the flow field and velocity distribution around and inside the net cages, the CFD-based porous media model was developed. For instance, Patursson et al. (2010) studied the fluid characteristics of a net panel under steady flow. A mean normalized absolute error of 6.2% between measured and modeled data was discovered. Zhao et al. (2013a); Zhao et al. (2013b) investigated the flow field around net panels using the porous media model. Their results showed that, when the number of net panels reached five, the velocity reduction from the downstream net panel was 42%. To examine the fluid forces and wave attenuation of the biofouling net cages, the porous media model was used (Bi et al., 2018). Their results revealed that the biofouling accumulation led to 10 times the hydrodynamic loads on nets. The porous media model was used to study the porous resistance coefficients of fishing net cages (Chen and Christensen, 2016). The relevant achievements have been applied to a floater-net system under both waves and current conditions (Chen and Christensen, 2018).

To examine the interactions between steady flow and the flexible nets the structural model (e.g., lumped-mass model) was used in conjunction with the porous media model (Bi et al., 2014a). Their coupled FSI model assumed that the steady-state condition was satisfied at each iteration. Chen and Christensen (2017) conducted the FSI analysis of an aquaculture net under steady flow. The FSI model coupled the porous media model and the lumped-mass structural model. Tu et al. (2020) examined the fluid-structure interaction of a net panel under current using the lattice Boltzmann method. The results indicated that the flow-velocity attenuation was mainly dependent on the net solidity. Martin et al. (2020) developed a Lagrangian approach for the coupled simulation of fixed net panels in a Eulerian fluid model. In contrast to the porous media model, the net was represented by the Lagrangian points. The Reynolds-averaged Navier-Stokes equations were solved in a Eulerian fluid domain. Most recently, a coupled fluid-structure partitioned scheme was used to examine the wake characteristics induced by the net deformation (Xu et al., 2022).

The finite element model, the porous media model and the FSI model have all significantly advanced the numerical modeling for aquaculture systems. However, there remains several issues that still need to be resolved. These are:

(1) Almost all the aquaculture nets/cages in numerical simulations are approximated by a system of equivalent cylinders. Hence, they neglect the helixes of the net twines. However, it still remains unclear how these helixes influence the general wake and turbulence characteristics of a net/cage.

(2) The use of the porous media model to approximate the aquaculture nets/cages risks influencing results so that they tend to a constant pressure zone, rather than a natural pressure drop. Also, the specific flow field of the individual net twines is missing. These drawbacks of the porous media model should be resolved, and the specific flow field of the individual net twines requires further explorations.

(3) During the CFD simulations, the Boussinesq hypothesis-based two-equation turbulence models, namely the k - ε and k - ω models, have been used to ascertain the underlying turbulence mechanisms of the aquaculture nets/cages. However, the selection of the turbulence models seems random.

Having considered these issues, we decided to model a piece of the aquaculture net using the natural helical net twines rather than approximations, as shown in Figure 1. The use of a representative net panel, could reduce the computational cost without losing the physical properties of the cage. For the purposes of this study the net modeled by the natural helical net twines is referred to as the twisted-twine net, and the equivalent-twine net means the net is approximated by a system of smooth cylinders. A subcritical Reynolds number $Re = 4.5 \times 10^3$ is selected based on the effective diameter of the net twine (McKenna et al., 2004; Evans and Ridge, 2005; Lader et al., 2015). The effects of helixes on the wake and turbulence characteristics of the nets, the specific flow field of the net twines, and the comparison of the turbulence models are all assessed.

The remainder of this paper is organized as follows. Firstly, we summarize the turbulence models used for evaluating flow characteristics of aquaculture nets/cages in Section 2. The strengths and weaknesses of each two-equation turbulence model are evaluated and compared. In Section 3 the governing equations and numerical solutions for the present study are outlined. Section 4 elaborates on the verifications of the present numerical method. The drag force, the second-order turbulence statistics are verified for both smooth and twisted bodies. Section 5 presents the numerical results regarding the effects of the helixes of net twines. Finally, the conclusions of this paper are presented in Section 6.

Review of turbulence models applied to flow through aquaculture nets/cages

Previously, all turbulence models used for evaluating flow characteristics of aquaculture nets/cages have been based on the Reynolds-averaged Navier-Stokes (RANS) framework. The primary purpose of turbulence modeling in RANS is to prompt equations that anticipate the time-averaged variables without calculating the complete turbulent flow as a function of time. Two groups of turbulence models, namely the k - ε models (Patursson et al., 2010; Zhao et al., 2013a; Zhao et al., 2013b; Bi et al., 2014a; Bi et al., 2014b; Winthereig-Rasmussen et al., 2016; Yao et al., 2016; Bui et al., 2020) and k - ω models (Tang et al., 2017), have been used for the preliminary estimation of flow around and inside aquaculture cages. However, for evaluating

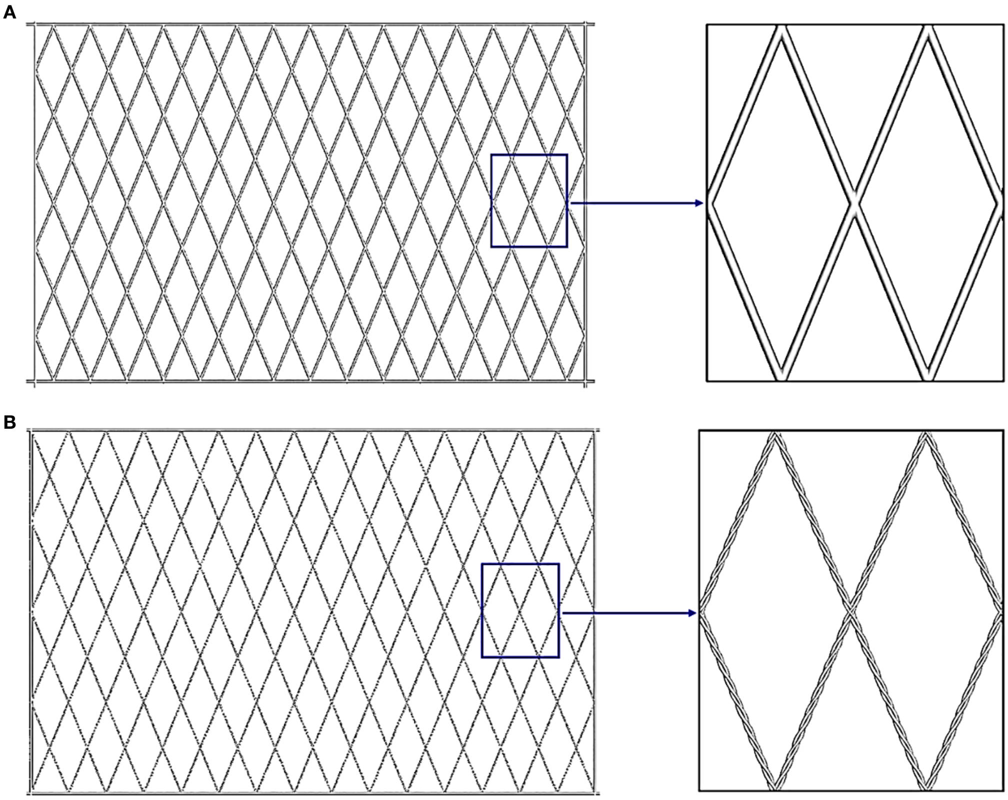

FIGURE 1
The representatives of the net panels, **(A)** the equivalent-twine net and **(B)** the twisted-twine net.

the flow field of aquaculture nets/cages, there is no such criterion to distinguish the applications of these turbulence models. Therefore, it is essential to compare these turbulence models to predict flow characteristics of aquaculture net structures precisely. We summarize the turbulence models applied to flow through aquaculture nets/cages in Table 1.

Reynolds numbers, illustrated in Table 1, reveal that the flow behind the nets is developed as turbulent flow (Zdravkovich, 1997). The turbulence kinetic energy k and the dissipation rate ε/ω shown in Table 1 are directly given by values (Patursson et al., 2010; Zhao et al., 2013a; Zhao et al., 2013b; Winthereig-Rasmussen et al., 2016), or they can be dependent on empirical formulae (Bi et al., 2014a; Bi et al., 2014b; Yao et al., 2016; Tang et al., 2017; Bui et al., 2020). I and l_τ are the turbulence intensity and the turbulence length scale. These are denoted as (ANSYS, 2017)

$$I = 0.16(Re_D)^{-0.125}, \quad l_\tau = 0.07L_c \tag{1}$$

where Re_D is the Reynolds number based on the hydraulic diameter of the domain, L_C is the characteristic length of the object. The turbulence intensity is dependent on the Reynolds number, and it significantly affects the turbulence kinetic energy k. However, the Boussinesq hypothesis assumes that the fluctuation velocity is isotropic, and the turbulence intensity is specified (Wilcox, 1998).

When using the medium turbulence parameters for k and ε, it was found that CFD simulations underestimated the drag coefficients and the velocity deficit much more than experiments did. These discrepancies could be attributed to the turbulence parameters used in the simulations. However, this could also be due to the resistance coefficients of the porous media. Despite the discrepancies, comparable results between CFD predictions and experimental measurements were obtained using values between the high and medium turbulence parameters. The coupled FSI models slightly underestimated the drag coefficients and velocity reductions of the nets. The turbulence parameters were calculated based on empirical formulae (Bi et al., 2014a; Bi et al., 2014b; Yao et al., 2016). Higher turbulence intensities should be responsible for underestimating hydrodynamic forces since the turbulence intensity from Table 1 is in a range of 2.2%~8%. In order to avoid over- or under-estimations it is recommended that the turbulence parameters, k and ε/ω should be selected based on field measurements.

The turbulence models have been used to resolve conditions such as transition in wake and transition in shear layers. According to (Wilcox, 1998), the equation of ε in the standard k - ε model is postulated, and it is not feasible for no-slip wall conditions along net twines. The realizable k - ε model was improved to modify the equation for ε, by introducing the effect of the mean flow distortion on turbulence dissipation. However, the difficulty has also been encountered when solving the epsilon equation. To accurately model the near-wall interaction the standard k - ω model was developed. This model performs better than the k - ε model in predicting the near-wall interactions. However, the model over-predicts shear stress and has issues with free stream flows. In addition, it is also susceptible to inlet boundary conditions. In comparison to the k - ε model, the standard k - ω model is more challenging to reach convergence. The shear stress transport (SST) k - ω model has gained popularity due to its excellent ability to predict separation and reattachment. This is achieved through the use of a blended function based on wall distance. The SST k - ω model works like k - ε model in the far field and like the standard k - ω model in the near-wall region. The wall damping effect that has been considered in (Tang et al., 2017) increased the grid number and left the turbulence intensity effect uncertain. As a result, the SST k - ω model overestimated the drag coefficients by 6.82% compared to the experimental data.

Furthermore, the CFD simulation results can also be affected by the near-wall treatment. The near-wall treatment can be attended with either the wall function or the near-wall model

TABLE 1 Summary of turbulence models applied to flow through aquaculture nets/cages.

Researchers	**methods**	***Re***	**Turbulence models**	***I***	***k***	**ε/ω**
Patursson et al. (2010)	porous media	429-2574	realizable k - ε	3%-8%	3.75×10^{-5}	2.5×10^{-7}
Zhao et al. (2013a)	porous media	440-1600	realizable k - ε	4%	6.11×10^{-5}	3.92×10^{-8}
Zhao et al. (2013b)	porous media	440-1600	realizable k - ε	4%	4.3×10^{-5}	2.81×10^{-7}
Bi et al. (2014a)	coupled FSI	150-5000	realizable k - ε	4%-6%	$1.5(UI)^2$	$C_\mu^{3/4} \cdot k^{3/2} / \ l_\tau$
Bi et al. (2014b)	coupled FSI	180-5000	realizable k - ε	4%-6%	$1.5(UI)^2$	$C_\mu^{3/4} \cdot k^{3/2} / \ l_\tau$
Yao et al. (2016)	coupled FSI	0-2400	standard k - ε	3.4%	$1.5(UI)^2$	$C_\mu^{3/4} \cdot k^{3/2} / \ l_\tau$
Winthereig-Rasmussen et al. (2016)	porous media	120-2500	realizable k - ε	2.2%	two values	two values
Tang et al. (2017)	one-way coupling	30-1000	SST k - ω	3.4%	$1.5(UI)^2$	$C_\mu^{3/4} \cdot k^{3/2} / \ l_\tau$
Bui et al. (2020)	porous media	10^6	standard k - ε	2.8%	$1.5(UI)^2$	$C_\mu^{3/4} \cdot k^{3/2} / \ l_\tau$

U is the mean velocity of the incoming flow and C_μ is a constant. Considering the difference between CFD simulations and field measurements, Winthereig-Rasmussen et al. (2016) used two different sets of the turbulence kinetic energy k and the dissipation rate ε. The medium turbulence parameters were based on empirical values. While the high turbulence parameters were reproduced from field measurements.

approaches. However, this is dependent on whether the wall function has been used or not. The use of the wall function reduces the computational cost, but the boundary layer profiles are assumed to be near equilibrium. In contrast, the near-wall model approach abandons the wall function, instead it modifies the wall with refined grids to capture transitions within the near-wall region. The near-wall model approach significantly improves the accuracy but raises a lower computational efficiency. A significant number of the studies in Table 1 use standard wall function, this makes the turbulent quantities less accurate. It is recommended that one should carefully select the wall functions to avoid resolving the near-wall layer and losing accuracy. In addition, the near-wall model approach is recommended if the computational resources are affordable. This paper uses the near-wall model approach with refined grids in the near-wall region.

It can be concluded that (1) The k - ε model underestimated the drag coefficients and the velocity reduction, while the SST k - ω model overestimated the drag coefficients. (2) Boussinesq hypothesis-based two-equations turbulence models lose accuracy due to assumption. Consequently, the accuracy may be improved if the turbulence parameters of k and ε/ω could be selected based on field measurements. (3) The near-wall treatment or other advanced techniques should be addressed to resolve the near-wall region and gain accurate results.

Computational model and numerical approach

Model description

In this paper we consider two diamond-mesh net panels with the dimension of 0.6m (length)×0.4m (height), as shown in Figure 2. The flow field and the drag force on a net panel are influenced by three parameters. These are the angle of attack, α, the solidity ratio, S_n, and the Reynolds number, Re. For the diamond-mesh nets, the solidity ratio represented by the hang ratios, E_1 and E_2, is defined as (Fredheim, 2005).

$$S_n = \frac{A_p}{A} = \frac{d_w}{l_w E_1 E_2} - \left(\frac{d_w}{2l_w}\right)\left(\frac{1}{E_1^2} + \frac{1}{E_2^2}\right) \tag{2}$$

Here, A_p and A are the projected and the outline areas of a net panel. d_w is the diameter of the net twine, l_w represents the length of the mesh bar. The hang ratios, E_1 and E_2, represent the diamond shape of a mesh and are functions of the mesh opening angle, 2θ, they can be denoted as (Fredheim, 2005)

$$E_1 = \frac{L}{2N_H l_w} = \frac{2N_H l_w \sin\theta}{2N_H l_w} = \sin\theta \tag{3}$$

$$E_2 = \frac{H}{2N_V l_w} = \frac{2N_V l_w \cos\theta}{2N_V l_w} = \cos\theta \tag{4}$$

Where L and H represent the length and height of the net panel, N_H and N_v are mesh numbers in horizontal and vertical directions.

As shown in Figure 2, the effective twine diameter d_w is 3mm. The hang ratios E_1 and E_2 can be adjusted by changing the mesh opening angle. In this manner, the hydrodynamic behaviors of diamond-mesh net panels can be examined in either a tensive or a loose condition. In this paper, $2\theta = 45°$, corresponds to solidity of 0.16, and was specifically selected for the numerical studies.

Governing equations and turbulence modeling

This paper conducts incompressible unsteady Reynolds-averaged Navier-Stokes (URANS) simulations using ANSYS Fluent (ANSYS, 2017). To effectively capture the unsteady flow effect induced by the wall-shear stress with respect to free stream

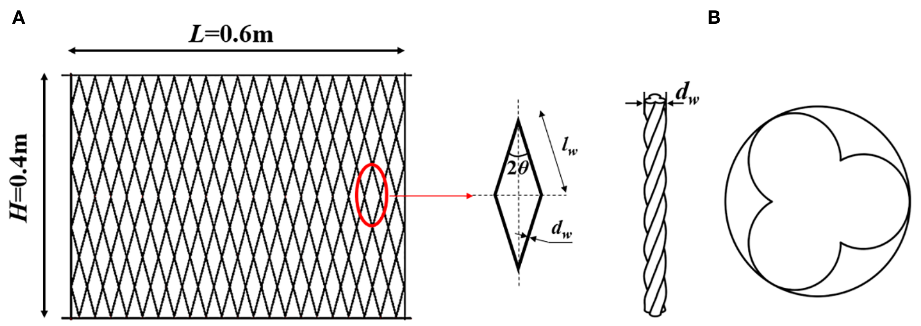

FIGURE 2
Geometric description of the net panel. **(A)** The overall geometry and **(B)** twisted twine and its cross-section. The effective diameter of the twisted twine is the diameter of the circumcircle (McKenna et al., 2004; Evans and Ridge, 2005; Lader et al., 2015).

velocity, the boundary layer needs to be resolved. The low Reynolds number near-wall turbulence modeling (e.g., URANS) seems suitable for this purpose (Palkin et al., 2016). On the other hand, as a physics-based low-fidelity simulation model, URANS is a computationally cheap representation of the high-fidelity such as large eddy simulations (LES). For the incompressible, viscous flow, the URANS equations regarding the conservation of mass and momentum are

$$\frac{\partial \overline{U_i}}{\partial x_i} = 0 \tag{5}$$

$$\frac{\partial \overline{U_i}}{\partial t} + \overline{U_j}\frac{\partial \overline{U_i}}{\partial x_j} = -\frac{1}{\rho}\frac{\partial \bar{P}}{\partial x_i} + v\frac{\partial^2 \overline{U_i}}{\partial x_j \partial x_j} - \frac{\partial \overline{U_i' U_j'}}{\partial x_j} \tag{6}$$

where $\overline{U_i}$ represents the time-dependent mean velocity, ρ is the fluid density, v is the kinematic viscosity of the fluid, $\overline{P}$ is the pressure, $\overline{U'}$ is the fluctuation velocity, i, j=1, 2, 3 (x, y, z), $\overline{U_i' U_j'}$ is the Reynolds stress.

The Reynolds stress turbulence model (Versteeg and Malalasekera, 2005), which is beyond the Boussinesq hypothesis, is used to resolve the six independent Reynolds stresses concerning the Reynolds stress transport equation and the dissipation rate of the turbulent kinetic energy as follows,

$$\frac{\partial \overline{U_i' U_j'}}{\partial t} + \overline{U_k}\frac{\partial \overline{U_i' U_j'}}{\partial x_k} = \frac{\partial}{\partial x_k}\left(\frac{v_t}{\sigma^k}\frac{\partial \overline{U_i' U_j'}}{\partial x_k}\right) - \left(\overline{U_i' U_k'}\frac{\partial \overline{U_j}}{\partial x_k} + \overline{U_j' U_j'}\frac{\partial \overline{U_i}}{\partial x_k}\right)$$
$$-C_1 \frac{\epsilon}{K}\left(\overline{U_i' U_j'} - \frac{2}{3}\delta_{ij}K\right) - C_2\left(P_{ij} - \frac{2}{3}\delta_{ij}P\right) - \frac{2}{3}\delta_{ij}\epsilon \tag{7}$$

where $K = (1/2)\overline{U_i' U_j'}$, the production P_{ij} is expressed as

$$P_{ij} = U_i' U_k' \frac{\partial \overline{U_j}}{\partial x_k} + U_j' U_k' \frac{\partial \overline{U_i}}{\partial x_k}, \qquad P = \frac{2}{3}P_{ii} \tag{8}$$

Here, The lower case 'k' signifies the turbulent kinetic energy, and U_k' is fluctuating velocity related to the turbulent kinetic energy, x_k is the position in the local coordinate system of the eddy. σ^k is the turbulent Prandtl number, $\sigma^k = 1.0$, $C_1 = 1.8$ and $C_2 = 0.52$ are constants that specified for the present case (Pope, 2001; Versteeg and Malalasekera, 2005).

The dissipation rate of the turbulent kinetic energy ε is calculated by

$$\frac{\partial \epsilon}{\partial t} + \overline{U_i}\frac{\partial \epsilon}{\partial x_i} = \frac{\partial}{\partial x_j}\left(v + \frac{v_t}{\sigma^\epsilon}\frac{\partial \epsilon}{\partial x_i}\right) - C_{\epsilon 1}\frac{\epsilon}{K}\overline{U_i' U_j'}\frac{\partial \overline{U_i}}{\partial x_j}$$
$$- C_{\epsilon 2}\frac{\epsilon^2}{K} \tag{9}$$

where the constants are $\sigma^\epsilon = 1.3, C_{\epsilon 1} = 1.44$ and $C_{\epsilon 2}$=1.92.

The Reynolds stress turbulence model (RSM) is particularly successful in reproducing the growth rate of the turbulence kinetic energy in the initial shear layer. As RSM naturally accounts for the stress anisotropy and phase lag between the stress and strain eigenvectors (Palkin et al., 2016). It has been used to predict the separation-induced transitions (Versteeg and Malalasekera, 2005; Yu and Yuan, 2014). The present study does not use wall functions because the RSM is free from any surface topography (Palkin et al., 2016).

Two non-dimensional parameters relevant to the present flow problems are given as follows:

$$Re = \frac{U_\infty d_w}{v} \tag{10}$$

$$C_D = \frac{2F_D}{\rho U_\infty^2 A_p} \tag{11}$$

Here, U_∞ is the free stream velocity, C_D represents the mean drag coefficient of the net panel, and A_p is the projected area. The Reynolds number calculated in Eq. (10) is based on the effective diameter of the net twine, as can be seen in Figure 2.

This work uses the non-dimensional computational domain with hexahedral grids. As exhibited in Figure 3, this domain uses the symmetry of the problem and is set as 2000d_w (length) × 1000d_w (width) × 1000 d_w (height) for the model (Lange et al., 1998; Bi et al., 2014a; Bi et al., 2017), d_w is the effective diameter of the net twine, which can be found in Figure 2 or from (McKenna et al., 2004; Evans and Ridge, 2005; Lader et al., 2015). We set the left and right sides of the domain as velocity inlet and pressure outlet. The pressure condition is set as zero normal pressure gradient at the inlet boundary. At the outlet boundary, the velocity condition is specified as zero normal gradient boundary conditions. Top, bottom, front and back sides are implemented as symmetry boundaries. To model an undisturbed flow channel slip, no slip walls are imposed on the net panel.

The domain is divided into the background and the refined regions. The refined region signifies the net panel and is surrounded by the background region. The prism captures the near-wall turbulent flow characteristics around net twines. For the equivalent-twine net, the height of the first prism layer, is dependent on the flow velocity (Reynolds number), is set as $3 \times 10^{-3} d_w$, $d_w = 3 \times 10^{-3}$m. Whereas, for the twisted-twine net, the height of the first prism layer is $2 \times 10^{-3} d_w$. With 15 prism layers being applied to each net, the total grid numbers of the computational domain are maximally 13.6 million for the equivalent-twine net and 19.9 million for the twisted-twine net.

Boundary conditions and discretization

We use the finite volume method (FVM) with structured grids to discretize the governing equations. The coupled scheme is implemented for pressure-velocity coupling. The discretization of the convective terms is conducted by the semi-implicit method for pressure-linked equations (SIMPLE) scheme. The spatial discretization of the pressure and momentum is conducted *via*

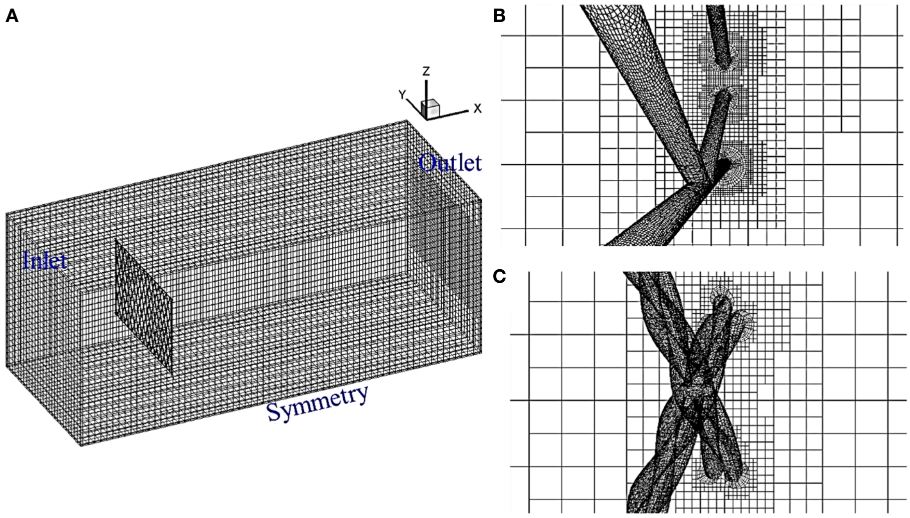

FIGURE 3
The schematics of the computational domain and the hexahedral grids. **(A)** The overall computational domain, **(B)** and **(C)** zoom-in views and prism layers around the net twines.

second-order and second-order upwind differencing schemes. The specific dissipation rate and Reynolds stresses are discretized using the first-order upwind scheme. The time step is $5 \times 10^{-3} d_w$, dw~O (10^{-3}) to the Reynolds number. We begin with some low inflow turbulence to initialize the turbulence equations. For instance, the initial turbulence intensity of 2.2% and $v_t/v \approx 5$ are used in the present study (Wilcox, 1998; Pope, 2001; Palkin et al., 2016). Once the turbulence field (e.g., eddy viscosity or turbulent stresses) is well established, the inflow turbulence is then switched off.

Verifications

This section conducts URANS and RSM simulations at subcritical Reynolds to verify the present flow solver. Two cases have been examined; these are (1) flow past a circular cylinder, (2) grid independence studies for equivalent- and twisted-twine nets. The specific physical questions raised in this section are:

i. What is the suitable grid strategy for flow past the aquaculture net?
ii. What are the dynamics of the shear layer and how does it affect the very near wake?
iii. How does the coherent motion affect the mean flow and the Reynolds stresses?

To address these questions, hydrodynamic characteristics and turbulence statistics of these structures are reported. Particularly, comparisons are conducted between smooth and twisted structures to gain insights into the first- and second-order turbulence statistics.

Flow past a circular cylinder

Flow past a smooth circular cylinder (referred to as flow past a circular cylinder) has been considered a classical problem in flow mechanics for centuries (Zdravkovich, 1997). There has been a surge in the numerical modeling of flow past a circular cylinder using various numerical simulations with the rapid growth of computing power. The purposes of investigating flow past a circular cylinder including (Jiang and Cheng, 2021)

(1) Resolving fundamental flow behaviors, e.g., flow structures, wake characteristics, turbulence statistics and hydrodynamic forces.
(2) Guiding practical applications, e.g., flow control (Choi et al., 2008; Yan et al., 2018), vortex-induced vibration (Williamson and Govardhan, 2004; Gsell et al., 2018).
(3) Testing the accuracy and robustness of new numerical methods and schemes.

The most well-studied case among different *Re* values is Re=3900, where flow characteristics and numerical findings have been reported extensively (Jiang and Cheng, 2021). It is worth mentioning that Parnaudeau et al. (2008) studied the flow past a circular cylinder at Re=3900 based on PIV experiments and LES. The experimental results suggested that the wake recirculation length, L_r, serves as the best indicator for determining the accuracy of the numerical simulation. Therefore, the present numerical results have been compared against the experimental results from (Parnaudeau et al., 2008); these include the hydrodynamic characteristics and the turbulence statistics. Three different grids based on the rectangle computational domains (Figure 4) are used in the present study for flow past circular cylinder to study the grid independence, as shown in Table 2.

In the present study, the rectangle computational domain is (30*D*) length × (20*D*) width × (20*D*) height, as shown in Figure 4. The grid numbers for three different domains are 1.8million, 2.6 million and 3.3 million, respectively. From Table 2, we see that the overall drag coefficient is smaller than the experimental measurement (e.g., $\lessapprox$2.7% variation in C_D), but the Strouhal number and the wake recirculation length is larger than the experimental measurement (e.g., $\lessapprox$1.4% variation in S_t and $\lessapprox$6.6% variation in L_r). The hydrodynamic forces and wake recirculation length show that the flow solver is not sensitive to the grids. We use a Medium grid to further examine the second-order turbulence statistics along the wake centerline at three typical locations of x/D = 1.06, 1.54 and 2.02, as exhibited in Figure 5. Considering the computing efficiency and convergence, statistics are acquired throughout 30 vortex shedding cycles.

Figure 5 shows the present mean velocities and fluctuations at *Re* = 3900 in comparison with the experimental results from (Parnaudeau et al., 2008) at three *x*-locations in the very near

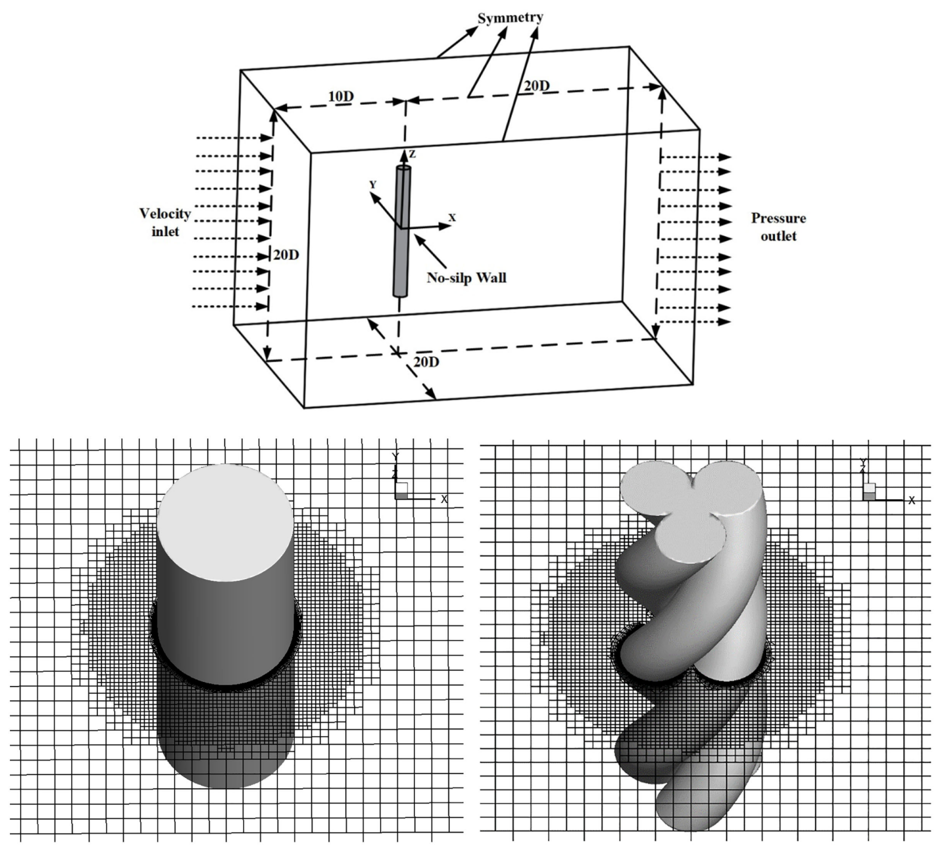

FIGURE 4
Computational domain and the prism layers for circular and twisted cylinders.

TABLE 2 Grid independence study of flow past a circular cylinder at *Re* = 3900.

Researcher	Method	C_D	S_t	L_r/D
Present numerical (Coarse)	URANS	0.959	0.211	1.61
Present numerical (Medium)	URANS	0.963	0.209	1.59
Present numerical (Fine)	URANS	0.961	0.208	1.60
Parnaudeau et al. (2008)	PIV	0.99 ± 0.05	0.208 ± 0.002	1.51 ± 0.1

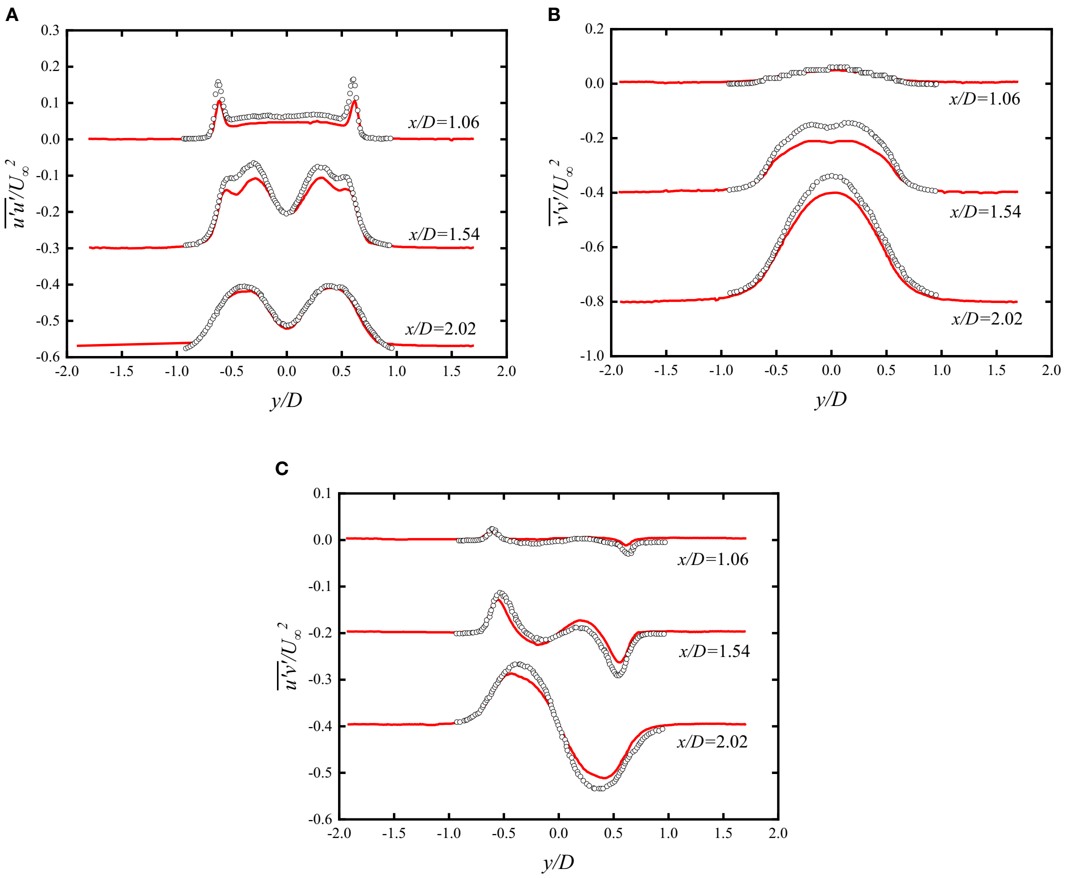

FIGURE 5
Normal and shear Reynolds stress component profiles for circular cylinders at Re=3900. (a) The variance of the streamwise velocity fluctuations ¯(u'u')/U_∞2. (b) Variance of the transverse velocity fluctuations ¯(v'v')/U_∞2. (c) Covariance of the velocity fluctuations ¯(u'v')/U_∞2. The solid red curve represents the present URANS simulation; empty black circles are experimental data reproduced from (Parnaudeau et al., 2008).

wake ($x/D \le 3$). The $\overline{u'u'}/U_\infty^2$ profiles in Figure 5A show a typical double-peak shape, mostly caused by the symmetrical shear layer transition. The present study has the same shape as the experiments of (Parnaudeau et al., 2008) at three selected positions. The peak values of $\overline{u'u'}/U_\infty^2$ at x/D = 1.06 and 1.54 are slightly lower than the experiments of (Parnaudeau et al., 2008), while a perfect match is found at x/D = 2.02. The $\overline{v'v'}/U_\infty^2$ profiles approach peak values at y/D = 0 as shown in Figure 5B, and the peak value increases alongside the downstream distance. The discrepancy exists between the present numerical simulations and experiments from (Parnaudeau et al., 2008). This discrepancy is mainly attributed to the transition of the shear layer. The $\overline{u'v'}/U_\infty^2$ show anti-symmetric profiles and the present numerical results are close to the experiments from (Parnaudeau et al., 2008). Overall, the present numerical results show a good agreement with the experiments of (Parnaudeau et al., 2008), demonstrating the accuracy and robustness of the present URANS approach in simulating flow past a circular cylinder. In particular, the present numerical approach has sufficient accuracy for predicting the first-order statistics at Re = 3900.

Grid independence study for equivalent-twine and twisted-twine nets

The equivalent-twine and twisted-twine nets characterized with the twine diameter d_w=3mm and S_n = 0.16 are selected to evaluate the grid sensitivity and numerical accuracy. This study examines different computational domains and y^+, as illustrated in Table 3. The domain dimension increases exponentially with a factor of $\sqrt{2}$, and the values of y^+ are adjusted around 1.0. The testing free stream velocity remains 1m/s, and the corresponding Reynolds number is 3000. C_D represents the mean drag coefficient and is calculated based on Eq. (11).

The numbers in the parentheses represent the grid numbers for twisted nets. Table 3 shows that the effect of domain dimension on the drag coefficient seems insignificant.

TABLE 3 Grid independent study at different domains and y^+.

Cases	Domain dimension/Grid number	C_D-smooth	C_D-twisted
Computational domain			
D1	$7L_C \times 3.5\ L_C \times 3.5\ L_C$	0.828	0.915
D2	$10\ L_C \times 5\ L_C \times 5\ L_C$	0.825	0.911
D3	$14\ L_C \times 7\ L_C \times 7\ L_C$	0.824	0.907
y^+			
1.15	280 (300) × 190 (200) × 190 (200)	0.822	0.931
1.0	295 (315) × 200 (220) × 200 (220)	0.831	0.918
0.85	310 (330) × 210 (240) × 210 (240)	0.838	0.922

However, a higher C_D has been witnessed when using D1 as the computational domain. This indicates that C_D could be slightly overestimated if the domain is relatively small. C_D is obtained to verify the grid sensitivity at the near-wall region (e.g., y^+). The results show that the grids in the near-wall region affect the C_D; thus, the grids in the near-wall region should be resolved carefully. Overall, the grid convergence is satisfied after the comparison of drag coefficients.

We see that the drag coefficients for twisted-twine nets (i.e., C_D-twisted) are larger than that of the equivalent-twine nets (i.e., C_D -smooth); this is also evident from (Tsukrov et al., 2011 and Wang et al., 2021). Eventually, the D2 domain and $y^+ = 1$ are used to verify the present numerical solver. The numerical predictions are compared with the experimental results of a yellow brass Chain-link diamond netting from (Tsukrov et al., 2011) and a four-strand braided diamond netting (i.e., ultra-cross knotless netting) from (Zhou et al., 2015). The twine diameter and the solidity of the yellow brass Chain-link diamond netting are 4 mm and $S_n = 0.18$; for the four-strand braided diamond netting, the solidity is 0.16. The samples of the netting are shown in Figure 6, and the comparisons of the drag coefficients for equivalent-twine and twisted-twine nets are exhibited in Figure 7.

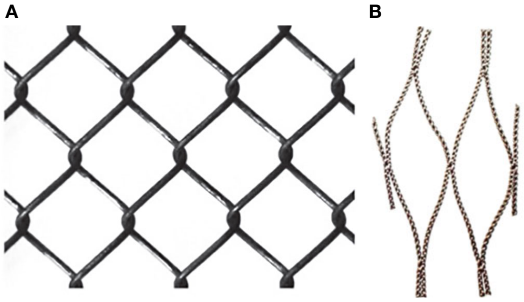

FIGURE 6
The samples of the netting. **(A)** The yellow brass ChainLink diamond netting, reproduced from (Tsukrov et al., 2011). **(B)** The four-strand braided diamond netting, reproduced from (Zhou et al., 2015).

Figure 7A reveals that the comparative results of drag coefficients for the yellow brass Chain-link diamond netting are close to each other (e.g., $\lesssim$12.7% variation in C_D). However, the drag coefficients obtained from the present numerical simulations are overall smaller than that in (Zhou et al., 2015), as shown in Figure 7B. It is worth mentioning that in their study, Zhou et al. (2015) examined a four-strand twisted netting, which is slightly different from what we study in the present work, because in our study a three-strand netting is used. In addition, Zhou et al. (2015) also claimed that two-strand netting showed a lower drag coefficient in comparison to that of the three-strand, even though the two-strand netting owns a larger solidity. Hence, it is reasonably established in Figure 7B that the drag coefficient of the present three-strand twisted netting is lower than that of the four-strand from (Zhou et al., 2015). In summary, alongside the angle of attack, the Reynolds number and the solidity, structure patterns such as woven type of the net twines also significantly affect the drag coefficient of the netting.

Verifications in this section demonstrate that the present URANS framework is valid in predicting flow past smooth and twisted bodies regarding cylinders and nets. Particularly, it is more compatible in predicting second-order turbulence statistics. Next, we will provide specific wake and turbulence characteristics of the target nets since the verifications have been extensively exhibited.

Results and discussion

To examine the effects of helixes on the vortex formations in the wake, Figure 8 exhibits the comparison of the instantaneous vortex structures of the equivalent-twine and twisted-twine nets at $Re = 4500$ and AOA = 90°. The three-dimensional vortex structures are visualized based on the Q-criterion and it is defined as $Q = -(S_{ij}\text{-}S_{ij}\text{-}\Omega_{ij}\Omega_{ij})/2$, where S_{ij} is the strain rate and Ω_{ij} is the rotation rate tensor (Hunt et al., 1988). The Q-criterion is colored by iso-contours of the streamwise velocity.

The fully turbulent effect is established with the observation of small-scale vortex structures in the instantaneous field of the wake. Vortex shedding overall is well-organized but not as regular as the classical Karman vortex. There is little wake

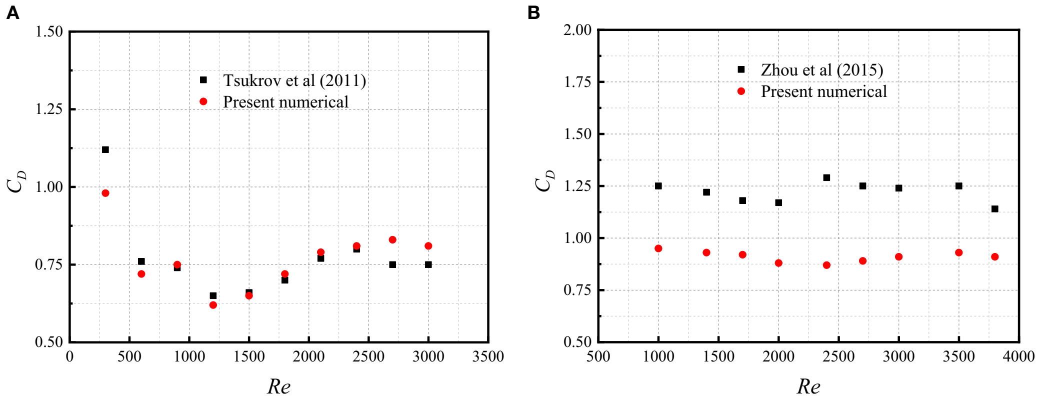

FIGURE 7
The dependence of drag coefficient on the Reynolds number. **(A)** Drag coefficients of the yellow brass ChainLink diamond netting. **(B)** Drag coefficients of four-strand braided diamond netting.

interference between net twines under a certain net solidity of 0.16, but vortex interaction does exist when flow passes through the net twines. The vortex structures of the twisted-twine net are much smaller than that of the equivalent-twine net. As the inner shear layer of the twisted-twine net is disturbed by the helixes. Furthermore, small-scale vortices are observed to be attached in the turbulent boundary layer of the twisted-twine net, and the shear layer seems to be suppressed by the helixes. Consequently, the separated shear layer at subcritical Reynolds is turbulent, represented by small-scale vortices. As a result, the fluctuating velocity and the Reynolds normal stress components in the shear layer decrease.

Three selected horizontal planes perpendicular to the net are used to present the two-dimensional instantaneous streamlines of the individual net twines. These horizontal planes are defined as $z = 0$ (Middle) and $z = \pm 0.14$m (Top and Bottom), based on the net height. Two-dimensional instantaneous streamlines of the net twines in these three selected planes are depicted in Figure 9 to provide close-up views of the turbulence characteristics. The vortex structures generated by the flow separation show distinct features. Symmetric vortices form behind the equivalent net twine and single vortices appear behind the twisted twines. The vortices behind the twisted twines show wall-attached characteristics after the separation point. The recirculation length, L_r, of the equivalent net twine is around 2.2 d_w, which is longer than that of the twisted twine ($1.6d_w$).

The unsteady flow velocity fluctuations caused by the vortex shedding give rise to the Reynolds stresses in the near wake. Moreover, the transition to turbulence in the laminar shear layer also contributes to the Reynolds stresses. Therefore, to better understand the turbulence characteristics in the wake, it is vitally important to examine the Reynolds stresses. Figure 10 depicts the normal and shear Reynolds stresses in the near and far wake regions of the equivalent-twine and the twisted-twine nets. The Reynolds normal stresses $\overline{u'u'}/U_\infty^2$, $\overline{v'v'}/U_\infty^2$ and $\overline{w'w'}/U_\infty^2$ show symmetric profiles while the Reynolds shear stress $\overline{u'v'}/U_\infty^2$ has an anti-symmetric profile. Moreover, the amplitude of Reynolds stress fluctuations for the equivalent-twine net is higher than that of the twisted-twine net.

Of all the Reynolds stresses, $\overline{u'u'}/U_\infty^2$ show the highest fluctuations. The maximum value is found to be 0.13 U_∞^2 in the near wake of the equivalent-twine net. In comparison to the equivalent-twine net, there is a conspicuous reduction in the fluctuation magnitude of the $\overline{u'u'}/U_\infty^2$ for the twisted-twine net. In particular, a nearly 23% reduction in the $\overline{u'u'}/U_\infty^2$ is evident between the two nets. This significant reduction is caused by the decrease in streamwise velocity fluctuations in the near wake. The Reynolds normal stress $\overline{u'u'}/U_\infty^2$ is also related to the vortex formation (Williamson, 1996). The location of the maximum $\overline{u'u'}/U_\infty^2$ closely follows the extent of the recirculation zone. This causes the vortex formation length to decrease.

The $\overline{v'v'}/U_\infty^2$ and the $\overline{w'w'}/U_\infty^2$ are related to the transverse velocity, contributing to the fluctuating kinetic energy in the wake (Ma et al., 2000; Zhu et al., 2020). The magnitudes of the Reynolds stresses $\overline{v'v'}/U_\infty^2$ and $\overline{w'w'}/U_\infty^2$ show their maximum values due to the vortices formed in the shear layers. For the equivalent-twine net, the maximum $\overline{v'v'}/U_\infty^2$ and $\overline{w'w'}/U_\infty^2$ are found to be 0.11 U_∞^2 and 0.10 U_∞^2 in the near wake. For the twisted-twine net, the fluctuation amplitudes of $\overline{v'v'}/U_\infty^2$ and $\overline{w'w'}/U_\infty^2$ decrease compared to the equivalent-twine net.

The Reynolds shear stress $\overline{u'v'}/U_\infty^2$ contributes to the momentum transport in the wake of the net (Matsumura and Antonia, 1993). The Reynolds shear stresses show anti-symmetric profiles mostly because the anti-symmetric vortex shedding dominates the wake. For the equivalent-twine net, the

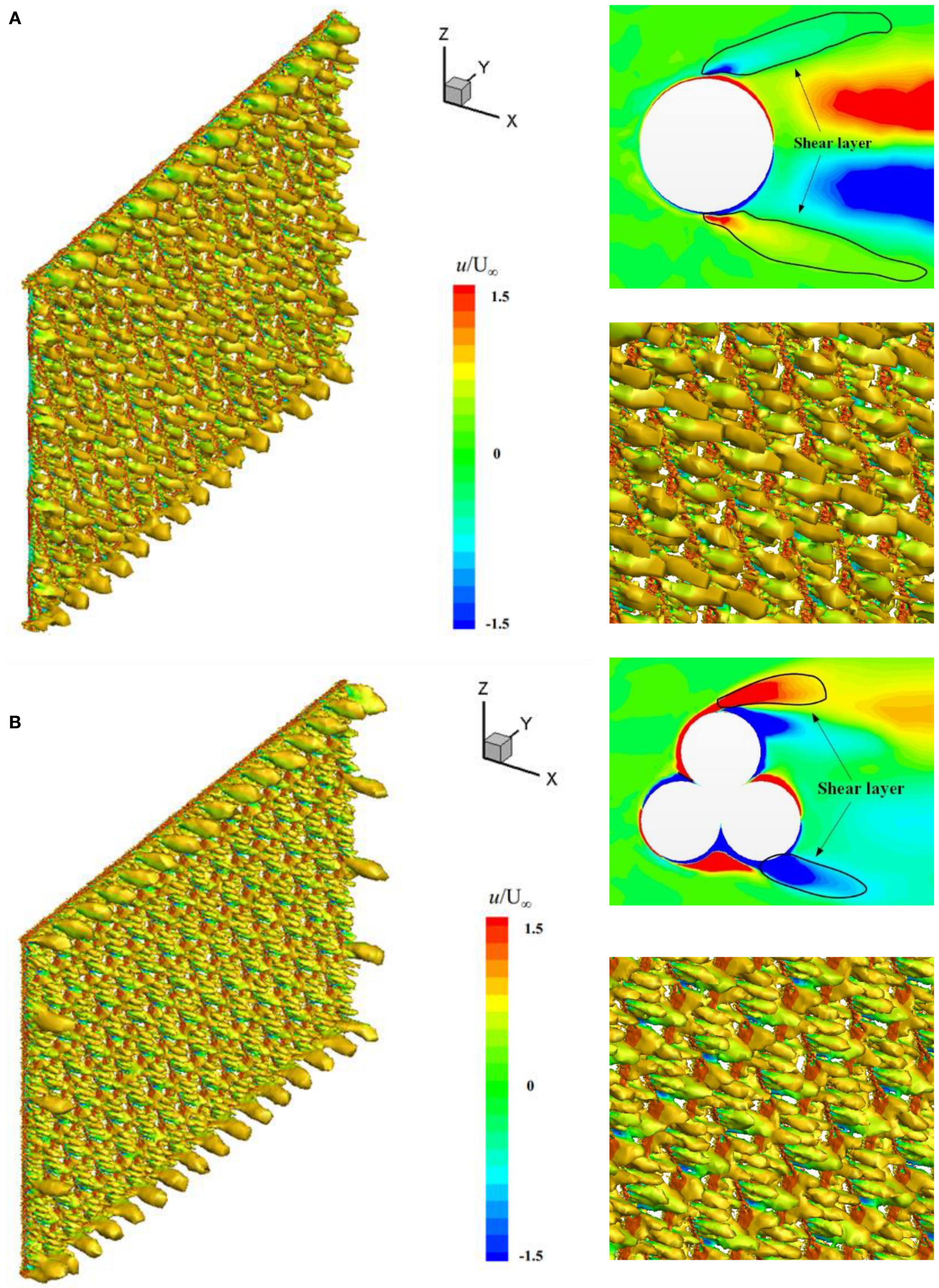

FIGURE 8
Instantaneous vortex structures and detailed shear layers of the individual twines at *Re* = 4500. **(A)** Equivalent-twine net and **(B)** twisted-twine net.

maximum $\overline{u'v'}/U_\infty^2$ is found to be 0.01 U_∞^2. The magnitude of $\overline{u'v'}/U_\infty^2$ decreases significantly due to the addition of the helixes on the twisted twines.

Figures 11, 12 depict the turbulence kinetic energy (TKE) contours and statistics for both equivalent-twine and twisted-twine nets. The TKE is associated with momentum, heat transport and turbulence intensity (Matsumura and Antonia, 1993; Pope, 2001). In addition, the TKE can be used to approximate turbulence diffusion. Thus, the TKE is one of the most critical variables in a turbulent flow. Understanding the

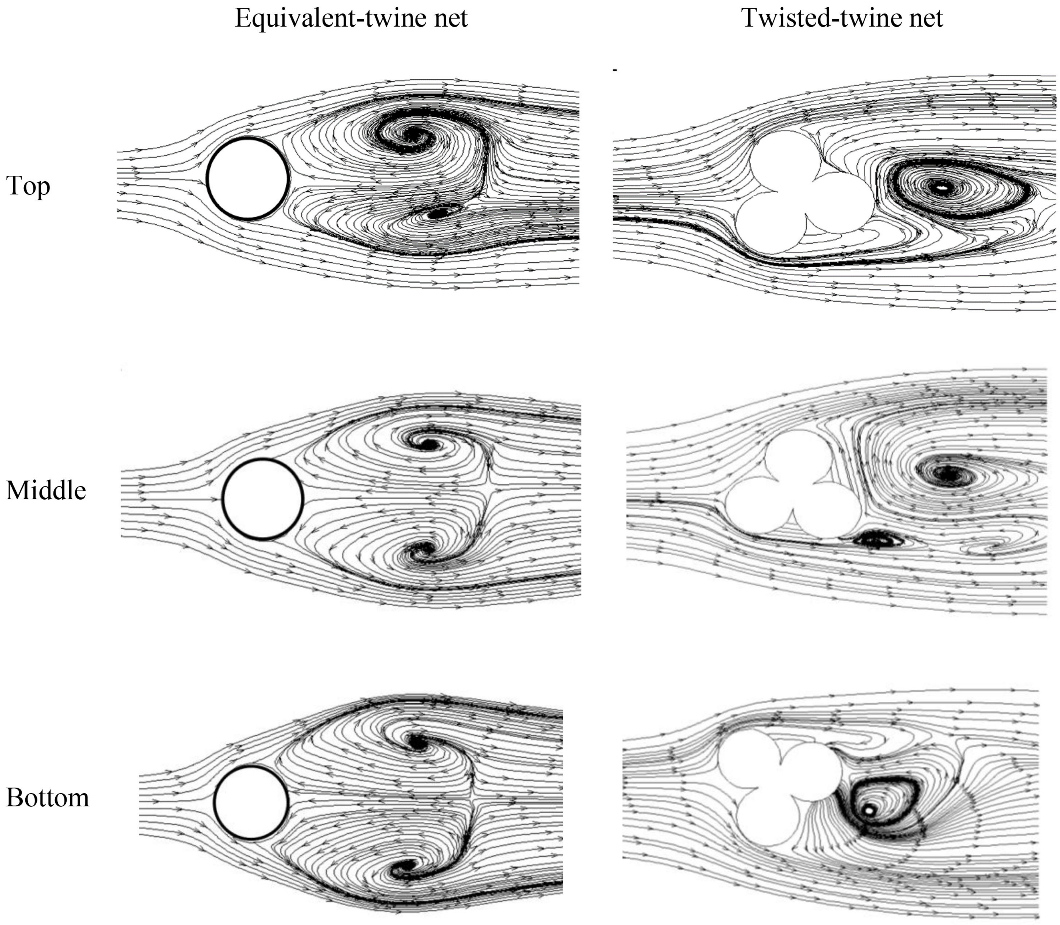

FIGURE 9
Streamlines around the equivalent net twines (left column) and the twisted net twines (right column) at different planes of the nets for *Re* = 4500.

turbulence fluctuations (usually the fluctuating velocity) is instructive to examine the TKE. This study follows the definition of (Wilcox, 1998) in which TKE is half the trace of the Reynolds stress tensor, and it is defined as $k = (\overline{u'u'} + \overline{v'v'} + \overline{w'w'})/2U_\infty^2$.

Figure 11 shows that the TKE of the equivalent-twine net is larger than that of the twisted-twine net. This is due to the helixes on the twisted twines which hinder the development of the flow. This then results in less fluctuating velocities in the near wake. Consequently, the wider turbulent region appears in the wake of the equivalent-twine net, while the twisted-twine net shows a narrower turbulent region. The observation from Figure 11 has also been confirmed by Figure 12, where the statistics show detailed profiles for these two different nets. The average difference of the TKE for these two different nets is 16%. Which means at least 3.3% of the fluctuating velocity is lost due to the effect of the helixes. Furthermore, the energy in the wake of the twisted-twine net is relatively low because of the galloping response induced by the helixes. It can be concluded that the helixes could cause a decrease in turbulent kinetic energy.

Conclusions

In this paper, two diamond-mesh net panels, namely the equivalent-twine and the twisted-twine nets with the dimension of 0.6m (length)×0.4m (height), are numerically examined to understand the wake and turbulence characteristics of the aquaculture nets. To capture the unsteady flow effect induced by the wall-shear stress regarding the free stream velocity, Unsteady Reynolds-averaged Navier-Stokes (URANS) simulations are conducted. The subcritical Reynolds number $Re = 4.5 \times 10^3$ is selected for all simulation cases based on the effective diameter of the net twine. The Reynolds stress model (RSM) is used to resolve the separation-induced transition problems.

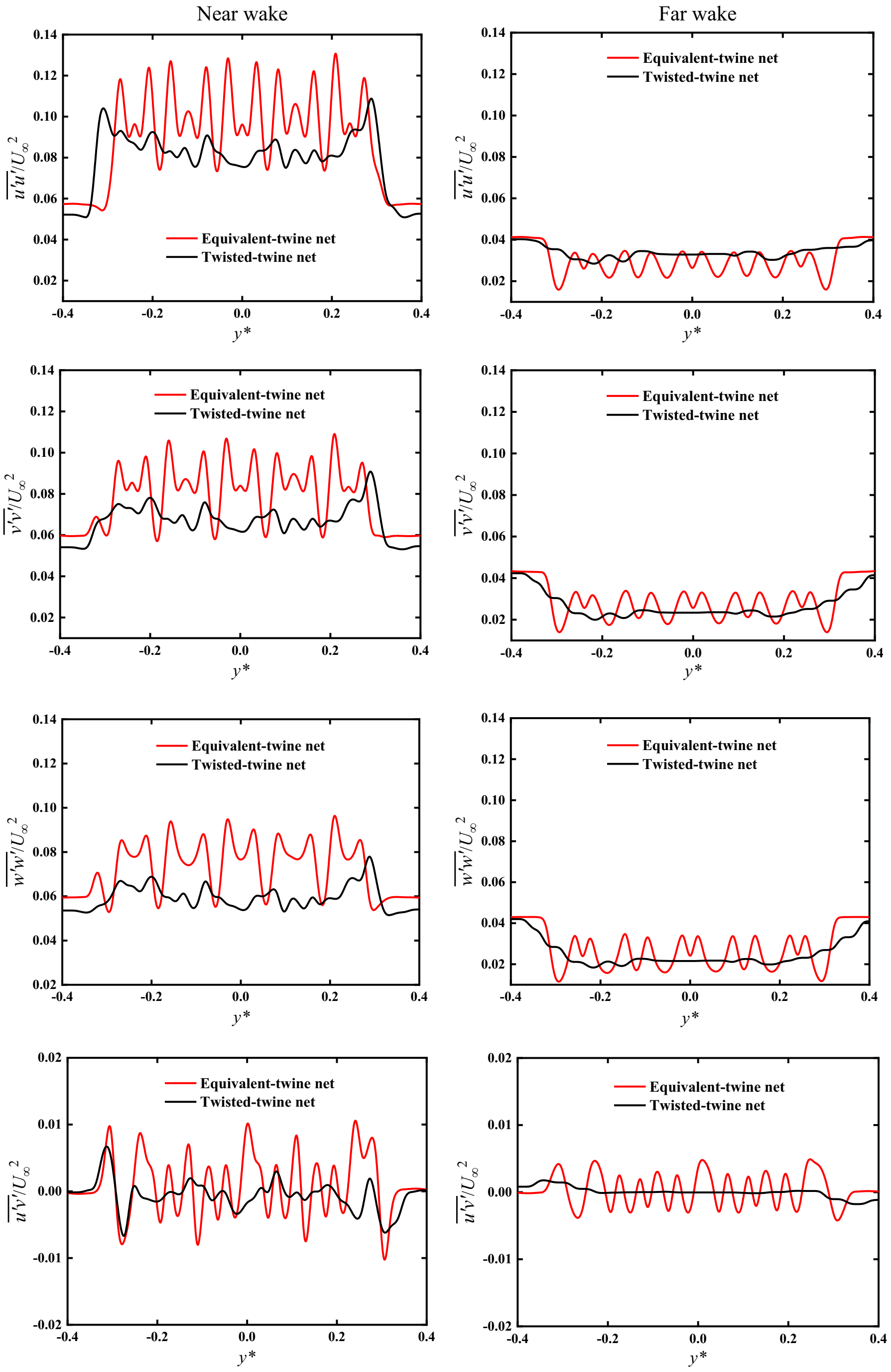

FIGURE 10
Profiles of the normal and shear Reynolds stress components in the near- and far-wake regions "*" means the dimensionlessization of y. y*=y (m)/1(m) ,"m" means Unit of length – meter.

The overall vortex shedding for these two nets is well organized but not as regular as the classical Karman vortex. Due to the helixes the vortex structures of the twisted-twine net are smaller compared to the equivalent-twine. Two-dimensional close-up views show that symmetric vortices form behind the equivalent net twine and single vortices appear behind the twisted twines. The recirculation length of the equivalent twine is longer than that of the twisted twine. Similar to the mean velocity profiles, the Reynolds normal and shear stresses

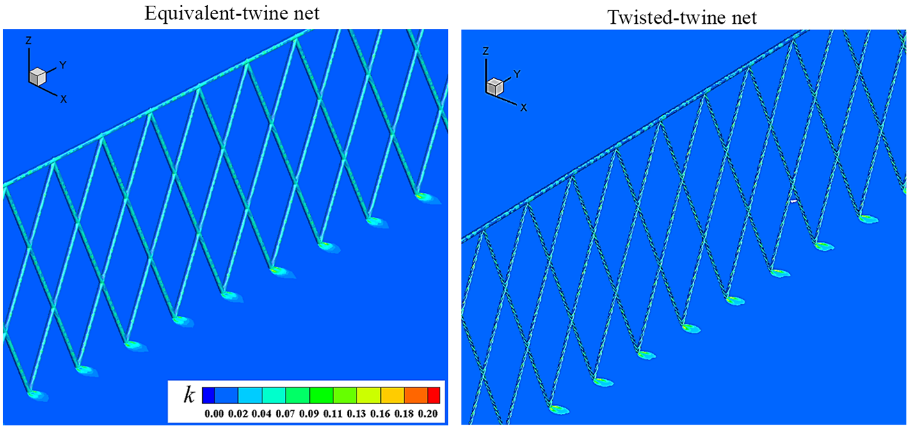

FIGURE 11
Comparison of the turbulent kinetic energy contours by the URANS model at AOA = 90°.

show symmetric and anti-symmetric profiles, respectively. $\overline{u'u'}/U_\infty^2$ causes the decrease of the vortex formation length, $\overline{v'v'}/U_\infty^2$ and $\overline{w'w'}/U_\infty^2$ provide the most contribution to the fluctuating kinetic energy, and $\overline{u'v'}/U_\infty^2$ contributes to the momentum transport in the wake. Compared to the other Reynolds stress components, $\overline{u'u'}/U_\infty^2$ shows the highest fluctuations and the maximum value is 0.13 U_∞^2 in the near wake of the equivalent-twine net. The turbulent regions and the statistics clearly show that the helixes on the twisted twines lead to decreased turbulence kinetic energy.

This study provides insight into understanding the drag coefficient discrepancy between the equivalent-twine and the twisted-twine nets based on their wake and turbulent mechanisms. Engineers need to properly identify the net type for preliminary design of marine aquaculture cages to avoid over- or under-estimating the drag forces. Future studies should focus on wake and turbulent characteristics of three-dimensional net cages to better guide the design of marine aquaculture systems.

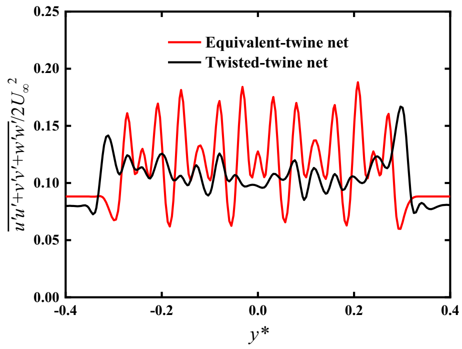

FIGURE 12
Comparison of the turbulent kinetic energy along the transverse direction of the equivalent-twine and the twisted-twine nets.

Data availability statement

The original contributions presented in the study are included in the article/supplementary materials. Further inquiries can be directed to the corresponding author.

Author contributions

LX completed the numerical calculation and writing of the paper, PL performed the numerical analysis of the paper, HQ provided financial support, and ZX performed the typesetting and revision of the paper. All authors contributed to the article and approved the submitted version.

Funding

This work was financially supported by the National Natural Science Foundation of China (Grant No. 51909040), Natural Science Foundation of Heilongjiang Province (Grant No. LH2020E073), the Key Technology Research and Development Program of Shandong (Grant No. 2020CXGC010702), the Stable Supporting Fund of Science and Technology on Underwater Vehicle Technology (Grant No. JCKYS2022SXJQR-11), the Jiangsu Province Science Foundation for Youths (Grant No. BK20220221), and the High-tech Ship Research Projects Sponsored by the Ministry of Industry and Information Technology (2019[357]).

Conflict of interest

The authors declare that the research was conducted in the absence of any commercial or financial relationships that could be construed as a potential conflict of interest.

Publisher's note

References

ANSYS (2017). *ANSYS fluent 18.2 user's guide* (Canonsburg, PA, USA: ANSYS, Inc.).

Bi, C.-W., Balash, C., Matsubara, S., Zhao, Y.-P., and Dong, G.-H. (2017). Effects of cylindrical cruciform patterns on fluid flow and drag as determined by CFD models. *Ocean Eng.* 135, 28–38. doi: 10.1016/j.oceaneng.2017.02.032

Bi, C.-W., Chen, Q.-P., Zhao, Y.-P., Su, H., and Wang, X.-Y. (2020). Experimental investigation on the hydrodynamic performance of plane nets fouled by hydroids in waves. *Ocean Eng.* 213, 107839. doi: 10.1016/j.oceaneng.2020.107839

Bi, C.-W., Zhao, Y.-P., Dong, G.-H., Wu, Z.-M., Zhang, Y., and Xu, T.-J. (2018). Drag on and flow through the hydroid-fouled nets in currents. *Ocean Eng.* 161, 195–204. doi: 10.1016/j.oceaneng.2018.05.005

Bi, C.-W., Zhao, Y.-P., Dong, G.-H., Xu, T.-J., and Gui, F.-K. (2013). Experimental investigation of the reduction in flow velocity downstream from a fishing net. *Aquacult. Eng.* 57, 71–81. doi: 10.1016/j.aquaeng.2013.08.002

Bi, C.-W., Zhao, Y.-P., Dong, G.-H., Xu, T.-J., and Gui, F.-K. (2014a). Numerical simulation of the interaction between flow and flexible nets. *J. Fluids Struct.* 45, 180–201. doi: 10.1016/j.jfluidstructs.2013.11.015

Bi, C.-W., Zhao, Y.-P., Dong, G.-H., Zheng, Y.-N., and Gui, F.-K. (2014b). A numerical analysis on the hydrodynamic characteristics of net cages using coupled fluid–structure interaction model. *Aquacult. Eng.* 59, 1–12. doi: 10.1016/j.aquaeng.2014.01.002

Bui, C. M., Ho, T. X., and Khieu, L. H. (2020). Numerical study of a flow over and through offshore fish cages. *Ocean Eng.* 201, 107140. doi: 10.1016/j.oceaneng.2020.107140

Chen, H., and Christensen, E. D. (2016). Investigations on the porous resistance coefficients for fishing net structures. *J. Fluids Struct.* 65, 76–107. doi: 10.1016/j.jfluidstructs.2016.05.005

Chen, H., and Christensen, E. D. (2017). Development of a numerical model for fluid-structure interaction analysis of flow through and around an aquaculture net cage. *Ocean Eng.* 142, 597–615. doi: 10.1016/j.oceaneng.2017.07.033

Chen, H., and Christensen, E. D. (2018). Simulating the hydrodynamic response of a floater–net system in current and waves. *J. Fluids Struct.* 79, 50–75. doi: 10.1016/j.jfluidstructs.2018.01.010

Cheng, H., Li, L., Ong, M. C., Aarsæther, K. G., and Sim, J. (2021). Effects of mooring line breakage on dynamic responses of grid moored fish farms under pure current conditions. *Ocean Eng.* 237, 109638. doi: 10.1016/j.oceaneng.2021.109638

Choi, H., Jeon, W.-P., and Kim, J. (2008). Control of flow over a bluff body. *Annu. Rev. Fluid Mech.* 40, 113–139. doi: 10.1146/annurev.fluid.39.050905.110149

DeCew, J., Fredriksson, D., Lader, P., Chambers, M., Howell, W., Osienki, M., et al. (2013). Field measurements of cage deformation using acoustic sensors. *Aquacult. Eng.* 57, 114–125. doi: 10.1016/j.aquaeng.2013.09.006

Evans, J. J., and Ridge, I. M. L. (2005). *Rope and rope-like structures[J]* Vol. 20 (WIT Transactions on State-of-the-art in Science and Engineering).

Fredheim, A. (2005). Current forces on net structure. (PhD Thesis)[J]. Trondheim, Norway Norwegian University of Science and Technology, , 139.

Fredriksson, D., DeCew, J., Lader, P., Volent, Z., Jensen, Ø., and Willumsen, F. (2014). A finite element modeling technique for an aquaculture net with laboratory measurement comparisons. *Ocean Eng.* 83, 99–110. doi: 10.1016/j.oceaneng.2014.03.005

Fredriksson, D. W., DeCew, J., Swift, M. R., Tsukrov, I., Chambers, M. D., and Celikkol, B. (2004). The design and analysis of a four-cage grid mooring for open ocean aquaculture. *Aquacult. Eng.* 32 (1), 77–94. doi: 10.1016/j.aquaeng.2004.05.001

Fredriksson, D. W., DeCew, J. C., and Tsukrov, I. (2007). Development of structural modeling techniques for evaluating HDPE plastic net pens used in marine aquaculture. *Ocean Eng.* 34 (16), 2124–2137. doi: 10.1016/j.oceaneng.2007.04.007

Fredriksson, D. W., Swift, M. R., Irish, J. D., Tsukrov, I., and Celikkol, B. (2003). Fish cage and mooring system dynamics using physical and numerical models with field measurements. *Aquacult. Eng.* 27 (2), 117–146. doi: 10.1016/S0144-8609(02)00043-2

Gsell, S., Bourguet, R., and Braza, M. (2018). Three-dimensional flow past a fixed or freely vibrating cylinder in the early turbulent regime. *Phys. Rev. Fluids* 3 (1), 013902. doi: 10.1103/PhysRevFluids.3.013902

Hunt, J., Wray, A., and Moin, P. (1988). Eddies, streams, and convergence zones in turbulent flows. 2 *Proc. Summer Program (Center Turbul. Res. 1988)*, 193–208.

Jiang, H., and Cheng, L. (2021). Large-Eddy simulation of flow past a circular cylinder for reynolds numbers 400 to 3900. *Phys. Fluids* 33 (3), 034119. doi: 10.1063/5.0041168

Klebert, P., and Su, B. (2020). Turbulence and flow field alterations inside a fish sea cage and its wake. *Appl. Ocean Res.* 98, 102113. doi: 10.1016/j.apor.2020.102113

Lader, P. F., and Fredheim, A. (2006). Dynamic properties of a flexible net sheet in waves and current–a numerical approach. *Aquacult. Eng.* 35 (3), 228–238. doi: 10.1016/j.aquaeng.2006.02.002

Lader, P., Fredriksson, D. W., Guenther, J., Volent, Z., Blocher, N., Kristiansen, D., et al. (2015). Drag on hydroid-fouled nets–an experimental approach. *China Ocean Eng.* 29 (3), 369–389. doi: 10.1007/s13344-015-0026-y

Lader, P., Jensen, A., Sveen, J. K., Fredheim, A., Enerhaug, B., and Fredriksson, D. (2007). Experimental investigation of wave forces on net structures. *Appl. Ocean Res.* 29 (3), 112–127. doi: 10.1016/j.apor.2007.10.003

Lange, C. F., Durst, F., and Breuer, M. (1998). Momentum and heat transfer from cylinders in laminar crossflow at 10– 4≨ Re≨ 200. *Int. J. Heat Mass Transf.* 41 (22), 3409–3430. doi: 10.1016/S0017-9310(98)00077-5

Liu, L., Kinoshita, T., Wan, R., Bao, W., and Itakura, H. (2012). Experimental investigation and analysis of hydrodynamic characteristics of a net panel oscillating in water. *Ocean Eng.* 47, 19–29. doi: 10.1016/j.oceaneng.2012.03.013

Ma, X., Karamanos, G.-S., and Karniadakis, G. (2000). Dynamics and low-dimensionality of a turbulent near wake. *J. Fluid Mech.* 410, 29–65. doi: 10.1017/S0022112099007934

Martin, T., Kamath, A., and Bihs, H. (2020). A Lagrangian approach for the coupled simulation of fixed net structures in a eulerian fluid model. *J. Fluids Struct.* 94, 102962. doi: 10.1016/j.jfluidstructs.2020.102962

Matsumura, M., and Antonia, R. (1993). Momentum and heat transport in the turbulent intermediate wake of a circular cylinder. *J. Fluid Mech.* 250, 651–668. doi: 10.1017/S0022112093001600

McKenna, H. A., Hearle, J. W., and O'Hear, N. (2004). *Handbook of fibre rope technology* (Woodhead publishing).

Palkin, E., Mullyadzhanov, R., Hadziabdic, M., and Hanjalic, K. (2016). Scrutinizing URANS in shedding flows: The case of cylinder in cross-flow in the subcritical regime. *Flow Turbul. Combust.* 97 (4), 1–30. doi: 10.1007/s10494-016-9772-z

Park, S., Lee, J., and Lee, C. W. (2021). Design evaluation of a fish cage mooring system with different bridle line connections using model experiments and simulations. *Aquacult. Eng.* 94, 102177. doi: 10.1016/j.aquaeng.2021.102177

Parnaudeau, P., Carlier, J., Heitz, D., and Lamballais, E. (2008). Experimental and numerical studies of the flow over a circular cylinder at reynolds number 3900. *Phys. Fluids* 20 (8), 085101. doi: 10.1063/1.2957018

Patursson, Ø., Swift, M. R., Tsukrov, I., Simonsen, K., Baldwin, K., Fredriksson, D. W., et al. (2010). Development of a porous media model with application to flow through and around a net panel. *Ocean Eng.* 37 (2-3), 314–324. doi: 10.1016/j.oceaneng.2009.10.001

Pope, S. B. (2001). *Turbulent flows* (IOP Publishing).

Priour, D. (2003). Analysis of nets with hexagonal mesh using triangular elements. *Int. J. numer. Methods Eng.* 56 (12), 1721–1733. doi: 10.1002/nme.635

Su, B., Kelasidi, E., Frank, K., Haugen, J., Føre, M., and Pedersen, M. O. (2021). An integrated approach for monitoring structural deformation of aquaculture net cages. *Ocean Eng.* 219:108424. doi: 10.1016/j.oceaneng.2020.108424

Swift, M. R., Fredriksson, D. W., Unrein, A., Fullerton, B., Patursson, O., and Baldwin, K. (2006). Drag force acting on biofouled net panels. *Aquacult. Eng.* 35 (3), 292–299. doi: 10.1016/j.aquaeng.2006.03.002

Tang, M.-F., Xu, T.-J., Dong, G.-H., Zhao, Y.-P., and Guo, W.-J. (2017). Numerical simulation of the effects of fish behavior on flow dynamics around net cage. *Appl. Ocean Res.* 64, 258–280. doi: 10.1016/j.apor.2017.03.006

Tang, H. J., Yang, R. Y., and Yao, H. C. (2021). Experimental and numerical investigations of a mooring line failure of an aquaculture net cage subjected to currents. *Ocean Eng.* 238, 109707. doi: 10.1016/j.oceaneng.2021.109707

Tsukrov, I., Drach, A., DeCew, J., Swift, M. R., and Celikkol, B. (2011). Characterization of geometry and normal drag coefficients of copper nets. *Ocean Eng.* 38 (17-18), 1979–1988. doi: 10.1016/j.oceaneng.2011.09.019

Tsukrov, I., Eroshkin, O., Fredriksson, D., and Robinson, M. (2003). Finite element modeling of net panels using a consistent net element. *Ocean Eng.* 30, 251–270. doi: 10.1016/S0029-8018(02)00021-5

Tsukrov, I., Eroshkin, O., Paul, W., and Celikkol, B. (2005). Numerical modeling of nonlinear elastic components of mooring systems. *IEEE J. Ocean. Eng.* 30 (1), 37–46. doi: 10.1109/JOE.2004.841396

Tsukrov, I., Ozbay, M., Swift, M. R., Celikkol, B., Fredriksson, D. W., and Baldwin, K. (2000). Open ocean aquaculture engineering: numerical modeling. *Mar. Technol. Soc. J.* 34 (1), 29–40. doi: 10.4031/MTSJ.34.1.4

Tu, G., Liu, H., Ru, Z., Shao, D., Yang, W., Sun, T., et al. (2020). Numerical analysis of the flows around fishing plane nets using the lattice Boltzmann method. *Ocean Eng.* 214, 107623. doi: 10.1016/j.oceaneng.2020.107623

Versteeg, H. K., and Malalasekera, W. (2005). *An introduction to computational fluid dynamics* (New York: Wiley).

Wang, G., Martin, T., Huang, L., and Bihs, H. (2021). Modelling the flow around and wake behind net panels using large eddy simulations. *Ocean Eng.* 239, 109846. doi: 10.1016/j.oceaneng.2021.109846

Wilcox, B. (1998). *Turbulence modeling for CFD | clc* (Turbulent Flow).

Williamson, C. H. (1996). Vortex dynamics in the cylinder wake. *Annu. Rev. Fluid Mech.* 28 (1), 477–539. doi: 10.1146/annurev.fl.28.010196.002401

Williamson, C. H., and Govardhan, R. (2004). Vortex-induced vibrations. *Annu. Rev. Fluid Mech.* 36, 413–455. doi: 10.1146/annurev.fluid.36.050802.122128

Winthereig-Rasmussen, H., Simonsen, K., and Patursson, Ø. (2016). Flow through fish farming sea cages: Comparing computational fluid dynamics simulations with scaled and full-scale experimental data. *Ocean Eng.* 124, 21–31. doi: 10.1016/j.oceaneng.2016.07.027

Xu, Z., and Qin, H. (2020). Fluid-structure interactions of cage based aquaculture: From structures to organisms. *Ocean Eng.* 217, 107961. doi: 10.1016/j.oceaneng.2020.107961

Xu, L., Qin, H., Li, P., and Xu, Z. (2022). Numerical modeling of flexible net panels under steady flow using a coupled fluid–structure partitioned scheme. *Appl. Sci.* 12 (7), 3399. doi: 10.3390/app12073399

Yan, T., Wang, R., Bao, Y., Zhou, D., Zhu, H., Ping, H., et al. (2018). Modification of turbulent wake characteristics by two small control cylinders at a subcritical reynolds number. *Phys. Fluids* 30 (10), 105106. doi: 10.1063/1.5046447

Yao, Y., Chen, Y., Zhou, H., and Yang, H. (2016). Numerical modeling of current loads on a net cage considering fluid–structure interaction. *J. Fluids Struct.* 62, 350–366. doi: 10.1016/j.jfluidstructs.2016.01.004

Yu, K. T., and Yuan, X. (2014). *Introduction to computational mass transfer* Vol. XI (Berlin Heidelberg: Springer-Verlag), 337.

Zdravkovich, M. M. (1997). *Flow around circular cylinders: Volume 2: Applications* (Oxford university press).

Zhao, Y.-P., Bi, C.-W., Dong, G.-H., Gui, F.-K., Cui, Y., Guan, C.-T., et al. (2013a). Numerical simulation of the flow around fishing plane nets using the porous media model. *Ocean Eng.* 62, 25–37. doi: 10.1016/j.oceaneng.2013.01.009

Zhao, Y.-P., Bi, C.-W., Dong, G.-H., Gui, F.-K., Cui, Y., and Xu, T.-J. (2013b). Numerical simulation of the flow field inside and around gravity cages. *Aquacult. Eng.* 52, 1–13. doi: 10.1016/j.aquaeng.2012.06.001

Zhao, Y.-P., Li, Y.-C., Dong, G.-H., Gui, F.-K., and Wu, H. (2008). An experimental and numerical study of hydrodynamic characteristics of submerged flexible plane nets in waves. *Aquacult. Eng.* 38 (1), 16–25. doi: 10.1016/j.aquaeng.2007.10.004

Zhou, C., Xu, L., Hu, F., and Qu, X. (2015). Hydrodynamic characteristics of knotless nylon netting normal to free stream and effect of inclination. *Ocean Eng.* 110, 89–97. doi: 10.1016/j.oceaneng.2015.09.043

Zhu, H., Ping, H., Wang, R., Bao, Y., Zhou, D., Wei, X., et al. (2020). Dynamic response of a cable with triangular cross section subject to uniform flow at reynolds number 3900. *Phys. Fluids* 32 (4), 045103.

frontiers | Frontiers in Marine Science

TYPE Original Research
PUBLISHED 08 December 2022
DOI 10.3389/fmars.2022.1057419

OPEN ACCESS

EDITED BY
Wei-Bo Chen,
National Science and Technology
Center for Disaster Reduction
(NCDR), Taiwan

REVIEWED BY
Jinhai Zheng,
Hohai University, China
Hassan Saghi,
University of Zagreb, Croatia
Bang-Fuh Chen,
National Sun Yat-sen
University, Taiwan
Xiaosen Xu,
Jiangsu University of Science and
Technology, China

*CORRESPONDENCE
Chunwei Bi
bichunwei@ouc.edu.cn

SPECIALTY SECTION
This article was submitted to
Ocean Solutions,
a section of the journal
Frontiers in Marine Science

RECEIVED 18 October 2022
ACCEPTED 16 November 2022
PUBLISHED 08 December 2022

CITATION
Zhu X, Dong G, Bi C and Zhao Y
(2022) Wave diffraction of a hybrid
wind turbine foundation with a
double-layer aquaculture cage.
Front. Mar. Sci. 9:1057419.
doi: 10.3389/fmars.2022.1057419

Wave diffraction of a hybrid wind turbine foundation with a double-layer aquaculture cage

Xiaokang Zhu[1], Guohai Dong[1], Chunwei Bi[2]* and Yunpeng Zhao[1]

[1]State Key Laboratory of Coastal and Offshore Engineering, Dalian University of Technology, Dalian, China, [2]Fisheries College, Ocean University of China, Qingdao, China

A hybrid wind turbine foundation combined with a double-layer offshore net cage for marine aquaculture is proposed in this paper. To study the diffraction and hydrodynamic loads on the structure for waves with small steepness, a numerical model was established using linear potential theory and solved using the eigenfunction expansion method. A porosity parameter was introduced to describe the hydrodynamic characteristics of the net panels. The model was validated based on existing numerical results and experimental data. An empirical formula was derived to calculate the porosity parameter based on the opening ratios of the nets. The wavefield and wave force were calculated and analyzed by setting different porosity parameters, spacings between the exterior net and interior net, radius ratios of the exterior net to the wind turbine tower and thicknesses of the friction wheel. Noticeable differences in the wave elevation were observed between the upstream and downstream sides of the nets. At downstream sites, the wavefield exhibits different profiles, particularly for structures with low porosities. Sloshing modes were observed that impacted the force and wave elevation at certain frequencies. For the common fishing nets with large porosities, the spacing between the nets does not have a significant impact on the wavefield and wave force acting on the structure. Moreover, the radius and thickness of the friction wheel have a non-negligible influence on the force acting on the structure, which also narrows the intervals between adjacent sloshing frequencies. In summary, this study provides a perspective for the engineering design and hydrodynamic analysis of a hybrid wind turbine foundation with a double-layer aquaculture cage.

KEYWORDS

hybrid wind turbine foundation, aquaculture cage, wave diffraction, hydrodynamic load, linear potential theory, eigenfunction expansion method

1 Introduction

In recent years, the offshore fish farming industry has developed rapidly based on its cost-effective productivity and environmentally friendly characteristics. Additionally, offshore wind farms are thriving as a result of increasing demand for clean wind energy. The concept of integrating offshore aquaculture with wind turbine systems is a relatively novel trend that aims to take full advantage of sea space and provide additional profits to balance the cost of constructing and maintaining wind farms. However, when deployed in offshore areas, hybrid structures may encounter intense wave conditions. Furthermore, based on the shielding effects of net panels and diffraction of waves by the wind turbine foundation, hydrodynamic characteristics tend to be relatively complex. A structure may bear increased wave loads, which introduces more uncertainty regarding the durability of the structure. Therefore, investigating the fluid-structure interactions is critical for ensuring the reliability and longevity of integrated systems, which is an important domain that has been studied by many researchers.

Extensive numerical simulations and laboratory experiments have been conducted to study the hydrodynamic characteristics of offshore net cages. Aarsnes et al. (1990) studied the distribution of water flow velocity in several groups of square cages and the attenuation of the water flow velocity in the cages was summarized. Lader et al. (2003) conducted a series of model tests, studied the stress and deformation of a cage under uniform flow, and measured a velocity attenuation of approximately 20% inside the cage. Tsukrov et al. (2003) developed a finite-element model to study the hydrodynamic responses of net panels to environmental loads They found that for each net panel, 21 special net elements were adequate to analyze the overall hydrodynamics of the net cage. Huang et al. (2006) developed a numerical model to simulate the dynamic properties of an offshore net cage system. In their model, the cage net was divided into several plane surface elements to calculate external forces. Zhao et al. (2007) adopted a lumped-mass model and calculated the hydrodynamic force on a net using the Morison equation. Bao et al. (2009) used linear potential theory by applying Darcy's law to a porous boundary and calculated the hydrodynamic force on a net cage using the eigenfunction expansion method. Patursson et al. (2010) investigated the flow characteristics through and around a net panel through computational fluid dynamics (CFD) and laboratory measurements. A finite-volume method was used to solve the Reynolds-averaged Navier-Stokes equations and the k-ϵ turbulence model was adopted to describe the flow field. Bi et al. (2014) developed a numerical approach using the lumped-mass model to simulate the configuration of flexible nets and a porous media model to calculate the flow field. They discovered that the shielding effect of the fishing net increases as the number of nets increases. Recently, Ma et al. (2022) proposed a novel semi-analytical solution to describe the hydrodynamics of a flexible cylindrical net cage based on linear potential flow theory and the membrane vibration equation of cylindrical shells. It was found that at certain wave frequencies, the horizontal wave force acting on the cage would vanish. Apart from traditional gravity cages, several novel methods could be applied to the study of large semisubmersible aquaculture facilities. Liu et al. (2020) combined the Morison equation and the potential flow theory to analyze the hydrodynamic characteristic of a semisubmersible aquaculture facility. A good agreement was obtained between the presented method and the experimental data. Saghi (2019); Saghi et al. 2022) developed a numerical wave tank using coupled VOF-FDM method and further put forward a machine learning method for the prediction of hydrodynamic performance of floating objects. Their method was feasible and might be applied to the analysis of large aquaculture facilities, including the simulation of interaction with solitary waves.

In addition to typical environmental conditions, net panels are also subject to biofouling. Biofouling refers to the accumulation of marine organisms that may induce a significant increase in the hydrodynamic loads acting on net panels and limit the water exchange and oxygen supply inside aquaculture cages (Braithwaite et al., 2007; Klebert et al., 2013). Swift et al. (2006) tested the drag forces on biofouled plane nets through field experiments and compared them to the results of clean nets measured during experiments in a towing tank. A 240% increase in the drag coefficient was observed for the maximally biofouled plane net. Lader et al. (2015) studied the drag increase on nets caused by the biofouling of colonial hydroids. They created models of twines with artificial hydroid fouling and tested drag forces in a towing tank. Bi et al. (2015); Bi et al. (2017) studied the hydrodynamic characteristics of a single offshore net cage and a square array of offshore net cages with biofouling using a three-dimensional CFD model. They found that the damping effects of the cage array increased with increasing biofouling.

The novel concept of combining aquatic offshore net cages with offshore wind turbines has been studied by a few researchers in recent years. Buck (2004); Buck and Krause (2012) conducted a feasibility study on the multifunctional use of offshore wind farms and mariculture in the North Sea area and initiated a design project focusing on investigating the possibility of adding a net cage within the foundation of a tripod wind turbine. Jiang (2017) proposed the concept of combining a net cage with an offshore wind turbine with a jacket foundation and performed mechanical analysis using the finite-element method software ANSYS. Zheng and Lei (2018) proposed a floating offshore wind turbine integrated with a steel fish farming cage. Through comparative study, it was shown that the anti-overturning ability, surge, heave and pitch motions of the proposed structure outperformed those of OC3Hywind and OC4DeepCwind. Chu and Wang (2020); Chu et al. (2022) proposed a novel offshore fish farm that combined a floating spar with a fish cage. A partially porous wave fence was installed on the structure to attenuate wave energy. Hydrodynamic analysis revealed that the proposed structure has advantages in terms of stable motion responses while heaving and pitching against wave and current forces.

Offshore wind turbines can be categorized into several types according to their foundations, namely traditional fixed foundations such as monopiles, jackets, and tripods, and floating types such as tension leg platforms, as well as spar types and semi-submersible types (Jahani et al., 2022). The monopile type is the most prevalent foundation based on its cost-effective capacity. However, in deep sea areas, traditional monopile foundations fail to provide adequate support to withstand complex soil conditions. Therefore, as shown in Figure 1A, a novel solution was developed by installing a circular friction wheel made of steel or gravel at the mudline. According to Wang et al. (2018); Wang and Li (2020), this foundation has advantages in terms of imparting greater shear stress to resist lateral deformation and inducing additional vertical stresses in the soil beneath and in front of the foundation. Thus far, several laboratory tests and numerical simulations have been conducted to evaluate the performance of this hybrid monopile foundation (Lehane et al., 2014; Arshi and Stone, 2015; Yang et al., 2019; Wang et al., 2022). The results have been promising. However, considering different types of soil, the size of the friction wheel may be sufficiently wide to occupy vast sea areas, resulting in the waste of sea space. Therefore, in this paper, we propose a novel compound structure that integrates an offshore net cage with a hybrid monopile wind turbine foundation. As shown in Figures 1B, C, the offshore net cage mainly consists of an interior and exterior net, and supporting beams. Unlike traditional aquaculture cages,

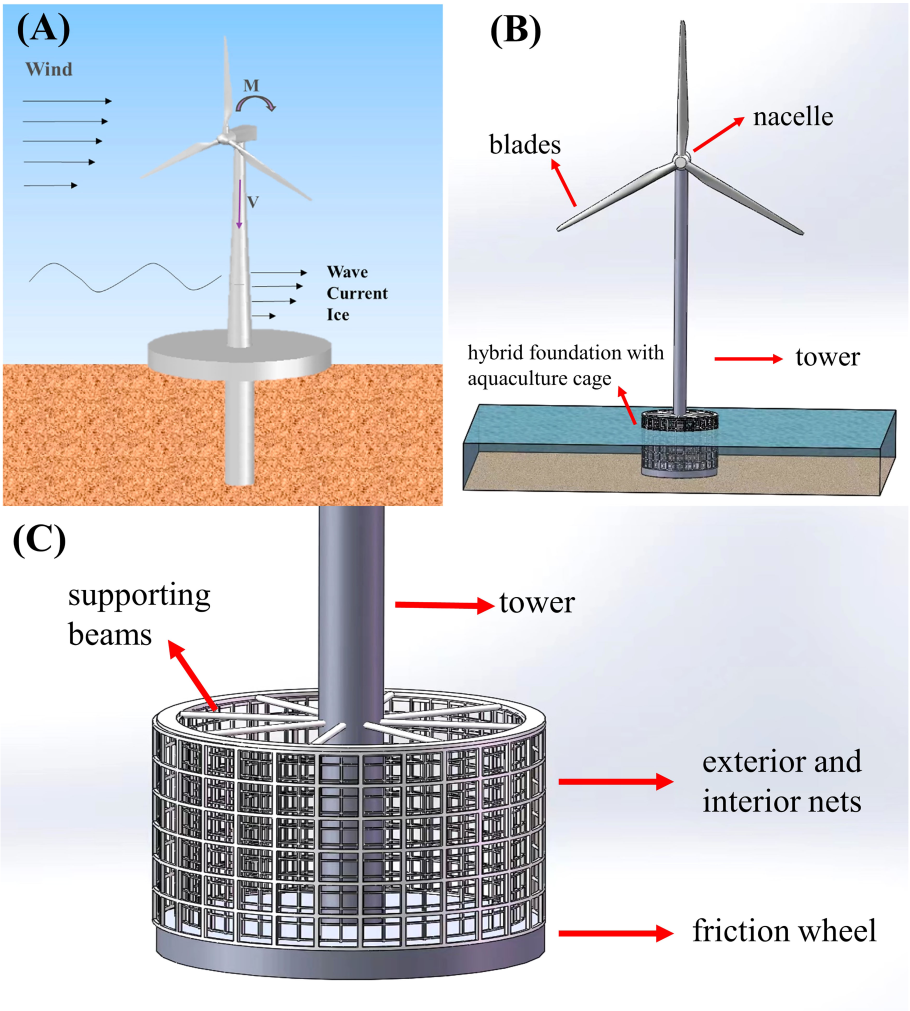

FIGURE 1
Hybrid monopile foundation for offshore wind turbine. **(A)** Hybrid monopile foundation with a friction wheel (Wang et al., 2018). **(B)** Hybrid monopile foundation with a double-layer aquaculture cage. **(C)** Details of the hybrid foundation with a double-layer aquaculture cage.

this combined system is bottom seated and can provide more stability. Additionally, an extra exterior net made of reinforced steel is incorporated to protect cultivated fish from natural predators. Finally, the system is self-sufficient because the wind turbine can generate electricity to power the instruments equipped on the net cage. Considering these advantages, this study addresses the wave diffraction and hydrodynamic characteristics of the proposed system to provide a better understanding of its interaction with waves with small steepness. In the following sections, we use the linear potential theory and eigenfunction expansion method to analyze the force and wavefield with respect to the aforementioned hybrid system.

The remainder of this paper is organized as follows. Section 2 describes the theoretical basis and analytical solutions of the numerical model. Section 3 presents the verification of the model with comparison to other published numerical models. Section 4 presents the determination of the non-dimensional porosity parameter and verification of the model with experimental data. Section 5 presents and discusses results based on a parametric study. Finally, our conclusions are summarized in Section 6. The appendix provides further detailed explanations of the proposed numerical method.

2 Numerical model

2.1 Theoretical formulation

A numerical model of the hybrid wind turbine foundation and aquaculture cage system is presented in Figure 2. The fluid domain is divided into three regions: Ω_1, Ω_2, and Ω_3. The symbols a_0, a_1, a_2, h, d, and s denote the wind turbine tower radius, interior net radius, friction wheel radius, static water depth, and depth and thickness of the friction wheel, respectively. The exterior net is located at the edge of the friction wheel. With the origin located at the still water level and z axis pointing vertically upward, a cylindrical coordinated system (r, θ, z) is established at the center of the wind turbine tower.

We assume that the fluid is irrotational, inviscid, incompressible and the wave steepness is small. Therefore, a numerical model based on the linear potential theory can be applied to solve this problem. The structure is subjected to regular surface waves propagating in the positive x direction with a wave amplitude A and angular frequency ω. The complex potential function can be written as $\Phi(r,\theta,z,t)=Re\{\phi(r,\theta,z)e^{-\mathrm{i}\omega t}\}$, where Re denotes the real part of the complex potential expression, $\phi(r,\theta,z)$ is the spatial potential, i is the imaginary unit, and $e^{-\mathrm{i}\omega t}$ is a time-dependent term. In the following discussion, we separate the spatial and temporal terms, and focus on the solution of the spatial potential $\phi(r,\theta,z)$.

As shown in Figure 2, the entire fluid domain is divided into three regions. Region I is located outside the exterior net with $r>a_2$ and $-h<z<0$, as defined by Ω_1 . Region II is located between the interior and exterior nets with $a_1<r<a_2$ and $-d<z<0$, as defined by Ω_2 . Region III is located inside the interior net with $a_0<r<a_1$ and $-d<z<0$, as defined by Ω_3 . The potential in these three regions satisfies the Laplace equation as follows:

$$\nabla^2\phi^{(j)} = 0,\ for\ j = 1, 2, 3\ in\ \Omega\,. \tag{1}$$

Furthermore, the potential also satisfies the free-surface condition, seabed condition, and solid-body condition on top of the friction wheel as follows:

$$\frac{\partial\phi^{(j)}}{\partial z} - \frac{\omega^2}{g}\phi^{(j)} = 0,\ for\ z = 0\ \ and\ \ j = 1, 2, 3, \tag{2}$$

$$\frac{\partial\phi^{(1)}}{\partial z} = 0,\ for\ z = -h, \tag{3}$$

$$\frac{\partial\phi^{(j)}}{\partial z} = 0,\ for\ z = -d\ \ and\ \ j = 2, 3, \tag{4}$$

where g is the gravitational acceleration.

In region I, the diffracted wave potential must satisfy the Sommerfeld condition when the distance r approaches infinity as follows:

$$\lim_{r\to\infty}\sqrt{r}\left(\frac{\partial}{\partial r} - \mathrm{i}k_0\right)\left(\phi^{(1)} - \phi^{(0)}\right) = 0, \tag{5}$$

where $\partial/\partial r$ denotes the partial derivative with respect to r, k_0 is the wavenumber, and $\phi^{(0)}$ is the incident wave potential.

In region I and region III, the potential must satisfy the impermeable boundary condition on the friction wheel and wind turbine tower surface as follows:

$$\frac{\partial\phi^{(3)}}{\partial r} = 0,\ for\ r = a_0\ \ and\ \ -d < z < 0, \tag{6}$$

$$\frac{\partial\phi^{(1)}}{\partial r} = 0,\ for\ r = a_2\ \ and\ \ -h \le z \le -d\,. \tag{7}$$

On the common surface of these three regions, the potential must satisfy the following matching conditions:

$$\frac{\partial\phi^{(1)}}{\partial r} = \frac{\partial\phi^{(2)}}{\partial r} = i\sigma_2\left(\phi^{(2)} - \phi^{(1)}\right),\ for\ r = a_2\ \ and\ -h < z \le 0, \tag{8}$$

$$\frac{\partial\phi^{(2)}}{\partial r} = \frac{\partial\phi^{(3)}}{\partial r} = i\sigma_1\left(\phi^{(3)} - \phi^{(2)}\right),\ for\ r = a_1\ \ and\ -d \le z \le 0, \tag{9}$$

where the matching conditions in Equations (8) and (9) follow the fine-pore assumption, the fluid flow passing through the porous medium obeys Darcy's law (Chwang and Chan, 1998). The normal velocity of the flow follows the continuity condition and is linearly proportional to the pressure difference through the porous medium, so a linear pressure drop is adopted here (Taylor, 1956). Additionally, $\sigma=b/\lambda$, where λ is the wavelength and b is a non-dimensional porosity parameter introduced for convenience, which is defined as follows (Zhao et al., 2010a):

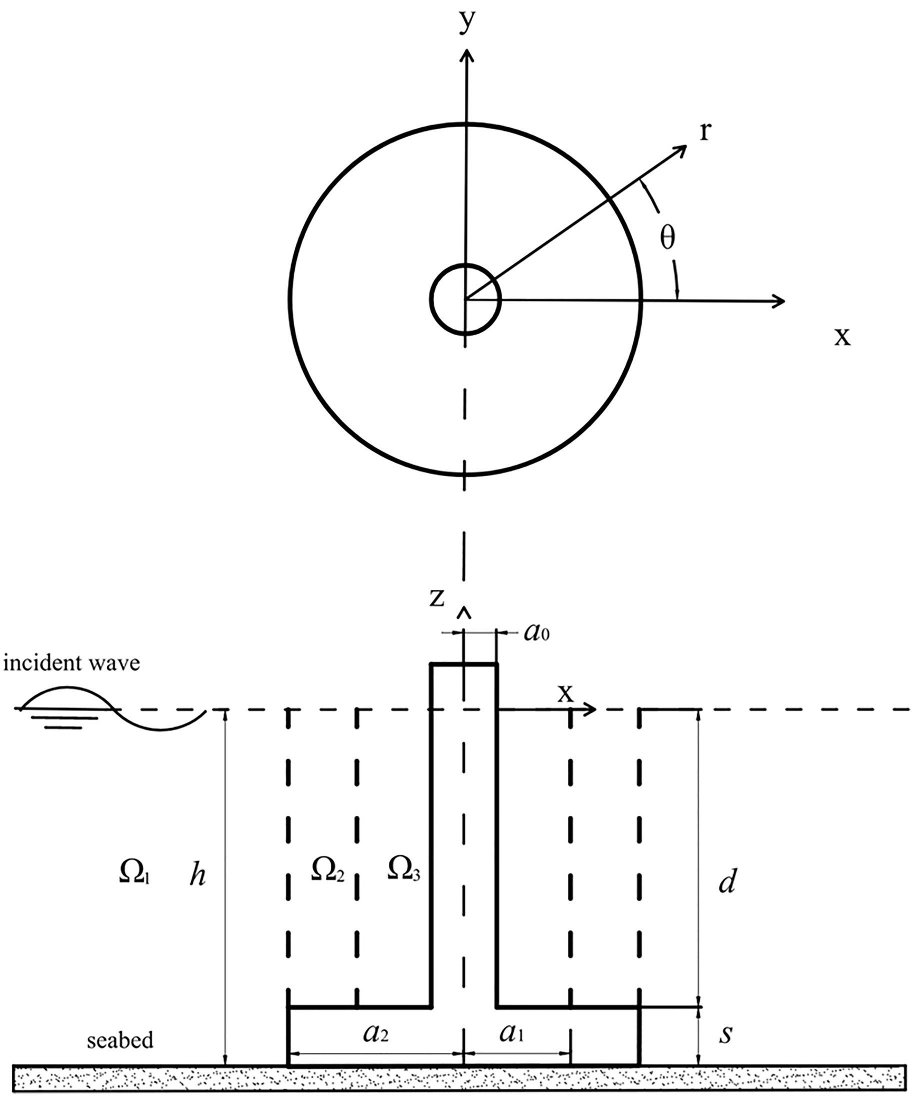

FIGURE 2
Sketch of the hybrid structure and division of the fluid domain.

$$b = \rho \lambda l \omega / \mu \,. \tag{10}$$

where ρ is the density of water, μ denotes the dynamic viscosity coefficient of the fluid, and l represents the porosity coefficient with dimensions of length. The coefficient b represents the porosity characteristics of porous materials and $b = 0$ indicates that the surface is impermeable. In contrast, as b increases to infinity, the surface becomes completely permeable, which can be considered as a non-existent medium. The determination of the non-dimensional porosity parameter b and the feasibility of the numerical model are discussed in Section 4.

2.2 Analytical solution

The problem presented above is solved using the eigenfunction expansion method. With different eigenfunctions defined in these regions and specific boundary values matched on common surfaces, the velocity potential of each region can be obtained.

The expansion series of the velocity potential in region I, denoted as $\phi^{(1)}$, which satisfies the free surface, seabed, and Sommerfeld conditions, is written as

$$\phi^{(1)} = -\frac{\mathrm{i}g\zeta_0}{\omega}\sum_{n=-\infty}^{\infty} e^{in\theta}\left(\mathrm{i}^n J_n(k_0 r) Z_0(k_0 z) + \sum_{m=0}^{\infty} A_{nm} R_n(k_m r) Z_m(k_m z)\right), \tag{11}$$

where ζ_0 is the amplitude of the incident wave, A_{nm} ($n, m = 0, 1, 2, \ldots$) are unknown coefficients, and the eigenvalues k_m($m = 0, 1, 2, 3, \ldots$) can be obtained using the following dispersion relation:

$$\omega^2 = \begin{cases} gk_0 \tanh(k_0 h), & m = 0 \\ -gk_m \tan(k_m h), & m = 1, 2, 3, \ldots \end{cases}$$

The radial eigenfunctions $R_n(k_m r)$ are defined as

$$R_n(k_m r) = \begin{cases} \mathrm{H}_n(k_0 r)/H_n(k_0 a_2), & m = 0 \\ K_n(k_m r)/K_n(k_m a_2), & m = 1, 2, 3, \ldots \end{cases}$$

where H_n is a Hankel function of the first kind and K_n is a modified Bessel function of the second kind. The vertical eigenfunctions $Z_m(k_m z)$ are expressed as

$$Z_m(k_m z) = \begin{cases} \cosh k_0(z+h)/\cosh k_0 h, & m = 0 \\ \cos k_m(z+h)/\cos k_m h, & m = 1, 2, 3, \ldots \end{cases}$$

which form an orthogonal set in [-h, 0].

The velocity potential in region II, which satisfies the appropriate free surface and boundary conditions, can be expressed as

$$\phi^{(2)} = -\frac{\mathrm{i}g\zeta_0}{\omega}\sum_{n=-\infty}^{\infty} e^{in\theta}\left(\sum_{l=\mathbf{0}}^{\infty} B_{nl} V_n^{(1)}(\lambda_l r) Z_l(\lambda_l z) + \sum_{l=0}^{\infty} C_{nl} V_n^{(2)}(\lambda_l r) Z_l(\lambda_l z)\right), \quad (12)$$

where the eigenvalues λ_l($l = 0, 1, 2, 3, \ldots$) can be obtained using the following dispersion relation:

$$\omega^2 = \begin{cases} g\lambda_0 \tanh(\lambda_0 d), & l = 0 \\ -g\lambda_l \tan(\lambda_l d), & l = 1, 2, 3, \ldots \end{cases}$$

where $\omega = \sqrt{gk_0 \tanh(k_0 h)}$. The radial eigenfunctions are defined as follows:

$$V_n^{(1)}(\lambda_l r) = \begin{cases} \mathrm{J}_n(\lambda_0 r)/J_n(\lambda_0 a_1), & l = 0 \\ I_n(\lambda_l r)/I_n(\lambda_l a_1), & l = 1, 2, 3, \ldots \end{cases}$$

and

$$V_n^{(2)}(\lambda_l r) = \begin{cases} \mathrm{H}_n(\lambda_0 r)/H_n(\lambda_0 a_1), & l = 0 \\ K_n(\lambda_l r)/K_n(\lambda_l a_1), & l = 1, 2, 3, \ldots \end{cases},$$

where J_n is a Bessel function of the first kind and I_n is a modified Bessel function of the first kind. The vertical eigenfunction $Z_l(\lambda_l z)$, which forms an orthogonal set in [− d, 0], can be written as

$$Z_l(\lambda_l z) = \begin{cases} \cosh\lambda_0(z+d)/\cosh\lambda_0 d, & l = 0 \\ \cos\lambda_l(z+d)/\cos\lambda_l d, & l = 1, 2, 3, \ldots \end{cases}$$

The velocity potential in region III, which satisfies the appropriate free surface and structural boundary conditions, can be expressed as

$$\phi^{(3)} = -\frac{\mathrm{i}g\zeta_0}{\omega}\sum_{n=-\infty}^{\infty} e^{in\theta}\sum_{l=0}^{\infty} D_{nl} W_n(\lambda_l r) Z_l(\lambda_l z). \quad (13)$$

The radial eigenfunctions are expressed as

$$W_n(\lambda_l r) = \begin{cases} \mathrm{J}_n(\lambda_0 r) - \frac{J_n'(\lambda_0 a_0)}{H_n'(\lambda_0 a_0)} H_n(\lambda_0 r), & l = 0 \\ I_n(\lambda_l r) - \frac{I_n'(\lambda_l a_0)}{K_n'(\lambda_l a_0)} K_n(\lambda_l r), & l = 1, 2, 3, \ldots \end{cases}$$

Then, by using the orthogonality of the vertical eigenfunctions, four sets of algebraic equations that satisfy the continuity condition on the common surface of these three regions can be obtained.

$$\int_{-d}^{0} \frac{\partial \phi^{(2)}}{\partial r} Z_m(k_m z)dz = \int_{-h}^{0} \frac{\partial \phi^{(1)}}{\partial r} Z_m(k_m z)dz, \quad r = a_2, \quad (14)$$

$$\int_{-d}^{0}\left(\phi^{(2)} - \frac{1}{\mathrm{i}\sigma_2}\frac{\partial \phi^{(2)}}{\partial r}\right) Z_l(\lambda_l z)dz = \int_{-d}^{0} \phi^{(1)} Z_l(\lambda_l z)dz, \quad r = a_2, \quad (15)$$

$$\int_{-d}^{0} \frac{\partial \phi^{(3)}}{\partial r} Z_l(\lambda_l z)dz = \int_{-d}^{0} \frac{\partial \phi^{(2)}}{\partial r} Z_l(\lambda_l z)dz, \quad r = a_1, \quad (16)$$

$$\int_{-d}^{0}\left(\phi^{(3)} - \frac{1}{\mathrm{i}\sigma_1}\frac{\partial \phi^{(3)}}{\partial r}\right) Z_l(\lambda_l z)dz = \int_{-d}^{0} \phi^{(2)} Z_l(\lambda_l z)dz, \quad r = a_1. \quad (17)$$

By truncating n, m, and l in Equations (11), (12), and (13) for N, M, and L, respectively, Equations (14) to (17) can be rewritten as matrix equations that can be solved using standard mathematical techniques and the unknown coefficients A_{nm}, B_{nl}, C_{nl}, and D_{nl} can be determined. Therefore, the specific velocity potential in each region can be obtained. This solution procedure is detailed in the Appendix.

After determining the velocity potential, the horizontal force can be obtained by integrating the pressure over the average wet surface, which is expressed as

$$f_x^{(1)} = -i\omega\rho a_0 \int_0^{2\pi}\int_{-d}^{0} \phi^{(3)}(a_0, \theta, z)\cos\theta d\theta dz, \quad (18)$$

$$f_x^{(2)} = i\omega\rho a_1 \int_0^{2\pi}\int_{-d}^{0}\left[\phi^{(3)}(a_1, \theta, z) - \phi^{(2)}(a_1, \theta, z)\right] cos\theta d\theta dz, \quad (19)$$

$$f_x^{(3)} = i\omega\rho a_2 \int_0^{2\pi}\int_{-d}^{0}\left[\phi^{(2)}(a_2, \theta, z) - \phi^{(1)}(a_2, \theta, z)\right]\cos\theta d\theta dz, \quad (20)$$

$$f_x^{(4)} = -i\omega\rho a_2 \int_0^{2\pi}\int_{-h}^{-d} \phi^{(1)}(a_2, \theta, z)\cos\theta d\theta dz, \quad (21)$$

$$f_x^{(tol)} = f_x^{(1)} + f_x^{(2)} + f_x^{(3)} + f_x^{(4)}. \quad (22)$$

where $f_x^{(1)}$, $f_x^{(2)}$, $f_x^{(3)}$, and $f_x^{(4)}$denote the horizontal forces acting on the wind turbine tower, interior net, exterior net, and friction wheel, respectively, and $f_x^{(tol)}$ denotes the total force exerted on the entire structure.

Furthermore, the wave elevation on the free surface can be computed using the following linear Bernoulli equation:

$$\eta = -\frac{1}{g}\frac{\partial \Phi(r,\ \theta,\ z,\ t)}{\partial t} = \frac{i\omega}{g}\phi(r,\ \theta,\ z)e^{-i\omega t}. \tag{23}$$

In the following section, the dimensionless wave elevation $|\eta|/\zeta_0$ is considered for calculating the wavefield and wave elevation.

3 Verification with existing numerical models

To derive accurate calculation results, 50 non-zero truncating terms were adopted throughout our calculations (i.e., M = N = L = 50). In this section, we present several published results that validate the numerical model developed in this study. Note that the dimensionless porosity parameters are expressed in different forms, namely b, τ, and G, and the conversion relationship is $b=2\pi G=2\pi/\tau$.

First, a bottom-mounted submerged cylinder was selected for verification, which corresponds to the case of a single friction wheel. The dimensionless forces acting on the friction wheel were calculated for $a_0 = 0$, $b_1 = b_2 =$ 1E10, $a_2/h = 0.5$, and $d/h = 0.3$. Figure 3 presents a comparison between the results obtained using the proposed model and another analytical solution presented by Li and Liu, 2019 for a bottom-mounted submerged cylinder. The horizontal axis represents the dimensionless wavenumber k_0h and the vertical axis represents the dimensionless horizontal force on the cylinder. In this figure, a good agreement can be observed between the two results.

Second, a bottom-mounted cylinder with an upper porous net and inner column was considered to validate the proposed numerical model. The comparison results correspond to the cases where the interior net does not exist and the porosity of the exterior net is set to different values. The parameters $d/h = 0.5$, $a_2/h = 1.0$, $a_0/a_2 = 0.5$, $G_1 =$ 1E10, $G_2 = 0.1 + 0.1i$ (i.e., case 1), and $G_2 = 0.4 + 0.4i$ (i.e., case 2) were selected to validate the calculation of the total horizontal force on the structure. In Figure 4A, the proposed model agrees well with the corresponding results presented by Teng et al. (2001). To validate the wave elevation calculation along the exterior net in different directions, the following parameters were chosen: $ka_2 = 1.0$, $d/h = 0.5$, $a_2/h = 1.0$, $a_0/a_2 = 0.5$, $G_1 =$ 1E10, $G_2 = 0.0$ (i.e., case 1), and $G_2 = 0.4$ (i.e., case 2). In Figure 4B, the vertical axis represents the dimensionless wave elevation and the horizontal axis represents the degree along the exterior net, which is consistent with the results presented by Teng et al. (2001). To verify the calculation of the wave elevation on the upstream side of the exterior net, the following parameters were chosen: $d/h = 0.5$, $a_2/h = 1.0$, $a_0/a_2 = 0.5$, $G_1 =$ 1E10, and $G_2 =$ 0.0, 0.1, and 0.4. Figure 4C reveals a good agreement between the compared numerical models.

Finally, the accuracy of cases in which the interior net is considered were validated with another numerical model presented by Liu et al. (2018). A bottom-mounted cylinder with an inner column and double nets was considered as an example. This is a special case of the model in which the friction wheel is ignored. To investigate the effects of different porosities of the interior and exterior nets on the horizontal force acting on the structure, $\tau_0 = 20$ was considered with various porosity effect parameter ratios τ_1/τ_2. In this verification, the parameters were set to $a_0 = 5$, $a_0/h = 4$, $a_2/a_0 = 2.0$, and $a_1/a_0 = 1.5$. Different parameter ratios (i.e., $\tau_1/\tau_2 = 0$,

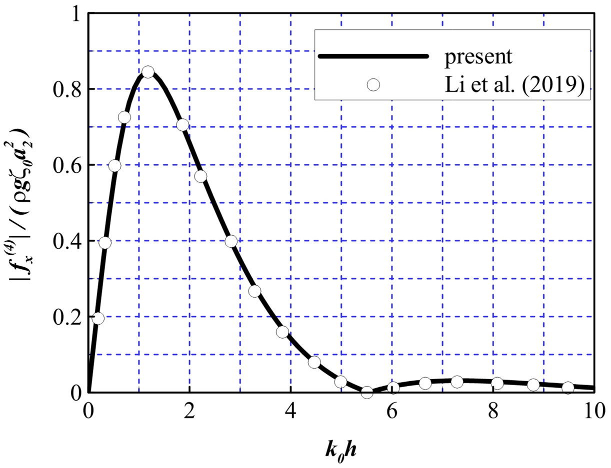

FIGURE 3
Comparison of the non-dimensional horizontal force to the results derived by Li et al. (2019).

1, 3, 7, 1E10) are represented in Figure 5A–C, which represent the horizontal forces on the wind turbine tower, interior net, and exterior net, respectively. One can see that the results of the two solution methods are identical.

4 Determination of the non-dimensional porosity parameter *b*

In Section 2, a linear pressure drop model was adopted for the simplicity of modeling. In actual cases, considering a porous medium, the pressure drop Δp through the porous boundary is mainly composed of two terms, a linear drag term due to the viscosity of the fluid and a drag term proportional to the square of the velocity due to the separation of flow, which is similar to the Darcy-Forchheimer equation (Forchheimer, 1901). According to Sollitt and Cross (1972), the pressure drop on the two sides of a porous medium can be written as:

$$\Delta p = \frac{\nu U}{l\tau} + \rho C_d \frac{|U|U}{\tau^2}, \tag{24}$$

where ν is the kinematic viscosity coefficient, l is a typical length related to the thickness of the porous medium, τ is the opening ratio, C_d is a proper drag coefficient and U is the locally average velocity of the flow close to the porous medium. Based on the continuity condition, the average velocity of the flow through the holes of the porous medium is expressed as U/τ. For the interaction of waves with a porous cylinder, the average velocity can be expressed as $U = \bar{U}\cos(k\vec{x} - \omega t)$, and $\vec{x} = (x, y)$ is the position vector, $\bar{U}$ is the velocity amplitude of the fluid particles. The latter term in Equation (24) could be linearized using Lorenz's principle of equivalent work, expressed as:

$$|U|U = \frac{8}{3\pi}\bar{U}U\,. \tag{25}$$

According to Zhao et al. (2010a), Equation (24) can then be written as:

$$U = \frac{A\tau^2}{1+B\tau}\frac{\Delta p}{\rho\omega\lambda}\,. \tag{26}$$

In which, $A = 3\pi\omega\lambda/(8C_d\bar{U})$ and $B = 3\pi\mu/(8C_d\rho l\bar{U})$. So, it can be speculated that the relationship of b-τ might take the form:

$$b = \frac{A\tau^2}{1+B\tau}\,. \tag{27}$$

Then, based on the experimental data, a suitable b can be chosen for each τ, thus A and B are determined. It should be noted that the effect of viscosity might have an influence on the wave interaction with cylinders. Although the pressure drop model has considered a viscosity term, the linear potential method might fail in the prediction for fluid with large viscosity as it assumes the fluid to be ideal, which is, inviscid and irrotational. Generally, the Keulegan-Carpenter (KC)

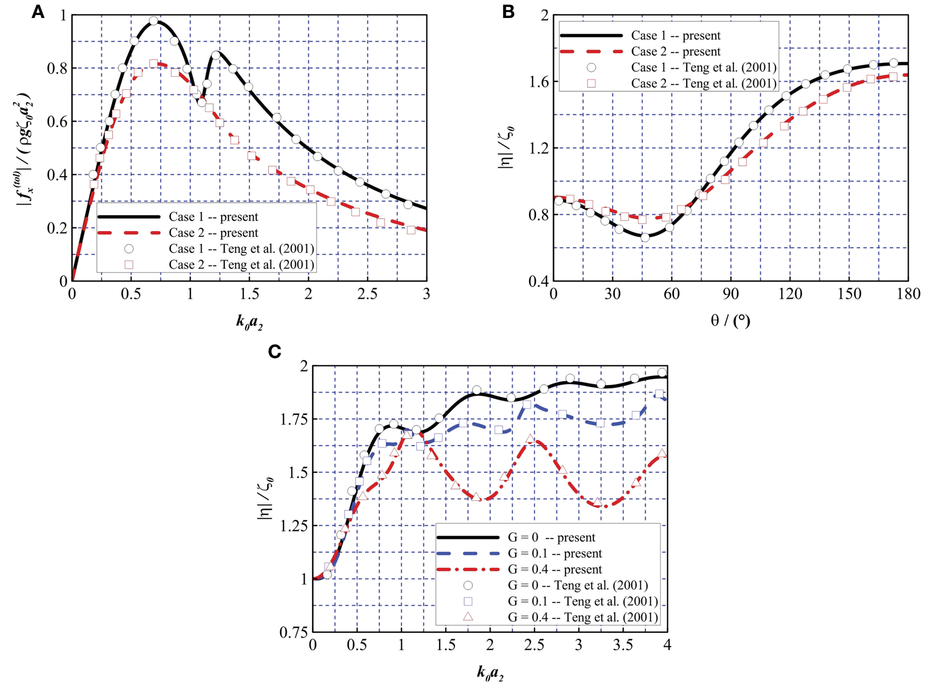

FIGURE 4

Comparison of the non-dimensional force and wave elevation to the results derived by Teng et al. (2001). **(A)** $|f_x^{(tol)}|/\ (\rho g\zeta_0 a_2^2)$ and **(B, C)** $|\eta|/\zeta_0$.

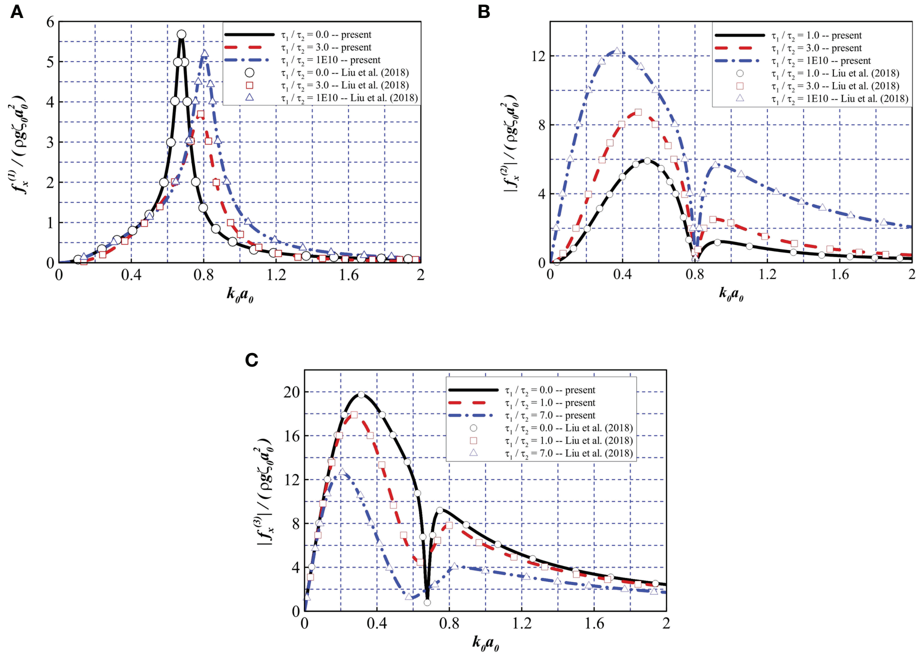

FIGURE 5
Comparison of the dimensionless force to the results derived by Liu et al. (2018). Force **(A)** on the wind turbine tower, **(B)** on the interior net, and **(C)** on the exterior net.

number is adopted to describe the relationship between viscous force and inertial force of an object in an oscillating flow field, which is defined as (Liu and Li, 2016):

$$KC = \frac{\bar{U}T}{\delta} = \frac{T}{\delta}\left(\frac{1}{h}\int_{-h}^{0} u_m dz\right) = \frac{T}{\delta}\left[\frac{1}{h}\int_{-h}^{0}\frac{gk\zeta}{\omega}\frac{\cosh k(z+h)}{\cos kh}dz\right] = \frac{\epsilon L^2}{2\pi h\delta}\,, \quad (28)$$

where u_m is the amplitude of horizontal fluid velocity of incident wave, $\bar{U}$is the depth-averaged value of u_m, δ represents the thickness of porous medium, k is the wavenumber ($k = 2\pi/L$), L is the wavelength, and takes the following form:

$$L = \frac{gT^2}{2\pi}\tanh(kh)\,. \quad (29)$$

So, for the wave interaction with a fixed porous cylinder, if the water depth h and the wave period T are unchanged, the value of L remains constant and the KC number is proportional to the value of ϵ, which further implies that the viscosity effect is less dominant for wave cases with small wave steepness.

From Equation (28), the average velocity of fluid is written as:

$$U = \frac{1}{h}\int_{-h}^{0}\frac{gk\zeta}{\omega}\frac{\cosh k(z+h)}{\cosh kh}dz = \frac{\zeta\omega}{kh} = \frac{\zeta\sqrt{gk\tanh(kh)}}{kh}\,. \quad (30)$$

As explained before, term $\sqrt{gk\tanh(kh)}/kh$ is a constant given that h and T remain unchanged, so the averaged velocity is proportional to the wave steepness ζ in such cases. Combined with Equation (26) and Equation (27), it can be concluded that not only does the non-dimensional porosity parameter b vary with different opening ratios τ, it also varies with different wave steepness ζ.

As pointed before, there exists a positive correlation between the wave steepness and KC numbers. In reference to the work of Honji (1981); Hall (1984) and Sarpkaya (1986), for oscillating flow around a cylinder with KC numbers less than 0.75, the flow is laminar, stable and attached to the wall of cylinder. Zhao et al. (2010a); Zhao et al (2010b) noted that both the experimental data and numerical analysis indicated little relevance between the force acting on the porous structure and viscous effects within a low KC number range of 0.065 – 0.84 for a maximum wave steepness $\epsilon = 0.09$. Mackay et al. (2021a) also stated that the effect of viscosity was not significant for wave conditions of low KC numbers with small wave steepness. For the interaction between porous structure and oscillating fluid with low KC numbers, the accuracy of the numerical model based on linear potential theory is good according to related work by Li et al. (2006); Suh et al. (2011) and Molin and Legras (1990); Molin (2001); Molin (2011). Therefore, the present numerical model may be considered reliable for the subsequent analysis concerning interaction of the structure with waves of small steepness.

To further derive an empirical formula for a bottom-mounted porous cylinder and test the feasibility of the present method for interaction between the structure and waves with small steepness, the non-dimensional horizontal force on a bottom-mounted porous cylinder was investigated.

The porosities τ were set to 0.1, 0.2 and 0.3, with the radius $a_1/h = 1/4$ and $h = 1.0$ m, and the wave slope $\epsilon = k\zeta$ was set to 0.05 to constrain the influence of viscosity, turbulence and possible nonlinear effects (e.g., wave break). Furthermore, a constant $a = h/8$ was defined. To test the feasibility of the method, the following steps are advised:

1. Select proper values of b to match the frequency domain curves of horizontal excitation force for $\tau = 0.1$ and 0.3 with the experimental data.
2. Calculate the coefficients A and B in Equation (27) using the data from step 1.
3. After the $b - \tau$ relation is obtained, calculate the non-dimensional porosity parameter b with respect to $\tau = 0.2$. Then evaluate the discrepancies with experimental data.

Figure 6A depicts the relationship between b and τ after choosing the proper porosity parameter b for the opening ratio τ. The value of b for $\tau = 0.2$ was calculated using the following empirical formula:

$$b = \frac{946.8\tau^2}{1+7.7\tau}. \quad (31)$$

From Figure 6B, it can be observed that the discrepancies between the numerical results and experimental data from Mackay et al. (2021a) are relatively small and acceptable. A good agreement is found between the compared data for the frequencies with 0.8< kh<1.5. The measurements for the higher frequencies with kh >1.5 are consistently lower than the predicted results from the numerical model. Resort to the Equations (28) and (29), for the wave cases with the same water depth h and wave period T, the wavelength L decreases as kh increases, thus leading a decrease of KC number. Therefore, the viscous effect becomes less important to the force acting on the cylinder and it causes a decrease of force acting on the structure. Another reason could be that although the estimation of b is based on a complete pressure drop model, the numerical method still adopts a linear pressure drop model, so the quadratic term may sometimes be a little overestimated or underestimated. Nevertheless, the presented method still exhibits a relatively satisfactory accuracy. Compared with some potential theory models based on boundary element method (BEM) and quadratic pressure drop model (Liu and Li, 2017; Mackay et al., 2021b), the present method does not require iteration to calculate the normal velocities and avoids the procedures of meshing and removing irregular frequencies, which are issues for BEM programs (Liu, 2019; Liu et al., 2020; Ma et al., 2022).

To further investigate the accuracy of the predicted b derived by Equation (31), the non-dimensional force on cylinders with opening ratio $\tau = 0.2$ was compared with experimental data. The wave steepness ϵ was set to 0.05 as previously suggested, and the radii of a_1 were set to $3h/16$, $4h/16$, $6h/16$. From Figure 7A, it is found that the agreement is good overall for the compared data. The discrepancies at higher frequencies with $kh > 1.5$ are also observed, similar to the aforementioned case. Figure 7B shows the non-dimensional force on porous cylinder with an inner solid cylinder, in which, the ratio of outer to inner cylinder a_1/a_0 was to 2.0 and the radius of the inner cylinder a_0 was set to $h/8$, the wave steepness ϵ was set to 0.05 and the opening ratios τ of the outer cylinder were set to 0.1, 0.2,0.3 and 1. $\tau = 1$ corresponds to the case with only the inner solid cylinder. It can be observed that in the particular case where only the inner cylinder is considered, the numerical results are consistent with the experimental data. This indicates that the effects of viscosity and turbulence have a small influence on the total horizontal force for a solid cylinder with the range of conditions considered here. It is noted that the comparison between the numerical method and the experimental data shows a similar trend as Figure 6B. Overall, the discrepancies are acceptable. Moreover, it

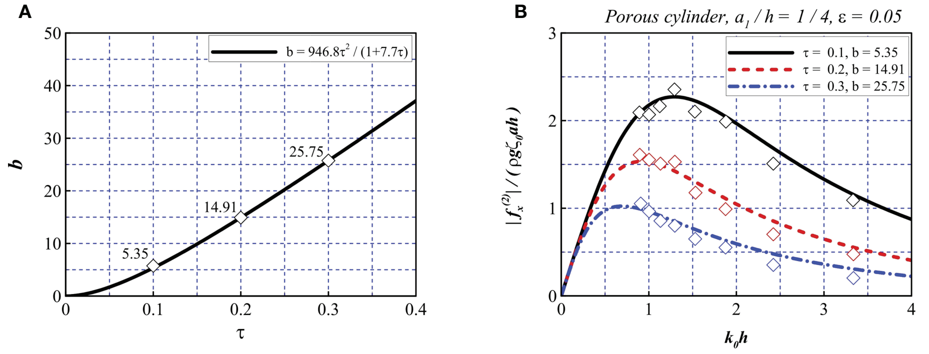

FIGURE 6
Determination of the non-dimensional parameter b. **(A)** The relationship between the non-dimensional porosity parameter b and the opening ratio τ. **(B)** Validation of the numerical model (solid line) with experimental data (diamonds).

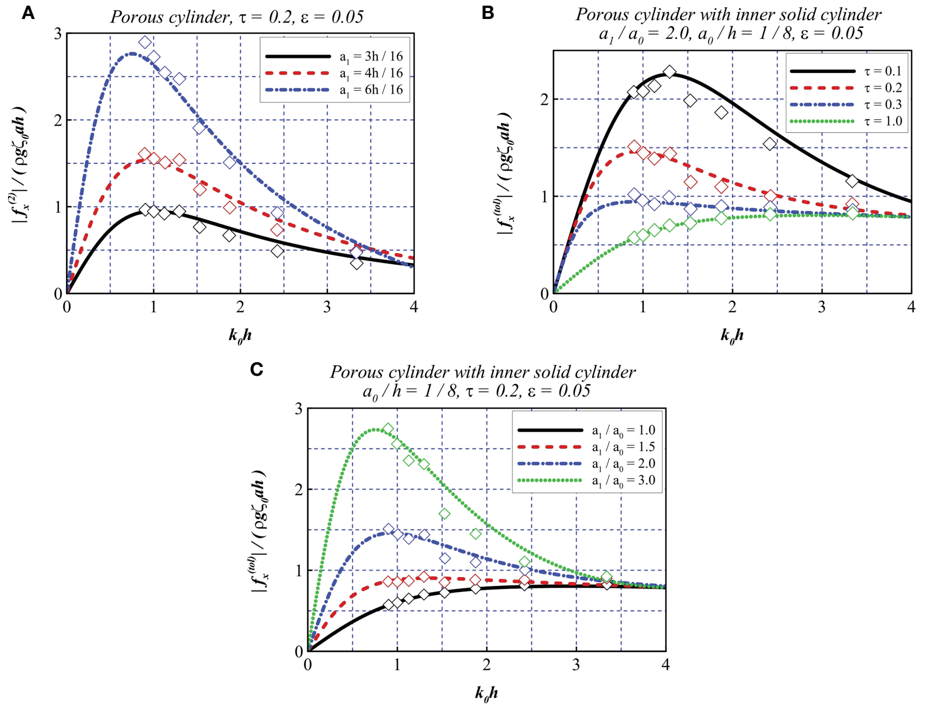

FIGURE 7
Comparison of non-dimensional horizontal force from the numerical model (solid line) and experimental data (diamonds). **(A)** Wave loads on a porous cylinder. **(B, C)** Wave loads on a porous cylinder with inner solid cylinder.

is also noted that adding a porous cylinder does not obviously increase the wave loads at higher frequencies with $kh > 2.5$. Figure 7C reveals the effect of the radius of the outer porous cylinder on the total horizontal force acting on the compound structure. The ratios of outer to inner cylinder a_1/a_0 were set to 1.0, 1.5, 2.0 and 3.0. The consistence between compared data is also satisfactory overall.

From the above discussion, it is found that the experimental data is well replicated by the presented numerical model. An empirical formula was also derived and tested. The numerical method based on linear potential theory and linear pressure drop model of porous medium is feasible for cases with small wave steepness and low KC numbers.

5 Results and discussion

5.1 Wavefield at the free surface

As mentioned previously, the proposed model is a combination of offshore wind turbine foundations and aquaculture infrastructure. The interactions between these components may be complex as a result of the shielding of the nets and diffraction effect of the wind turbine foundation. The manner in which waves act on a structure may have different characteristics under different environmental conditions. Furthermore, investigation of the wavefield is of great importance for enhancing the protection of aquatic creatures in fisheries. Therefore, special attention should be devoted to the wavefields within and adjacent to the model. In this section, we examine the cases with different net porosities. Moreover, cases of different net spacing are added for comparison. It should be noted that the discussion is suitable for cases with small wave steepness as stated in Section 4.

Referring to Balash et al. (2009); DeCew et al. (2010), and Kristiansen and Faltinsen (2012), the opening ratio of common fishing nets typically ranges from 0.7 to 0.9. According to Bi et al. (2018), in biofouling cases, the ratio can decrease to approximately 0.2. In the following discussion, we set $\epsilon = 0.05$, $\tau = 0.25$ to 0.85, and b to a minimum of 20 and maximum of 90 according to Equation (31).

The parameters were set to $a_2/a_0 = 5.0$, $a_1/a_2 = 0.9$, $h/a_0 = 10.0$ and $s/a_0 = 2.0$ with $b_1 = b_2 = 90$ for Figures 8A–D, which represents the common porosity of the fishing nets, and $b_1 = b_2 = 20$ for Figures 8E–H, which represents the case of biofouling. Moreover, $a_1/a_2 = 0.5$ and $b_1 = b_2 = 90$ were adopted for Figures 8I–L to investigate the impact of net spacings on the wavefield. Under the defined parameters, the wavefields of four different wavenumbers (i.e., $k_0a_0 = 0.51$, 0.82, 1.25, and 1.64) are

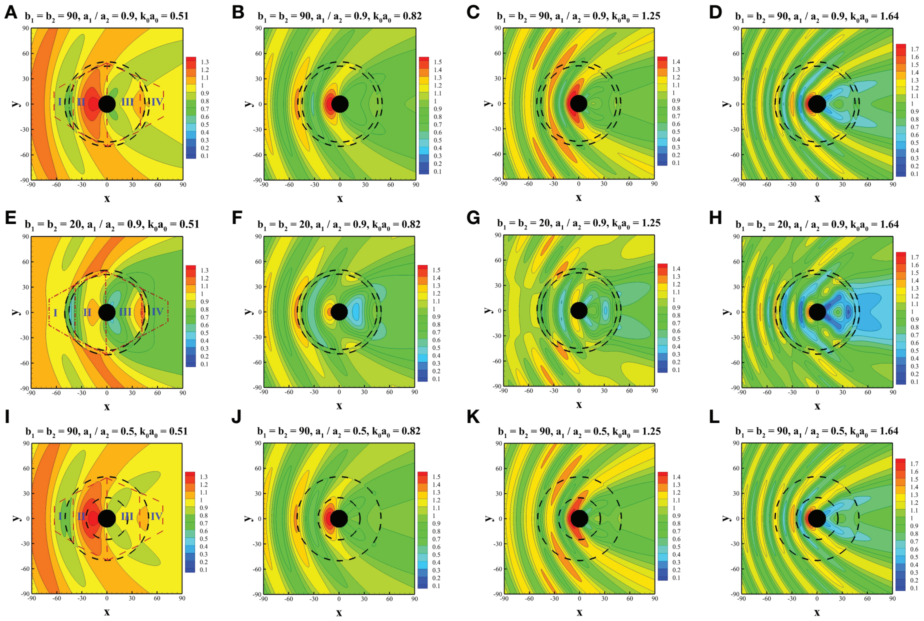

FIGURE 8
Comparison of wavefield at various wavenumbers. **(A–D)** $b_1 = b_2 = 90$, $a_1/a_2 = 0.9$, **(E–H)** $b_1 = b_2 = 20$, $a_1/a_2 = 0.9$, and **(I–L)** $b_1 = b_2 = 90$, $a_1/a_2 = 0.5$.

presented in Figures 8A–L, where the central shaded circles represent the wind turbine tower and the surrounding dashed lines represent the interior and exterior nets. To illustrate the phenomena to be discussed more clearly, four zones are defined divided within or adjacent to the structure, as shown in Figures 8A, E, I. Zone I is near the upstream part of the exterior net, zone II is between the exterior net and the upstream part of the wind turbine tower, zone III is between the downstream part of the wind turbine tower and the exterior net, and zone IV is located near the downstream part of the exterior net.

In general, with a decrease in porosity (i.e., parameter *b* decreases from 90 to 20), the wave elevation in zones II and III decreases significantly, which is intuitive based on the increased shielding effect of the two nets. Furthermore, the wave elevations on the upstream and downstream sides of the wind turbine tower decrease as the porosity decreases. Therefore, by reducing net porosity, the force acting on the wind turbine tower can be reduced. In particular, based on the combined effect of the pressure drop between the windward and leeward sides of the nets and the wave diffraction by the wind turbine tower and friction wheel, the wave elevation adjacent to the nets exhibits different characteristics. Figures 8E, G reveal that in zone I, the elevation at the windward side of the exterior net is greater than that in Figures 8A, C, but the elevation on the leeward side of the interior net is smaller. In zone IV, the wave elevation on the leeward side of the exterior net is significantly reduced with a decrease in the porosity parameter. Furthermore, a net with smaller porosity provides better shielding from water in the rear of the entire structure. In zone II, the wave elevation in Figures 8E-H is generally smaller than that in Figures 8A–D. In zone III, the wavefield exhibits more complex profiles than in zone II. However, generally speaking, Figures 8E–H show less significant wave elevation than Figures 8A-D, which reflects the improved shielding effect of nets with small porosity. However, there are several interesting phenomena to be observed. As shown in Figure 8F, the lowest elevation can be observed near the center of zone III. In Figures 8G, H, the lowest wave run-up appears near the windward side of the interior net. Furthermore, in Figure 8H, a sharp increase in wave elevation can be observed near the center of zone III, which is surrounded by an area with low wave elevation.

In comparison between wavefield of various net spacings, it is found that the discrepancies are less apparent regarding Figures 8A–D and Figures 8I–L. Some minor differences are discovered. As shown in Figure 8I, an area with smaller wave elevation exists near the upstream side of the exterior net in zone I. Moreover, due to the attenuation of the double nets, compared with Figure 8J, the wave elevation is smaller at the center of zone II in Figure 8B. The similar phenomenon is also found in comparison between Figures 8D, L. In Figure 8D, lower wave elevation is discovered near the leeward side of the interior net in zone II. In comparison between Figures 8C, K, smaller wave elevation is found near the leeward side of exterior net of zone II in Figure 8K, while slightly larger wave elevation is found near the interior net of zone II. This may be attributed to the composition of waves reflected by the interior net and propagating through the exterior net. Generally speaking, as the porosity of a fishing net is normally large, the spacings of the nets may have a less noticeable impact on the wavefield.

Based on the analysis above, a more complex wavefield tends to occur for cases with larger wavenumbers and smaller porosities. A large elevation difference may occur between the windward and leeward sides of the net, particularly for nets with smaller porosities. Furthermore, based on the interaction between shielding and diffraction effects, the wavefield may exhibit various profiles in different zones.

To explore the wavefield further, deeper quantitative analysis was conducted to highlight the wave elevation characteristics with different wavenumbers. As shown in Figure 9, eight sites are defined within or along the entire structure. Sites 1, 5, and 8 lie in the open water close to the exterior net. Sites 2, 4, and 7 are located at the middle point of the radius of the exterior net. Sites 3 and 6 are located at the wall of the wind turbine tower.

Figure 10A presents the wave elevation at site 1. In this figure, one can see that with a decrease in the porosity parameter b, the elevation increases, which confirms the phenomena discussed previously. Additionally, the curve peaks shift toward higher wavenumbers and the curve troughs shift toward lower wavenumbers as the porosity parameter decreases. Interestingly, minor troughs can be observed within $0< k_0a_0< 0.34$, $0.54< k_0a_0< 0.91$, and $1.18< k_0a_0< 1.64$, indicating that a small-porosity net can lead to a prominent disturbance at site 1, thereby causing intensive oscillation of the wave run-up at these frequencies. Figure 10B represents the wave elevation at site 2. With an increase in the porosity parameter, the elevation increases, in contrast to Figure 10A, demonstrating that with larger porosity parameters, the shielding effect becomes less obvious. Similar to Figure 10A, minor troughs can be observed between curve peaks and within the intervals of $0< k_0a_0< 0.5$, $0.5< k_0a_0< 0.77$, $0.77< k_0a_0< 1.32$, and $1.32< k_0a_0< 1.75$, where wave elevation is evidently reduced. However, smaller porosity parameters seem to have less influence on the performance of attenuating wave elevation within the ranges adjacent to the curve peaks. Figures 10C–G reveals similar trends corresponding to the cases at sites 3, 5, 6, and 7, respectively. Figure 10D represents the wave elevation at site 4. One can see that within the range $0< k_0a_0< 0.40$, the wave elevation increases as the porosity parameter b decreases and minor troughs emerge. In contrast, within the remaining range of $0.40< k_0a_0< 2.00$, the wave elevation decreases as b decreases, exhibiting a complex trend in areas on the downstream side of the structure. In particular, at $k_0a_0 = 0.89$, the dotted curve (i.e., $b_1 = b_2 = 20$) exhibits an approximately 60% decrease in wave elevation. In Figure 10H, the curves exhibit a more complex trend at site 8. In the ranges of $0< k_0a_0< 0.14$ and $0.93< k_0a_0< 1.31$, the wave elevation increases as the porosity parameter decreases. In the remaining ranges, we observe the opposite phenomena. Particularly in the range of $1.31< k_0a_0< 1.68$, despite the increase in b, the elevation seems to exhibit a sluggish increase. The discussion above may indicate complex interaction among the nets, wind turbine foundation and the incoming waves.

Figure 11A presents the wave elevation at site 1. It can be observed that the spacing of the nets does not have a significant impact on the wave elevation at site 1. At frequencies with $0.74< k_0a_0< 1.06$ and $1.10< k_0a_0< 1.39$, the wave elevation first slightly decreases then slightly increases with the decrease of the net spacing. Figure 11B depicts the wave elevation at site 3. At lower frequencies with $0< k_0a_0< 0.57$, the discrepancies are relatively small for various net spacings. In the range of $0.58< k_0a_0< 1.51$, the differences between various cases are noticeable. Due to the reflection of the wind turbine tower, the trend of curves for various net spacing is complex and not obvious. Figure 11C reveals the wave elevation at site 5, generally speaking, the wave elevation increases as the net spacing increases in the range of $0< k_0a_0< 0.89$. It can be observed

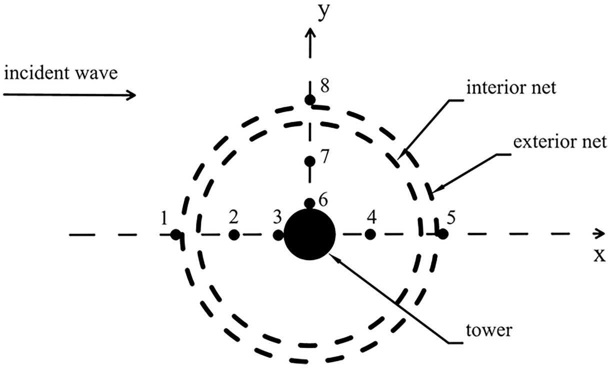

FIGURE 9
Layout of measurement sites for investigating wave elevation with different wavenumbers.

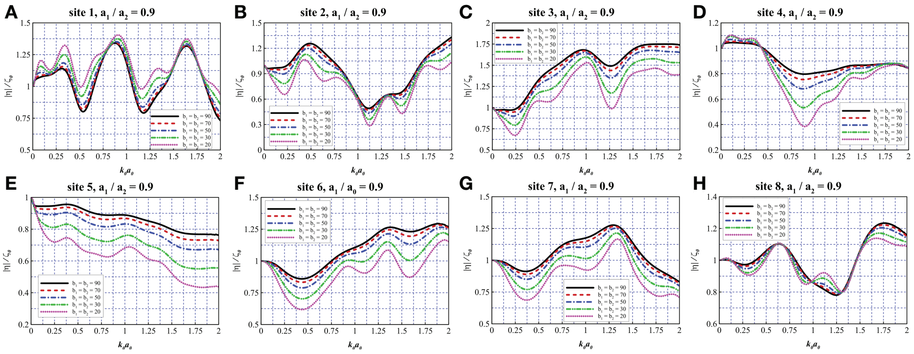

FIGURE 10
Comparison of wave elevation at different measurement sites with various porosity parameters. **(A–H)** a1/a2 = 0.9, site 1-8.

that the case with the largest spacing $a_1/a_2 = 0.3$ exhibits the highest wave elevation and the case with the smallest spacing $a_1/a_2 = 0.9$ exhibits the lowest wave elevation at frequencies with 0< $k_0a_{0<}$ 0.89 and 1.43< $k_0a_{0<}$ 2.0. In Figure 11D, the cases with a small net spacing may induce lower wave elevation at frequencies with 0< $k_0a_{0<}$ 0.52. At higher frequencies, cases with smaller net spacing may induce higher wave elevation in the range of 0.52< $k_0a_{0<}$ 1.06 and 1.06< $k_0a_{0<}$ 2.0. In general, the case with the largest spacing $a_1/a_2 = 0.3$ induces the highest wave elevation at site 6. From Figure 11E, it is found that the spacing of the nets does not have an obvious impact on the wave elevation at site 8. The case with the smallest spacing $a_1/a_2 = 0.9$ may have a better performance in attenuating wave elevation at lower frequencies with 0< k_0a0< 1.03.

5.2 Wave force

In this section, we present parametric studies investigating the effects of different characteristics on the wave loads acting on the structure. As a result of the biofouling effect, the net porosity may exhibit a sharp decrease, affecting the hydrodynamic performance of the structure. The spacings between the nets may also have an impact on the force acting on the structure. Furthermore, for various soil mechanics properties, special designs can be applied to the bottom friction wheel. Consequently, the effects of the total porosity parameter, the spacing between the nets, ratio of the radius of the friction wheel to the wind turbine tower, and thickness of the friction wheel were considered for analysis.

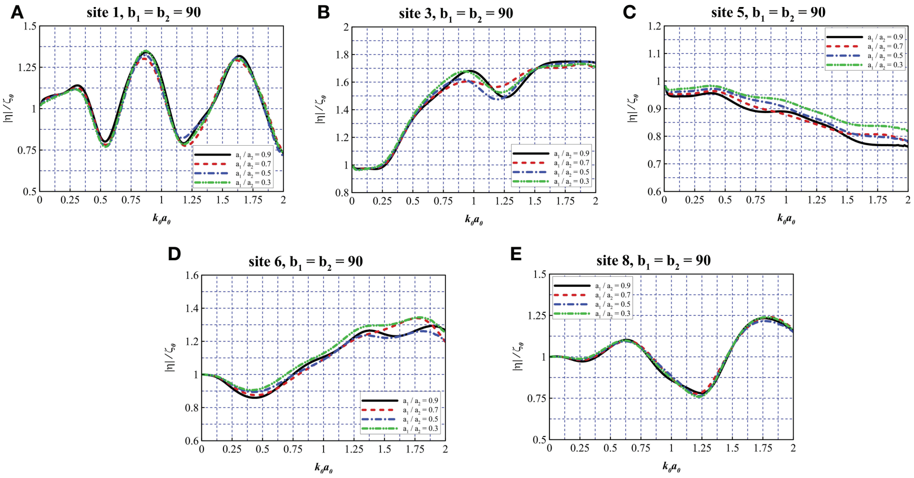

FIGURE 11
Comparison of wave elevation at different measurement sites with various net spacing. **(A–E)** b1 = b2 =90, site 1, 3, 5, 6, 8.

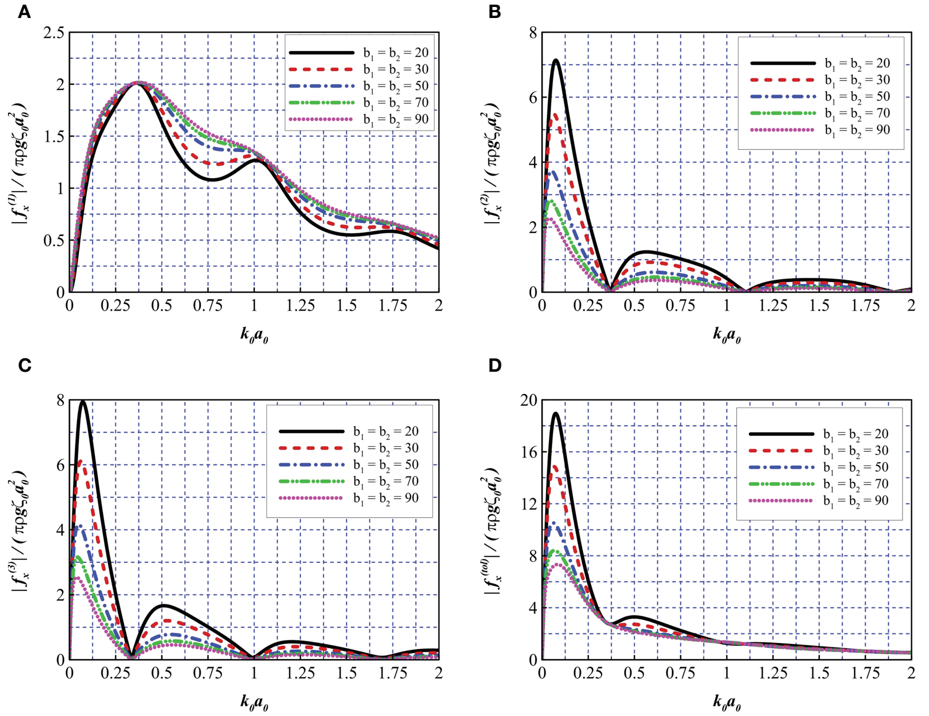

FIGURE 12
Comparison of wave force for different total porosity parameters. **(A)** $|f_x^{(1)}|/(\pi\rho g\zeta_0 a_0^2)$, **(B)** $|f_x^{(2)}|/(\pi\rho g\zeta_0 a_0^2)$, **(C)** $|f_x^{(3)}|/(\pi\rho g\zeta_0 a_0^2)$, and **(D)** $|f_x^{(\mathrm{tol})}|/(\pi\rho g\zeta_0 a_0^2)$.

5.2.1 Effects of the porosity parameter *b*

In this section, the parameters $a_2/a_0 = 5$, $a_1/a_2 = 0.9$, $h/a_0 = 10$, and $s/a_0 = 2$ were fixed. By introducing five different total porosity parameters $b_0 = 40, 60, 100, 140$, and 180 (i.e., $b_1 = b_2 = 20, 30, 50, 70, 90$), the effects of total net porosity on the force acting on the structure were investigated.

As shown in Figure 12A, with an increase in the total porosity parameter, the force exerted on the wind turbine tower exhibits an overall growth trend. In Figures 12B, C, one can see that the curves exhibit an opposite trend. With a greater total porosity, less wave force acts on the interior and exterior nets. This indicates that nets with small porosities have a better shielding effect on the wind turbine tower. Overall, because the exterior net is more exposed to incoming waves with larger radii, more force is exerted. Interestingly, there are some points along the curves located close to zero (i.e., $k_0a_0 = 0.37$, 1.10, and 1.90 in Figure 12B, and $k_0a_0 = 0.33$, 0.99, and 1.69 in Figure 12C, where the sloshing modes are satisfied. In each figure, the curves exhibit almost the same sloshing mode frequencies. The sloshing mode frequencies of the two nets are slightly different. The exterior net has a lower oscillating frequency than the interior net. Near the sloshing mode frequencies, there are some major or minor peaks (i.e., $k_0a_0 = 0.36, 1.01, 1.73$), where the force is eminently weakened. As a result, near such frequencies, the tower is more likely to be damaged and it is desirable to avoid such peaks such that the wind turbine tower is better protected from severe wave conditions. Furthermore, by reconsidering the peaks and troughs in Figure 10, it was determined that some of them occurred near these frequencies, which further demonstrates the pattern of sloshing phenomena. Figure 12D indicates that low porosity (i.e., $b_1 = b_2 = 20$) causes the entire structure to bear greater wave forces at low wavenumbers. Compared to the peak value of 7.33 on the dotted line (i.e., $b_1 = b_2 = 90$), the solid line (i.e., $b_1 = b_2 = 20$) has a peak value of 18.9, representing a significant 158% increase. However, at high wavenumbers $k_0a_0 > 1.0$, this phenomenon is less prominent. Among the frequencies in question (i.e., the range of approximately $0.37 < k_0a0 < 0.87$), there may be a minor peak for low porosity because such frequencies are between the sloshing modes shown in Figures 12B, C.

5.2.2 Effects of the spacing between the nets (a_1/a_2)

In this section, the wave loads acting on the structure with different spacings between the nets a_1/a_2 were investigated. The parameters $a_2/a_0 = 5$, $h/a_0 = 10$, $s/a_0 = 2$ and $b_1 = b_2 = 90$ were

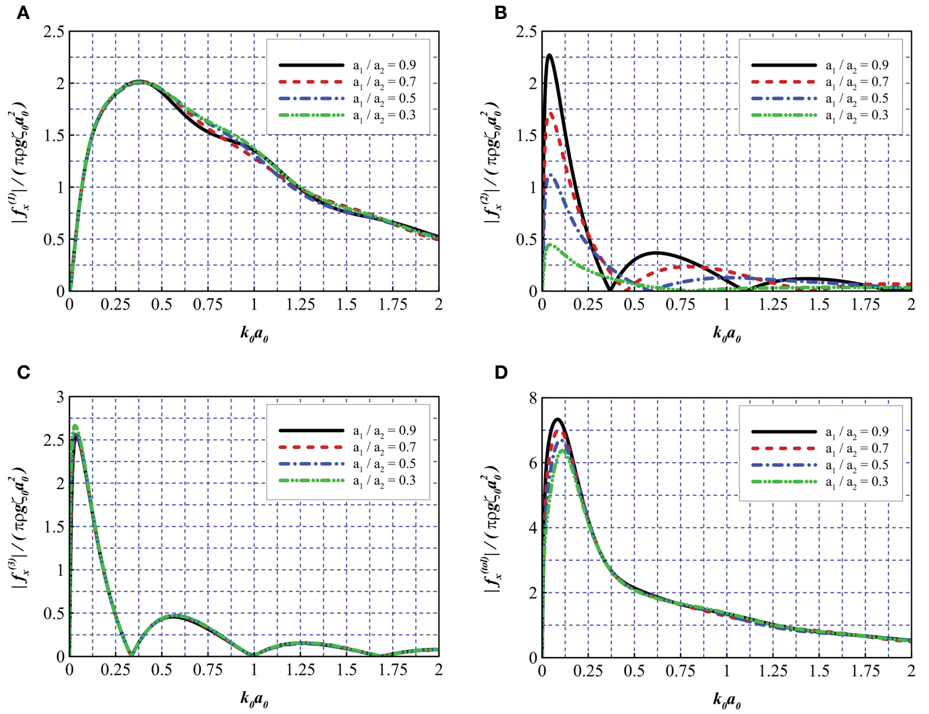

FIGURE 13
Comparison of wave force for different net spacing. **(A)** $|f_x^{(1)}|/(\pi\rho g\zeta_0 a_0^2)$, **(B)** $|f_x^{(2)}|/(\pi\rho g\zeta_0 a_0^2)$, **(C)** $|f_x^{(3)}|/(\pi\rho g\zeta_0 a_0^2)$, and **(D)** $|f_x^{(tol)}|/(\pi\rho g\zeta_0 a_0^2)$.

fixed, four different spacings between the nets were considered: $a_1/a_2 = 0.3$, 0.5, 0.7 and 0.9.

Figure 13A depicts the non-dimensional horizontal force on the wind turbine tower. It can be observed that the values for various net spacings are overall identical in the ranges of $0< k_0a_0< 0.47$ and $1.63< k_0a_0< 2.0$, indicating that the net spacing does not have an obvious impact on the wave loads of the wind turbine tower for the conditions we consider here. In the range of $0.47< k_0a_0< 1.63$, similar to the phenomenon discussed in Section 5.1, the trends of these curves are complex and less obvious. Overall, the case with the largest net spacing $a_1/a_2 = 0.3$ tends to exhibit more force on the wind turbine tower compared with other cases. From Figure 13B, it is found that the wave loads exerted on the interior net sharply decrease as the net spacing increase due to significant decrease of the area of the interior net, especially for a frequency range within $0< k_0a_0< 1.26$. Furthermore, the figure indicates that the sloshing mode frequencies for the interior net increase as the spacing of the net increases. Figure 13C shows that the net spacing does not obviously change the wave loads on the exterior net, except for frequencies near the first peak. Figure 13D illustrates that in the range of $0< k_0a_0< 0.16$, the wave loads acting on the whole structure decrease as the spacing of nets increases, which is similar to what Figure 13B indicates. Moreover, the curve peak shifts to higher frequencies as the spacing of nets increases. At higher frequencies (i.e., $k_0a_0 > 0.16$), the curves are overall consistent.

5.2.3 Effects of the ratio of friction wheel to wind turbine tower radius (a_2/a_0)

In practical use, the radius of the friction wheel may be set to various values to ensure the stability of the foundation based on different soil properties. In the following discussion, the parameters $a_1/a_2 = 0.9$, $h/a_0 = 10$, $s/a_0 = 2$, and $b_1 = b_2 = 90$ were fixed, and four different radius ratios of $a_2/a_0 = 2$, 3, 5, and 7 were considered.

In Figure 14A, with an increase in the radius ratio a_0/a_2, the peak frequency gradually shifts toward lower wavenumbers. The radius ratio appears to have a less significant impact on the force exerted on the wind turbine tower. In Figures 14B, C, with a greater radius ratio, the curves exhibit more frequencies satisfying the sloshing mode within the range $0< k_0a_0< 2$, which indicates that a large radius ratio can narrow the intervals between adjacent sloshing mode frequencies. For cases with large radius ratios (i.e., $a_2/a_0 = 5$ and 7), the sloshing phenomena become more apparent. At such frequencies (i.e., $k_0a_0 = 0.38$ and 1.04 on the blue line, and $k_0a_0 = 0.31$, 0.75, and 1.25 on the green line), humps can be observed in Figure 14A, which are attributed to the sloshing phenomena, as discussed in Section 5.2.1. Figure 14D reveals that the net panels have a limited capacity to dissipate wave energy within the low-frequency range (where the wavelength is sufficiently large) and that a structure with a larger radius ratio tends to experience a higher total wave force within the range 0<

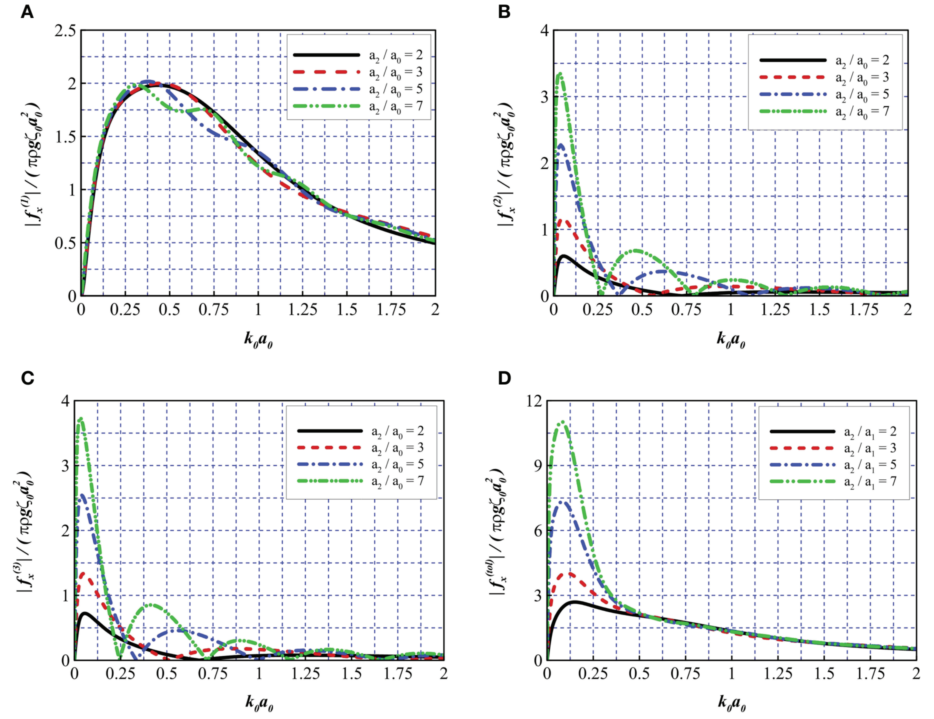

FIGURE 14
Comparison of wave force for different radius ratios of the friction wheel to the wind turbine tower. **(A)** $|f_x^{(1)}|/(\pi\rho g\zeta_0 a_0^2)$, **(B)** $|f_x^{(2)}|/(\pi\rho g\zeta_0 a_0^2)$, **(C)** $|f_x^{(3)}|/(\pi\rho g\zeta_0 a_0^2)$, and **(D)** $|f_x^{(tol)}|/(\pi\rho g\zeta_0 a_0^2)$.

$k_0a_0< 0.5$, leading to a nearly 300% increase compared to the cases of $a_2/a_0 = 2$ and $a_2/a_0 = 7$. However, for higher wave frequencies, the radius ratio has little influence on the total wave force.

5.2.4 Effects of the thickness of the friction wheel (s/a_0)

In this section, the force acting on the structure with different thicknesses of the friction wheel s/a_0 was investigated. The parameters $a_2/a_0 = 5$, $a_1/a_2 = 0.9$, $h/a_0 = 10$, and $b_1 = b_2 = 90$ were fixed, while four different thicknesses of the friction wheel were considered: $s/a_0 = 1.5$, 2.0, 4.0, and 7.0.

Figure 15A reveals that in the range of $0< k_0a_0<1.0$, the wave force on the wind turbine tower is reduced with an increase in the thickness of the friction wheel. However, at higher frequencies (i.e., $1.0< k_0a_0< 2.0$), the curves exhibit very similar trends and values. Figures 15B, C indicate that structures with a greater wheel thickness exert less wave force on the double nets. Furthermore, a greater wheel thickness (i.e., $s/a_0 = 7.0$) leads to lower oscillating frequencies in the first sloshing mode (e.g., the corresponding wavenumber is reduced from 0.33 to 0.26, as shown in Figure 15C, while rarely affecting other higher oscillating modes (i.e., at $k_0a_0 =$ 0.99 and 1.68). Figure 15D reveals that with an increase in wheel thickness, larger peaks can be observed within the first oscillating frequency and a nearly 200% increase can be observed compared to $s/a_0 = 1.5$ and $s/a_0 = 7.0$. In the high-frequency range (i.e., $k_0a_0 > 0.5$), the total wave force exhibits little change, except for at $s/a_0 = 7.0$, where the curve reaches a low trough at $k_0a_0 = 0.79$. This may be a comprehensive result of fewer wave loads acting on the tower based on the reduction of the stream surface and shielding of the nets. Additionally, as the upper part of the friction wheel approaches the free surface, the friction wheel begins to dominate the interaction of incoming waves with the entire structure.

6 Conclusions

In this study, the wave diffraction of a hybrid wind turbine foundation with a double-layer aquaculture cage was investigated. A numerical model based on the linear potential theory was established and solved using the eigenfunction expansion method. The feasibility and accuracy of the proposed method were verified and compared to existing numerical models and experimental data. Subsequently, the wave elevation, wavefield, and horizontal force acting on the structure were calculated by performing parametric studies. Note that the assumption of small wave steepness was adopted throughout the study. Based on the results, our main findings can be summarized as follows:

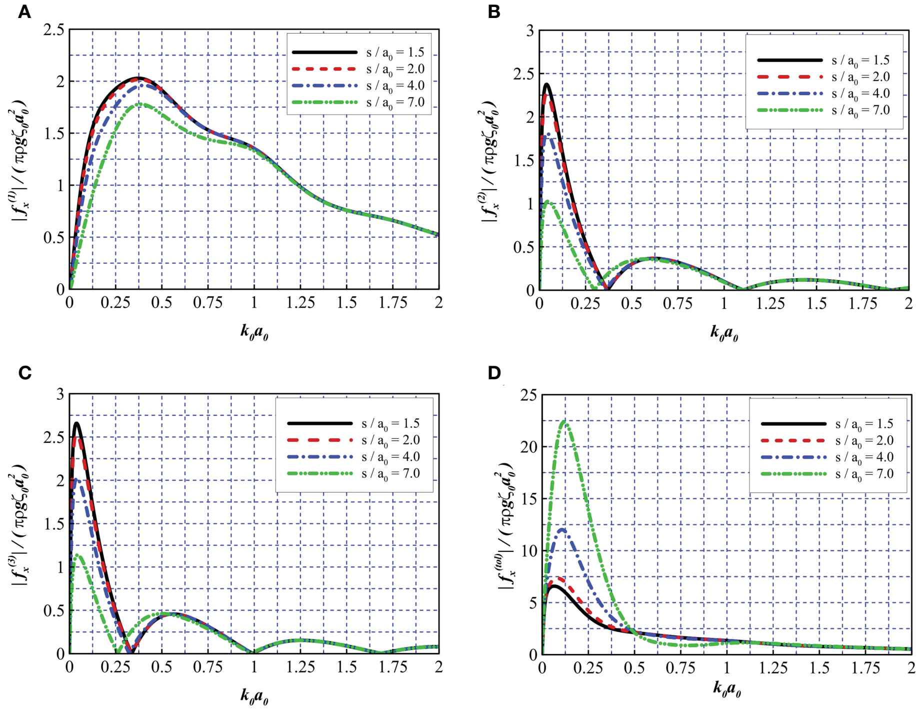

FIGURE 15

Comparison of wave force for different thicknesses of the friction wheel. **(A)** $|f_x^{(1)}|/(\pi\rho g\zeta_0 a_0^2)$, **(B)** $|f_x^{(2)}|/(\pi\rho g\zeta_0 a_0^2)$, **(C)** $|f_x^{(3)}|/(\pi\rho g\zeta_0 a_0^2)$, and **(D)** $|f_x^{(tol)}|/(\pi\rho g\zeta_0 a_0^2)$.

I. A noticeable difference in elevation was found between the upstream and downstream sides of the net system, which caused a large run-up accumulation at leeward sites. In general, the wave elevation within the hybrid system was reduced for structures with low net porosities (i.e., $b_1 = b_2 = 20$). In the downstream and side areas of the structure, the wavefield exhibited complex profiles and wave elevation might be significantly attenuated as a result of the shielding effect of nets and diffraction of waves by the wind turbine tower foundation (e.g., a 60% maximum decrease in wave elevation was observed at the middle point of the downstream areas for $b_1 = b_2 = 20$).

II. Sloshing modes were discovered, which had a non-negligible impact on the wave elevation and wave loads acting on the structure. At these oscillating frequencies (e.g., $k_0a_0 = 0.36$, 1.01, 1.73 for $b_1 = b_2 = 20$), the force and wave run-up on the wind turbine tower were at their peak, whereas at between the oscillating frequencies, the force on the wind turbine tower decreased and the force on the nets increased. One possible method to avoid peak values is to adjust the geometrical parameters of the structure such as the radius and thickness of the friction wheel.

III. Structures with nets of low porosities withstood greater wave loads acting on them. In the present study, a 158% maximum increase in the total wave load was observed by reducing b from 90 to 20. However, nets of low porosities tended to provide a better shielding for the wind turbine tower. Furthermore, net porosity had little influence on the sloshing-mode frequencies of the structure.

IV. For common fishing nets with relatively large porosities, the spacing between the double nets did not have a significant impact on the wavefield and wave loads on the structure.

V. In this study, by increasing the radius ratio of the exterior net to the wind turbine tower, the wave force on the wind turbine tower was slightly reduced, whereas on other parts, it increased significantly within the first oscillating frequency (i.e., approximately $0< k_0a_0< 0.25$). However, at higher wavenumbers (i.e., $0.5< k_0a_0< 2.0$), the wave loads acting on the tower were similar in value. Furthermore, by increasing the radius ratio, the intervals between adjacent sloshing mode frequencies were narrowed.

VI. By increasing the thickness of the friction wheel, the wave force on the wind turbine tower was reduced, whereas the force on other parts generally increased. Furthermore, the interval of the first sloshing mode (i.e., $0< k_0a_0< 0.33$) was narrowed, whereas other sloshing modes were negligibly affected by the increase in thickness of the friction wheel.

Compared with previous research, this paper presents a deeper investigation into the physical implication of the non-dimensional porosity parameter b, derives an empirical formula for the bottom-seated porous cylinder structure and discusses the feasibility of the linear potential theory based numerical model combined with a linear pressure drop model for tackling the problem of interaction between waves with small steepness and structures with porous medium. This paper puts forward a novel hybrid aquaculture system combined with wind turbine. Furthermore, the wavefield and wave loads on this novel structure are thoroughly studied. Special phenomena (e.g., sloshing) are discovered, which further reveal the hydrodynamics of the structure. The abovementioned findings may provide useful information in practical engineering when considering a structure's interaction with waves of small steepness. For instance, in order to avoid sloshing mode frequencies which may cause severe wave loads acting on the wind turbine tower, geometrical properties of the structure should be designed carefully according to the local sea conditions. The effect of biofouling is also nonnegligible, as it leads to apparent changes of the wavefield and drastic increases of the wave loads acting on the whole structure. Moreover, the size of the friction wheel also impacts the wave force acting on the structure, so the properties of both hydrodynamics and soil mechanics should be taken into consideration. As mentioned before, the present method provides a simplified and feasible approach to investigate the hydrodynamics of structures with porous media for wave cases of small steepness and KC numbers. However, when wave steepness and KC numbers become larger, the present model may fail in obtaining satisfactory results compared with experimental data, because it does not consider viscosity, turbulence or other non-linear effects. Therefore, a more comprehensive and accurate numerical method might be needed to tackle these problems, which will be the main topic of our future work. Furthermore, experiments shall be conducted to investigate hydrodynamic characteristics of the proposed hybrid aquaculture system.

Data availability statement

The original contributions presented in the study are included in the article/supplementary material. Further inquiries can be directed to the corresponding author.

Author contributions

XZ: Conceptualization, methodology, programming and writing the original draft. GD: Data curation, funding acquisition and supervision. CB: Writing, review, editing, investigation, methodology and supervision. YZ: Resources and investigation. All authors contributed to the article and approved the submitted version.

Funding

This work was financially supported by the National Natural Science Foundation of China (project nos. 31972843 and 31872610) and LiaoNing Revitalization Talents Program (project nos. XLYC907139 and XLYC2007045).

Conflict of interest

The authors declare that the research was conducted in the absence of any commercial or financial relationships that could be construed as potential conflict of interest.

Publisher's note

References

Aarsnes, J. V., Rudi, H., and Løland, G. (1990). "Current forces on cage, net deflection," in *Engineering for offshore fish farming* (Glasgow: Thomas Telford Publishing), (137–152).

Arshi, H. S., and Stone, K. J. L. (2015). "Improving the lateral resistance of offshore pile foundations for deep water application," in *Proc., 3rd int. symp. on frontiers in offshore geotechnics* (London, UK: CRC Press).

Balash, C., Colbourne, B., Bose, N., and Raman-Nair, W. (2009). Aquaculture net drag force and added mass. *Aquacultural Eng.* 41 (1), 14–21. doi: 10.1016/j.aquaeng.2009.04.003

Bao, W., Kinoshita, T., and Zhao, F. (2009). Wave forces acting on a semi-submerged porous circular cylinder. *Proc. Institution Mechanical Engineers Part M: J. Eng. Maritime Environ.* 223 (3), 349–360. doi: 10.1243/14750902JEME145

Bi, C. W., Zhao, Y. P., and Dong, G. H. (2015). Numerical study on the hydrodynamic characteristics of biofouled full-scale net cage. *China Ocean Eng.* 29 (3), 401–414. doi: 10.1007/s13344-015-0028-9

Bi, C. W., Zhao, Y. P., Dong, G. H., Wu, Z. M., Zhang, Y., and Xu, T. J. (2018). Drag on and flow through the hydroid-fouled nets in currents. *Ocean Eng.* 161, 195–204. doi: 10.1016/j.oceaneng.2018.05.005

Bi, C. W., Zhao, Y. P., Dong, G. H., Xu, T. J., and Gui, F. K. (2014). Numerical simulation of the interaction between flow and flexible nets. *J. Fluids Structures* 45, 180–201. doi: 10.1016/j.jfluidstructs.2013.11.015

Bi, C. W., Zhao, Y. P., Dong, G. H., Xu, T. J., and Gui, F. K. (2017).). numerical study on wave attenuation inside and around a square array of biofouled net cages. *Aquacultural Eng.* 78, 180–189. doi: 10.1016/j.aquaeng.2017.07.006

Braithwaite, R. A., Carrascosa, M. C. C., and McEvoy, L. A. (2007). Biofouling of salmon cage netting and the efficacy of a typical copper-based antifoulant. *Aquaculture* 262, 219–226. doi: 10.1016/j.aquaculture.2006.11.027

Buck, B. H. (2004). *Farming a high energy environment: Potentials and constraints of sustainable offshore aquaculture in the German bight (North Sea)* (Bremen: University of Bremen). dissertation.

Buck, B. H., and Krause, G. (2012). "Integration of aquaculture and renewable energy systems," in *Encyclopaedia of sustainability science and technology*, vol. 1 . Ed. R. A. Meyers (New York: Springer Science + Business Media LLC), 511–533. doi: 10.1007/978-1-4419-0851-3_180

Chu, Y. I., and Wang, C. M. (2020). Hydrodynamic response analysis of combined spar wind turbine and fish cage for offshore fish farms. *Int. J. Struct. Stability Dynamics* 20 (9), 2050104. doi: 10.1142/S0219455420501047

Chu, Y. I., Wang, C. M., and Zhang, H. (2022). A frequency domain approach for analyzing motion responses of integrated offshore fish cage and wind turbine under wind and wave actions. *Aquacultural Eng.* 97, 102241. doi: 10.1016/j.aquaeng.2022.102241

Chwang, A. T., and Chan, A. T. (1998).). interaction between porous media and wave motion. *Annu. Rev. Fluid Mech.* 30, 53–84. doi: 10.1146/annurev.fluid.30.1.53

DeCew, J., Tsukrov, I., Risso, A., Swift, M. R., and Celikkol, B. (2010). Modeling of dynamic behavior of a single-point moored submersible fish cage under currents. *Aquacultural Eng.* 43 (2), 38–45. doi: 10.1016/j.aquaeng.2010.05.002

Forchheimer, P. (1901). Wasserbewegung durch boden. *Z. Ver. Dtsch. Ing* 45, 1782–1788.

Hall, P. (1984). On the stability of unsteady boundary layer on a cylinder oscillating transversely in a viscous fluid. *J. Fluid Mech.* 146, 347–367. doi: 10.1017/S0022112084001907

Honji, H. (1981). Streaked flow around an oscillating circular cylinder. *J. Fluid Mech.* 107, 509–520. doi: 10.1017/S0022112081001894

Huang, C.-C., Tang, H.-J., and Liu, J.-Y. (2007). Dynamical analysis of net cage structures for marine aquaculture: numerical simulation and model testing. *Aquacult. Eng.* 35 (3), 258–270. doi: 10.1016/j.aquaeng.2006.03.003

Jahani, K., Langlois, R. G., and Afagh, F. F. (2022). Structural dynamics of offshore wind turbines: A review. *Ocean Eng.* 251, 111136. doi: 10.1016/j.oceaneng.2022.111136

Jiang, (2017). *Design and mechanical properties analysis of aquaculture net cage installed on jacket wind turbine base* (Zhenjiang: Jiangsu University of Science and Technology).

Klebert, P., Lader, P., Gansel, L., and Oppedal, F. (2013). Hydrodynamic interactions on net panel and aquaculture fish cages: a review. *Ocean Eng.* 58, 260–274. doi: 10.1016/j.oceaneng.2012.11.006

Kristiansen, T., and Faltinsen, O. M. (2012). Modelling of current loads on aquaculture net cages. *J. Fluids Structures* 34, 218–235. doi: 10.1016/j.jfluidstructs.2012.04.001

Lader, P. F., Enerhaug, B., Fredheim, A., and Krokstad, J. (2003). "September. modelling of 3D net structures exposed to waves and current," in *3rd international conference on hydroelasticity in marine technology* (Oxford, UK: Department of Engineering Science, The University of Oxford), (19–26).

Lader, P., Fredriksson, D. W., Guenther, J., Volent, Z., Blocher, N., Kristiansen, D., et al. (2015). Drag on hydroid-fouled nets–an experimental approach. *China Ocean Eng.* 29 (3), 369–389. doi: 10.1007/s13344-015-0026-y

Lehane, B. M., Pedram, B., Doherty, J. A., and Powrie, W. (2014). Improved performance of monopiles when combined with footings for tower foundations in sand. *J. geotechnical geoenvironmental Eng.* 140 (7), 04014027. doi: 10.1061/(ASCE)GT.1943-5606.0001109

Li, A. J., and Liu, Y. (2019). New analytical solutions to water wave diffraction by vertical truncated cylinders. *Int. J. Naval Architecture Ocean Eng.* 11 (2), 952–969. doi: 10.1016/j.ijnaoe.2019.04.006

Li, Y., Liu, Y., and Teng, B. (2006). Porous effect parameter of thin permeable plates. *Coast. Eng. J.* 48 (4), 309–336. doi: 10.1142/S0578563406001441

Liu, Y. (2019). HAMS: A frequency-domain preprocessor for wave-structure interactions–theory, development, and application. *J. Mar. Sci. Eng.* 7, 81. doi: 10.3390/jmse7030081

Liu, H. F., Bi, C. W., and Zhao, Y. P. (2020). Experimental and numerical study of the hydrodynamic characteristics of a semisubmersible aquaculture facility in waves. *Ocean Eng.* 214, 107714. doi: 10.1016/j.oceaneng.2020.107714

Liu, Y., and Li, Y. (2016). Predictive formulas in terms of keulegan-carpenter numbers for the resistance coefficients of perforated walls in jarlan-type caissons. *Ocean Eng.* 114, 101–114. doi: 10.1016/j.oceaneng.2016.01.007

Liu, Y., and Li, H. (2017). Iterative multi-domain BEM solution for water wave reflection by perforated caisson breakwaters. *Eng. Anal. Boundary Elements* 77, 70–80. doi: 10.1016/j.enganabound.2016.12.011

Liu, H., Zhang, L., Chen, H., Zhang, W., and Liu, M. (2018). Wave diffraction by vertical cylinder with multiple concentric perforated walls. *Ocean Eng.* 166, 242–252. doi: 10.1016/j.oceaneng.2018.08.025

Ma, C., Bi, C. W., and Xu, Z. (2022). Dynamic behaviors of a hinged multi-body floating aquaculture platform under regular waves. *Ocean Eng.* 243, 110278. doi: 10.1016/j.oceaneng.2021.110278

Mackay, E., Liang, H., and Johanning, L. (2021b). A BEM model for wave forces on structures with thin porous elements. *J. Fluids Struct.* 102, 103246. doi: 10.1016/j.jfluidstructs.2021.103246

Mackay, E., Shi, W., Qiao, D., Gabl, R., Davey, T., Ning, D., et al. (2021a). Numerical and experimental modelling of wave interaction with fixed and floating porous cylinders. *Ocean Eng.* 242, 110118. doi: 10.1016/j.oceaneng.2021.110118

Ma, M., Zhang, H., Jeng, D. S., and Wang, C. M. (2022). Analytical solutions of hydroelastic interactions between waves and submerged open-net fish cage modeled as a porous cylindrical thin shell. *Phys. Fluids* 34 (1), 017104. doi: 10.1063/5.0076659

Molin, B. (2001). On the added mass and damping of periodic arrays of fully or partially porous disks. *J. Fluids Struct.* 15, 275–290. doi: 10.1006/jfls.2000.0338

Molin, B. (2011). Hydrodynamic modeling of perforated structures. *Appl. Ocean Res.* 33 (1), 1–11. doi: 10.1016/j.apor.2010.11.003

Molin, B., and Legras, J.-L. (1990). Hydrodynamic modeling of the Roseau tower stabilizer. in. *Proc. 9th OMAE Conf.* 1, 329–336.

Patursson, Ø., Swift, M. R., Tsukrov, I., Simonsen, K., Baldwin, K., Fredriksson, D. W., et al. (2010). Development of a porous media model with application to flow through and around a net panel. *Ocean Eng.* 37 (2-3), 314–324. doi: 10.1016/j.oceaneng.2009.10.001

Saghi, H. (2019). A parametric study on wave–floating storage tank interaction using coupled VOF-FDM method. *J. Mar. Sci. Technol.* 24, 454–465. doi: 10.1007/s00773-018-0564-0

Saghi, H., Mikkola, T., and Hirdaris, S. (2022).). A machine learning method for the evaluation of hydrodynamic performance of floating breakwaters in waves. *Ships Offshore Structures* 17 (7), 1447–1461. doi: 10.1080/17445302.2021.1927358

Sarpkaya, T. (1986). Force on a circular cylinder in viscous oscillatory flow at low keulegan–carpenter numbers. *J. Fluid Mech.* 165, 61–71. doi: 10.1017/S0022112086002999

Sollitt, C., and Cross, R. (1972). "Wave transformation through permeable breakwaters," in *13th international conference on coastal engineering* (New York: ASME) 1827–1846.

Suh, K. D., Kim, Y. W., and Ji, C. H. (2011). An empirical formula for friction coefficient of a perforated wall with vertical slits. *Coast. Eng.* 58 (1), 85–93. doi: 10.1016/j.coastaleng.2010.08.006

Swift, M. R., Fredriksson, D. W., Unrein, A., Fullerton, B., Patursson, O., and Baldwin, K. (2006). Drag force acting on biofouled net panels. *Aquacultural Eng.* 35 (3), 292–299. doi: 10.1016/j.aquaeng.2006.03.002

Taylor, G. (1956). Fluid flow in regions bounded by porous surfaces. *Proc. R. Soc London Ser. A* 234, 456–475. doi: 10.1098/rspa.1956.0050

Teng, B., Zhao, M., and Li, Y. C. (2001). Wave diffraction from a cylinder with porous upper wall and an inner column. *Acta Oceanol. Sin.* 23 (6), 133–142. doi: 10.3321/j.issn:0253-4193.2001.06.016

Tsukrov, I., Eroshkin, O., Fredriksson, D., Swift, M. R., and Celikkol, B. (2003). Finite element modeling of net panels using a consistent net element. *Ocean Eng.* 30 (2), 251–270. doi: 10.1016/S0029-8018(02)00021-5

Wang, X., and Li, J. (2020). Parametric study of hybrid monopile foundation for offshore wind turbines in cohesionless soil. *Ocean Eng.* 218 (3), 108172. doi: 10.1016/j.oceaneng.2020.108172

Wang, X., Li, S., and Li, J. (2022). Load bearing mechanism and simplified design method of hybrid monopile foundation for offshore wind turbines. *Appl. Ocean Res.* 126, 103286. doi: 10.1016/j.apor.2022.103286

Wang, X., Zeng, X., Yang, X., and Li, J. (2018). Feasibility study of offshore wind turbines with hybrid monopile foundation based on centrifuge modeling. *Appl. Energy* 209, 127–139. doi: 10.1016/j.apenergy.2017.10.107

Yang, X., Zeng, X., Wang, X., Berrila, J., and Li, X. (2019). Performance and bearing behavior of monopile-friction wheel foundations under lateral-moment loading for offshore wind turbines. *Ocean Eng.* 184, 159–172. doi: 10.1016/j.oceaneng.2019.05.043

Zhao, F., Bao, W., Kinoshita, T., and Itakura, H. (2010a). Theoretical and experimental study on a porous cylinder floating in waves. *J. offshore mechanics Arctic Eng.* 133 (1), 11301. doi: 10.1115/1.4001435

Zhao, F., Bao, W., Kinoshita, T., and Itakura, H. (2010b). Interaction of waves and a porous cylinder with an inner horizontal porous plate. *Appl. Ocean Res.* 32 (2), 252–259. doi: 10.1016/j.apor.2009.11.003

Zhao, Y. P., Bi, C. W., Dong, G. H., Gui, F. K., Cui, Y., Guan, C. T., et al. (2013). Numerical simulation of the flow around fishing plane nets using the porous media model. *Ocean Eng.* 62, 25–37. doi: 10.1016/j.oceaneng.2013.01.009

Zhao, Y. P., Li, Y. C., Dong, G. H., Gui, F. K., and Teng, B. (2007). Numerical simulation of the effects of structure size ratio and mesh type on three-dimensional deformation of the fishing-net gravity cage in current. *Aquacultural Eng.* 36 (3), 285–301. doi: 10.1016/j.aquaeng.2007.01.003

Zheng, X. Y., and Lei, Y. (2018). Stochastic response analysis for a floating offshore wind turbine integrated with a steel fish farming cage. *Appl. Sci.* 8 (8), 1229. doi: 10.3390/app8081229

Appendix

After truncating m to M and l to L, we can establish a set of matrix equations based on Equations (14) to (17).

From Equation (14), based on the orthogonal relationship $\int_{-h}^{0} Z_{m_1}(k_{m_1}z)Z_{m_2}(k_{m_2}z)dz = 0,\ m_1 \neq m_2$, we can get

$$\left\{a_{0m}^{(1)}\right\} + \left[a_{mm}^{(1)}\right]\{A_{nm}\} = \left[b_{ml}^{(1)}\right]\{B_{nl}\} + \left[c_{ml}^{(1)}\right]\{C_{nl}\}. \quad \text{(i)}$$

The matrix coefficients are given by

$$\left\{a_{0m}^{(1)}\right\} = \begin{cases} \mathrm{i}^n k_0 J_n'(k_0 a_2)\displaystyle\int_{-h}^{0} Z_0^2(k_0 z)dz, & m = 0 \\ 0, & m = 1,\ 2,\ 3,\ \ldots,\ M \end{cases}$$

$$\left[a_{mm}^{(1)}\right] = diag\left(k_m R_n'(k_m a_2)\int_{-h}^{0} Z_m^2(k_m z)dz\right), m = 0, 1, 2, 3, \ldots, M$$

$$b_{ml}^{(1)} = \lambda_l V_n^{(1)'}(\lambda_l a_2)\int_{-d}^{0} Z_l(\lambda_l z)Z_m(k_m z)dz,\ l = 0,\ 1,\ 2,\ 3,\ \ldots,\ L,\quad m = 0,\ 1,\ 2,\ 3,\ \ldots,\ M$$

$$c_{ml}^{(1)} = \lambda_l V_n^{(2)'}(\lambda_l a_2)\int_{-d}^{0} Z_l(\lambda_l z)Z_m(k_m z)dz,\ l = 0,\ 1,\ 2,\ 3,\ \ldots,\ L,\quad m = 0,\ 1,\ 2,\ 3,\ \ldots,\ M$$

where "diag" indicates the matrix diagonalization of a vector. The integrals of the vertical eigenfunctions are given by

$$\int_{-h}^{0} Z_m^2(k_m z)dz = \begin{cases} \dfrac{\tanh(k_0 h) + k_0 h\ \mathrm{sech}^2(k_0 h)}{2k_0}, & m = 0 \\ \dfrac{\tan(k_m h) + k_m h\ \sec^2(k_m h)}{2k_m}, & m = 1, 2, 3, \ldots, M \end{cases}$$

$$\int_{-d}^{0} Z_l(\lambda_l z)Z_m(k_m z)dz = \begin{cases} \dfrac{-\lambda_0 \tanh(\lambda_0 d) + k_0 \tanh(k_0 h) + k_0 \mathrm{sech}(\lambda_0 d)\mathrm{sech}(k_0 h)\sinh(k_0(d-h))}{k_0^2 - \lambda_0^2}, & l = 0,\ m = 0 \\ \dfrac{\lambda_l \tan(\lambda_l d) + k_0 \tanh(k_0 h) - k_0 \sec(\lambda_l d)\mathrm{sech}(k_0 h)\sinh(k_0(h-d))}{k_0^2 + \lambda_l^2}, & l = 1,\ 2,\ 3,\ \ldots,\ L,\ m = 0 \\ \dfrac{\lambda_0 \tanh(\lambda_0 d) + k_m \tan(k_m h) - k_m \mathrm{sech}(\lambda_0 d)\sec(k_m h)\sin(k_m(h-d))}{k_m^2 + \lambda_0^2}, & l = 0,\quad m = 1,\ 2,\ 3,\ \ldots,\ M \\ \dfrac{-\lambda_l \tan(\lambda_l d) + k_m \tan(k_m h) + k_m \sec(\lambda_l d)\sec(k_m h)\sin(k_m(d-h))}{k_m^2 - \lambda_l^2}, & l = 1,\ 2,\ 3,\ \ldots,\ L,\quad m = 1,\ 2,\ 3,\ \ldots,\ M \end{cases}$$

.

From Equation (15), based on the orthogonal relationship $\int_{-d}^{0} Z_{l_1}(\lambda_{l_1}z)Z_{l_2}(\lambda_{l_2}z)dz = 0,\ l_1 \neq l_2$, we can derive

$$\left\{a_{0l}^{(2)}\right\} + \left[a_{lm}^{(2)}\right]\{A_{nm}\} = \left[b_{ll}^{(2)}\right]\{B_{nl}\} + \left[c_{ll}^{(2)}\right]\{C_{nl}\}. \text{(ii)}$$

The matrix coefficients are expressed as

$$a_{0l}^{(2)} = \mathrm{i}^n J_n(k_0 a_2)\int_{-d}^{0} Z_l(\lambda_l z)Z_0(k_0 z)dz,\ l = 0,\ 1,\ 2,\ 3,\ \ldots,\ L \quad ,$$

$$a_{lm}^{(2)} = R_n(k_0 a_2)\int_{-d}^{0} Z_l(\lambda_l z)Z_m(k_m z)dz,\ l = 0,\ 1,\ 2,\ 3,\ \ldots,\ L,\quad m = 0,\ 1,\ 2,\ 3,\ \ldots,\ M \quad ,$$

$$\left[b_{ll}^{(2)}\right] = diag\left(\left[V_n^{(1)}(\lambda_l a_2) - \frac{1}{\mathrm{i}\sigma_2}\lambda_l V_n^{(1)\prime}(\lambda_l a_2)\right]\int_{-d}^{0} Z_l^2(\lambda_l z)dz\right),\ l = 0,\ 1,\ 2,\ 3,\ \ldots,\ L$$

$$\left[c_{ll}^{(2)}\right] = diag\left(\left[V_n^{(2)}(\lambda_l a_2) - \frac{1}{\mathrm{i}\sigma_2}\lambda_l V_n^{(2)\prime}(\lambda_l a_2)\right]\int_{-d}^{0} Z_l^2(\lambda_l z)dz\right),\ l = 0,\ 1,\ 2,\ 3,\ \ldots,\ L \quad ,$$

where the integral of the eigenfunction is defined as

$$\int_{-d}^{0} Z_l^2(\lambda_l z)dz = \begin{cases} \dfrac{\tanh(\lambda_0 d) + \lambda_0 d\mathrm{sech}^2(\lambda_0 d)}{2\lambda_0}, & l = 0 \\ \dfrac{\tan(\lambda_l d) + \lambda_l d\sec^2(\lambda_l d)}{2\lambda_l}, & l = 1,\ 2,\ 3,\ \ldots,\ L \end{cases}$$

From Equation (16), we can get

$$\left[d_{ll}^{(3)}\right]\{D_{nl}\} = \left[b_{ll}^{(3)}\right]\{B_{nl}\} + \left[c_{ll}^{(3)}\right]\{C_{nl}\}. \text{(iii)}$$

The matrix coefficients are expressed as

$$\left[d_{ll}^{(3)}\right] = diag\left(\lambda_l W_n'(\lambda_l a_1)\int_{-d}^{0} Z_l^2(\lambda_l z)dz\right),\ l = 0,\ 1,\ 2,\ 3,\ \ldots,\ L \quad ,$$

$$\left[b_{ll}^{(3)}\right] = diag\left(\lambda_l V_n^{(1)\prime}(\lambda_l a_1)\int_{-d}^{0} Z_l^2(\lambda_l z)dz\right),\ l = 0,\ 1,\ 2,\ 3,\ \ldots,\ L$$

$$\left[c_{ll}^{(3)}\right] = diag\left(\lambda_l V_n^{(2)\prime}(\lambda_l a_1)\int_{-d}^{0} Z_l^2(\lambda_l z)dz\right),\ l = 0,\ 1,\ 2,\ 3,\ \ldots,\ L$$

From Equation (17), we can get

$$\left[d_{ll}^{(4)}\right]\{D_{nl}\} = \left[b_{ll}^{(4)}\right]\{B_{nl}\} + \left[c_{ll}^{(4)}\right]\{C_{nl}\}. \text{(iv)}$$

The matrix coefficients are expressed as

$$\left[d_{ll}^{(4)}\right] = diag\left(\left[W_n(\lambda_l a_1) - \frac{1}{\mathrm{i}\sigma_1}\lambda_l W_n'(\lambda_l a_1)\right]\int_{-d}^{0} Z_l^2(\lambda_l z)dz\right),\ l = 0,\ 1,\ 2,\ 3,\ \ldots,\ L$$

$$\left[b_{ll}^{(4)}\right] = diag\left(V_n^{(1)}(\lambda_l a_1)\int_{-d}^{0} Z_l^2(\lambda_l z)dz\right),\ l = 0,\ 1,\ 2,\ 3,\ \ldots,\ L$$

$$\left[c_{ll}^{(4)}\right] = diag\left(V_n^{(2)}(\lambda_l a_1)\int_{-d}^{0} Z_l^2(\lambda_l z)dz\right),\ l = 0,\ 1,\ 2,\ 3,\ \ldots,\ L$$

Equations(i) to (iv) constitute a system of linear algebraic equations. All the unknown coefficients in the velocity potentials can be determined by solving this system of linear algebraic equations.

Frontiers in Marine Science

TYPE Original Research
PUBLISHED 07 February 2023
DOI 10.3389/fmars.2023.1134278

OPEN ACCESS

EDITED BY
Zhao Yunpeng,
Dalian University of Technology, China

REVIEWED BY
Binzhen Zhou,
South China University of Technology, China
Hung-Jie Tang,
National Cheng Kung University, Taiwan

*CORRESPONDENCE
Peng Li
✉ peng.li@hrbeu.edu.cn

SPECIALTY SECTION
This article was submitted to Marine Fisheries, Aquaculture and Living Resources, a section of the journal Frontiers in Marine Science

RECEIVED 30 December 2022
ACCEPTED 20 January 2023
PUBLISHED 07 February 2023

CITATION
Yu S, Qin H, Li P, Gong F and Tian Y (2023) Experimental study on drag characteristics of the practical rigid net under different current conditions.
Front. Mar. Sci. 10:1134278.
doi: 10.3389/fmars.2023.1134278

Experimental study on drag characteristics of the practical rigid net under different current conditions

Songchen Yu[1,2], Hongde Qin[1,2], Peng Li[1,2,3]*, Fangyu Gong[1,2] and Yu Tian[3]

[1]Science and Technology on Underwater Vehicle Laboratory, Harbin Engineering University, Harbin, China, [2]College of Shipbuilding Engineering, Harbin Engineering University, Harbin, China, [3]Yantai Research Institute and Graduate School of Harbin Engineering University, Yantai, China

The net structure of a cage is an important component to ensure the survival environment of aquaculture. In order to ensure the safety of the net, an experimental study on practical rigid nets is conducted in this paper. The drag force characteristics of the nets with different mesh sizes and different twine thicknesses are analyzed, and the impact of 90° and 45° attack angles on the drag force characteristics of the net are further studied. The empirical formulae for calculating the drag force of the net under different attack angles are given. The calculated drag forces are compared with the literature, and the results are in good agreement. Particularly, the current velocity is taken as one of the variables in the formulae to include the influence of nonlinear factors caused by the extreme current velocity in the drag force calculation.

KEYWORDS

practical net, drag force, attack angle, empirical formula, current velocity

Highlights

- The relationship between the drag force of the net and the current velocity is quadratic polynomial.
- Under a similar mesh size, the thicker the net twine, the greater the drag force, especially at 90° attack angle.
- The drag force of net at attack angle of 90° is basically ("$\sqrt{2}$") times that at 45°.
- The empirical formulae of the average drag force including the influence of nonlinear factors on the net are given.

1 Introduction

The aquaculture industry has been developing vigorously over the past five decades (Xu and Qin, 2020). Due to limited space in coastal areas and the aggravation of environmental pollution, transformation to pelagic aquaculture has become a new goal (Costa-Pierce and Bridger, 2002; Fredriksson et al., 2003; Klebert et al., 2015). New types of fish farms, such as a semi-submersible offshore fish farm (Yu et al., 2021), deep-sea aquaculture vessel (Li et al., 2019), have been put into use in recent years. In order to ensure the safety of large-scale aquaculture fishery, the strength of the rigid fish nets fixed by the frames cannot be ignored. There is a need to focus on the hydrodynamic responses of the net under extreme sea conditions to guide the design and application of offshore cages.

Improving the understanding of the interaction between currents and net in aquaculture cages is crucial for the development of efficient and sustainable aquaculture in the future (Klebert et al., 2013). Different modeling methods have been developed, such as lumped mass method (Li et al., 2006), four-sided super-elements (Lader et al., 2003), consistent finite net elements (Tsukrov et al., 2003), current blockage model (Santo, 2022), and Kriging metamodel (Wang et al., 2022a) to better simulate the deformation and tension distribution of the net as well as the volume reductions of the net cages (Lader et al., 2008). Moreover, Cheng et al. (2020) have reviewed 11 commonly used hydrodynamic models comprehensively. However, a growing number of scholars pay attention to the study of hydrodynamic responses, including the flow field variations and drag force characteristics of the net.

For normal and tangential drag coefficients, Zhan et al. (2006) and Niño et al. (2020) carried out an experiment study. Endresen and Føre (2022) carried out a numerical simulation on the new formulae. Empirical values for normal drag coefficients are proposed by Tsukrov et al. (2011) for various types of copper netting, and Cha et al. (2013) compared the drag coefficients of copper alloy nets with knotless fabric nets. In addition, the drag coefficients of nylon nets (Zhou et al., 2015) and knotless polyethylene nets (Tang et al., 2017; Tang et al., 2019) under different attack angles were studied. It is concluded that the normal drag coefficient is determined by the synergistic control of Reynolds number (Re) and solidity ratio, and the solidity ratio has a dual influence on the drag coefficient of inclined netting panels. To compare with the numerical results, Balash et al. (2009) conducted an experiment to measure the hydrodynamic loads, including drag force and added mass on plane nets with differing mesh geometry under steady and oscillating flows. Taking the effects of the net solidity, the net material, and the knot pattern into account, Dong et al. (2019) investigated the hydrodynamic force on net panels in waves by experiments, and a wave force model for the net panel was proposed. Considering the offshore cages with fine-mesh nettings used for young sardine culture, Shimizu et al. (2018) studied the drag coefficient on fine-mesh nettings, tending to avoid the effects of blocking. The open-source hydrodynamic toolbox REEF3D is adopted to investigate the hydrodynamic drag on the net, and the simulation accuracy is in good agreement with flume experiments and previous research (Wang et al., 2022b).

According to the linear free-wake equations in conjunction with an eddy viscosity formulation, the relationship between the drag coefficient and the wake velocity was derived by Løland (1993), and the behavior of the near- and far-field wake was investigated. To investigate the reduction of flow velocity downstream from a fishing net, a series of laboratory experiments was conducted by Bi et al. (2013). They found that the reduction in flow velocity tended to increase with the increasing attack angle, that is, the angle between the plane net and the vertical direction, and the reduction factors under different numbers of nets were given. Porous media models were used for simulating the fishing nets in order to obtain the flow field variation around the net panel efficiently (Patursson et al., 2010; Zhao et al., 2013; Bi et al., 2014). Based on one-way coupling combining the shear stress turbulent k-omega model and the large deformation nonlinear structural finite element model, a fluid–structure interaction model was carried out to evaluate the flow field distribution through the net (Zou et al., 2020). Wang et al. (2021) proposed computational meshing strategies which are suitable for smooth and fabric twines, and the fluid flow through a fixed net panel is qualitatively analyzed.

Although relevant experimental or numerical studies on the plane net have been conducted by scholars, there are few experimental research considering the extreme current velocity. In this paper, an experimental study on the drag force characteristics of the practical rigid plane net is carried out, and the influence of the twine thickness and mesh size on the drag force characteristics of the net is analyzed. At the same time, the relationship of the drag force between two attack angles is obtained. The empirical formulae of the drag force on the plane net at different attack angles with the variables of current velocity and solidity are given.

In what follows, we first introduce the parameters of the physical models and experimental set up in Section 2; this part also includes test conditions and data processing. Section 3 gives the numerical calculation method and the numerical model. The comparative results of drag force at different attack angles and current velocities are exhibited in Section 3; the empirical formulae and a thorough explanation of the results and errors are also discussed. This is followed by the conclusions of this paper in Section 4.

2 Experiments

2.1 Physical model

The rigid nets used in the experiment are the practical size used in offshore cages. The size of the nets varies according to the size of different aquaculture products. Table 1 illustrates the parameters of the nets used for the experiment, where d is the diameter of the net twine and l_1 l_2 are the side lengths of the mesh. The side length of the mesh is the distance between the axes of two adjacent twines Ensuring that the mesh area is consistent, the equivalence mesh side length is $l = \sqrt{l_1 \cdot l_2}$ in order to calculate the net solidity S_n, and here the net solidity can be written as follows (Kristiansen and Faltinsen, 2012):

$$S_n = \frac{2d}{l} - \left(\frac{d}{l}\right)^2 \tag{1}$$

TABLE 1 Parameters of stainless steel nets.

Group	Name	l_1/mm	l_2/mm	l/mm	d/mm	S_n
1	S1	23.42	24.88	24.14	1.70	0.136
	S2	24.64	25.00	24.82	2.16	0.166
2	S3	35.10	37.60	36.33	2.22	0.118
	S4	35.74	37.84	36.78	3.06	0.159
3	S5	45.22	46.90	46.05	3.10	0.130
	S6	44.78	48.18	46.45	4.12	0.170
4	S7	55.20	56.40	55.80	3.12	0.109
	S8	54.82	57.00	55.90	4.12	0.142
5	S9	65.50	67.62	66.55	3.10	0.091
	S10	65.64	68.50	67.05	4.12	0.119

As described in Table 1, the nets in groups 1–5 have a similar mesh size but different twine diameters, respectively. Figure 1 shows some of the nets used for the experiment, where Figures 1A–D correspond to S3, S4, S5, and S6.

2.2 Experimental setup

Laboratory tests of practical rigid nets under extreme current conditions were conducted at a horizontal circulating water channel in Harbin Engineering University, Heilongjiang, China. The dimensions of the circulating water channel are 7 m (length) × 1.7 m (width) × 1.8 m (deep) with a constant water depth of 1.5 m. The range of flow velocity that can be created by the circulating water channel is 0.3–2.0 m/s, and the equipment is shown in Figure 2.

In order to ensure the stability of the net under extreme current conditions, a frame structure is designed in this paper. The position of the net is fixed by the frame, and the net is connected with the frame by self-locking plastic ribbons. The upstream of the frame is designed as streamline to reduce interference to the flow. The top of the frame is connected with a connector, which can adjust the attack angle. The top end of the connector is connected with a single component force measuring balance, and the data interaction with the dynamic signal testing system is realized through cables to complete the transformation of electrical signals and force signals. The measuring range of the balance in this paper is 100 kgf, and the precision is ± 0.001 kgf, which can effectively ensure the accuracy of the balance reading under extreme current conditions. The top of the balance is connected with a ship-like structure, which can effectively reduce the interference to the water flow. The top of the ship-like structure is

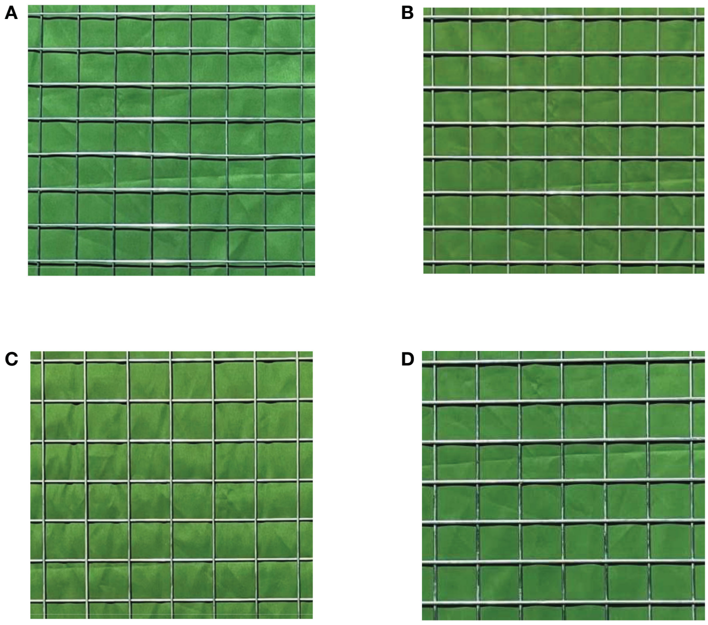

FIGURE 1
Nets with different twine diameters, where **(A)** S3 and **(B)** S4 are two nets corresponding to group 2 and **(C)** S5 and **(D)** S6 are two nets corresponding to group 3.

FIGURE 2
Circulating water channel used for the experiment.

fixed on two rigid brackets, which can span over the circulating water channel. The schematic of the experimental setup is shown in Figure 3.

2.3 Test conditions

Large-scale fish farms like the semi-submersible offshore fish farms are likely to suffer from severe environment in the ocean. Since the hydrodynamic characteristics of the net structure on the fish farm are greatly affected by current, a series of extreme current conditions is tested in this study. According to the geographical characteristics of the sea area where the semi-submersible offshore fish farm is put into use, namely, the Arctic Ocean nearby Norway, which is characterized by the frequent occurrence of the Norwegian warm current, the normal current velocity is 0.25–0.53 m/s. The velocity range given in this paper is $V = 0.3–1.3$ m/s, with an interval of 0.1 m/s. There is a certain error between the actual current velocity and the designed current velocity, as shown in Table 2. V is the designed current velocity, and V_P is the actual current velocity with the largest difference from the designed current velocity in all working conditions. The error range E is ± 2.667%.

2.4 Data processing

Before the experiment under each working condition, it is necessary to carry out balance reset in the data acquisition system. Acquiring of data should be started before the designed current velocity is given. In order to eliminate the effects of noises, the average value of 10 s force data should be read and recorded after stabilization. Moreover, the experiment interval of each case is 5–8 min to avoid water surface interference. Each case is suggested to be repeated two to three times to ensure reproducibility. The procedure of data processing is as follows:

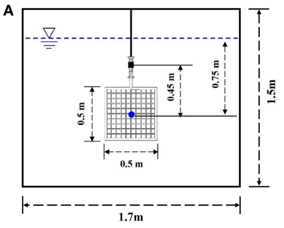

front view

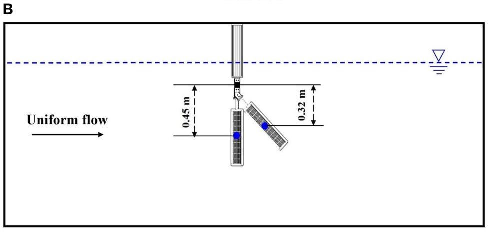

side view

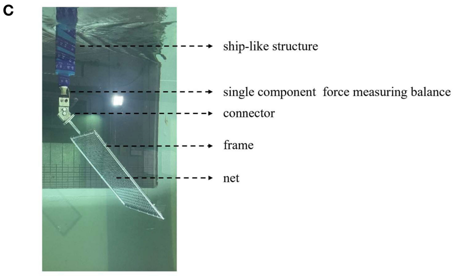

component diagram

FIGURE 3
Schematic of the experimental setup.

TABLE 2 Error between the designed current velocity and actual current velocity.

V (m/s)	V_p (m/s)	E
0.3	0.292	2.667%
0.4	0.395	1.250%
0.5	0.496	0.800%
0.6	0.597	0.500%
0.7	0.697	0.429%
0.8	0.803	0.375%
0.9	0.903	0.333%
1.0	1.003	0.300%
1.1	1.103	0.273%
1.2	1.207	0.583%
1.3	1.306	0.462%

(1) Obtain the raw data from the single component force measuring balance.
(2) Read and record the average value of 10-s force data after each current velocity reaches a steady state.
(3) Repeat the case for two to three times after a 5–8-min experiment interval.

3 Results

According to the Morrison formula, the drag force of rigid net in this paper is calculated numerically, namely:

$$F_\mathrm{D} = C_\mathrm{D}\frac{\rho}{2}A_\mathrm{p}V^2 \tag{2}$$

where C_D is the drag coefficient—according to the empirical value, C_D is taken as 1.2, ρ is the density of water, V is the current velocity, and A_p is the projection area of the net. A_p can be calculated by the solidity S_n, with data given in Table 1. Under the attack angle of 90°, $A_{\mathrm{p\_}}90$ can be written as follows:

$$A_{\mathrm{p\_90}} = A\,{}^{\cdot}S_\mathrm{n} \tag{3}$$

where A is the area of the net panel, $A = l_\mathrm{i}^2$ and l_i is the inner length of the frame. In this paper, li=0.486m. Under the attack angle of 45°, $A_{\mathrm{p\_45}}$ can be written as follows:

$$A_{\mathrm{p\_45}} = \frac{\sqrt{2}}{2}A\,{}^{\cdot}S_\mathrm{n} \tag{4}$$

3.1 Drag force under different current velocities

Figure 4 shows the drag force comparisons of the rigid nets between the experiments and numerical results in groups 1–5 under the current velocities of 0.3–1.3 m/s, with an interval of 0.1 m/s and attack angle of 90°. It can be seen that the relationship between the drag force of the net and the current velocity is quadratic polynomial, regardless of the numerical results or the experimental results. By comparing the drag force of each group in Figure 4, it can be indicated that, under a similar mesh size, the thicker the net twine, the greater the drag force, and the numerical values are basically consistent with the experimental results. In addition, by comparing the numerical and experimental results of the nets in each group, the error is relatively large under the condition of large current velocity, and the error comes from three probable aspects. First of all, as mentioned in Section 2.2, a frame structure is used in the experiments to fix the net model, then the drag force of the net is the total measured force minus the empty frame force, in the condition of the same current velocity and attack angle, which can result in errors on the results during the experiments. Moreover, the existence of the mesh hinders the flow of water, as the moment that the water flows through the net mesh the flow region of the water suddenly becomes narrow. According to the continuity equation, when the overall volume of flow is unchanged, the current velocity will increase when the flow region is getting narrow. Therefore, when passing through the net mesh, an acceleration in the velocity direction will be produced by the current, that is, a force will be generated in the current direction. According to Newton's Third Law this time, a force opposite to the current direction but with the same value will be generated on the net, which will be different from the numerical results. Finally, there is a certain error between the practical current velocity generated by the propeller and the designed current velocity. As mentioned in Section 2.3, the practical current velocity may be slightly greater or less than the designed current velocity, which will affect the drag force of the net in the experiment. The combined influence of three factors leads to the difference between the experimental results and the numerical results. Figure 5 illustrates the drag force comparisons of the rigid nets between the experiments and numerical results in groups 1–5 under the current velocities of 0.3–1.3 m/s, with an interval of 0.1 m/s and attack angle of 45°. From Figure 5, it can be observed that the drag force variation trend is similar, and the drag force of the net in each group under 45° and 90° attack angles seems to have a quadratic polynomial relationship with the increase of current velocity. As the projected area of the net under the attack angle of 45° is obviously less

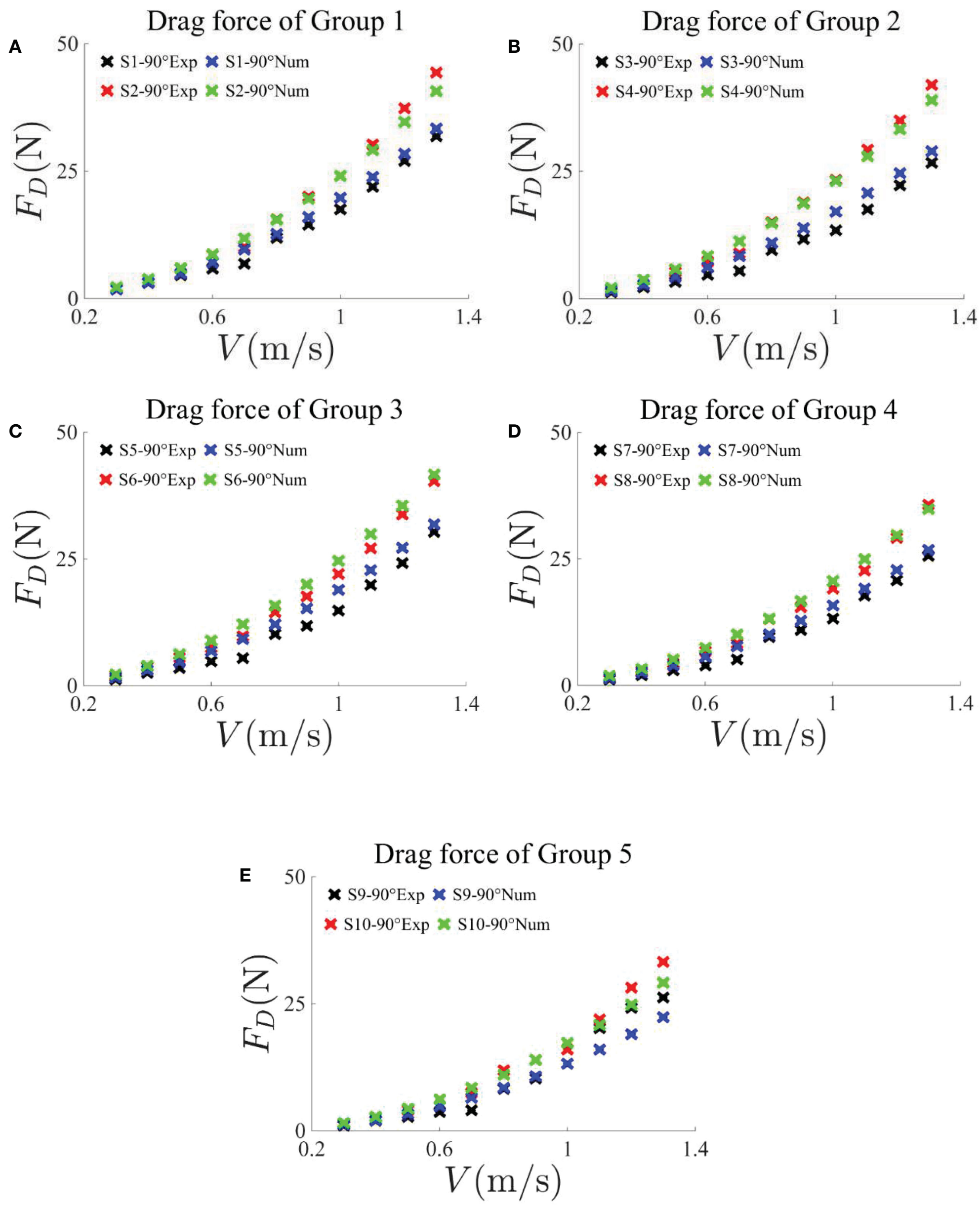

FIGURE 4
Comparisons of average drag force on net panels in groups 1–5 obtained by experiments and numerical simulations under an attack angle of 90°. The current velocities are in the range 0.3–1.3 m/s, with an interval of 0.1 m/s.

than that under 90°, the drag force of the net is obviously small. At the same time, compared with the numerical results, the experimental results under the attack angle of 45° are also smaller. In addition to the probable errors mentioned, another influencing factor existed. When the strain gauge in the force measuring balance is subjected to force or moment, electric charges will be generated at its two ends, which will be transmitted to the data acquisition system through the data line for the force value to be read. When the attack angle is 90°, the force measuring balance is not affected by the net. However, when the attack angle is 45°, the center of the net deviates from the vertical direction of the force measuring balance, and a force moment will be generated by the weight coming from the stainless steel net. It should be noted that, before measuring the drag force of the net, a balancing and zeroing step was taken to eliminate the impact of anthropic factor, namely, the process of net replacement. The impact of the force moment acting on the force measuring balance is also eliminated by this step, which will result in errors.

3.2 Drag force under different attack angles

Figures 6A–J are the drag force comparisons of each net obtained by experiments and numerical simulations under 90° and 45° attack angles. The velocity is 0.3–1.3 m/s, and the interval is 0.1 m/s. It can be observed that the experimental average drag forces are in good agreement with the numerical results. By comparing the drag force in each group, it can be seen that, under the same attack angle and similar mesh size, the thicker the net twine, the greater the drag force,

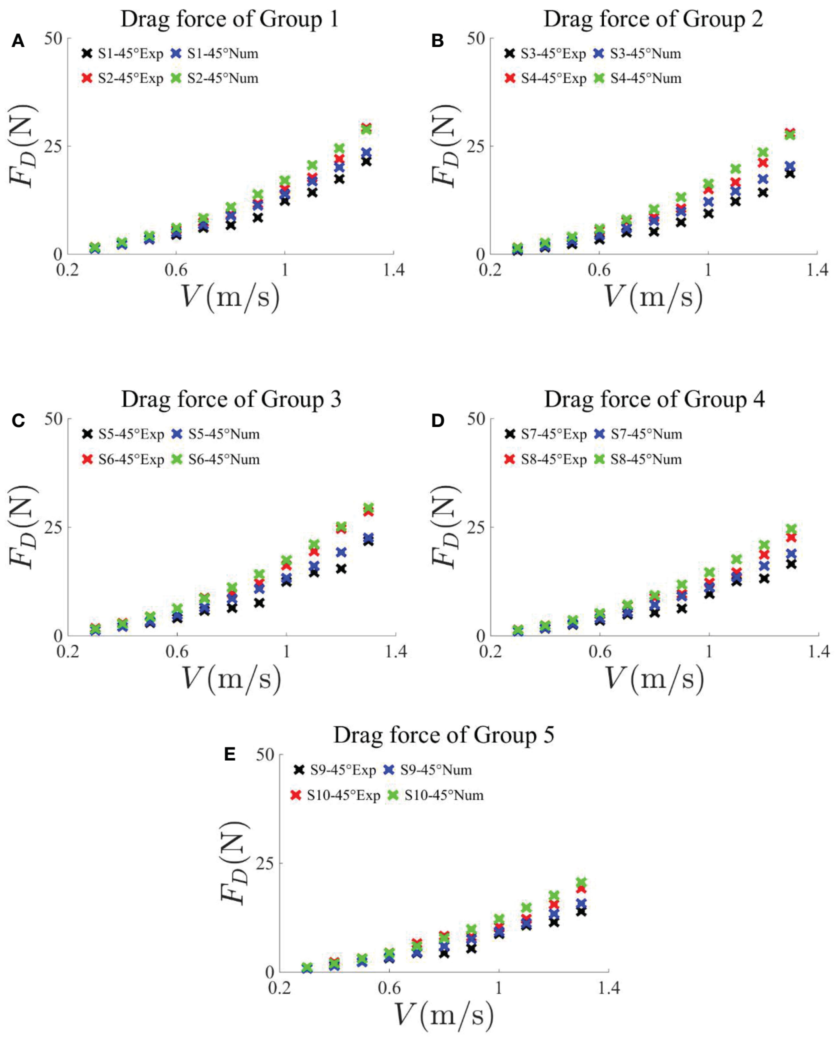

FIGURE 5
Comparisons of average drag force on net panels in Groups 1–5 obtained by experiments and numerical simulations under an attack angle of 45°. The current velocities are in the range 0.3–1.3 m/s, with an interval of 0.1 m/s.

and it is more obvious under the attack angle of 90°. At the same time, with the increase of the current velocity, in terms of the degree of increase of the drag force from a thin twine net to a thick twine net, 90° attack angle is larger than 45° attack angle. In addition, since the projected area under 90° attack angle is larger than that at 45° attack angle, the drag values obtained by experiments and numerical simulations under 90° are both larger than that under 45°. At the same time, by comparing the values of drag force in Figure 6, it can be found through calculation that the drag force at 90° is basically $\sqrt{2}$ times that at 45° because the projected area of the upstream at 90° is $\sqrt{2}$ times that at 45°.

3.3 Fitting formulae of the drag force

Figure 7 shows the fitting curve of experimental drag force with different solidity under different current velocities, where Figure 7A is attack angle of 90° and Figure 7B is attack angle of 45°. Comparing Figures 7A, B, we can see a similar trend of the fitting curve variations. Under the same current velocity, the drag force increases linearly with the increase of solidity, and this linear relationship is more stable when the current velocity is low. At the same time, when the current velocity increases, the slope of the fitting line increases. Under the attack angle of 90°, when the current velocity reaches above 1.1 m/s, the linear relationship starts to be unstable. This is due to the influence of nonlinear factors caused by large flow velocity. Compared with the condition at an attack angle of 90°, the linear relationship between drag force and solidity at an attack angle of 45° under the same current velocity is more stable. It can be speculated that the projection area of the net under the attack angle of 45° is smaller, and it is less affected by the nonlinear factors of extreme current velocity. The fitting formulas of drag force and solidity corresponding to different current velocities at 90° and 45° can be obtained from Figure 7, and the slope k is taken, as shown in Table 3.

Figure 8 is the fitting curve of slope k under different current velocities in Table 3, where (A) is 90° attack angle and (B) is 45° attack angle. The relationship between the slope k and the current velocity is quadratic polynomial, and the increase of k at 90° attack angle is obviously greater than that at 45° attack angle, and under the same current velocity, the slope k at 90° is about $\sqrt{2}$ times of 45°. The fitting

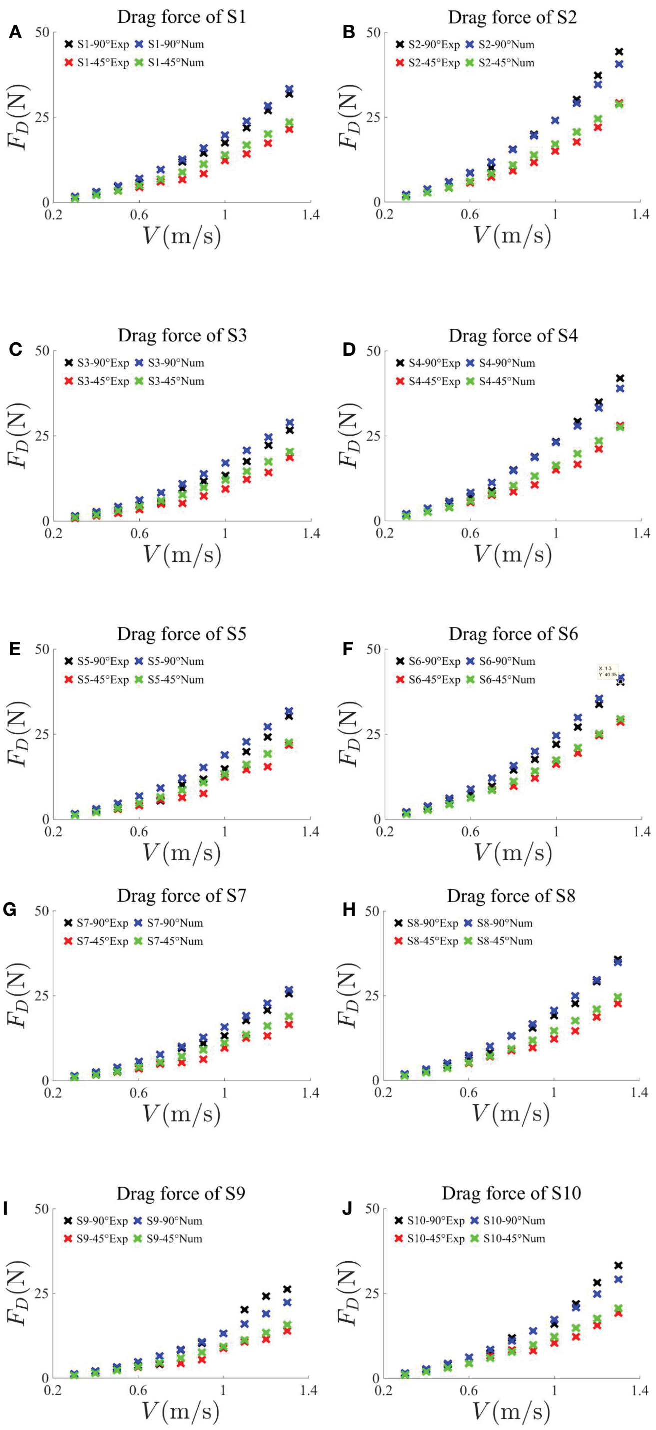

FIGURE 6
Comparisons of average drag force on net panels of group 1 **(A)** S1 and **(B)** S2, group 2 **(C)** S3 and **(D)** S4, group 3 **(E)** S5 and **(F)** S6, group 4 **(G)** S7 and **(H)** S8, and group 5 **(I)** S9 and **(J)** S10 with a similar mesh size obtained by experiments and numerical simulations under an attack angle of 90° and 45°, respectively. The current velocities are in the range 0.3–1.3 m/s, with an interval of 0.1 m/s.

curve formula of slope k and current velocity V can be obtained from Figure 8, namely:

$$k = \begin{cases} 198.43V^2 - 81.881V + 20.883 & \alpha = 90^\circ \\ 123.88V^2 - 51.029V + 17.177 & \alpha = 45^\circ \end{cases} \tag{5}$$

By combining Table 3 and Formula (5), we can get the relationship between the drag force of the net and current velocity, that is:

$$F_{\mathrm{D}} = \begin{cases} (198.43V^2 - 81.881V + 20.883)\cdot S_n & \alpha = 90^\circ \\ (123.88V^2 - 51.029V + 17.177)\cdot S_n & \alpha = 45^\circ \end{cases} \tag{6}$$

According to the empirical formulae for the drag coefficient of plane nets in a steady current established by Milne (1972) [Formula (7)] and Fridman and Danilov (1967) [formula (8)], the drag force of

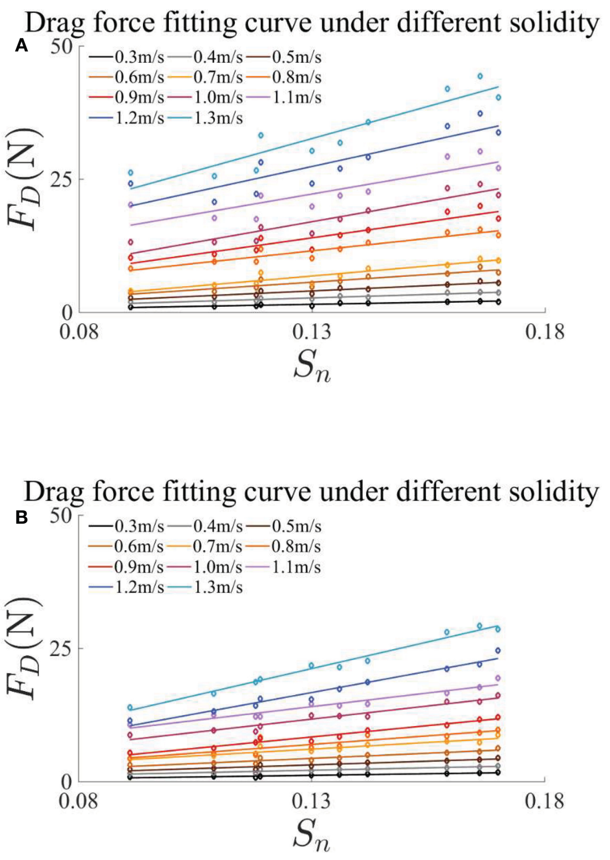

FIGURE 7
Fitting curves of drag force with different solidity values under an attack angle of **(A)** 90° and **(B)** 45°, respectively.

the rigid nets at the attack angle of 90° in this paper can be obtained.

$$C_d = 1 + 1.37S_n + 0.78S_n^2 \tag{7}$$

$$C_d = 3(2S_n/Re)^{0.07} \tag{8}$$

Figures 9 and 10 illustrate the comparison of the drag force of S5, S6, S7, and S8 obtained by the empirical formula in this paper and by Milne (1972) as well as by Fridman and Danilov (1967) under different current velocities. The attack angle is 90° and 45°, respectively. Comparing Figures 9 and 10, it can be found that the drag force variation caused by the attack angle is consistent with the previous analysis. Moreover, it can be seen in Figures 9 and 10 that the drag force value calculated by the empirical formula in this paper is in good agreement with that calculated according to the drag force coefficient of previous scholars. The difference between the drag force of this paper and that of previous scholars is relatively large when the current velocity is large. On the one hand, this paper may focus on the nonlinear effect caused by the extreme current velocity. The current velocity and solidity are taken as the main variables of the empirical formula in this paper. On the other hand, there is a certain error between the practical current velocity and the designed current velocity mentioned previously, which leads to a certain error in the calculated drag force.

4 Conclusion

For the average drag force under different current velocities and attack angles, the experimental average drag forces are in good agreement with the numerical results. The relationship between the drag force of the net and the current velocity is quadratic polynomial. Under a similar mesh size, the thicker the net twine, the greater the drag force, and it is more obvious under the attack angle of 90°. The drag force at 90° is basically $\sqrt{2}$ times that at 45° because of the projected area under different attack angles. The empirical formulae of the drag force on the net are given; the results were compared with the literatures and were found to be in good agreement.

In addition, the error between the numerical and experimental results is relatively large under the condition of large current velocity, and the experimental error comes from three probable aspects: (1) measurement error of the drag force on empty frame and the frame with net, (2) an acceleration in the velocity direction will be produced by the current when the current is passing through the net according to the continuity equation, that is, a force will be generated in the

TABLE 3 Slope *k* of linear fitting formula corresponding to different current velocities at attack angles of 90° and 45°.

V (m/s)	*k*	
	Attack angle of 90°	Attack angle of 45°
0.3	11.971	9.503
0.4	21.339	16.79
0.5	31.665	24.613
0.6	44.605	34.111
0.7	54.063	47.336
0.8	89.325	54.573
0.9	108.76	65.967
1.0	132.51	90.995
1.1	169.84	108.08
1.2	209.62	130.68
1.3	250.67	165.62

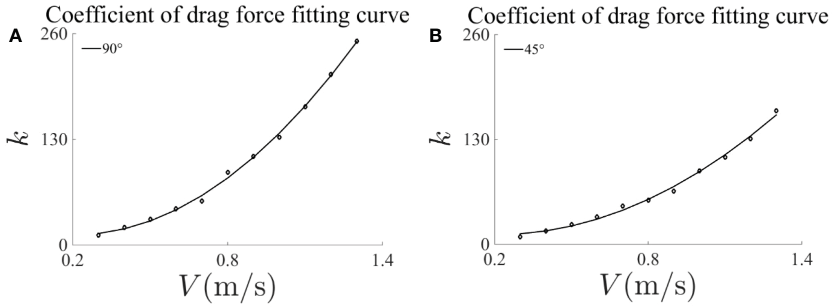

FIGURE 8
Coefficient of drag force fitting curve with different current velocities under an attack angle of **(A)** 90° and **(B)** 45°, respectively.

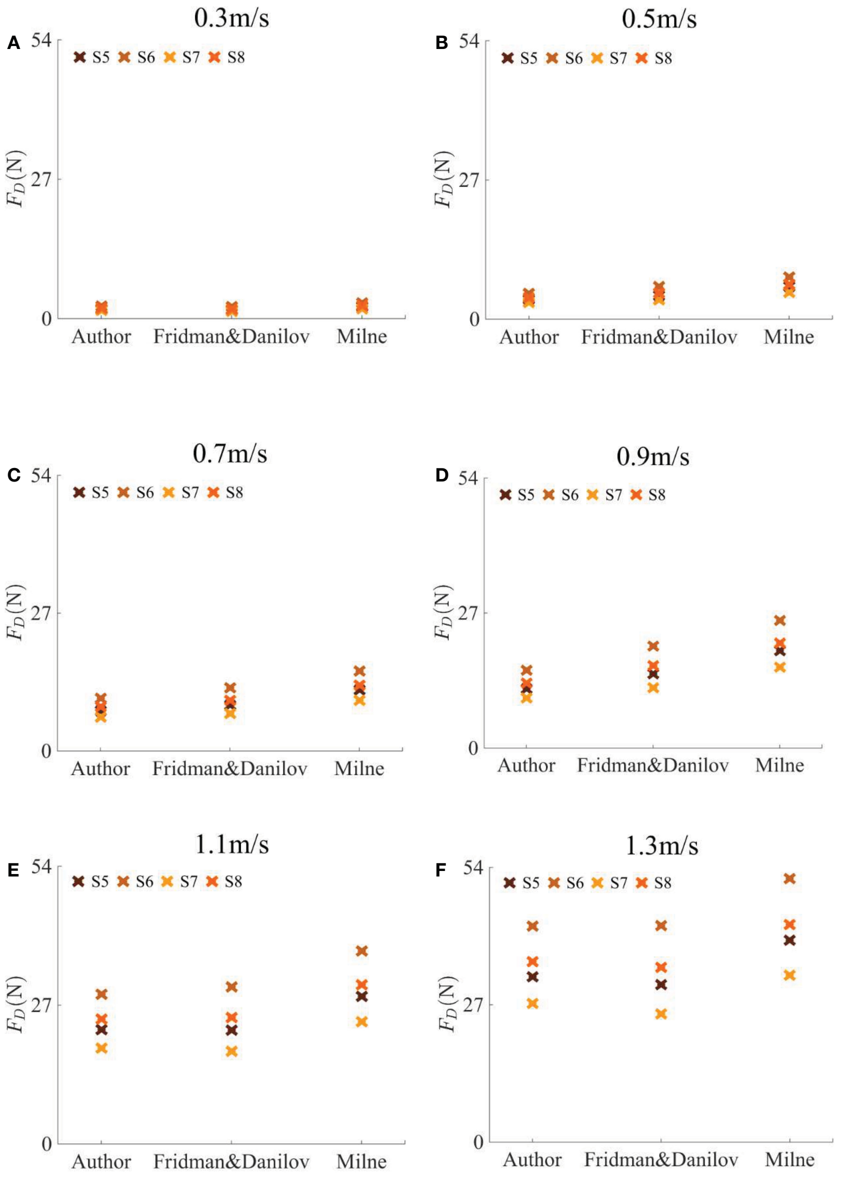

FIGURE 9
Comparisons of the drag force of S5, S6, S7 and S8 at the attack angle of 90°. The data are calculated by the empirical formula in this paper and by Milne (1972) as well as by Fridman and Danilov (1967) under different current velocities.

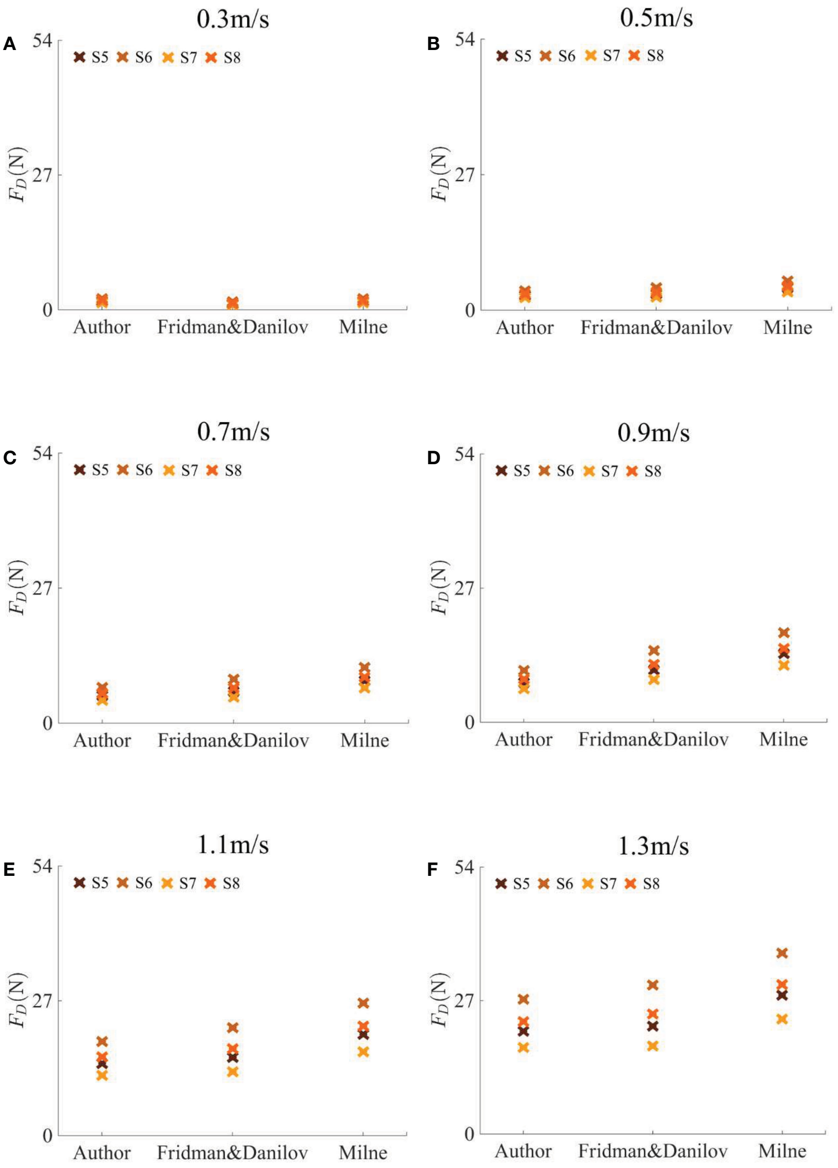

FIGURE 10
Comparisons of the drag force of S5, S6, S7 and S8 at the attack angle of 45°. The data are calculated by the empirical formula in this paper and by Milne (1972) as well as by Fridman and Danilov (1967) under different current velocities.

current direction. A force opposite to the current direction but with the same value will be generated on the net at this time according to Newton's Third Law, which will be different from the numerical results, and (3) the certain error between the practical current velocity generated by the propeller and the designed current velocity. Finally, a moment will be generated by the weight coming from the stainless steel net at the attack angle of 45°. The impact of the moment acting on the force measuring balance is eliminated by balancing and zeroing step, which will result in errors.

Data availability statement

The original contributions presented in the study are included in the article/supplementary material. Further inquiries can be directed to the corresponding author.

Author contributions

SY: Physical model experiments, Validation, Investigation, Data curation and analysis. Writing - original draft. HQ: Supervision, Project administration. PL: Supervision, Project administration, Funding acquisition. FG: Physical model experiments. YT: Physical model experiments. All authors contributed to the article and approved the submitted version.

Funding

This work is financially supported by the National Natural Science Foundation of China (grant numbers 51909040 and 52231011). The Research Fund from Stable Supporting Fund of Science and Technology on Underwater Vehicle Technology (grant number JCKYS2022SXJQR-11), and the Key Technology Research and Development Program of Shandong (grant number 2020CXGC010702) are also greatly acknowledged.

Conflict of interest

The authors declare that the research was conducted in the absence of any commercial or financial relationships that could be construed as a potential conflict of interest.

Publisher's note

References

Balash, C., Colbourne, B., Bose, N., and Raman-Nair, W. (2009). Aquaculture net drag force and added mass. *Aquacultural Engineering.* 41 (1), 14–21. doi: 10.1016/j.aquaeng.2009.04.003

Bi, C. W., Zhao, Y. P., Dong, G. H., Xu, T. J., and Gui, F. K. (2013). Experimental investigation of the reduction in flow velocity downstream from a fishing net. *Aquacultural Engineering.* 57, 71–81. doi: 10.1016/j.aquaeng.2013.08.002

Bi, C. W., Zhao, Y. P., Dong, G. H., Xu, T. J., and Gui, F. K.. (2014). Numerical simulation of the interaction between flow and flexible nets. *J. Fluids Structures.* 45, 180–201. doi: 10.1016/j.jfluidstructs.2013.11.015

Cha, B. J., Kim, H. Y., Bae, J. H., Yang, Y. S., and Kim, D. H.. (2013). Analysis of the hydrodynamic characteristics of chain-link woven copper alloy nets for fish cages. *Aquacultural Engineering.* 56, 79–85. doi: 10.1016/j.aquaeng.2013.05.002

Cheng, H., Li, L., Aarsæther, K. G., and Ong, M. C.. (2020). Typical hydrodynamic models for aquaculture nets: A comparative study under pure current conditions. *Aquacultural Engineering.* 90, 102070. doi: 10.1016/j.aquaeng.2020.102070

Costa-Pierce, B. A., and Bridger, C. J. (2002). The role of marine aquaculture facilities as habitats and ecosystems. *Responsible Mar. aquaculture.*, 105–144. doi: 10.1079/9780851996042.0105

Dong, G. H., Tang, M. F., Xu, T. J., Bi, C. W., and Guo, W. J.. (2019). Experimental analysis of the hydrodynamic force on the net panel in wave. *Appl. Ocean Res.* 87, 233–246. doi: 10.1016/j.apor.2019.04.005

Endresen, P. C., and Føre, H. M. (2022). Numerical Modelling of Drag and Lift Forces on Aquaculture Nets: Comparing New Numerical Load Model with Physical Model Test Results. Proceedings of the ASME 2022 41st International Conference on Ocean, Offshore and Arctic Engineering. Volume 4: Ocean Space Utilization. Hamburg, Germany. V004T05A002. ASME.

Fredriksson, D. W., Swift, M. R., Irish, J. D., Tsukrov, I., and Celikkol, B.. (2003). Fish cage and mooring system dynamics using physical and numerical models with field measurements. *Aquacultural Engineering.* 27 (2), 117–146. doi: 10.1016/S0144-8609(02)00043-2

Fridman, A. L., and Danilov, Y. A. (1967). Ob osobennostyah soprotivleniya rybolovnoi seti. *Rybolovnoe Hozyajstvo* 6, 38–40.

Klebert, P., Lader, P., Gansel, L., and Oppedal, F.. (2013). Hydrodynamic interactions on net panel and aquaculture fish cages: A review. *Ocean Engineering.* 58 (4), 260–274. doi: 10.1016/j.oceaneng.2012.11.006

Klebert, P., Patursson, Ø., Endresen, P. C., Rundtop, P., Birkevold, J., and Rasmussenb, H. W.. (2015). Three-dimensional deformation of a large circular flexible sea cage in high currents: field experiment and modeling. *Ocean Engineering.* 104, 511–520. doi: 10.1016/j.oceaneng.2015.04.045

Kristiansen, T., and Faltinsen, O. M. (2012). Modelling of current loads on aquaculture net cages. *J. Fluids Structures.* 34, 218–235. doi: 10.1016/j.jfluidstructs.2012.04.001

Løland, G. (1993). Current forces on, and water flow through and around, floating fish farms. *Aquaculture Int.* 1 (1), 72–89. doi: 10.1007/BF00692665

Lader, P., Dempster, T., Fredheim, A., and Jensen, Ø.. (2008). Current induced net deformations in full-scale sea-cages for Atlantic salmon (Salmo salar). *Aquacultural Engineering.* 38 (1), 52–65. doi: 10.1016/j.aquaeng.2007.11.001

Lader, P. F., Enerhaug, B., Fredheim, A., and Krokstad, J.. (2003) in *3rd International Conference on Hydroelasticity in Marine Technology.* 19–26 (The University of Oxford Oxford, UK: Department of Engineering Science).

Li, L., Jiang, Z. Y., Ong, M. C., and Hu, W. F.. (2019). Design optimization of mooring system: an application to a vessel-shaped offshore fish farm. *Eng. Structures.* 197, 109363. doi: 10.1016/j.engstruct.2019.109363

Li, Y. C., Zhao, Y. P., Gui, F. K., and Teng, B.. (2006). Numerical simulation of the hydrodynamic behaviour of submerged plane nets in current. *Ocean Engineering.* 33 (17-18), 2352–2368. doi: 10.1016/j.oceaneng.2005.11.013

Milne, P. H. (1972). “Fish and shellfish farming in coastal waters,” in *Fishing news (Books)* (London: UNIPub).

Niño, Y., Vidal, K., Tamburrino, A., Zamorano, L., Beltrán, J. F., Estay, G., et al. (2020). Normal and tangential drag forces of nylon nets, clean and with fouling, in fish farming. *Exp. Study. Water.* 12 (8), 2238. doi: 10.3390/w12082238

Patursson, Ø., Swift, M. R., Tsukrov, I., Simonsen, K., Baldwin, K., Fredriksson, D. W., et al. (2010). Development of a porous media model with application to flow through and around a net panel. *Ocean Engineering.* 37 (2-3), 314–324. doi: 10.1016/j.oceaneng.2009.10.001

Santo, H. (2022). On the application of current blockage model to steady drag force on fish net. *Aquacultural Engineering.* 97, 102226. doi: 10.1016/j.aquaeng.2022.102226

Shimizu, H., Mizukami, Y., and Kitazawa, D. (2018). Experimental study of the drag on fine-mesh netting. *Aquacultural Engineering.* 81, 101–106. doi: 10.1016/j.aquaeng.2018.03.005

Tang, H., Hu, F. X., Xu, L. X., Dong, S. C., Zhou, C., and Wang, X. F.. (2017). The effect of netting solidity ratio and inclined angle on the hydrodynamic characteristics of knotless polyethylene netting. *J. Ocean Univ. China.* 16 (5), 814–822. doi: 10.1007/s11802-017-3227-6

Tang, H., Hu, F. X., Xu, L. X., Dong, S. C., Zhou, C., and Wang, X. F.. (2019). Variations in hydrodynamic characteristics of netting panels with various twine materials, knot types, and weave patterns at small attack angles. *Sci. Rep.* 9 (1), 1–13. doi: 10.1038/s41598-018-35907-1

Tsukrov, I., Drach, A., DeCew, J., Swift, M. B., and Celikkol, B.. (2011). Characterization of geometry and normal drag coefficients of copper nets. *Ocean Engineering.* 38 (17-18), 1979–1988. doi: 10.1016/j.oceaneng.2011.09.019

Tsukrov, I., Eroshkin, O., Fredriksson, D., Swift, M. B., and Celikkol, B.. (2003). Finite element modeling of net panels using a consistent net element. *Ocean Engineering.* 30 (2), 251–270. doi: 10.1016/S0029-8018(02)00021-5

Wang, G., Martin, T., Huang, L. Y., and Bihs, H.. (2021). Modelling the flow around and wake behind net panels using large eddy simulations. *Ocean Engineering.* 239, 109846. doi: 10.1016/j.oceaneng.2021.109846

Wang, G., Martin, T., Huang, L. Y., and Bihs, H.. (2022a). An improved screen force model based on CFD simulations of the hydrodynamic loads on knotless net panels. *Appl. Ocean Res.* 118, 102965. doi: 10.1016/j.apor.2021.102965

Wang, G., Martin, T., Huang, L. Y., and Bihs, H.. (2022b). Modeling the flow around and the hydrodynamic drag on net meshes using REEF3D. *J. Offshore Mechanics Arctic Engineering.* 144 (1), 011902. doi: 10.1115/1.4051408

Xu, Z. J., and Qin, H. D. (2020). Fluid-structure interactions of cage based aquaculture: From structures to organisms. *Ocean Engineering.* 217, 107961. doi: 10.1016/j.oceaneng.2020.107961

Yu, S. C., Qin, H. D., Li, P., and Xu, Z. J.. (2021). Nonlinear vertical accelerations and mooring loads of a semi-submersible offshore fish farm under extreme conditions. *Aquacultural Engineering.* 95, 102193. doi: 10.1016/j.aquaeng.2021.102193

Zhan, J. M., Jia, X. P., Li, Y. S., Sun, M. G., Guo, G. X., and Hu, Y. Z.. (2006). Analytical and experimental investigation of drag on nets of fish cages. *Aquacultural engineering.* 35 (1), 91–101. doi: 10.1016/j.aquaeng.2005.08.013

Zhao, Y. P., Bi, C. W., Dong, G. H., Gui, F. K., Cui, Y., Guan, C. T., et al (2013). Numerical simulation of the flow around fishing plane nets using the porous media model. *Ocean Engineering.* 62, 25–37. doi: 10.1016/j.oceaneng.2013.01.009

Zhou, C., Xu, L. X., Hu, F. X., and Qu, X. Y.. (2015). Hydrodynamic characteristics of knotless nylon netting normal to free stream and effect of inclination. *Ocean Engineering.* 110, 89–97. doi: 10.1016/j.oceaneng.2015.09.043

Zou, B. Q., Thierry, N. N.B., Tang, H., Xu, L. X., Dong, S. C., and Hu, F. X. (2020). The deformation characteristics and flow field around knotless polyethylene netting based on fluid structure interaction (FSI) one-way coupling. *Aquaculture and Fisheries.* 7(1), 89–102.

Frontiers in Marine Science

TYPE Original Research
PUBLISHED 13 February 2023
DOI 10.3389/fmars.2023.1136844

EDITED BY
Fukun Gui,
Zhejiang Ocean University, China

REVIEWED BY
Ray-Yeng Yang,
National Cheng Kung University, Taiwan
Peng Li,
Harbin Engineering University, China

*CORRESPONDENCE
Xiuchen Li
lxc@dlou.edu.cn

SPECIALTY SECTION
This article was submitted to
Marine Fisheries, Aquaculture and Living Resources,
a section of the journal
Frontiers in Marine Science

RECEIVED 03 January 2023
ACCEPTED 31 January 2023
PUBLISHED 13 February 2023

CITATION
Zhang H, Li P, Zhang H, Huang W, Zhang G, Mu G and Li X (2023) Design and experiment of cone disk centrifugal shellfish seeding device.
Front. Mar. Sci. 10:1136844.
doi: 10.3389/fmars.2023.1136844

Design and experiment of cone disk centrifugal shellfish seeding device

Hanbing Zhang[1,2,3], Pengpeng Li[1], Haonan Zhang[1], Wei Huang[1], Guochen Zhang[1,2,3], Gang Mu[1,2,3] and Xiuchen Li[1,2,3]*

[1]College of Mechanical and Power Engineering, Dalian Ocean University, Dalian, China, [2]Key Laboratory of Environment Controlled Aquaculture (Dalian Ocean University), Ministry of Education, Dalian, China, [3]Research & Development Center of Fisheries Equipment and Engineering, Dalian, Liaoning, China

This paper designed a centrifugal shellfish seeding device with a conical disc structure to improve the seeding efficiency and uniformity of the centrifugal shellfish seeding device. The dynamic model of the shellfish seedling moving on the conical disk is established, and the main parameters affecting the shellfish seedling's movement characteristics are determined as the cone angle of the impeller, the speed of the impeller, and the offset angle of the blade. Using the EDEM software and the shellfish seedlings blanking rate as the influencing factors, a single factor simulation test was performed. The research found that the variation trend of shellfish seedlings distribution in a single statistical area gradually decreased along the horizontal direction of both sides, with the origin being the center of the seedling sowing device. Test orthogonal rotation simulations using the variation coefficient of seedlings distribution uniformity and the effective job width as evaluation indicators. Use Design Expert software to optimize the structure of the seedling sowing device based on the test results, and determine the optimal structure with the maximum width and the minimum variation coefficient as constraints: the impeller cone angle is 7.72°, and the blade offset angle is -0.9°. Use the above-mentioned seeding device for simulation and actual seeding testing. The simulation results show that when the impeller speed is 750r/min and the blanking rate is 0.65kg/s, the variation coefficient of seedlings distribution uniformity and the effective job width are 12.84% and 24.98m, respectively, while the actual test results are 13.77% and 23.25m, respectively. The object of the seeding performance test was commonly used size shellfish seedlings of the Philippines clam. The results showed that the impeller speed, blanking rate, quadratic term of shellfish seedling size, quadratic term of blanking rate, and interactive term of impeller speed and blanking rate had significant effects on the variation coefficient of the distribution uniformity of shellfish seedlings ($P<0.01$). Shellfish seedling size, impeller speed, and interactive term of impeller speed and blanking rate all had a significant impact on job width ($P<0.01$). The results of this study provide a reference for the mechanized design of shellfish seeding.

KEYWORDS

shellfish seeding device, conical spiral, centrifugal, discrete element simulation, coefficient of distributed variation

1 Introduction

Shellfish are the biological species with the highest proportion of marine aquaculture production in China, living in shallow seas and intertidal tidal mudflats containing sediment, and are cultivated on a large scale by fishermen due to their high edible and economic value (Fishery Administration Bureau of Ministry of Agriculture and Rural Affairs, 2021). However, due to the unique working conditions, seedlings are still primarily sown manually at this stage (National Fisheries Technology Extension Station, 2008; Yuan et al., 2014), posing issues such as high labor intensity, low operational efficiency, and a high crushing rate of shellfish seedlings. The traditional artificial seeding method is no longer capable of meeting the production requirements of large-scale shellfish farming. The use of mechanized seedling sowing devices can significantly improve seedling sowing efficiency, reduce shellfish damage, and lower labor costs (Liu et al., 2014; Liu et al., 2020).

Currently, mechanical seeding methods include grooved wheel type, drag type, air suction type, and so on (Keith et al., 2000; Yuan et al., 2018; Li et al., 2019). These methods, however, cannot meet the actual needs of a shellfish seeding operation. In comparison to the preceding scheme, the centrifugal seeding device has the advantages of a simple structure, a wide operating range, and high operational efficiency. The specific centrifugal seeding implementation scheme can refer to the operation mode of centrifugal fertilization and seeding in agriculture (Lv et al., 2016; Liu et al., 2017; Yang et al., 2019). In terms of centrifugal fertilization, Dintwa et al. (2004) established the particle flow model of centrifugal fertilizer applicator, analyzed the movement of particles on the rotating disk, deduced the motion equation of particles on the centrifugal flat disk and cone disk, and provided a theoretical basis for centrifugal fertilizer applicator design optimization. Coetzee et al (Coetzee and Lombard, 2011). used discrete element modeling to investigate the effect of disc speed, blanking position, blanking rate, and blade angle on fertilization results, and they found that discrete element modeling simulation can accurately predict the actual operation situation. Artur (2015) investigated the effect of disc speed, fertilizer feed position, and blade angle on fertilizer spatial distribution. It was demonstrated that changing the working parameters can influence the distribution results in order to adapt to different work requirements. In China, Yongguang Hu et al. (2016) designed a tea garden fertilizer spreader and investigated the effects of the fertilizer spreader's walking speed, number of centrifugal disc blades, and blade offset angle on the fertilizer spreader's operating performance during the fertilization process. Yinyan Shi et al. (2018) created a surface variable fertilizer spreader with a centrifugal uniform fertilizer cover and investigated the effects of fertilizer discharge flow, disc speed, and travel speed on the spreader's performance. Guozhong Zhang et al. (2021) created a lotus root field centrifugal side-throwing fertilizer spreader. By developing a model, the main influencing factors were identified as fertilizer spreader rotation speed, blade inclination Angle, and blade deflection Angle, and the effects of fertilizer spreader rotation speed, blade inclination Angle, blade deflection Angle, and fertilizer feeding rate on the working performance of the fertilizer spreader were investigated.

In the research of shellfish bottom seeding device, Frederick et al. (1977) developed a centrifugal oyster seeding device in the research of shellfish bottom seeding device, which transported oyster seedlings from the cabin to the centrifugal plate at the stern of the ship *via* the conveyor belt and then spread them by the centrifugal plate. Keith et al. (2000) created an air suction bottom sowing clam pulling seedling device that can be moved on the seabed by divers or traction devices, and the seedlings can be spread from the silo to the seabed *via* suction. In China, Wei Huang et al. (2022) created a centrifugal beach shellfish seeding device. The number of blades, centrifugal disk speed, and traveling speed were found to be the factors influencing the variation coefficient of distribution of shellfish seedlings through simulation analysis and beach test verification. Gang Mu et al. (2019) created a beachside shellfish seeding machine that could seed shellfish seedlings at a distance and quantitatively based on the variety, size, and geology of the beachside, effectively reducing seedling injury, increasing seedling survival, and greatly improving seeding efficiency. Zhe Li et al. (2019) invented a suspension type seedling release device that can prevent seedlings from being carried by ocean currents to sea areas unsuitable for shellfish seedling growth, effectively improve shellfish seedling survival rates, and avoid a large number of shellfish seedlings concentrated in a specific location, which is conducive to the spread and reproduction of shellfish seedlings. Jian Liang et al. (2021) invented a portable wind-swept shellfish seeding machine that ejects seedlings from the seeding port *via* the air flow generated by the fan, achieving automatic seedling seeding and addressing issues such as low efficiency, high labor intensity, high cost, and uneven seeding of shellfish in tidal flats. Chunting Yuan et al. (2018) invented a bottom-seeding device for benthic shellfish seedlings in shallow sea, addressing the issue of seedlings being washed away from the set area due to the influence of waves, tides, and other factors.

The current shellfish bottom sowing device, on the other hand, has a small operation area and poor seeding uniformity, making it unsuitable for large-scale shellfish breeding on the beach. In order to address the existing issues, this paper designed a cone disk centrifugal shellfish seeding device for use on the beach. The main factors influencing the movement of shellfish seedlings were determined by analyzing the movement of shellfish particles. EDEM discrete element software was used to simulate the seeding process. The structural parameters of the seeding device were optimized based on simulation results, and the operating parameters of the seeding device were optimized based on actual seeding test results, with the goal of providing a reference for the design of mechanized shellfish seeding devices.

2 Structure and working principle of centrifugal seeding device

Figure 1 depicts the centrifugal seeding device developed in this paper, which consists primarily of a hopper, blanking device, conical seeding tray, frame, and other components. 1. Hopper and blanking device 2. Switch and speed regulating mechanism 3. Guard board 4. Shelter plate 5. Hook 6. Generator box 7. Electric motor 8. Conical seeding tray 9. Blanking port 10. Slide rail 11. Belt pulley 12. Frame

The shellfish seedlings fall to the surface of the conical seeding tray through the blanking device due to gravity in the hopper. The shellfish seedlings are subjected to centrifugal force and Coriolis force

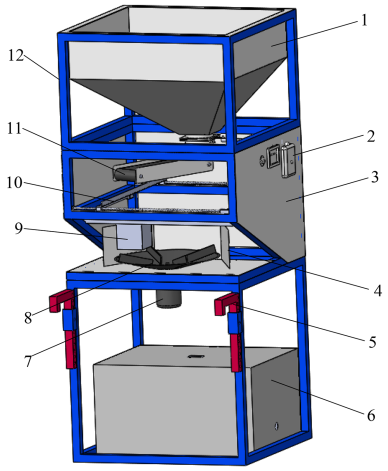

FIGURE 1
Centrifugal seeding device.

while rotating with the blade, gradually move to the blade's edge, and are thrown out of the conical impeller disk at a certain speed before being sown in the operation area.

3 Design of key components

3.1 Design of hopper and blanking device

Figure 2 depicts the design of the hopper. The upper half of the hopper is a cuboid, whereas the lower half is an asymmetric construction. To avoid shellfish seedling arching in the hopper, the angle of repose on one side is greater than the angle of repose of the shellfish seedling accumulation, the upper section is 1500mm long, 1100mm wide, and 300mm high, the lower half is 400mm high, and the hopper volume is 833L. The interior is lined with 4mm thick EVA material, which acts as a cushion when the shellfish seedlings fall and keeps them from breaking. Figure 2 depicts the blanking device, to adjust the blanking rate of shellfish seedlings, the opening between the blanking baffle and the chute is controlled by a motor and gear transmission mechanism. The blanking opening is 20cm wide and designed as a square, use formula (1) to calculate the flow rate of the blanking port ω relation with blanking opening width D_0 and seedling size D (Yi, ; Qin et al., 1966; Chen et al., 2019).

$$\omega = c\rho_B(D_0 - KD)^{2.5} \tag{1}$$

Wherein, ρ_B is the density of shellfish seedlings (non bulk density), c and K are dimensionless parameters, their values depend on the shape and friction of the shellfish seedlings, generally $0.5<c<0.7$, $1.2<K<3$.

When c is 0.6 and K is 2, ω=5.56kg/s=20016kg/h, that is, when the width of the blanking opening is 20cm, 20t can be sown per hour when the blanking opening is fully open.

3.2 Design of conical seeding mechanism

The conical seeding tray, as shown in Figure 3, is primarily made up of a conical impeller disc with a diameter of 600mm and a blade with a length of 310mm. It is 3D printed with resin and internally covered with 4mm EVA material. The shellfish will rotate with the conical impeller's blade as a result of centrifugal force as it rotates, and when the blade reaches the edge of the impeller plate, it will be thrown from the plate. It will eventually spread to the working area after a certain amount of time.

The impeller disc has a conical structure to increase the operation efficiency and job width, a protection cover is added inside the conical disc to prevent shellfish from falling to the bottom of the cone plate and causing blockage. To gather the shellfish seedlings, the upper end of the blade is bent in the direction of rotation. The blade offset angle can be adjusted to change the sowing area and range.

4 Motion analysis of shellfish seedling on impeller disk

Establish a radius of R and a cone angle of α_d, as shown in Figure 4. Straight blades extend directly to the edge of the impeller disk and are offset from the pitch radius r_p. Shellfish seedlings are fed into the impeller disk of the seeding device through the blanking port at the bottom of the hopper. The blanking port's inner diameter is r_i, its outer diameter is r_o, and the range angle is Φ. The blanking port's initial angle is Ψ. The impeller disk is installed on the traction device, the traction device's speed is v_s, and the disk's angular velocity is ω.

Figure 5 shows the trajectory of the shellfish seedlings randomly falling on a certain position on the impeller disk through the initial angle ($\Psi<\Phi_L<\Psi+\Phi$) and radius ($r_i<r_L<r_o$) to define the initial position of the seedlings. Where r_L is the radius from the center of the disc when the seedlings fall, θ_L is the angle at which the seedlings fall, θ_p is the angle of the shellfish when the impeller disk moves to different positions, Ψ is the initial angle of the blanking port, Φ is the

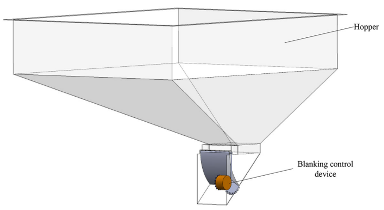

FIGURE 2
Hopper and blanking control device.

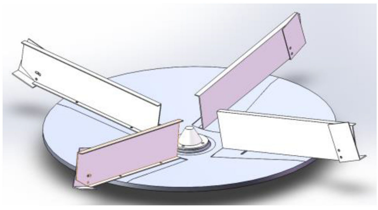

FIGURE 3
Conical seeding mechanism.

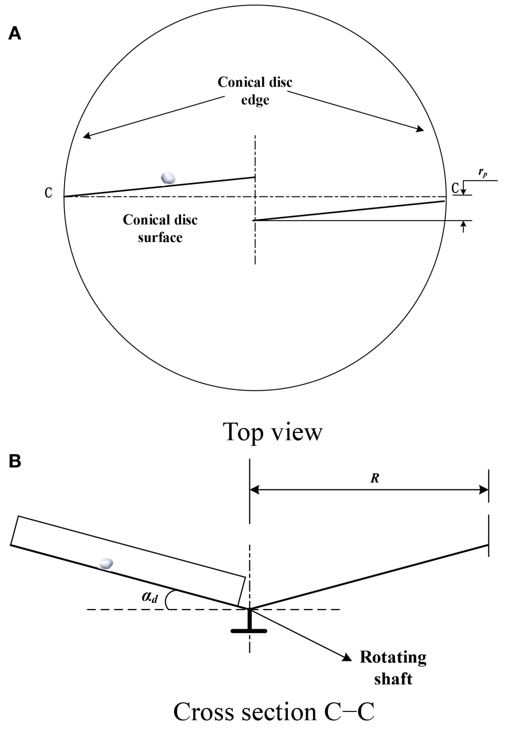

FIGURE 4
Schematic diagram of conical impeller disk. **(A)** Top view **(B)** Cross section C–C.

angle of the blanking port, r_i is the inner diameter of the blanking port, r_o is the outer diameter of the blanking port, R is the radius of the disc, and v_{tot} is the exit velocity of the shellfish seedling at the edge of the disc. The particles of shellfish seedlings are placed in a specific position (R, θ_p) disengage the bladed disc.

Figure 6 illustrates the velocity analysis of a shellfish seedling moving on an impeller disk. Where α_{tot} is the angle between the horizontal plane and the exit direction of the seedling; β_{tot} is the angle between the driving direction and the ejection direction of the seedling on the horizontal plane; v_s is the motion speed relative to the ground; v_v is the velocity component of v_{tot} in the vertical direction; v_o is the exit velocity of shellfish seedling under the static state of the bladed disc (v_s=0); v_h is the horizontal component of the exit velocity of the shellfish seedling under the static state of the impeller disk; v_{toth} is the total horizontal component of the exit velocity of the shellfish seedling under the unsteady state of the impeller disk; ω is the angular velocity when the disc rotates; θ_L is the angle of the initial position of the shellfish seedling on the impeller disk relative to the driving direction; θ_p is the angle of the seedling position relative to the initial position; α_o is the included angle between the vertical line of the particle outlet direction and the ground (horizontal plane) under the stable state of the impeller disk; α_{tot} is the total vertical angle of the exit direction of the shellfish seedling relative to the ground under the unsteady state of the impeller disk; β_o is the horizontal outlet angle of the shellfish seedling under the stable state of the impeller disk; β_{tot} is the total horizontal exit angle of the shellfish seedling under the unstable state.

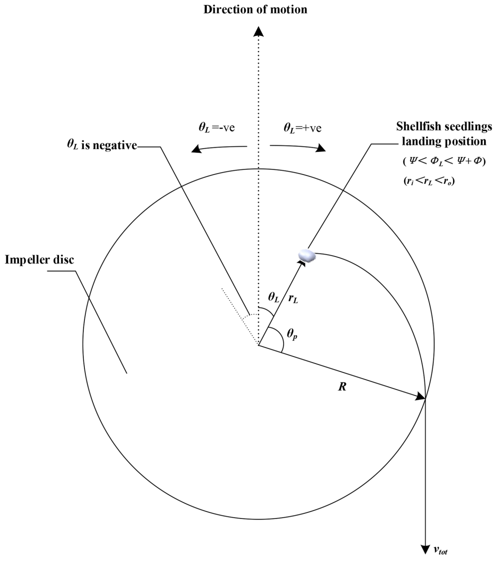

FIGURE 5
Top view of the trajectory of shells on the impeller disk.

The rebound between the blade and the shellfish seedling is not taken into account in the process of establishing the motion equation, assuming that the shellfish seedling maintains contact with the blade at all times from dropping on the impeller disk to exiting the impeller disk. Figure 7 depicts the top view and front view of the shellfish seedling under stress study on the conical impeller disk. Where r_p is the blade pitch radius, R is the diameter of the impeller disk, and r is the distance between the shellfish seedling and the horizontal direction of the rotation center, ω is the angular velocity of impeller disk rotation.

The shellfish seedling on the conical impeller disk are mainly subjected to centrifugal force F_c, gravity F_g, Coriolis force F_{co} and friction force F_f. In the Figure 7, the axis of the conical impeller disk serves as the origin of the (XYZ) coordinate system, which is constructed along the surface of the blade and the conical disk. If we establish the force balance equation along the X-axis, we can obtain:

$$F = F_c \cos\alpha \cos\beta - F_g \sin\alpha \cos\beta - F_f \tag{2}$$

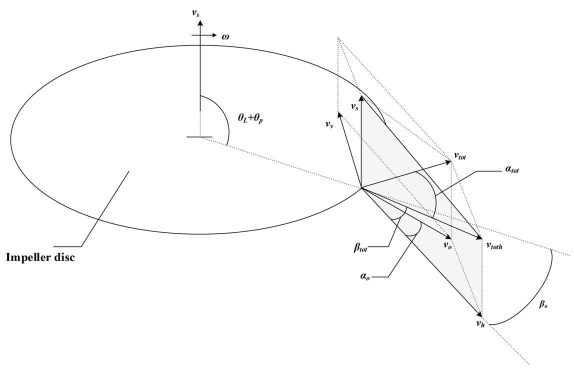

FIGURE 6
Speed analysis of shellfish on the impeller disc.

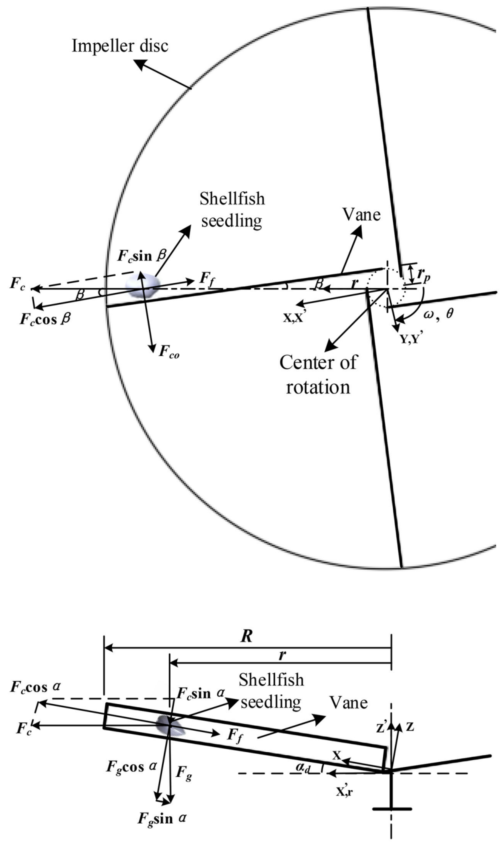

FIGURE 7
Analysis of the force of shellfish on the impeller disk.

In which case the pitch angle β is:

$$\beta = \arcsin\left(\frac{r_p}{r}\right) \tag{3}$$

When the blade offset direction is opposite to the impeller disk rotation direction, $r_p > 0$, and when the blade offset direction is the same as the impeller disk rotation direction, $r_p < 0$. The cone angle α_d is the included angle between the blade and the horizontal plane when the blade is placed radially. The friction force between the shellfish seedling and the blade and the friction between the shellfish seedling and the conical blade disc adds up to the force operating on the shellfish seedling.

$$F_f = \mu_d(F_g\cos\alpha + F_c\sin\alpha) + \mu_v(F_g\sin\alpha\sin\beta + F_{co} - F_c\sin\beta) \tag{4}$$

Where μ_d is the coefficient of friction between the blade and the shellfish seedling and μ_v is the coefficient of friction between the seedling shellfish and the cone impeller disk. The vector representations of Coriolis force and centrifugal force are as follows:

$$F_c = m\omega^2 r\hat{r} \tag{5}$$

$$F_{co} = 2m(\omega \times v) = 2m\omega\cos\alpha\frac{\mathrm{d}x}{\mathrm{d}t}\hat{y} \tag{6}$$

The analytical expression of gravity is:

$$F_g = mg \tag{7}$$

Where g is the acceleration of gravity, $\hat{r}$ and $\hat{y}$ is the unit vector in the radial and Y directions. By substituting formula (5) ~ (7) into formula (4), the equation of motion of the shellfish seedling on the conical impeller disk can be written:

$$\begin{aligned}&\frac{\mathrm{d}^2x}{\mathrm{d}t^2} + 2\mu_v\omega\cos\alpha\frac{\mathrm{d}x}{\mathrm{d}t} - \omega^2 r(\cos\alpha\cos\beta + \mu_v\sin\beta - \mu_d\sin\alpha)\\&+g(\sin\alpha\cos\beta + \mu_d\cos\alpha + \mu_v\sin\alpha\sin\beta) = 0\end{aligned} \tag{8}$$

The aforementioned analysis shows that the impeller speed ω, impeller cone angle α, and blade offset angle β all have an impact on the motion trajectory of the shellfish seedling on the impeller disc.

5 Discrete element simulation optimization test

The EDEM discrete element simulation software was used to perform single factor experiments and rotation orthogonal combination experiments, analyze the influence of different parameters on the working performance of the centrifugal seeding device, perform response surface analysis and variance analysis on the simulation results, and optimize the seeding device's key parameters.

5.1 Parameter setting of simulation model

Only import the three-dimensional model of the key component conical seeding mechanism in EDEM to reduce the amount of simulation calculation. The conical seeding mechanism is made of resin material. To prevent the shellfish particles from leaving the calculation domain during simulation, the shellfish bearing surface in EDEM software is set to 30m×50m; the seeding mechanism is 1m away from the bearing surface; and the contact between the shellfish and the shellfish is Hertz-Mindlin (no slip). Because the EDEM only contains regular spherical particle models, it is necessary to scan the three-dimensional model of the clam and import it, and then use multiple spherical particles to fill to create the simulation model of the clam. Reference (Huang, 2022) specifies the simulation parameters of the clam: Poisson's ratio 0.35, density 1367kg/m^3, elastic modulus 8.2MPa. Poisson's ratio of resin material is 0.38, density is 1.117g/cm^3, and elastic modulus is 1GPa; the elastic recovery coefficient between particles is 0.1, the static friction coefficient is 0.36, and the dynamic friction coefficient is 0.01; the elastic recovery coefficient, static friction coefficient and dynamic friction coefficient between particles and conical seeding mechanism are 0.15, 0.266 and 0.157 respectively.

5.2 Statistics of simulation data

After the simulation is completed, a statistical grid perpendicular to the seeding direction is established in the EDEM post-processing, and the grid size is 1m × 30m, the sowing direction is defined as vertical, and at the same time, the distribution variation coefficient of the shellfish seedlings in this direction is taken as the seedings uniformity index. The quality of the shellfish seedlings in each row is counted, and the distribution variation coefficient is calculated, and the variation coefficient and the effective width are used to assess how well the seeding device operates. As shown in Figure 8. Taking the center of the seedling sowing device as the origin, the distribution of shellfish seedlings in a single statistical area gradually decreases along the horizontal direction on both sides, and the distance between the two sides of a single statistical area that reaches the highest peak and half of the seedlings fall is defined as the effective job width.

The calculation formula of coefficient of variation Cv is

$$Cv = \frac{S}{\overline{m}} \times 100\,\% \tag{24}$$

In formula

$$S = \sqrt{\frac{\sum_{i=1}^{n}(m_i - \overline{m})^2}{n-1}} \tag{25}$$

$$\overline{m} = \frac{1}{n} \cdot \sum_{i=1}^{n} m_i \tag{26}$$

Where, S is the standard deviation of shellfish seedlings quality, g; m_i is the mass of shellfish seedlings in the statistical area of line i, g; $\overline{m}$ is the average quality of shellfish seedlings in the statistical area, g; n is the number of grid lines in the statistical area.

5.3 Single factor simulation test

To investigate the distribution characteristics of shellfish seedlings after sowing and the influence of a single factor on the distribution law of shellfish seedlings, a single factor simulation test was first performed to change the value of the single factor to be investigated, while the values of the other factors remained constant at the middle value. For results statistics, the rotation center's position was defined as the origin of the coordinate axis.

5.3.1 Effect of impeller speed on the distribution of shellfish seedlings

Set the test conditions as follows: the impeller cone angle is 10°, the blade offset angle is 0°, and the blanking rate is 0.7kg/s. In order to prevent the crushing rate of the shellfish seedlings from being too high due to excessive rotating speed, the range of the rotating speed of the impeller disk is 500~900 r/min, and the increment is 100 r/min. Figure 9A) displays the measured transverse distribution of shellfish seedlings. At low speeds, the dispersion of shellfish seedlings is limited and rather dense. The width, distribution range, and variation coefficient of the regularity of the dispersion of shellfish seedlings all steadily rise with an increase in impeller speed. The explanation behind this is that when the impeller speed increases, the distribution of shellfish seedlings becomes more uniform, the distance and width of sowing increase, and the initial speed at which shellfish seedlings leave the blade edge increases.

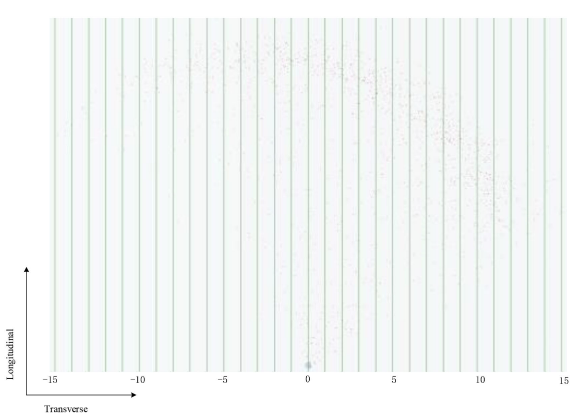

FIGURE 8
Shellfish seeding simulation diagram.

5.3.2 Effect of impeller cone angle on the distribution of shellfish seedlings

Set the test conditions as follows: rotating speed is 700r/min, blade offset angle is 0°, blanking rate is 0.7kg/s, impeller cone angle within the range of 0°~20°, and increment is 5°. Figure 9B) displays the shellfish seedlings distribution. The breadth of shellfish seedlings gradually grows as the impeller cone angle increases, and the variation coefficient of the evenness of the distribution of shellfish seedlings first declines and then increases. In order to make the distribution of shellfish seedlings more uniform, the distribution coefficient of variation can be decreased by altering the cone angle.

5.3.3 Effect of blade offset angle on the distribution of shellfish seedlings

Set the test conditions as follows: rotating speed is 700r/min, impeller cone angle is 10°, blanking rate is 0.7kg/s, blade offset angle value range -10°~10°, and the increment is 5°. Figure 9C) displays the dispersion status of shellfish seedlings. The coefficient of variance of shellfish seedlings distribution uniformity drops initially and subsequently increases. The direction of shellfish seedings is mostly affected by the blade offset angle. With a blade offset angle of -10° to 10°, the seedings direction progressively shifts from the right to the left side of the rotation center, and the width gradually rises. As a result, this factor can be used to adjust the direction and width of shellfish seedings.

5.3.4 Effect of blanking rate on the distribution of shellfish seedlings

Set the test conditions as follows: rotating speed is 700r/min, impeller cone angle is 10°, blade offset angle is 0°, blanking rate value range 0.5~0.9kg/s, increment is 0.1kg/s. Figure 9D) displays the shellfish seedlings distribution. When all other elements are held constant, as the blanking rate rises, the width stays the same, the peak value gradually rises, and the variation coefficient of the uniformity of the distribution of shellfish seedlings gradually rises. The simulation findings demonstrate that as the degree of blanking grows, the concentration of shellfish seedlings in the distribution region steadily rises.

5.4 Rotary orthogonal combination test

5.4.1 Orthogonal combination test of rotation of conical impeller disc

The effects of impeller speed n, impeller cone angle α, blade offset angle β, blanking rate v, and their interaction terms on the distribution

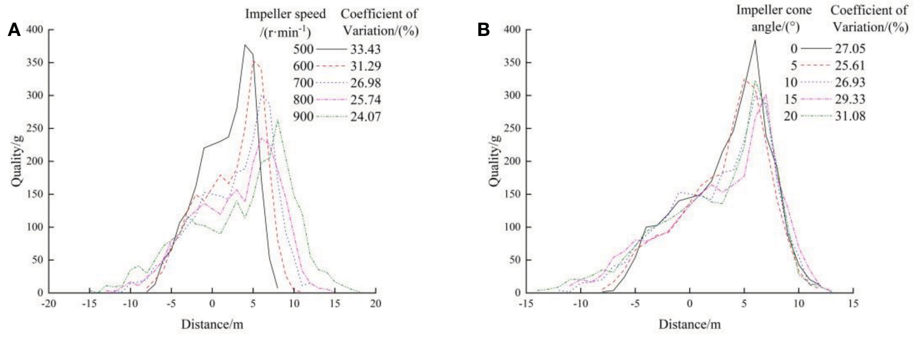

Effects of impeller speed on shellfish seeding distribution

Effects of impeller cone angle on shellfish seeding distribution

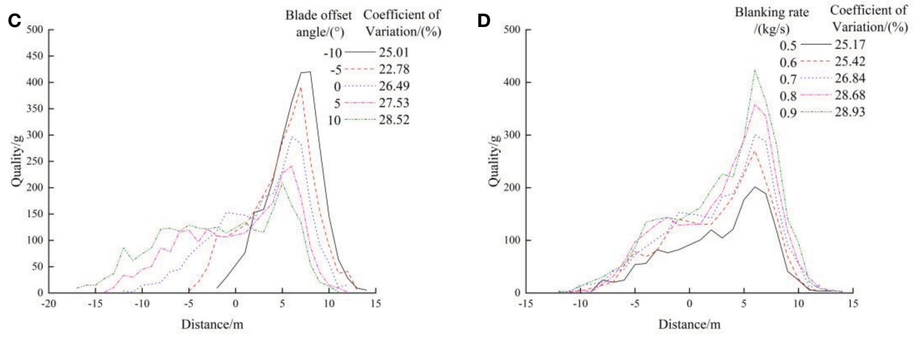

Effects of blade offset angle on shellfish seeding distribution

Effects of blanking rate on shellfish seeding distribution

FIGURE 9
Effects of single factor on shellfish seeding distribution. **(A)** Effects of impeller speed on shellfish **(B)** Effects of impeller cone angle on seeding distribution shellfish seeding distribution **(C)** Effects of blade offset angle on shellfish **(D)** Effects of blanking rate on shellfish seeding distribution seeding distribution.

coefficient of variation *Cv* and width *L* were examined in order to optimize the performance of the seeding device. The rotary orthogonal combination test was also carried out. According to the definition of American ASAE (, ; Geneva (Switzerland) International Organization for Standardization's scientific contributions, 1984; Jones et al., 2008), the effective width is defined as the distance between the statistical region where the distribution quality of shellfish seedlings is half of the peak quality and the seeding device. Prepare a four factor five horizontal rotation orthogonal combination test and optimize the results for structural parameters (Ren, 2009; Xu and He, 2010). The test arm length should be set to 2. Table 1 displays the level coding table, whereas Table 2 displays the test scheme and results.

5.4.2 Analysis of test results

Use Design-8.0.6 software to conduct regression analysis on the test results, and remove the non significant items about the evaluation indicators in turn. The results of variance analysis are shown in Table 3 and Table 4.

The lack of fit term of the variance analysis of the distribution coefficient of variation of shellfish seedlings is 0.1640>0.05, and the lack of fit term is not significant, it shows that the model can accurately capture the impact of numerous factors on the distribution coefficient of variation. The distribution of shellfish seedlings' variation coefficient *Cv* and different affecting factors are modeled by the following regression equation:

$$C_v = 13.43 - 1.52n + 7.63\alpha + 1.77\beta + 2.81v + 2.24\alpha\beta + 1.30\alpha v + 2.61\alpha^2 \quad (27)$$

The lack of fit term of variance analysis of job width is 0.1626 > 0.05, which is not significant, demonstrating the model's ability to accurately depict the influence law of several factors on job width. The following is the regression equation between job width *L* and different affecting factors:

$$L = 22.64 + 1.80n + 3.90\alpha + 0.68\beta + 0.29v + 0.67n\alpha - 0.71\alpha v - 0.67\alpha^2 - 1.41\beta^2 - 0.57v^2 \quad (28)$$

5.4.3 Interaction analysis

Response surface analysis was performed on the interaction items with significant impact on the evaluation indicators using Design expert 8.0.6 software, as shown in Figure 10.

When the rotating speed of the impeller is 700r/min and the blanking rate is 0.70kg/s, the response surface of the blade offset angle and the cone angle of the impeller to the variation coefficient of the seedlings

TABLE 1 Factor level coding table.

Level code	Impeller speed n (r/min)	Impeller cone angle α (°)	Blade offset angle β (°)	Blanking rate v (kg/s)
-2	600	0	-6	0.60
-1	650	3	-3	0.65
0	700	6	0	0.70
1	750	9	3	0.75
2	800	12	6	0.80

distribution is shown in Figure 10A). When the blade offset angle of the impeller is fixed, the cone angle of the impeller is directly proportional to the variation coefficient of the distribution of shellfish seedlings; when the cone angle of the impeller is fixed, the blade offset angle is directly proportional to the variation coefficient of the distribution of shellfish seedlings.

When the blade offset angle is 0° and the blanking rate is 0.70kg/s, the response surface of the impeller cone angle and impeller speed to the job width is shown in Figure 10C). The speed of the impeller is proportional to the job width when the cone angle of the impeller is fixed; and the cone angle of the impeller is proportionate to the job width when the speed of the impeller is fixed.

When the speed of the impeller is 700r/min and the offset angle of the blade is 0°, the response surface of the blanking rate and the cone angle of the impeller to the variation coefficient of the seedlings distribution and the job width is shown in Figure 10B, D). When the cone angle of the impeller is fixed, the blanking rate is directly proportional to the variation coefficient of the shellfish seedlings distribution and inversely proportional to the job width. When the blanking rate is constant, the cone angle of the impeller is proportional to the variation coefficient of the seedlings distribution and the job width.

5.4.4 Parameter optimization

The results of the variance and response surface analyses show that the influence of various factors on the distribution variation coefficient of shellfish seedlings is greater than the influence of the operating width. To optimize the operating parameters, the central composite response surface design of Design Expert software is used. The operating efficiency and seeding effect are thoroughly examined. The optimization goals are to minimize the distribution variation coefficient and maximize the effective operating width. When the impeller speed is 750 r/min, the blanking rate is 0.65kg/s, the impeller cone angle is 7.72°and the blade offset angle is -0.9°, the distribution variation coefficient is 12.84% and the job width is 24.98m.

6 Performance test of seeding device

In order to verify the operation performance of the seeding device, a 30 * 30m experimental site is arranged for bench test and whole machine test. The test scenario is shown in Figure 11.

TABLE 2 Test scheme and results.

Test No.	n (r/min)	α (°)	β (°)	v (kg/s)	Cv (%)	L (m)
1	650	3	-3	0.65	9.08	13
2	750	3	-3	0.65	7.13	15
3	650	9	-3	0.65	18.62	21
4	750	9	-3	0.65	13.08	25
5	650	3	3	0.65	7.42	13
6	750	3	3	0.65	6.33	14
7	650	9	3	0.65	27.49	22
8	750	9	3	0.65	20.63	27
9	650	3	-3	0.75	10.06	12
10	750	3	-3	0.75	9.95	16
11	650	9	-3	0.75	24.72	19
12	750	9	-3	0.75	22.08	25
13	650	3	3	0.75	13.12	15
14	750	3	3	0.75	10.63	17
15	650	9	3	0.75	35.04	21
16	750	9	3	0.75	32.53	25
17	600	6	0	0.70	16.24	18
18	800	6	0	0.70	9.64	26
19	700	0	0	0.70	7.24	13
20	700	12	0	0.70	38.52	25
21	700	6	-6	0.70	12.36	14
22	700	6	6	0.70	14.33	18
23	700	6	0	0.60	7.04	18
24	700	6	0	0.80	16.57	21
25	700	6	0	0.70	12.75	20
26	700	6	0	0.70	15.85	22
27	700	6	0	0.70	12.83	21
28	700	6	0	0.70	13.69	22
29	700	6	0	0.70	12.45	22
30	700	6	0	0.70	13.02	22

6.1 Bench test

Install the blade on the conical impeller, the impeller taper is 7.72°, and the blade offset angle is -0.9°, according to the results of optimization of the above simulation parameters. Prepare a bench for the actual seeding test. The shellfish seedlings are used clam seedlings from the Philippines, which are classified as large, medium, or small based on shell length. Table 5 shows its physical characteristics after measurement.

TABLE 3 ANOVA of coefficient of variation of shellfish distribution.

Variation source	Sum of squarcs	Degree of freedom	Mean square	*F* value	*P* value
Model	2038.83	14	145.63	46.54	<0.0001
n	55.18	1	55.18	17.63	0.0008
α	1395.83	1	1395.83	446.05	<0.0001
β	74.94	1	74.94	23.95	0.0002
v	189.34	1	189.34	60.51	<0.0001
$\alpha\beta$	80.60	1	80.60	25.76	0.0001
αv	26.91	1	26.91	8.60	0.0103
α^2	187.19	1	187.19	59.82	<0.0001
Lack of fit	39.06	10	3.91	2.48	0.1640
Pure error	7.87	5	1.57		
Total	2085.77	29			

6.1.1 Single size shellfish seedling test

The verification test was performed with medium-sized shellfish seedlings at the same impeller speed and blanking rate, as shown in Figure 12A). The simulation time is the same as the actual seeding time, and the measurement is repeated three times. The results revealed that the average measured mean value of the distribution variation coefficient of shellfish seedlings was 13.77%, the effective job width was 23.25 m, and the errors with the simulation results were respectively 7.24% and 6.92%, and the crushing rate of shellfish seedlings was less than 3%. According to the analysis, the main causes of the above errors are stone inclusion in shellfish seedlings, measurement errors of structure and operation parameters, and the influence of air resistance in the actual seeding process.

TABLE 4 ANOVA of job width.

Variation source	Sum of squarcs	Degree of freedom	Mean square	*F* value	*P* value
Model	542.75	14	38.77	26.57	< 0.0001
n	77.65	1	77.65	53.23	< 0.0001
α	365.12	1	365.12	250.28	< 0.0001
β	10.95	1	10.95	7.50	0.0152
v	2.07	1	2.07	1.42	0.2520
$n\alpha$	7.20	1	7.20	4.93	0.0422
αv	7.99	1	7.99	5.48	0.0335
α^2	12.34	1	12.34	8.46	0.0108
β^2	54.30	1	54.30	37.22	< 0.0001
v^2	8.90	1	8.90	6.10	0.0260
Lack of fit	18.23	10	1.82	2.49	0.1626
Pure error	3.66	5	0.73		
Total	564.64	29			

6.1.2 Different shellfish seedlings working performance test

In order to study the actual operation performance of the seeding device under the same operating parameters, the three factor and three horizontal rotation orthogonal combination tests were carried out with the shellfish seedling size *A*, impeller speed *n* and blanking rate τ as the factors, the distribution variation coefficient *Cv* and width *L* as the influencing indexes. The level coding table is shown in Table 6. The bench test scheme and results are shown in Table 7.

6.1.3 Analysis of test results

Use Design-8.0.6 software to conduct regression analysis on the test results, and remove the non-significant items about the evaluation indicators in turn. The results of variance analysis are shown in Tables 8 and 9.

The lack of fit term of the variance analysis of the distribution coefficient of variation of shellfish seedlings is 0.3987>0.05, and the lack of fit term is not significant, it shows that the model can better reflect the influence of various influencing factors on the distribution coefficient of variation. The variation coefficient of seedlings distribution uniformity is significantly affected by impeller speed, blanking rate, the quadratic term of seedling size, the quadratic term of blanking rate, and the interaction term of impeller speed and blanking rate. The regression equation describing the relationship between the variation coefficient *Cv* of shellfish seedlings distribution and the influencing factors is given:

$$Cv = 12.97 + 0.3987A - 2.24n - 3.13\tau - 2.66n\tau + 2.55A^2 + 3.23\tau^2 \qquad (29)$$

The lack of fit term of variance analysis of job width is 0.5017 > 0.05, which is not significant, demonstrating that the model can better reflect the influence of various influencing factors on job width. The shellfish seedling size, impeller speed, impeller speed and blanking rate all have a significant impact on the job width. The regression equation for the relationship between width *L* and various factors is:

$$L = 11.78 - 0.75A + 3.50n + 0.50\tau - 0.75n\tau + 0.47n^2 \qquad (30)$$

6.1.4 Interaction analysis

Figure 12A) displays the impeller speed and blanking rate reaction surfaces to the shellfish seedlings distribution variation coefficient while the shellfish seedling size remain constant. The blanking rate is directly proportional to the seedlings distribution's variation coefficient when the impeller speed is constant; when the blanking rate is constant, the impeller speed is inversely proportional to the seedlings distribution's variation coefficient.

Figure 12B) displays the impeller speed and blanking rate reaction surface to job width when the shellfish seedling size will not change. The blanking rate is proportional to the job width when the impeller speed is constant; when the blanking rate is constant, the impeller speed is also proportional to the job width.

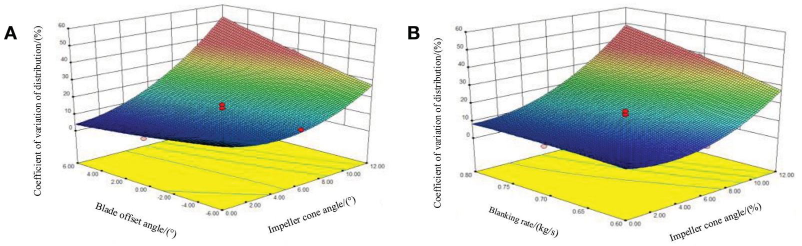

Interaction of blade offset angle and impeller cone angle on distribution coefficient of variation

Interaction of blanking rate and impeller cone angle on distribution coefficient of variation

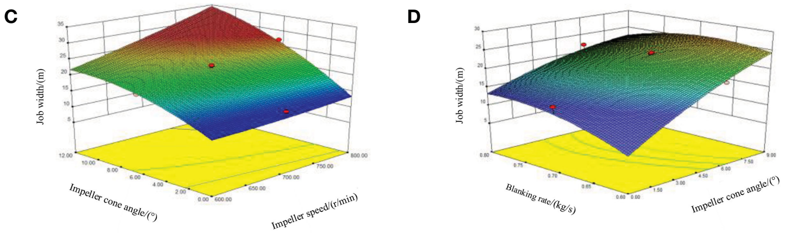

Interaction of blade offset angle and impeller speed on Job width

Interaction of blanking rate and impeller cone angle angle on Job width

FIGURE 10
Response surface diagram. **(A)** Interaction of blade offset angle and impeller cone **(B)** Interaction of blanking rate and impeller cone angle angle on distribution coefficient of variation on distribution coefficient of variation **(C)** Interaction of blade offset angle and impeller speed **(D)** Interaction of blanking rate and impeller cone angle on Job width angle on Job width.

6.2 Whole machine test

Place the seeding device at the tail of the traction device and drive at an even speed to simulate the offshore seeding operation, as shown in Figure 12B). At this time, the impeller disk is 1.5m above the ground. The seeding process begins when the traction device's tail enters the site 4m and ends when the vehicle's tail drives out of the site 4m. The mass of shellfish seedlings in the unit grid was counted after each test, and the distribution variation coefficient *Cv* was calculated.

Four factor and three level orthogonal experiments were carried out to investigate the effect of travel speed on distribution coefficient of variation. Table 10 shows the factor level coding table; Table 11 shows the whole machine test scheme and results. The size of *R* in the analysis results in Table 10 shows that the influence on the distribution variation coefficient *Cv* in the traveling process is in the order of shellfish seedling size, blanking rate, travel speed, and impeller speed.

7 Conclusion

1) This paper designed a cone disc centrifugal shellfish seedling sowing device on the beach to improve the breadth and evenness of shellfish seedlings. The main factors influencing the force and movement of a single shellfish seedling on the cone disc were determined by analyzing its movement characteristics. The results of a single factor simulation test revealed that the distribution of shellfish seedlings in a single statistical area decreased gradually along the horizontal direction of both sides, with the origin being the center of the seeding device.

2) The rotary orthogonal combination test was performed with four factors and five levels. The design expert software was used to perform variance analysis and response surface analysis on the test results. The results showed that the interaction between the impeller cone angle and the blade offset angle, the impeller cone angle and the blanking rate had a significant effect, and the quadratic term of the

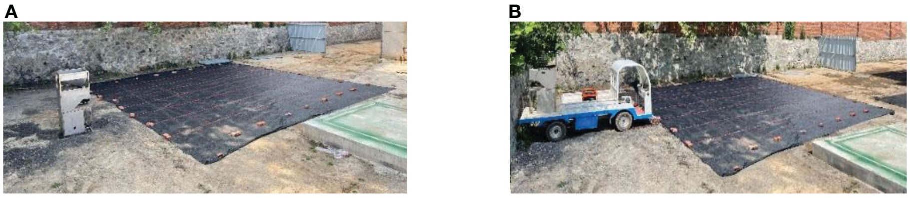

Bench test

Whole machine test

FIGURE 11
Test site. **(A)** Bench test **(B)** Whole machine test.

TABLE 5 Physical characteristics of shellfish seedlings.

Shellfish seedling size	Shell length/(mm)	Particle density/(g/cm^3)	Static pressure strength/(N)
Large (A_1)	35.08	1.78	105.23
Medium (A_2)	25.54	1.27	95.57
Small (A_3)	15.02	0.95	90.65

TABLE 6 Factor level coding table.

Level code	Shellfish seedling size *A*	Impeller speed *n* (r/min)	Blanking rate τ (kg/s)
-1	A_1	300	0.6
0	A_2	500	0.7
1	A_3	700	0.8

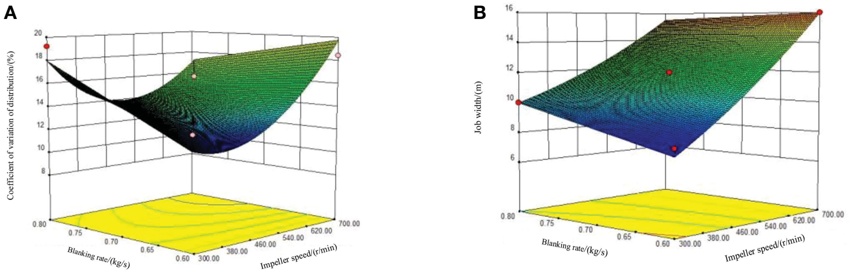

Interaction of impeller speed and blanking rate on distribution coefficient of variation

Interaction of impeller speed and blanking rate on job width

FIGURE 12
Response surface diagram. **(A)** Interaction of impeller speed and blanking rate on **(B)** Interaction of impeller speed and blanking rate distribution coefficient of variation on job width.

impeller cone angle had an extremely significant effect on the distribution variation coefficient of shellfish seedlings (*P*<0.01). The interaction between the impeller speed and the impeller cone angle, the impeller cone angle and the blanking rate, and the quadratic term of the impeller cone angle, the blade offset angle, and the blanking rate all have a significant effect on the job width (*P*<0.05).

TABLE 7 Bench test scheme and results.

No.	*A*	*n* (r/min)	τ (kg/s)	*Cv* (%)	*L* (m)
1	A_1	300	0.7	16.6	8
2	A_3	300	0.7	18.75	9
3	A_1	700	0.7	12.31	8
4	A_3	700	0.7	14.23	10
5	A_1	500	0.6	22.94	12
6	A_3	500	0.6	23.39	10
7	A_1	500	0.8	15.09	11
8	A_3	500	0.8	13.76	12
9	A_2	300	0.6	17.65	12
10	A_2	700	0.6	18.43	12
11	A_2	300	0.8	19.21	12
12	A_2	700	0.8	9.35	13
13	A_2	500	0.7	14.72	12
14	A_2	500	0.7	13.76	16
15	A_2	500	0.7	13.45	17
16	A_2	500	0.7	11.58	15
17	A_2	500	0.7	11.51	15

3) Design Expert software's central composite response surface design was chosen. The optimization objectives were the lowest coefficient of variation and the greatest effective width. The impeller cone angle and the blade offset angle were 7.72° and - 0.9°, respectively, after optimization. The impeller with the critical parameters was installed in the seeding device, and the simulation optimization test was run. The coefficient of variation was 12.84%, and the effective

TABLE 8 ANOVA of coefficient of variation of shellfish distribution.

Variation source	Sum of squarcs	Degree of freedom	Mean square	*F* value	*P* value
Model	223.39	6	37.23	15.33	0.0002
A	1.27	1	1.27	0.5239	0.4858
n	40.01	1	40.01	16.48	0.0023
τ	78.13	1	78.13	32.17	0.0002
$n\tau$	28.30	1	28.30	11.66	0.0066
A^2	27.40	1	27.40	11.28	0.0073
τ^2	44.18	1	44.18	18.20	0.0016
Lack of fit	16.31	6	2.72	1.36	0.3987
Pure error	7.97	4	1.99		
Total	247.67	16			

TABLE 9 ANOVA of job width.

Variation source	Sum of squarcs	Degree of freedom	Mean square	*F* value	*P* value
Model	107.69	5	21.54	102.76	< 0.0001
A	4.50	1	4.50	21.47	0.0007
n	98.00	1	98.00	467.57	< 0.0001
τ	2.00	1	2.00	9.54	0.0103
$n\tau$	2.25	1	2.25	10.73	0.0074
n^2	0.94	1	0.94	4.51	0.0573
Lack of fit	1.51	7	0.22	1.08	0.5017
Pure error	0.80	4	0.20		
Total	110.00	16			

TABLE 10 Factor level coding table.

Level code	Travel speed *v* (m/s)	Shellfish seedlings size *A*	Blanking rate *τ* (kg/s)	Impeller speed *n* (r/min)
1	0.51	A_1	0.6	300
2	0.77	A_2	0.7	500
3	1.02	A_3	0.8	700

TABLE 11 Whole machine test scheme and results.

No.		*v* (m/s)	*A*	*τ* (kg/s)	*n* (r/min)	*Cv* (%)
1		1	1	1	1	22.07
2		2	1	2	2	18.41
3		3	1	3	3	15.68
4		1	2	2	3	18.01
5		2	2	3	1	12.51
6		3	2	1	2	14.96
7		1	3	3	2	9.87
8		2	3	1	3	15.24
9		3	3	2	1	12.37
Cv	k_1	16.65	18.72	17.42	15.65	
	k_2	15.38	15.16	16.26	14.41	
	k_3	14.33	12.49	12.68	16.31	
	R	2.31	6.22	4.73	1.89	

operating width was 24.98m. The bench verification test revealed that the average values of the above indicators are 13.77% and 23.25 m, respectively, and the errors with the simulation results are 7.24% and 6.92%. The crushing rate is less than 3%, which meets the requirements for beach shellfish seeding.

4) On the seeding device, seedlings from the Philippines of three commonly used specifications were tested. The test results showed that the seedling spreader's rotation speed had a wide range of adaptability, the job width increased and the coefficient of variation of uniformity decreased under high-speed rotation of the seedling tray, and the seeding effect was better; however, the breaking rate of medium seedlings and small seedlings is higher under high rotating speed of the seedling tray, so they are not suitable for operation under high rotating speed. The test results can be used to select operation parameters for shellfish seedlings of various specifications.

Data availability statement

The original contributions presented in the study are included in the article/supplementary material. Further inquiries can be directed to the corresponding author.

Author contributions

HBZ, XL, GZ, GM contributed to the conception and design of thepaper and give modification suggestions. PL wrote the manuscript. HNZ draw the graph. WH carry out statistical analysis. All authors contributed to the article and approved the submitted version.

Funding

This research was funded by National Key R&D Program of China(2019YFD0900701); Education Department of Liaoning Province (LJKMZ20221112); Science and Technology Innovation Fund of Dalian(2021JJ12SN33); Key Laboratory of Environment Controlled Aquaculture (Dalian Ocean University) Ministry of Education (202212).

Conflict of interest

The authors declare that the research was conducted in the absence of any commercial or financial relationships that could be construed as a potential conflict of interest.

Publisher's note

References

Artur, P. (2015). The impact of structural and operational parameters of the centrifugal disc spreader on the spatial distribution of fertilizer. *Agric. Agric. Sci. Proc.* 7, 215–222. doi: 10.1016/j.aaspro.2015.12.021

(2006). *American Society of agricultural and biological engineers procedure for measuring distribution uniform and calibrating granular broadcast spreaders*.

Chen, H., Nan, J., Gao, H., and Wang, M. (2019). Study on the relationship between velocity of particulate matter and beverloo formula[J]. *Univ. Phys.* 38 (9), 6. doi: 10.16854 /j.cnki.1000-0712.180687

Coetzee, C. J., and Lombard, S. G. (2011). Discrete element method modelling of a centrifugal fertiliser spreader. *Biosyst. Eng.* 109 (4), 308–325. doi: 10.1016/j.biosystemseng.2011.04.011

Dintwa, E., Liedekerke Van, P., Olieslagers, R., Tijskens, E., and Ramon, H. (2004). Model for simulation of particle flow on a centrifugal fertiliser spreader. *Biosyst. Eng.* 87 (4), 407–415. doi: 10.1016/j.biosystemseng.2003.12.009

Fishery Administration Bureau of Ministry of Agriculture and Rural Affairs (2021). *2021 China fisheries statistical yearbook* (Beijing: China Agricultural Press), 17–57.

Frederick, L., Garrett, J., Frederick, L., and Gordon, B. M. (1977). *Apparatus for planting seed oysters: US4052961*, Vol. 10. 11.

Geneva (Switzerland) International Organization for Standardization's scientific contributions (1984). *Equipment for distributing fertilizers-test methods-part 2: Fertilizer distributors in lines*.

Huang, W. (2022). *Design and experimental study of centrifugal shellfish seeding equipment* (Dalian Ocean University). doi: 10.16535/j.cnki.dlhyxb.2021-270

Huang, W., Li, X., Mu, G., Zhang, G., Bai, Y., Zhang, H., et al. (2022). Design and experiment of centrifugal shoal shellfish seeding device. *J. Dalian Ocean Univ.* 37 (02), 320–328.

Hu, Y., Yang, Y., Xiao, H., and Li, P. (2016). Simulation and parameter optimization of centrifugal fertilizer spreader for tea plants. *Trans. Chin. Soc. Agric. Machinery* 47 (5), 77–82. doi: 10.6041/j.issn.1000-1298.2016.05.011

Jones, J. R., Hayden, L. G., and Yule, I. J. (2008). A statistical comparison of international fertiliser spreader test methods-confidence in bout width calculations. *Powder Technology* 184 (3), 337–351. doi: 10.1016/j.powtec.2007.09.004

Keith, W., Rob, J., Doug, S., Fred, L., and Reinhold, S. (2000). *Machine for planting shellfish seedings: US6082303*, Vol. 07. 04.

Liang, J., Li, Y., Liang, S., Guo, Y., Shun, X., You, H., et al. (2021). *A portable windswept shellfish seeding machine: CN213404549 U*, Vol. 06. 11.

Liu, C., Li, Y., Song, J., Ma, T., Wang, M., Wang, X., et al. (2017). Performance analysis and test of centrifugal disc fertilizer spreader based on EDEM. *Trans. Chin. Soc. Agric. Eng.* 33 (14), 32–39. doi: 10.11975/j.issn.1002-6819.2017.14.005

Liu, W., Zhang, H., Li, X., Zhang, G., Zhang, Q., Qu, S., et al. (2020). Analysis of biomechanical properties of juvenile Manila clam for mechanization sowing. *J. Dalian Ocean Univ.* 35 (3), 455–461. doi: 10.16535/j.cnki.dlhyxb.2019-241

Liu, Y., Zheng, J., and Qiu, T. (2014). Research and development status and trend of shellfish facility breeding engineering. *Fishery modernization* 41 (05), 1–5. doi: 10.3969/j.issn.1007-9580.2014.05.001

Li, Z., Xu, G., Xu, K., and Zhang, H. (2019). *Towed seedling release device: CN110089463A*, Vol. 08. 06.

Lv, J., Shang, Q., Yang, Y., et al. (2016). Performance analysis and test of tapered disc fertilizer sprinkling device. *Trans. Chin. Soc. Agric. Eng.* 32 (11), 16–24. doi: 10.11975/j.issn.1002-6819.2016.11.003

Mu, G., Wei, X., Li, X., Li, Z., Li, J., Liu, Z., et al. (2019). *Mud flat shellfish seedling planting machine: CN208768735U*, Vol. 04. 23.

National Fisheries Technology Extension Station (2008). Healthy cultivation technology of shellfish in tidal flats. *Chin. Aquat. products* 6), 52–53.

Qin, J., Chen, H., Tu, Z., and Cui, X. (1966). The flow of solid particles through the orifice. *J. Chem. Eng.* 2), 115–123.

Ren, L. (2009). *Regression design and optimization* (Beijing: Science Press).

Shi, Y., Chen, M., Wang, X., Morice, O. O., Li, C., Ding, W., et al. (2018). Design and experiment of a variable rice surface fertilizer spreader with centrifugal uniform fertilizer cover. *Trans. Chin. Soc. Agric. Machinery* 49 (03), 86–93+113. doi: 10.6041/j.issn.1000-1298.2018.03.010

Xu, X., and He, M. (2010). *Experimental Design and application of Design-Expert and SPSS.* (Beijing: Science Press).

Yang, L., Chen, L., Zhang, J., Shun, H., Liu, H., Li, M., et al. (2019). Test and analysis of uniformity of centrifugal disc spreading. *Trans. Chin. Soc. Agric. Machinery* 50 (sup 1), 108–114. doi: 10.6041/j.issn.1000-1298.2019.S0.018

Yi, M. (1973). Flow of solid particles through orifice-gravity flow and negative pressure differential flow of granular material through vertical and inclined pipe orifice. *Chem. Eng.* 1973 (1), 2–17.

Yuan, C., Liu, Q., and Liu, Y. (2018). Shallow seabed sowing device for de-mersal shellfish larvae and using method of shallow seabed sowing device: CN105900878B. Vol. 08. 03.

Yuan, H., Shen, H., Wang, L., and Shi, L. (2014). Ecological culture technology of Philippine clam beach. *Aquatic science and technology information* 1, 54–56.

Zhang, G., Wang, Y., Liu, H., Ji, C., Hou, Q., Zhou, Y., et al. (2021). Design and experiments of the centrifugal side throwing fertilizer spreader for lotus root fields. *Trans. Chin. Soc. Agric. Eng.* 37 (19), 11.

frontiers | Frontiers in Marine Science

TYPE Original Research
PUBLISHED 13 February 2023
DOI 10.3389/fmars.2023.1122855

OPEN ACCESS

EDITED BY
Zhao Yunpeng,
Dalian University of Technology, China

REVIEWED BY
Peng Li,
Harbin Engineering University, China
Shuxue Liu,
Dalian University of Technology, China

*CORRESPONDENCE
Hung-Jie Tang
✉ hjtang@thl.ncku.edu.tw

SPECIALTY SECTION
This article was submitted to Marine Fisheries, Aquaculture and Living Resources, a section of the journal Frontiers in Marine Science

RECEIVED 13 December 2022
ACCEPTED 30 January 2023
PUBLISHED 13 February 2023

CITATION
Tang H-J, Yang R-Y and Yao H-C (2023) Experimental and numerical study on the hydrodynamic behaviors of mooring line failure on a net cage in irregular waves and currents. *Front. Mar. Sci.* 10:1122855. doi: 10.3389/fmars.2023.1122855

Experimental and numerical study on the hydrodynamic behaviors of mooring line failure on a net cage in irregular waves and currents

Hung-Jie Tang[1]*, Ray-Yeng Yang[2] and Hao-Cheng Yao[2]

[1]Tainan Hydraulics Laboratory, National Cheng Kung University, Tainan, Taiwan, [2]Department of Hydraulic and Ocean Engineering, National Cheng Kung University, Tainan, Taiwan

The failure of mooring lines in net cages could lead to the death or escape of farmed fish, which causes huge economic losses and immeasurable ecological impacts. Therefore, it is very important to ensure the safety of the cage mooring system in practical applications. This study experimentally and numerically investigates the hydrodynamic behaviors of the mooring line failure on a net cage in irregular waves and currents. For the model test, a 1:25 scaled net cage model with eight-point mooring is installed in a wave tank. The two load cells in its upstream mooring lines and a gyroscope on its floating collar are used to measure the mooring force and the rotational motions, respectively. A cutting device equipped with a pneumatic cylinder and a blade is used to cut the line. A self-developed numerical model is specifically established for the model test for cross-validation. Both experimental and numerical results are analyzed and compared in the time and frequency domains. The results show that the mooring load in the remaining line significantly increases as one of the upstream mooring lines is disconnected. Meanwhile, a significant yaw rotation of the floating collar is observed. The results indicate that the maximum tension, drift displacement, and rotational angles significantly increase as the current velocity increases.

KEYWORDS
mooring line failure, net cage, irregular waves, flume experiment, numerical simulation

1 Introduction

Marine cage culture is becoming an important part of the fishing industry in many countries near oceans (FAO, 2022). In Taiwan, although the cage culture industry has developed well over the past two decades, mooring line failure still happens (Tang et al., 2020). When a mooring line fails, the floating collars collide with each other, and the fish net becomes entangled. Massive amounts of farmed fish may die in the net or escape from the cage. This kind of event can result in considerable economic losses and immeasurable ecological impacts. Moreover, a strong tidal current occurs in the Taiwan Strait every day, and more than three typhoons on average hit Taiwan every year. In addition, the development of the cage culture toward the far deep ocean is inevitable due to conflict with other ocean activities. Therefore, it is essential to study mooring line failures on net cages in irregular waves and currents for future development.

In recent decades, the hydrodynamic characteristics of marine net cage systems had been extensively investigated *via* laboratory experiments, numerical simulations, and field measurements. Tsukrov et al. (2003) employed a finite element model with consistent net elements to simulate the hydrodynamic responses of net panels and evaluated the performance of a tension-leg net cage. Fredriksson et al. (2003) used a stochastic approach to analyze the motion of a central-spar net cage and the tension generated in the anchor lines by the waves. The results provided valuable insights into the net cage dynamics in open waters. DeCew et al. (2005) investigated the dynamics of a modified gravity cage subjected to regular and random waves in a wave tank. Huang et al, 2006; Huang et al, 2007) conducted a series of experiments to investigate the mooring forces on a net cage subjected to waves and currents. Zhao et al. (2007) applied a lumped mass numerical model to simulate the motion of a gravity cage subjected to the simultaneous actions of waves and currents. Their results were consistent with the experimental data. Dong et al. (2010) developed a numerical model to simulate the mooring line tension and the body motion of a net cage subjected to irregular waves and validated it against their experimental results. Huang et al. (2010) developed a numerical model for a single-point mooring net cage in irregular waves and currents and validated it against field measurements. Kristiansen and Faltinsen (2015) used a numerical and experimental model to investigate the mooring loads of an aquaculture net cage with a floater in waves and currents. Moe-Føre et al. (2016) studied the structural responses of high-solidity net cage models in uniform flow. For good reviews on the research development of net cages, the readers can refer to Guo et al. (2020) and Xu and Qin (2020).

Recently, studies on the mooring line failure of net cages have attracted much attention. Yang et al. (2020) developed a time domain numerical model to investigate the effects of the mooring line failure on a net cage under various waves and currents. Tang et al. (2020) explored the mooring line failure-induced dynamic responses of net cages in irregular waves and currents and found significant changes in the tension spectra in both the wave- and lower-frequency regions. Subsequently, they conducted a laboratory experiment to verify their numerical model for a net cage suffering from the mooring line failure in currents (Tang et al., 2021). Cheng et al. (2021) studied the effect of mooring line breakage on the dynamic responses of grid-moored fish farms subjected to currents. They showed that the breakage at one mooring line is unlikely to immediately cause a progressive collapse of the fish farm at a current velocity of less than 0.5 m/s; however, it may cause a structural collapse, and fish may escape when the current and waves increase. Hou et al. (2022) investigated the reliability of the mooring system of net cages with one damaged mooring line and indicated that the failure of one mooring line significantly affects the failure probability for the remaining mooring lines. Tang et al. (2022a) assessed the two potential disasters of mooring line failure and anchor sinking regarding the seabed sand waves in an offshore wind farm area in Taiwan. Tang et al. (2022b) investigated the dynamic responses of the successive failure of two mooring lines on a net cage through numerical simulations and model tests. Results showed that the mooring tension, cage movement, and remaining cage volume responses were higher after the second failure than after the first.

In this study, a model test is performed, and a numerical model is used to investigate the dynamic responses of the mooring line failure on a net cage subjected to irregular waves and currents. First, the influence of the mooring line failure on the remaining line tensions and the floating collar rotations is estimated by comparing it to the intact mooring state. The influence of the current velocity on the mooring line failure is then obtained by increasing the inflow velocity with the same incident irregular waves. All results are analyzed in both the time and frequency domains. The power spectral density and linear transfer functions of tensions and motions are also analyzed. The remainder of this paper is structured as follows: Section 2 describes the model test; Section 3 introduces the numerical model; Section 4 compares the mooring tension and the rotational motion under the intact and failed states of mooring; Section 5 investigates the influence of increasing the current velocity on the mooring line failure of a net cage in irregular waves and currents, and Section 6 draws the conclusions and recommendations for future work.

2 Experimental method

2.1 Experimental setup

Figures 1, 2 present the net cage model adopted in this study. Table 1 lists its specifications. The wave tank size is 50 m in length, 7 m in width, and 1.2 m in depth. The position of the model is about 30 m to the wave maker, 20 m to the end wall, and 3.5 m to the side wall. The wave and current directions were set similarly to the x-axis direction; thus, the mooring system was symmetrical to the environmental force. The full-scale net cage had a 30 m-diameter inner floating collar and a 12.5 m-deep net installed in water with a 20 m constant water depth. Froude scaling with a geometric similarity was adopted in the model test. The model scale was 1:25. Table 1 also presents the corresponding full-scale values. However, duplicating the geometric similarity, especially netting, was almost impossible. Thus, the corresponding full-scale values listed in Table 1 were provided only for reference (Huang et al., 2006; Kristiansen and Faltinsen, 2015).

The net cage model consisted of a floating collar, a net chamber, a tube sinker, a buoy, and a mooring line attached to the wave tank bottom. Two upstream mooring lines were deployed through two pulleys connected to two load cells fixed to a plate laid on the tank wall. Both load cells were an LT6-5 type (SSK Company, Japan) with 0.2% FS reproducibility, 0.2% FS linearity, 0.05% RO/°C temperature characteristic, ±10 V output voltage, 500 Ω input and output resistance, and between −15 and 75°C operating temperature range. The maximum force recorded during the test was 49.05 N. An IMU (MTW2-3A7G6, Xsens, The Netherlands) was installed on the floating collar edge to measure the rotational motions. Three acoustic Doppler velocimeters (ADVs, Nortek, Norway) were installed on the front of the net cage model to simultaneously measure the inflow velocity. The three ADVs were evenly spaced at

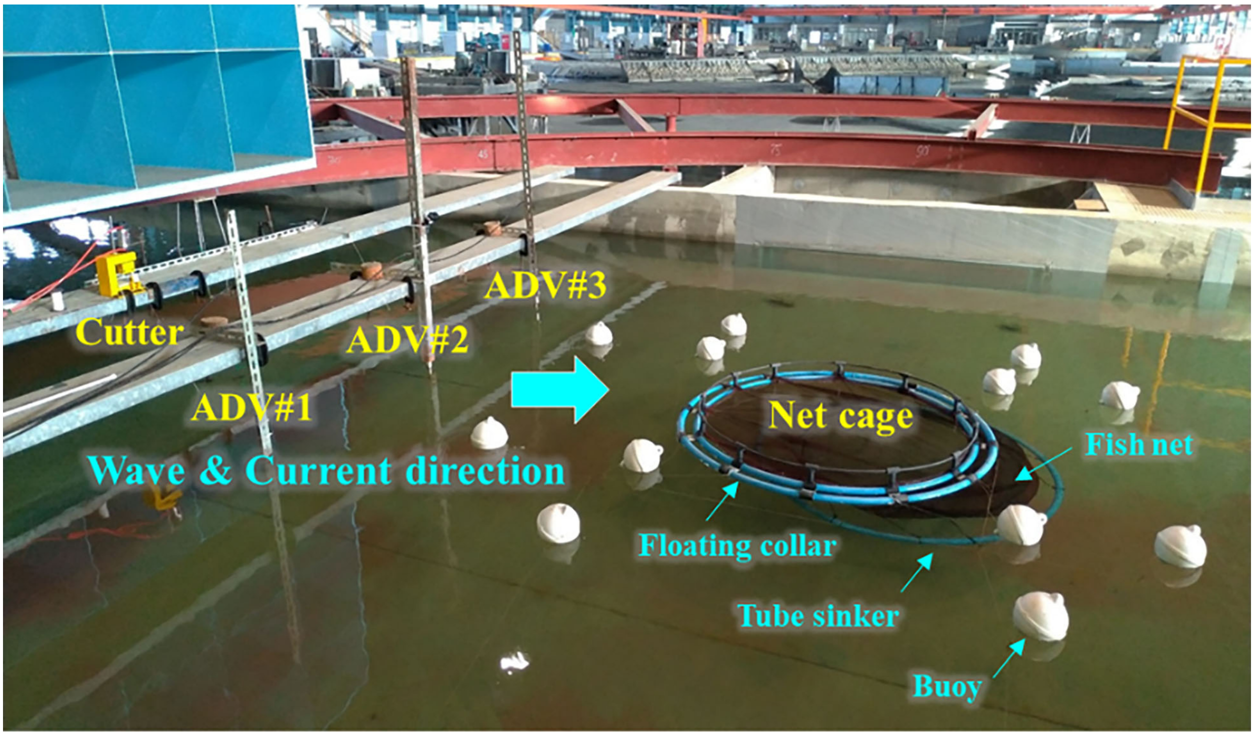

FIGURE 1
Photo of the net cage model installed in a wave tank.

100 cm intervals, with the mean measurement value taken as the inflow velocity. We installed two LED markers on the center of the floating collar and the tube sinker to try to measure the surge and heave motions following Tang et al. (2022b). However, the wave tank bottom was a sandy bed covered with an iron plate, and the wave-generating process made the water quality so muddy that the image processing method was not applicable. Therefore, only the rotational motion results were available for the experiment.

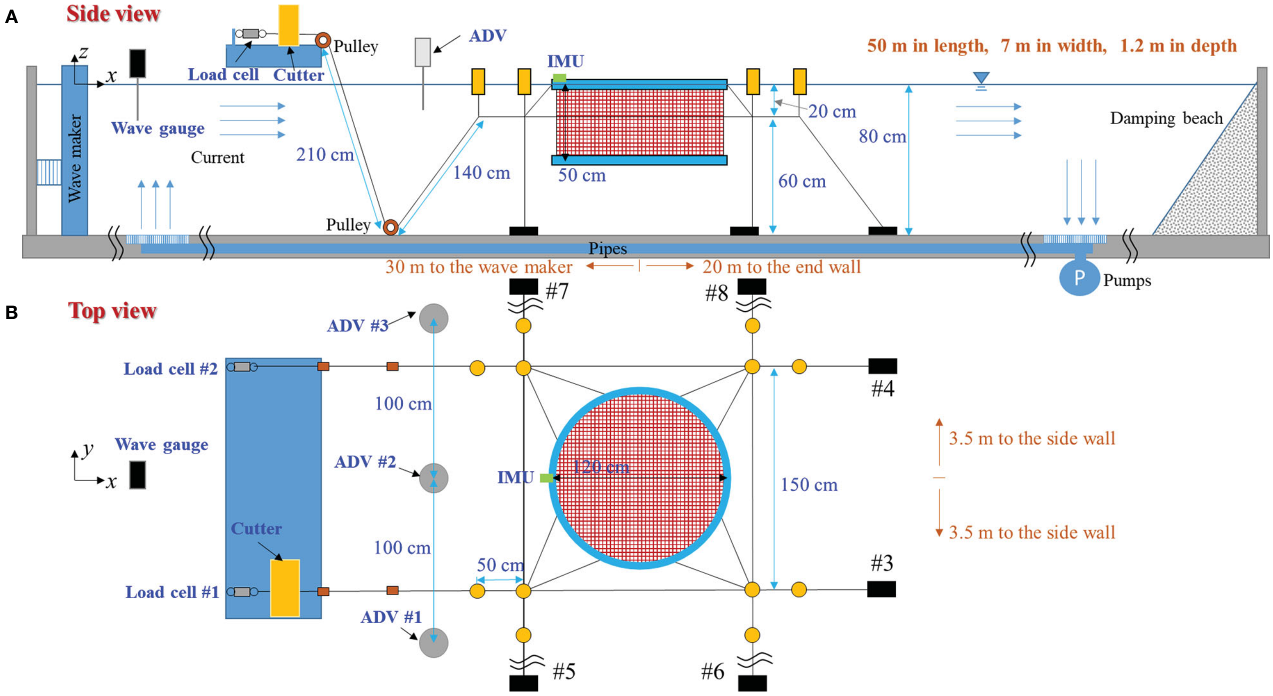

FIGURE 2
Schematic diagram of the model test.

TABLE 1 Specifications of the net cage model.

Component	*Specification*	*Model scale*	*Full scale*	*Scale ratio*
Floating collar	Inner circumference	377.0 cm	94.25 m	1:25
	Outer circumference	408.4 cm	102.1 m	1:25
	Tube diameter	3.4 cm	0.85 m	1:25
	Density	0.950 g/cm^3	950 kg/m^3	1:1
	Total mass	3,724 g	58,188 kg	1:25^3
	Total buoyancy	6,774 g	105,844 kg	1:25^3
Fish net	Twine diameter	0.02 cm	0.5 cm	1:25
	Mesh size	0.60 cm	15 cm	1:25
	Solidity	0.128	0.128	1:1
	Net depth	50 cm	12.5 m	1:25
	Density	1.14 g/cm^3	1140 kg/m^3	1:1
	Young's modulus	2.424 GPa	2.424 GPa	1:1
	Total mass	71.5 g	1,117 kg	1:25^3
Tube sinker	Circumference	408.4 cm	102.1 m	1:25
	Tube diameter	3.4 cm	0.85 m	1:25
	Total mass	1,320 g	20,625 kg	1:25^3
	Density	0.95 g/cm^3	950 kg/m^3	1:1
Mooring line	Diameter	0.265 cm	6.625 cm	1:25
	Unit mass	0.039 g/cm	2.437 kg/m	1:25^2
	Density	1.14 g/cm^3	1140 kg/m^3	1:1
	Young's modulus	0.753 GPa	0.753 GPa	1:1
Buoy	Diameter	15 cm	3.75 m	1:25
	Buoyancy	1,450 g	22,656 kg	1:25^3
	Total mass	230 g	3,594 kg	1:25^3

Two methods presented in existing studies can make the mooring line failure happen in a laboratory environment. The first method is the usage of the line cutting device (Figure 1) proposed by Tang et al. (2021). The device composes of a blade and a pneumatic cylinder that provides cutting power by means of an air compressor. The second approach is the electromagnet described by Tang et al. (2022b), wherein power can be turned off to disconnect the mooring line. The first method was adopted herein because the second method was proposed after this experiment.

2.2 Experimental procedure

Figure 3 illustrates the experimental procedure flowchart. The no-load offset readings of the load cells, wave gauges, gyro, and ADVs were initially recorded. The pre-tension of the two mooring lines was then checked using the measurements of two load cells and by adjusting the difference between them to less than 5%. This was done to ensure that the forces in the mooring system were symmetrical. The current velocity was then increased to a predetermined value. A 30 min elapse was allowed for the flow field stabilization. Irregular waves were generated by the wave maker according to the JONSWAP spectrum. The steps comprising the main part of the experiment are presented here. First, the measurements were collected from the load cells and the ADVs of the mooring system in intact condition for 5 min (300 s). The mooring line cutting test was then conducted, and recording started. The button was pressed after 40 s to cut the mooring line linked to load cell #1. The remaining recording length was 260 s. Finally, the test data were checked, and the wave and current generators were stopped if found to be in order.

As for the duration time for the irregular wave measurements, the typical 15–30-min sample duration in the natural sea is generally considered a reasonable compromise considering the battery life and the deployment time. For example, a wave-measuring buoy may be used for a year deployment with three hourly records using 15 min sample durations or a 2 month deployment reporting every hour using 30 min sample durations (Pecher and Kofoed, 2017). In previous studies, a 20 min duration time was commonly adopted in a full-scale net cage in the natural sea (e.g., Fredriksson et al., 2003; Fredriksson et al., 2005; Huang et al., 2010). This time duration includes 120–200 waves for 6 to 10 s wave periods. The long duration

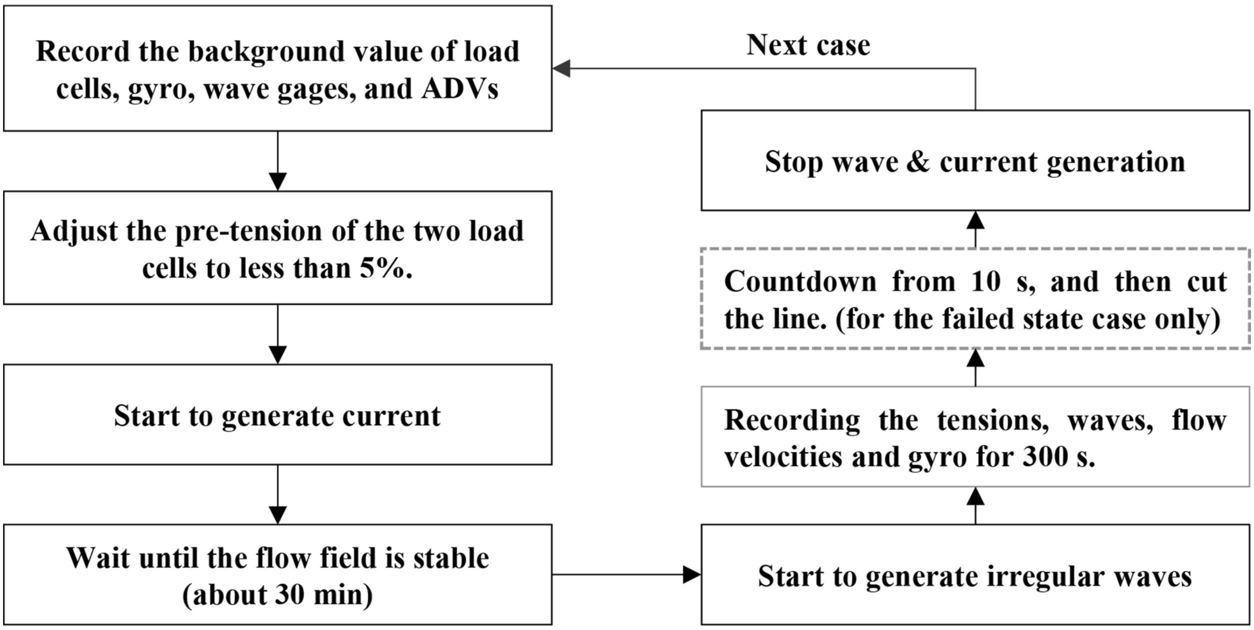

FIGURE 3
Flowchart of a single experimental case.

of irregular waves in the wave tank can cause wave reflections that must be considered. According to that, the recording time for the model test is scaled down from 20 to 4 min based on the scale ratio of time. Moreover, the total measurement time is extended to 5 min to sufficiently capture the dynamic responses after the failure.

3 Numerical model

The numerical model aimed to cross-check the experimental results. Therefore, the numerical simulations used the same input parameters of the net cage model listed in Table 1. The subsequent sections will provide a brief introduction to the numerical method.

3.1 Environmental loads

The numerical domain was considered herein as a three-dimensional (3D) space with a uniform bottom and adopted a superposition principle of linear velocity potential functions to represent a flow field, including a steady uniform current and an irregular progressive wave, given as

$$\phi(x,y,z,t) = -(U_x x + U_y y) + \sum_{i=1}^{N_w} \frac{A_i g}{\omega_{e_i}} \frac{\cosh k_i(h+z)}{\cosh k_i h} \cos(k_{x_i} x + k_{y_i} y - \omega_i t + \epsilon_i) \quad (1)$$

where U_x and U_y are the components of a uniform current in the x and y directions, respectively; (x,y,z) is a position coordinate; N_w is the total number of wave components; A_i is the i-th wave amplitude; ω_i is the i -th wave angular frequency; $\omega_{e_i}=\omega_i-(k_{x_i}U_x+k_{y_i}U_y)$ is referred to as the i-th apparent wave angular frequency; k_i is the i-th wave number; $k_{xi}=k_k cos\alpha$ is the component of the wave number in the x-direction ; $k_{yi}=k_i sin\alpha$ is the component of the wave number in the y-direction , where α is an apparent angle defined as the angle between the irregular wave and current directions; ϵ_i is the i-th wave phase angle randomly distributed between 0 and 2 π ; g is gravity; t is time; and h is the water depth. The water surface elevation η is calculated as

$$\eta = \sum_{i=1}^{N_w} A_i \sin(k_{x_i} x + k_{y_i} y - \omega_i t + \epsilon_i) \quad (2)$$

The correspondent dispersion relation for the wave/current coexisted field is given as

$$\omega_{e_i}2 = gk_i \tan hk_i h \quad (3)$$

We obtain a 3D velocity field, where velocity is defined as $V=-\nabla\phi$, by taking the derivative of Eq. (1) with respect to (x,y,z)

$$\left\{ \begin{array}{l} u = U_x + \sum_{i=1}^{N_w} \dfrac{A_i g k_{x_i} \cosh k_i(h+z)}{\omega_{e_i} \cosh k_i h} \sin(k_{x_i} x + k_{y_i} y - \omega_i t + \epsilon_i) \\ v = U_y + \sum_{i=1}^{N_w} \dfrac{A_i g k_{y_i} \cosh k_i(h+z)}{\omega_{e_i} \cosh k_i h} \sin(k_{x_i} x + k_{y_i} y - \omega_i t + \epsilon_i) \\ w = -\sum_{i=1}^{N_w} \dfrac{A_i g k_i \sinh k_i(h+z)}{\omega_{e_i} \cosh k_i h} \cos(k_{x_i} x + k_{y_i} y - \omega_i t + \epsilon_i) \end{array} \right\} \quad (4)$$

Similarly, the local accelerations for the 3D field are obtained as follows by taking the derivative of Eq. (4) with respect to t

$$\left\{\begin{array}{l} \frac{\partial u}{\partial t} = -\sum_{i=1}^{N_w} \frac{\omega_i A_i g k_{x_i} \cosh k_i(h+z)}{\omega_{e_i} \cosh k_i h} \cos\left(k_{x_i}x + k_{y_i}y - \omega_i t + \epsilon_i\right) \\ \frac{\partial v}{\partial t} = -\sum_{i=1}^{N_w} \frac{\omega_i A_i g k_{y_i} \cosh k_i(h+z)}{\omega_{e_i} \cosh k_i h} \cos\left(k_{x_i}x + k_{y_i}y - \omega_i t + \epsilon_i\right) \\ \frac{\partial w}{\partial t} = -\sum_{i=1}^{N_w} \frac{\omega_i A_i g k_i \sinh k_i(h+z)}{\omega_{e_i} \cosh k_i h} \sin\left(k_{x_i}x + k_{y_i}y - \omega_i t + \epsilon_i\right) \end{array}\right\} \tag{5}$$

Velocity and acceleration fields are then applied to the Morison equation based on the lumped mass method to obtain the hydrodynamic forces acting on the net cage (Huang et al., 2006; Huang et al., 2007; Huang et al., 2010).

The incident wave spectrum $S(f)$ obtained from the wave gauge records in the experiment (Figure 4) was applied to the numerical simulation to better fit with the experiment. For computational efficiency, the exponential frequency cutoff method (Hsu et al., 2007) was used to decompose the incident wave spectrum $S(f)$ into 100 wave components. Let the lowest and highest cutoff frequencies be f_{min} and f_{max}, respectively. The frequency of each wave component is then given as

$$f_{i+1} = f_i + \left[\left(\frac{f_{max}}{f_{min}}\right)^{1/(N_w-1)} - 1\right] f_i \tag{6}$$

where N_w is the number of wave components. Typically, f_{min}=0.1f_p and f_{max}=5f_p are adopted in the numerical simulation, where f_p is the peak frequency. The wave amplitude and the angular frequency of each wave component are written as

$$A_i = \sqrt{2S(f_i)\Delta f_i},\ \omega_i = 2\pi f_i \tag{7}$$

When irregular waves are generated in the numerical model, random phase angles will appear in the water elevation, velocity, and acceleration, as shown by Eqs. (2), (4), and (5), respectively. Therefore, a phase difference between the numerical and experimental results is ineluctable.

In order to reduce transient responses and prevent numerical instabilities, there is usually a build-up stage in which wave dynamics and object motions are ramped up smoothly to their full value. In this study, the duration of the build-up stage was set to 20 seconds.

3.2 Equation of motion

In this study, the net cage model was assumed to be deployed in water at a uniform depth and subjected to irregular waves and uniform currents. To calculate the hydrodynamic forces acting on the cage system, the whole system was divided into small elements

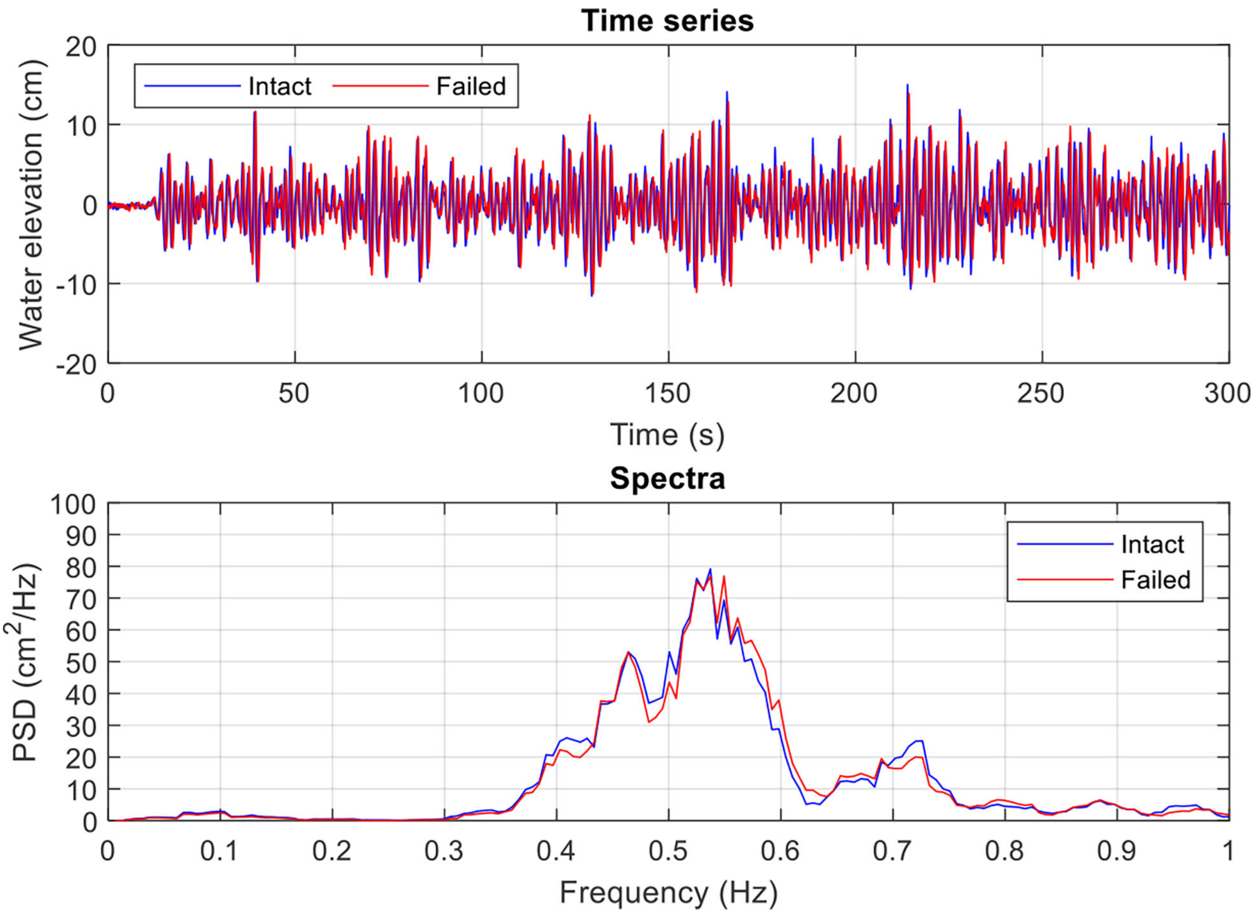

FIGURE 4
Time series and power spectral density of the incident waves.

according to the lumped mass method. These elements were chosen to be relatively small compared with the characteristic wavelength to simplify the numerical calculations. In this manner, the scattering effect between any element and the flow field can be neglected. We appropriately applied the Morison equation to the net cage components. All net cage model components were divided into two categories: deformable and rigid. The deformable parts included the fish nets and the mooring lines, whereas the rigid parts included the nondeformable floating collar and the tube sinker.

In this study, each deformable component comprised several elements and nodes assigned with numbers. For each element, the external forces were calculated, and the resultant force was evenly distributed among the corresponding nodes. Thus, each node contained the lumped mass of all neighboring elements and their corresponding forces. Its equation of motion is expressed as follows:

$$\sum\nolimits_{j=1}^{N_e} m_j \ddot{x}_k = \sum\nolimits_{j=1}^{N_e} F_{D_j} + F_{I_j} + F_{B_j} + F_{W_j} + F_{T_j} \tag{8}$$

where subscript k denotes the node number, $j = 1, \ldots$; N_e denotes all neighboring elements associated with node k; N_e represents the total number of neighboring elements; m_j is the mass matrix; x is the position vector; and F_{D_j}, F_{I_j}, F_{B_j}, F_{W_j}, and F_{T_j} represent the vectors of the drag, inertia, buoyant, gravity, and tension forces, respectively, on element j. Details on the external force modeling of the cage components can be found in the previous works of Huang et al, 2006; Huang et al, 2007.

The motion of the rigid components of the net cage system, including the floating collar and the tube sinker, can be resolved by the rigid body motion with six degrees of freedom (DOF) in a 3D space. The three translation motions can be expressed as

$$\begin{cases} \ddot{x}_G = \dot{y}_G \omega_3 - \dot{z}_G \omega_2 + \frac{1}{m_G} \sum\nolimits_{k=1}^{N_n} F_{x_k} \\ \ddot{y}_G = \dot{z}_G \omega_1 - \dot{x}_G \omega_3 + \frac{1}{m_G} \sum\nolimits_{k=1}^{N_n} F_{y_k} \\ \ddot{z}_G = \dot{x}_G \omega_2 - \dot{y}_G \omega_1 + \frac{1}{m_G} \sum\nolimits_{k=1}^{N_n} F_{z_k} \end{cases} \tag{9}$$

and the three rotational motions can be expressed as

$$\begin{Bmatrix} \dot{\omega}_1 = -\frac{1}{I_1}(I_3 - I_2)\omega_2 \omega_3 + \frac{1}{I_1} \sum\nolimits_{k=1}^{N_n} M_{1_k} \\ \dot{\omega}_2 = -\frac{1}{I_2}(I_1 - I_3)\omega_3 \omega_1 + \frac{1}{I_2} \sum\nolimits_{k=1}^{N_n} M_{2_k} \\ \dot{\omega}_3 = -\frac{1}{I_3}(I_2 - I_1)\omega_1 \omega_2 + \frac{1}{I_3} \sum\nolimits_{k=1}^{N_n} M_{3_k} \end{Bmatrix} \tag{10}$$

where subscripts 1 to 3 and x, y, and z correspond to the body and global coordinate systems, respectively; (x_G , y_G , z_G) are the coordinates of the center of gravity; (ω_1 , ω_2 , ω_3) are the angular velocities along the principal axes; m_G is the body mass; (F_{x_k} , F_{y_k} , F_{z_k}) and (M_{1_k} , M_{2_k} , M_{3_k}) are the components of the resultant forces and moments acting at the lumped mass node k; N_n is the number of nodes in the body; and (I_1 , I_2 , I_3) are the principal moments of the rigid body inertia. For the floating collar and the tube sinker, I_1=$0.5m_G R^2$, I_2=$0.5m_G R^2$, and I_3=$m_G R^2$, where R is the rigid body radius.

We can obtain a solution with a short time increment by applying the fourth-order Runge–Kutta method to the equation of motion in the net cage system [Eqs. (10)–(12)]. The path of each node, including the mass center of the rigid body, is accordingly depicted herein. By computing the neighboring node distance, the tension force of the flexible part is obtained and used as the input tension data for the next time step until the required time interval is spent.

In this work, the net cage model was divided into 844 elements and 791 nodes, and the time step for the numerical integration was 0.0001 s. The number of nodes and elements and the time step in the preliminary stage were determined through time domain convergence tests. The total number of elements on the fish net was 480, including 24 and 20 in the circumferential and depth direction of the net, respectively. The element on each mooring line was 25.

3.3 Force on the net

The hydrodynamic forces on the netting were calculated using the screen model (Huang et al., 2006; Kristiansen and Faltinsen, 2012). In the algorithm, the whole netting structure was divided into many small screens (or elements), with each screen containing many mesh twines. The tension, buoyancy, and gravity forces acting on each screen represented the sum of the forces exerted on the twines in the screen. Finally, the total forces on the screen were assumed to be evenly distributed among the nodes. The drag $C_D(\beta)$ and lift $C_L(\beta)$ coefficients depended on the flow attack angle β . They can be determined using the experimental results by Løland (1991).

$$C_D(\beta) = 0.04 + (- 0.04 + 0.33S_n + 6.54S_n2 - 4.88S_n3) \cos(\beta) \tag{11}$$

$$C_L(\beta) = (- 0.05S_n + 2.3S_n2 - 1.76S_n3) \sin(2\beta) \tag{12}$$

The solidity ratio S_n is the ratio between the area covered by the twines in the screen and the total area of the screen. It is expressed as follows for a knotless net:

$$S_n = \frac{2D}{\lambda} - \left(\frac{D}{\lambda}\right)^2 \tag{13}$$

where D is the twine diameter and λ is half of the mesh size. The fluid particle velocity was slightly retarded after entering the net cage. This phenomenon is known as the shielding effect. A velocity reduction coefficient of 0.85 was adopted for the rear part of the nets (Løland, 1991).

3.4 Simulation of the mooring line failure

All anchor points in the intact mooring state were considered as fixed nodes to simulate the net cage dynamics. To do that, the equation of motion of all anchor points was set to $\ddot{x}_k = 0$. It is to ensure all anchor points will not move. In contrast, anchor point #1 was changed to a free node and allowed to move freely according to the equation of motion to simulate the mooring line failure (Yang et al., 2020). In the other word, we can lift the restriction of the anchor point ($\ddot{x}_k = 0$), then it will move freely in the next time step depending on the external forces as shown in Eq. (8). In this study, a predetermined time of 40 s after the start of the simulation was set as the moment of failure occurrence. The experimental setup showed a total simulation time of 300 s. The results were then compared with those in the experiments.

4 Influence of the mooring line failure on dynamic responses

4.1 Model test A

Table 2 lists the input wave and current conditions, where A1 is the intact mooring condition and A2 is the mooring line failure condition implemented according to the flowchart shown in Figure 3. The significant wave height (Hs) and wave period (Tz) were obtained from the wave gauge recordings using the zero up-crossing analysis method. The current velocity (*U*) was taken from the average of the three ADVs. The difference in the input conditions between the two test cases was less than 1.10%. Figure 4 shows the time history and the power spectral density (PSD) of the incident irregular waves. The two PSDs were obtained using the fast Fourier transform (FFT) analysis with 2^{12} = 4096 data points ranging from 50 to 213.84 s (approximately 91 wave periods). The sampling rate was 25 Hz. The PSDs were then smoothed by the moving average method with seven points. The two cases showed great agreement in both the time and frequency domains. The wave spectra under the intact and failed states were very close, having a similar 0.54 Hz peak frequency. However, a minor peak response was observed near 0.73 Hz, which may have resulted from the reflected waves caused by the limited wave tank length. Overall, the repeatability of the irregular waves and current generation in the experiment was excellent. For comparison reasons, these two wave spectra were used to generate irregular waves in the time series for the numerical model in the case of the intact and failed mooring states, respectively.

TABLE 2 Input irregular wave and current conditions in model test A.

Case	Hs (cm)	Tz (s)	U (cm/s)	Remark
A1	13.55	1.82	24.35	Intact
A2	13.61	1.84	24.43	Failed
Difference (%)	0.44	1.10	0.33	

4.2 Tension responses caused by the mooring line failure

Figure 5 shows the time series of the tension response of Line 2 under the intact and failed states of mooring and compares the difference between the experiment and simulation. The intact condition was used to quantify the actual influence of the mooring line failure. The comparison revealed that the tension in Line 2 greatly increased after Line 1 failed at 40 s in both the experiment and simulation. In the experiment, the maximum tensions for the intact and failed states were 13.2 and 20.9 N, respectively. The mean values were 4.9 and 10.2 N, and the standard deviations were 2.0 and 3.0 N,

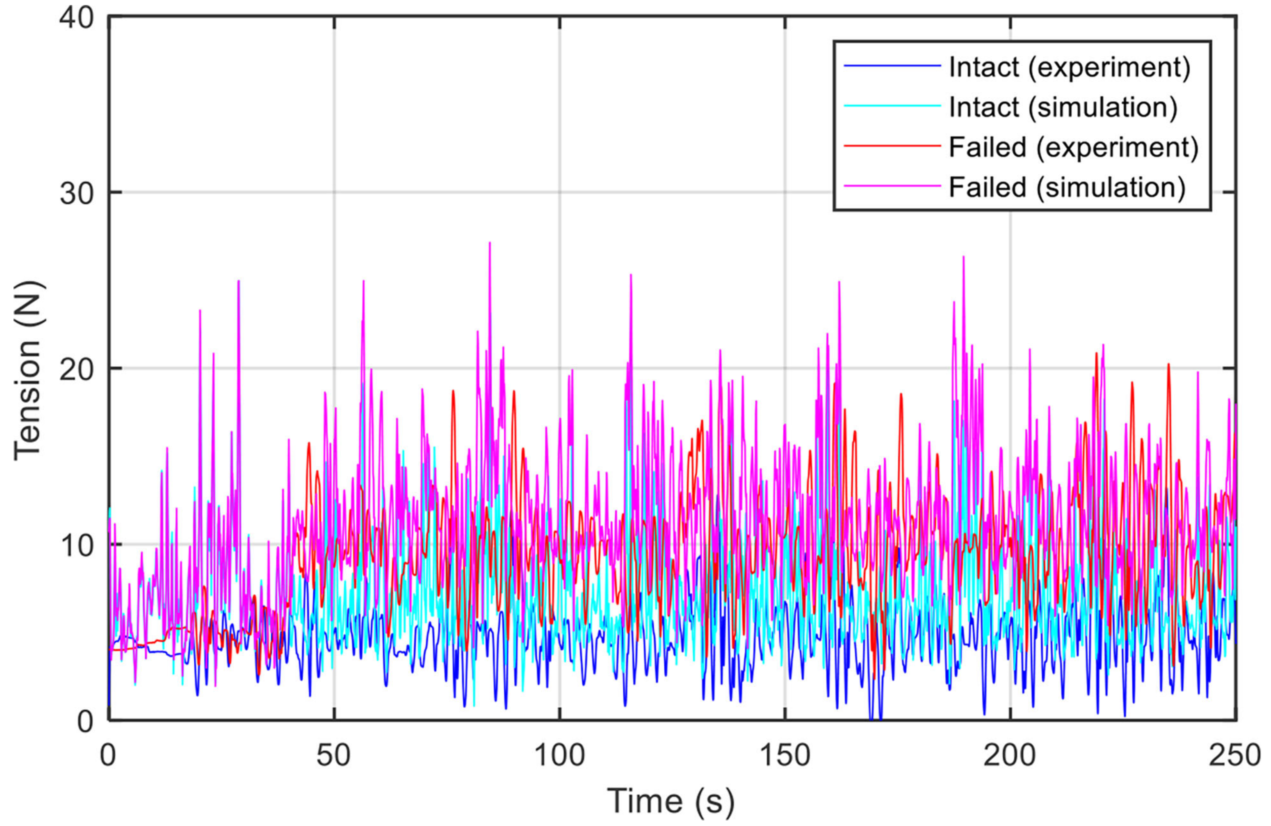

FIGURE 5
Time series tension responses of Line 2 under the intact and failed states of mooring.

respectively. In the simulation, the maximum tensions for the intact and failed states were 23.1 and 27.1 N, respectively. The mean values were 7.2 and 12.1 N, and the standard deviations were 3.1 N and 3.5 N, respectively. Both results showed that the mooring line failure increased the tension response not only in magnitude but also in amplitude. However, the simulation results were overestimated. The difference between the experiment and simulation should be caused by the limitation of the numerical models that ignored the wave–body interactions. Moreover, numerically perfect symmetric mooring and uniform water current is nearly impossible to reproduce in an experimental setting. The shielding effect within the net and the damping effect of the wave–body interactions may lead to reduced mooring loads in the model tests. It is also difficult and sometimes impossible to accurately deploy the mooring system to ensure its symmetry in a model test. This will cause an asymmetrical cage movement and produce unexpected results. The motion of the floating collar induced by the asymmetric mooring will be described in the next section.

Figure 6 compares the PSD of tension of Line 2 in the frequency domain for both the experiment and simulation under intact and failed moorings. All PSDs were obtained using the FFT analysis based on the consideration mentioned earlier. The results of both intact and failed moorings between the experiment and simulation were comparable, except for the higher-frequency (within 0.6 and 1.0 Hz) and lower-frequency (close to 0.1 Hz) regions. The tension PSD for both the experiment and simulation showed a significant increase in both the wave- and low-frequency regions compared to the intact mooring. The former was related to the wave force, whereas the latter was related to the restoring force of mooring. In other words, the mooring line failure caused a more significant tension response in both wave- and lower-frequency regions. The peak frequency of the tension PSD was different from the wave PSD, which may be due to the complex coupling effect between the cage motion and its mooring.

The linear transfer function of the tension $H_{tension}(f)$ of the net cage using the auto-spectral technique was applied to better understand the frequency response of the tension under irregular waves (Fredriksson et al., 2003; Dong et al., 2010; Huang et al., 2010).

$$H_{tension}(f) = \sqrt{\frac{S_{tt}(f)}{S_{\eta\eta(f)}}} \tag{14}$$

where $S_{tt}(f)$ is the auto-spectra of the mooring tension and $S_{\eta\eta}(f)$ is the auto-spectra of the incident waves.

Figure 7 compares the transfer function of tension in Line 2 for the experiment and simulation under the intact and failed mooring states. The resonant frequency of the tension response was found within 0.2–0.3 Hz for both the experiment and simulation. The response amplitude in the resonant frequency region turned into two peaks when the mooring line failure happened. The comparison results also showed that the numerical model can precisely simulate the response frequency but overestimate its response amplitude. The discrepancy between the experiment and simulation was mentioned earlier. Overall, the numerical simulation results are acceptable for the engineering feasibility analysis purpose.

4.3 Rotational motion response due to the mooring line failure

According to existing studies (Tang et al., 2020; Yang et al., 2020), a significant yaw motion can be observed after cutting an upstream

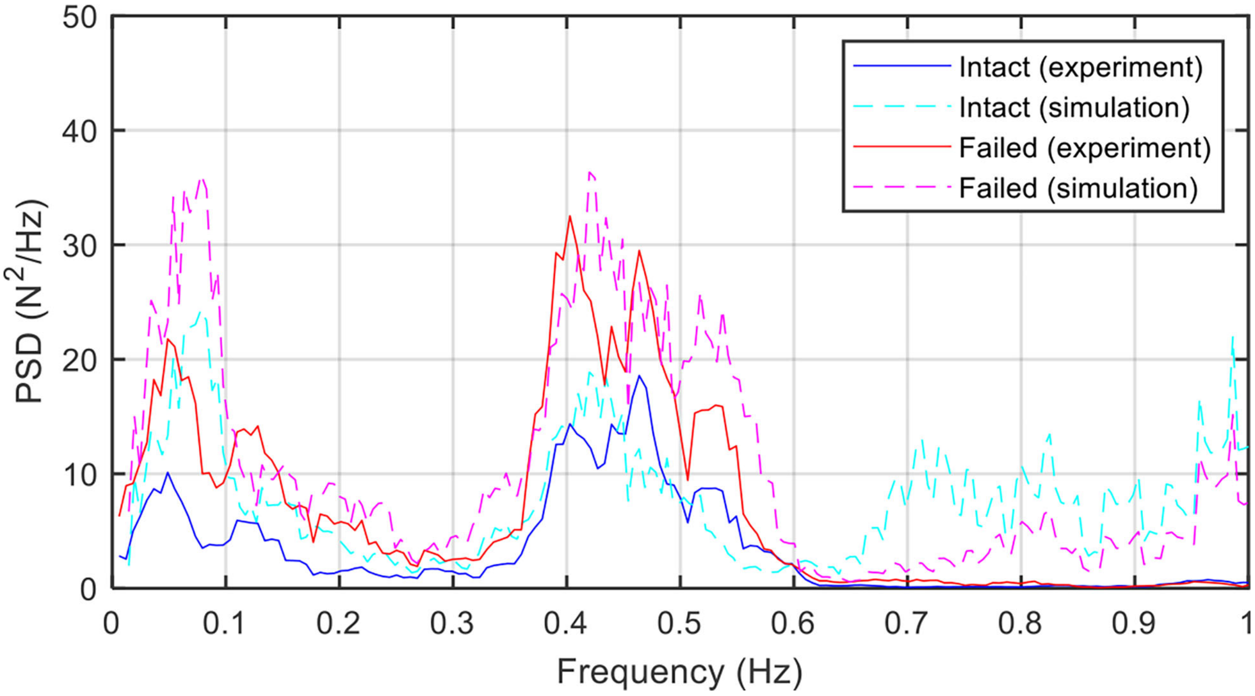

FIGURE 6
Power spectral density of the mooring tension in Line 2.

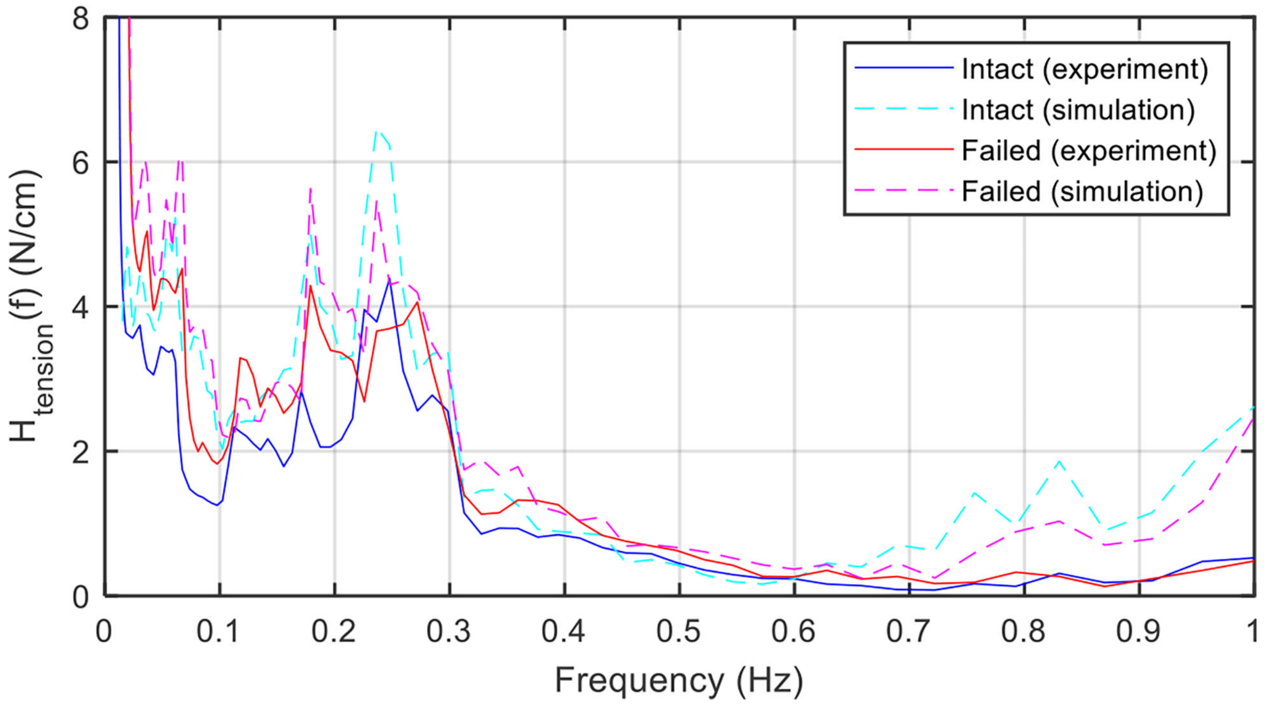

FIGURE 7
The transfer function of the mooring tension in Line 2.

mooring line. Therefore, we deployed an IMU on the floating collar to measure its rotational motions, including the roll, pitch, and yaw. However, we did not record the translational motions (i.e., surge, sway, and heave) because the IMU was not installed at the gravity center of the floating collar. Table 2 lists the test conditions in this case.

The incident direction of the waves and currents was aligned in the x -axis direction symmetric to the net cage model layout (Figures 1, 2). Therefore, the surge, heave, and pitch of the floating collar under the intact condition were the major responses, and its roll and yaw motions were minor and negligible. Thus, if the mooring layout is not exactly symmetric, some unwanted or unexpected motion components will occur. However, this was hard, even impossible, to prevent in the experiment.

Figure 8 compares the time series of the experimental and simulated roll, pitch, and yaw motions under intact and failed mooring conditions. In the intact state of the experiment, the roll and yaw were small compared to the pitch, but still visibly vibrated compared to the simulated ones because the mooring system was not perfectly symmetrical, thereby leading to differences in the motion response and the resulting mooring response between the experiment and simulation. In the failed state of the experiment, a significant increase in the yaw motion above 20° was observed after cutting the line at 40 s. It then started to balance and reach a stable value. Its amplitude was much smaller than the pitch amplitude. A similar yaw motion was also observed compared to the simulation, but only by approximately 8°. This difference could have been caused by the tightened bridle in the simulation, but not fully tightened in the experiment (Tang et al., 2022b). The fully symmetrical and tightened mooring in the simulation could also be the source of discrepancy in the roll and pitch responses compared to the experiment.

Similarly, the linear transfer function of the motion response of the net cage under irregular waves was calculated as follows using the auto-spectral technique:

$$H_{roll}(f)=\sqrt{\frac{S_{rr}(f)}{S_{\eta\eta(f)}}};$$

$$H_{pitch}(f)=\sqrt{\frac{S_{pp}(f)}{S_{\eta\eta(f)}}};\quad H_{yaw}(f)=\sqrt{\frac{S_{yy}(f)}{S_{\eta\eta(f)}}}\qquad(15)$$

where $S_{rr}(f)$, $S_{pp}(f)$, and $S_{yy}(f)$ are the auto-spectra of the roll, pitch, and yaw motions of the floating collar, respectively.

Figure 9 compares the linear transfer functions of the experimental and simulated roll, pitch, and yaw rotations under intact and failed mooring conditions. The intact state showed almost no response of the roll and yaw in the simulation. By contrast, the low- and resonant frequency (0.2–0.3 Hz) responses of the roll and yaw were observed in the experiment. The differences were caused by the fully symmetrical and tightened mooring lines. Nevertheless, the transfer functions of the pitch were close to each other. The experimental peak values of the roll, pitch, and yaw within 0.2–0.3 Hz slightly decreased in the failed state than in the intact state. However, the simulated peak values of the three rotations significantly increased when their intact and failed states were compared. This difference may be the error source of the higher transfer function response of the mooring tension in Figure 7.

4.4 6 DOF motion response due to the mooring line failure

The experimental results were considered to be more representative and referenceable. However, the three translational

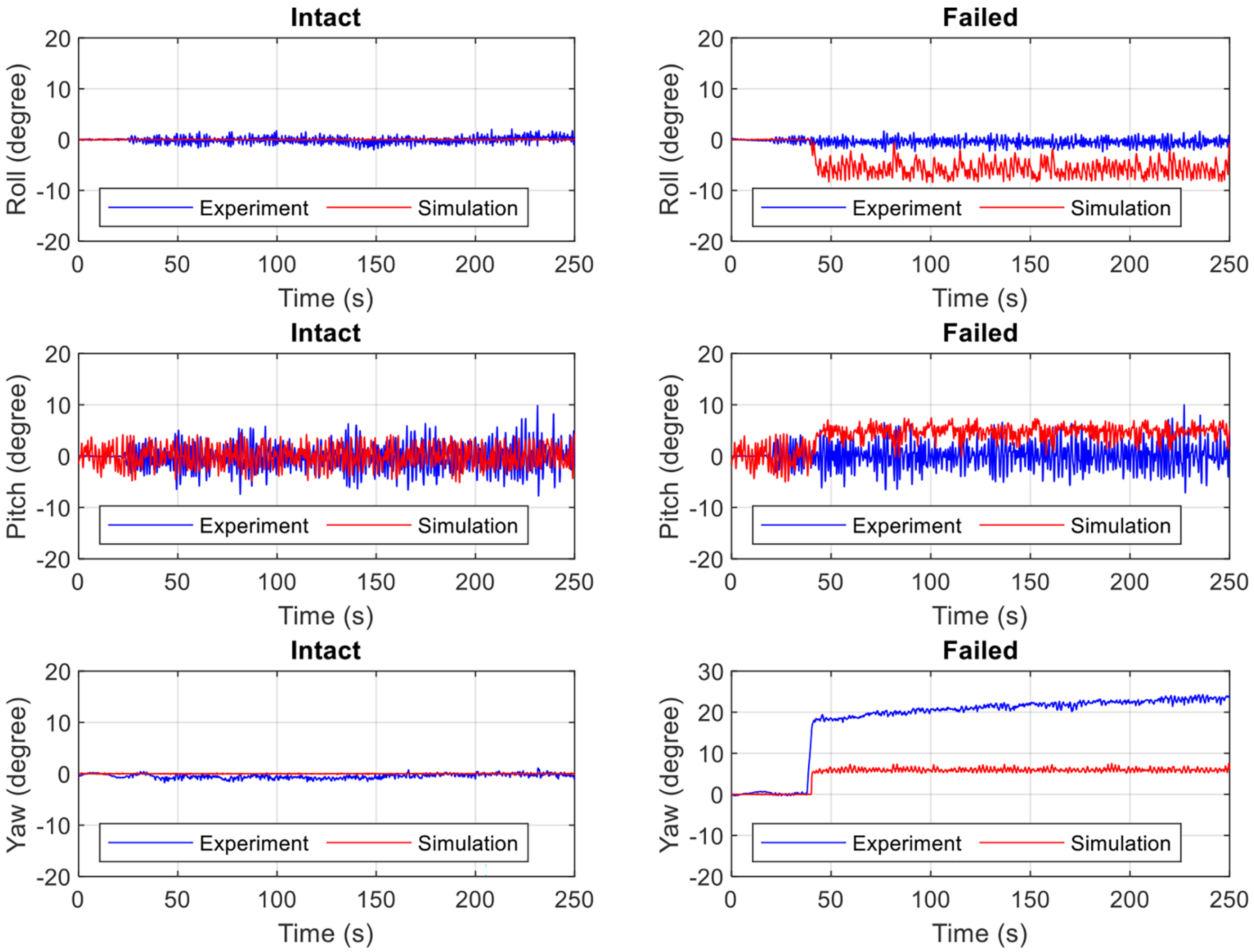

FIGURE 8
Time series of the roll, pitch, and yaw rotations of the floating collar in the experiment and simulation under the intact and failed states.

motions (i.e., surge, sway, and heave) of the floating collar were not available in the experiment. Therefore, in this section, we will only discuss the 6 DOF motions in the numerical simulations.

Figure 10 compares the transfer function of the 6 DOF motions of the floating collar under the intact and failed mooring conditions. Comparing the translational motions, the pitch and heave responses within the resonant frequency of 0.2–0.3 Hz decreased with the mooring line failure, while the low-frequency response increased. The transfer function of sway significantly increased as the mooring system transitioned from an intact to a failed state. Comparing the rotational motions, the transfer functions of the roll and yaw became significant, while the pitch frequency shifted to a lower frequency. The low-frequency response significantly increased.

5 Influence of the current velocity on the mooring line failure

5.1 Model test B

The current forces can play a more important role than the waves due to the drag force dominant characteristic of the netting structure (Huang et al., 2007). Therefore, it is important to study the influence of increasing the current velocity on the mooring line failure. In this case study, three different current velocities traveling with the same irregular waves (cases B1 to B3) toward the *x*-axis direction were used (Table 3). The significant wave height and period were obtained by using the zero up-crossing analysis method (see Section 4.1). The current velocity was the average value of the three ADVs. The input parameters used in the wave-generating procedure of the experiment for the three cases were identical. Results showed that the wave period slightly increased when the current velocity was increased. By contrast, the wave height significantly decreased. Figure 11 compares the wave spectra for cases B1 to B3. The wave amplitude changed as the current velocity increased. This is known as the characteristics of the wave–current interaction (Thomas, 1981; Ryu et al., 2003).

5.2 Influence on the tension response

Figure 12 compares the experimental and numerical time series of the mooring forces for cases B1 to B3. The results indicated a significant increase in tension before and after the mooring line

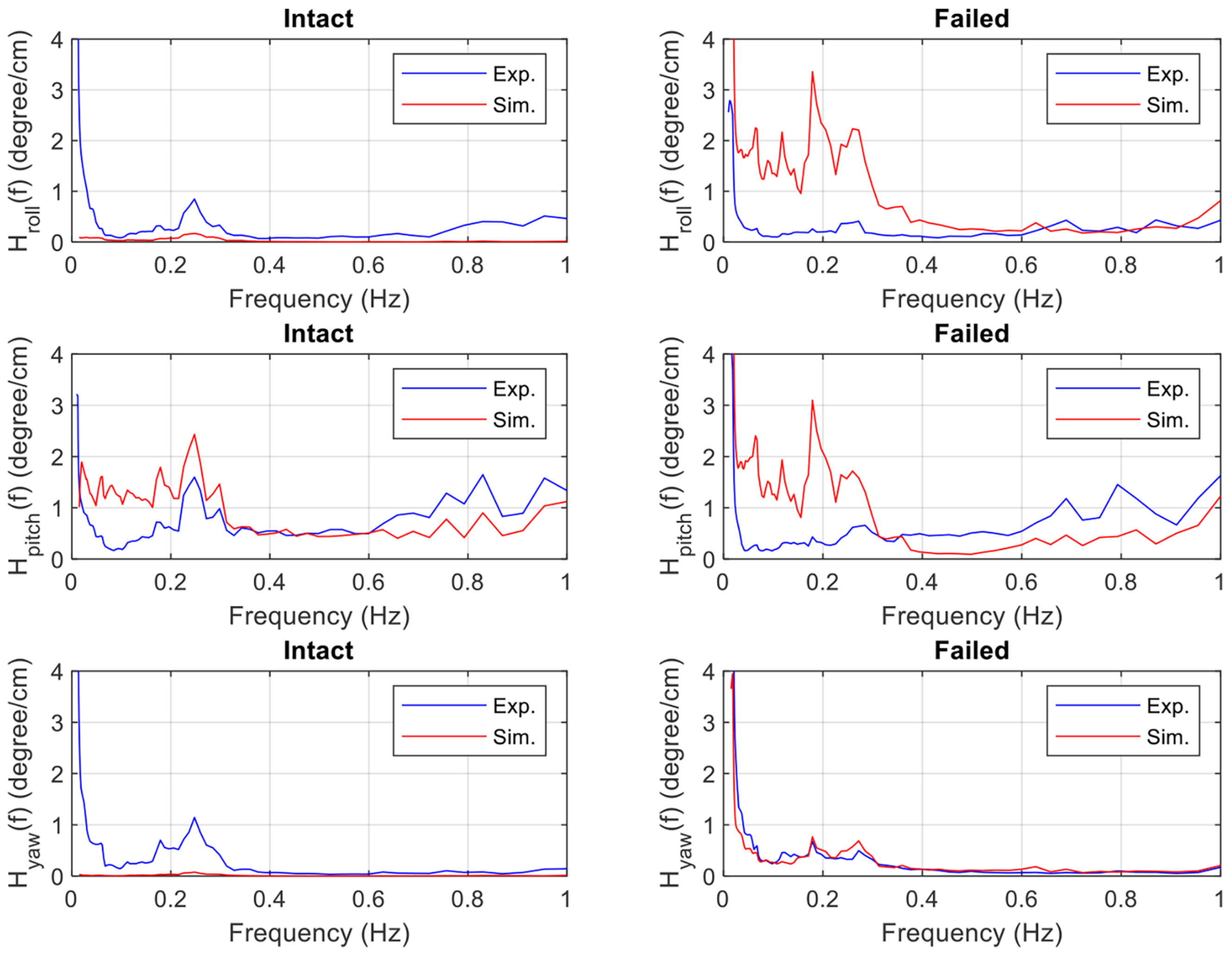

FIGURE 9
Transfer functions of the roll, pitch, and yaw motions of the floating collar in the experiment and simulation under the intact and failed states.

failure at 40 s with an increasing inflow velocity. However, the response was stronger in the numerical results, which may be due to the mooring lines being fully tightened in the numerical model. In Figure 13, the experimental and simulated maximum tension and standard deviation increased with the increasing inflow velocity. The numerical results were higher than the experimental ones. The difference decreased with the increasing inflow velocity.

Figure 14 compares the effects of increasing the current velocity on the tension spectrum after the mooring line failure. Although the wave height was suppressed by increasing the current velocity (Table 3), the tension spectrum in the wave-frequency region can still be significantly increased. However, increasing the current velocity did not have an obvious effect in the low-frequency region. The comparison revealed that the numerical tension spectrum was not very smooth and showed some response in the high-frequency region, which may be due to the strong motion of the floating collar with tightened mooring lines.

Figure 15 compares the effect of increasing the current velocity on the linear transfer function of tension after the mooring line failure. The tension spectrum was normalized by the wave spectrum; hence, the linear transfer function of tension showed a different trend than the tension spectrum. The comparison results illustrated similar trends between the experiment and simulation. The peak occurring in the resonant frequency region (0.2–0.3 Hz) increased as the velocity increased from U = 11.78 to U = 24.43 cm/s, but decreased as the velocity increased from U = 24.43 to U = 29.95 cm/s. This may be due to the increased rate of tension being slowed down when the velocity increased from U = 24.43 to U = 29.95 cm/s (Figure 13). After being normalized by the wave spectrum, the line transfer function of case B3 became lower than that of case B2.

5.3 Influence on the motion response

The influence of increasing the current velocity on the 6 DOF motion of the floating collar resulting from the mooring line failure was investigated through numerical simulations. Figure 16 compares the time series of the 6 DOF motion of the floating collar for cases B1 to B3. Prior to failure, the increased current velocity significantly affected the surge, heave, and pitch, but only slightly affected the sway, roll, and yaw because the waves and currents were symmetrical with

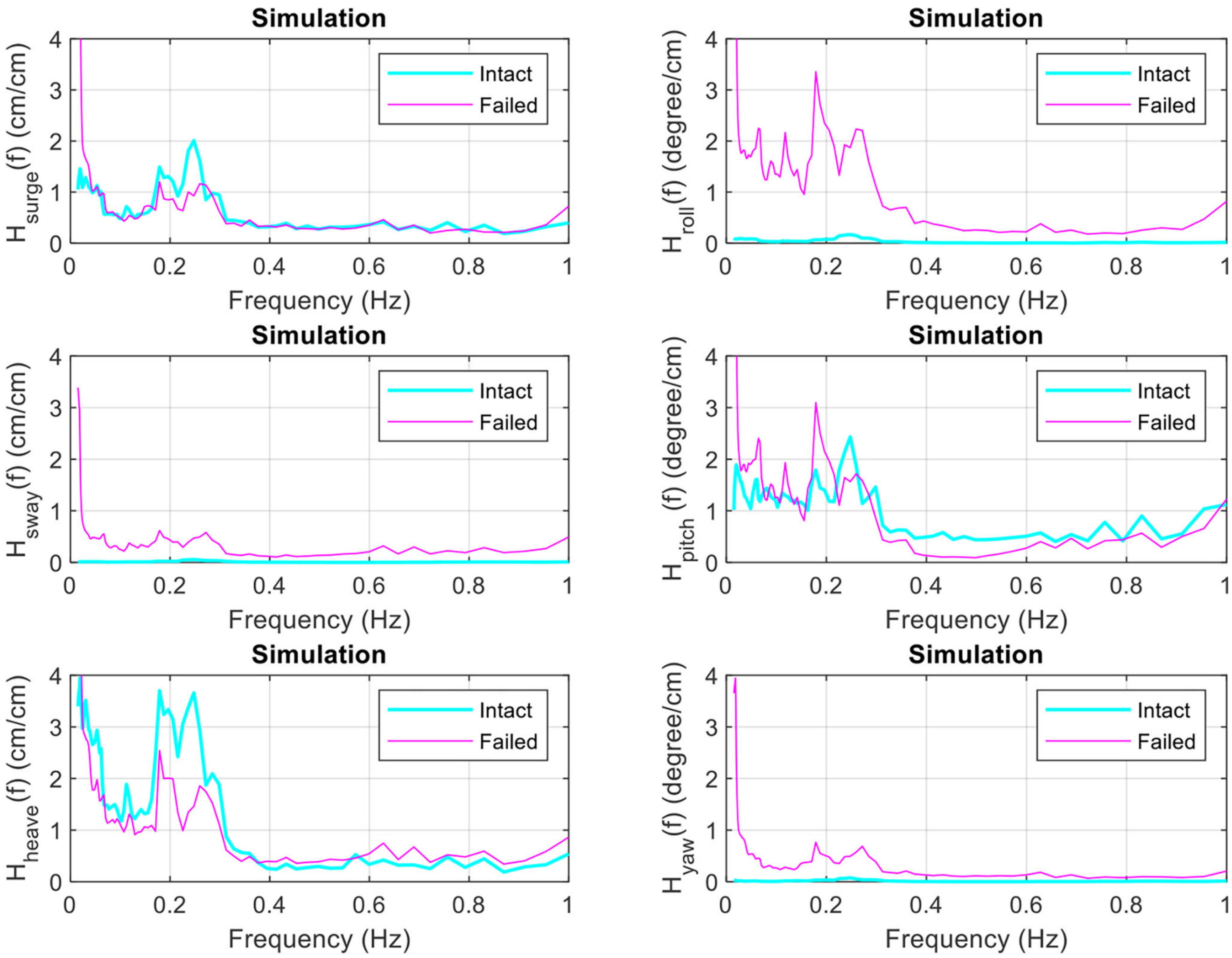

FIGURE 10
Transfer functions of the 6 DOF motions of the floating collar under intact or failed mooring (numerical simulation).

respect to the cage's mooring system. The mooring system becomes asymmetrical when a failure occurs, which can have significant effects on the sway, roll, and yaw. Consequently, the 6 DOF motion of the floating collar increased as the current velocity increased. Figure 17 compares the linear transfer function of the 6 DOF motion of the floating collar for cases B1 to B3. Results showed that the resonant frequency responses of the surge, sway, heave, roll, and yaw decreased as the current velocity increased. However, the pitch response increased from B1 to B2 and decreased from B2 to B3. The reason for this may be similar to that in Figure 15. Overall, the influence of increasing the current velocity can cause larger drift displacement and rotational angle, but a lower response amplitude.

6 Conclusion

In this study, a net cage model was tested in a wave tank to study the effect of the mooring line failure on its dynamic response. A self-developed numerical model for the model test was used for cross-validation. Two cases of the mooring line failure for the net cage in

TABLE 3 Input irregular wave and current conditions in model test B.

Case	Hs (cm)	Tz (s)	U (cm/s)	Remark
B1	14.37	1.78	11.78	Failed
B2	13.61	1.84	24.43	Failed
B3	12.48	1.83	29.95	Failed

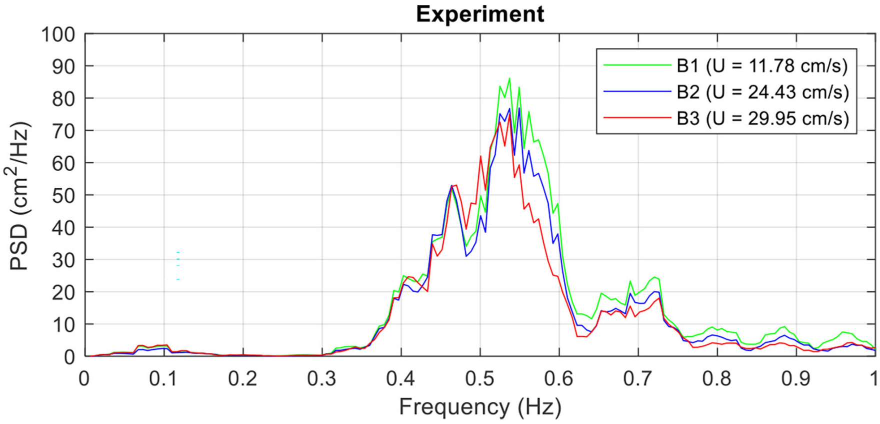

FIGURE 11
Power spectral density of the irregular waves with different coplanar current velocities.

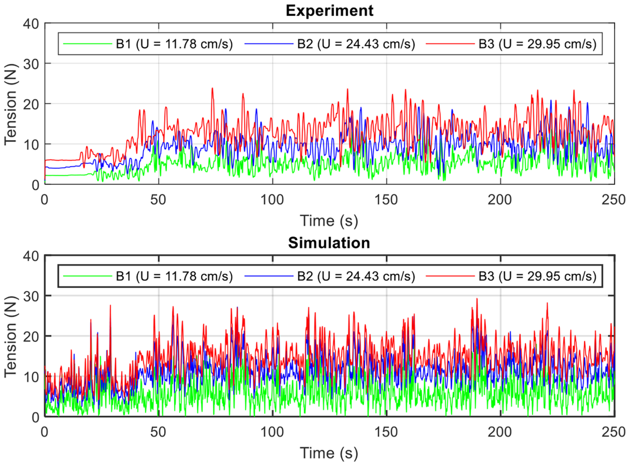

FIGURE 12
Influence of the current velocity on the time series mooring force under the mooring line failure of a net cage in irregular waves and currents.

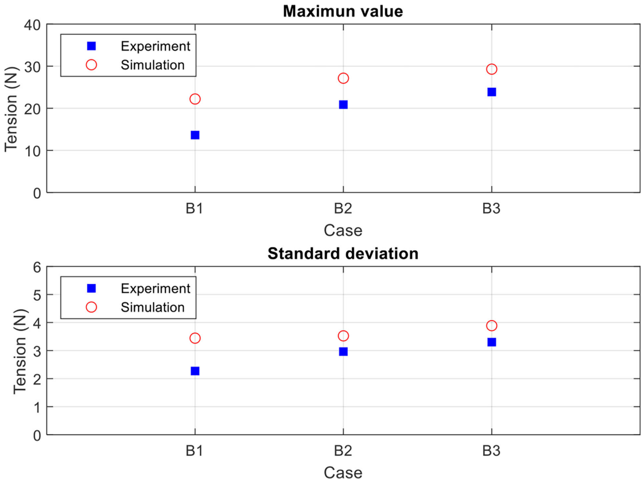

FIGURE 13
Influence of the current velocity on the maximum, mean, and minimum values and the standard deviations of the mooring force under the mooring line failure of a net cage in irregular waves and currents.

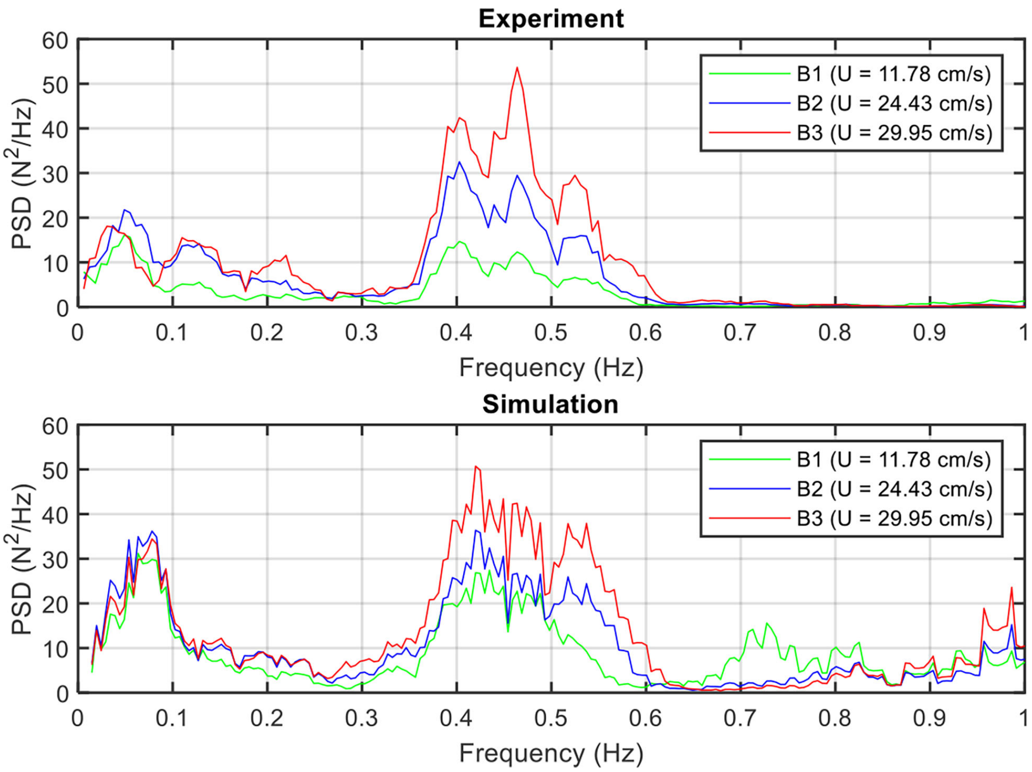

FIGURE 14
Influence of the current velocity on the power spectral density of the mooring force under the mooring line failure of a net cage in irregular waves and currents.

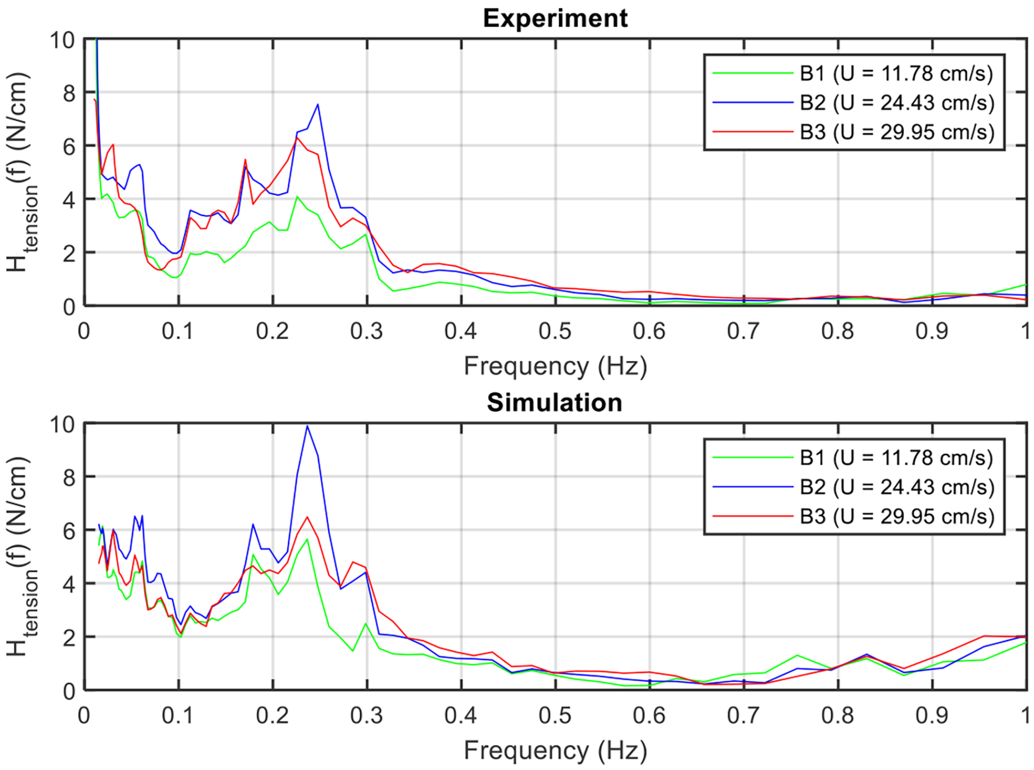

FIGURE 15
Influence of the current velocity on the linear transfer function of the mooring force under the mooring line failure of a net cage in irregular waves and currents.

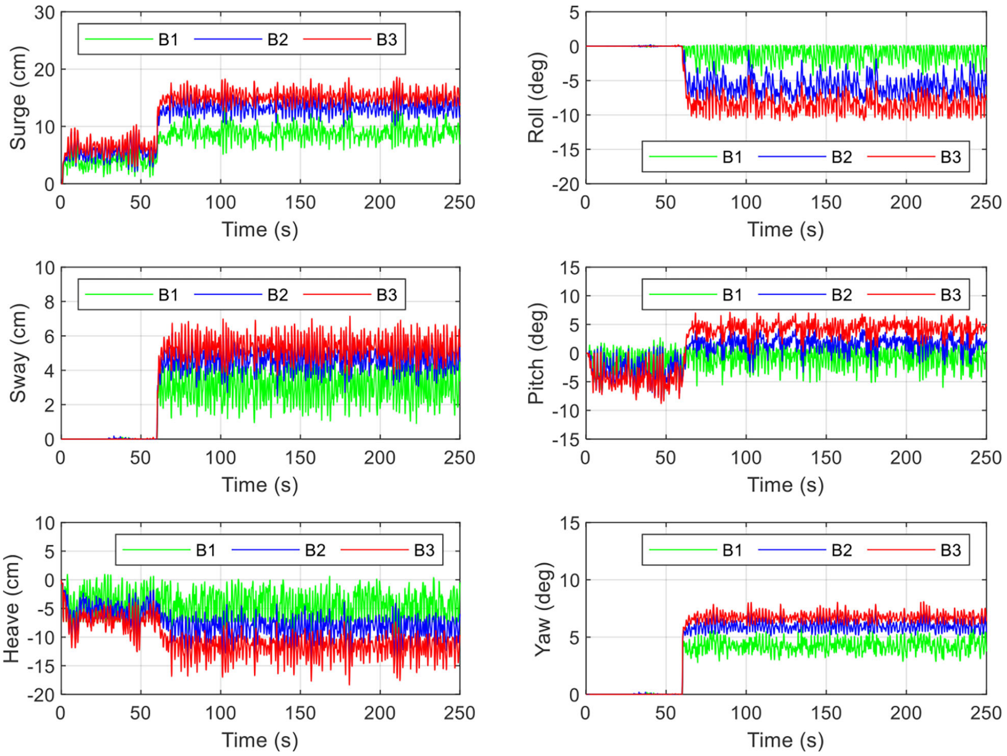

FIGURE 16
Influence of the current velocity on the time series 6 DOF motions of the floating collar under the mooring line failure of a net cage in irregular waves and currents (numerical simulation).

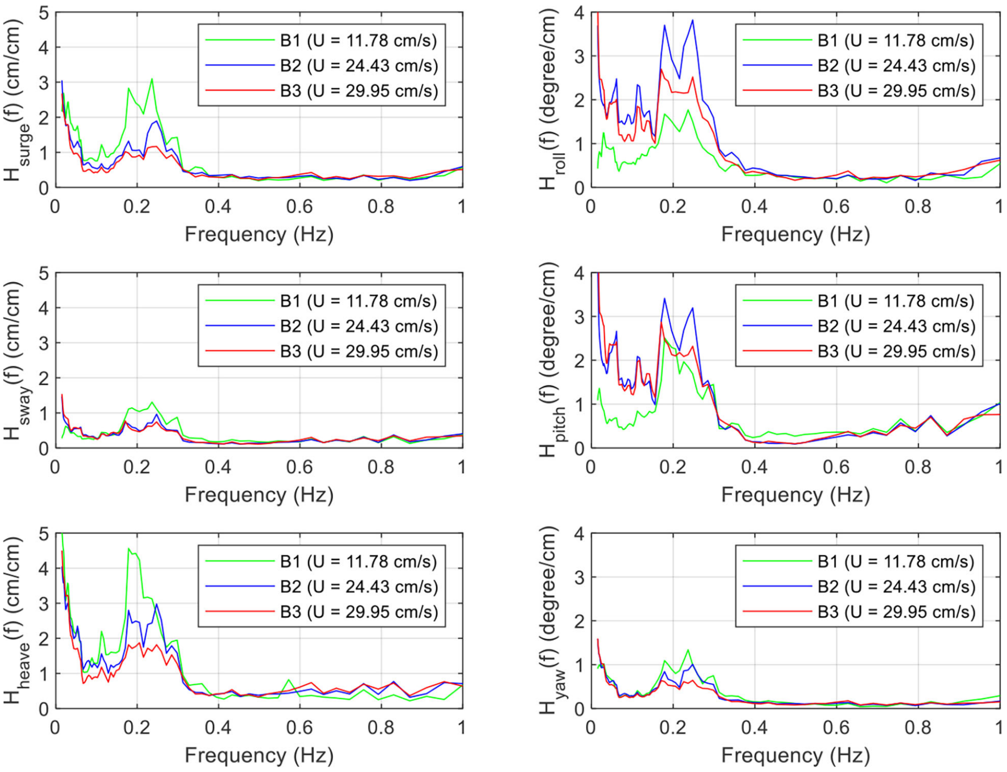

FIGURE 17
Influence of the current velocity on the linear transfer function of the 6 DOF motions of the floating collar under the mooring line failure of a net cage in irregular waves and currents (numerical simulation).

irregular waves and currents were investigated. The first case involved a comparative study of the intact and failed cage moorings. Results showed that the mooring line failure leads to a higher mooring tension in the remaining line, a higher spectral response in the wave- and low-frequency regions, and a significant yaw motion of the floating collar. The second case showed the effect of increasing the current velocity on the mooring line failure. Increasing the velocity led to an increase in the mooring tension, drift displacement, and rotation angle.

However, the numerical model overestimated the mooring line tension, and the experimental and numerical results of the floating collar rotation motion were inconsistent. Therefore, future work is recommended to improve the mooring system symmetry for the model test and the numerical model accuracy by considering the wave–body interactions.

Data availability statement

The raw data supporting the conclusions of this article will be made available by the authors, without undue reservation.

Author contributions

H-JT: Conceptualization, methodology, software, validation, investigation, writing–review and editing, visualization, project administration, funding acquisition. H-CY: Conceptualization, methodology, validation, investigation. R-YY: Conceptualization, methodology, resources, writing–review and editing, supervision, project administration, funding acquisition. All authors contributed to the article and approved the submitted version.

Funding

This work was financially supported by the National Science and Technology Council of Taiwan, Project No. 109-2222-E-006-003-MY2 and 111-2218-E-019-001.

Conflict of interest

The authors declare that the research was conducted in the absence of any commercial or financial relationships that could be construed as a potential conflict of interest.

Publisher's note

References

Cheng, H., Li, L., Ong, M. C., Aarsæther, K. G., and Sim, J. (2021). Effects of mooring line breakage on dynamic responses of grid moored fish farms under pure current conditions. *Ocean Eng.* 237, 109638. doi: 10.1016/j.oceaneng.2021.109638

DeCew, J., Fredriksson, D. W., Bougrov, L., Swift, M. R., and Eroshkin O. and Celikkol, B. (2005). A case study of a modified gravity type cage and mooring system using numerical and physical models. *IEEE J. Oceanic Eng.* 30 (1), 47–58. doi: 10.1109/JOE.2004.841400

Dong, G. H., Xu, T. J., Zhao, Y. P., Li, Y. C., and Gui, F. K. (2010). Numerical simulation of hydrodynamic behavior of gravity cage in irregular waves. *Aquacultural Eng.* 42, 90–101. doi: 10.1016/j.aquaeng.2009.12.004

FAO (2022). *The state of world fisheries and aquaculture 2022 – towards blue transformation* (Rome, Italy: Food and Agriculture Organization of the United Nations).

Fredriksson, D. W., Swift, M. R., Eroshkin, O., Tsukrov, I., Irish, J. D., and Celikkol, B. (2005). Moored fish cage dynamics in waves and currents. *IEEE J. Oceanic Eng.* 30 (1), 28–36. doi: 10.1109/JOE.2004.841412

Fredriksson, D. W., Swift, M. R., Irish, J. D., Tsukrov, I., and Celikkol, B. (2003). Fish cage and mooring system dynamics using physical and numerical models with field measurements. *Aquacultural Eng.* 27, 117–146. doi: 10.1016/S0144-8609(02)00043-2

Guo, Y. C., Mohapatra, S. C., and Guedes Soares, C. (2020). Review of developments in porous membranes and net-type structures for breakwaters and fish cages. *Ocean Eng.* 200, 107027. doi: 10.1016/j.oceaneng.2020.107027

Hou, H. M., Liu, Y., Dong, G. H., and Xu, T. J. (2022). Reliability assessment of mooring system for fish cage considering one damaged mooring line. *Ocean Eng.* 257, 111626. doi: 10.1016/j.oceaneng.2022.111626

Hsu, T. W., Hsiao, S. C., Ou, S. H., Wang, S. K., Yang, B. D., and Chou, S. E. (2007). An application of boussinesq equations to Bragg reflection of irregular waves. *Ocean Eng.* 34, 870–883. doi: 10.1016/j.oceaneng.2006.02.005

Huang, C. C., Tang, H. J., and Liu, J. Y. (2006). Dynamical analysis of net cage structures for marine aquaculture: Numerical simulation and model testing. *Aquacultural Eng.* 35 (3), 258–270. doi: 10.1016/j.aquaeng.2006.03.003

Huang, C. C., Tang, H. J., and Liu, J. Y. (2007). Modeling volume deformation in gravity-type cages with distributed bottom weights or a rigid tube-sinker. *Aquacultural Eng.* 37 (2), 144–157. doi: 10.1016/j.aquaeng.2007.04.003

Huang, C. C., Tang, H. J., and Wang, B. S. (2010). Numerical modeling for an *in situ* single-point-mooring cage system. *IEEE J. Oceanic Eng.* 35 (3), 565–573. doi: 10.1109/JOE.2010.2050351

Kristiansen, T., and Faltinsen, O. M. (2012). Modelling of current loads on aquaculture net cages. *J. Fluids Structures* 34, 218–235. doi: 10.1016/j.jfluidstructs.2012.04.001

Kristiansen, T., and Faltinsen, O. M. (2015). Experimental and numerical study of an aquaculture net cage with floater in waves and current. *J. Fluids Structures* 54, 1–26. doi: 10.1016/j.jfluidstructs.2014.08.015

Løland, G. (1991). Current forces on and flow through fish farms. *Doctoral Thesis*. (Trondheim, Norway: The Norwegian Institute of Technology).

Moe-Føre, H., Lader, P. F., Lien, E., and Hopperstad, O. S. (2016). Structural response of high solidity net cage models in uniform flow. *J. Fluids Structures* 65, 180–195. doi: 10.1016/j.jfluidstructs.2016.05.013

Pecher, A., and Kofoed, J. P. (2017). "Handbook of ocean wave energy," in *Ocean engineering & oceanography* (Springer), 7, 67–68. doi: 10.1007/978-3-319-39889-1

Ryu, S., Kim, M. H., and Lynett, P. J. (2003). Fully nonlinear wave-current interactions and kinematics by a BEM-based numerical tank. *Comput. Mechanics* 32, 336–346. doi: 10.1007/s00466-003-0491-7

Tang, H. J., Chiang, W. S., and Nan, F. H. (2022a). Engineering feasibility assessment of cage aquaculture in offshore wind power generation areas in Taiwan. *Sustainability* 14 (18), 11705. doi: 10.3390/su141811705

Tang, H. J., Yang, R. Y., and Yao, H. C. (2021). Experimental and numerical investigations of a mooring line failure of an aquaculture net cage subjected to currents. *Ocean Eng.* 238, 109707. doi: 10.1016/j.oceaneng.2021.109707

Tang, H. J., Yao, H. C., and Yang, R. Y. (2022b). Experimental and numerical studies on successive failures of two mooring. *Ocean Eng.* 266, 113243. doi: 10.1016/j.oceaneng.2022.113243

Tang, H. J., Yeh, P. H., Huang, C. C., and Yang, R. Y. (2020). Numerical study of the mooring system failure of aquaculture net cages under irregular waves and current. *Ocean Eng.* 216, 108110. doi: 10.1016/j.oceaneng.2020.108110

Thomas, G. P. (1981). Wave-current interaction: An experimental and numerical study. part 1. linear waves. *J. Fluid Mechanics* 110, 457–474. doi: 10.1017/S0022112081000839

Tsukrov, I., Eroshkin, O., Fredriksson, D., Swift, M. R., and Celikkol, B. (2003). Finite element modeling of net panels using a consistent net element. *Ocean Eng.* 30 (2), 251–270. doi: 10.1016/S0029-8018(02)00021-5

Xu, Z., and Qin, H. (2020). Fluid-structure interactions of cage based aquaculture: From structures to organisms. *Ocean Eng.* 217, 107961. doi: 10.1016/j.oceaneng.2020.107961

Yang, R. Y., Tang, H. J., and Huang, C. C. (2020). Numerical modeling of the mooring system failure of an aquaculture net cage system under waves and currents. *IEEE J. Oceanic Eng.* 45 (4), 1396–1410. doi: 10.1109/JOE.2019.2941768

Zhao, Y. P., Li, Y. C., Dong, G. H., Gui, F. K., and Teng, B. (2007). A numerical study on dynamic properties of the gravity cage in combined wave-current flow. *Ocean Eng.* 34 (17–18), 2350–2363. doi: 10.1016/j.oceaneng.2007.05.003

frontiers | Frontiers in Marine Science

TYPE Original Research
PUBLISHED 02 March 2023
DOI 10.3389/fmars.2023.1131522

EDITED BY
Fukun Gui,
Zhejiang Ocean University, China

REVIEWED BY
Yong Tang,
Shanghai Ocean University, China
Zonghang Zhang,
Shantou University, China
Ying Liu,
Dalian Ocean University, China

*CORRESPONDENCE
Binbin Xing
✉ xingbinbin@dlou.edu.cn
Leiming Yin
✉ yinleiming@dlou.edu.cn

†These authors share first authorship

SPECIALTY SECTION
This article was submitted to
Marine Fisheries, Aquaculture and Living
Resources,
a section of the journal
Frontiers in Marine Science

RECEIVED 25 December 2022
ACCEPTED 20 February 2023
PUBLISHED 02 March 2023

CITATION
Song M, Gong D, Cui X, Yu X, Xu P, Xing B
and Yin L (2023) Study on feeding behavior
and biological sound of *Sebastes schlegelii*.
Front. Mar. Sci. 10:1131522.
doi: 10.3389/fmars.2023.1131522

Study on feeding behavior and biological sound of *Sebastes schlegelii*

Mingyuan Song†, Dehua Gong†, Xiaojie Cui, Xiaoming Yu,
Pengxiang Xu, Binbin Xing* and Leiming Yin*

College of Fisheries and Life Science, Dalian Ocean University, Dalian, China

The construction of marine ranches can enrich and conserve the fishery resources and improve the marine ecosystem, which helps realize the sustainable utilization of these resources. *Sebastes schlegelii* is a major breeding and releasing fish species in the marine ranches of North China. Its behavioral characteristics can be understood better by researching its vocalization, which will provide data support for constructing acoustic taming marine ranches with *S. schlegelii* as the target fish species. However, there are few studies focusing on its sounds and behaviors. Therefore, based on the passive acoustic monitoring technology, the audios of underwater noises made by *S. schlegelii* were extracted using an AQH hydrophone. The high-definition internet protocol camera was used to monitor the behavior change of *S. schlegelii*. Then, by collating and replaying the collected audios and videos, the feeding behavior and biological noises of *S. schlegelii* were matched to analyze their relationship. Results are as follows: (1) The noise of chewing settling granular baits (Φ5.0 mm) has a main frequency band and sound pressure level of 2000~4500 Hz and 96.53 ± 0.65 dB, respectively; in this feeding process, the main frequency band and sound pressure level of the swimming noise are 25~400 Hz and 95.63 ± 0.38 dB, respectively; the values are 500~700 Hz and 97.34 ± 4.91 dB, respectively, for the noise of flapping the water with the tail. (2) The sound signals emitted by *S. schlegelii* are mostly presented as single pulses during normal habitation or ingestion of baits on the surface of the water tank. However, *S. schlegelii* will attack and fight against each other when scrambling for baits, during which these signals are presented as continuous pulses. To sum up, the vocalization of *S. schlegelii* is closely related to feeding activities, and the sounds produced under different behaviors have specific biological significance.

KEYWORDS
***Sebastes schlegelii*, biological sound, behavior, marine ranch, passive acoustics**

1 Introduction

The classification and identification of economic fish is of great significance to the development and utilization of marine fishery resources. It is a feasible method to identify fish through the characteristics of fish vocal spectrum (Chen et al., 2021). The vocalization of fish usually associates with specific behaviors, so monitoring this vocalization can help identify different behavioral characteristics (Myrberg et al., 1965; Luh and Mok, 1986; Lobel and Kerr, 1999; Bertucci et al., 2010). Fish can make different sounds by various methods, such as the sound of whirlpool or spoondrift produced by swinging fins or tails, the sound of chewing baits, the sound of moving vertebrae, and the sound from the resonance and squeeze of swim bladders, of which the last one is the loudest. There are two types of fish: physostomi and physoclisti. The former refers to the fish whose swim bladders are connected to the esophagus through a pneumatic duct. It is categorized as the lower-grade Osteichthyes, such as carps. The latter refers to the fish without a pneumatic duct. It is categorized as the higher-grade Osteichthyes, such as perches (Fish and Mowbray, 1971; Sprague, 2000a; Sprague et al., 2000b). Vocation is an important part of fish behavior. Different behaviors correspond to different sounds. Fish's courtship, breeding, feeding, swimming and other behaviors will produce different sounds (Holt and Johnston, 2014; Picciulin et al., 2020; Mackiewicz et al., 2021). In addition, some vocal fish make sounds when a predator is approaching or when it is caught (Ladich, 2022).The characteristics of sound intensity and frequency produced by different behaviors of fish are different (Qu et al., 2021). Thus, much work is needed to adequately characterize vocal species, acoustic features, and behavioral contexts, and to build sound repertoires, which will contribute to researching the soundscape of fish shoals and provide important vocal library data for identifying the distribution of fish populations (Tricas and Boyle, 2014).

The passive acoustic monitoring (PAM) technology is also known as passive sonar. Without a special sound emission system, this technology detects the underwater targets and determines their states and natures by receiving the radiated noise made by themselves, thus locating, tracking, and identifying them. It is a non-intrusive and non-invasive observation method (noiseless input) (Cato et al., 2005) used to evaluate the biodiversity, monitor the habitat environment, and locate the spawning fish (Lindseth and Lobel, 2018). In 2008, Anderson et al. first investigated the vocalization of fish in freshwater areas using this method and found that *Oyster Toadfish*, *Ophidion marginatum*, *Ameiurus nebulosus*, and *Ietalurus Punetaus* could produce sounds (Anderson et al., 2008). In 2008, Aalbers and Drawbridge first combined the underwater video surveillance with this method, with a finding that the size and gender of *Atractoscion nobilis* could be distinguished by its vocalization (Aalbers and Drawbridge, 2008).

Many scholars carried out time-domain and frequency analyses on the acoustic spectra of fish and proposed that the acoustic frequency was significantly different in diverse types of fish. The frequency of *Anguilli Formes* is 350 Hz, and that of *Stromateus* can reach 2000 Hz (Shen et al., 2014). The main frequency range of *Bahaba taipingensis* vocalization is 0~1000 Hz The main frequency segment of *Sebasticus marmoratus*' vocalization ranges from 68 to 175 Hz. (Zhang et al., 2013).

In marine environments, the energy in the forms of light, heat, or electromagnetic wave will attenuate quickly, but sound signals can be transmitted over long distances, which differs from the situation in air environments on land. For this reason, the PAM technology has become the best method to research fish vocalization by recording and analyzing underwater sound signals. In addition, PAM technology can not only monitor fish, but also be used to locate the spawning grounds of some fish based on the identified sound frequency (Picciulin et al., 2020). However, this technology can only detect the underwater noises in marine environments and the sounds produced by marine species, which merely reflects a part of the sonic characteristics of these species.In some cases, the acoustic spectra of vocal species are unidentified or misidentified (Sprague and Luczkovich, 2001; Mann and Jarvis, 2004; Anderson et al., 2008). Under such circumstances, the soundscape in fish habitats can be monitored by combining passive acoustics and optics to match the collected acoustic spectra with corresponding species and behaviors, thus exploring the relationship between the soundscape and these behaviors. This lays a foundation for researching the fish vocalization and the impact of man-made noise on this soundscape (Tricas and Boyle, 2014).

Korean rockfish (*Sebastes schlegelii*), belonging to the Sebastes of Scorpaenidae in the Scorpaeniformes (Xu et al., 2018), mainly lives in the northwest Pacific Ocean. It is an important commercial fish species in China, primarily distributed in the Bohai Sea, Yellow Sea, and East China Sea (Feng et al., 2021). In 1974, Hallacher studied the swim bladder muscle of nearly 30 types of fish in the Scorpaeniformes and speculated that the fish of Sebastes with this muscle could produce sounds (Hallacher, 1974). However, the fish of Scorpaenidae are rarely reported in respect of vocalization (Nichols, 2005; Širović and Demer, 2009).

S. schlegelii is a major breeding and releasing fish species in typical marine ranches of North China. There is also vocal behavior in the wild population of *S.schlegelii*, but there are few studies on using acoustic technology to monitor the wild population of it. This work seeks to analyze the relationship between biological noises and behaviors of *S. schlegelii*. PAM was used to obtain the acoustic spectrum characteristics of the indoor *S.schlegelii*, aiming to provide data support for identifying the *S.schlegelii* population and studying its cluster behavior in the marine ranch demonstration area. At the same time, it provides scientific basis for controlling fish population activities, establishing a modern marine fishery production model of ecological health, environmental friendliness and resource protection, and optimizing and improving the construction of marine ranch with *S.schlegelii* as the target in the future.

2 Materials and methods

2.1 Experimental materials

The test fish, *S. schlegelii*, were purchased from a fish farm in Dalian City, Liaoning Province, China. They were provisionally cultured in a cylinder-shaped canvas water tank (Φ200cm×150cm) for 7 d and fed with settling granular baits (Φ5.0 mm) at 8:00 every day. The water was changed daily by half, before which the residual baits and feces at the bottom of the tank were cleaned using a bottom suction pump. Seven days later, 90 healthy fish with the body length of 22.44 ± 0.90 cm and the weight of 185.13 ± 15.45 g were selected for our experiment and averagely divided into 3 groups. Then, these fish were raised in open cylinder-shaped fiberglass reinforced plastic (FRP) water tanks (Φ100cm×90cm). In each tank, there were 3 air stones (diameter: 43 mm; height: 43 mm; pore size: 8 mm) connected to the aerator (ACO-007; power: 185 W; voltage: 220 V) through plastic hoses. In addition, a water pump (power: 80 W) was connected to each tank through PVC tubes, thus forming a circulating water system. The water temperature was 20.41 ± 0.87 °C; the salinity was 25.85 ± 0.77%.

2.2 Behavioral surveillance

The high-definition internet protocol camera (Hikvision, China) was used to monitor the behaviors of test fish. The behavioral surveillance videos and underwater noise audios were collected synchronously. Thereinto, videos were collated and saved using the HIK VISION software. By replaying and analyzing these videos and audios, the fish behaviors were matched with biological noises. The monitoring method is that each camera monitors one experimental water tank, and the height and monitoring Angle of each group of cameras are consistent to ensure that the whole water tank picture can be recorded completely. The population dynamics and behavioral characteristics of test fishes were obtained by video playback.

2.3 Sound collection and analytical methods

According to the methods proposed by Yin et al. (2017), hydrophones were set at 2 measuring points in each water tank where the water was 70 cm deep in each group of experiments and were connected to a lead weight to make them vertically fixed to two positions at the center of the tank, as shown in Figure 1 (Yin et al., 2017). The two points refer to surface measuring point and bottom measuring point, of which the former is 20 cm away from the surface, located in a water layer for the feeding activities of *S. schlegelii*, and the latter is 60 cm away from the surface, located in a water layer for the normal habitation of this fish species.

In this experiment, the behaviors and noises were monitored for a total of 15 days, during which audios were recorded at 8:00~8:30 and 16:00~16:30 every day. we collected the circulating water system as well as the feeding and swimming noises of *S. schlegelii* under the shutdown of this aerator and system. Within the frequency band of 20 Hz~20 kHz, these noises were measured 5 times at each point at an interval of over 10 min, with each time lasting for 120 s. The AQH20k-1062 hydrophone (sensitivity: -193 dB re 1V μPa^{-1}, Aquasound, Japan) was connected to a system-provided professional recorder to collect noise audios, which were saved offline in the file format of Wav. according to the bit rate of 16 $bits{\cdot}s^{-1}$ and the sampling frequency of 96 kHz.

Based on the methods suggested by Craven et al. (2009), these audios were replayed and discriminated by iZotope RX 5 Audio Editor to remove the man-made noise (Craven et al., 2009). Then, in combination with the behavioral surveillance videos previously recorded by a high-definition internet protocol camera, the audios were analyzed and processed using the AQ Level Meter1607 to draw frequency spectra. Finally, we carried out the 1/3 octave analysis to study the test fish's swimming noise, feeding noise, and vocalization.

2.4 X-ray image acquisition

After measuring the body length and weight of *S. schlegelii*, the X-ray image was collected. Before shooting, calibrate, preheat and

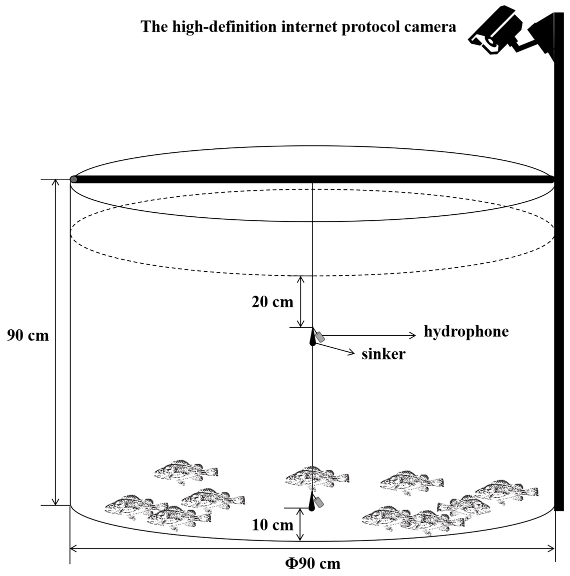

FIGURE 1
Schematic diagram for measuring points of hydrophones in the FRP water tank.

adjust the parameters of the equipment according to the operation manual. According to the method of Guan et al., (2011), use MS-222 to anesthetize Sebastian Hsu. After *S. schlegelii* enters the deep anesthesia period, place it on the self-made bracket to obtain the high-definition X-ray image of *S. schlegelii*.

3 Results

3.1 Measurement and analysis of the biological noises of *S. schlegelii*

The biological noises produced by *S. schlegelii* were collected after the aerator and circulating water system were shut down. The noises of chewing settling granular baits and swimming as well as the vocalization data were extracted for spectral characteristic and 1/3 octave analyses, with the frequency bandwidth set at 20~5000 Hz. After the equipment shutdown, the feeding noise made by *S. schlegelii* has an SPL of about 103.06 dB, which is 13 dB higher than that of the background noise (90.85 dB) in the water tank.

In the whole feeding process (Figures 2, 3), the noise in the water tank shows a primary peak of 80 Hz and 3150 Hz at low and high frequency bands, respectively. The sound detected at the low frequency band of 25~400 Hz is caused by swimming. The sound detected within 1000~2000 Hz is produced by *S. schlegelii* when it flaps the water with its tail during feeding or stirs the water during ingesting. This fish species can make a "click" sound when chewing baits, which is detected at the frequency band of 2000~4500 Hz.

After feeding, *S. schlegelii* swims back to the bottom of the water tank. When it swims without vocalization, the noise has an SPL of about 95.29 dB at the low frequency band of 25~400 Hz. It makes a "coo" sound when swimming at the bottom of the tank, and this sound is monitored at the main frequency band of 80~315 Hz, showing an SPL of about 95.23 dB. It can be seen that this SPL is close to that of the swimming noise (95.29 dB) but is approximately 5 dB higher than that of the background noise (90.85 dB). The main biological noises made by *S. schlegelii* in the water tank are classified in Table 1.

When the aerator and circulating water system are turned on, the background noise in the water tank without any test fish shows an SPL of 92.04 dB at the frequency band of 80~100 Hz, an SPL of 95.86 dB at the frequency band of 1000~2500 Hz, and an SPL of 92.09 dB at the frequency band of 2500~4500 Hz. The overall SPL is 7.41 dB higher than that of the feeding noise made by *S. schlegelii*.

3.2 Acoustic features of *S. schlegelii*

According to the X-ray image and anatomy map of *S. schlegelii*, its swim bladders are located behind the skull and right below the vertebrae, as shown in Figure 4. The "coo" sound made by it during the experiment presents a sound wave composed of several single pulses and a set of continuous pulses, which, with similar waveforms, have the same frequency band of about 140 Hz (Figure 5A). As shown in Figure 5B, the mean width and average pulse interval of single pulses are 15.83 ± 2.11 ms and 175.63 ± 67.01 ms, respectively; those of continuous pulses are 15.92 ± 2.06 ms and 161.57 ± 22.69 ms, respectively.

3.3 Behavioral surveillance of *S. schlegelii*

The behavior change of *S. schlegelii* was synchronously recorded using a high-definition internet protocol camera during the collection of underwater noises, as shown in Figure 6. We obtained 30 audio clips, in all clips, the swimming noise could be detected. It was found that the feeding and swimming noises produced by *S. schlegelii* could be detected in 15 clips recorded within 8:00~8:30.

By analyzing the audio data of 120 s collected during the bait casting on the first day and replaying the video data about fish behaviors using a high-definition internet protocol camera at the speed of ×0.5, we obtained 17 clips of chewing baits, and 11 clips of flapping the water with the tail during feeding. The vocalization of *S. schlegelii* was detected in 31 clips, of which 28 ones presented single pulses and 2 ones presented continuous pulses. The test fish swam back to the bottom of the water tank and moved freely after eating the baits on the water surface, making a single-pulse "coo" sound.

At the time intervals of 88 s~90 s and 105 s~108 s, the test fish scrambled for the baits sunk into the bottom, and larger fish chased and attacked smaller ones (Figure 7). Meanwhile, a "coo" sound

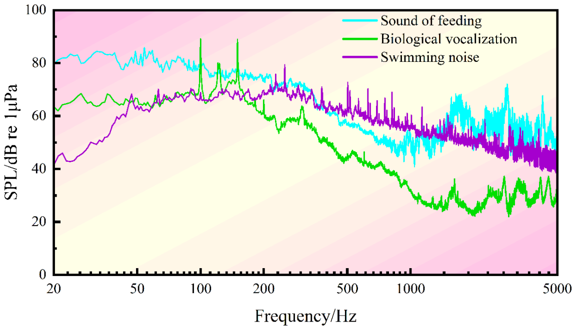

FIGURE 2
Spectral characteristics of noise during the feeding of *S. schlegelii*.

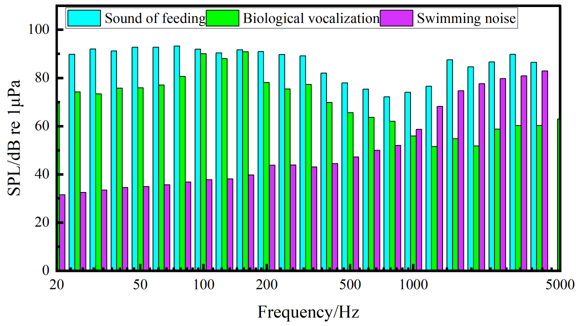

FIGURE 3
1/3 octave analysis of sound during the feeding of *S. schlegelii*.

with continuous pulses was detected. In combination with the video data, we found that this sound was made by the test fish when they attacked others. In this 15-day experiment, the sound with continuous pulses could be detected in 14 days, except the 9th day, and it emerged when the test fish scrambled for baits at the bottom of the water tank.

The sounds of chewing baits or flapping the water with the tail were not monitored in all 15 audio clips recorded at 16:00~16:30. We analyzed the audio data of 120 s collected at this time interval on the first day and obtained 15 clips containing the swimming noise and 6 clips containing the single-pulse "coo" sound. In the whole experiment, this sound could be detected at the bottom of the water tank in 13 days, except the 4th, 7th, and 12th days. Thereinto, the sound with continuous pulses was also monitored on the 3rd and 8th days. In combination with the video data, it was found that *S. schlegelii* may chase and fight against each other in the water tank during daily activities, during which it also made a sound with continuous pulses.

In this experiment, we collected a total of 30 audio clips, of which half recorded the noises during the feeding of *S. schlegelii*, and the other half recorded the noises during its daily activities. Thereinto, those collected during feeding include: the noises of chewing baits and swimming, the vocalization (with single and continuous pulses), and the noise of flapping the water with the tail; those collected during daily activities include: the swimming noise, and the single-pulse sound.

Within 120 s at the time interval of 8:00~8:30, the noises of chewing baits and swimming occurred 14.06 ± 3.17 and 16.40 ± 2.44 times, respectively; the sounds with single and continuous pulses were detected 20.67 ± 5.04 and 2.53 ± 1.31 times, respectively; the noise of flapping the water with the tail occurred 11.47 ± 2.65 times. Within 120 s at the time interval of 16:00~16:30, the swimming noise was monitored 11.60 ± 2.47 times; the single-pulse sound was detected 4.20 ± 2.66 times, as shown in Figure 8. These observations showed that *S. schlegelii* was more active between 8:00 and 8:30, during which the swimming noise and its vocalization occurred more frequently than those at the time interval of 16:00~16:30. The noise of flapping the water with the tail was not monitored within 16:00~16:30, because the test fish all moved freely at the bottom of the water tank when no baits were cast.

4 Discussion

Under the equipment shutdown, the low-frequency noise (<1 kHz) is mainly caused by ground vibration and water flow (Bart et al., 2001), which may mute the feeding and swimming noises at low frequencies (Takemura, 1988; Fujieda et al., 1993). *S. schlegelii* eats fast when baits are cast into the water tank, with the following manifestations: it swims faster to ingest baits, producing the sounds caused by the splashing of water and the swinging of tail. This feeding mode indicates that the test fish are vivacious (Phillips, 1989). The feeding noise is primarily influenced by the properties of baits: the peak frequency of noise made by chewing varies with the hardness of baits.Furthermore, the duration of feeding is determined by the amount and particle distribution of baits, which refer to the settling granular baits in this experiment. During bait casting, the test fish swim faster to the surface of the water tank for feeding. The "click" sound produced by *S. schlegelii* during chewing and swallowing is detected at the main frequency band of 2~4.5 kHz. By contrast, the main frequency band of the feeding noise made by *Oncorhynchus mykiss* and *Scophthalmus maximus* is measured to be 4~6 kHz when they swim faster to the

TABLE 1 Biological noise classification and main acoustic frequency bands of *S. schlegelii* in the water tank.

Biological noise classification	Main frequency band/Hz	Sound pressure level/dB
Feeding noise	2000~4500	96.53 ± 0.65
Swimming noise	25~400	95.63 ± 0.38
Slapping water noise	500~700	97.34 ± 4.91
Biological noise	80~315	95.32 ± 0.12

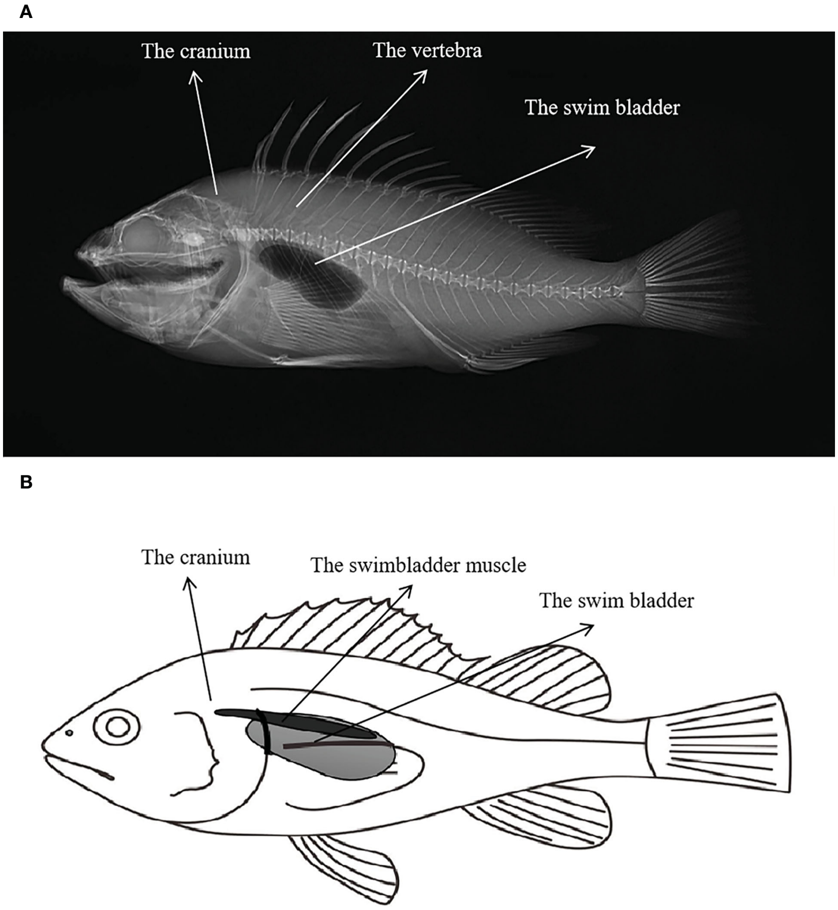

FIGURE 4
(A) X-ray image of *S.schlegelii*; **(B)** Schematic diagram of the location of the swim bladder and swimbladder muscle of *S.schlegelii*.

surface of the water tank to eat granular baits (Lagardere et al., 2004), which is similar to that of the feeding noise made by *S. schlegelii* within 6 kHz.

However, *Scophthalmus maximus* has a special feeding frequency of 7~9 kHz, which is attributed to its exclusive suction feeding mode (Lagardere et al., 2004). This mode is also observed in *Cyprinus carpio*, with the maximum acoustic energy of 7~9 kHz (Takemura, 1988). However, *S. schlegelii* does not eat in this mode. The bony fish have the most diverse vocalization mechanisms in all vertebrates (Ladich and Fine, 2006). In 1974, Hallacher studied nearly 30 types of fish in the Scorpaeniformes and speculated that the fish of Sebastes with a swim bladder muscle could produce sounds (Hallacher, 1974). This hypothesis is supported by the observations of Zhang et al. (2013) made during the study on morphological structures of the acoustic system and acoustic features of *Sebasticus marmoratus* (Zhang et al., 2013). The “glouglou” sound with continuous pulses produced by this fish species is monitored at the main frequency band of 68~175 Hz.

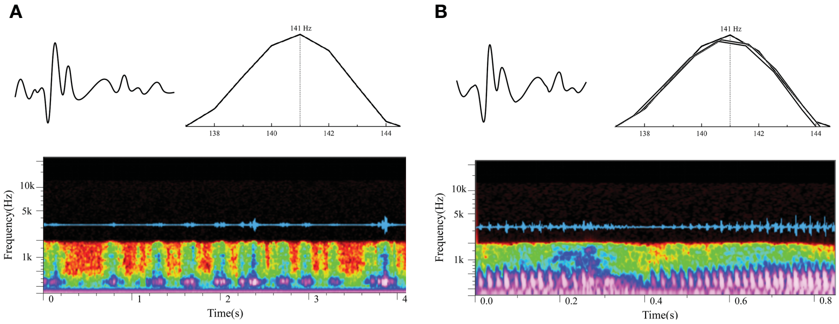

FIGURE 5
Vocalization of *S. schlegelii* [**(A)** oscillogram and spectrogram of single pulses; **(B)** oscillogram and spectrogram of continuous pulses].

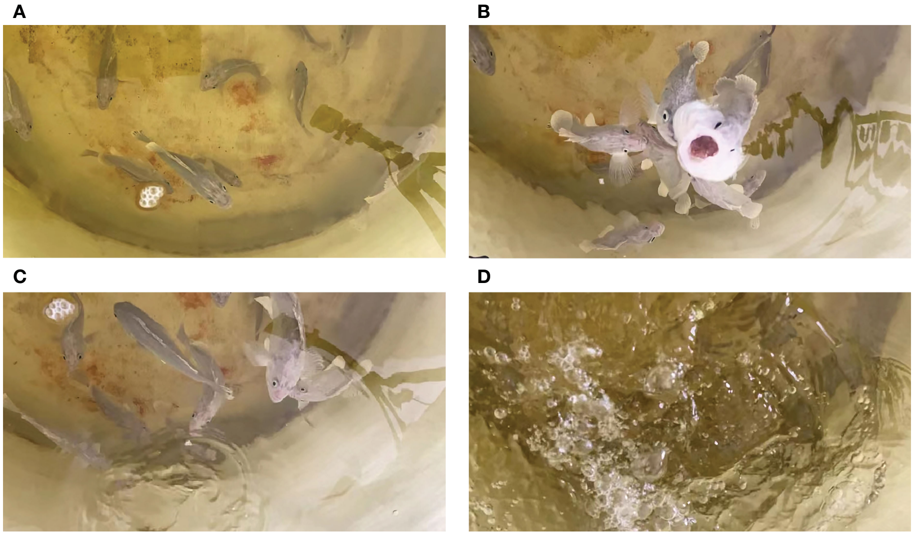

FIGURE 6
Behavioral surveillance of *S. schlegelii* in the FRP water tank. [**(A)** Before bait casting, the test fish moved freely at the bottom of the water tank; **(B)** During bait casting, the test fish swam to the surface of the water tank to eat baits; **(C)** After feeding, a single test fish slapped the water with its tail; **(D)** After feeding, several test fish slapped the water with their tails].

Based on the morphological and behavioral analyses, it is deduced that *Sebasticus marmoratus* makes a sound by contracting its swim bladder muscle.

In this study, *S. schlegelii* can produce a "coo" sound with continuous pulses, and the primary peak of this sound at the low frequency band is basically consistent with that of *Sebasticus marmoratus*. The reason may be that both *S. schlegelii* and *Sebasticus marmoratus* belong to the Scorpaenidae, with similar swim bladders and vocal muscles. The sounds produced by them are caused by the vibration of swim bladders and retractor muscles. However, the fish in different families and genera have distinct acoustic frequencies, and there are also certain differences in their vocalization mechanisms. For example, the pharyngeal jaw apparatus also involves in sound production in the Cichlidae and Pomacentridae (Rice and Lobel, 2003). The Doradidae, Pimelodidae, Mochokidae, and Ariidae have two kinds of sound-

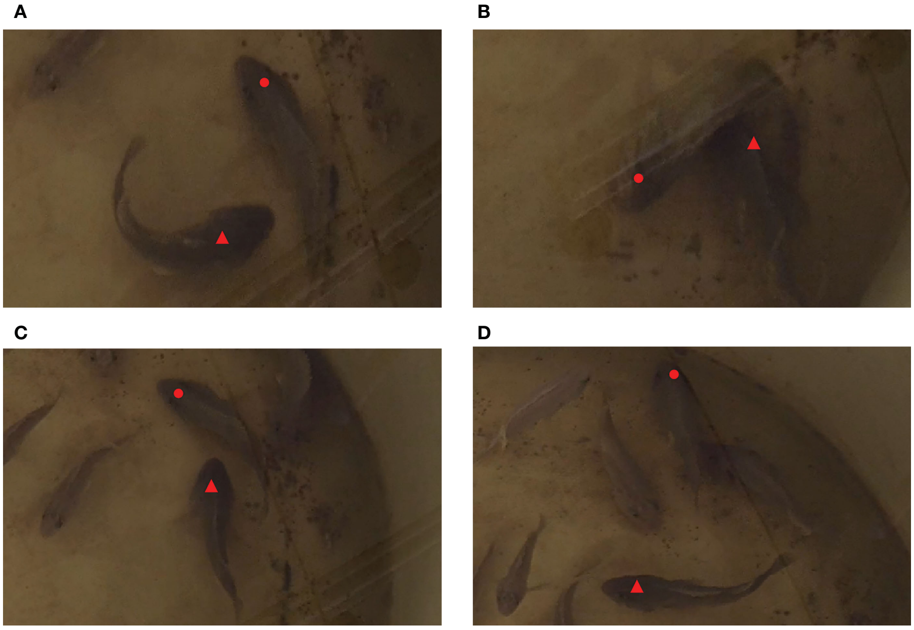

FIGURE 7
Behavior change of *S. schlegelii* at the bottom of the water tank (▲ for larger fish; • for smaller fish. **(A)** Larger fish chased smaller fish; **(B)** Larger fish ingested the baits at the bottom of the tank; **(C)** Larger fish continued to chase smaller fish; **(D)** Smaller fish escaped faster, and larger fish stopped chasing and attacking.).

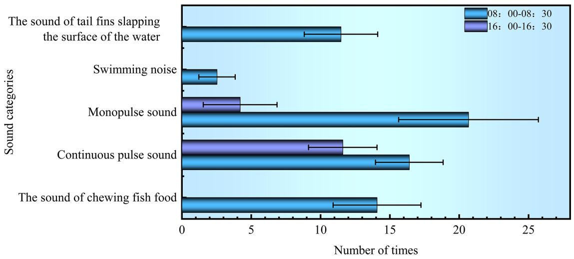

FIGURE 8
Composition of biological noises of *S. schlegelii* in the water tank.

production mechanisms (Ladich and Fine, 2006). They can make a stridulation through pectoral spines and produce a low-frequency sound by vibrating swim bladders (Fine and Ladich, 2003).

The Sciaenidae can also make a sound, with the main frequency band of 300~800 Hz (Chen et al., 2021). The main frequency bands of sounds produced by *Nibea albiflora* and cultured *Larimichthys crocea* are 300~800 Hz and 550~800 Hz, respectively (Ren et al., 2016). In addition to the difference in vocalization mechanisms, the vocalization modes also vary with different fish species or with different behaviors of the same species (Akamatsu et al., 2002; Zhang et al., 2013; Lindseth and Lobel, 2018; Chen et al., 2021). For instance, the longsnout seahorse can produce two types of "click" sounds (50~800 Hz) during feeding and courting. Zhang et al. (2013) believed that the sounds with single and continuous pulses made by *Sebasticus marmoratus* in a territorial invasion test could reflect its different states in the face of invasion (Zhang et al., 2013).

Our study shows that *S. schlegelii* can produce sounds both with single and continuous pulses, which are speculated to be made under different behaviors. By matching the video and audio data, we obtained that the two kinds of sounds were produced during the normal feeding and the scrambling for baits, which verified the above conjecture. The sound signals emitted by *S. schlegelii* are mostly presented as single pulses during normal habitation and ingestion but presented as continuous pulses during attacking. Fish can produce sounds when they are interfered or threatened. In the same species, fish usually vocalize during attacking and fighting, but rarely make a sound during defending and escaping (Ladich, 1997). This phenomenon is also verified in this study.

The PAM technology can be used to monitor the underwater soundscape and collect the vocalization of underwater organisms in indoor and outdoor environments, including fish, marine mammals, crustaceans, etc (Kikuchi et al., 2015; Putland et al., 2018; Emmons et al., 2021; Muñoz-Duque et al., 2021). Aalbers and Drawbridge (2008) proposed that this technology could be combined with behavioral surveillance to make up for its deficiency of non-visualization (Aalbers and Drawbridge, 2008). The combination was performed in this study to research the feeding behavior and biological noises of *S. schlegelii* by matching sounds with behaviors, which solved the problem of non-visualization during acoustic monitoring. However, these sounds and behaviors were only monitored during feeding. Therefore, the behavioral surveillance shall be combined with PAM technology in future studies to explore the acoustic features of *S. schlegelii* in the face of territorial invasion. Meanwhile, the vocalization mechanisms of this fish species shall be further explored using morphological and behavioral methods, thus providing better data support for the research on the sounds and behaviors of *S. schlegelii*.

In summary, taking *S. schlegelii* as an example, analyzing the relationship between its biological noise information and its behavior can provide scientific basis for controlling the action of fish stocks in the future, creating a modern marine fishery production mode of ecological health, environmental friendliness and resource conservation, and optimizing and improving the construction of marine pasture with *S. schlegelii* as the target fish species.

Data availability statement

The original contributions presented in the study are included in the article/supplementary material. Further inquiries can be directed to the corresponding authors.

Ethics statement

The animal study was reviewed and approved by Dalian Ocean University. Written informed consent was obtained from the owners for the participation of their animals in this study.

Author contributions

MS and DG conceived and designed the experiment. BX and LY conducted the experiment. XC, XY and PX are involved in data analysis. MS and DG wrote the manuscript. MS and DG contributed equally to this work and share first authorship. All authors contributed to the article and approved the submitted version.

Funding

This research was supported by National Natural Science Foundation of China (No. 31672673) and the Science and Technology Innovation Fund of Dalian, China (No. 2021JJ11CG001).

Acknowledgments

We would like to thank the Fish Behavior Laboratory of Dalian Ocean University and the Center for Marine Ranching Engineering Science Research for providing experimental sites and technical support for this study. Thank all the authors for their valuable time. Without the hard work of all the authors, we could not complete this study.

Conflict of interest

The authors declare that the research was conducted in the absence of any commercial or financial relationships that could be construed as a potential conflict of interest.

The reviewer YL declared a shared parent affiliation with the authors to the handling editor at the time of review.

Publisher's note

References

Aalbers, S. A., and Drawbridge, M. A. (2008). White seabass spawning behavior and sound production. *Trans. Am. Fish. Soc.* 137 (2), 542–550. doi: 10.1577/T04-058.1

Akamatsu, T., Okumura, T., Novarini, N., and Yan, H. Y. (2002). Empirical refinements applicable to the recording of fish sounds in small tanks. *J. Acoustical Soc. America* 112 (6), 3073–3082. doi: 10.1121/1.1515799

Anderson, K. A., Rountree, R. A., and Juanes, F. (2008). Soniferous fishes in the Hudson river. *Trans. Am. Fish. Soc.* 137 (2), 616–626. doi: 10.1577/T05-220.1

Bart, A. N., Clark, J., Young, J., and Zohar, Y. (2001). Underwater ambient noise measurements in aquaculture systems: A survey. *Aquacult. Eng.* 25 (2), 99–110. doi: 10.1016/S0144-8609(01)00074-7

Bertucci, F., Beauchaud, M., Attia, J., and Mathevon, N. (2010). Sounds modulate males' aggressiveness in a cichlid fish. *Ethology* 116 (12), 1179–1188. doi: 10.1111/j.1439-0310.2010.01841.x

Cato, D. H., Noad, M. J., and McCauley, R. D. (2005). *Passive acoustics as a key to the study of marine animals* (New York: Cambridge University Press).

Chen, D. H., Lin, J. H., Yi, X. J., and Jiang, P. F. (2021). Research on band energy extraction and classification of three kinds of fishes sound signals. *Tech. Acoustics.* 40 (2), 254–259. doi: 10.16300/j.cnki.1000-3630.2021.02.017

Craven, A., Carton, A. G., McPherson, C. R., and McPherson, G. (2009). Determining and quantifying components of an aquaculture soundscape. *Aquacult. Eng.* 41 (3), 158–165. doi: 10.1016/j.aquaeng.2009.07.003

Emmons, C. K., Hanson, M. B., and Lammers, M. O. (2021). Passive acoustic monitoring reveals spatiotemporal segregation of two fish-eating killer whale orcinus orca populations in proposed critical habitat. *Endangered Species Res.* 44, 253–261. doi: 10.3354/esr01099

Feng, A. X., Wang, F., Sun, C. F., Zhang, Y. G., and Liu, Y. X. (2021). Artificial breeding techniques and breeding and releasing methods of sebastes schlegelii. *Sci. Fish. Farming* 04, 64–65. doi: 10.14184/j.cnki.issn1004-843x.2021.04.039

Fine, M. L., and Ladich, F. (2003). Sound production, spine locking and related adaptations. *Catfishes* 1, 249–290. doi: 10.1007/978-94-007-1060-3_10

Fish, M. P., and Mowbray, W. H. (1971). Sounds of western north Atlantic fishes. *Copeia* 1, 190–190. doi: 10.2307/1441636

Fujieda, S., Matsuno, Y., Yamanaka, Y., Chung, Y. J., and Kishimoto, C. (1993). *Feature of the swimming sound for fishes in the netting cages at the culture ground* (Memoirs of Faculty of Fisheries Kagoshima University).

Guan, S. G., Guan, J., Liu, H. J., Zheng, Y. Y., Liu, M. X., Gao, X., et al. (2011). Anesthetic effect of MS-222 on juveniles of sebastes schlegeli. *Mar. Sci.* 35 (05), 100–105.

Hallacher, L. E. (1974). The comparative morphology of extrinsic gasbladder musculature in the scorpionfish genus sebastes (Pisces: Scorpaenidae). *Proc. California Acad. Sci. 4th Ser.* 40, 59–86.

Holt, D., and Johnston, C. (2014). Sound production and associated behaviours in blacktail shiner cyprinella venusta: A comparison between field and lab. *Environ. Biol. Fishes* 97, 1207–1219. doi: 10.1007/s10641-013-0208-5

Kikuchi, M., Akamatsu, T., and Takase, T. (2015). Passive acoustic monitoring of Japanese spiny lobster stridulating sounds. *Fish. Sci.* 81 (2), 229–234. doi: 10.1007/s12562-014-0835-6

Ladich, F. (1997). Agonistic behaviour and significance of sounds in vocalizing fish. *Mar. Freshw. Behav. Phy.* 29 (1-4), 87–108. doi: 10.1080/10236249709379002

Ladich, F. (2022). Shut up or shout loudly: Predation threat and sound production in fishes. *Fish. Fish.* 23 (1), 227–238. doi: 10.1111/faf.12612

Ladich, F., and Fine, M. L. (2006). Sound-generating mechanisms in fishes: a unique diversity in vertebrates. *Commun. Fishes* 1, 3–43.

Lagardere, J. P., Mallekh, R., and Mariani, A. (2004). Acoustic characteristics of two feeding modes used by brown trout (Salmo trutta), rainbow trout (Oncorhynchus mykiss) and turbot (Scophthalmus maximus). *Aquaculture* 240 (1-4), 607–616. doi: 10.1016/j.aquaculture.2004.01.033

Lindseth, A. V., and Lobel, P. S. (2018). Underwater soundscape monitoring and fish bioacoustics: A review. *Fishes* 3 (3), 36. doi: 10.3390/fishes3030036

Lobel, P. S., and Kerr, L. M. (1999). Courtship sounds of the pacific damselfish, abudefduf sordidus (Pomacentridae). *Biol. Bull.* 197 (2), 242–244. doi: 10.2307/1542627

Luh, H. K., and Mok, H. K. (1986). Sound production in the domino damselfish, dascyllus trimaculatus (Pomacentridae) under laboratory conditions. *Japanese J. Ichthyol.* 33 (1), 70–74. doi: 10.11369/jji1950.33.70

Mackiewicz, A., Putland, R., and Mensinger, A. (2021). Effects of vessel sound on oyster toadfish opsanus tau calling behavior. *Mar. Ecol. Prog. Ser.* 662, 115–124. doi: 10.3354/meps13634

Mann, D. A., and Jarvis, S. M. (2004). Potential sound production by a deep-sea fish. *J. Acoustical Soc. America* 115 (5), 2331–2333. doi: 10.1121/1.1694992

Muñoz-Duque, S., López-Casas, S., Rivera-Gutiérrez, H., and Jiménez-Segura, L. (2021). Bioacoustic characterization of mating calls of a freshwater fish (Prochilodus magdalenae) for passive acoustic monitoring. *Biota Colombiana* 22 (1), 108–121. doi: 10.21068/c2021.v22n01a07

Myrberg, A. A.Jr., Kramer, E., and Heinecke, P. (1965). Sound production by cichlid fishes. *Science* 149 (3683), 555–558. doi: 10.1126/science.149.3683.555

Nichols, B. (2005). *Characterizing sound production in nearshore rockfishes (Sebastes spp.)* (USF Tampa Graduate Theses and Dissertations).

Phillips, M. J. (1989). The feeding sounds of rainbow trout, salmo gairdneri Richardson. *J. Fish. Biol.* 35 (4), 589–592. doi: 10.1111/j.1095-8649.1989.tb03008.x

Picciulin, M., Fiorin, R., Facca, C., and Malavasi, S. (2020). Sound features and vocal rhythms as a proxy for locating the spawning ground of sciaena umbra in the wild. *Aquat. Conservation: Mar. Freshw. Ecosyst.* 30 (7), 1299–1312. doi: 10.1002/aqc.3340

Putland, R. L., Mackiewicz, A. G., and Mensinger, A. F. (2018). Localizing individual soniferous fish using passive acoustic monitoring. *Ecol. Inf.* 48, 60–68. doi: 10.1016/j.ecoinf.2018.08.004

Qu, R., Liu, H., Liu, J. W., and Zhang, Y. L. (2021). Acoustic signal characteristics of largemouth bass in feeding process and the effects of breeding. *Fishery Modernization.* 48 (6), 55–63. doi: 10.3969/j.issn.1007-9580.2021.06.008

Ren, X. M., Gao, D. Z., Yao, Y. L., Yang, F., Liu, J. F., and Xie, F. J. (2016). Occurrence and characteristic of sound in large yellow croaker (pseudosciaena crocea). *J. Dalian Ocean Univ.* 22 (2), 123–128. doi: 10.16535/j.cnki.dlhyxb.2007.02.009

Rice, A. N., and Lobel, P. S. (2003). The pharyngeal jaw apparatus of the cichlidae and pomacentridae: Function in feeding and sound production. *Rev. Fish. Biol. Fish.* 13 (4), 433–444. doi: 10.1007/s11160-004-8794-0

Shen, W. X., Hu, Q. S., Li, C. X., and Shentu, J. K. (2014). Fish voice spectrum analysis and research. *BioTechnol.: Indian J.* 10 (23).

Širović, A., and Demer, D. A. (2009). Sounds of captive rockfishes. *Copeia* 2009 (3), 502–509. doi: 10.1643/CP-08-121

Sprague, M. W. (2000a). The single sonic muscle twitch model for the sound-production mechanism in the weakfish, cynoscion regalis. *J. Acoustical Soc. America* 108 (5), 2430–2437. doi: 10.1121/1.1315296

Sprague, M. W., and Luczkovich, J. J. (2001). Do striped cusk-eels ophidion marginatum (Ophidiidae) produce the "chatter" sound attributed to weakfish cynoscion regalis (Sciaenidae)? *Copeia* 2001 (3), 854–859. doi: 10.1643/0045-8511(2001)001[0854:dsceom]2.0.co;2

Sprague, M. W., Luczkovich, J. J., Pullinger, R. C., Johnson, S. E., Jenkins, T., and DANIEL, H. J.III (2000b). Using spectral analysis to identify drumming sounds of some north Carolina fishes in the family sciaenidae. *J. Elisha Mitchell Sci. Soc.* 116(2), 124–145.

Takemura, A. (1988). The attraction effect of natural feeding sound in fish. *Bull. Fac. Fish. Nagasaki Univ.* 63, 1–4.

Tricas, T. C., and Boyle, K. S. (2014). Acoustic behaviors in Hawaiian coral reef fish communities. *Mar. Ecol. Prog. Ser.* 511, 1–16. doi: 10.3354/meps10930

Xu, G. C., Li, J. J., Li, X. S., Wang, X. Y., and Wang, H. B. (2018). The offshore cage culture technology of sebastes schlegelii. *J. Aquacult.* 39 (6), 23–26. doi: 10.3969/j.issn.1004-2091.2018.06.010

Yin, L. M., Chen, X. Z., Zhang, X. G., Li, L. Z., and Huang, H. L. (2017). The morphology of sonic system and sound characteristics of the marbled rockfish sebasticus marmoratus. *Mar. Fish.* 39 (3), 314–321. doi: 10.13233/j.cnki.mar.fish.2017.03.009

Zhang, X. G., Xie, W., Guo, H. Y., Hu, Q. S., Pan, Y. J., and Song, J. K. (2013). The morphology of sonic system and sound characteristics of the marbled rockfish sebasticus. *J. Shanghai Ocean Univ.* 22 (05), 672–677.

frontiers | Frontiers in Marine Science

TYPE Original Research
PUBLISHED 06 March 2023
DOI 10.3389/fmars.2023.1135757

OPEN ACCESS

EDITED BY
Fukun Gui,
Zhejiang Ocean University, China

REVIEWED BY
Lianhui Wu,
Tokyo University of Marine Science and Technology, Japan
Hongzhou Chen,
Zhejiang Ocean University, China

*CORRESPONDENCE
Xiaohua Huang
huangx-hua@163.com

SPECIALTY SECTION
This article was submitted to Marine Fisheries, Aquaculture and Living Resources, a section of the journal Frontiers in Marine Science

RECEIVED 01 January 2023
ACCEPTED 14 February 2023
PUBLISHED 06 March 2023

CITATION
Pang G, Zhang S, Liu H, Zhu S, Yuan T, Li G, Han X and Huang X (2023) Hydrodynamic response analysis for a new semi-submersible vessel-shaped fish farm platform based on numerical simulation. *Front. Mar. Sci.* 10:1135757. doi: 10.3389/fmars.2023.1135757

Hydrodynamic response analysis for a new semi-submersible vessel-shaped fish farm platform based on numerical simulation

Guoliang Pang[1,2], Song Zhang[1], Haiyang Liu[2], Shiyao Zhu[3], Taiping Yuan[1,2], Gen Li[1,2], Xiangxi Han[4] and Xiaohua Huang[1,2]*

[1]Key Laboratory of Open-Sea Fishery Development, South China Sea Fisheries Research Institute, Chinese Academy of Fishery Science, Ministry of Agriculture and Rural Affairs, Guangzhou, China, [2]Key Laboratory of Efficient Utilization and Processing of Marine Fishery Resources of Hainan Province, Sanya Tropical Fisheries Research Institute, Sanya, China, [3]School of Engineering and Information Technology, University of New South Wales, Canberra, NSW, Australia, [4]Key Laboratory of Beibu Gulf Offshore Engineering Equipment and Technology, Education Department of Guangxi Zhuang Autonomous Region, Beibu Gulf University, Qinzhou, China

Due to polluted environments, limited resources, and restricted space in coastal aquaculture, the use of a large-scale aquaculture platform in deep-sea areas has become more important in fish farming. However, the environment in the deep sea is complex and harsh, which threatens the safety of the fish farm platform due to extreme weather. In this work, we developed a new semi-submersible vessel-shaped truss fish farm platform with single-point mooring, considering different operating conditions. The dynamic performance of the platform was analyzed numerically. Firstly, a numerical model of the fish farm platform was created. A physical model test was then executed to verify the numerical model. The results from the numerical model were found to be in good agreement with the experimental results. Subsequently, the dynamic response of the platform under different wave conditions was analyzed based on the validated numerical model. The results showed that the new semi-submersible vessel-shaped fish farm platform had good adaptability to extreme sea conditions. The experimental and numerical analyses of the hydrodynamic responses of the fish farm platform facilitated the design, analysis, and application of the large deep-sea fish farm platform.

KEYWORDS

vessel-shaped fish farm platform, SPM, Hydrodynamic response, mooring tension, numerical simulation

1 Introduction

With population growth, economic progress, and rapid urbanization, the demand for food has increased exponentially. As an indispensable part of the human diet, fish is not only a source of high-quality protein but is also key to ensuring food security in the future. Owing to traditional marine fisheries having been fully developed or overexploited, mariculture is playing an important role in meeting the demand for fish (Chu et al., 2020). Mariculture can be classified into coastal, off-the-coast, and deep-sea types. In recent years, problems such as the degradation of water quality, the frequent occurrence of biological diseases, and environmental pollution have existed in coastal and off-the-coast mariculture areas, which have directly hindered the sustainable development of the mariculture industry. Therefore, research on deep-sea mariculture based on a large-scale fish farm platform has become more and more important worldwide (Xu and Qin, 2020).

Traditional high-density polyethylene (HDPE) net cages have been commonly used, and analysis of the corresponding hydrodynamic responses has been widely performed using numerical and experimental methods (Fredriksson et al., 2003; Fredriksson et al., 2007; Zhao et al., 2007; Kristiansen and Faltinsen, 2012; Kristiansen and Faltinsen, 2015; Huang et al., 2016; Gansel et al., 2018; Huang et al., 2018). However, the environment in the deep sea is extremely complex and harsh. As a result, the large steel fish farm platform is becoming the one of available facilities for developing deep-sea aquaculture and various forms of large steel fish farm platforms have been being developed intensely developed, and the large steel fish farm platform is one of the available facilities for developing deep-sea aquaculture. A lot of experimental and numerical studies on the hydrodynamic characteristics of these fish farm platforms have also been carried out. Rui (2018) established the finite element model (FEM) of “Ocean Farm 1” based on SESAM and analyzed the hydrodynamic properties of the platform under different wave conditions. It was found that the influence of the cage net on the amplitude of the motion of the platform was not large, but the effect on the mean position of the body cannot be neglected. Zhao et al. (2019) carried out a physical model test of a fish farm platform similar to “Ocean Farm 1” and analyzed the motion and mooring characteristics of the platform under different draught conditions. In addition, Liu et al. (2020, 2021) utilized a numerical simulation method to study the hydrodynamic characteristics of a platform in waves and uniform currents. Moreover, in order to understand the flow field characteristics of a fish farm platform under waves and currents, computational fluid dynamics (CFD) was used by a number of researchers instead of the classical potential flow theory (Martin et al., 2020; Wang et al., 2021; Wang et al., 2022). Li et al. (2018a, 2018b, 2019) presented a vessel-shaped offshore fish farm and conducted a systematic study on the coupled dynamic response and optimization of the mooring lines. In addition, to improve the rate of sea utilization, Lei et al. (2020, 2021) presented a novel offshore floating wind turbine integrated with a steel fish farming cage. With regard to the structural security of the fish farm platform, Yu et al. (2019) studied the local and global responses of an offshore fish farm subjected to ship impacts, while Wang et al. (2020) gave a set of test methods for evaluating the fatigue strength of a copper alloy netting structure. Previous studies indicate that the development of deep-sea mariculture was the consensus in the industry. However, there was no agreement on the types of facilities suitable for this activity. Thus, corresponding studies on types of fish farm platforms have been conducted all over the world. Still, one thing is clear: a fish farm platform with excellent hydrodynamic performance is necessary to develop deep-sea mariculture.

The “DEHAI 1” fish farm platform (Figure 1A) is a semi-submersible vessel-shaped truss platform with single-point mooring (SPM) developed in 2018 by the South China Sea Fisheries Research Institute, Chinese Academy of Fishery Sciences (Huang et al., 2020). This platform successfully resisted the attack of super typhoon Mangkhut in 2018 (Figure 1B), making it the first fish farm platform in the world to “pass the test” against a grade 17 super typhoon. Following that, similar fish farm platforms with different cultured water volumes were designed and stationed in Hong Kong and Hainan, China. However, it should be noted that the current DEHAI series fish farm platforms are all arranged in sheltered sea areas close to the shore and that the operating water depths are all less than 20 m.

To develop deep-sea mariculture and cope with the harsh environment in deep-sea areas, a new semi-submersible vessel-

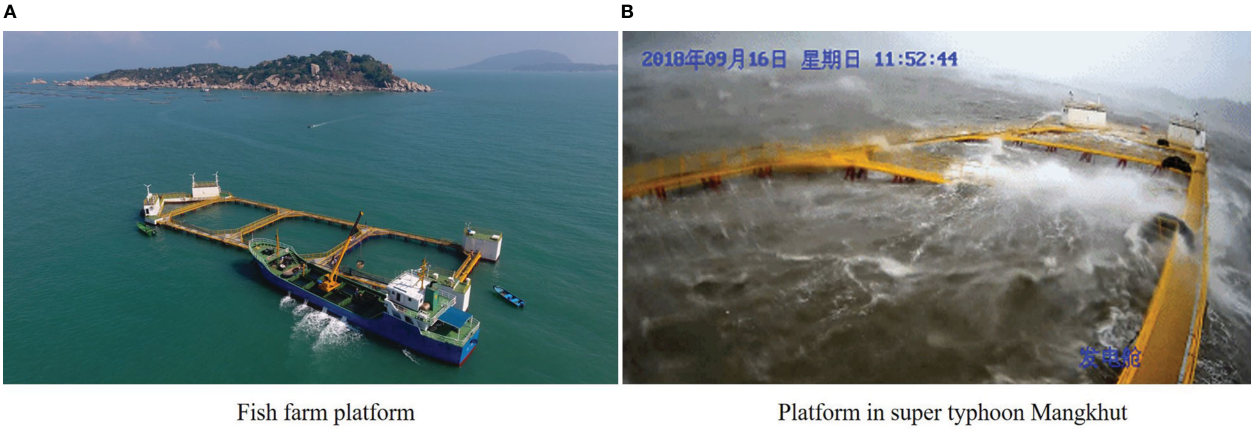

Fish farm platform

Platform in super typhoon Mangkhut

FIGURE 1
DEHAI series DEHAI 1 fish farm platform.

shaped fish farm platform with SPM was presented based on technological accumulation from the DEHAI series fish farm platforms. There are structural differences between the new fish farm platform and the current DEHAI series platforms. These are described in detail in a subsequent section. For this new fish farm platform, the hydrodynamic characteristics need to be analyzed. This paper is organized as follows. The numerical model of the fish farm platform is established in *Section 2*. The physical model test and the verification of the numerical model of the fish farm platform are presented in *Section 3*. An analysis of the hydrodynamic characteristics of the platform based on the verified model is presented in *Section 4*. The applicability of the new fish farm platform to deal with extreme sea conditions, which was evaluated through the aspects of motion response and mooring line tension, is discussed in *Section 5*. Finally, the conclusions of this research are presented in *Section 6*.

2 Numerical model establishment

2.1 Fish farm platform parameters

The diagram of the developed semi-submersible vessel-shaped fish farm platform and the definition of the coordinate system are shown in Figure 2. This platform mainly consisted of a steel tube truss, pontoons in the bow and stern, a baffle, and a mooring system. The net was tied to the adjacent truss steel tubes to form three cultured spaces. The baffle in the bow was used to resist the current. The ballast tanks are located at the bottom of the pontoons. The new fish farm platform and the current DEHAI series platforms mainly differed in terms of pontoon type. The pontoons of the new platform had a small waterplane area, and the platform can have different draughts by adjusting the ballast. Figure 3A shows the two draught conditions of the fish farm platform: normal condition and survival condition. In most cases, the platform was in normal condition for aquaculture production. During extreme weather, the platform will dive the main body through the water. This is referred to as the survival condition in this paper. Due to the pontoons being built with a small waterplane area, the wave and current load acting on the fish farm platform under the survival condition would be reduced, which could help in coping with extreme ocean environments.

A “Y”-type SPM system has been used in the new fish farm platform. Two mooring lines come out of the fairleads of the pontoons in the bow, and these two lines converge at one point into one line. A steel clump weight was arranged at the convergence point, with the end of the mooring line serving as an anchor. Figure 3B shows the diagram of the vertical and lateral views of the fish farm platform. From the figure, the “Y”-type SPM in vertical view can be clearly seen. Due to the weathercock effect from the SPM, the fish farm platform will be moored at the position with the least environmental force. In addition, the platform rotates around the mooring point, which will increase the diffusion space of waste and excreta in the aquaculture area to ensure the quality of the aquaculture water.

The main structure of the fish farm platform is 102.2 m long, 35.1 m wide, and 9 m high. The cultured water volume is nearly 20,000 m^3. The main parameters of the fish farm platform are shown in Table 1.

2.2 Numerical tool and hydrodynamic theory

An analysis of the hydrodynamic responses of the new semi-submersible vessel-shaped fish farm platform was implemented based on the hydrodynamic software AQWA (ANSYS, 2018). According to the structural characteristics of the platform, two types of elements were used in the simulation. The baffle and pontoons in the bow and stern were simulated using a panel method based on potential flow theory. For the steel tube truss system, the Morison equation was used to calculate the wave force of the steel tubes.

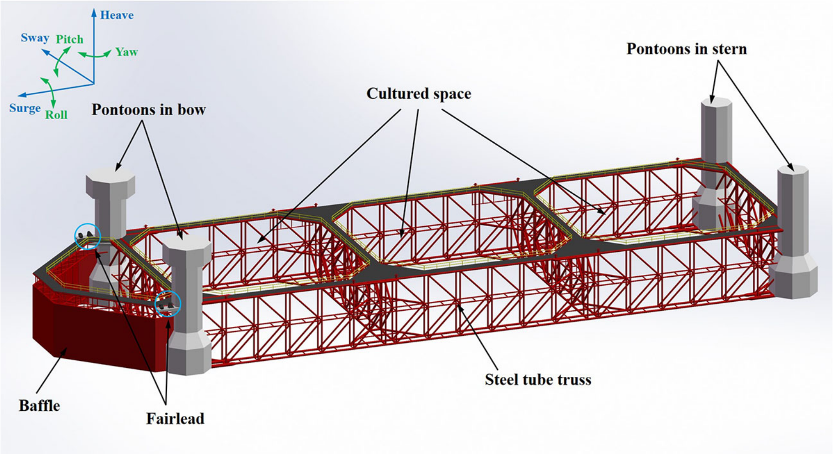

FIGURE 2
Diagram of the new semi-submersible vessel-shape fish farm platform.

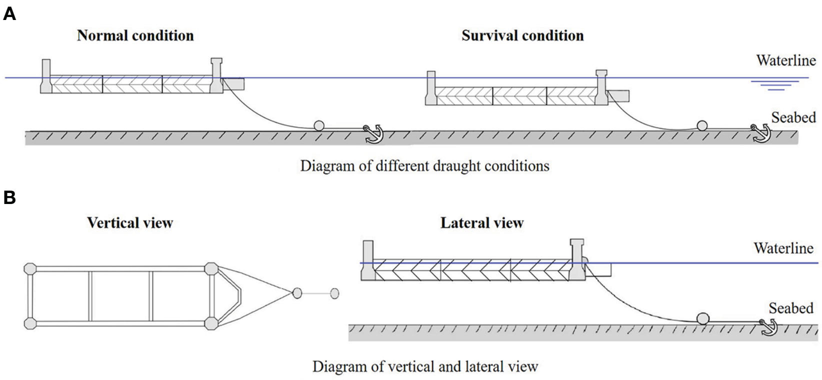

FIGURE 3
Diagram of fish farm platform under different draughts and different views.

TABLE 1 Fish farm platform parameters.

Component	Parameter	Value
Main body of platform	Length (m)	102.2
	Width (m)	35.1
	Height (m)	9
	Draught in normal condition (m)	8.2
	Draught in survival condition (m)	14
	Operating water depth (m)	30
Pontoons	Height of pontoons in the bow (m)	17.5
	Height of pontoons in the stern (m)	17.0
	Shape	Eight prism
Mooring steel chain	Length (m)	90
	Weight per meter (kg/m)	84.12
	Fracture force (N)	2,940,000

The floating body's dynamic equation under different environmental loads can be expressed as:

$$(M + \Delta M)\ddot{X} + (B_{\mathbf{rad}} + B_{\mathbf{vis}})\dot{X} + (K_{\mathbf{sw}} + K_{\mathbf{m}})X$$
$$= F_1 + F_{2\mathbf{low}} + F_{2\mathbf{high}} + F_{\mathbf{w}} + F_{\mathbf{c}} + F_{\mathbf{other}} \tag{1}$$

where M is the mass matrix of the floating body; ΔM is the added mass matrix; B_{rad} and B_{vis} are the radiation and viscous damping matrices, respectively; K_{sw} is the stiffness matrix of still water; and K_{m} is the mooring stiffness matrix. F_1 is the first-order wave frequency load; $F_{2\mathrm{low}}$ is the second-order low-frequency load; $F_{2\mathrm{high}}$ is the second-order high-frequency load; F_{w} is the wind load; F_{c} is the current load; and F_{other} denotes other loads.

The flow field was assumed to be inviscid, irrotational, and incompressible. The fluid motion can be described using the three-dimensional (3D) potential flow theory. There is unsteady velocity potential, Φ, in the flow field, which can be classified into either incident potential, Φ_{I}; diffraction potential, Φ_{D}; or radiation potential, Φ_{R}.

$$\Phi = \Phi_{\mathbf{I}} + \Phi_{\mathbf{D}} + \Phi_{\mathbf{R}} \tag{2}$$

The Φ_{I} variable is known, while Φ_{D} and Φ_{R} can be obtained using corresponding methods. With a known velocity potential, Φ, the pressure distribution of the flow field can be calculated to obtain the overall fluid force acting on the floating body.

The Morison equation is usually employed to calculate the fluid forces acting on the cross-section of a slender structure, and it can be expressed as:

$$dF = \frac{1}{2}\rho D C_{\mathbf{d}}|u_{\mathbf{f}} - u_{\mathbf{s}}|(u_{\mathbf{f}} - u_{\mathbf{s}}) + \rho A C_{\mathbf{m}}\dot{u}_{\mathbf{f}} - \rho A(C_{\mathbf{m}} - 1)\dot{u}_{\mathbf{s}} \tag{3}$$

where C_{d} is the drag coefficient; D is the characteristic drag diameter; u_{f} is the transverse directional fluid particle velocity; u_{s} is the transverse directional structure velocity; C_{m} is the inertia coefficient; $C_{\mathrm{a}}(C_{\mathrm{a}} = C_{\mathrm{m}} - 1)$ is the added mass coefficient; and A is the cross-sectional area.

2.3 Fish farm platform model

The geometric model of the fish farm platform was created using the DM module in ANSYS Workbench. The surface bodies were used to simulate the baffle and the pontoons, while the truss system of the platform was simulated by the line bodies. The geometric model of the fish farm platform is shown in Figure 4A.

The geometric model was then imported into the AQWA module. Considering mesh convergence and computational efficiency, the maximum element size was set to 0.5 m, and the automatic meshing technology in AQWA was used to generate the mesh. The FEM of the fish farm platform (Figure 4B) had 32,219 elements in total. The floating and diving of the fish farm platform are achieved by adjusting the ballast water of the pontoon, with the ballast water being simulated by the mass point in AQWA. The corresponding ballast water parameters under normal operating and extreme survival conditions are shown in Tables 2, 3. After the mooring lines were arranged, the final numerical model of the fish farm platform was updated, as shown in Figure 5.

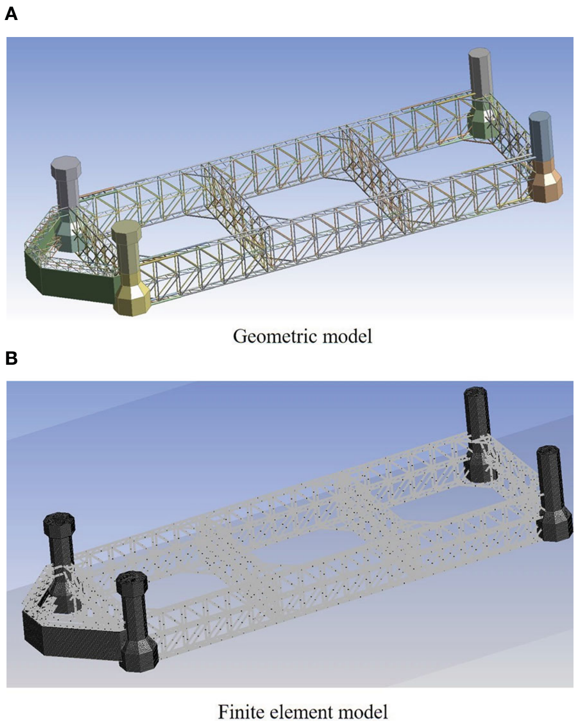

FIGURE 4
Model of fish farm platform.

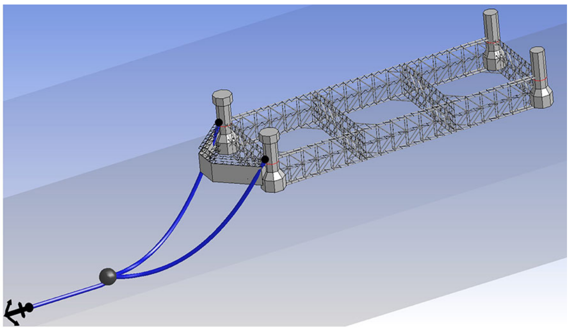

FIGURE 5
Model of fish farm platform with mooring lines.

FIGURE 6
Physical model of fish farm platform.

3 Model verification

3.1 Physical model test

In order to validate the numerical model of the fish farm platform, a physical model test was conducted at the Rudong Test Base of the China Academy of Fishery Sciences. Considering the actual platform size, wave tank conditions, and the model cost, among other factors, the model scale was set to 1:40. The physical model of the fish farm platform is shown in Figure 6.

Figure 7 shows the physical model test site condition. The measuring point was fixed to the platform, and the platform's 6 DOF (degrees of freedom) motion was measured using the 3D motion capture system. A wave height gauge and a flow meter were arranged to monitor the wave height and flow velocity, respectively. Strain-type tension gauges were adopted to measure the mooring line tension. The maximum tension from the tension gauges was recorded,

TABLE 2 Ballast water parameters under normal operating conditions.

Draught 8.2 m	Mass (kg)	I_{xx} (kg·m^2)	I_{yy} (kg·m^2)	I_{zz} (kg·m^2)
Ballast water in the bow (left)	128,690.3471	438,075	438,075	677,935
Ballast water in the bow (right)	128,690.3471	438,075	438,075	677,935
Ballast water in the stern (left)	106,316.7612	423,223	423,223	558,458
Ballast water in the stern (right)	106,316.7612	423,223	423,223	558,458

TABLE 3 Ballast water parameters under extreme survival conditions.

Draught 14 m	Mass (kg)	I_{xx} (kg·m^2)	I_{yy} (kg·m^2)	I_{zz} (kg·m^2)
Ballast water in the bow (left)	208,619.73	1,310,000	1,310,000	1,000,000
Ballast water in the bow (right)	208,619.73	1,310,000	1,310,000	1,000,000
Ballast water in the stern (left)	204,827.52	1,970,000	1,970,000	766,860.69
Ballast water in the stern (right)	204,827.52	1,970,000	1,970,000	766,860.69

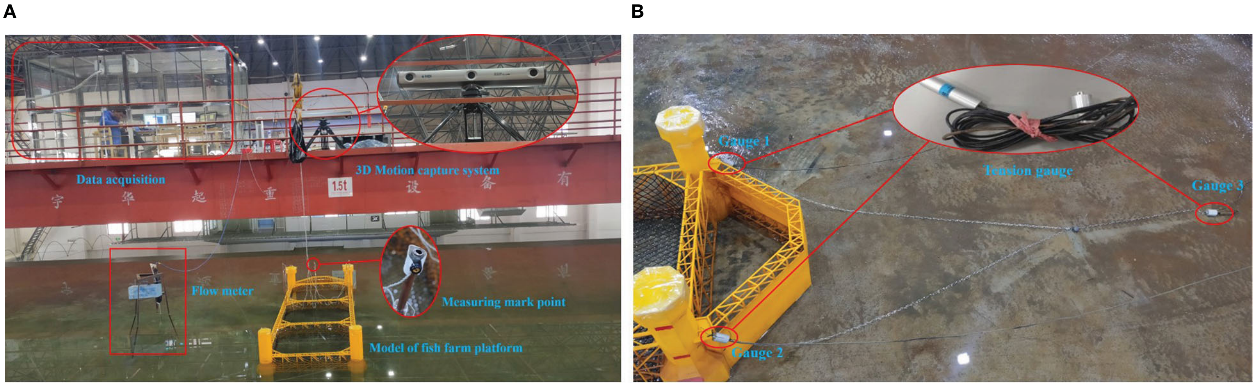

Overall condition of the test

Mooring system in test and tension gauge

FIGURE 7
Physical modeling test site condition.

which usually occurred at gauge 1 or gauge 2 (Figure 7). Because of symmetry, the two tensions from gauges 1 and 2 were almost the same.

3.2 Motion response and mooring line tension comparison

Three regular wave conditions (*H* = 5 m, *T* = 9 s; *H* = 6 m, *T* = 11 s; and *H* = 7 m, *T* = 13 s) were selected for comparative verification. The results showed that the motion response values in roll, sway, and yaw were small due to the adoption of the Y-type SPM. Thus, only the motion responses in the heave and pitch of the physical model test and the numerical simulation were compared, as shown in Figure 8. It was noted that the numerical simulation curves showed good agreement with the physical model test curves. Figure 9 shows the maximum mooring line tension of the physical model test and the numerical simulation under different wave conditions. The maximum error occurred in the *H* = 7 m, *T* = 13 s wave condition, with a value of 4.35%. The comparison of the motion response and mooring line tension between the

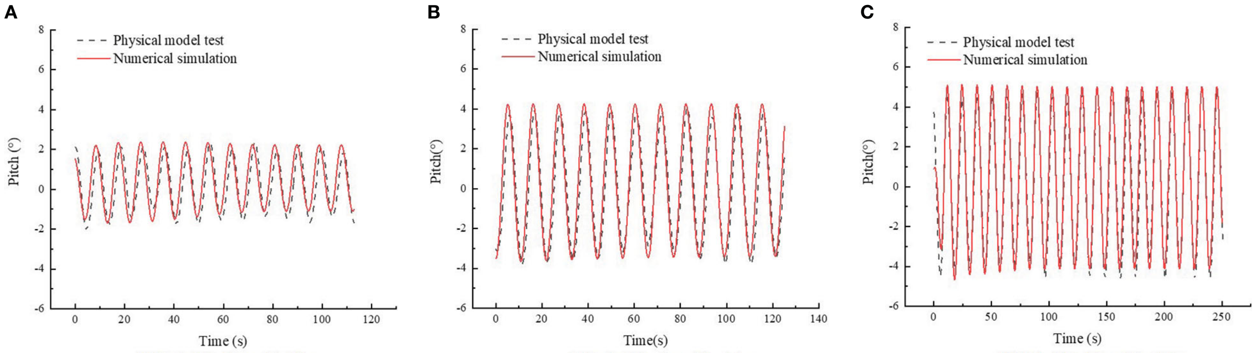

Pitch H=5m T=9s

Pitch H=6m T=11s

Pitch H=7m T=13s

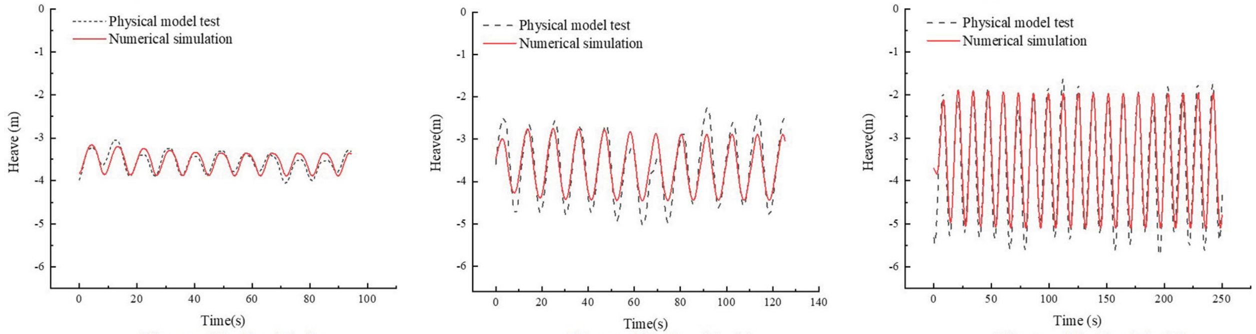

Heave H=5m T=9s

Heave H=6m T=11s

Heave H=7m T=13s

FIGURE 8
Comparison of motion responses between physical model test and numerical simulation under different wave conditions.

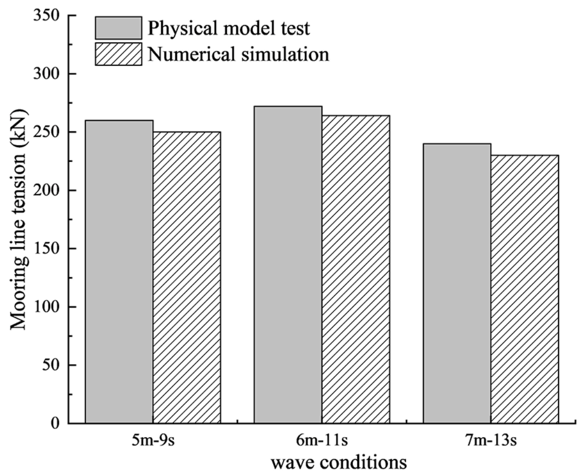

FIGURE 9
Comparison of mooring line tension peak between physical model test and numerical simulation.

physical model test and the numerical simulation demonstrated the effectiveness of the numerical model of the fish farm platform and the corresponding modeling method.

4 Motion response and mooring characteristic analysis

4.1 Motion response

To study the response characteristics of the fish farm platform with different wave parameter changes, the platform's motion response and mooring characteristics were analyzed under a series of regular waves. Nine groups of wave conditions were considered, with wave heights from 6 to 10 m and wave periods from 9 to 13 s. The wave conditions are shown in Table 4. It should be noted that, as the platform was in normal condition most of the time, only the draught of 8.2 m was considered. In addition, for this type of SPM vessel-shaped platform, the motion responses in roll, sway, and yaw were very small; thus, only the motion responses in pitch, heave, and surge were analyzed.

Figure 10 shows the motion response of the fish farm platform under different wave conditions. It was found that the motion response was positively correlated with the wave height and wave period in the pitch and heave motions. When the wave height increased from 6 to 10 m, the average amplitude increases were 41.47%, 21.89%, and 41.50%, respectively, corresponding to the pitch motion under wave periods of 9, 11, and 13 s, respectively. In addition, when the wave period increased from 9 to 13 s, the average amplitude increases of the pitch motion under wave heights of 6, 8, and 10 m were 138.27%, 137.77%, and 138.33%, respectively. These indicate that the pitch motion was more sensitive to the change of wave period than of wave height. Similar results were obtained for the heave motion, as shown in Figure 10B, which also illustrates the correlation between the pitch and heave motions. The difference was that, under the condition of a large wave period, the heave motion increased more obviously with increasing wave height. Similarly, surge motion also increased with the increase in wave height, but there was no obvious correlation with the change in wave period.

4.2 Mooring line tension and laid length

The mooring line tension values of the fish farm platform under different wave conditions are shown in Figure 11. It was observed

TABLE 4 Different wave conditions.

Conditions	1	2	3	4	5	6	7	8	9
Wave height (m)	6	8	10	6	8	10	6	8	10
Wave period (s)	9	9	9	11	11	11	13	13	13

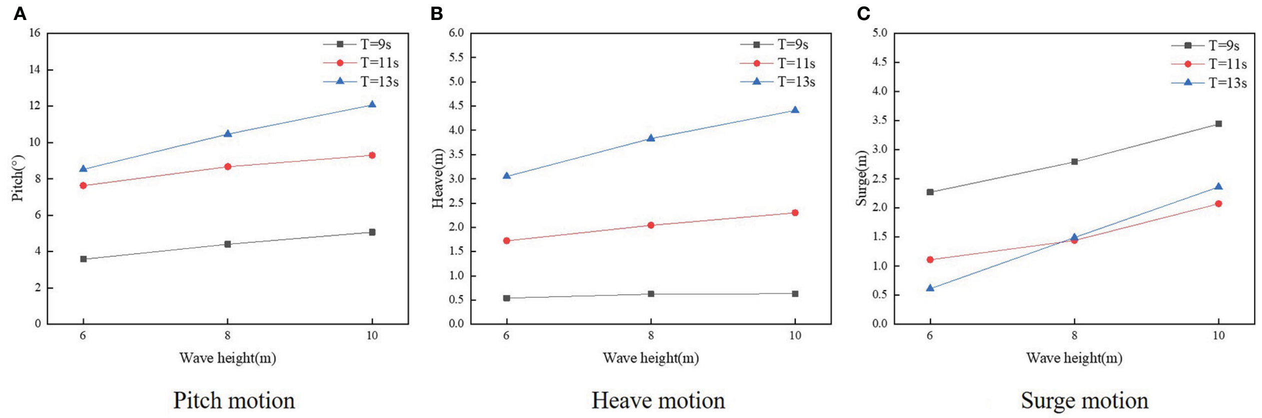

FIGURE 10
Motion response of fish farm platform under different wave conditions.

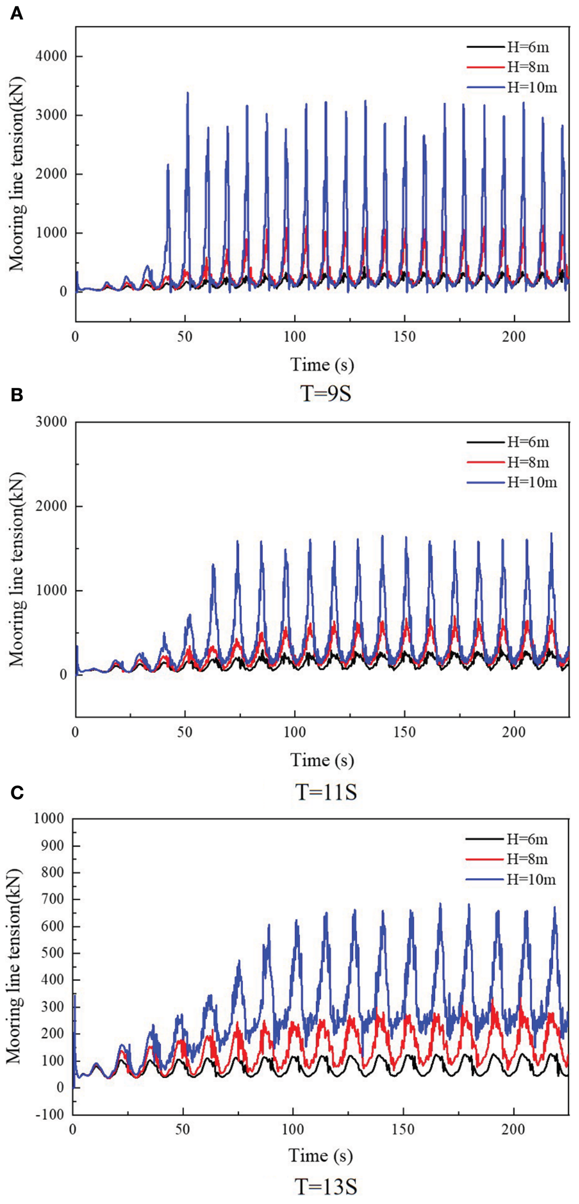

FIGURE 11
Mooring line tension of fish farm platform under different wave conditions.

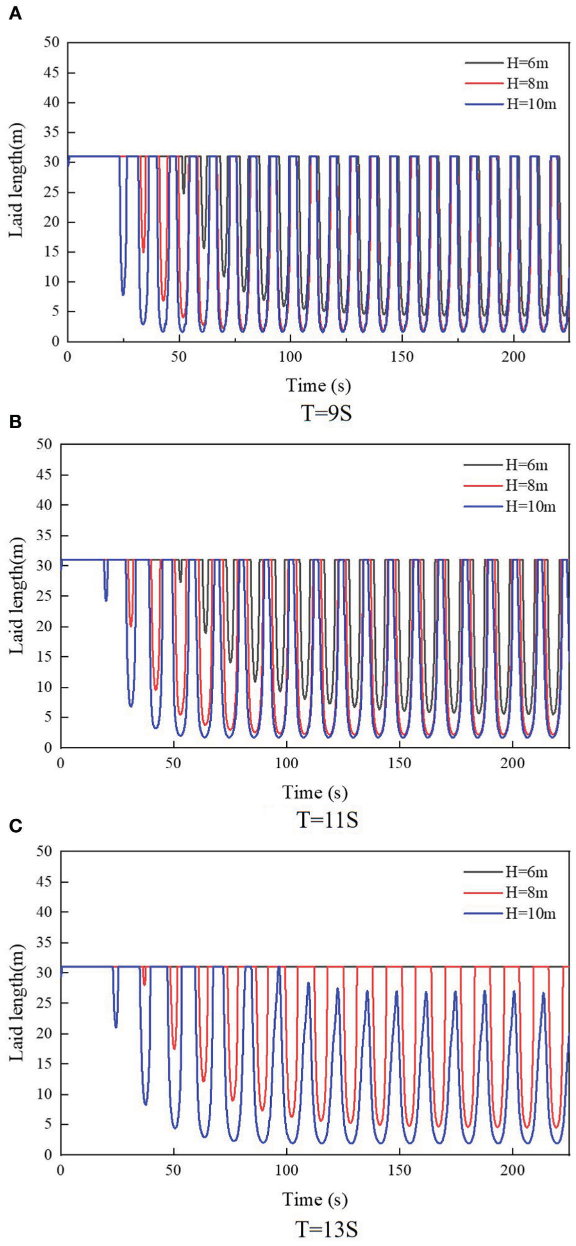

FIGURE 12
Time-domain curves of laid length of fish farm platform under different wave conditions.

that the mooring line tension was positively correlated with the wave height and negatively correlated with the wave period. Compared with the condition of small wave height, especially under the condition of large wave height, the mooring line tension increased more with the decrease of wave period.

Figure 12 shows the laid length of the fish farm platform under different wave heights. It was found that the minimum laid length was negatively correlated with the wave height; that is, the higher the wave height, the shorter the minimum laid length. A comparison of the laid length of the fish farm platform under different wave periods found that the minimum laid length was positively correlated with the wave period; that is, the longer the wave period, the greater the minimum laid length. A close check of Figures 11, 12 revealed a correlation between laid length and mooring line tension. A high mooring line tension corresponded to a short laid length, and with a large laid length, the mooring line tension would be low. It was concluded that, in addition to the mooring line tension of the fish farm platform, the laid length of the mooring line is also a key factor in judging mooring safety. A long laid length not only can ensure the anchor's bottom grasping ability but also plays a buffer role under the dynamic load transmitted by the connected platform.

To further understand the hydrodynamic characteristics of the fish farm platform under different wave conditions, the wave steepness parameter was adopted. Nine wave steepness independent variables were calculated, as shown in Table 4. The motion response and mooring line tension of a fish farm platform were obtained and illustrated in Figures 10, 12. The motion response and the mooring line tension of the fish farm platform under different wave steepness conditions are shown in Figure 13.

It can be seen that the pitch and heave motions showed consistent change characteristics with the increase of wave steepness, proving the correlation between these two motions. In addition, the overall change trends of the surge motion and mooring tension significantly increased with the increase of wave steepness. This indicates that surge motion played an important role in the increase of the mooring force. Moreover, attention should be paid to waves with high steepness values when designing a mooring system.

5 Applicability of the platform to deal with extreme sea conditions

5.1 Motion response

The new semi-submersible vessel-shaped fish farm platform in this study was designed to deal with extreme ocean conditions by diving the main body of the platform through the water. To evaluate the applicability of the platform in extreme sea conditions, its hydrodynamic characteristics under diving conditions were analyzed and compared with those under normal operating conditions. The same wave conditions were considered, as listed in Table 4.

Figure 14 shows the motion response comparison of the fish farm platform under the normal condition and the survival condition. It was observed that, with the increase in the draught, the motion response of the platform decreased to varying degrees. In detail, the pitch motion under the survival condition was smaller than that under the normal condition, but the range of decrease was not very large. The average decreases for the three wave periods were 17.52%, 18.66%, and 4.53%, respectively. The heave motion obviously decreased with the increase in the draught, and the decrease became larger with the increase in the wave period. The average decreases during the three wave periods were 21.67%, 26.84%, and 29.83%, respectively. With regard to the surge motion, in two groups of waves with periods of 9 and 11 s, the surge motion of the platform decreased with the increase in diving depth. When the wave height was 10 m and the wave period was 11 s, the decrease was the largest, which was 59.5%. However, the surge motions of the platform under both normal and survival conditions were almost the same under the wave group with a

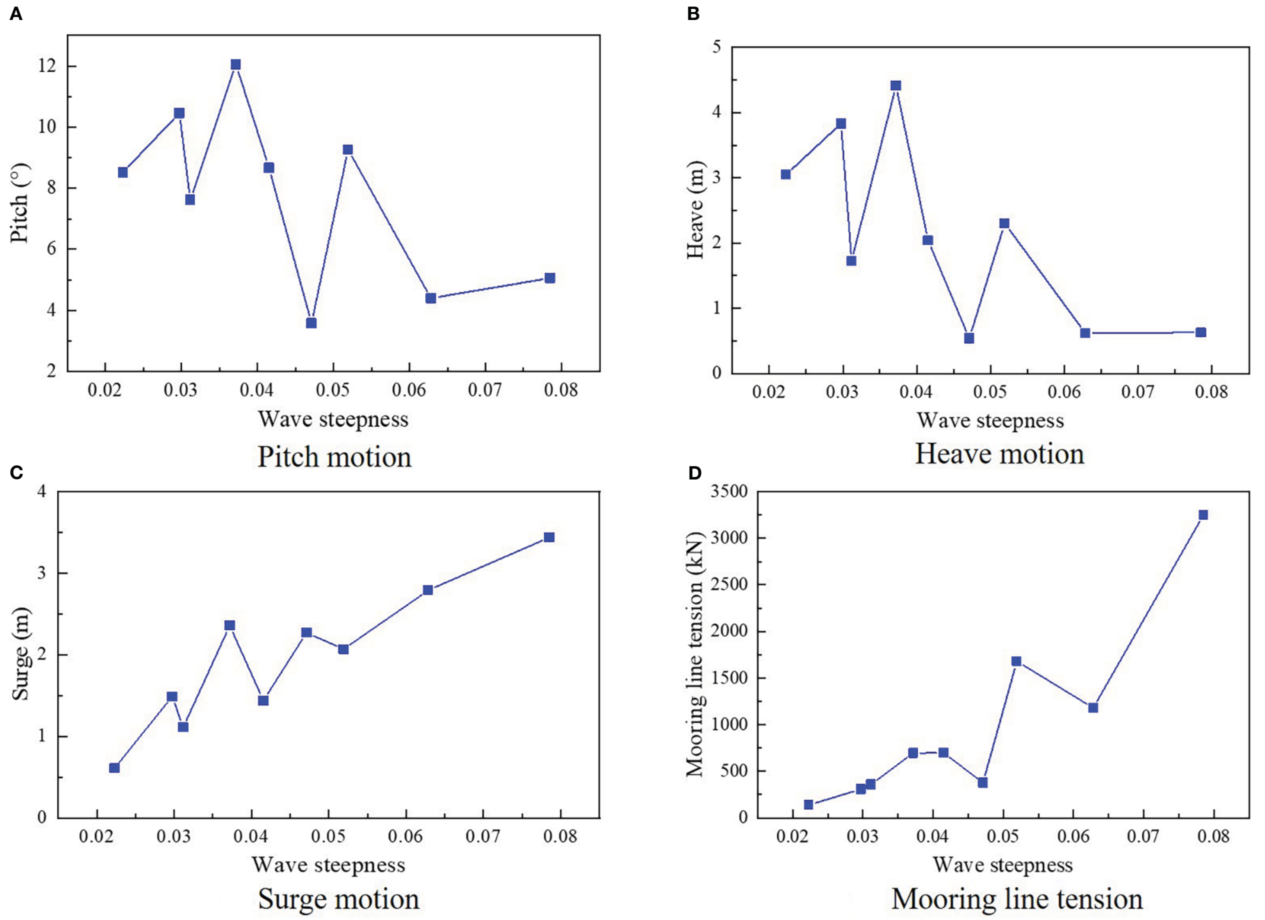

FIGURE 13
Motion response and mooring line tension of fish farm platform under different wave steepness.

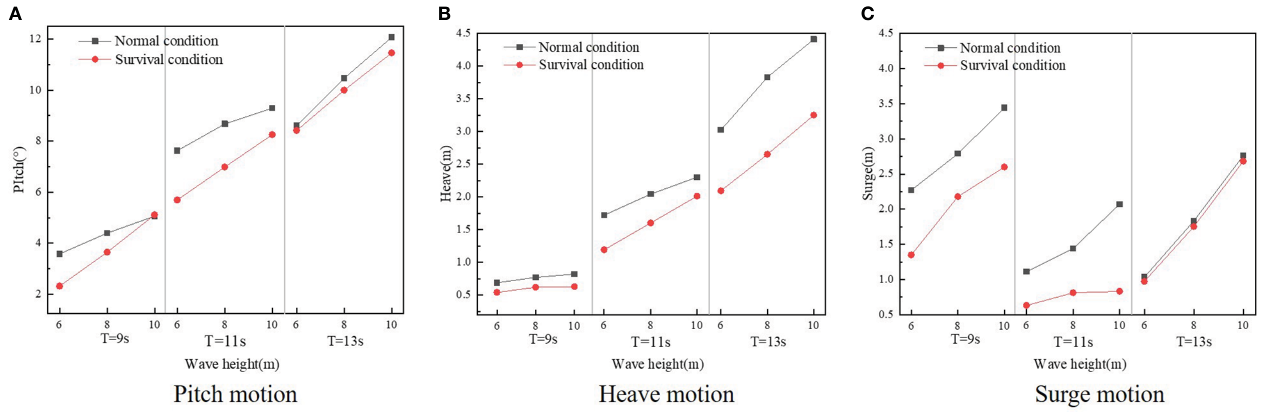

FIGURE 14
Motion response comparison of fish farm platform under different operating conditions.

period of 13 s. These results indicate that the new fish farm platform can improve its seakeeping performance under extreme conditions by diving its main body through the water.

5.2 Mooring line tension

The mooring line tension of the fish farm platform under the survival condition was calculated and compared to that under the normal condition. The comparison results are shown in Figure 15. It was found that the mooring line tension of the fish farm platform under the survival condition had the same response law as the platform under the normal condition with changes in wave height and wave period. The mooring line tension was positively correlated with the wave height and negatively correlated with the wave period. In addition, under all wave conditions, the mooring line tension of the platform under the survival condition was less than that under the normal condition. This is mainly due to the impact of the wave and current on the fish farm platform decreasing as the main structure of the platform dives into deeper water. In addition, it was found that the laid length increased with the increase of the draught of the platform, which reduced the initial mooring line tension. Furthermore, it should be noted that the decrease in mooring line tension between normal and survival conditions increased with the increase in wave height. This indicates that, in terms of mooring line tension, the new fish farm platform can deal with severe ocean conditions well by adjusting the draught of the platform.

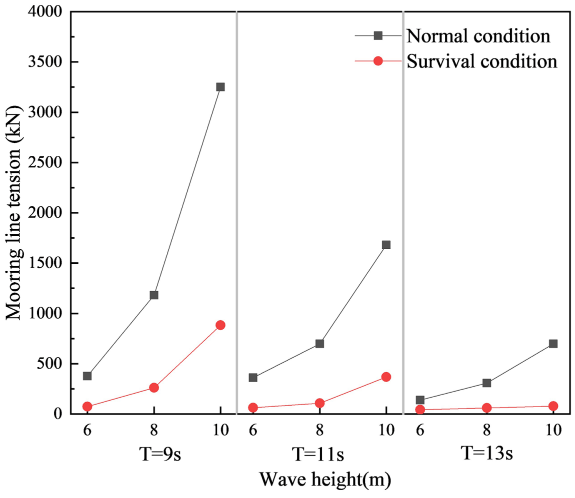

FIGURE 15
Mooring line tension comparison of fish farm platform under different operating conditions.

6 Conclusion

In this study, a new semi-submersible vessel-shaped fish farm platform was developed. The hydrodynamic numerical model of the fish farm platform was established based on the AQWA software, and the corresponding physical model test was carried out to verify the numerical model. Based on the verified model, the hydrodynamic performance of the platform under different wave conditions was analyzed. The applicability of the platform to deal with extreme ocean conditions was studied from two aspects: motion response and mooring line tension. The conclusions drawn are as follows:

1) The motion response numerical simulation results agreed well with the physical model test results. The maximum error in mooring line tension was less than 5%. between the numerical and the physical model's test. The numerical model of the fish farm platform was fully verified, and the corresponding modeling method provided a reference for the establishment of a hydrodynamic model of a large truss fish farm platform.
2) There were correlations between pitch and heave motions. They were all positively correlated with wave height and wave period. The platform's mooring line tension was positively correlated with wave height and negatively correlated with wave period. In addition, surge motion

played an important role in the increase of mooring tension. Waves with large steepness values should be considered when designing a mooring system.

3) The new fish farm platform improved its seakeeping performance under extreme conditions by diving its main body through the water. The mooring line tension of the platform under the survival condition was much lower than that under the normal condition. This expressed the new semi-submersible vessel-shaped fish farm platform's ability to deal with extreme ocean conditions. The choice of a small waterplane area provided a reference for the design of a large fish farm platform.

Data availability statement

The original contributions presented in the study are included in the article/supplementary material. Further inquiries can be directed to the corresponding author.

Author contributions

All authors certify that they have participated sufficiently in the work to take public responsibility for the appropriateness of the experimental design and method, and the collection, analysis, and interpretation of the data. All authors contributed to the article and approved the submitted version.

Funding

This work was financially supported by the National Natural Science Foundation of China (no. 32173024); the Science and Technology Special Fund of Hainan Province (no. ZDYF2021XDNY305); the Hainan Provincial Natural Science Foundation of China (no. 322QN438); the Central Public-Interest Scientific Institution Basal Research Fund, South China Sea Fisheries Research Institute, CAFS (no. 2021TS04); and the Fund of the Key Laboratory of Open-Sea Fishery Development, Ministry of Agriculture and Rural Affairs, P.R. China (no. LOF2021-04). The authors would like to express gratitude to these foundations.

Conflict of interest

The authors declare that the research was conducted in the absence of any commercial or financial relationships that could be construed as a potential conflict of interest.

Publisher's note

References

ANSYS, AQWA (2018). *Aqwa theory manual* (Canonsburg, PA, USA: ANSYS, Inc).

Chu, Y. I., Wang, C. M., Park, J. C., and Lader, P. F. (2020). Review of cage and containment tank designs for offshore fish farming. *Aquaculture* 519, 734928. doi: 10.1016/j.aquaculture.2020.734928

Fredriksson, D. W., Decew, J. C., and Tsukrov, I. (2007). Development of structural modeling techniques for evaluating HDPE plastic net pens used in marine aquaculture. *Ocean Eng.* 34 (16), 2124–2137. doi: 10.1016/j.oceaneng.2007.04.007

Fredriksson, D. W., Swift, M. R., Irish, J. D., Tsukrov, I., and Celikkol, B. (2003). Fish cage and mooring system dynamics using physical and numerical models with field measurements. *Aquacultural Eng.* 27 (2), 117–146. doi: 10.1016/S0144-8609(02)00043-2

Gansel, L. C., Oppedal, F., Birkevold, J., and Tuene, S. A. (2018). Drag forces and deformation of aquaculture cages full-scale towing tests in the field. *Aquacultural Eng.* 81, 46–56. doi: 10.1016/j.aquaeng.2018.02.001

Huang, X. H., Guo, G. X., Tao, Q. Y., Liu, H. Y., Wang, S. M., and Hao, S. H. (2016). Numerical simulation of deformations and forces of a floating fish cage collar in waves. *Aquacultural Eng.* 74, 111–119. doi: 10.1016/j.aquaeng.2016.07.003

Huang, X. H., Guo, G. X., Tao, Q. Y., Liu, H. Y., Wang, S. M., and Hao, S. H. (2018). Dynamic deformation of the floating collar of a net cage under the combined effect of waves and current. *Aquacultural Eng.* 83, 47–56. doi: 10.1016/j.aquaeng.2018.08.002

Huang, X. H., Liu, H. Y., Hu, Y., Tao, Q. Y., Wang, S. M., and Liu, Z. X. (2020). Hydrodynamic performance of a semi-submersible offshore fish farm with a single point mooring system in pure waves and current. *Aquacultural Eng.* 90, 102075. doi: 10.1016/j.aquaeng.2020.102075

Kristiansen, T., and Faltinsen, O. M. (2012). Modelling of current loads on aquaculture net cages. *J. Fluids Structures* 34, 218–235. doi: 10.1016/j.jfluidstructs.2012.04.001

Kristiansen, T., and Faltinsen, O. M. (2015). Experimental and numerical study of an aquaculture net cage with floater in waves and current. *J. Fluids Structures* 54, 1–26. doi: 10.1016/j.jfluidstructs.2014.08.015

Lei, Y., Zhao, S. X., Zheng, X. Y., and Li, W. (2020). Effects of fish nets on the nonlinear dynamic performance of a floating offshore wind turbine integrated with a steel fish farming cage. *Int. J. Struct. Stability Dynamics* 20 (3), 2050042. doi: 10.1142/S021945542050042X

Lei, Y., Zheng, X. Y., Li, W., Zheng, H., Zhang, Q., Zhao, S., et al. (2021). Experimental study of the state-of-the-art offshore system integrating a floating offshore wind turbine with a steel fish farming cage. *Mar. structures* 80, 103076. doi: 10.1016/j.marstruc.2021.103076

Li, L., Jiang, Z., Hoilang, Av, and Ong, M. C. (2018a). Numerical analysis of a vessel-shaped offshore fish farm. *J. Offshore Mechanics Arctic Eng.* 140, 041201. doi: 10.1115/1.4039131

Li, L., Jiang, Z. Y., Ong, M. C., and Hu, W. F. (2019). Design optimization of mooring system: An application to a vessel-shaped offshore fish farm. *Eng. Structures* 197, 109363. doi: 10.1016/j.engstruct.2019.109363

Li, L., Jiang, Z., Wang, J. G., and Hu, W.F. (2018b) Numerical study on the heading misalignment and current velocity reduction of a vessel-shaped offshore fish farm. *J. Offshore Mechanics Arctic Eng.* 141, 051602. doi: 10.1115/1.4042266

Liu, H. F., Bi, C. W., Xu, Z., and Zhao, Y. P. (2021). Hydrodynamic assessment of a semi-submersible aquaculture platform in uniform fluid environment. *Ocean Eng.* 237, 109656. doi: 10.1016/j.oceaneng.2021.109656

Liu, H. F., Bi, C. W., and Zhao, Y. P. (2020). Experimental and numerical study of the hydrodynamic characteristics of a semisubmersible aquaculture facility in waves. *Ocean Eng.* 214, 107714. doi: 10.1016/j.oceaneng.2020.107714

Martin, T., Tsarau, A., and Bihs, H. (2020). A numerical framework for modelling the dynamics of open ocean aquaculture structures in viscous fluids. *Appl. Ocean Res.* 106, 102410. doi: 10.1016/j.apor.2020.102410

Rui, D. (2018). *Numerical modeling and analysis of a semi-submersible fish-cage* (Trondheim, Norway: Norwegian University of Science and Technology).

Wang, G., Martin, T., Huang, L., and Bihs, H. (2021). A numerical study of the hydrodynamics of an offshore fish farm using REEF3D. *J. Offshore Mechanics Arctic Eng.* 144, 021301. doi: 10.1115/1.4052865

Wang, G., Martin, T., Huang, L., and Bihs, H. (2022). Numerical investigation of the hydrodynamics of a submersible steel-frame offshore fish farm in regular waves using CFD. *Ocean Eng.* 254, 111362. doi: 10.1016/j.oceaneng.2022.111528

Wang, S., Shen, W., Guo, J., Yuan, T. P., Qiu, Y., Tao, Q. Y., et al. (2020). Engineering prediction of fatigue strength for copper alloy netting structure by experimental method. *Aquacultural Eng.* 90, 102087. doi: 10.1016/j.aquaeng.2020.102087

Xu, Z., and Qin, H. (2020). Fluid-structure interactions of cage based aquaculture: From structures to organisms. *Ocean Eng.* 217, 107961. doi: 10.1016/j.oceaneng.2020.107961

Yu, Z., Amdahl, J., Kristiansen, D., and Bore, P. T. (2019). Numerical analysis of local and global responses of an offshore fish farm subjected to ship impacts. *Ocean Eng.* 194, 106653. doi: 10.1016/j.oceaneng.2019.106653

Zhao, Y. P., Guan, C. T., Bi, C. W., Bi, C. W., Liu, H. F., Cui, Y., et al. (2019). Experimental investigations on hydrodynamic responses of a semi-submersible offshore fish farm in waves. *J. Mar. Sci. Eng.* 7, 238. doi: 10.3390/jmse7070238

Zhao, Y. P., Li, Y. C., Dong, G. H., Gui, F. K., and Teng, B. (2007). A numerical study on dynamic properties of the gravity cage in combined wave-current flow. *Ocean Eng.* 34, 2350–2363. doi: 10.1016/j.oceaneng.2007.05.003

Frontiers in Marine Science

TYPE Original Research
PUBLISHED 10 March 2023
DOI 10.3389/fmars.2023.1140285

OPEN ACCESS

EDITED BY
Fukun Gui,
Zhejiang Ocean University,
China

REVIEWED BY
Hung-Jie Tang,
National Cheng Kung University,
Taiwan
Haocai Huang,
Zhejiang University,
China

*CORRESPONDENCE
Ruosi Zha
zhars@mail.sysu.edu.cn

SPECIALTY SECTION
This article was submitted to
Marine Fisheries, Aquaculture
and Living Resources,
a section of the journal
Frontiers in Marine Science

RECEIVED 08 January 2023
ACCEPTED 20 February 2023
PUBLISHED 10 March 2023

CITATION
Huang W and Zha R (2023) Numerical studies on internal flow in pipelines of an aquaculture vessel and flow control using a special branch pipe.
Front. Mar. Sci. 10:1140285.
doi: 10.3389/fmars.2023.1140285

Numerical studies on internal flow in pipelines of an aquaculture vessel and flow control using a special branch pipe

Wenyun Huang[1,2,3] and Ruosi Zha[4]*

[1]Fishery Machinery and Instrument Research Institute, Chinese Academy of Fishery Science, Shanghai, China, [2]Key Laboratory of Ocean Fishing Vessel and Equipment, Ministry of Agriculture, Shanghai, China, [3]Joint Laboratory for Open Sea Fishery Engineering, Pilot National Laboratory for Marine Science and Technology (Qingdao), Shandong, Qingdao, China, [4]School of Ocean Engineering and Technology, Sun Yat-sen University & Southern Marine Science and Engineering Guangdong Laboratory (Zhuhai), Zhuhai, China

Introduction: Regarded as the world's largest smart-aquaculture vessel so far, Guoxin No. 1, has achieved remarkable success in aim to develop large-scale cruising aquaculture platforms. Guoxin No. 1 is 816 feet long with 15 fish farming tanks, which has a tank capacity of up to 900,000 square feet. It is of great practical interest to study the pipe flow rate distribution involving oxygen and novel flow control schemes for internal flows of aquacultural facilities connecting fish farming tanks.

Methods: In this paper, three-dimensional numerical investigations on internal flow in a T-type pipeline and its flow control are carried out. A single pump is designed to convert water to two separate farming tanks through a pipeline system, which is composed of one main inlet pipe and two outlet pipes with the same diameter as that of the inlet pipe. A horizontal arrangement of the pipes, in which the flow rate of an outlet pipe must be half of the inflow rate, is firstly studied for validation. To guarantee a balanced oxygen supply, equilibrium outflow rates can be achieved as a consequence of using a branch with a smaller diameter installed on the main inlet pipe. 3-D unsteady RANS solvers were employed to simulate the incompressible viscous flow and the pipe walls were assumed as rigid bodies.

Results: A couple of flow rates and three pipe angles were then investigated to assess the change of the outflow rates. Based on the simulations, a flow control scheme was proposed including to optimize the central included angle between the main inlet pipe and the small branch pipe, and the inflow rate of the branch pipe in order to balance the outflow rates. The results show that the central included angle has a significant influence on the flow field and flow rate of the two outlet pipes.

Discussion: If the angle was fixed, it can be indicated that adjusting the flow rate of the branch inlet can be an efficient method to unify the flow rate of the outlet pipes and improve the water exchange among fish farming tanks.

KEYWORDS

offshore fish farming, aquaculture vessel, flow in pipes, flow control, computational fluid dynamics, internal flow

1 Introduction

During the operation of aquaculture vessels (Aryawan and Putranto, 2018), water with oxygen and nourishment must be carefully supplied by using a large number of pipes and pumps. For example, fresh seawater with saturated oxygen content is continuously needed to satisfy the oxygen requirement from the fish living in farming tanks. A single pump is designed to convert water with oxygen to two tanks *via* intricate pipelines for higher operating efficiency. It is therefore important to study the dynamic balance of oxygen in the aquaculture tanks for aquaculture vessels.

Compared with the traditional aquaculture systems with net cages, cruising aquaculture vessels have the advantage of mobility, preventing it from coming into contact with rough seas (Hvas et al., 2021). Good growth and survival rates of cultured fish, e.g., *Pseudosciaena crocea*, can be obtained according to Li et al. (2022). For cruising aquaculture vessels, a higher fish rearing density in tanks than farming in traditional aquaculture cages can be considered and a shortened rearing cycle can be obtained. In addition, a structural form of the vessel shape can decrease the sea loads on aquaculture vessels (Ma et al., 2022). However, the improvement of farming environment is challenged by large-amplitude ship motions in waves (Tello et al., 2011), the phenomenon of violent sloshing (Faltinsen, 2017), and the control of onboard sound levels and vibrations (Mansi et al., 2019). Different from the land-based fish farming systems (Zhang et al., 2011), the large length–width ratio of a ship leads to challenges in arrangement of farming tanks, pipes, and pumps. Therefore, the flow rates from pumps to farming tanks should be designed controllably and efficiently while the development of aquaculture vessels tends to be larger and smarter. Water flow rates (Oca and Masalo, 2013) are being considered as one of the primary factors for the safety of aquatic animals and the sustainability of aquaculture platforms equipped with fish culture tanks and support systems. Pump-driven water flows with different flow rates have an impact on the structural strength of pipeline systems (Costa et al., 2006) and the oxygen-rich environment of farming tanks in aquaculture engineering (Lekang, 2020).

As an example of cruising aquaculture vessels, Guoxin No.1 (or Guoxin 1), the first tanker-sized aquaculture vessel in the world that weighted 100,000 dwt, has been delivered by China (Editorial Staff, 2022). Aimed at producing high-quality farmed fish on a large scale (more than 3,700 tons annually), Guoxin 1 was jointly developed and built in 2020 by Qingdao Conson Development Group, China State Shipbuilding Corporation Limited (CSSC), the National Pilot Laboratory of Marine Science and Technology (Qingdao), and the Chinese Academy of Fisheries Science. A total of 15 aquaculture tanks and numerous pipes were equipped on this 250 by 45 m vessel. According to The Fish Site (2020), Guoxin 1 can sail with a maximum speed of 10 knots to avoid substantial hazards, e.g., typhoons, red tides, and pollution. After beginning operations in the Yellow Sea, Guoxin 1 delivered its first batch of 65 tons of large yellow croaker (Chen et al., 2020), which lives in aquaculture tanks in the deep sea with 100 nautical miles offshore. In the future, the Conson Group desired to build 50 of these mobile aquaculture vessels, each of which is anticipated to generate 200,000 tons of fish annually and have an economic value of more than $1.68 billion. To guarantee the fish output, a steady and healthy living environment in all aquaculture tanks must be created by circulating the seawater to keep an enclosed and controllable aquatic environment. Studies on flow pattern in aquaculture tanks (Duarte et al., 2011) have been extensively carried out, including experimental studies and numerical simulations. For example, particle tracking velocimetry (PTV) techniques were used to evaluate the flow pattern for the design of aquaculture tanks to obtain better culture conditions and improve water use efficiency (Oca et al., 2004; Oca and Masaló, 2007). Oca and Masalo (2013) and Masaló and Oca (2014) studied the influence of flow rate, water depth, and water inlet and outlet on flow field in aquaculture circular tanks. For the recirculating aquaculture system and biofloc technology system, the influences of macro-infrastructure on the microenvironment in 68 aquaculture tanks, e.g., the hydrodynamic characteristics, were reviewed by Zhao et al. (2022). Computational fluid dynamics (CFD) has been employed to study the flow field and pollutant particle distribution in aquaculture fish tanks (Xue et al., 2022). The discrete phase model (DPM) was used to study particle motion within fluid flows. Guo et al. (2020) applied the CFD method to investigate the flow characteristics including residence time and velocity uniformity in a force-rolling aquaculture tank by using the solver FLOW3D.

Complicated flows inside tee pipes have become a hot topic in the offshore and oil industry. For example, Han et al. (2020) studied the laminar flow pattern in blind tee pipes considering the influences of different pipe length and end-structure shapes by using the CFD software ANSYS CFX. The Large eddy simulation (LES) method was adopted by Zhou et al. (2019) to simulate the varied flow rate of the branch pipeline in a T-junction for thermal-mixing pipe flows. For farming systems, a flow driven by pumps in the main pipe with fresh seawater with saturated oxygen can be divided into several flows using tee pipes and flows can also join together in pipes with branches. It is assumed that two identical farming tanks demand the same water flow rate for oxygen balance. Different flow rates will be obtained due to the altitude difference of pipes and tanks. To overcome this problem, the unbalanced flow rates should be eliminated by using flow rate control schemes to improve the efficiency of water supply. Extensive study has been done on flow control in a variety of fields including aquaculture (Edwards and Finn, 2015). In the work of Padala and Zilber (1991), expert systems in aquaculture were reviewed including monitoring and control of feeding, temperature, water quality, flow, oxygen, and water level to optimize production efficiency in tilapia culture. For water level control, Ullah and Kim (2018) applied Kalman filters in a proposed optimization scheme for maintaining target water level fish farm tank to obtain a minimum energy consumption by adjusting pumping flow rate and target filling levels. Li et al. (2019) proposed a hybrid data-driven and model-assisted control strategy for water pump control, namely, modified active disturbance rejection control (MADRC). For the combination between aquatic live and crops, which is called aquaponics, water flow rate control based on pump specification and height was studied to avoid siphon malfunctionality (Romli et al., 2018). Water level management can be carried out to reduce the cost of using pumps with variable speed. Control strategies are of primary importance in conducting flow rate control. Urrea and

Páez (2021) investigated four control strategies including classical Proportional–Integral–Derivative (PID), Gain Scheduling (GS), Internal Model Control (IMC), and Fuzzy Logic (FL) for the water level control of an inverted conical tank system. As part of smart and sustainable aquaculture farms, pumps and valves can be used to achieve the optimal flow, and the water and aeration pipe networks were introduced by Kassem et al. (2021).

However, little effort has been made to study the flow control in pipes for cruising aquaculture vessels. In this work, the internal flow field inside a tee pipe and a scheme of using a branch to control flow rates were numerically studied by the solver STAR-CCM+. A special branch with high-speed water was manually installed on the wall of the main inflow segment to change the flow rate on the outlet. The varied flow rates of the two outlet pipes were then evaluated. The influence of the central included angle between the main input pipe and the small branch pipe and that of the branch pipe's inflow rate were addressed based on three-dimensional simulations. For the development of pipe systems, the distribution of inflow rates in pipes was recognized as a key point to control the outflow rates for pumping seawater to different aquaculture tanks. Other sections of this paper is organized as follows. In *Section 2*, numerical methods and mathematical models were introduced first. Then, the computational setup including the geometry, computational domain as well as coordinate systems, and boundary conditions are presented in *Section 3*, which is followed by numerical results and discussions on the flow rate distribution and flow pattern inside the pipe system. Finally, preliminary conclusions of this work are given accordingly.

2 Numerical methods

2.1 Governing equations

The governing equations for the incompressible viscous flow are Reynolds-averaged Navier-Stokes (RANS) equations, i.e., the continuity equation and momentum equation, which can be written as follows:

$$\frac{\partial u_i}{\partial x_i} = 0 \tag{1}$$

$$\rho \frac{\partial u_i}{\partial t} + \rho u_j \frac{\partial u_i}{\partial x_j} = - \frac{\partial p}{\partial x_i} + \frac{\partial}{\partial x_j}\left[\mu\left(\frac{\partial u_i}{\partial x_j} + \frac{\partial u_j}{\partial x_i}\right)\right] + \frac{\partial}{\partial x_j}\left(- \rho \overline{u_i' u_j'}\right) \tag{2}$$

where u_i ($i = 1, 2,$ and 3) denotes the velocity components along the x-, y-, and z-axis, respectively. p is the pressure, ρ is the density of fluid, μ is the dynamic viscosity of fluid, and $-\rho\overline{u_i' u_j'}$ are the terms of Reynolds stresses (Lai et al., 1991).

2.2 Turbulence modeling

The Reynolds stresses can be solved based on the Boussinesq hypothesis using the eddy viscosity turbulence models. Based on the assumptions of eddy viscosity models, the Reynolds stresses are computed by:

$$-\rho\overline{u_i' u_j'} = \mu_t\left(\frac{\partial u_i}{\partial x_j} + \frac{\partial u_j}{\partial x_i}\right) - \frac{2}{3}\rho k \delta_{ij} \tag{3}$$

where μ_t represents the eddy viscosity, δ_{ij} is the Kronecker delta, $k = \frac{1}{2}\overline{u_i' u_j'}$ is the turbulent kinetic energy that can be solved from the transport equations. As an example of the one-equation eddy viscosity model, the Spalart-Allmaras (SA) model (Spalart and Allmaras, 1992) solves a transport equation for the modified diffusivity, $\tilde{\nu}$, to determine the turbulence eddy viscosity, μ_t. For particular flows, the SA model has good convergence and robustness. However, the turbulence length and time scales are not as clearly defined. In this paper, two-equation eddy viscosity models were employed to solve the Reynolds stresses in RANS equations, in which both the velocity and length scale are solved using separate transport equations. The turbulence length scale is estimated from the kinetic energy and its dissipation rate. The most popular turbulence models include the standard k - ε model (Launder and Spalding, 1983), the standard k - ω model (Wilcox, 2008), and the shear stress transport (SST) k - ω model (Menter, 1994).

In the standard k - ε model (Launder and Spalding, 1983), the turbulent eddy viscosity is calculated as:

$$\mu_t = \rho C_\mu f_\mu k T \tag{4}$$

where C_μ is a model coefficient, f_μ is a damping function, and T is the turbulent time scale calculated by:

$$T = \max\ \left(T_e, C_t\sqrt{\frac{\nu}{\varepsilon}}\right) \tag{5}$$

where $T_e = \frac{k}{\varepsilon}$ is the large-eddy time scale, C_t is a model coefficient, and ν is the kinematic viscosity. The transport equations for the turbulent kinetic energy, k, and the turbulence dissipation rate, ε, are written as:

$$\frac{\partial}{\partial t}(\rho k) + \nabla \cdot (\rho k \bar{v}) = \nabla \cdot \left[\left(\mu + \frac{\mu_t}{\sigma_k}\right) \nabla k\right] + P_k + S_k - \rho(\varepsilon - \varepsilon_0) \tag{6}$$

$$\frac{\partial}{\partial t}(\rho \varepsilon) + \nabla \cdot (\rho \varepsilon \bar{v}) = \nabla \cdot \left[\left(\mu + \frac{\mu_t}{\sigma_\varepsilon}\right) \nabla \varepsilon\right] + \frac{1}{T_e} C_{\varepsilon 1} P_\varepsilon - C_{\varepsilon 2} f_2 \rho\left(\frac{\varepsilon}{T_e} - \frac{\varepsilon_0}{T_0}\right) + S_\varepsilon \tag{7}$$

where σ_k, σ_ε, $C_{\varepsilon 1}$ and $C_{\varepsilon 2}$ are the model coefficients, P_k and P_ε are the production terms, f_2 is a damping function, and S_k S_ε are the source terms.

Different from the standard k - ε model, C_μ is a variable rather than a constant in solving the turbulent eddy viscosity for the realizable k - ε. model (Shih et al., 1994). The transportation of dissipation rate was rewritten. The realizable k - ε model performs better for capturing the mean flow of complex structures and for flows involving rotation. For the present simulations, the realizable k - ε two-layer model (Shih et al., 1994) with an all y^+ wall treatment (Mockett et al., 2012) was applied.

2.3 Spatial and temporal discretization

2.3.1 Finite volume discretization

In this work, the finite volume method (Moukalled et al., 2016) was employed for the spatial discretization of governing equations. The discretized convective term at a face can be written as:

$$(\phi \rho v \cdot a)_f = (\dot{m}\phi)_f = \dot{m}_f \phi_f \tag{8}$$

where ϕ_f is an arbitrary fluid property at the face of a grid cell. $\dot{m}_f$ denotes the mass flow rate at the face of a grid cell. A second-order upwind (SOU) scheme was employed, in which the convective flux is calculated as follows.

$$(\dot{m}\phi)_f = \begin{cases} \phi_0 + \left(x_f - x_0\right) \cdot (\nabla \phi)_{r,0} & \text{for } \dot{m}_f \geq 0 \\ \phi_1 + \left(x_f - x_1\right) \cdot (\nabla \phi)_{r,1} & \text{for } \dot{m}_f < 0 \end{cases} \tag{9}$$

The minimum and maximum bounds of the neighboring cell values can be obtained and employed to limit the reconstruction gradients. For example, the Venkatakrishnan limiter (Venkatakrishnan, 1995) was used to improve the numerical stability in the present simulations.

The discretized diffusive flux through internal cell faces of a grid cell is written as follows.

$$D_f = (\Gamma \nabla \phi \cdot a)_f \tag{10}$$

where Γ stands for the face diffusivity.

2.3.2 Implicit time integration

In the paper, the Euler implicit scheme (He, 2008) was employed for implicit time integration. The transient term can be discretized by:

$$\frac{d}{dt}(\rho \phi v)_0 = \frac{(\rho \phi v)_0^{n+1} - (\rho \phi v)_0^n}{\Delta t} \tag{11}$$

where n is the nth time step and Δt is the time step size. Note that the Euler implicit scheme is only a first-order temporal scheme.

3 Computational setups

3.1 Geometries

In Guoxin 1, the number of water pumps was less than that of aquaculture tanks. With the purpose of saving energy, it was assumed that a single water pump was able to supply water to two aquaculture tanks by a flow diverter, which is composed of one main inlet pipe and two outlet pipes. Note that the three pipes are jointed together in a T-type with the same diameters, as shown in Figure 1A. The length and the diameter of the inlet/outlet pipe are $L = 3$ m and $\phi_1 = \phi_2 = \phi_3 = 0.7$ m, respectively. The T-type pipe with a special branch pipe for water flow control is shown in Figure 1B. The inlet branch is equipped on the wall of the main inlet pipe, with an angle of inclination a. The length and the diameter of the inlet branch are set as $l = 1.5$ m and $\phi = 0.15$ m, respectively.

Water flows from the water pump to the main inlet pipe with a given flow rate and is then diverted into the two outlet pipes to two farming tanks with oxygen. Water also flows from the inlet branch and joins in the main inlet pipe to control the flow rate of the two outlet pipes. To simplify the simulations, the thickness and roughness of the pipe walls are neglected. It is also assumed that the oxygen level of seawater can be proportional to the amplitude of flow rate.

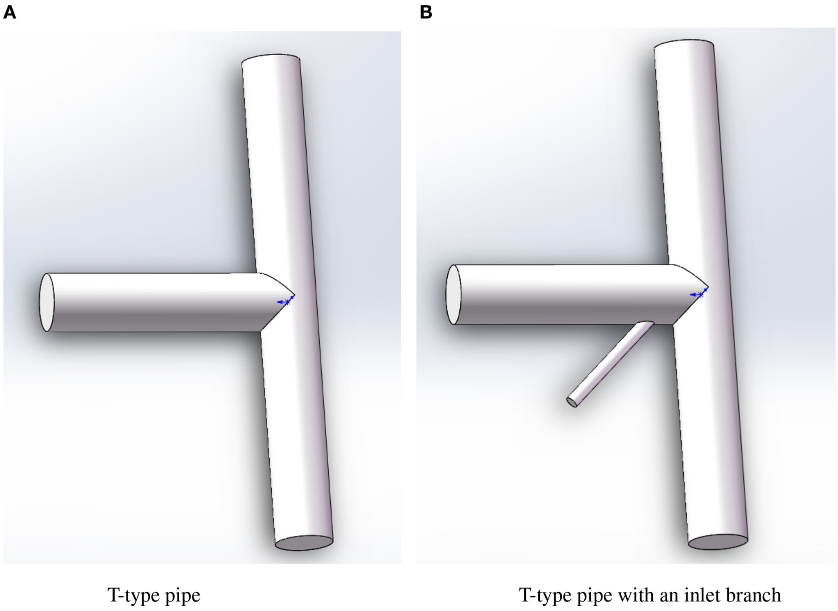

FIGURE 1
T-type pipes without and with a branch pipe for flow control. **(A)** T-type pipe. **(B)** T-type pipe with an inlet branch.

3.2 Computational domain and boundary conditions

The computational domain of T-type pipes without and with a branch inlet for flow control is shown in Figure 2. A coordinate system was established in which the origin was located at the center of the lower outlet. Q_1, Q_2, Q_3, and Q represent the flow rate at the main inlet, the upper outlet, the lower outlet, and the branch inlet, respectively. For the boundary conditions, the no-slip wall boundary condition was imposed on the pipe wall. Mass flow inlet and pressure outlet boundary conditions were employed for the inlet and outlet boundaries, respectively. A reference pressure equivalent to one standard atmospheric pressure was exerted on the upper outlet.

3.3 Grid generation

In this paper, a polyhedral meshing model, which utilizes an arbitrary polyhedral cell shape to generate the core mesh with complicated geometries, was taken advantage of in the STAR-CCM+ solver. As an example, the details of grid generation for the T-type pipe with a branch inlet are shown in Figure 3. Five layers of boundary layer mesh were built to deal with the large amplitude of velocity gradient within boundary layers near the wall. The grid growth ratio was 1.5 and the non-dimensional size of the first grid height near the wall, y^+, can be unified for the internal flows.

As shown in Figure 3A, the red part represents the polyhedral grids on the inlet and outlet surfaces while the blue part stands for the polyhedral grids on the wall surfaces of the T-type pipe. The grids near the connection between the main inlet pipe and the branch inlet pipe are also smoothed to improve the grid quality and numerical stability. Figure 3B presents the sliced section at the center of $Y = 0$ and its inner grids of the pipes. The boundary layer mesh can be observed and the inner grids are smoothed adjacent to the wall. Since the diameter of the branch inlet was relatively small, a fine base size was required to solve the flow fields accurately. Finally, the total number of grids in this paper ranges from 278,094 to 4,555,934.

3.4 Case matrix

A case matrix with various geometries, physical models, and detailed operating conditions is summarized below and presented in Table 1. Note that "TBD" is short for "to be determined", which can be determined by the present simulations.

In the following studies, simulations on flow rate distributions for the T-type pipe without a branch were firstly carried out. Since the diameters of the main inlet and two outlets are the same, the ideal outflow rate for the outlet can be determined as $Q_2 = Q_3 = Q_{1/2}$ based on the conservation of mass. Firstly, the gravitational acceleration was not considered. The numerical methods were verified based on convergence studies. In this case, the result of $Q_2 = Q_3$ should be satisfied for the numerical simulations. The effect of the gravitational acceleration was then studied by comparing the results of the first two cases listed in Table 1. In this case, $Q_2 \neq Q_3$ would be obtained for the numerical results, while the condition $Q1 = Q_2 + Q_3$ should always be satisfied.

Thereafter, simulations on flow rate distributions for the T-type pipe with a branch were comprehensively investigated. A given inflow rate for the branch inlet with $Q = 650$ (m^3/h) was imposed for the branch with various included angles from 30°C to 60°C. The effect of the branch inlet was addressed. Afterwards, a couple of inflow rates for the branch inlet was tested numerically to understand how the outflow rates in two outlets can be balanced. Note that the ideal outflow rate should be $Q_2 = Q_3 = (Q + Q_1)/2$,

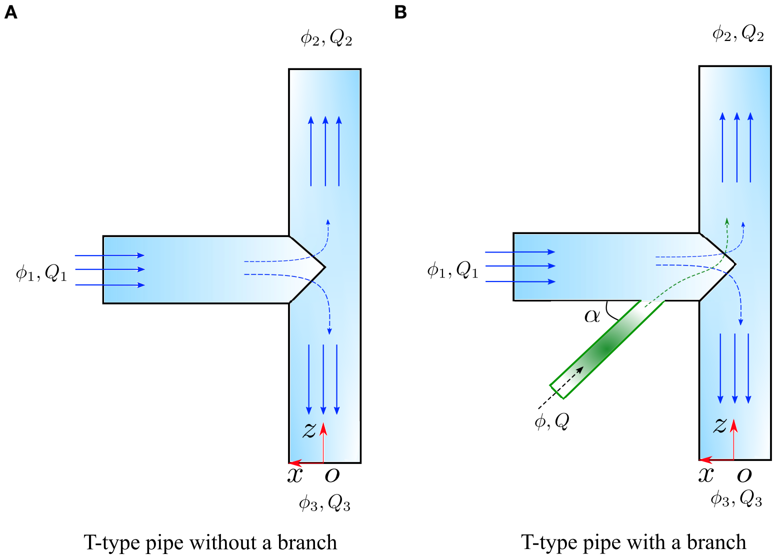

T-type pipe without a branch T-type pipe with a branch

FIGURE 2
Computational domain of T-type pipes for flow control **(A)** T-type pipe without a branch **(B)** T-type pipe with a branch pipe.

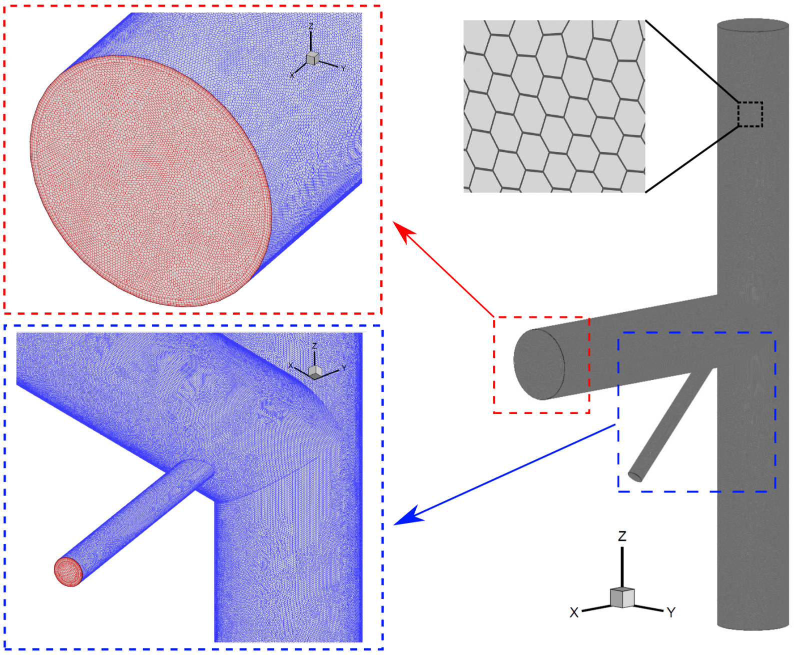

A Polyhedral grids on body surfaces

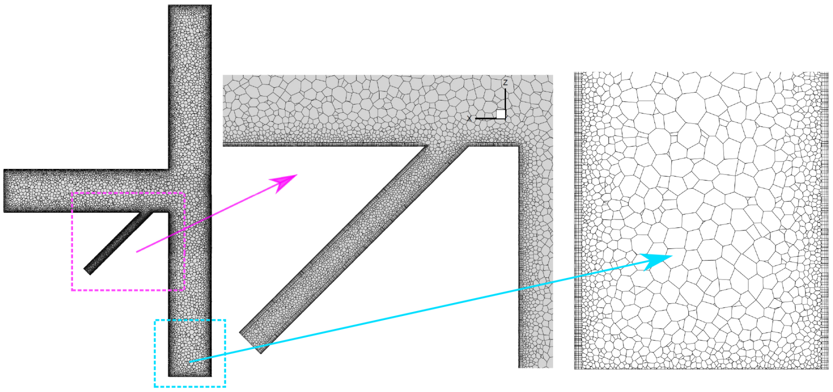

B Inner grids with a slice at $Y = 0$

FIGURE 3
Grid generation for the T-type pipe with a branch **(A)** Polyhedral grids on body surfaces **(B)** Inner grids with a slice at Y = 0.

TABLE 1 Case matrix for 3-D simulations of water flows inside T-type pipes.

Geometry	Included Angle	Physical Model	Inflow Rate	Inflow Rate	Ideal Outflow Rate
	α(°)	Gravity	Q_1 (m^3/h)	Q (m^3/h)	$Q_2 = Q_3$ (m^3/h)
Without a branch	–	False	5,000	0	2,500
Without a branch	–	True	5,000	0	–
With a branch	45	True	5,000	650	2,825
With a branch	60	True	5,000	650	2,825
With a branch	30	True	5,000	650	2,825
With a branch	45	True	5,000	TBD	TBD
With a branch	60	True	5,000	TBD	TBD
With a branch	30	True	5,000	TBD	TBD

which is dependent on the adjustable inflow rate for the branch inlet.

It should be noted that the Reynolds number, Re, ranged from 1.5×10^6 (branch inlet) to 2.5×10^6 (main inlet).

4 Numerical results and discussions

4.1 Verification for a T-type pipe

Convergence studies with various grid sizes and time steps are provided in Table 2. A total of seven cases were carried out, including five grid sizes and three time steps. The physical model, gravity, was not activated for these simulations.

For spatial convergence, five cases with different grid sizes in terms of $\Delta l = 5.00 \times 10^{-3}$ to 2.00×10^{-2} m were firstly investigated. Note that for these cases, the time step was kept the same. The convergence of the outflow rates at the upper outlet and lower outlet to Δl is shown in Figures 4A, B. It can be seen that the time histories of Q_2 and Q_3 converged to a constant value with the simulation time increased for all the cases. The final result was obtained by using the average of the results in the range of the last 500 steps. Finally, the converged results of spatial convergence are shown in Figure 5A. It can be seen that numerical results converged with the increase of the total number of grids. To save the computational resources, in the following studies, $\Delta l = 7.07 \times 10^{-3}$ m was applied instead of the setting with the finest grids. In comparison to the analytical value of the ideal outflow rate, the discrepancies between the present numerical results and the analytical value were smaller than 1%.

Furthermore, a temporal convergence study was carried out using three time steps. The convergence of the outflow rates at the upper outlet and lower outlet to Δt is presented in Figures 4C, D. Oscillations of the outflow rate were observed if the time step was large. It was found that the time histories converged with the increase of the simulation time. The converged results of temporal convergence are shown in Figure 5B, which are insensitive to the change in time step for implicit simulations. In the following studies, $\Delta t = 5 \times 10^{-3}$ s was adopted.

Therefore, a good accuracy was obtained and the numerical simulations were verified based on the convergence studies. The best-practice settings were obtained with a target grid size $\Delta l = 7.07 \times 10^{-3}$ m and a time step $\Delta t = 5 \times 10^{-3}$ s. The total number of grids was then 2,476,472 for the case of the T-type pipe without a branch inlet. The same settings can be applied for simulations of the T-type pipe with a branch inlet.

4.2 Effect of gravity

In this section, the influence of gravitational acceleration on the flow rate distribution of the two outflows in the T-type pipe without a branch is presented. Qualitatively, the flow rate at the upper outlet would be reduced and that at the lower outlet would be increased due to the effect of gravity. Despite the physical model, the geometry, grids, and operating conditions were kept the same for the cases without and with gravity.

Time histories of the outflow rates Q_2 and Q_3 are compared in Figure 6A and the final converged results are presented in Figure 6B. It can be seen that the convergence speed was higher and the fluctuation of the flow rates was smaller for the case with gravity. Finally, the flow rates Q_2 = 2,340.59m$^{3/}$h and Q_3 2,659.40m^3/h were obtained for the case with gravity. The result for $Q_1 = Q_2 + Q_3$ was also obtained with a high accuracy. Therefore, the effect of gravity led to a certain flow rate deduction for the upper outlet and a flow rate increment for the lower outlet. The difference in flow rate between the upper outlet and the lower outlet could be up to 320 m^3/h, equivalent to 12.8% of the ideal outflow rate.

The flow patterns for the T-type pipe without and with gravity were obtained by the present simulations. Figure 7 presents the contours of velocity field for the central section of the T-type. In addition, the velocity distributions on the upper and lower outlet surfaces are also compared. For the physical model without gravitational accelerations, the flow pattern indicates a good symmetrical feature for the upper segment and the lower segment of the pipe. The contours of velocity for the upper outlet and the lower outlet are basically the same. It can be seen that the flow velocity in the lower segment is higher than that in the upper segment because of the effect of gravity. Moreover, the velocity contour shows non-symmetry for the result on the upper outlet and that on the lower outlet.

The pressure contours for the central section of the T-type without and with gravity are shown in Figure 8. Two zones of low

TABLE 2 Convergence studies of flow rates using T-type pipe without a branch.

Case	Geometry	Inflow Rate	Target Grid Size	Target	Total Number	Time Step
No.		Q_1 (m^3/h)	Δl (m)	y^+	of Grids	Δt (s)
1	Without a branch	5,000	5.00×10^{-3}	150	4,555,934	5.00×10^{-3}
2	Without a branch	5,000	7.07×10^{-3}	150	2,476,472	5.00×10^{-3}
3	Without a branch	5,000	1.00×10^{-2}	150	1,127,837	5.00×10^{-3}
4	Without a branch	5,000	1.41×10^{-2}	150	622,945	5.00×10^{-3}
5	Without a branch	5,000	2.00×10^{-2}	150	278,094	5.00×10^{-3}
6	Without a branch	5,000	7.07×10^{-3}	150	2,476,472	1.00×10^{-2}
7	Without a branch	5,000	7.07×10^{-3}	150	2,476,472	2.50×10^{-3}

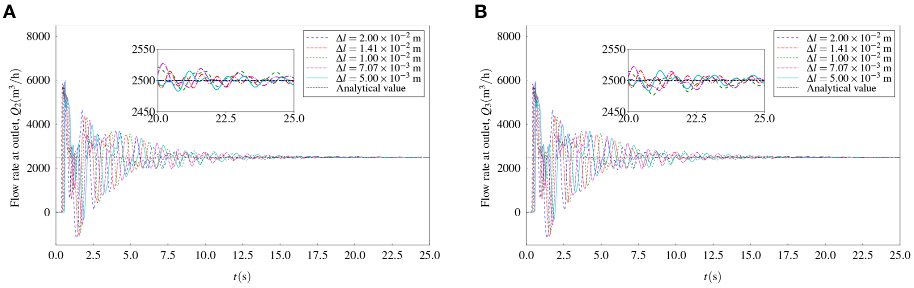

Spatial convergence of Q_2 Spatial convergence of Q_3

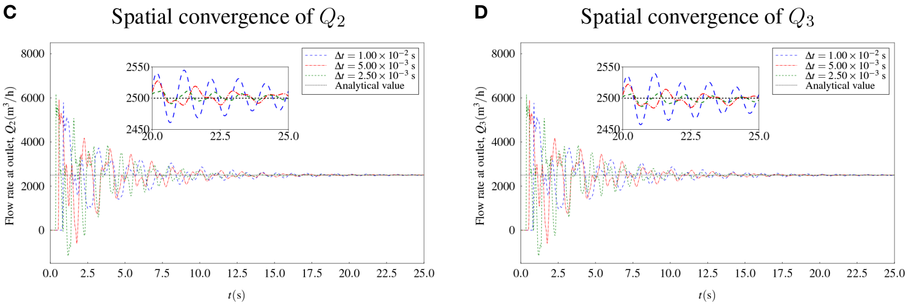

Temporal convergence of Q_2 Temporal convergence of Q_3

FIGURE 4
Convergence studies of flow rates on grid size **(A)** Spatial convergence of Q2 **(B)** Spatial convergence of Q3 **(C)** Temporal convergence of Q2 **(D)** Temporal convergence of Q3.

pressure can be observed near the perpendicular corners. A range of high pressure represented by red color was found due to the flow affecting the pipe wall. The influence of gravitational acceleration on pressure contours for the central section of the T-type was concluded as trivial.

To clearly show the detailed flow pattern inside the T-type pipe, a Line Integral Convolution (LIC) technology (Cabral and Leedom, 1993) was adopted. Based on the surface LIC algorithm, vectors defined on an arbitrary surface can be projected onto the surface and then from physical space into screen space where an image of LIC is computed. The LIC texture using velocity vectors with vorticity contours for the central section of the T-type is shown in Figure 9. Higher vorticity can be found near the corner at the connection of the inlet pipe and the outlet pipes. The influence of gravity on the flow field reduced the magnitude of vorticity near the upper corner.

In addition, the three-dimensional streamlines are extracted and presented in Figure 10. The flow fields are contoured by pressures. The streamlines started from the inlet, and laminar flow was found in the inlet segment of the T-type pipe. After the flow affecting the vertical wall surface, the streamlines began to rotate and twist and vortices were generated. With the limitation of the pipe wall, the water flow rotated along the *Zz*-axis and flushed out at the upper and lower outlet. It can also be observed that the streamlines differed a little for the two cases without and with gravity.

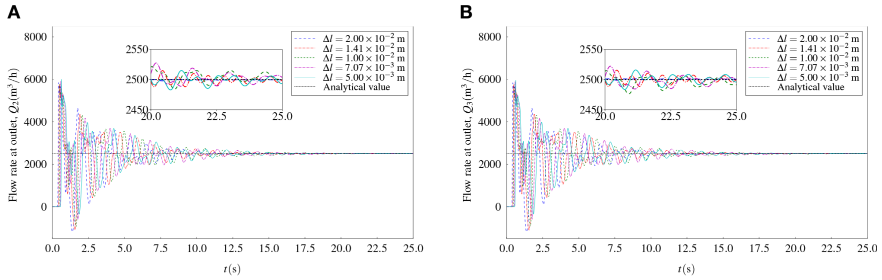

Spatial convergence of Q_2 Spatial convergence of Q_3

FIGURE 5
Results of convergence studies of flow rates **(A)** Results of spatial convergence **(B)** Results of temporal convergence.

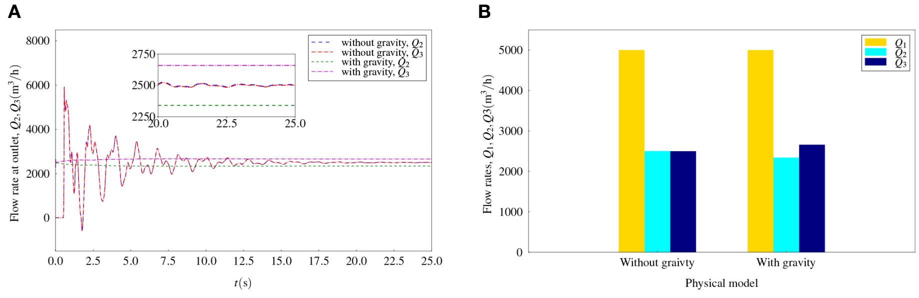

Time histories of flow rates

Flow rates at inlet and outlet

FIGURE 6
Flow rates for flows without and with gravity **(A)** Time histories of flow rates **(B)** Flow rates at inlet and outlet.

4.3 T-type pipe with a branch

The branch inlet was designed to control the flow rate inside the T-type pipe. Employing the best-practice settings, more studies were carried out to study the flow rates in the T-type pipe with a branch inlet. Two parameters were investigated for flow control, including the flow rate at the branch inlet and the included angle between the branch inlet pipe and the main inlet pipe.

The outflow rates Q_2 and Q_3 for the case without and with a branch inlet were compared. In this case, the included angle was fixed as $\alpha = 45°$. The flow rate at the main inlet pipe, Q_1, was fixed as 5,000 m$^{3/}$h. It was assumed that Q = 500m^3/h for flow rate at the branch inlet as an example, and time histories of flow rates at the upper and lower outlets and the final converged values are presented in Figures 11A, B, respectively. It can be concluded that the joint of the branch inlet flow leads to an increase in flow rates at both the upper and lower outlets. A new condition, i.e., $Q_1^{\}} = Q + Q_1 = Q_2 + Q_3$, has been satisfied. However, it is not enough to address the right flow rate at the branch inlet to balance the result of Q_2 and Q_3. Therefore, an interpolation process was carried out to determine the TBD value of Q. Six more cases were studied and the flow rate at the branch inlet Q ranged from 635 to 650 m^3/h. As shown in Figure 12, with the increase in flow rate at the branch inlet, the flow rate at the upper outlet tends to increase and that at the lower outlet tends to decrease. The intersection point crossing the curve of the ideal flow rate at each outlet should be the balance point. By using linear interpolation, the intersection point can be found as Q = 641.42m^3/h. Therefore, the flow rate Q_2 = 2,820.42m^3/h and $Q_{3\,=}$ 2,821.00m^3/h were obtained, which can be regarded as $Q_2 \approx Q_3$ within the error margin, and the ideal outflow rate was Q_t = 2820.71 m^3/h.

In the following studies, a change of the included angle of the branch inlet pipe, α, was applied to propose a flow control scheme to balance the outflow rates at the upper and lower outlet. Preliminary studies have been carried out for three included angles, i.e., α = 30°, 45°, and 60°. The same branch inlet flow rate Q = 650m^3/h was firstly applied to these cases to address the effect of the included angle of the branch inlet pipe. As shown in Figure 13A,

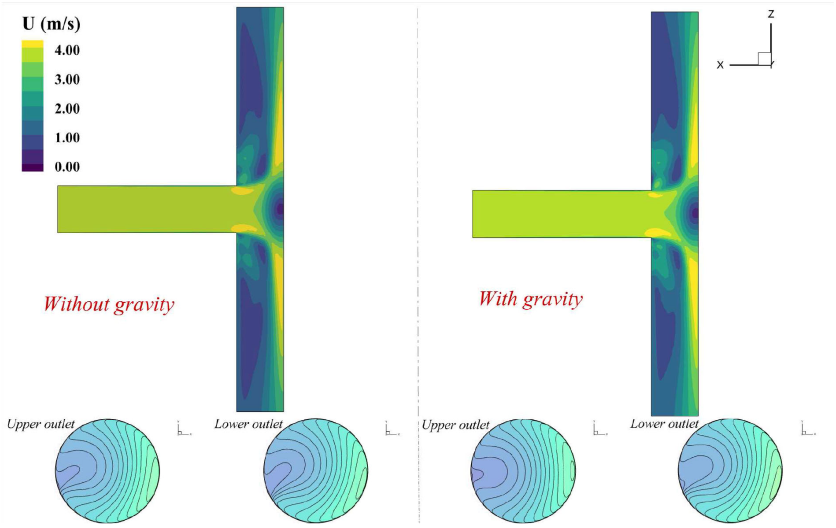

FIGURE 7
Contours of velocity field for flows without and with gravity.

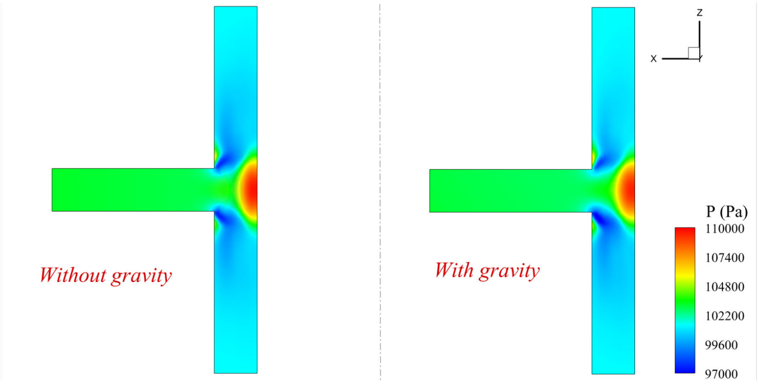

FIGURE 8
Contours of pressure field for flows without and with gravity.

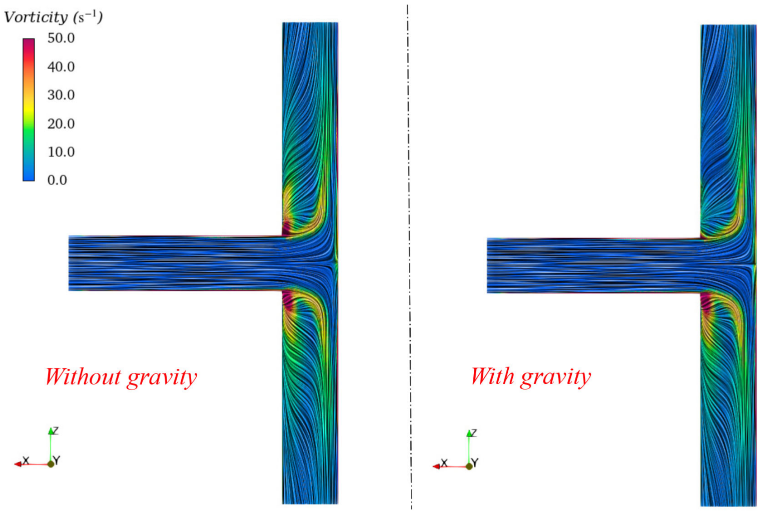

FIGURE 9
Contours of vorticity field with LIC for flows without and with gravity.

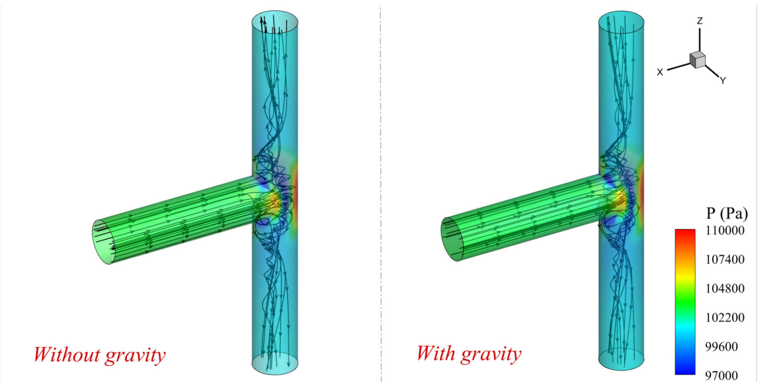

FIGURE 10
3-D streamlines for flows without and with gravity.

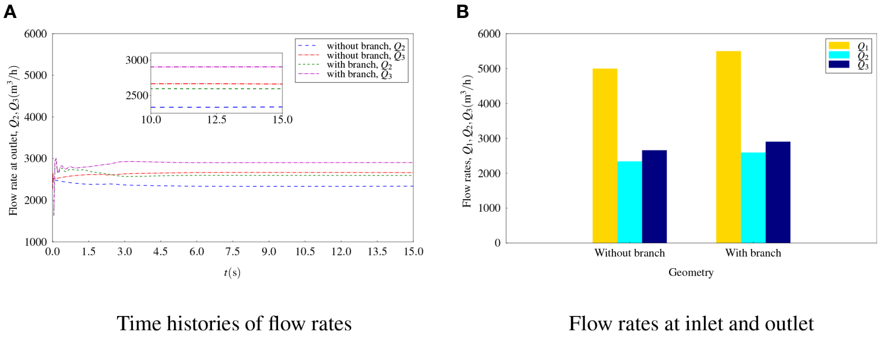

Time histories of flow rates

Flow rates at inlet and outlet

FIGURE 11
Flow rates for flows without and with a branch with a fixed angle **(A)** Time histories of flow rates. **(B)** Flow rates at inlet and outlet

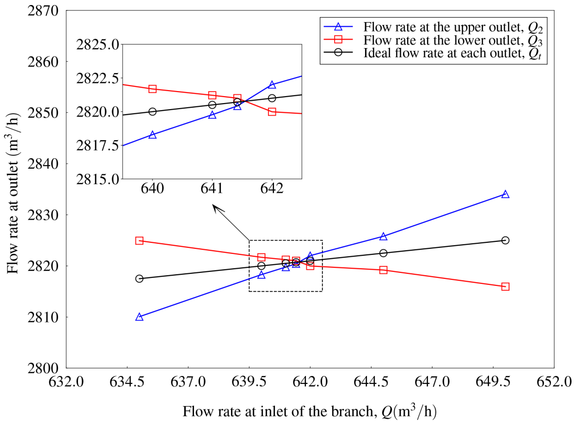

FIGURE 12
Flow rate at outlet with various flow rates at inlet of the branch (α = 45°).

time histories of the outflow rates at the upper and lower outlet converged along with the increase of simulation time. The final converged results as shown in Figure 13B were different for Q_2 and Q_3. $Q_2 < Q_3$ was observed for the results of $\alpha = 30°$. With the increase of the included angle, the flow rate Q_2 increased but the flow rate Q_3 decreased, while the flow rate of the branch inlet was fixed. For the included angle $\alpha = 45°$, $Q_2 > Q_3$. If the angle reached 60°C, the difference between Q_2 and Q_3 was quite large.

Similarly, interpolations were carried out to find out the balance point for the flow rate at the branch inlet with various included angles. The results for the case with $\alpha = 30°$ and $\alpha = 60°$ are shown in Figures 14, 15, respectively. For example, the error between Q_2 = 2835.06 m^3/h and Q_3 = 2835.16 m^3/h was less than 0.1\% (the ideal flow rate is 2835.11 m^3/h at the outlet as shown in Figure 14. It can be regarded as a balance flow rate at upper and lower outlets was obtained when the flow rate at the branch inlet was Q = 670.21m^3/h. Finally, the intersection points can be found as Q = 670.21m^3/h and Q = 505.98m^3/h for the case with $\alpha = 30°$ and $\alpha = 60°$, respectively.

Detailed flow fields for the T-type pipe with three included angles of the branch inlet pipe were analyzed by the present simulations. Note that the inflow rate at the balance point was presented. The contours of velocity field for the central section of the T-type and for the upper and lower outlet surfaces are shown and compared in Figure 16. For all the three cases, a high-speed inflow from the branch was obtained since the diameter of the branch inlet was much smaller than the diameter of the main inlet pipe. The high-speed inflow entering the main stream was then decelerated and the water flows in the outlet segment pipe became more turbulent. The velocity contours for the upper outlet and the lower outlet were changed due to the introduction of the branch

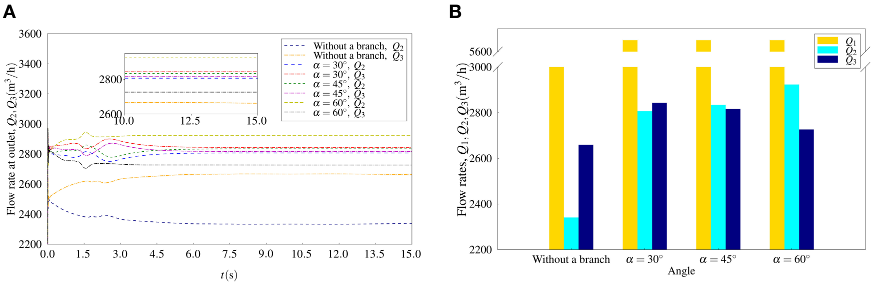

FIGURE 13
Flow rates for flows without and with a branch with various angles **(A)** Time histories of flow rates **(B)** Flow rates at inlet and outlet.

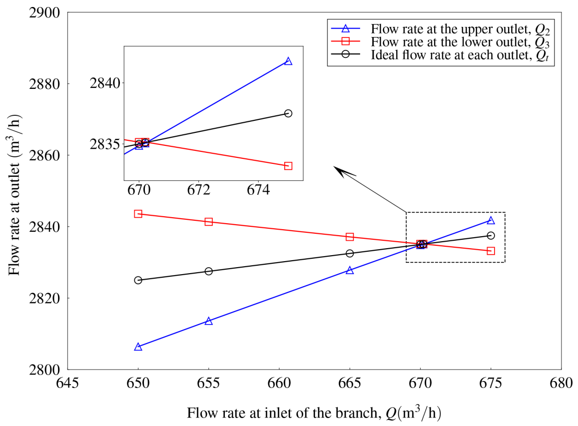

FIGURE 14
Flow rate at outlet with various flow rates at inlet of the branch (α = 30°).

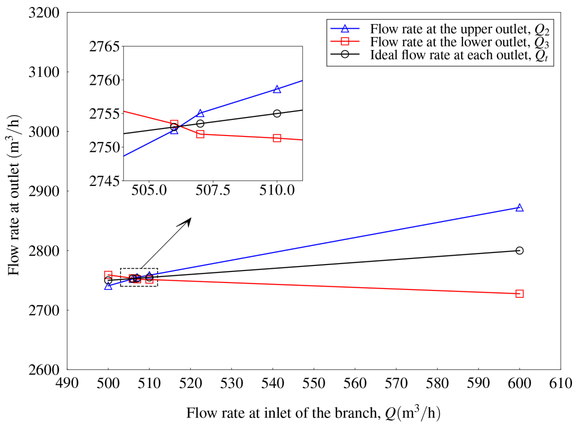

FIGURE 15
Flow rate at outlet with various flow rates at inlet of the branch (α = 60°).

inflow. In terms of the geometry of the branch, it can be seen that the flow velocity was quite asymmetrical for contours on the upper outlet and the lower outlet, especially for the case with an included angle α = 60°.

The pressure contours for the central section of the T-type with various included angles are shown in Figure 17. Two zones of low pressure can be observed near the perpendicular corners. The smaller the included angle was, the fewer changes in pressure distribution can be observed. For a large included angle, e.g., α = 60, the zone of low pressure was expanded and the original shape of high pressure was affected.

The LIC texture using velocity vectors with vorticity contours for the T-type with various included angles is shown in Figure 18. Vortices can be found near the corner at the connection of the inlet pipe and the outlet pipes, and the corner near the branch inlet pipe. The three-dimensional streamlines are extracted and presented in Figure 19, as well as the pressure contours. The streamlines rotated much more violently for the case with a large included angle like α = 60°. Compared with that of the flow in the upper segment pipe, the vorticity of the flow in the lower segment pipe was higher due to the effect of the branch inlet pipe.

5 Conclusions

In this paper, we studied the flow rates in a flow diverter, i.e., a T-type pipe, and its flow control using a special branch for water pumping systems in the cruising aquaculture vessel, Guoxin 1. To obtain a balanced oxygen supply for two farming tanks, a balanced water flow rate should be guaranteed if one pump is available. The flow rate at the outlet can be influenced by several factors, e.g., the gravitational acceleration, the flow rate at the branch inlet, and the included angle

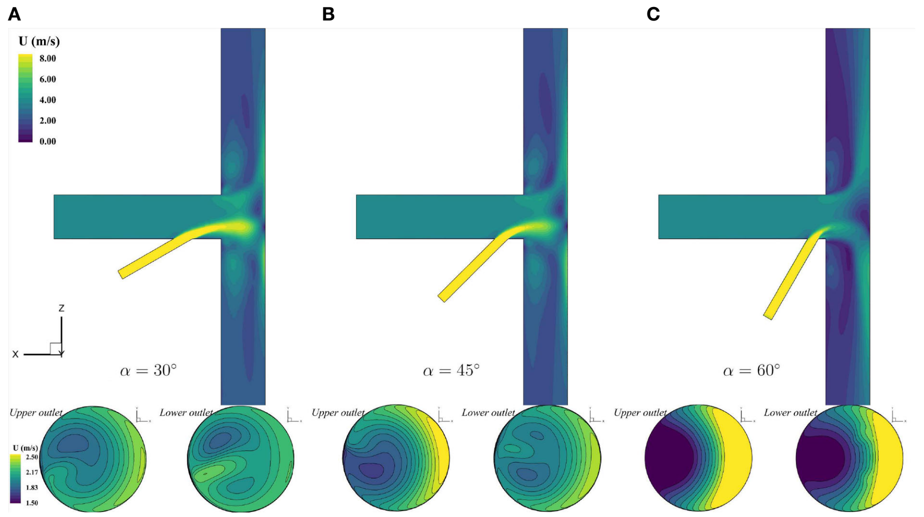

FIGURE 16
Contours of velocity field for flows with various angles **(A)** α = 30° **(B)** α = 45° **(C)** α = 60°.

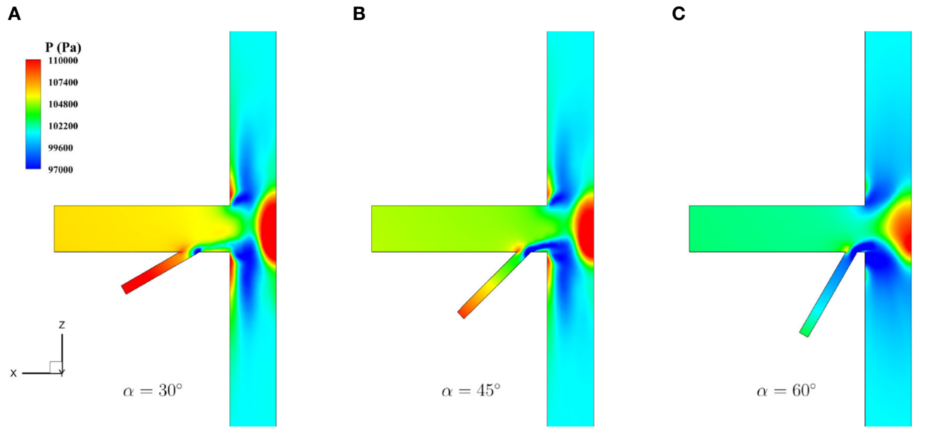

FIGURE 17
Contours of pressure field for flows with various angles **(A)** α = 30° **(B)** α = 45° **(C)** α = 60°.

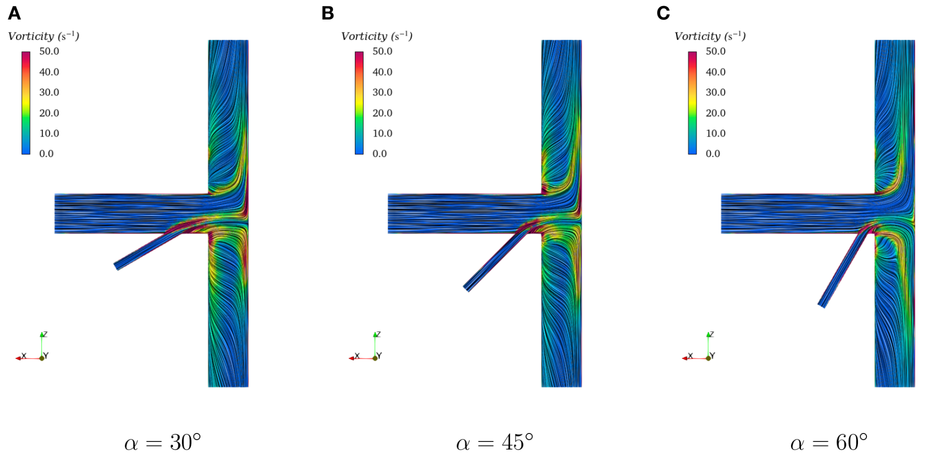

FIGURE 18
Contours of vorticity field with LIC for flows with various angles **(A)** α = 30° **(B)** α = 45° **(C)** α = 60°.

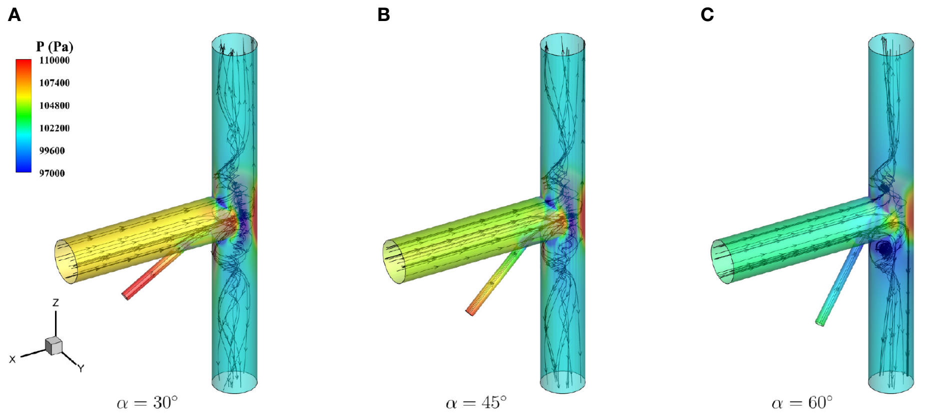

FIGURE 19
3-D streamlines for flows with various angles **(A)** α = 30° **(B)** α = 45° **(C)** α = 60°.

between the branch inlet pipe and the main inlet pipe. Equilibrium outflow rates were desired to efficiently supply the oxygen to different aquaculture tanks. The following conclusions can be drawn based on the numerical results in this work. The research of this paper can provide a reference for the oxygen supply between aquaculture tanks to maintain a healthy culturing environment.

1. Gravity would affect the unbalanced flow rate due to the altitude difference in multiple farm tanks, especially in cruising aquaculture vessels. According to the present three-dimensional simulations, the difference in flow rate at the upper and lower outlet could be as large as 12.8%.
2. It is reasonable for the flow control in the tee pipe to adopt a branch inlet with a small diameter and a high-speed water inflow. A balance point can be interpolated by adjusting the flow rate at the branch inlet to obtain equilibrium outflow rates in two outlets.
3. The branch inlet for flow control should be equipped with a reasonable included angle with the main inlet pipe. A high inflow rate at the branch inlet is required if the included angle was small. However, the advantage of a small included angle is the low impact of the additional flow on the flow patterns. It can be concluded that a low-speed inflow rate at the branch inlet for the branch with a large included angle is necessary while the flow field is significantly affected by the additional inlet flow.

Data availability statement

The raw data supporting the conclusions of this article will be made available by the authors, without undue reservation.

Author contributions

WH: Conceptualization, writing, reviewing, editing, and data analysis. RZ: Numerical simulations, supervision, writing, reviewing, and editing. All authors contributed to the article and approved the submitted version.

Funding

This work was financially supported by the National Key Research and Development Program of China (Grant No.2022YFD2401101), the Program of Qingdao National Laboratory for Marine Science and Technology (Grant No.2022QNLM030001-3), and the National Natural Science Foundation of China (Grant No. 52201394).

Conflict of interest

The authors declare that the research was conducted in the absence of any commercial or financial relationships that could be construed as a potential conflict of interest.

Publisher's note

References

Aryawan, W., and Putranto, T. (2018). The hydrodynamics performance of aquaculture fishing vessel in variation of deadrise angle and sponson. *Int. J. Mechanical Production* 8, 263–272. doi: 10.24247/ijmperdapr201829

Cabral, B., and Leedom, L. C. (1993). "Imaging vector fields using line integral convolution," in *Proceedings of the 20th annual conference on Computer graphics and interactive techniques*. 263–270. Association for Computing Machinery Anaheim, CA, United States

Chen, Y., Huang, W., Shan, X., Chen, J., Weng, H., Yang, T., et al. (2020). Growth characteristics of cage-cultured large yellow croaker larimichthys crocea. *Aquac. Rep.* 16, 100242. doi: 10.1016/j.aqrep.2019.100242

Costa, N., Maia, R., Proenca, M., and Pinho, F. (2006). Edge effects on the flow characteristics in a 90 deg tee junction. 128(6), 1204-1217 doi: 10.1115/1.2354524

Duarte, S., Reig, L., Masaló, I., Blanco, M., and Oca, J. (2011). Influence of tank geometry and flow pattern in fish distribution. *Aquac. Eng.* 44, 48–54. doi: 10.1016/j.aquaeng.2010.12.002

Editorial Staff (2022) *China Delivers guoxin 1, world's first tanker-sized aquaculture vessel that will produce more than 3,700 tons per year*. Available at: https://aquaculturemag.com/2022/06/10/china-delivers-guoxin-1-worlds-first-tanker-sized-aquaculture-vessel-that-will-produce-more-than-3700-tons-per-year/.

Edwards, K., and Finn, D. (2015). Generalised water flow rate control strategy for optimal part load operation of ground source heat pump systems. *Appl. Energy* 150, 50–60. doi: 10.1016/j.apenergy.2015.03.134

Faltinsen, O. (2017). Sloshing. *Adv. Mechanics* 47, 201701. doi: 10.6052/1000-0992-16-017

Guo, X., Li, Z., Cui, M., and Wang, B. (2020). Numerical investigation on flow characteristics of water in the fish tank on a force-rolling aquaculture platform. *Ocean Eng.* 217, 107936. doi: 10.1016/j.oceaneng.2020.107936

Han, F., Ong, M. C., Xing, Y., and Li, W. (2020). Three-dimensional numerical investigation of laminar flow in blind-tee pipes. *Ocean Eng.* 217, 107962. doi: 10.1016/j.oceaneng.2020.107962

He, Y. (2008). The euler implicit/explicit scheme for the 2d time-dependent navier-stokes equations with smooth or non-smooth initial data. *Mathematics Comput.* 77, 2097–2124. doi: 10.1090/S0025-5718-08-02127-3

Hvas, M., Folkedal, O., and Oppedal, F. (2021). Fish welfare in offshore salmon aquaculture. *Rev. Aquac.* 13, 836–852. doi: 10.1111/raq.12501

Kassem, T., Shahrour, I., El Khattabi, J., and Raslan, A. (2021). Smart and sustainable aquaculture farms. *Sustainability* 13, 10685. doi: 10.3390/su131910685

Lai, Y., So, R., Anwer, M., and Hwang, B. (1991). "Calculations of a curved-pipe flow using reynolds stress closure," in *Proceedings of the Institution of Mechanical Engineers, Part C: Mechanical Engineering Science*, Vol. 205. 231–244. SAGE Publications Sage UK: London, England

Launder, B. E., and Spalding, D. B. (1983). "The numerical computation of turbulent flows," in *Numerical prediction of flow, heat transfer, turbulence and combustion* (Elsevier), 96–116. Numerical Prediction of Flow. Heat Transfer, Turbulence and Combustion, 3

Lekang, O.-I. (2020). *Aquaculture engineering* (John Wiley & Sons) Norwegian University of Life Science, Blackwell Publishing.

Li, Z., Guo, X., and Cui, M. (2022). Numerical investigation of flow characteristics in a rearing tank aboard an aquaculture vessel. *Aquac. Eng.* 98, 102272. doi: 10.1016/j.aquaeng.2022.102272

Li, G., Pan, L., Hua, Q., Sun, L., and Lee, K. Y. (2019). Water pump control: A hybrid data-driven and model-assisted active disturbance rejection approach. *Water* 11, 1066. doi: 10.3390/w11051066

Ma, C., Zhao, Y.-P., and Bi, C.-W. (2022). Numerical study on hydrodynamic responses of a single-point moored vessel-shaped floating aquaculture platform in waves. *Aquac. Eng.* 96, 102216. doi: 10.1016/j.aquaeng.2021.102216

Mansi, F., Cannone, E. S. S., Caputi, A., De Maria, L., Lella, L., Cavone, D., et al. (2019). Occupational exposure on board fishing vessels: Risk assessments of biomechanical overload, noise and vibrations among worker on fishing vessels in southern italy. *Environments* 6, 127. doi: 10.3390/environments6120127

Masaló, I., and Oca, J. (2014). Hydrodynamics in a multivortex aquaculture tank: effect of baffles and water inlet characteristics. *Aquac. Eng.* 58, 69–76. doi: 10.1016/j.aquaeng.2013.11.001

Menter, F. R. (1994). Two-equation eddy-viscosity turbulence models for engineering applications. *AIAA J.* 32, 1598–1605. doi: 10.2514/3.12149

Mockett, C., Fuchs, M., and Thiele, F. (2012). Progress in des for wall-modelled les of complex internal flows. *Comput. Fluids* 65, 44–55. doi: 10.1016/j.compfluid.2012.03.014

Moukalled, F., Mangani, L., and Darwish, M. (2016). "The finite volume method," in *The finite volume method in computational fluid dynamics* (Springer), 103–135. Springer International Publishing

Oca, J., and Masaló, I. (2007). Design criteria for rotating flow cells in rectangular aquaculture tanks. *Aquac. Eng.* 36, 36–44. doi: 10.1016/j.aquaeng.2006.06.001

Oca, J., and Masalo, I. (2013). Flow pattern in aquaculture circular tanks: Influence of flow rate, water depth, and water inlet & outlet features. *Aquac. Eng.* 52, 65–72. doi: 10.1016/j.aquaeng.2012.09.002

Oca, J., Masaló, I., and Reig, L. (2004). Comparative analysis of flow patterns in aquaculture rectangular tanks with different water inlet characteristics. *Aquac. Eng.* 31, 221–236. doi: 10.1016/j.aquaeng.2004.04.002

Padala, A., and Zilber, S. (1991). "Expert systems and their use in aquaculture," in *Rotifer and microalgae culture systems. proceedings of a US-Asia workshop*, 221–227. Honolulu, HI the publisher is the Oceanic Institute.

Romli, M. A., Daud, S., Raof, R. A. A., Ahmad, Z. A., and Mahrom, N. (2018). Aquaponic growbed water level control using fog architecture. *J. Physics: Conf. Ser.* 1018, 012014. doi: 10.1088/1742-6596/1018/1/012014

Shih, T.-H., Liou, W. W., Shabbir, A., Yang, Z., and Zhu, J. (1994). A new k-epsilon eddy viscosity model for high reynolds number turbulent flows. Computers & Fluids. (Elsevier) 24(3), 227-238 doi: 10.1016/0045-7930(94)00032-T

Spalart, P., and Allmaras, S. (1992). "A one-equation turbulence model for aerodynamic flows," in *30th aerospace sciences meeting and exhibit*. 439. American Institute of Aeronautics and Astronautics Reno, NV, U.S.A.

Tello, M., e Silva, S. R., and Soares, C. G. (2011). Seakeeping performance of fishing vessels in irregular waves. *Ocean Eng.* 38, 763–773. doi: 10.1016/j.oceaneng.2010.12.020

The Fish Site (2020) *Chinese Start construction of 200,000-tonne mobile fish farm*. Available at: https://thefishsite.com/articles/chinese-start-construction-of-first-200-000-tonne-mobile-fish-farm.

Ullah, I., and Kim, D. (2018). An optimization scheme for water pump control in smart fish farm with efficient energy consumption. *Processes* 6, 65. doi: 10.3390/pr6060065

Urrea, C., and Páez, F. (2021). Design and comparison of strategies for level control in a nonlinear tank. *Processes* 9, 735. doi: 10.3390/pr9050735

Venkatakrishnan, V. (1995). Convergence to steady state solutions of the euler equations on unstructured grids with limiters. *J. Comput. Phys.* 118, 120–130. doi: 10.1006/jcph.1995.1084

Wilcox, D. C. (2008). Formulation of the kw turbulence model revisited. *AIAA J.* 46, 2823–2838. doi: 10.2514/1.36541

Xue, B., Zhao, Y., Bi, C., Cheng, Y., Ren, X., and Liu, Y. (2022). Investigation of flow field and pollutant particle distribution in the aquaculture tank for fish farming based on computational fluid dynamics. *Comput. Electron. Agric.* 200, 107243. doi: 10.1016/j.compag.2022.107243

Zhang, S.-Y., Li, G., Wu, H.-B., Liu, X.-G., Yao, Y.-H., Tao, L., et al. (2011). An integrated recirculating aquaculture system (RAS) for land-based fish farming: The effects on water quality and fish production. *Aquac. Eng.* (Elsevier) 45(3), 93-102. doi: 10.1016/j.aquaeng.2011.08.001

Zhao, Y., Xue, B., Bi, C., Ren, X., and Liu, Y. (2022). Influence mechanisms of macro-infrastructure on micro-environments in the recirculating aquaculture system and biofloc technology system. *Rev. Aquac.*. doi: 10.1111/raq.12713

Zhou, M., Kulenovic, R., and Laurien, E. (2019). "Large-Eddy simulation of thermal-mixing pipe-flow close to a horizontal t-junction with flow-rate variations in the branch pipe," in *International Congress on Advances in Nuclear Power Plants, ICAPP2019*. American Nuclear Society Juan-les-pins, France 12-15

Frontiers in Marine Science

TYPE Original Research
PUBLISHED 16 March 2023
DOI 10.3389/fmars.2023.1134888

EDITED BY
Zhao Yunpeng,
Dalian University of Technology, China

REVIEWED BY
Changsu Xu,
Northeast Agricultural University, China
Peng Li,
Harbin Engineering University, China

*CORRESPONDENCE
Guochen Zhang
zhangguochen@dlou.edu.cn
Xiuchen Li
lxc@dlou.edu.cn

†These authors have contributed equally to this work and share first authorship

SPECIALTY SECTION
This article was submitted to Marine Fisheries, Aquaculture and Living Resources, a section of the journal Frontiers in Marine Science

RECEIVED 31 December 2022
ACCEPTED 20 February 2023
PUBLISHED 16 March 2023

CITATION
Li H, Mu G, Zhang H, Wu H, Liu F, Sun Z, Zhang Q, Wang Y, Wang Y, Li X and Zhang G (2023) Design and testing of a mechanized brush-screen cooperative vibration harvester for mudflat-buried shellfish based on the discrete element method.
Front. Mar. Sci. 10:1134888.
doi: 10.3389/fmars.2023.1134888

Design and testing of a mechanized brush-screen cooperative vibration harvester for mudflat-buried shellfish based on the discrete element method

Hangqi Li[1†], Gang Mu[2†], Hanbing Zhang[2], Hao Wu[1], Fawei Liu[2], Zhenyin Sun[2], Qian Zhang[2], Yizhou Wang[2], Yurui Wang[2], Xiuchen Li[2*] and Guochen Zhang[1,2*]

[1]College of Engineering, Shenyang Agricultural University, Shenyang, China, [2]College of Mechanical and Power Engineering, Dalian Ocean University, Dalian, China

Introduction: To enhance the application of mechanized harvesting and supplement research on harvesting theory in mudflat-buried shellfish harvesting in China, a brush-screen cooperative mudflat-buried shellfish vibration harvester was designed.

Methods: The harvester is primarily composed of a crank rocker double-layer vibrating screen, two stage rolling brush, and a conveyor chain. White clams (*Mactra veneriformis*) cultured in mudflats were used as the research objects in this paper, and the mechanics and motion states of the shellfish on the vibrating screen were analyzed. The shellfish harvesting simulation response surface experiments based on the discrete element method (DEM) were conducted to analyze the influence of the main operating parameters on the quantity of shellfish harvested.

Results: The results revealed that the number of shellfish harvested was significantly influenced ($p < 0.01$) by vibrating screen amplitude, first-stage spiral rolling stainless steel brush rotation rate, and harvester travel speed. The optimal combination of key parameters was 1.4 mm, 40 rpm, and 10 m/min, respectively. With these values, the projected shellfish crushing rate was 2.82% and the shellfish harvesting efficiency was 125 pieces/m^2. The equipment was then manufactured and the shellfish harvesting verification test was performed under the same operating parameters as the simulation. Test results indicated that the harvesting efficiency of the equipment was 114 pieces/m^2 and the shellfish crushing rate was 6.97%.

Discussion: The shellfish harvesting work could be completed by the equipment effectively and with low loss. The results of this study provide a theoretical reference for a novel mechanized method of harvesting mudflat-buried shellfish.

KEYWORDS

mudflat-buried shellfish, vibratory screening, discrete element simulation, Mechanization harvester, response surface experiments

1 Introduction

Shellfish aquaculture is a key sector in the fisheries industry of China, with a production of 15 million tons in 2021 (Fisheries Administration Bureau of Ministry of Agriculture China, 2022). It accounts for 28.7% of total fishery aquaculture production nationwide and has significantly advanced the economic development of fishery aquaculture in China. Mudflats serve as the principal habitat for shellfish, and the area of mudflat shellfish culture in China was 562 thousand hectares in 2021 (Fisheries Administration Bureau of Ministry of Agriculture China, 2022). Shellfish production is directly influenced by harvesting efficiency, which is a crucial factor in shellfish culture. Traditional mudflat-buried shellfish (shellfish) harvesting is mostly performed manually and is ineffective, labor intensive, and involves high labor costs, among other drawbacks. This makes manual harvesting unsuitable for the large-scale aquaculture of shellfish.

Through years of development, commercial dredge (Miguel B. Gaspar et al., 2002; Yamasaki et al., 2002) and hydraulic dredge has become widely employed (Mu et al., 2020). It utilizes high-pressure water jets on the seafloor to spread the sediment and then catch shellfish using nets with rake teeth. Hydraulic dredge can be classified into several types, such as the hydraulic clam rake dredge (Glude et al., 1952), hydraulic escalator dredge (Kyte and Chew, 1975; Coen, 1995), hydraulic suction dredge (Meyer et al., 1981; Smolowitz, 1982; Morello et al., 2005; Fahy and Carroll, 2007), or tractor dredge (Hall et al., 1990; Beukema, 1995; Hall and Harding, 1997; Robinson and Richardson, 1998), depending on the depth of the marine environment. Despite the high efficiency of hydraulic dredge, it has been banned in China due to its negative impact on sustainable shellfish production (China, M. O. A, 2013), including the choking and death of shellfish, poor selectivity, and loss of mudflat sediment. Rotary tooth dredging and hydraulic vibratory dredging are the two basic categories of mechanized dredging method. The rotary tooth mechanized dredge is a type of bottom equipment towed by a fishing boat that is mainly used to catch buried shellfish and convey them to netting gear. Three main types of tooth harvesters include spring-loaded teeth (Haven et al., 1973; Haven et al., 1979), rotating conveyors (Collier and McLaughlin, 1983), and rotating drum teeth (Badino et al., 2004), depending on the rake tooth arrangement. Rotary tooth mechanized dredge offer low dragging resistance, high production, and adequate selectivity. However, their structure is more complex, they consume more energy, and they disturb the natural habitat of the seafloor. The development of vibratory harvesters has attracted much attention as shellfish production has grown in scope. Vibratory harvesting softens the mudflat sediment by using mechanized stimulation, and then the vibration of the mesh screen encourages the separation of shellfish and sediment as well as the subsequent collection of shellfish in the meshing gear. Vibratory harvesting offers several advantages such as high production, good selectivity, low ecological impact, etc. The hydraulic vibratory dredge manufactured in Netherlands, and the mixture of shellfish and sediment was rinsed with seawater by nozzles, and the shellfish was screened with a vibrating device in harvesting progress. (Rambaldi et al., 2001). The crank-rocker mechanism caused high-frequency vibration of the fixed rake teeth, which loosened the sediment and allowed the shellfish to be harvested and conveyed to the deck. The ebb tide bare mudflat clam vibratory harvester, designed by Dewey, lowered the cost of harvesting manila clams (*Ruditapes philippinarum*) by 3-5% (Pacific Shellfish Institute, 2014). The scale of manila clam farming on the west coast of the United States has increased by a considerable 40% in recent years due to the application of the vibratory harvester (Saurel et al., 2014). The British Columbia Shellfish Growers Association of Canada assessed the effects of the shellfish vibratory harvester manufactured by Taylor Shellfish Ltd. on mudflat ecology and found no appreciable difference between the environmental effects of manual harvesting and vibratory harvesting. The impact of vibratory harvesting was even less severe than that of natural factors such as wind and waves (Hoyseth, 2009; Stirling, 2013; Landry, 2017). The Nantong Agricultural Mechanization Technology Promotion Center in Jiangsu Province, China, manufactured a self-propelled hard clam (*Meretrix meretrix*) harvester that was towed by a crawler (Lu et al., 2021). The hard clams were first shoveled up along with sediment by the shovel plate teeth. Then, the hard clams were cleaned, screened, and conveyed with the aid of three cleaning roller brushes and a conveyor chain. Finally, the hard clams that met the harvesting specifications were conveyed into a collection basket. In summary, several researches from various countries worldwide have investigated shellfish harvesters and the mechanization of shellfish harvesting. There are now excellent evaluation systems for mudflat sediment damage, biological behavior, and water quality changes. However, the study of mechanized shellfish harvesting in China is rudimentary and still in the early stages of empirical design and testing. Several issues still require addressing, including the insufficient application of mechanized shellfish harvesting, paucity of research on harvesting theory, absence of design and manufacturing experience, and weak ecological evaluation system for mudflats. Consequently, shellfish harvesters and methods have become one of the fundamental factors limiting the healthy and sustainable development of the shellfish aquaculture industry in China (Mu et al., 2020).

To address the above issues, a brush-screen cooperative shellfish vibratory harvester was designed, and white clams (*Mactra veneriformis*) cultured in mudflats were used as the research objects. Besides, mechanics and kinematic models of shellfish on the vibrating screen were established through theoretical analysis. Mechanized shellfish harvesting was simulated using a combination of the discrete element method (DEM) and the response surface method, thereby achieving the design of the main harvesting mechanism and determining the operating parameters. After the simulations were completed, a shellfish vibratory harvester was manufactured and shellfish harvesting verification tests were conducted on shellfish farming mudflats. This project serves as a reference for the design and development of mechanized shellfish harvesters.

2 Harvesting structure and working principles

An illustration of the shellfish vibratory harvester is shown in Figure 1. The harvester is mainly composed of a first-stage spiral rolling stainless steel brush (first-stage brush), crank rocker double-layer vibrating screen, second-stage rolling plastic brush (second-stage brush), conveying chain, shellfish collection basket, power system, steering device, and other components. When the harvester is working, the harvesting depth of the vibrating screen can be manually adjusted using a handle according to the depth of the buried shellfish. Because mudflat sediment has high water content and easily clumps together, it can be efficiently screened and conveyed with the combined use of a first-stage brush, second-stage brush, and crank rocker type double-layer vibrating screen. The first layer vibrating screen works in tandem with the first-stage brush to excavate, loosen, and shovel the mudflat sediment and shellfish mixture into the first layer vibrating screen to realize the excavation and preliminary screening. The second-stage brush is placed at the connecting point of the first and second layers of the vibrating screen to crush the unbroken large pieces of sediment from the first layer vibrating screen and sweep the shellfish into the second layer vibrating screen. The mudflat sediment and juvenile shellfish are mostly screened out in the second layer vibrating screen, while the shellfish of the required size are retained for harvesting by being transferred to the conveyor chain at the end of the second layer vibrating screen. The screened shellfish are then transported along the conveying chain to the collection basket, thereby completing the harvesting process. To avoid mechanical interference between the screens during the reciprocating screening process of the double-layer vibrating screen and according to the design demand of each vibrating screen layer, the structure of each layer vibrating screen is designed with two inclination angles. Thus, the inclination angles of the tail ends of the first and second layers are equal.

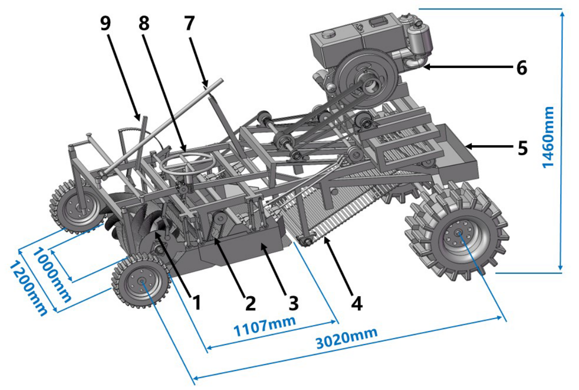

FIGURE 1
Structural diagram of the shellfish vibrating harvester. 1. First-stage brush; 2. Second-stage brush; 3. Crank rocker double-layer vibrating screen; 4. Conveying chain; 5. Shellfish collection basket; 6. Power system; 7. Steering device; 8. Catch depth adjustment handle; 9. First-stage brush adjustment device.

3 Motion analysis of shellfish on the vibrating screen

The crank rocker double-layer vibrating screen, an essential component of the vibratory shellfish harvester, mainly consists of a cylinder strip swing separating screen, an eccentric mechanism (eccentric bearing, bearing seat), a swing rod, and connecting rod, among other parts. The screening effect on the sediment and shellfish is directly influenced by the structural parameters and operating parameters of the crank rocker double-layer vibration screen. The screen is simplified into a planar six-rod mechanism, which comprises a crank rocker mechanism combined with a parallelogram mechanism, as shown in Figure 2. The cylinder strip swing separating screen (BC) is hinged on the frame through the front and rear pendulum (BE and CD), the crank (OA) performs a uniform circular motion with angular velocity ω, and the connecting rod AB pushes the cylinder strip swing separating screen (BC) to perform a reciprocating motion.

The force and relative motion state of a single shellfish mass on the vibrating screen were analyzed, ignoring the tumbling of the shellfish and their contact with one another. As Figure 3 shows, the principal forces acting on the shellfish on the vibrating screen are the screen surface support force F_n, gravity G, screen surface friction force F_f, and inertia force P. The movement of the shellfish is determined by the direction of the combined force on the shellfish. Due to uncertainty in the motion state of the shellfish on the vibrating screen, a motion analysis was carried out to obtain the displacement, velocity, and acceleration equations of the vibrating screen.

Displacement of the vibrating screen (x):

$$x = r\cos\omega t\,. \tag{1}$$

The velocity of the vibrating screen (v):

$$v = -\omega r\sin\omega t\,. \tag{2}$$

Acceleration of the vibrating screen (a):

$$a = -\omega^2 r\cos\omega t\,. \tag{3}$$

where α is the screen inclination angle (°), r represents the crank length (m), ω denotes the crank angular velocity (rad/s), and t is the time (s).

In the shellfish harvesting process, the motion state of the shellfish on the vibrating screen can be divided into backward sliding (sliding toward the tail point B of the vibrating screen), forward sliding (sliding toward the front point C), and jumping states. Force analysis of the shellfish under the backward and forward sliding limit conditions is displayed in Figure 3. According to the results of the shellfish force analysis, the following conditions should be satisfied when the material slides forward, slides backward, or jumps on the vibrating screen.

When the shellfish slides forward, as shown in Figure 3A, the direction of inertia force is downward along the direction of vibration, and the acceleration is positive.

$$P\cos(\epsilon - \alpha) + G\sin\alpha - F_f > 0, \tag{4}$$

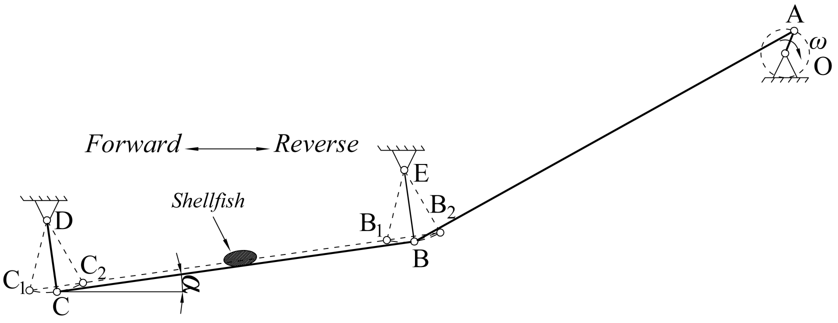

FIGURE 2
Vibrating screen mechanism diagram.

$$Gsin\alpha + Psin(\epsilon - \alpha) - F_n = 0, \quad (5)$$

$$F_f = \mu F_n, \quad (6)$$

$$\mu = tan\varphi, \quad (7)$$

$$P = m\omega^2 rcos\omega t\,. \quad (8)$$

Combining Equations 4-8 yields Equation 9:

$$\omega^2 rcos\omega tcos(\epsilon - \alpha + \varphi) > gsin(\varphi - \alpha), \quad (9)$$

where m denotes the shellfish mass (kg), ϵ represents the horizontal swing direction angle (°), α is the inclination angle of the vibrating screen with a value range of 5-14°, μ signifies the static friction coefficient between the vibrating screen and the shellfish, φ represents the static friction angle between the vibrating screen and the shellfish (°), and g is the acceleration due to gravity (m/s^2).

When the shellfish slides backward, as shown in Figure 3B, the inertia force direction is upward along the direction of vibration.

$$Pcos(\epsilon - \alpha) - Gcos\alpha - F_f > 0, \quad (10)$$

$$Psin(\epsilon - \alpha) + F_n = Gcos\alpha, \quad (11)$$

$$F_f = \mu F_n\,. \quad (12)$$

Equation 13 is generated by combining Equations 10-12:

$$\omega^2 rcos\omega tcos(\epsilon - \alpha - \varphi) > gsin(\varphi + \alpha)\,. \quad (13)$$

When the shellfish jumps, the conditions required for the shellfish to leave the vibrating screen are expressed using Equation 14:

$$F_n = Gcos\alpha - Psin(\epsilon - \alpha) < 0, \quad (14)$$

which can be simplified as:

$$gcos\alpha < \omega^2 rcos\omega tsin(\epsilon - \alpha)\,. \quad (15)$$

The motion index D characterizes the motion state of the shellfish and makes it easier to analyze the impact of each structural parameter on the shellfish motion state.

Shellfish forward motion index D_f:

$$D_f = K\frac{cos(\epsilon - \alpha + \varphi)}{sin(\varphi - \alpha)}\,. \quad (16)$$

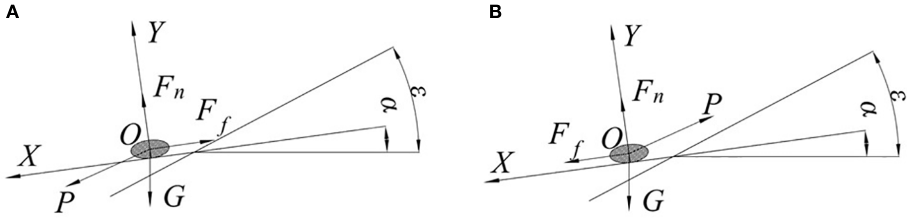

FIGURE 3
Force analysis of the shellfish motion state on the vibrating screen: **(A)** shellfish slides forward, **(B)** shellfish slides backward. The horizontal direction of the vibrating screen is set as the X-axis positive direction, while upward on the vertical screen surface is set as the Y-axis positive direction.

Shellfish backward motion index D_b:

$$D_b = K\frac{cos(\epsilon-\alpha-\varphi)}{sin(\varphi+\alpha)}. \quad (17)$$

Shellfish jumping motion index D_j:

$$D_j = K\frac{sin(\epsilon-\alpha)}{cos\alpha}, \quad (18)$$

$$K = \frac{\omega^2 r}{g}, \quad (19)$$

where K denotes vibration intensity.

From Equations 17-19, it can be observed that the motion index D of the shellfish on the vibration screen is related to α, ϵ, r, ω, and φ. Due to the high-water content of mudflat sediment, it is difficult to separate shellfish and sediment. Thus, to improve screening efficiency, the shellfish and sediment mixture must undergo double movement on the vibration screen to increase the screening time, and ensure that D_b is greater than D_f. To improve the efficiency of shellfish conveying, the difference between D_b and D_f should be maximized. This leads to an increase in D_j, shortens the shellfish harvesting time, and improves shellfish conveying efficiency.

The average static friction angle (φ) between the shellfish and the vibrating screen surface (stainless steel) was measured using the inclined plate method ($\varphi = 25°$) (González-Montellano et al., 2012; Ramírez-Gómez et al., 2014). According to the empirical value of the picker design and the size of the harvester structure, the structural parameters were chosen as r = 0.01 m, ω = 30 rad/s, and $\epsilon_1 = 30°$ for the first layer, $\epsilon_2 = 35°$ for the second layer of the vibrating screen. The range of values for α is 5-14°. Figure 4 illustrates the change curve of the shellfish motion index (D) on the vibrating screen under various screen inclination angles (α).

As Figure 4 reveals, the D_b value of the shellfish on the vibrating screen gradually decreases with increasing α, while D_f steadily increases as α rises. Additionally, D_j falls slightly with an increase in α, but the change is insignificant. To improve the shellfish harvesting efficiency in the first layer of the vibrating screen and reduce harvesting energy consumption, it is necessary to reduce the length of the front section of the vibrating screen that receives the excavated mudflat sediment and increase the inclination of the front section in the first layer of the vibrating screen. Thus, we set the inclination of the front section in the first layer of the vibrating screen as $\alpha_{1-1} = 11°$ and the inclination of the screen at the tail end to $\alpha_{1-2} = 8°$. To improve the efficiency of shellfish screening and conveying in the second layer of the vibrating screen, the inclination of the front section in the second layer of the vibrating screen was set as $\alpha_{2-1} = 8°$, while the inclination of the screen at the tail end was selected as $\alpha_{2-2} = 5°$.

4 Shellfish harvesting DEM simulation

4.1 DEM modeling of shellfish harvesting

In this study, the mudflat sediments and white clams in the shellfish culture area of Panjin City, Liaoning Province, China (40°42′4″N, 121°8′56″E) were used as the research objects. The mudflat DEM models (white clam DEM model (Mu, 2019; Liu et al., 2020; Li et al., 2021) and mudflat sediment DEM model (Asaf et al., 2007; Bahrami et al., 2020) were established accurately using EDEM software (EDEM, 2018, DEM Solutions Ltd., Edinburgh, UK), as Table 1 shows. According to shellfish harvesting requirements, stainless steel (Cabiscol et al., 2018; Bahrami et al., 2020) and plastic were selected as the contact material. Besides, the simulation contact parameters are shown in Table 2.

To improve simulation efficiency, the diameter of the mudflat sediment DEM model (x_1 = 0.14mm) was proportionally enlarged by five times to reduce the total number of particles in the soil box. In EDEM software, a virtual plane (length, width: 980mm, 190mm) was added 200mm above the soil box (length, width, and height: 1000 mm, 200 mm, and 200 mm) and two particle factories (30 pieces of shellfish particles and 60,000 pieces of mudflat sediment particles) were added to the virtual plane. The shellfish and mudflat

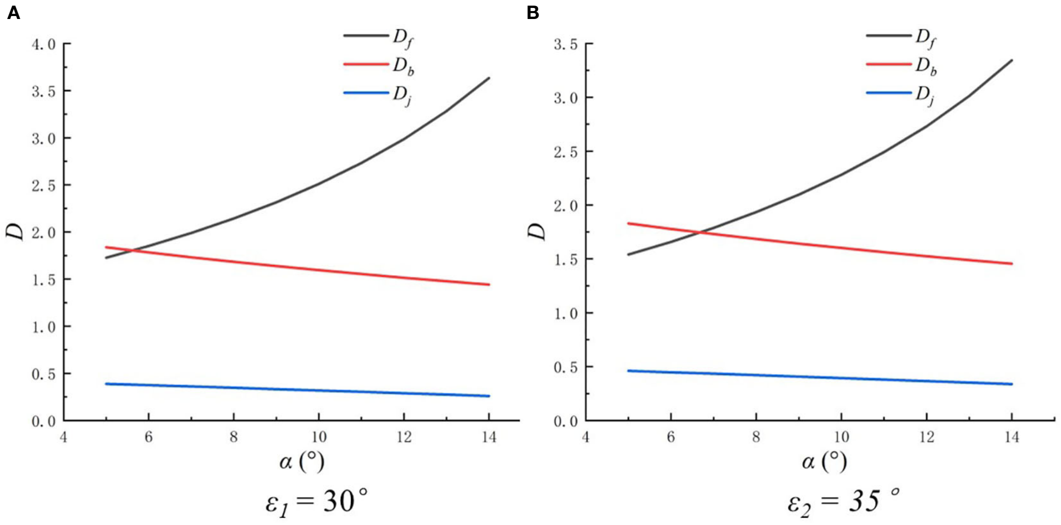

FIGURE 4
The shellfish motion index change curve under different horizontal swing direction angles: **(A)** $\epsilon_1 = 30°$, **(B)** $\epsilon_2 = 35°$.

TABLE 1 Characteristic material parameters for white clams (CL), stainless steel (SS), plastic (PA), and mudflat sediment (MS).

Property	Symbol				Value			
	CL	SS	PL	MS	CL	SS	PA	MS
Poisson's ratio	μ_P	μ_{SS}	μ_{PL}	μ_{MS}	0.33	0.31	0.34	0.30
Elasticity modulus (GPa)	E_P	E_{SS}	E_{PL}	E_{MS}	0.15	190.00	2.32	83.00
Density (g·mm^{-3})	ρ_P	ρ_{SS}	ρ_{PL}	ρ_{MS}	1.58	7.86	1.13	2.05

TABLE 2 Simulation contact parameters of different DEM models.

Parameters	MS-MS	MS-SS	MS-CL	CL-SS	CL-CL	PA-CL	PA-MS
Coefficient of restitution (e)	0.30	0.50	0.10	0.38	0.32	0.38	0.50
Coefficient of static friction (μs)	0.50	0.83	0.10	0.23	1.25	0.23	0.83
Coefficient of rolling friction (μ_r)	0.30	0.15	0.30	0.34	0.33	0.34	0.15
JKR surface energy (J·m^{-2})	8.11	0.00	0.00	0.00	0.00	0.00	0.00

JKR surface energy is often applied to simulate cohesion between fine and moist particles (Johnson et al., 1971).

sediment particles were evenly distributed in the soil box at the same time with an initial velocity of 5m/s, and the mudflat DEM model was established, as shown in Figure 5.

The three-dimensional structure of the shellfish vibratory harvester was simplified. Ultimately, only the essential components were retained, including the double-layer vibrating screen, first-stage brush, second-stage brush, conveying chain, and collection basket. The width of the vibrating screen was also reduced to 200 mm (reduction ratio 5:1).

The simplified three-dimensional structures of the harvester were imported into EDEM software, then the inclination angles of the first and second vibrating screens were set according to the results obtained in Section 2. The axle centers of the first-stage brush and second-stage brush were subsequently added with the clockwise rotation motions respectively, the second-stage brush's rotation rate was same as the first-stage brush's rotation rate (Table 3). And two linear reciprocating motions (frequency: 15 Hz, Reciprocal motion displacement: 20 mm, amplitude in Table 3) were added to the double-layer vibrating screen, the conveyor speed was 0.2m/s. Further, a linear motion (parallel to the conveyor surface toward the oblique rear) was added to the conveying chain, and the linear motion in X- direction was added to all simplified key structures, respectively, and set the travel speed (Table 3).

To reduce the simulation time, the shellfish was defined to have been harvested upon reaching the end of the second layer vibrating screen. To count the quantity of shellfish harvested, a grin bin group was added to the tail of the equipment, as shown in Figure 5.

Electronic universal testing equipment was used to determine that the least force required to break a shellfish was 86 N and that a shellfish was damaged when it was subjected to a force greater than 80 N during the harvesting simulation process. To measure the

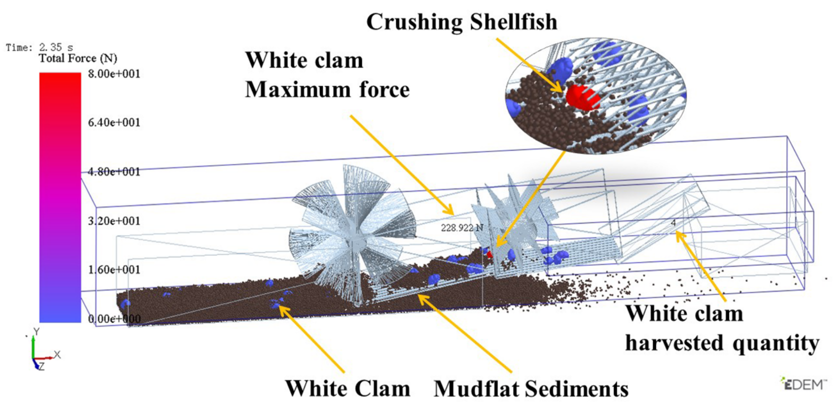

FIGURE 5
DEM simulation of shellfish vibratory harvesting.

TABLE 3 Single-factor test for clam harvesting simulation.

Level	First-stage brush rotation rate (rpm)	Amplitude (mm)	Travel speed (m/min)
1	18	0.8	7
2	27	1.2	8
3	36	1.6	9
4	45	2.0	10

maximum force of shellfish during the harvesting process, a grin bin group was added to the whole soil box. According to the shellfish force value, the number of shellfish forces greater than 80 N was counted, and the shellfish crushing rate was calculated. A reference legend representing the force applied to the shellfish was inserted on the left side of Figure 5 and run throughout the simulation. The force applied during the harvesting process was judged by where and how the shellfish were crushed by observing the change in color of the shellfish surface.

4.2 Shellfish harvesting single factor simulation test

4.2.1 Materials and methods

The yield of shellfish, screening effectiveness, and harvesting area was affected directly by the structure and operating paraments of the harvester. The parameters included the first-stage brush rotation rate, harvester travel speed, vibrating screen amplitude (vibration along the y-axis direction), etc.

The design of the single-component simulation for shellfish harvesting is presented in Table 3. The factor rotation method was used to determine the optimal range of values for each factor and the test indexes were the quantity of shellfish harvested and the shellfish crushing rate ϕ_c (Equation 18). The optimal range of values for each factor was obtained using the factor rotation method.

$$\varnothing_c = \frac{N_c}{N_t} \times 100\,\%, \tag{20}$$

where N_c represents the number of crushed shellfish and $N_t$is the quantity of total shellfish harvested, according to the EDEM software.

4.2.2 Results and analysis

4.2.2.1 Influence of first-stage brush rotation rate

The quantity of shellfish harvested first increased and then decreased when the rotational rate of the first-stage brush increased and all other conditions remained constant. The maximum number of shellfish harvested was 14 pieces when the rotation rate of the first-stage brush was 27 rpm, as Figure 6 indicates. Additionally, the shellfish crushing rate initially declined and then grew as the first-stage brush rotational rate increased. When the first-stage brush rotational rate was 36 rpm, the shellfish crushing rate was 0%. Under the same conditions, the volume of mudflat sediment cut per unit of time was higher at a slow first-stage brush rotational rate. This made it more difficult to screen the shellfish and sediment effectively, thereby reducing the harvesting efficiency. Conversely, when the first-stage brush rotational rate was faster, the volume of sediment cut decreased and the efficiency of the vibrating screen increased. However, the shellfish were more easily broken by the brush, thus increasing the shellfish crushing rate. By considering the number of shellfish harvested and the shellfish crushing rate, the ideal first-stage brush rotational rate range was 27-45 rpm.

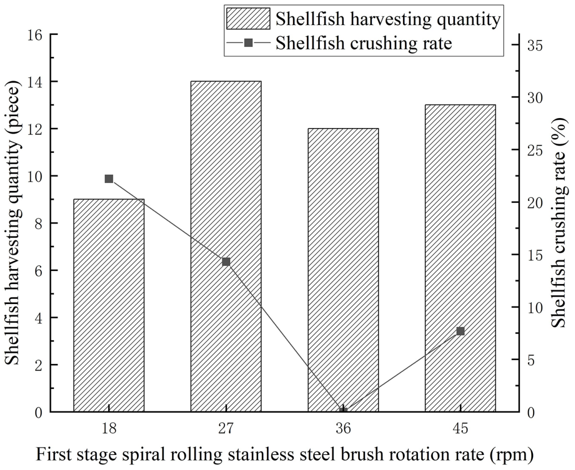

FIGURE 6
Influence of first-stage brush rotation rate on shellfish harvesting.

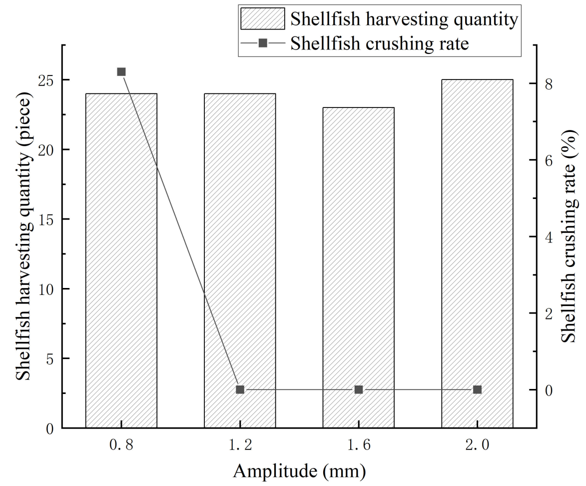

FIGURE 7
Influence of amplitude on shellfish harvesting.

4.2.2.2 Influence of screen vibration amplitude

The effect of amplitude on shellfish harvesting simulation is shown in Figure 7. The quantity of shellfish harvested gradually rose as the amplitude increased, but the difference in the quantity of shellfish harvested between different amplitudes was negligible. Under constant conditions, higher vibration amplitudes led to greater heights from which the sediment and shellfish fell onto the vibrating screen. Also, they fell more quickly onto the screen surface, making them easier to sift and boosting shellfish harvesting efficiency. When the vibration amplitude was 1.2 mm, 1.6 mm, or 2.0 mm, the quantity of shellfish harvested was similar and the shellfish crushing rate was 0. However, larger amplitudes resulted in higher energy consumption and greater structural strength requirements for the machine. After comprehensive consideration, the amplitude range of the vibrating screen was established in the range of 0.8-1.6 mm.

FIGURE 8
Influence of travel speed on shellfish harvesting.

4.2.2.3 Effect of harvester travel speed

The results for shellfish harvesting under various travel speeds are presented in Figure 8. When the travel speed of the harvester increased, the quantity of harvested shellfish gradually decreased, while the shellfish crushing rate remained constant at 0. The front end of the vibrating screen moved along an inclined sinusoidal vibration curve (Awuah et al., 2022), and as the harvesting equipment traveled faster, the sinusoidal curve cycle displacement became longer and the wave crests grew farther apart from one another. This resulted in shellfish leakage and reduced the quantity of shellfish harvested. However, as the harvester's travel speed grew, the area it could harvest in a given amount of time and the harvesting efficiency also rose. Given the quantity of shellfish being harvested and the harvesting efficiency, the travel speed of the harvester was chosen in the range of 8-10 m/min.

4.3 Response surface simulation experiment

To obtain the optimal operating and structural parameters of the vibratory shellfish harvester, the Box-Behnken experimental design method was chosen in the design of the harvesting simulation response surface experiment with Design-Expert software (Design-Expert v8.0.6.1, Stat-Ease, Minneapolis, MN, USA). Besides, the response surface experiment factors were coded according to those listed in Table 4. Both the quantity of shellfish harvested (N_t) and the shellfish crushing rate (ϕ_{c1}) were employed as response variables.

The results of the shellfish harvesting response surface simulation experiments are displayed in Table 5. The maximum and minimum number of shellfish harvested under various parameters were 25 pieces and 21 pieces, respectively, while the shellfish crushing rate varied from 0% to 8.7%.

4.3.1 Influence on shellfish harvesting quantity

A multivariate fitted regression equation (Eq. 21) between the quantity of shellfish harvested and each factor was created using Design-Expert software by removing insignificant factors from the analysis results of the shellfish harvesting simulation tests (Table 6).

$$N_s = 22.00 + 0.88A + 0.38B + 0.75C - 0.50AB - 0.25AC - 0.25BC + 0.75A^2 + 1.25B^2 . \tag{21}$$

According to the results of the ANOVA model on the factors determining the quantity of shellfish harvested (Table 6), A, B, C, AB, A^2, and B^2 had significant effects on the quantity of shellfish harvested. Besides, AC and BC had insignificant effects on the quantity of shellfish harvested. Specifically, the three factors of B^2, C, and A had the largest impact on the quantity of harvested shellfish. The fitted model for the quantity of harvested shellfish was highly significant ($P< 0.0001$), indicating that the significance level of the model was high. The results of the last five sets of replicate tests in Table 5 were the same because the shellfish vibration harvesting simulation test conditions remained constant. Moreover, the P values for lack of fit and

TABLE 4 Response surface experiment factor codes.

Level	A. Screen vibration amplitude (mm)	B. First-stage brush rotation rate (rpm)	C. Travel speed (m/min)
High 1	1.4	32	10
Mid 0	1.2	36	9
Low -1	1.0	40	8

pure errors of the misfit term for the shellfish harvesting quantity were all 0. The model coefficient of determination $R^2 = 0.9891$ indicated a good fit between the actual and predicted values established by the regression equation. The determination correction coefficient $R_2^{adj} = 0.9751$ also indicated that the equation was reliable. The *Adeq Precision* was 28.460, suggesting excellent equation accuracy. The coefficient of variation (*CV*) of the multivariate fitted equation was 0.82%, indicating high experiment reliability.

The influence of test factors on the quantity of shellfish harvested is presented in Figure 9A. When the screen vibration amplitude was fixed, the quantity of harvested shellfish initially decreased and then increased as the rotational rate of the first-stage brush increased. The quantity of shellfish harvested rose with an increase in vibration amplitude, and the influence of amplitude was more pronounced. The bounce height and the falling speed of the shellfish and sediment both grew as the amplitude of the vibrating screen increased, thereby enhancing screening efficiency. The vibrating screen and the shellfish both experienced relative displacement while the harvester moved forward and the shellfish were bouncing up from the screen. When the shellfish bounced off the screen surface, the harvester advanced forward, and a relative displacement was generated between the vibrating screen and the shellfish. The greater the height at which the shellfish bounced and the further they were displaced backward, the more efficiently the shellfish were conveyed and harvested.

TABLE 5 Results of the shellfish harvesting response surface simulation tests.

Number	A	B	C	N_t/piece	ϕ_{b1}/%
1	1.0	32	9	22	0.0
2	1.4	32	9	25	8.0
3	1.0	40	9	24	4.2
4	1.4	40	9	25	0.0
5	1.0	36	8	21	0.0
6	1.4	36	8	23	8.7
7	1.0	36	10	23	4.3
8	1.4	36	10	24	8.3
9	1.2	32	8	22	4.0
10	1.2	40	8	23	4.3
11	1.2	32	10	24	0.0
12	1.2	40	10	24	4.2
13	1.2	36	9	22	4.2
14	1.2	36	9	22	4.2
15	1.2	36	9	22	4.2
16	1.2	36	9	22	4.2
17	1.2	36	9	22	4.2

When the travel speed was fixed, as shown in Figure 9B, the quantity of shellfish harvested grew as the vibration amplitude increased. Additionally, the quantity of shellfish harvested increased with a rise in harvester travel speed when the amplitude was fixed. The quantity of shellfish harvested was optimal when both speed and amplitude were at their maximums, and amplitude had a greater influence on the quantity of shellfish harvested. When the travel speed was fixed, the quantity of shellfish harvested initially decreased and then increased with an increase in the rotational rate of the first-stage brush, as shown in Figure 9C. When the rotational rate of the rolling brush was fixed, the number of shellfish harvested rose with an increase in travel speed. Furthermore, the harvester's travel speed had a more significant influence on the quantity of shellfish harvested.

4.3.2 Influence on shellfish crushing rate

The results of the shellfish crushing rate simulation tests are shown in Table 6. The shellfish crushing rate model is not statistically significant ($P > 0.05$), the precision (*Adeq Precision*) is 7.933, the model variance $CV = 50.52\%$, the equation coefficient of determination $R^2 = 0.6665$, and the correction coefficient of determination $R_2^{adj} = 0.4664$. These figures indicate because the reliability and precision of the shellfish crushing rate simulation test were low, the response surface experiment reliability was poor. The primary cause of shellfish crushing was that the shellfish were crushed between the rolling brush and the vibrating screen, which was not related to each test factor.

4.3.3 Simulation and optimization of key harvester parameters

The objective and constraint functions were established according to the requirements of shellfish harvesting. By combining the boundary conditions of the key factors, the results of the shellfish vibration harvesting simulation response surface experiments were optimally solved using the optimization module in Design-Expert software.

$$\begin{cases} Max\ \ N_s(A,B,C) \\ Min\ \ \varnothing_c\,(A,B,C) \end{cases}, \tag{22}$$

$$\begin{cases} 1.0mm \le A \le 1.4mm \\ 28rpm \le B \le 32rpm \\ 8m/min \le C \le 10m/min \end{cases}. \tag{23}$$

The optimal key factor combination of the shellfish vibration harvesting simulation was obtained through statistical analysis. The

TABLE 6 ANOVA results of factors influencing shellfish harvesting quantity and shellfish crushing rate.

Source	Shellfish harvesting quantity					Shellfish crushing rate				
	Sum of Squares	df	Mean Square	*F* Value	*P* value	Sum of Squares	df	Mean Square	*F* value	*P* value
Model	22.69	9	2.52	70.59	<0.0001**	94.47	9	10.50	2.77	0.0964
A	6.13	1	6.13	171.50	<0.0001**	34.03	1	34.03	8.99	0.0200*
B	1.13	1	1.13	31.50	0.0008**	0.0612	1	0.0612	0.0162	0.9024
C	4.50	1	4.50	126.00	<0.0001**	0.0050	1	0.0050	0.0013	0.9720
AB	1.00	1	1.00	28.00	0.0011**	37.21	1	37.21	9.82	0.0165*
AC	0.25	1	0.25	7.00	0.0331*	5.52	1	5.52	1.46	0.2664
BC	0.25	1	0.25	7.00	0.0331*	3.80	1	3.80	1.00	0.3497
A^2	2.37	1	2.37	66.32	<0.0001**	1.16	1	1.16	0.3064	0.5971
B^2	6.58	1	6.58	184.21	<0.0001**	11.81	1	11.81	3.12	0.1207
C^2	0.000	1	0.000	0.000	1.0000	1.52	1	1.52	0.4002	0.5471
Residual	0.25	7	0.036			26.51	7	3.79		
Lack of Fit	0.25	3	0.083			26.51	3	8.84		
Pure Error	0.000	4	0.000			0.0000	4	0.0000		
Cor Total	22.94	16				120.98	16			

* indicates a significant effect (0.01< P< 0.05); ** indicates a highly significant effect (P< 0.01).

ideal screen vibration amplitude was 1.4 mm, the first-stage brush rotation rate was 40 rpm, and the harvester travel speed was 10 m/min. Subsequently, the quantity of shellfish harvested was calculated by unit area under simulation conditions as N_{ta} = 125 pieces/m^2, while the shellfish crushing rate ϕ_{b1} = 2.90%.

5 Shellfish harvesting verification test

According to the results of the simulation, a brush-screen cooperative shellfish vibratory harvester was manufactured completely. Based on the optimized results of the response surface experiment, the harvester was debugged. A verification test of shellfish harvesting was carried out using the vibratory shellfish harvester in the white clam growing area of Panjin City, Liaoning Province, China, in September 2021, as depicted in Figure 10. The site environment in the test was a sandy mudflat, the moisture (W_s) was 45.55%, the average penetration force at 100mm depth was 3.8N, and the sediment average diameter x_2 was 0.09mm. A rectangular test area of 15 m × 1 m was created on the mudflat. The test area was divided into three equal parts lengthwise and then marked. The quantity of shellfish harvested (N_r) and the shellfish crushing rate (ϕ_{b2}) in the collection baskets were counted every 5 m the harvester traveled. The quantity of shellfish harvested and the quantity of shellfish crushed was obtained by manual counting, and the shellfish crushing rate was calculated. Also, the relative error (E) in the quantity of shellfish harvested, the quantity of shellfish harvested per unit area (N_{ra}), and the absolute value in the crushing rate error ($\triangle\phi_b$) were calculated according to Equations (24)-(26).

$$E = \frac{|N_h - N_s|}{N_s} \times 100\,\%, \tag{24}$$

$$N_{ha} = \frac{N_h}{5}, \tag{25}$$

$$\Delta \varnothing_b = |\varnothing_{b1} - \varnothing_{b2}|\,. \tag{26}$$

Here, E denotes the relative error, $N_h$represents the number of shellfish harvested in the harvesting verification test, N_{ha} is the quantity of shellfish harvested per unit area (piece/m^2), and $\triangle\phi_b$ signifies the absolute value of the crushing rate error.

The results of the shellfish vibration harvesting verification test reveal that the average quantity of shellfish harvested (N_a) was 571 pieces. Besides, as Figure 11 shows, N_{ha} = 114 pieces/m^2 and E = 8.80%. And the shellfish crushing rate was ϕ_{b2} = 6.97% and $\triangle\phi_b$ = 5.20%.

6 Discussion

6.1 Shellfish harvesting efficiency

The harvesting efficiency indicates the quantity (mass) of commercial shellfish harvested by the equipment per unit time in this paper. The quantity of shellfish harvested in the verification test was less than that in the simulation test, according to comparing the results of the simulation test and the verification test. The reason for the decreased in the quantity of harvested shellfish was possible that the shellfish density in the harvesting environments were smaller than that in the mudflat DEM model. Moreover, the juvenile shellfish were discarded onto the surface of the mudflat, leading to a decrease in shellfish harvesting quantity. The simulation results showed that

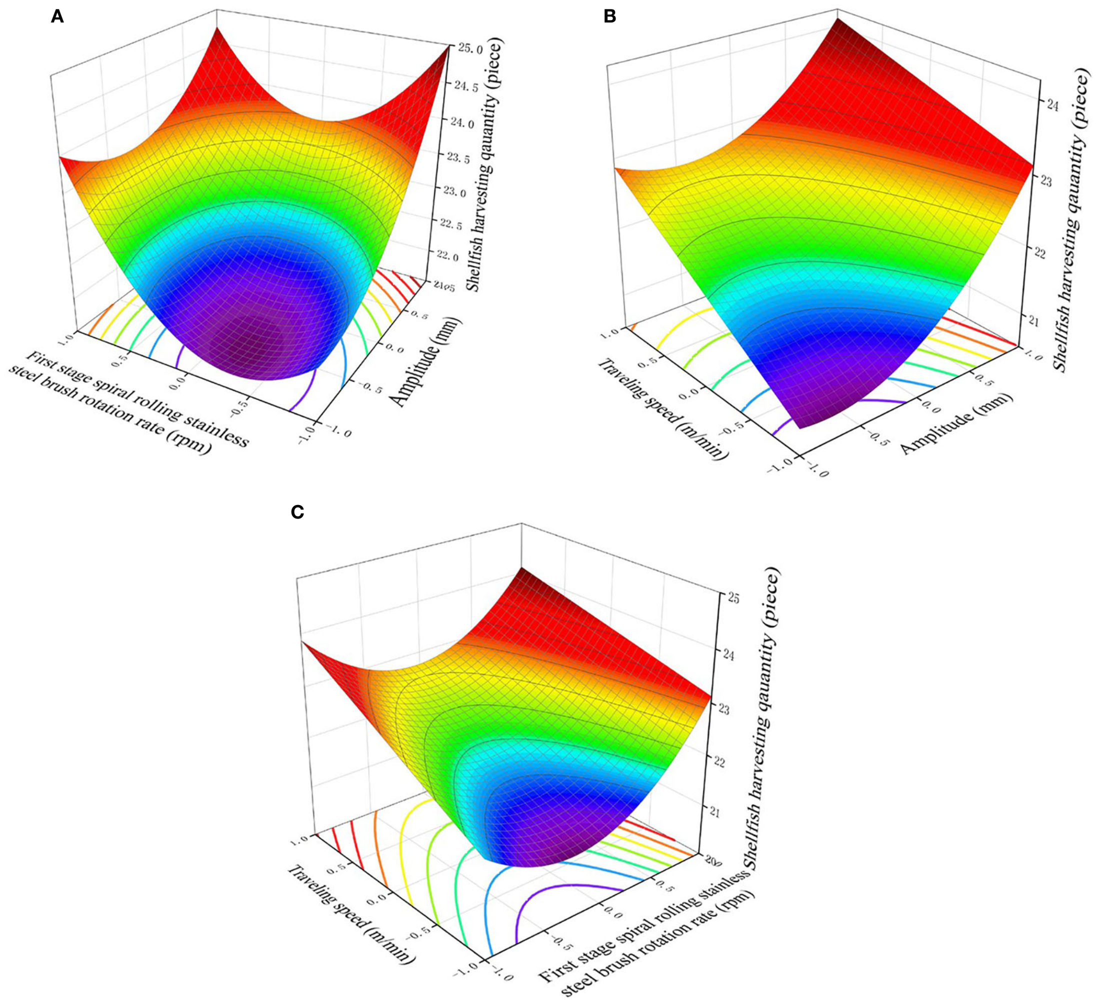

FIGURE 9
Influence of test factors on the quantity of shellfish harvested: **(A)** effect of first-stage brush rotation rate and amplitude on the number of shellfish, **(B)** effect of amplitude and travel speed on the number of shellfish, **(C)** effect of first-stage brush rotation rate and travel speed on the number of shellfish.

the harvester's travel speed and amplitude have significant effects on the quantity of shellfish harvested. Compared with the travel speed of other harvesters (Miguel B. Gaspar et al., 2002), the travel speed of the vibratory harvester is low (10 m/min), the lower shellfish harvesting efficiency. The main reason may be that the operating environment of vibratory harvester is “dry” mudflats, the adhesion force of sediments is strong, and it is difficult to separate sediments and shellfish. If the travel speed is too high, it is hard to effectively screen out sediment and shellfish, and there will be an accumulation in the vibrating screen. The operating environment of hydraulic dredge and commercial dredge are the submarine mudflats, sediment and shellfish are more easily to be separated in the action of seawater (Miguel B. Gaspar et al., 2002), with the faster travel speed (2 knots) and high harvesting efficiency. Vibration can speed up the screening efficiency, realize the separation of sediment and shellfish and the screening of juvenile shellfish back to the mudflats. Rambaldi et al. (2001) mentioned that the hydraulic vibratory dredge's shellfish harvesting efficiency and commercial shellfish harvesting proportion are 2 times and 3 times of commercial dredge respectively. Vibration can improve the harvesting efficiency, and realize the sustainable harvesting of mudflat shellfish and low ecological impact (Stirling, 2013).

6.2 Shellfish crushing rate

The higher shellfish crushing rate in the verification test than that in the simulation test, which was probably caused by the more complex environment and more influencing factors during the actual shellfish harvesting operation. Comparing the shellfish crushing rate of different type of harvesters, it was found that the shellfish crushing rate was the highest under the hydraulic dredge (Miguel B. Kauwling and Bakus, 1979; Gaspar et al., 2002), which was about 3-4 times higher than that of the vibratory harvester in this paper. The shellfish crushing rate of the vibratory harvester was 5.13% lower than that of the hydraulic vibratory dredge (Rambaldi et al., 2001). Such findings could be attributed to the fact that the operating environment of the hydraulic vibratory dredge was subwater, and the surface of the harvested shellfish was cleaner and more directly affected by the mechanical force. The surface of the harvested shellfish by the vibratory harvester

FIGURE 10
Shellfish vibration harvesting test: **(A)** The equipment harvesting operation, **(B)** The shellfish vibrating screening, **(C)** First-stage brush sediments cutting operation.

was attached to the sediment, which was an important factor in buffering the external force and protecting the shellfish. The lowest shellfish crushing rate of about 5% was observed under the commercial dredge(Miguel B. Gaspar et al., 2002). In addition, differences in shellfish hardness of different shellfish species may lead to different shellfish crushing results.

By observing the shellfish vibration harvesting process, it was found that the crushed shellfish is not directly caused by a single mechanism of the vibratory harvester, and the shellfish may be crushed at different stages of the shellfish harvesting process. In the initial stage of harvesting, when the first layer vibrating screen penetrates into the mudflat sediment, the shellfish are subjected to compaction forces exerted by the sediment and direct forces from the shovel of the first layer vibrating screen, which may cause some shellfish to be crushed (Vasconcelos et al., 2011). In the shellfish screening stage, the shellfish damage could be mainly attributed to the small gap size between the brush and the screen surface being small, the shellfish were subjected to the pressure of the bristles of the rolling brush, which might cause the shellfish to get crushed. Miguel B. Gaspar et al. (2002) indicated that the tooth spacing has a significant effect on the percentage of damaged and dead individuals (Yamasaki et al., 2002). In the shellfish vibratory harvesting process, when the shellfish moves to the combination part between the first layer vibrating screen and the second layer vibrating screen, the shellfish at the front end of the second layer vibrating screen was easily broken by the mechanical impact force, but the crushing is not caused by vibration (Rambaldi et al., 2001). In the early stages of harvesting, the large distance between the empty collection baskets and the drop opening of the conveyor chain creates the potential for crushing. As harvesting progresses and the drop height gradually decreases, the crushing problem can be alleviated. The same damage problem is also found in hydraulic dredging (Lambert and Goudreau, 2002). Through the analysis, it was found that the possibility of shellfish crushing exists in each of the above-mentioned harvesting links. In addition, the shellfish crushing may also be caused by the action of several links in the above-mentioned harvesting process together,

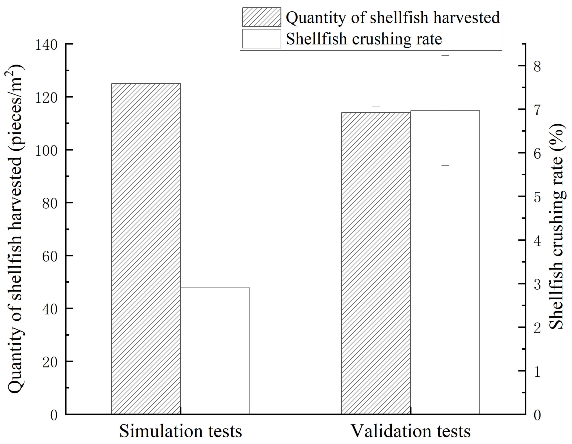

FIGURE 11
Results of shellfish harvesting simulation and verification test.

leading to the accumulation of the crushing until the shellfish is completely broken. In the subsequent upgrade, the structure of the vibratory harvester should be further optimized that prioritizing the reduction of shellfish crushing rate.

7 Conclusion

In this paper, the white clam was taken as the research object, and a mechanized brush-screen cooperative shellfish vibration harvester was designed. The mechanical and kinematic models of shellfish on the vibrating screen were established. A mudflat DEM model was established and the single-factor and response surface experiments of shellfish harvesting simulation were conducted in EDEM. The verification test was conducted on the mudflat to determine the accuracy of the simulation results. The conclusions of this paper are as follows.

(1) A crank rocker double-layer vibrating screen structure was designed, and the structural and operating parameters of the crank rocker double-layer vibrating screen were determined as $\alpha_{1\text{-}1} = 11°$, $\alpha_{1\text{-}2} = 8°$, $\alpha_{2\text{-}1} = 8°$, $\alpha_{2\text{-}2} = 5°$, $\epsilon_1 = 30°$, $\epsilon_2 = 35°$, $r = 0.01\text{m}$, $\varphi = 25°$, and $\omega = 30$ rad/s. The results provided a theory reference for shellfish harvesting simulation and harvester trial manufacturing.

(2) The quantity of shellfish harvesting was significantly influenced ($p< 0.01$) by vibrating screen amplitude, first-stage brush rotation rate, and harvester travel speed. The screen vibration amplitude was 1.4 mm, the first-stage brush rotation rate was 40 rpm, and the harvester travel speed was 10 m/min. Using these parameters, the error between the verification test and the simulation test is small and the shellfish harvesting work could be completed by the harvester effectively. For actual harvesting, it is recommended that the vibratory harvester be set to the above parameters for shellfish harvesting.

Data availability statement

The original contributions presented in the study are included in the article/supplementary material, further inquiries can be directed to the corresponding authors.

Author contributions

HL: Conceptualization, Methodology, data curation, performed research, writing - original draft. GM: Supervision, conceptualization, writing - review & editing. HZ: Methodology. HW: Investigation. FL: Performed research. ZS: Performed research. QZ: Data curation. YZW: Performed research. YZW: Performed research. XL: Project administration, funding acquisition, writing - review & editing. GZ: Supervision, writing - review & editing. All authors contributed to the article and approved the submitted version.

Funding

This research was funded by The National Key R&D Program of China, grant number 2019YFD0900701; The Science and Technology Innovation Project of Dalian, grant number 2021JJ12SN33; The Key Technology Projects of Dalian, grant number 2021JB11SN035.

Conflict of interest

The authors declare that the research was conducted in the absence of any commercial or financial relationships that could be construed as a potential conflict of interest.

Publisher's note

References

Asaf, Z., Rubinstein, D., and Shmulevich, I. (2007). Determination of discrete element model parameters required for soil tillage. *Soil Tillage Res.* 92, 227–242. doi: 10.1016/j.still.2006.03.006

Awuah, E., Zhou, J., Liang, Z., Aikins, K. A., Gbenontin, B. V., Mecha, P., et al. (2022). Parametric analysis and numerical optimisation of Jerusalem artichoke vibrating digging shovel using discrete element method. *Soil Tillage Res.* 219, 105344. doi: 10.1016/j.still.2022.105344

Badino, G., Bona, F., Maffiotti, A., Giovanardi, O., and Pranovi, F. (2004). Impact of mechanical clam harvesting on a benthic habitat: evaluation by means of sediment profile imaging. *Aquat. Conservation: Mar. Freshw. Ecosyst.* 14 (S1), S59–S67.

Bahrami, M., Naderi-Boldaji, M., Ghanbarian, D., Ucgul, M., and Keller, T. (2020). Simulation of plate sinkage in soil using discrete element modelling: Calibration of model parameters and experimental validation. *Soil Tillage Res.* 203, 203. doi: 10.1016/j.still.2020.104700

Beukema, J. (1995). Long-term effects of mechanical harvesting of lugworms arenicola marina on the zoobenthic community of a tidal flat in the wadden Sea. *Netherlands J. Sea Res.* 33, 219–227. doi: 10.1016/0077-7579(95)90008-X

Cabiscol, R., Finke, J. H., and Kwade, A. (2018). Calibration and interpretation of DEM parameters for simulations of cylindrical tablets with multi-sphere approach. *Powder Technol.* 327, 232–245. doi: 10.1016/j.powtec.2017.12.041

China, M. O. A (2013) *Notice of the ministry of agriculture on the prohibition of the use of thirteen types of fishing gear* (China: Ministry of Agriculture and Rural Affairs of the People's Republic of China). Available at: http://www.moa.gov.cn/nybgb/2013/dseq/201805/t20180510_6141830.htm (Accessed November 21, 2022).

Coen, L. D. (1995). *A review of the potential impacts of mechanical harvesting on subtidal and intertidal shellfish resources* (South Carolina: South Carolina Department of Natural Resources, Marine Resources Research).

Collier, J., and McLaughlin, D. (1983). A mechanical oyster harvester for south Carolina estuaries. *J. World Mariculture Soc.* 14, 295–301. doi: 10.1111/j.1749-7345.1983.tb00085.x

EDEM (2018). *EDEM*. (UK:DEM Solutions Ltd.).

Fahy, E., and Carroll, J. (2007). Consequences of hydraulic dredging for a razor clam ensis siliqua (L.) bed in the north-west Irish Sea. *Biol. Environment: Proc. R. Irish Acad.* 107, 115–128.

Fisheries Administration Bureau of Ministry of Agriculture China (2022). *China Fishery statistical yearbook 2022* (Beijing: China agriculture press).

Gaspar, M. B., Leita˜o, F., Santos, M. N., Sobral, M., Chı´Charo, Luı´S, Chı´Charo, A., et al. (2002). Influence of mesh size and tooth spacing on the proportion of damaged organisms in the catches of the Portuguese clam dredge fishery. *ICES J. Mar. Sci.* 59, 1228–1236. doi: 10.1006/jmsc.2002.1310

Glude, J., Spear, H., and Wallace, D. (1952). "The hydraulic clam rake, a new method of gathering seed clams". In:Proceedings of the National Shellfisheries Association, 163–166.

González-Montellano, C., Fuentes, J. M., Ayuga-Téllez, E., and Ayuga, F. (2012). Determination of the mechanical properties of maize grains and olives required for use in DEM simulations. *J. Food Eng.* 111, 553–562. doi: 10.1016/j.jfoodeng.2012.03.017

Hall, S., Basford, D., and Robertson, M. (1990). The impact of hydraulic dredging for razor clams ensis sp. on an infaunal community. *Netherlands J. Sea Res.* 27, 119–125. doi: 10.1016/0077-7579(90)90040-N

Hall, S. J., and Harding, M. J. (1997). Physical disturbance and marine benthic communities: the effects of mechanical harvesting of cockles on non-target benthic infauna. *J. Appl. Ecol.* 34, 497–517. doi: 10.2307/2404893

Haven, D. S., Loesch, J. G., and Whitcomb, J. P. (1973). *An investigation into commercial aspects of the hard clam fishery and development of commercial gear for the harvest of molluscs: final contract report for the period 1 July 1970 through 30 June 1973* (William & Mary: Virginia Institute of Marine Science).

Haven, D. S., Whitcomb, J. P., and Davis, Q. C. (1979). A mechanical escalator harvester for live oysters and shell. *Mar. Fisheries Rev.* 41 (12), 17–20.

Hoyseth, K. (2009) *Archived-does mechanical clam harvesting in BC pose any environmental risk?* (Canda: Government of Canada, Fisheries Oceans Canada, Communications Branch). Available at: https://www.dfo-mpo.gc.ca/aquaculture/rp-pr/acrdp-pcrda/projects-projets/P-08-03-005-eng.html (Accessed November 16, 2022).

Johnson, K. L., Kendall, K., and Roberts, A. (1971). "Surface energy and the contact of elastic solids". In:Proceedings of the royal society of London. A. mathematical, 301–313.

Kauwling, T. J., and Bakus, G. J. (1979). *Effects of hydraulic clam harvesting in the Bering Sea* (North Pacific Fishery Management Counci).

Kyte, M. A., and Chew, K. K. (1975). *A review of the hydraulic escalator shellfish harvester and its known effects in relation to the soft-shell clam, mya arenaria* (Washington: University of Washington).

Lambert, J., and Goudreau, P. (2002). *Performance of the new England hydraulic dredge for the harvest of stimpson's surf clams (Mactromeris polynyma)* (Canada, Department of Fisheries Oceans).

Landry, T. (2017) *The ecological effects of clam harvesting by mechanical means in St mary's bay, Nova Scotia* (Ottawa: Aquaculture Science Branch Fisheries and Oceans Canada). Available at: https://www.dfo-mpo.gc.ca/aquaculture/rp-pr/acrdp-pcrda/projects-projets/G-12-01-001-eng.html (Accessed November 15, 2022).

Li, H., Zhang, G., Li, X., Zhang, H., Zhang, Q., Liu, W., et al. (2021). Calibration of the discrete element method parameters in living juvenile Manila clam (Ruditapes philippinarum) and seeding verification. *AgriEngineering* 3, 894–906. doi: 10.3390/agriengineering3040056

Liu, W., Zhang, H., Li, X., Zhang, G., Zhang, Q., Qu, S., et al. (2020). Analysis of biomechanical properties of juvenile Manila clam for mechanization sowing. *J. Dalian Ocean Univ.* 35, 455–461.

Lu, J., Zhou, Y., Shen, C., Lu, S., Tu, L., and Xue, A. (2021). Design and experiment of self-propelled shellfish harvester. *Fishery modernization* 48, 85–90.

Meyer, T. L., Cooper, R. A., and Pecci, K. J. (1981). The performance and environmental effects of a hydraulic clam dredge. *Mar. fisheries Rev.* 43, 14–22.

Morello, E., Froglia, C., Atkinson, R. J., and Moore, P. (2005). Impacts of hydraulic dredging on a macrobenthic community of the Adriatic Sea, Italy. *Can. J. Fisheries Aquat. Sci.* 62, 2076–2087. doi: 10.1139/f05-122

Mu, G. (2019). *Study on key technology and design of chain-tine dredge for ruditapes philippinarum* (Doctorate, Dalian University of Technology).

Mu, G., Duan, F., Yang, J., Zhang, H., Li, X., Pan, L., et al. (2020). Research progress on burying shellfish harvesters: a review. *Journel Dalian Ocean Univ.* 35, 19–30.

Pacific Shellfish Institute (2014) *Evaluation and development of advanced farm management and harvesting tools for economically efficient and environmentally sustainable production of Manila clams* (Olympia: Pacific Shellfish Institute). Available at: https://www.pacshell.org/pdf/SKManila.pdf (Accessed November 22, 2022).

Rambaldi, E., Bianchini, M. L., Priore, G., Prioli, G., Mietti, N., and Pagliani, T. (2001). Preliminary appraisal of an innovative hydraulic dredge with vibrating and sorting bottom on clam beds (Chamelea gallina). *Hydrobiologia* 465, 169–173. doi: 10.1023/A:1014540824340

Ramírez-Gómez, Á., Gallego, E., Fuentes, J. M., González-Montellano, C., and Ayuga, F. (2014). Values for particle-scale properties of biomass briquettes made from agroforestry residues. *Particuology* 12, 100–106. doi: 10.1016/j.partic.2013.05.007

Robinson, R., and Richardson, C. (1998). The direct and indirect effects of suction dredging on a razor clam (Ensis arcuatus) population. *ICES J. Mar. Sci.* 55, 970–977. doi: 10.1006/jmsc.1998.0356

Saurel, C., Ferreira, J. G., Cheney, D., Suhrbier, A., and Cordell, J. (2014). Ecosystem goods and services from Manila clam culture in puget sound: a modelling analysis. *Aquaculture Environ. Interact.* 5 (3). doi: 10.3354/aei00109

Smolowitz, R. J. (1982). The design of an electrohydraulic dredge for clam surveys. *Mar. Fish Rev.* 44, 1–18.

Stirling, D. (2013) *Mechanized clam harvesting for coastal British Columbia - environmental implications* (Canada: Fisheries and Oceans Canada). Available at: https://www.dfo-mpo.gc.ca/aquaculture/rp-pr/acrdp-pcrda/projects-projets/p-08-03-005-eng.html (Accessed November 21, 2022).

Vasconcelos, P., Morgado-Andre, A., Morgado-Andre, C., and Gaspar, M. B. (2011). Shell strength and fishing damage to the smooth clam (Callista chione): simulating impacts caused by bivalve dredging. *Ices J. Mar. Sci.* 68, 32–42. doi: 10.1093/icesjms/fsq149

Yamasaki, S., Higano, J., and Watanabe, T. (2002). Foot damages of the clam meretrix lamarckii caused by clam dredging. *Bull. Japanese Soc. Sci. Fisheries* 68, 368–373. doi: 10.2331/suisan.68.368

frontiers | Frontiers in Marine Science

TYPE Original Research
PUBLISHED 27 March 2023
DOI 10.3389/fmars.2023.1132629

OPEN ACCESS

EDITED BY
Yang Jin,
Carnegie Institution for Science,
United States

REVIEWED BY
Hung-Jie Tang,
National Cheng Kung University, Taiwan
Ray-Yeng Yang,
National Cheng Kung University, Taiwan

*CORRESPONDENCE
Yun-Peng Zhao
✉ ypzhao@dlut.edu.cn

SPECIALTY SECTION
This article was submitted to
Marine Fisheries, Aquaculture and Living
Resources,
a section of the journal
Frontiers in Marine Science

RECEIVED 27 December 2022
ACCEPTED 06 March 2023
PUBLISHED 27 March 2023

CITATION
Chen Q-P, Bi C-W and Zhao Y-P (2023)
Prediction of wave force on netting under
strong nonlinear wave action.
Front. Mar. Sci. 10:1132629.
doi: 10.3389/fmars.2023.1132629

Prediction of wave force on netting under strong nonlinear wave action

Qiu-Pan Chen[1], Chun-Wei Bi[2] and Yun-Peng Zhao[1,3]*

[1]State Key Laboratory of Coastal and Offshore Engineering, Dalian University of Technology, Dalian, China, [2]Key Laboratory of Mariculture, Ministry of Education, Ocean University of China, Qingdao, China, [3]Ningbo Institute of Dalian University of Technology, Ningbo, China

Under the strong nonlinear wave environment, accurate simulation of wave force for aquaculture netting is an effective guarantee for cage design and safety. In this paper, the horizontal wave forces of a nylon square-mesh netting panel were obtained through a series of strong nonlinear regular wave tests, and their nonlinearity was analyzed by amplitude spectrum. Moreover, the Morison equation based on fifth-order Stokes wave theory was used to reasonably predict the wave force on the netting. The results showed that both wave and wave force have strong nonlinearity, especially the latter. The frequency domain characteristics of the test wave and wave force are similar, while the higher frequency components of the test force are more apparent. The predicted wave forces are in good agreement with the test values in time and frequency domain, and zero or higher frequency components of predicted force are more prominent with the increase of wave steepness. When the range of the Keulegan-Carpenter number is 35-120, the average drag and inertia coefficient of the predicted force are 2.4 and 2.1, respectively. The results can provide a more accurate assessment of the nonlinear wave force on aquaculture facilities.

KEYWORDS

netting panel, nonlinear wave, wave force, amplitude spectrum, hydrodynamic coefficient

1 Introduction

As a flexible structure with strong water permeability, netting plays an important role in aquaculture activities and is an important part of marine aquaculture facilities. Under the action of complex marine environmental, the load on the netting usually accounts for a large proportion in the aquaculture facilities (e.g., Martin et al., 2020; Endresen and Moe-Føre, 2022; Ma et al., 2022; Wang Y, et al., 2022; Zhao et al., 2022). The reasonable prediction of the hydrodynamic on netting is related to the structural safety of aquaculture facilities.

Many scholars believed that the drag force on netting represent the large contribution to hydrodynamic forces on traditional fish farms, so there were many researches on hydrodynamic of netting in steady flows. Zhan et al. (2006) conducted analytical and experimental investigation of drag on netting of fish cages, and the proposed new formulae was verified experimentally. Zhou et al. (2015) studied the drag effect of netting with various solidity ratios in their angle of incline to free stream, and found a dual effect of solidity on drag coefficient for inclined netting. The dual effect was described as a positive correlation in upper attack angle and a negative correlation in lower angle of attack. Moe-Føre et al. (2021) investigated the drag and lift coefficients for Raschel knitted netting considering high solidity netting and high towing velocities, and found that drag forces were close to proportional with the netting solidity for netting solidities ranging from 0.15 to 0.32. Tang et al. (2018) studied the hydrodynamic characteristics of nylon as well as polyethylene netting of different knot types and solidity ratios under varied attack angles and flow velocities. The drag coefficients of knotless nylon netting were dominant compared with knotless polyethylene netting when Reynolds number greater than 2200. Santo (2022) proposed a hydrodynamic model, based on the current blockage model commonly used in offshore engineering, to characterize steady drag force as well as velocity reduction factor on netting. In numerical terms, Zhao et al. (2013) simulated netting using the porous media model, and present the flow field around netting panel with different variable (such as inclination angles, spacing distances between two netting panel and netting panel numbers). Wang G, et al. (2022) proposed a new screen force model based on numerical simulations of a portion of knotless netting panels, and believed that the new model was superior to previously used screen force models for the simulation of the drag forces on and the velocity reduction downstream of netting panel. For biofouling problem in marine aquaculture activities, some researchers have also investigated the drag effect on netting with biofouling (e.g., Swift et al., 2006; Gansel et al., 2015; Lader et al., 2015; Bi et al., 2018).

For some aquaculture facilities, the netting must be exceeded the still water level. Hydrodynamics would be more dominated by waves than flows. Balash et al. (2009) measured the hydrodynamic forces on netting in waves that can be assumed as linear wave theory, and also simulated the forces with a proposed numerical model. They found that the drag and added mass coefficients were not well quantified by conventional nondimensional parameters (such as Keulegan-Carpenter and Reynolds numbers). Wang S, et al. (2022) investigated the hydrodynamic and deformation of a prototype pile-net configuration based on the lumped mass model, they found the force was mainly from the top half of the netting. Through the analysis of the above related researches, there would be a lack of in-depth research on the force and force prediction of netting under waves, especially strong nonlinear waves.

In this paper, a series of wave experiments of square-meshed nylon netting was conducted, and the horizontal wave force under strong nonlinear waves was studied. Meanwhile, Morison equation is used to reasonably predict the wave force in experience. The relevant research was helpful to make a more accurate assessment of the nonlinear wave force of marine aquaculture facilities.

2 Material and methods

2.1 Experimental setup

The wave experiments of the netting panel were carried out in a wave-current tank at the State Key Laboratory of Coastal and Offshore Engineering, Dalian University of Technology, China. The tank was 22 m long, 0.45 m wide, and 0.6 m deep. Both the side and bottom walls of the tank were made of smooth glass plates with minimal frictional drag. The effective length of the experiments was 16.5 m from the wave paddle to the wave absorber. A 40 × 51.5 cm clean netting panel with a solidity of 0.194 was placed in the flume 6.3 m downstream of the wave paddle (see Figure 1), and the water depth was 40 cm. The characteristic length of the twine in the plane of the netting was 4.5 mm and the mesh bar length was 5 cm. The nylon netting was fastened in a steel frame welded together with 6 mm steel bars, to form the netting panel.

The top edge of the netting was 14.5 cm above the still water level. The netting panel was tied to a 4 mm thick and 10 mm wide steel plate, which was attached to the force transducer with a connecting bracket. The details of netting panel in the flume are shown in Figure 2. Three wave gauges were used to measure wave elevation time series: G1 was placed 0.5 m upstream of the netting, G2 and G3 were placed 0.5 m and 1.0 m downstream of the netting, respectively. The three gauges were for verifying the stability of the wave surface near the netting and also studying the effect of netting on wave. The force transducer was capable of recording forces of up to 50 N with an accuracy of 0.005 N. The sampling rate for both wave force and wave elevation was set at 50 Hz.

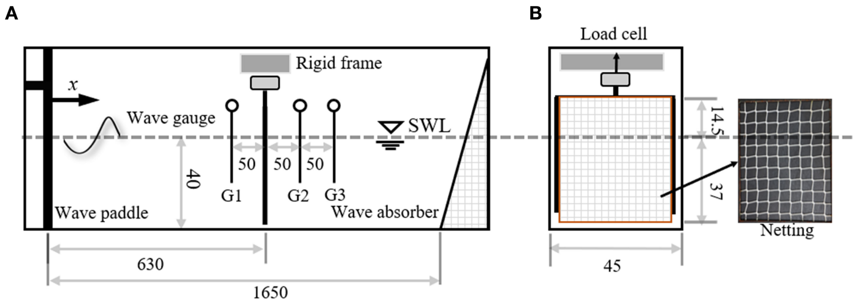

FIGURE 1
Sketch of the facility (unit: cm). **(A)** side elevation view; **(B)** Front elevation view.

FIGURE 2
Details of the netting panel in water.

2.2 Wave conditions

Netting is an important part of aquaculture cage exposed to ocean environment, and its hydrodynamic under strong nonlinear wave action is relatively complex. A total of five wave conditions were designed for this experiment (see Table 1). The wave height ranged from 3.95 to 11.62 cm, the wave period was 1.18 s, and the wave length was 1.89 m. Therefore, the wave steepness ranged from 0.021 to 0.061. Then, a common square-meshed nylon netting was taken as the research object, and its nonlinear wave force was analyzed under the five wave conditions.

2.3 Analysis methods

2.3.1 Low pass filter

For test data, the duration curve often has poor smoothness due to its complex high frequency components. When these high-frequency components are introduced unintentionally by the test, their existence will interfere with the further analysis of the experimental data. For these interferences, we consider using a low pass filter to remove them, so as to conduct more targeted research.

Low pass filter is of great significance for data analysis. Its principle is as follow:

$$G(f) = F(f)H \tag{1}$$

TABLE 1 Wave parameters in the experiment.

Items	Wave height H/cm	Wave period T/s	Wave length L/m	Wave steepness ϵ
W1	3.96	1.18	1.89	0.021
W2	6.05	1.18	1.89	0.032
W3	7.71	1.18	1.89	0.041
W4	9.76	1.18	1.89	0.052
W5	11.62	1.18	1.89	0.061

where $F(f)$ is the fast Fourier transform of the original data containing high-order vibration signals, $G(f)$ is the fast Fourier transform of the data after low pass filtering, and H is the transfer function shown below.

$$H = \begin{cases} 1, & f \le f_{cut} \\ 0, & f > f_{cut} \end{cases} \tag{2}$$

where f_{cut} was the cut-off frequency.

After the fast Fourier transform of the test data is processed by low pass filtering, the desired data of this study can be obtained by using the inverse fast Fourier transform method.

2.3.2 Hydrodynamic force model for netting in waves

The netting can be considered as a combination of many slender twines, and the hydrodynamic force on each twine can be calculated according to the Morison equation. Then the total hydrodynamic force of the netting can be calculated by summing the force of each twine. According to Morison equation, the wave force F_c of each twine included the drag force F_d and inertia force F_i, as follows:

$$F_c = F_d + F_i = 0.5\rho C_D D u|u| + \rho C_M A \dot{u} \tag{3}$$

Where ρ was the water density, D and A were the dimension of the twine normal to the wave and cross-sectional area of the twine, C_D and C_M were the drag and inertial coefficient, u and $\dot{u}$were horizontal velocity and acceleration of the water particles.

For describing the strong nonlinearity of the regular waves, the fifth-order Stokes wave theory was used for calculating the quasi-static wave force. In this way, the horizontal water particle velocity of wave action at twine was given as follow:

$$u = c\sum_{n=1}^{5} n\lambda_n \cosh[nk(z+d)]\cos[n(kx-\omega t)]$$

$$(-d \le z \le \eta) \tag{4}$$

Where ω, d, and k were angular frequency, water depth, and wave number, other parameters referred to Skjelbreia and Hendrickson (1960) and Nishimura et al. (1977).

The total force F_C of the netting can be predicted by summing the force of every twine calculated by Equation 3. The difference between measured force F_M and predicted force F_C of the netting according to Morison equation was as follow:

$$Q = \sum_{i=1}^{n} [F_C(i) - F_M(i)]^2 \tag{5}$$

Then, the least square method was used to solve the hydrodynamic coefficients C_D and C_M of the netting by following equation:

$$\partial Q / \partial C_D = 0, \ and \ \partial Q / \partial C_M = 0 \tag{6}$$

3 Results and discussion

3.1 Wave forces on netting

3.1.1 Low pass filtering for wave forces in the experiment

In order to obtain more stable wave forces of netting, the original signals of force collected from the experiment was processed by low pass filtering introduced in Section 2.3.1. Low pass filtering was a commonly used signal processing method, which aimed to remove irrelevant interference signals of high frequency. In this study, the netting was fixed on the steel frame. The high frequency response was not the performance of wave force, but the high frequency resonance signal of the frame. Considering the nonlinear property of the test wave, the cut-off frequency (5 Hz) was set to about 6 times the wave frequency.

Comparing the wave force processed by low pass filtering with the original force curve in Figure 3, the force was total wave force of frame and netting under W1 shown in Table 1. Compared with the original data, the data after low pass filtering had better smoothness, and the high-frequency vibration signal was filtered out. In addition, low pass filtering will also affect the amplitude of wave force. The amplitude of filtered data was significantly smaller than that of original data, although the impact was relatively limited.

The wave force after low pass filtering will better reflect the relationship between wave and the wave force caused by it. The frame force and the total force including the frame and the netting were filtered respectively. Finally, the wave force of the netting itself can be obtained by making a difference between the two.

3.1.2 Wave surface and wave force in time domain

The wave forces on the structure were directly caused by the directional propagation of water waves. To intuitively analyze the relationship between wave surface and wave force on netting, they were placed in a figure together. The wave surface curve at the target position were shown in Figure 4A, and the wave force curve of netting at the same position were shown in Figure 4B. The wave surface and force curves included all five wave conditions as shown in Table 1. The curves showed the data of two consecutive wave periods that start from the peak value.

The wave force curve continued the periodic and nonlinear characteristics of wave curve. The recurrence period of the force curve was wave period. The force curve had a relatively consistent phase change rules with the wave curve. In terms of nonlinear characteristics, the peak-valley ratio of wave surface was 1.19-1.47, while that of wave force was 1.41-1.63. The ratios showed that wave force had more significant horizontal asymmetry. Furthermore, there was little difference between the front and rear slope of the wave surface, while the front slope of the wave force was obviously lower than the rear slope, that is, the wave force had obvious vertical asymmetry.

The peak value of wave force and the corresponding wave height were taken as two-dimensional scattered data, and the change rule was shown in the figure. The limited scattered point data in Figure 5 can basically depict the function type of the relationship between wave force and wave height. Here, the scattered point data was fitted by using a quadratic polynomial, and the fitting curve was shown by the red dashed line in Figure 5. The fitting curve and scatter point data basically coincided, which was consistent with the assumption of Morison equation in Equation 3 because of the drag force played a leading role in wave force of the netting.

3.2 Frequency spectrum characteristic

3.2.1 Frequency spectrum characteristic for wave surface

The ocean waves can be affected by many complex factors, and often have strong nonlinearity. The amplitude spectrum (as shown

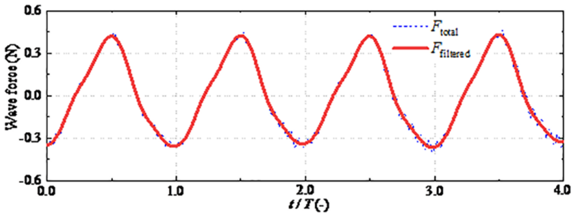

FIGURE 3
Details of the original and its filtered force for W1. Both the original and filtered force correspond to the netting with frame.

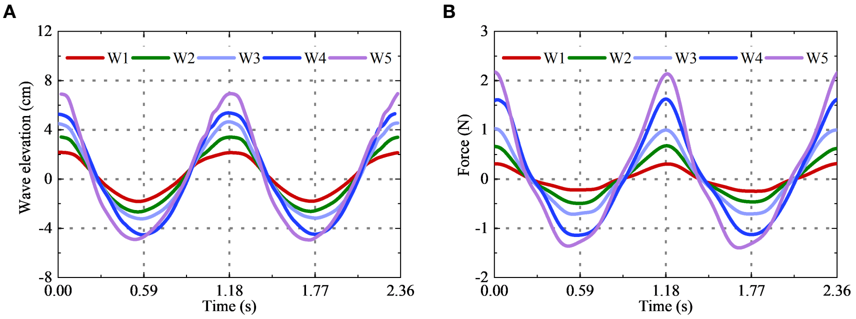

FIGURE 4
Time series of wave elevation and wave force for netting only. **(A)** wave elevation; **(B)** wave force.

in Figure 6) of the wave surface data under the test conditions can be obtained by a fast Fourier transformation. It can be used to characterize the nonlinear degree of the wave surface data. In order to study the characteristics of amplitude spectrum, its frequency coordinates were transformed to non-dimensional form, which showed the multiples of wave frequencies.

Amplitude spectrum analysis can separate the linear and nonlinear component of wave surface. It can be seen from the amplitude spectrum of each wave surface that the amplitude of wave surface was mainly dominated by wave frequency. The proportion of nonlinear components would increase with the increasing wave steepness, and the second-order component contributes the most. The frequency of nonlinear component was mainly the multiple frequency based on the wave frequency. The multiple frequency had a positive contribution to the horizontal asymmetry of the wave surface, which would distort the sinusoidal wave shape: the crest becomes steeper and the troughs become flatter. These were consistent with the characteristics of the wave surface curve shown in Figure 5. In addition, it was worth noting that the amplitude spectrum of wave surface has an obvious amplitude at the zero frequency. The component was mainly generated by the rise of the second-order wave surface, and was shown as the sinking of the mean water level. The sinking of the mean water level was related to the conservation of energy. The nonlinear term increased the kinetic energy of the water, which was bound to reduce the potential energy. The sinking was the amplitude at the zero frequency.

3.2.2 Frequency spectrum characteristic for wave force

According to Section 3.1, the wave force also had obvious nonlinear characteristics such as the wave surface. The wave forces were analyzed by using fast Fourier transform as in Section 3.2.1. The amplitude spectrum of wave force on the netting was obtained under various wave conditions (see Figure 7).

Compared with the amplitude spectrum of wave surface, the wave frequency component of wave force on netting still played an important role. There was also an obvious second-order component. However, the difference was that the third or higher-order components had an amplitude similar to that of the second-

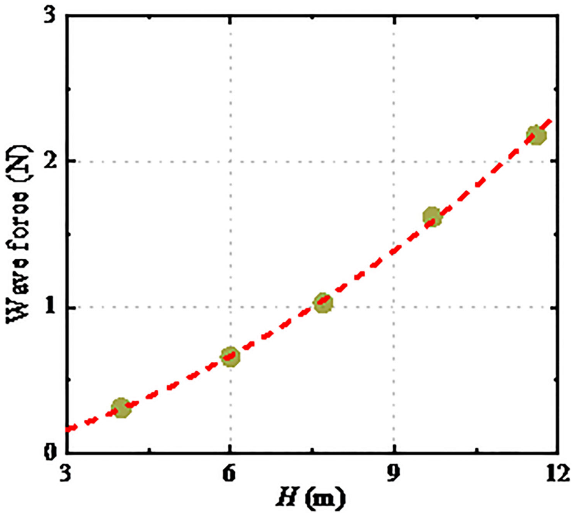

FIGURE 5
The positive amplitude of wave force as a function of wave height. The red dashed line is quadratic polynomial curve to fit the scatter data.

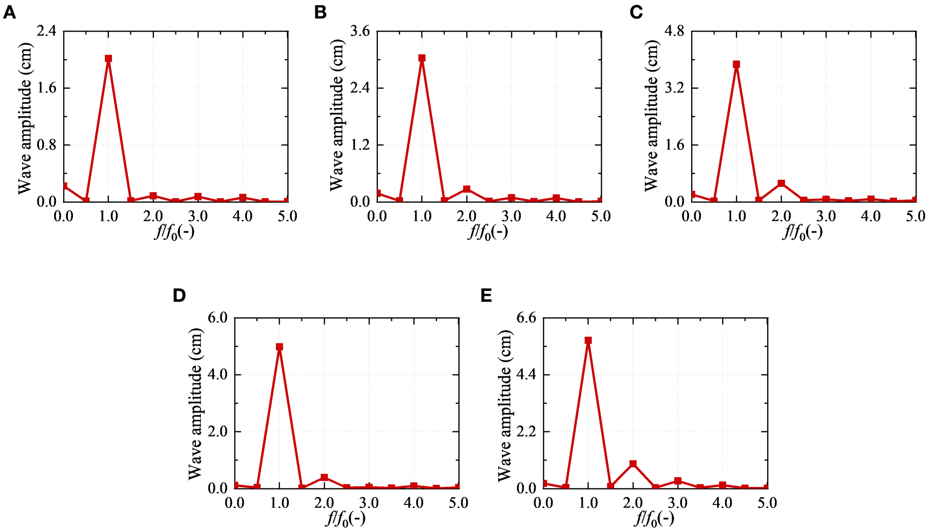

FIGURE 6
The amplitude spectrum of wave surface in the experiment. **(A)** W1, ϵ = 0.021; **(B)** W2, ϵ = 0.032; **(C)** W3, ϵ = 0.041; **(D)** W4, ϵ = 0.052; **(E)** W5, ϵ = 0.061.

order components. These meant that compared to the wave surface, the wave force had a greater horizontal asymmetry. The difference between wave surface and wave force in amplitude spectrum was consistent with their performance in curve feature.

In addition, the wave force also had a certain amplitude at the zero frequency, which was essentially different from the zero frequency of the wave surface. The zero frequency of wave surface was the change of the mean water level and did not contribute to the wave force. The amplitude at the zero frequency of wave force was mainly the second-order mean force (drift force) caused by the second-order problem. Both the multiple frequency component and zero frequency component of wave force would cause the increase of its horizontal asymmetry. However, the drift forces of the wave force measured in the test were smaller than those of the multiple frequency component.

3.3 The prediction of wave force

3.3.1 The predicted force in time domain

The time and frequency domain of the force of the netting have been described in detail above. On this basis, this section attempts to use Morison equation to predict the force of the netting. The dimension of the twine normal to the wave was much smaller

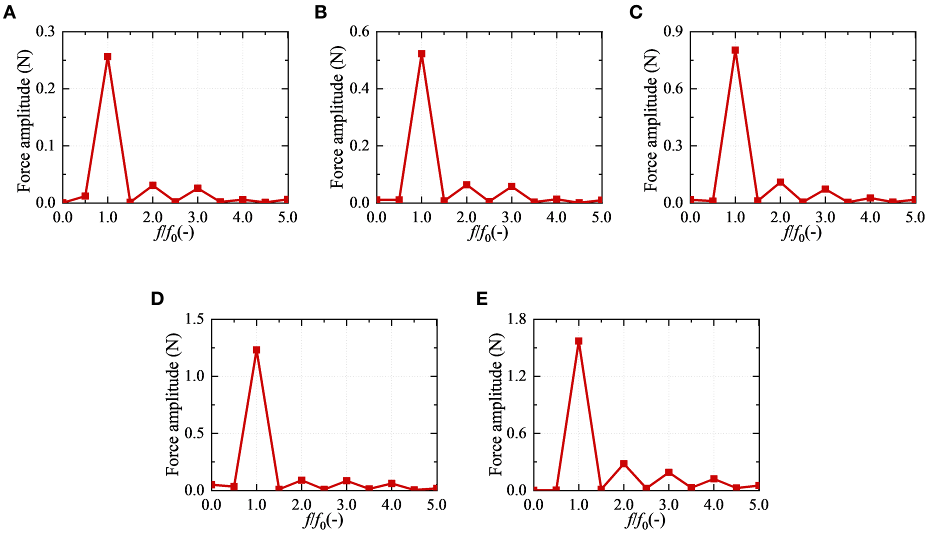

FIGURE 7
The amplitude spectrum of wave force in the experiment. **(A)** W1, ϵ = 0.021; **(B)** W2, ϵ = 0.032; **(C)** W3, ϵ = 0.041; **(D)** W4, ϵ = 0.052; **(E)** W5, ϵ = 0.061.

than the wave length, and each twine of the netting can be assumed as a small-scale component satisfying the Morison equation. Thus, the wave force of the whole netting can be simplified as the sum of Morison force of all twines. The least squares method can be used to fit the appropriate hydrodynamic coefficients for each wave condition (see Section 3.4), and then compare the predicted wave force with the test force, as shown in Figure 8.

When the wave steepness was small, the wave force predicted by Morison equation was in good agreement with the wave force measured in the test. With the increase of wave steepness, the predicted wave force deviated from the test value to varying degrees, mainly showing that the predicted wave force had higher horizontal asymmetry than the test value. In addition, their phases are basically the same, and both have obvious protrusions in front slope, while there were obvious depressions in rear slope. For this netting, the twines were not standard circular in cross-section, but nearly rectangular in shape. The inertia force corresponding to the effective volume of the netting cannot be ignored relative to the drag force corresponding to the effective projected area, which made a huge difference in the symmetry about front and rear slope.

3.3.2 The predicted force in frequency domain

Both the wave surface and wave force of the netting had strong nonlinearity, which greatly increased the difficulty of prediction. To study the nonlinear difference between the test and prediction values, the fast Fourier transform was performed on the corresponding wave surface and wave force in time domain to obtain their amplitude spectra. The comparison of the wave surface amplitude spectrum was shown in Figure 9A, and that of the wave force was shown in Figure 9B.

By comparing the test and prediction values of wave surface, it can be found that they were in good agreement, which was the basis for accurate prediction of wave force. The amplitudes of both were dominated by wave frequency, and the second-order frequency components accounted for the largest proportion of multiple frequency components. In addition, at the zero frequency, the sinking of the mean water level obtained from the test was always greater than that of the theoretical fifth-order wave surface. With the increase of wave steepness, the predicted amplitudes of wave force at multiple frequency and zero frequency were significantly greater than the corresponding test amplitude. These differences directly determined that the wave force predicted in time domain had more obvious nonlinear characteristics than the force tested (as shown in Figure 8).

3.4 Hydrodynamic coefficients

The hydrodynamic coefficients fitted by the predicted wave force were sorted and their variation rules with Keulegan-Carpenter number (KC number, $KC = u_{\max}T/D$, where $u_{\max}$ is the maximum horizontal velocity of the water particles) were shown in Figure 10. There, C_D was the drag coefficient, C_M was the inertial coefficient, and D was the dimension of the twine normal to the wave. In this study, the variation range of KC number is 35-120.

It can be seen from the figure that C_D decreased with the increasing KC number, while C_M remained basically unchanged. The variation range of C_D value was 2-2.82, with an average value of 2.4. The variation range of C_M was 1.99-2.23, with an average value of 2.1. Considering that the effective cross-section of the twine was nearly rectangular, its C_D value will be significantly greater than the empirical C_D value of slender rods with cylindrical section. In addition, due to the problems of the netting knitting process, its surface roughness was large, which would also increase its drag

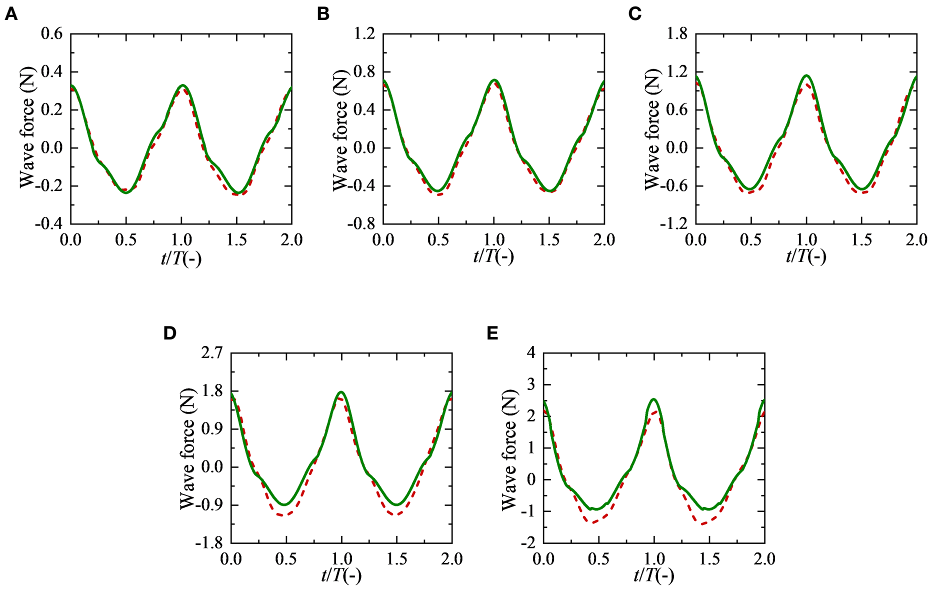

FIGURE 8
Comparison of the predicted wave force and the test force of netting in time domain. The green solid lines represent the predicted wave force and the red dashed lines represent the test force. **(A)** W1, ϵ = 0.021; **(B)** W2, ϵ = 0.032; **(C)** W3, ϵ = 0.041; **(D)** W4, ϵ = 0.052; **(E)** W5, ϵ = 0.061.

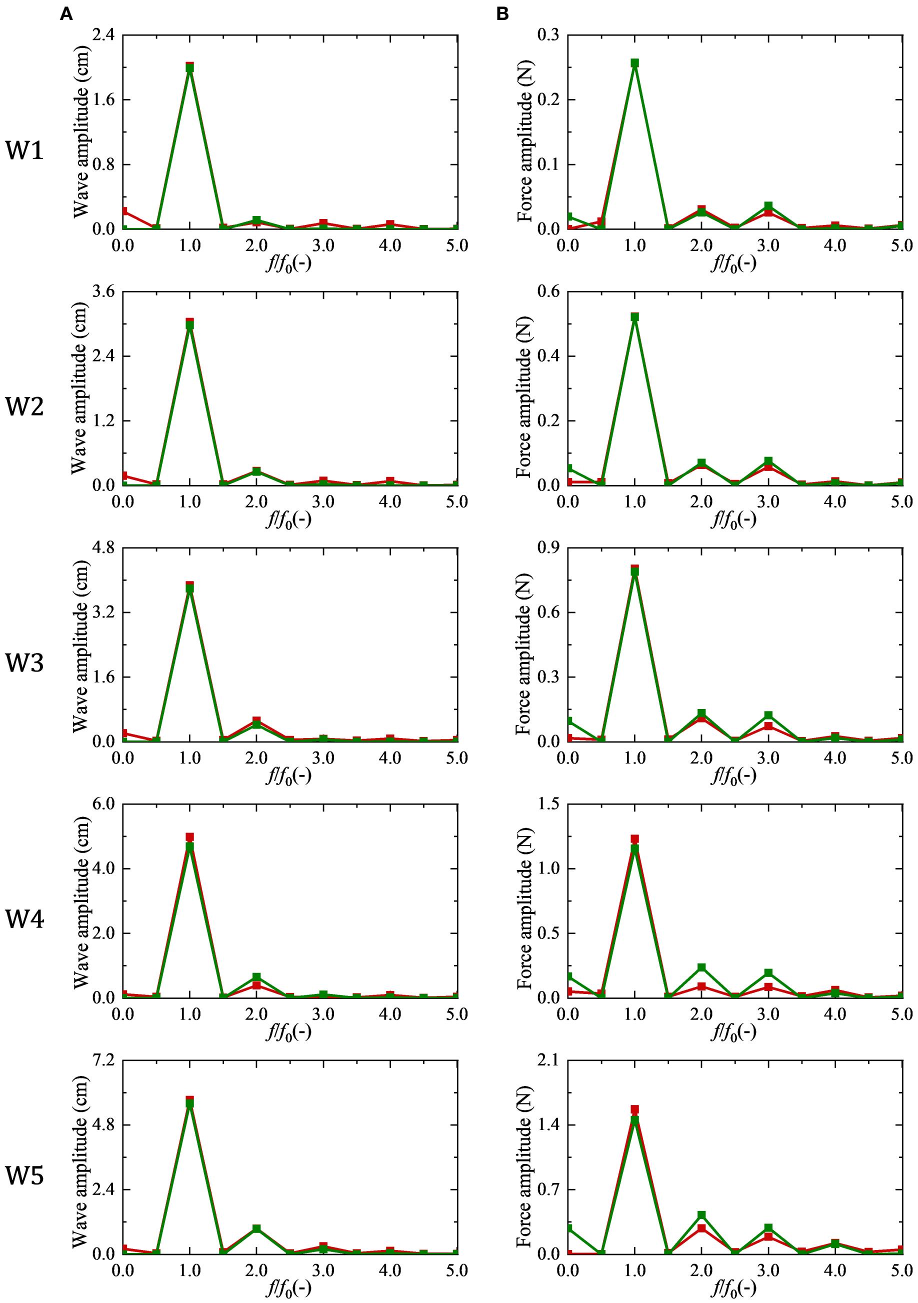

FIGURE 9
Comparison of the predicted wave force and the test force of netting in frequency domain. The green symbol with green line represents the amplitude spectrum of predicted wave force and the red symbol with red line represents the amplitude spectrum of the test force. **(A)** wave surface; **(B)** wave force.

coefficient. Therefore, the value range of drag coefficient obtained in this study had important practical significance and can provide reference for the design of anti-wave cage.

4 Conclusions

In this study, the horizontal wave force of a nylon netting was performed in a series of wave tests. The wave in the experiment had strong nonlinearity. The nonlinear characteristics of wave surface and wave force were analyzed by means of the fast Fourier transform method. Moreover, the wave forces of the netting were predicted based on Morison equation, and the accuracy of the predicted value was analyzed in time domain and frequency domain. The main results are as follows:

i. In the nonlinear wave test, wave force of the netting is more nonlinear than the wave surface. The positive

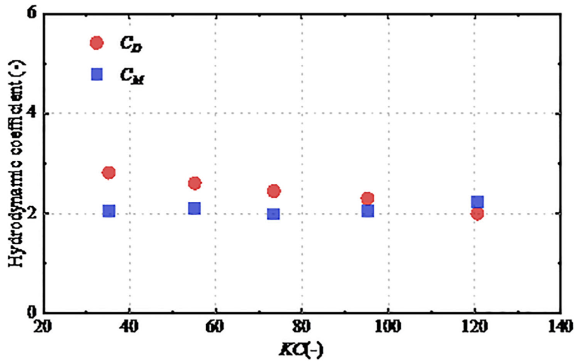

FIGURE 10
Hydrodynamic coefficients of the netting.

amplitude of wave force is basically proportional to the square of wave height.

ii. The wave surface and wave force are both dominated by wave frequency component. The second-order component contributes the most to the nonlinearity of the wave surface, while the third or higher-order components of the wave force have similar contribution as the second-order component.
iii. The wave forces predicted by the Morison equation agree well with the test values in time and frequency domain. As the wave steepness increases, the amplitude spectrum of predicted force at zero and multiple frequencies show obvious differences with the corresponding test values.
iv. The hydrodynamic coefficients of the test netting are quite different with single smooth cylinder mainly due to the cross-section and surface roughness of twine. The average C_D of the netting is about 2.4, and the average C_M is about 2.1.

Data availability statement

The datasets presented in this article are not readily available. Requests to access the datasets should be directed to Q-PC, chenqiupan@mail.dlut.edu.cn.

Author contributions

Q-PC experiment design, Data curation, Wave force prediction, Writing - original draft. C-WB: Supervision, Reviewing and Editing. Y-PZ: Conceptualization and Methodology. All authors contributed to the article and approved the submitted version.

Funding

This work was financially supported by the National Key R&D Program of China (no. 2019YFD0900902); National Natural Science Foundation of China (nos. 51822901, 31972843 and 31872610); LiaoNing Revitalization Talents Program (no. XLYC1907139); Dalian Technology Talents Program, project no. 2020RJ02.

Conflict of interest

The authors declare that the research was conducted in the absence of any commercial or financial relationships that could be construed as a potential conflict of interest.

Publisher's note

References

Balash, C., Colbourne, B., Bose, N., and Raman-Nair, W. (2009). Aquaculture net drag force and added mass. *Aquacult. Eng.* 41, 14–21. doi: 10.1016/j.aquaeng.2009.04.003

Bi, C.-W., Zhao, Y.-P., Dong, G.-H., Wu, Z.-M., Zhang, Y., and Xu, T.-J. (2018). Drag on and flow through the hydroid-fouled nets in currents. *Ocean Eng.* 161, 195–204. doi: 10.1016/j.oceaneng.2018.05.005

Endresen, P. C., and Moe-Føre, H. (2022). "Numerical modelling of drag and lift forces on aquaculture nets: Comparing new numerical load model with physical model test results," in *Proceedings of the ASME 2022* (Hamburg, Germany: 41st International Conference on Ocean, Offshore and Arctic Engineering).

Føre, H.M., Endresen, P.C., Norvik, C., and Lader, P.F. (2021). Hydrodynamic loads on net panels with different solidities. *J. Offshore Mech. Arc.* 143, 1–17. doi: 10.1115/1.4049723

Gansel, L. C., Plew, D. R., Endresen, P. C., Olsen, A. I., Misimi, E., Guenther, J., et al. (2015). Drag of clean and fouled net panels – measurements and parameterization of fouling. *PloS One* 10, 0131051. doi: 10.1371/journal.pone.0131051

Lader, P.F., Fredriksson, D.W., Guenther, J., Volent, Z., Blocher, N., Kristiansen, D., et al (2015). Drag on hydroid-fouled nets – An experimental approach. *China Ocean Eng.* 29, 369–389. doi: 10.1007/s13344-015-0026-y

Ma, C., Bi, C.-W., Xu, Z.-J., and Zhao, Y.-P. (2022). Dynamic behaviors of a hinged multi-body floating aquaculture platform under regular waves. *Ocean Eng.* 243, 110278. doi: 10.1016/j.oceaneng.2021.110278

Martin, T., Tsarau, A., and Bihs, H. (2020). A numerical framework for modelling the dynamics of open ocean aquaculture structures in viscous fluids. *Appl. Ocean Res.* 106, 102410. doi: 10.1016/j.apor.2020.102410

Nishimura, H., Isobe, M., and Horikawa, K. (1977). Higher order solutions of the stokes and cnoidal waves. *J. Fac. Eng. Univ. Tokyo Ser. B.* 34, 267–293.

Santo, H. (2022). On the application of current blockage model to steady drag force on fish net. *Aquacult. Eng.* 97, 102226. doi: 10.1016/j.aquaeng.2022.102226

Skjelbreia, L., and Hendrickson, J. (1960). Fifth order gravity wave theory. *Coast. Eng. Proc.* 1 (7), 184–196. doi: 10.9753/icce.v7.10

Swift, M. R., Fredriksson, D. W., Unrein, A., Fullerton, B., Patursson, O., and Baldwin, K. (2006). Drag force acting on biofouled net panels. *Aquacult. Eng.* 35, 292–299. doi: 10.1016/j.aquaeng.2006.03.002

Tang, H., Xu, L.-X., and Hu, F.-X. (2018). Hydrodynamic characteristics of knotted and knotless purse seine netting panels as determined in a flume tank. *PloS One* 13, 0192206. doi: 10.1371/journal.pone.0192206

Wang, S., Feng, D.-J., Gui, F.-K., and Xu, Z.-J. (2022). Dynamic behavior of the net of a pile-net-gapped enclosure aquaculture facility. *J. Mar. Sci. Eng.* 10, 1166. doi: 10.3390/jmse10091166

Wang, Y.-H., Fu, S.-X., Xu, Y.-W., Li, S., and Moan, T. (2022). Loads on a vessel-shaped fish cage steel structures, nets and connectors considering the effects of diffraction and radiation waves. *Mar. Struct.* 86, 103301. doi: 10.1016/j.marstruc.2022.103301

Wang, G., Martin, T., Huang, L.-Y., and Bihs, H. (2022). An improved screen force model based on CFD simulations of the hydrodynamic loads on knotless net panels. *Appl. Ocean Res.* 118, 102965. doi: 10.1016/j.apor.2021.102965

Zhan, J.-M., Jia, X.-P., Li, Y., Sun, M.-G., Guo, G.-X., and Hu, Y.-Z. (2006). Analytical and experimental investigation of drag on nets of fish cages. *Aquacult. Eng.* 35, 91–101. doi: 10.1016/j.aquaeng.2005.08.013

Zhao, Y.-P., Bi, C.-W., Dong, G.-H., Gui, F.-K., Cui, Y., Guan, C.-T., et al. (2013). Numerical simulation of the flow around fishing plane nets using the porous media model. *Ocean Eng.* 62, 25–37. doi: 10.1016/j.oceaneng.2013.01.009

Zhao, Y.-P., Chen, Q.-P., and Bi, C.-W. (2022). Numerical investigation of nonlinear wave loads on a trestle-netting enclosure aquaculture facility. *Ocean Eng.* 257, 111610. doi: 10.1016/j.oceaneng.2022.111610

Zhou, C., Xu, L.-X., Hu, F.-X., and Qu, X.-Y. (2015). Hydrodynamic characteristics of knotless nylon netting normal to free stream and effect of inclination. *Ocean Eng.* 110, 89–97. doi: 10.1016/j.oceaneng.2015.09.043

frontiers | Frontiers in Marine Science

TYPE Original Research
PUBLISHED 15 May 2023
DOI 10.3389/fmars.2023.1175852

OPEN ACCESS

EDITED BY
Yang Jin,
Johns Hopkins Medicine, United States

REVIEWED BY
Hung-Jie Tang,
National Cheng Kung University, Taiwan
Chunwei Bi,
Ocean University of China, China

*CORRESPONDENCE
Chang-tao Guan
✉ guanct@ysfri.ac.cn

RECEIVED 28 February 2023
ACCEPTED 14 April 2023
PUBLISHED 15 May 2023

CITATION
Cui Y, Wang G and Guan C-t (2023)
Numerical and experimental investigations of hydrodynamics of a fully-enclosed pile-net aquaculture pen in regular waves.
Front. Mar. Sci. 10:1175852.
doi: 10.3389/fmars.2023.1175852

Numerical and experimental investigations of hydrodynamics of a fully-enclosed pile-net aquaculture pen in regular waves

Yong Cui, Gang Wang and Chang-tao Guan*

Yellow Sea Fisheries Research Institute, Chinese Academy of Fishery Sciences, Qingdao, China

Large-scale aquaculture pen is one of the essential modes of offshore aquaculture being explored in recent years. In contrast to cage farming, the advantages are more significant as the larger cultural space for fish swimming, the closer-to-nature environment, and the improved ecological quality of fish. As a novel offshore aquaculture structure, fully-enclosed pile-net aquaculture pens (FPAPs) are generally deployed in exposed oceans, where severe waves and currents are of great dominance. The hydrodynamic characteristics of FPAPs in offshore areas deserve further investigation. In this paper, the numerical model of a typical FPAP in waves is proposed based on the finite element method (FEM), then wave loads on and induced motion responses of the FPAP are analyzed. The results show that the maximum loads on the structure and the maximum displacement of piles are closely proportional to the wave height. Secondly, the maximum stress of nets decreases as the embedded depth increases, while the deformation of nets tends to rise with the increase of pile spacing. At last, several structural optimal patterns are given to improve the safety of pen facilities. This work has laid a solid scientific foundation for designs and optimizations of FPAPs in the future.

KEYWORDS

fully-enclosed pile-net aquaculture pen (FPAP), offshore aquaculture, hydrodynamics, embedded depth, pile spacing

1 Introduction

Mariculture in China mainly consists of land-based and nearshore aquaculture, and these cultural regions considerably suffer from land-based pollution. Nevertheless, due to economic and social development as well as people's higher requirements on life, the space available for mariculture has been severely squeezed, resulting in increasingly prominent problems such as excessive farming density, frequent occurrence of diseases and environmental degradation. In order to realize the sustainable development of mariculture and reduce the impact of farming on coastal areas, it is urgent to expand the space for aquaculture and carry out offshore farming (Chu et al., 2020). The large-scale pile-net aquaculture pen is developed as one of the essential innovative modes, suitable for economic fish farming in China. Ordinarily located at the flat seabed with the continental shelves, the primary structures of large-scale aquaculture pens are composed of piles, side nets, rope constraints and affiliated facilities. It can be categorized into two typical types: Coast-connected pile-net aquaculture pen (CPAP, Figure 1A) and fully-enclosed pile-net aquaculture pen (FPAP, Figure 1B), of which the latter would suffer from severe sea states in offshore regions. Due to the shortage of systematic research on FPAPs, the structural design and engineering technology of large-scale pens are still nonetheless immature, and the abilities of anti-stormy waves need to be evaluated and then improved considerably. Therefore, it is universally recognized that hydrodynamic characteristics of the FPAP in waves have become a critical safety issue.

Without bottom nets and mooring systems, steel piles and side nets assembled in FPAPs have fully formed the cultural regions, indicating that side nets take an indispensable role in the whole aquaculture system. Nevertheless, flexible nets are the most fragile parts compared with piles in open oceans, hence numerous researches related to hydrodynamics of flexible nets have been conducted through model tests and numerical simulation in the past decades. Huang et al. (2018) established a numerical model to simulate the dynamic behavior of a floating net cage in waves and currents, based on the finite element method (FEM). Zhao et al. (2015) conducted a series of physical model experiments to investigate the hydrodynamic characteristics of a large fish farm containing one up to eight net pens with a scaling of 1:40. Cifuentes and Kim (2017) presented an analysis of a cage under combinations of current and wave loading, and the numerical results were validated with experimental data. Bi et al. (2013) conducted a series of laboratory experiments to investigate the reduction in flow velocity downstream from a fishing net in a current. Cui et al. (2014) presented a simulation model based on FEM to analyze the motion response and mooring line tension of a flatfish cage system in waves. Gharechae and Ketabdari (2020) developed a semi-analytical model to find the vertical motions and wave fields around elastic circular floaters of aquaculture fish cages in regular waves. Mohapatra et al. (2021) developed a mathematical model associated with wave interaction with a moored floating flexible cylindrical net cage based on linearized water wave theory. The analytical solution was obtained using the Fourier Bessel series solution and least squares approximation method along with matching the velocity and pressure at the fluid-structure interfaces. He et al. (2018) studied the influence of fish on the mooring loads of a floating net cage.

Initialized from pile-net coupled structures, Yang et al. (2020) investigated the hydrodynamic responses of a floating rope enclosure with different mooring systems in combined wave-current. Gui et al. (2020) and Chen et al. (2018) introduced a novel pile-column type net enclosure, which was mainly composed of piles and net panels. The mechanical properties of nets in waves and current were further investigated using FEM simulation, thereby the guidelines of design and construction have been provided. Zhao et al. (2022) reported a trestle-netting enclosure aquaculture facility combining an offshore steel trestle with a marine aquaculture facility in which the trestle acts as a supporting substructure. A full-scale finite element model of the system was established, then the structural responses subjected to wave were discussed innovatively.

To the authors' best knowledge, the hydrodynamic characteristics of FPAPs in waves are seldom studied systematically at present. The investigated case of FPAPs adopted in this study is "Lan-zuan No. 1" located in Laizhou Bay of China, which is mainly made up of steel pipe piles, with a volume of 160,000 m^3. It is justified in the field monitoring that the existence of deformations and vibrations in waves, threatening long-term safe operations. The hydrodynamic responses of the FPAP in waves are carried out through FEM and experimental validations. Thereby the crucial innovative significance of this study lies in filling the research gap, proposing the design or optimization recommendations from the perspectives of hydrodynamics.

2 Material and methods

2.1 Numerical methods

2.1.1 Finite element methods

The governing equations of dynamic responses of steel frames and nets in waves and currents are defined as follows (Tsukrov et al., 2003):

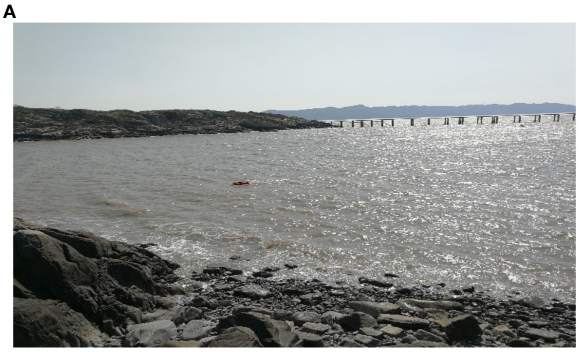

coast-connected pile-net aquaculture pen (CPAP)

fully-enclosed pile-net aquaculture pen (FPAP)

FIGURE 1
The categories of the large-scale aquaculture pens. **(A)** coast-connected pile-net aquaculture pen (CPAP). **(B)** fully-enclosed pile-net aquaculture pen (FPAP).

$$M\ddot{a}(t) + Ka(t) = F(t) \quad (1)$$

where M denotes the mass matrix, while K represents the stiffness matrix in the dynamic structural system. Resulting from the relative motion between structures and fluids, $F(t)$ represents the resultant nodal forces including hydrodynamic forces, gravity and buoyancy forces. $a(t)$ denotes the nodal displacement vectors, $\dot{a}(t)$ and $\ddot{a}(t)$ are the vectors of nodal velocity and acceleration, respectively. The numerical solution to $\dot{a}(t)$ in Eq. (1) is the typical Newmark- β time-advancement scheme. The governing equations as well as the detailed schemes have been implemented in the FEM parts of the commercial software ANSYS, of which modelling accuracies have been successfully validated in the flat-cage hydrodynamics investigations (Cui et al., 2013).

The pipe piles, net systems as well as beams are simulated using the PIPE element, with the capabilities of tension-compression, torsion, and bending. The applicability and accuracy of the PIPE element to simulate the hydrodynamics of nets and beams in waves and currents have been justified in Cui et al. (2013). The Morison model is further utilized to calculate the wave loads F_h on piles, nets and beams, which is given by

$$\{F_h/l\} = \frac{1}{2}C_D\rho_w d\left|\dot{U}_n\right|\dot{U}_n + \frac{1}{2}C_T\rho_w d\left|\dot{U}_t\right|\dot{U}_t + C_M\rho_w\frac{\pi}{4}d^2\left|\ddot{U}_n\right| \quad (2)$$

where C_D denotes the normal drag coefficient while C_T represents the tangential component. C_M denotes the inertia coefficient which is the addition of 1 and the added mass coefficient. ρ_w is the water density. d and l correspond to the diameters and lengths, respectively. $\dot{U}$ are the velocity vectors of relative motions between water particles and elements, while $\ddot{U}$ represents the acceleration vectors. The operational platform made of moderately-thick shell structures is modelled by the SHELL element, with linear, large rotation, and/or large strain non-linear properties (ANSYS Inc, 2009). It is the four-node element capable of simulating six degrees of freedom at each node, thus being widely applied in mechanics studies of offshore structures (Xia et al., 2019). In addition, COMBIN non-linear spring element is adopted to model elastic-plastic soil axial and lateral friction behavior, then the reaction force of soil on the pipe pile can be derived.

2.1.2 Mesh-grouping strategy

The computational loads can be excessively considerable in case of modelling with the actual number of meshes, resulting in the decrease of computational efficiencies. Therefore, a novel mesh-grouping method is utilized for the simplification of all net meshes. Proposed by Wan et al. (2007), the mesh-grouping strategy is to combine several original actual meshes into one so-called virtual mesh. The computational accuracies and efficiencies with various mesh-grouping strategies are discussed, combined with several hypotheses practically. That is, the geometric scale, the weights as well as the hydrodynamics loads should be kept consistent amongst the virtual mesh and the pre-merged meshes during mesh-grouping. It has been widely verified for FEM modelling of net cages and fishing gears in waves and currents (Bi et al., 2014; Cui et al., 2014; Huang et al., 2019), along with the Morison force model. Depicted through continuous bolded lines in Figure 2, the example of a virtual mesh is surrounded by certain physical meshes transversely and longitudinally.

Keeping the hydrodynamic loads on the virtual mesh and the pre-merged meshes consistent, the relevance of twine diameters can be derived with Morison force model as follows:

$$d_2 = \frac{NT_1 * NN_1}{n * NT_2 * NN_2} d_1 \quad (3)$$

Keeping the physical weights of the virtual mesh and the pre-merged meshes consistent, the material densities of twines can be derived as follows:

$$\rho_2 = \frac{n * NT_2 * NN_2}{NT_1 * NN_1} \rho_1 \quad (4)$$

where NN_1 and NN_2 are the numbers of longitudinal meshes during grouping, respectively; NT_1, NT_2 are the numbers of mesh in radial direction during grouping; n denotes the number of the grouping, that is, the number of the actual mesh bar contained in a grouped mesh bar; d_1 and ρ_1 are the twine diameter and density of physical meshes, respectively; d_2 and ρ_2 are the twine diameter and density of the grouped meshes, respectively.

2.1.3 Pipe-soil interaction model

The overall model restricts the freedom of Z direction (vertical direction) at the bottom node of the pile. In this model, the resistance of soil to pipe pile is simulated by setting p-y parameter of spring elements. Meanwhile, one end of the spring is connected to the pipe pile, and the other end is fully constrained. The constraint mode of the overall model of FPAP is shown in Figure 3.

The formula for calculating the p-y curve of pipe pile located in sandy soil is as follows (Zhao et al., 2007):

$$\begin{cases} p = AP_u \tan h\left[\frac{Kz}{AP_u} y\right] \\ A = \left(3.0 - 0.8\frac{z}{D}\right) \geq 0.9 \end{cases} \quad (5)$$

where p is the horizontal soil resistance acting on unit area of pile side at a certain depth z; y is the horizontal displacement at a certain depth z; P_u is the ultimate soil resistance per unit pile length; A is the coefficients; K is the initial modulus; D is the pile diameter.

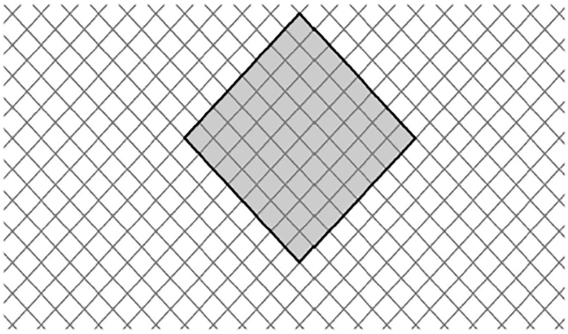

FIGURE 2
Overview of the grouped mesh.

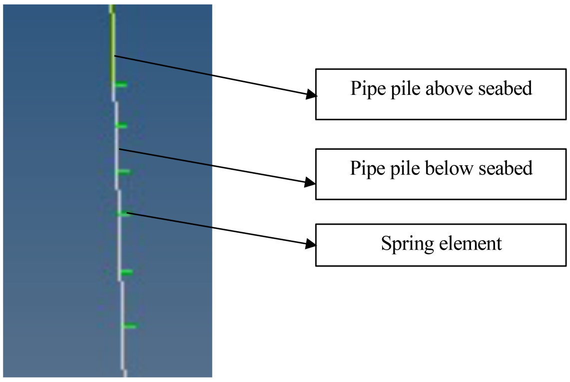

FIGURE 3
Overall model constraints.

2.2 Geometries of “Lan-zuan No.1” FPAP

The large-scale FPAP “Lan-zuan No.1” is mainly composed of pipe piles, nets, an operational platform and beams (see Figure 1B). The perimeter of steel FPAP is 400 m, of which the cultural area is 12,661 m^2, and the cultural volume is 160,000 m^3. The pen comprises 172 pipe piles, including one central pile and 171 circular pipe piles. The pipe pile uses spiral steel tubes with the diameter of 508 mm and wall thickness of 10 mm. Each pipe pile has a length of 26 m and is welded by two steel tubes of 13 m. The length of the pipe pile inserted into the seabed is 8.5 m. At low tide, the pipe pile is 5.1 m above the water level, and at high tide, it is 4.0 m above the water level. The pen is a structure of double-layer pipe piles, with the diameter of outer piles 127 m and inner piles 117 m. The distance between the inner and outer pipe piles is 5 m. The spacing of external pipe piles is also about 5 m. And the top layer of pipe piles is connected by “N” type beams. The scale of the corridor width is 1250 mm.

2.3 Numerical model of FPAP and cases set-up

The XY plane of the coordinate system is consistent with the horizontal plane. The Z-axis is determined by the right-hand rule and is compatible with the axis of the pipe pile. And the origin of coordinates is located at the center of the FPAP as well as the numerical model are depicted in Figure 4. The input wave scenarios, based on the fifth-order Stokes waves theory, are set based on the actual sea-state data, as described in Table 1.

3 Experimental validations

The local model tests were performed in a wave–current flume at the State Key Laboratory of Coastal and Offshore Engineering, Dalian University of Technology, Dalian, China. In order to project the hydrodynamics of the local model into a full-scale one at the large extent, the prototype FPAP have been extracted locally and then scaled to meet the flume test conditions (the test flume is 60.0 m long, 2.0 m wide while the depth corresponds to 1.8 m) using Froude scaling criterion (λ =1:20). In general, the heights and the diameters of pipe piles are 875 mm and 25 mm, respectively (see Figure 5).

In order to study the effects of pile spacing on wave force of the pen, three models with pile spacing of 250mm, 500mm and 750mm are tested respectively. The local model and prototype parameters are shown in Table 2. The schematic diagram of three finite element models with different pile spacing is shown in Figure 6.

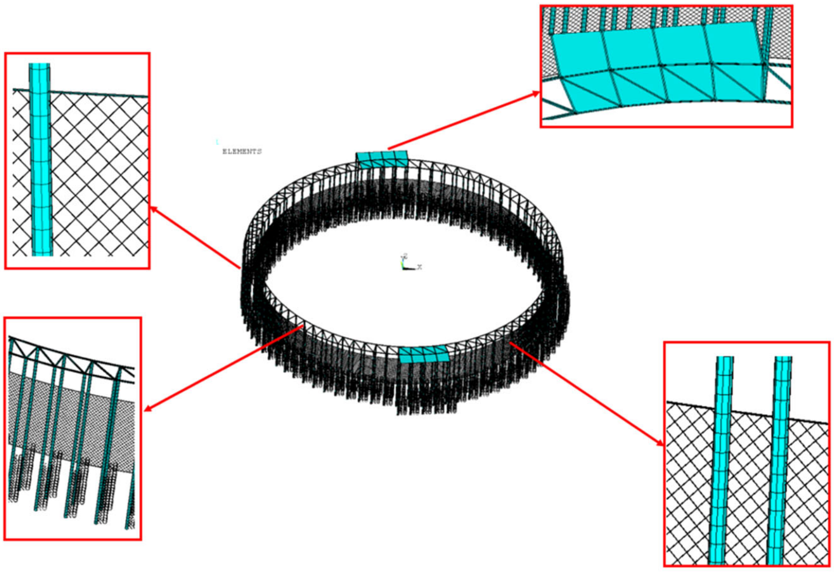

FIGURE 4
Overview of finite element models of the FPAP.

The wave load shown in Table 3 is applied to the local model to calculate the wave forces on the local model under different wave heights and periods.

According to the measurement method in the local model test, a full constraint is applied on the bottom of the local numerical model. The maximum force of the top point is extracted from the local model as the calculated wave force. The accuracy of the modeling method is verified by comparing the calculated wave force with the measured force of the pipe pile in the test as shown in Figure 7. From Figure 7, the average relative errors of the three spacing are 8.25%, 10.13% and 6.88% respectively. With the wave height of 50 mm, the local model receives less wave force, and the relative error between simulation and test is large, with the maximum relative error is 19%. The reason for the error between the experimental value and the simulated value may be that the mesh group method is adopted in the numerical simulation, and the influence of the grouped mesh on the waves is not considered. In addition, the details of the numerical model cannot be completely consistent with the model test, and there are small differences between the physical and numerical models (Liu et al., 2020). Therefore, the modelling accuracies and reasonability of the local model have been substantiated through the validations.

FIGURE 5
Local physical model test with scale of 1:20.

4 Results

4.1 Wave forces and displacements of pipe piles

The wave induced forces and displacements of pipe piles in various wave cases are evaluated in this section, wherein the maximum forces of the pen perpendicular to flow are extracted in Figure 8 and Figure 9.

Since the hydrodynamic loads vary periodically with the evolvement of waves, the maxima of forces and displacements of piles within a period are analyzed in each case. Figure 8 presents the maximum force on piles with various wave periods and wave heights. It can be observed from Figure 8 that the maximum wave forces are closely proportional to wave heights. In addition, no obvious correlation exists amongst maximum forces and wave periods. The maximum force of the pen reaches 476.5 kN for the case with wave height 3.00 m and wave period 6.19 s. Figure 9 shows the maximum displacement of pipe piles with wave inputs. The variation of displacements with wave inputs has the similar tendency with that of maximum force. The maximum displacement of the pipe pile is about 18.4 mm for the case with wave height 3.00 m and wave period 6.19 s.

4.2 Bending moments of pipe piles and nets deformation

It is illustrated in Figure 10 that the variation patterns of bending moments of the pipe pile with elevations. For each case, the uniform trend can be observed that both positive and negative bending moments increase firstly and then decrease with the elevation. The maximum bending moment is within the range of 3 m below the seabed. Furthermore, the second largest bending moment is approximately located at the free surface. The above analysis results are in accordance with the numerical results of Gui et al. (2020). Meanwhile, the bending moment with the same elevation rises with the increasing of wave height. Given the consistent wave heights,

TABLE 1 Wave cases for the FPAP.

Wave Case No.	1	2	3	4	5	6	7	8	9
Wave Height (m)	1.44	1.44	1.44	2.11	2.11	2.11	3.00	3.00	3.00
Wave Period (s)	5.73	6.19	7.45	5.73	6.19	7.45	5.73	6.19	7.45

TABLE 2 Local model and prototype parameters.

Parameter	Prototype(m)	Model(m)
Height of pipe pile	17.5	0.875
Height of nets	17.5	0.875
Pile spacing	5/10/15	0.25/0.50/0.75

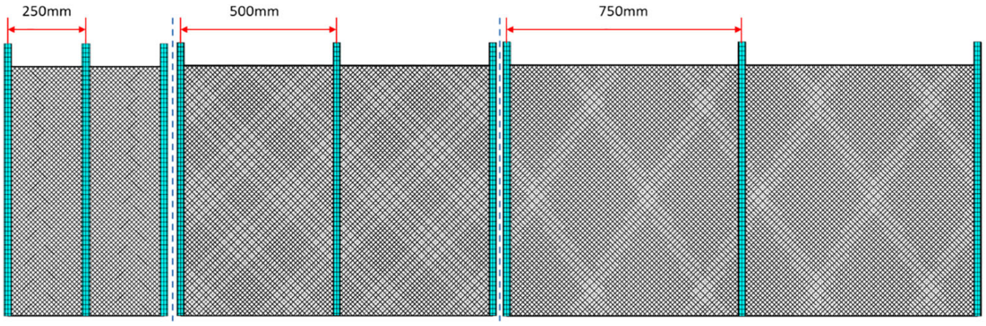

FIGURE 6
Three finite element models with different pile spacing.

there is no distinct correlation between bending moments and wave periods. For the case of which wave height is 3 m, the maximum bending moment of pile is 24609 N·m, which is still in the scope of the ultimate bending moment of pipe piles.

Figure 11 shows the variation of the deformations of nets in the streamwise direction with elevations. A general tendency can be detected that the displacement of nets increases first and then decreases with the elevation. The maximum displacement is within the range of 2 m beneath free surfaces. Moreover, the displacement of nets close to the free surface tends to zero. It is possibly attributed to the rope, of which the stiffness is considerably larger than the nets, assembled with the net panel at 500 mm above the sea. The maximum displacement is approximate 0.7 m corresponding to the case with wave height 1.44 m, while the maximum displacement reaches sharply to 1.6 m with wave height 3 m case, which is nevertheless doubled compared to the former one.

4.3 The first principal stresses of nets and beams

As the essential factor in the field of structural mechanics, the 1st principal stress has provided the maximum tensile stress induced in the part due to the hydrodynamic loadings, applied universally for the fragile materials. Thus, the rationalities of using this principle to evaluate stresses of nets and beams are justified. Figures 12 and 13 show the maximum stress of nets and beams in varying wave periods and heights, separately. It can be concluded from Figure 12 that the maximum stress of nets is significantly proportional to wave heights, while the maximum stresses are however presenting a downward trend with wave periods rising. Furthermore, it is noticeable in Figure 13 that the maximum stresses of beams exhibit the upward tendencies with the rise of wave heights, but is not dependent on the wave period. The maximum stress of nets reaches about 13.99 MPa with the case of wave height 3 m and wave period 5.73 s, while the maximum stress of beams is around 12.55 MPa with the case of the same wave height and wave period 6.19 s.

5 Discussion

In comparison with typical net cages, the large-scale FPAP is an innovative type of offshore aquaculture facility. The evident advantages have been introduced at present such as the large cultural region, close-to-nature farming environment to prevent diseases and substantially adaptive for the sea areas with flat trend of China's continental shelf. The relevance of designs and constructions of FPAP with hydrodynamic characteristics should be investigated further, thereby the effects of depths and spacings of pipe piles are discussed in this section.

TABLE 3 Wave conditions for the numerical calculation and the local physical experiment.

Wave Case No.	Prototype Value		Model Value	
	Wave Height (m)	Wave Period (s)	Wave Height (m)	Wave Period (s)
1	1	4.0	0.05	0.9
2	1	4.9	0.05	1.1
3	1	5.8	0.05	1.3
4	2	4.0	0.10	0.9
5	2	4.9	0.10	1.1
6	2	5.8	0.10	1.3
7	3	4.9	0.15	1.1
8	3	5.8	0.15	1.3

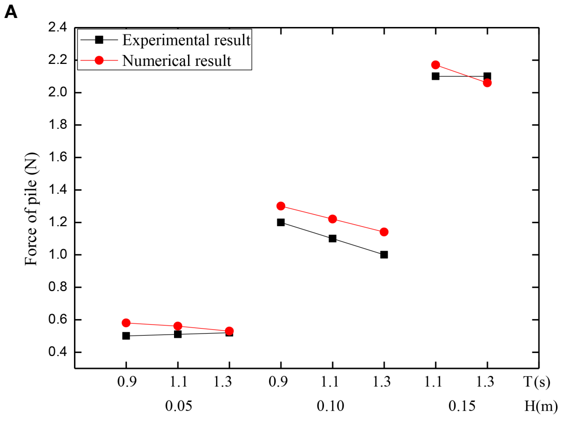

Pile spacing 250mm

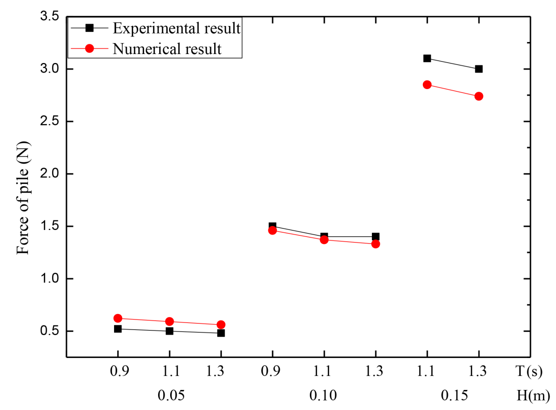

Pile spacing 500mm

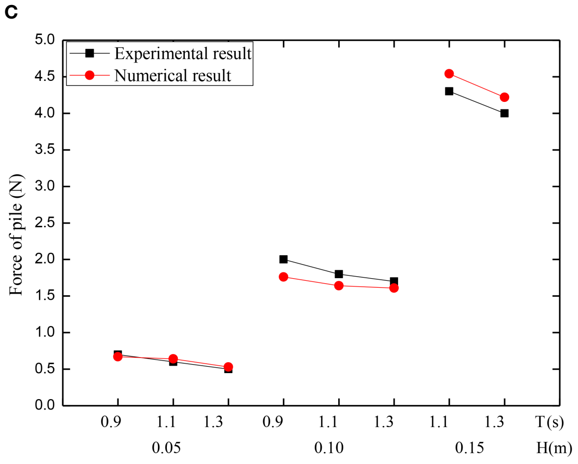

Pile spacing 750mm

FIGURE 7
Comparison of the pile force between the calculated and experimental values. **(A)** Pile spacing 250mm. **(B)** Pile spacing 500mm. **(C)** Pile spacing 750mm.

5.1 Effect of embedded depth

The costs of finance and resources for FPAP *in-situ* constructions are much more significant contrast with the that of typical deep-water fish cages, especially for offshore pilings. The selections of embedded depth are of great significance to ensure the stability of the FPAP and reduce the construction cost. It can be observed from Figure 14 that as the embedded depth continues to increase, the maximum stress of nets declines throughout all wave scenarios. Additionally, when the embedded depth is 7.5 m, the maximum tension of the nets is about 1% higher than that of 9.0 m on average. It has the implication that the embedded depth shows few impacts on the stress of side nets. Meanwhile, it is apparent from Figure 15 that the maximum displacement of piles exhibits a downward trend with embedded depths rising. It can be calculated that the maximum reduction reaches 9.2% with the rise of embedded depths, for the case of which wave height is 2.11 m and wave period is 5.73 s. The simulated results are also consistent with Gui et al. (2020) qualitatively and quantificationally.

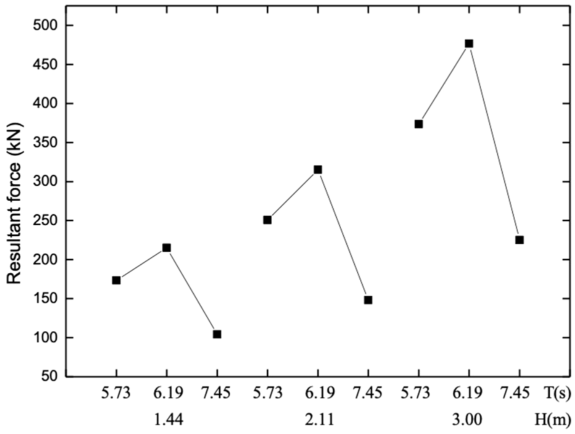

FIGURE 8
Maximum forces of pens.

Figure 16 shows that the maximum stresses of beams marginally increase with the embedded depth. A possible explanation lies in the position of the beam, which is closer to the water surface with the increase of embedded depth. Provided the embedded depth ranges from 7.5 m ~ 9.0 m, the maximum stresses of the beam rise by 2.2% on average across all wave cases. In general,

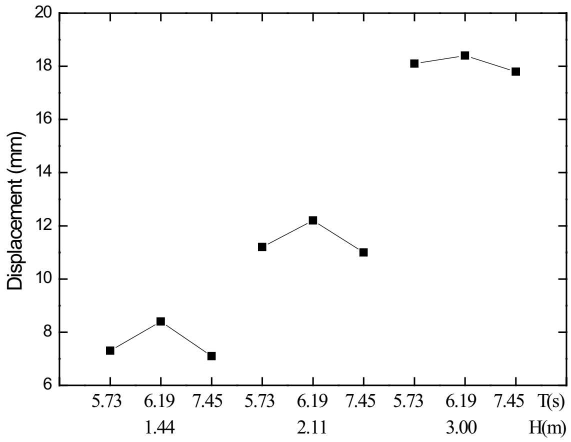

FIGURE 9
Displacements of pipe piles.

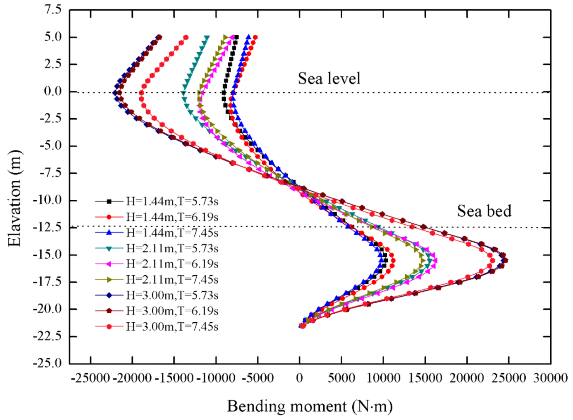

FIGURE 10
Variation of bending moments.

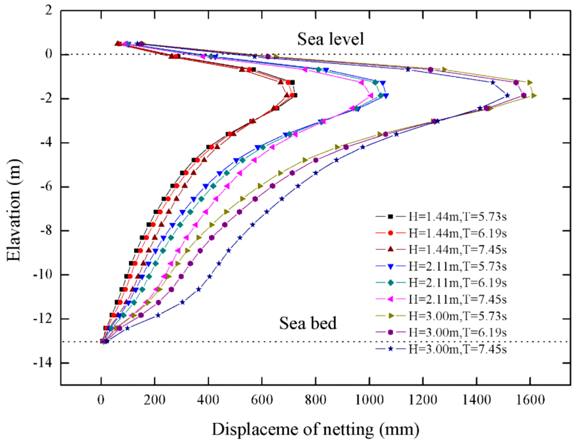

FIGURE 11
Variation of net deformations with varying waves inputs.

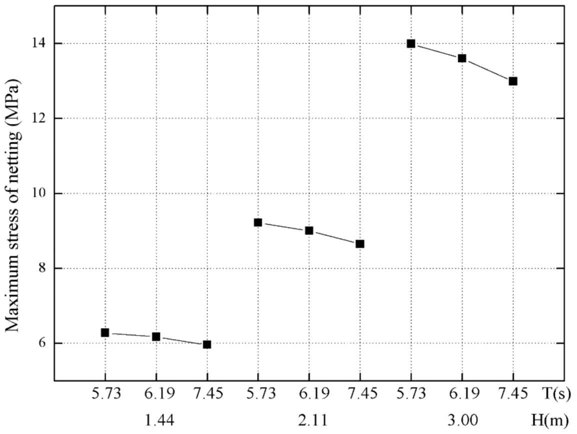

FIGURE 12
Maximum stress of nets.

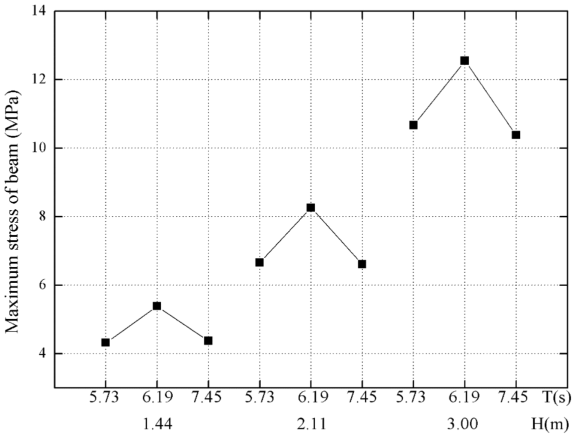

FIGURE 13
Maximum stress of beams.

the depth of pile piling has little effect on pile displacements, stresses of net twines and beams. To ensure the stability of the pen structure, embedded depth should be decided according to the specific conditions of seabed geology, otherwise the costs and the challenges of piling operations would be considerable. For the consideration of providing a more general recommendations for FPAP in other regions, the effects of a wider range of embedded depths on hydrodynamics and structural mechanics deserve further investigations in the future study.

5.2 Effect of pipe pile spacing

When the pile gap to diameter (L/D) is smaller than 4, the experimental results indicate wave transmission between piles can have a more significant influence, that is, the pile group effect (Xu, 2019). In addition to embedded depths, the selection of pipe pile spacing should also be considered on the basis of the safety of

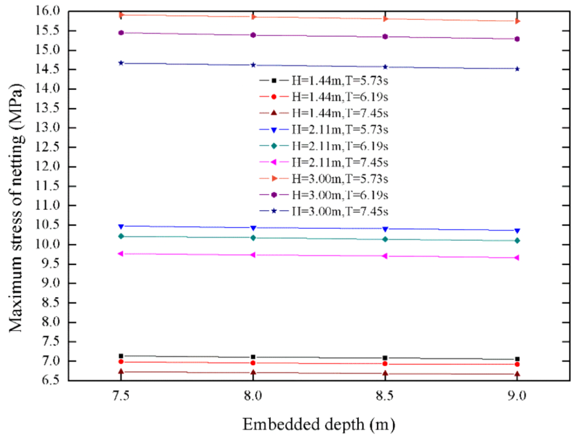

FIGURE 14
Maximum stress of nets.

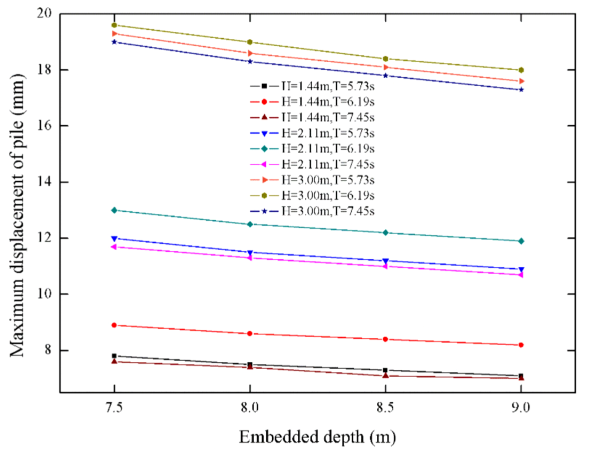

FIGURE 15
Maximum displacement of piles.

FPAPs and the cost of constructions. In order to study the influence of pipe pile spacing on the hydrodynamic properties of FPAPs, the distance between pipe piles is selected from 4.0 m to 6.2 m. The pile group effect is negligible to be ignored outside of this range. Figure 17 shows the maximum displacement of nets with elevations for three kinds of pile spacings. It can be noted that the deformations of nets tend to increase with the increase of pipe pile spacing, and the relative increment can reach 34%. Meanwhile, the maximum displacements of the nets across all cases can be simultaneously detected close to free surfaces, implying that the nets interacted with free surfaces should be reinforced to prevent the potential damages. Keeping the wave inputs and the embedded depth constant, it is pronounced from Figure 18 that the maximum displacements of piles get enhanced with enlarging the pile spacing. Given the shrinking of the number of pipe piles, the stiffness of the FPAP can be weakened and the induced distinct deformations of nets and beams would threaten the safety of the overall structure. The variation patterns of the stresses of nets and beams with pile-spacing are demonstrated in Figure 19 and Figure 20. It can be principally concluded that net stresses would decline while enlarging pile-spacing, and the varying trend of beam stresses is similar as that of the net stresses. The stresses of net twines and beams decrease by 2% and 4% on average while the pile spacings corresponding from 4.5 m to 5.5 m.

5.3 Structural optimizations

In this part, the case with the dominated induced displacements (pipe pile spacing 6.25 m, embedded depth 7.50 m, wave height 3.00 m, wave period 6.19 s) are utilized, taking the most extreme scenario into consideration. The wave forces in three directions, joint forces of the I-beam at the top of the pen and the welding points of piles are provided for the strength check of the welding site. As the area outlined in Figure 21, the maximum force on the top beam is about 12.53 kN.

Diverse from the typical offshore structures with piles, the flexible side-net systems are equipped with FPAPs. As demonstrated in Figure 22, the wave loads on and deformation of the nets in the proximity of free surfaces are the largest. After the deployment, it should be noticed that the bio-fouling issues of nets are quite substantial for a long duration, resulting in the surging of hydrodynamic drags. As a result, the nets of the FPAP needs to be cleaned timely to prevent net-mesh blockage and the induced damages.

In the Figure 23, the stress is relatively concentrated at the welding position of the beam composed of the walking board. The maximum stress in regular waves is 79.33 MPa for the case of which wave height 3.00 m and wave period 5.74 s. Due to the concentration of stresses, there is the possibility that the cracking event at the welded region can occur, emphasizing the dominance of welding qualities during constructions. It is recommended that the reinforcement plate as shown in Figure 24 be added at the weld position where the weld is prone to be damaged. Following the

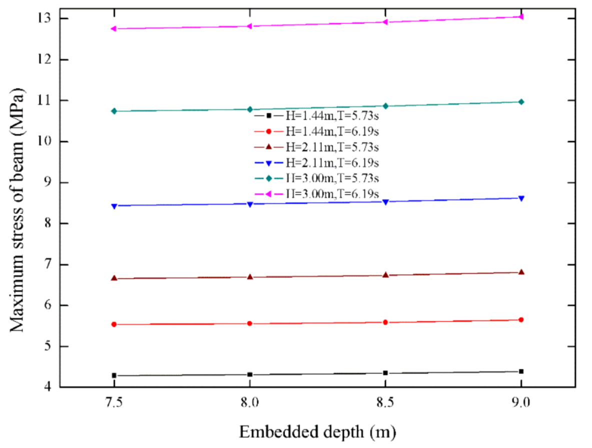

FIGURE 16
Maximum stress of beams.

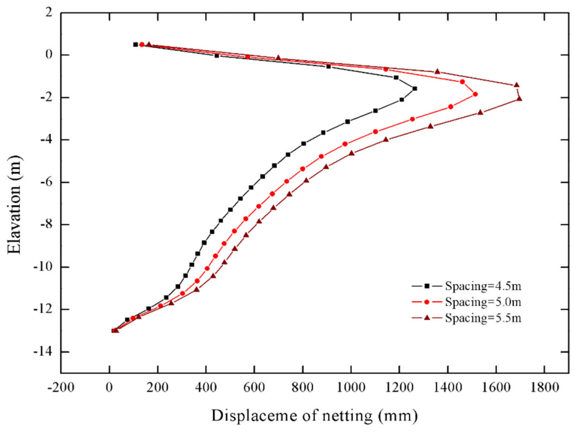

FIGURE 17
Displacement of nets with elevations.

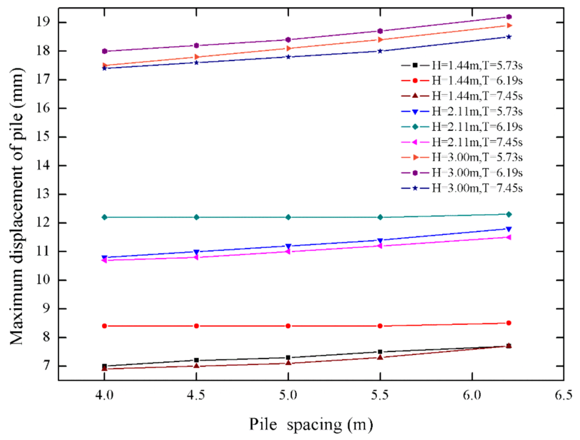

FIGURE 18
Maximum displacement of pile with pile spacings.

optimizations in the Figure 25, after adding the reinforced plate, the stress decreases from 79.33 MPa to 44.45 MPa, which greatly reduces the stress level and the risk of cracking.

6 Conclusions

In this study, the hydrodynamic responses of a novel FPAP in regular waves are investigated using the finite element modelling. The accuracies of numerical methods have been verified against the physical measurements, with the relative error of wave loads is about 10%. Then hydrodynamic loads on and structural responses of the FPAP are analyzed and discussed. The structural optimizations regarding reducing the stresses to prevent cracking are conducted finally. The conclusions are summarized as follows:

(1) The maximum force of the pen and the maximum displacement of the pipe pile are closely proportional to the wave height. In addition, the change of wave period has little effect on the force and deformation. The maximum bending moment is within the range of 3 m below the seabed. When wave height is 3 m, the maximum bending moment of pile is 24609 N·m. The displacement of nets increases first and then decreases with the structure elevation, and the maximum displacement is within the range of 2 m below the sea level. The maximum stress of nets is about 13.99 MPa and the maximum stress of beam is about 12.55 MPa.

(2) As the embedded depth continues to increase, the maximum stress of nets decreases under nine wave conditions. Meanwhile, the maximum displacement of pile exhibits a downward trend with increasing embedded depth. The maximum stress of beam increases slowly with the increase of embedded depth. In general, the depth of pile driving has little effect on the deformation of pipe pile, the stress of nets and beam.

(3) The deformation of nets tends to increase with the increase of pipe pile spacing, and the maximum displacement of pile exhibits a rising trend with increasing pile spacing under the same wave condition and embedded depth. Meanwhile, nets stress and beam stress will exhibit a downward trend for the pen with increasing pile spacing.

(4) Some suggestions on the optimization of the pen structure are given. The nets of the FPAP needs to be cleaned on time

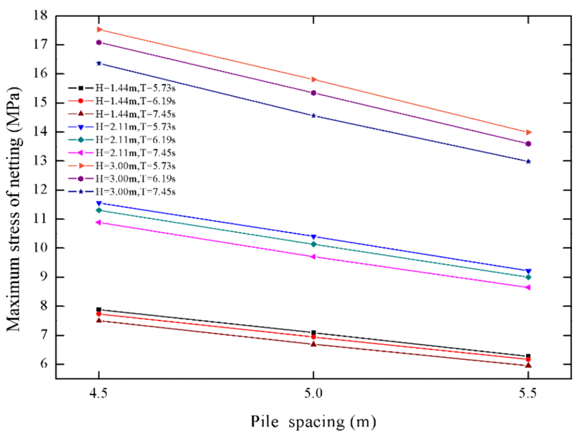

FIGURE 19
Maximum stress of nets with pile spacings.

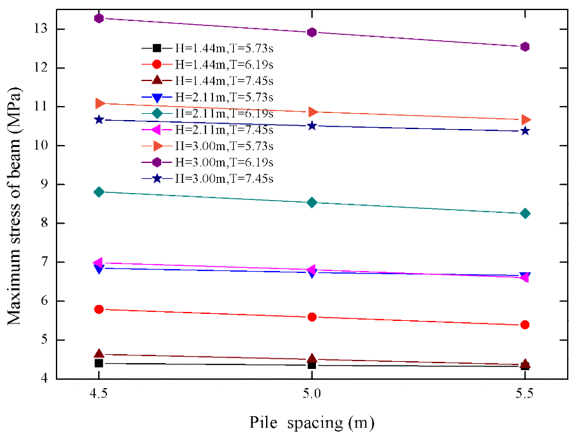

FIGURE 20
Maximum stress of beams with pile spacings.

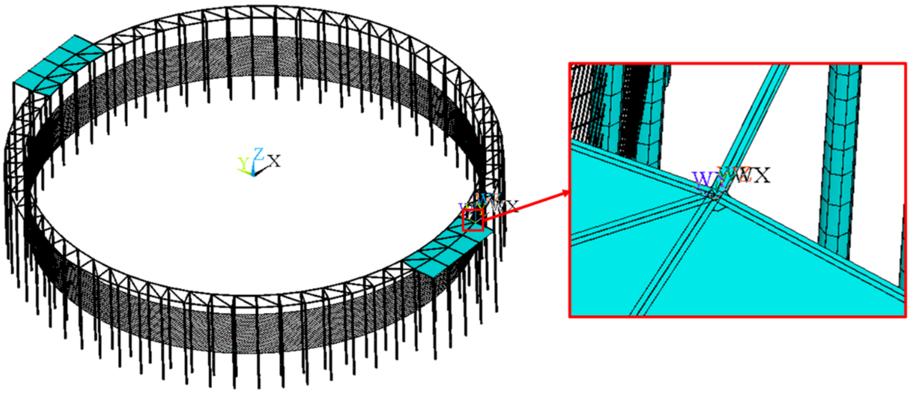

FIGURE 21
Position of maximum force point of pipe pile.

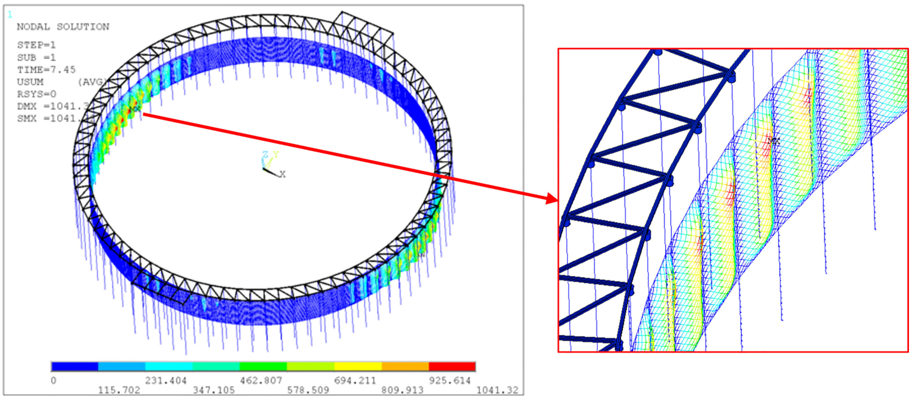

FIGURE 22
Position of maximum displacement of nets.

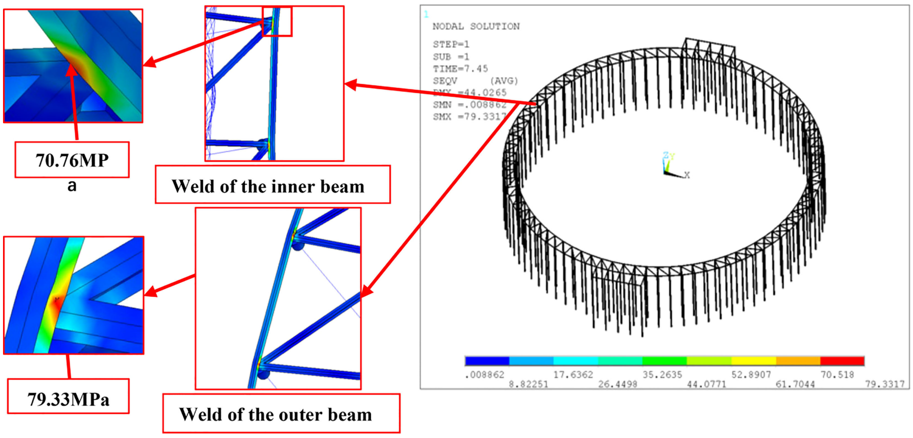

FIGURE 23
Stress results of beam of walking board.

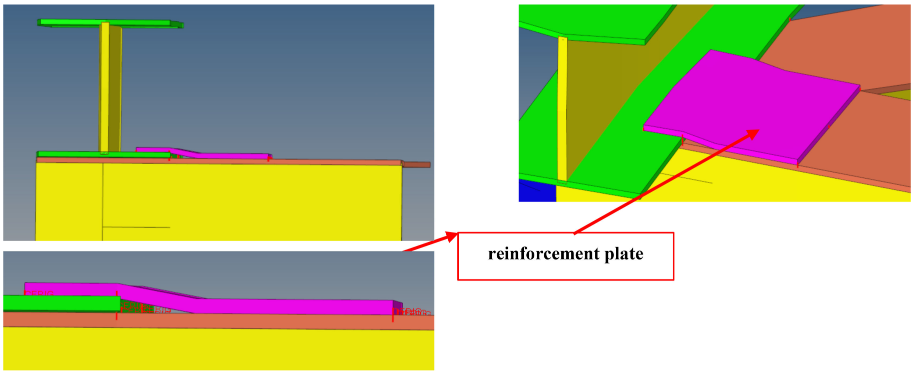

FIGURE 24
Suggestions on optimization of beam welding.

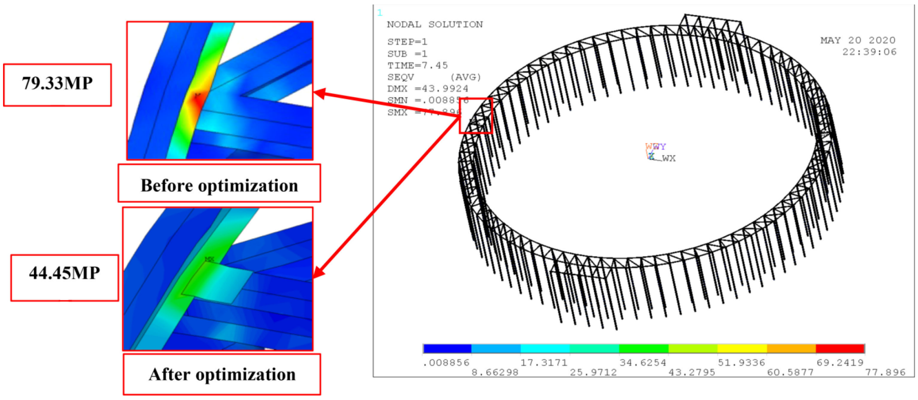

FIGURE 25
Stress before optimization and after optimization.

to prevent damage. It is recommended to add a reinforcement plate at the weld position where the weld is prone to cracking, which will greatly reduce the stress level and the risk of cracking.

Data availability statement

The original contributions presented in the study are included in the article/supplementary material. Further inquiries can be directed to the corresponding author.

Author contributions

YC: Data curation, formal analysis, funding acquisition, writing the original draft, review. GW: investigation, methodology, review. C-TG: investigation, funding acquisition, supervision. All authors contributed to the article and approved the submitted version.

Funding

This work was financially supported by the National Key R&D Program of China (No. 2019YFD0900902); National Natural Science Foundation of China (No. 31772898); Maritime S&T Fund of Shandong Province for Pilot National Laboratory for Marine Science and Technology (Qingdao) (No. 2018SDKJ0303-4); China Agriculture Research System of MOF and MARA (No. CARS-47-22); Central Public-interest Scientific Institution Basal Research Fund, CAFS (No. 2020TD51).

Conflict of interest

The authors declare that the research was conducted in the absence of any commercial or financial relationships that could be construed as a potential conflict of interest.

Publisher's note

References

ANSYS Inc (2009). *ANSYS user's manual* (Southpointe, 275 Technology Drive, Canonsburg, PA: ANSYS Inc.).

Bi, C.-W., Zhao, Y.-P., Dong, G.-H., Xu, T.-J., and Gui, F.-K. (2013). Experimental investigation of the reduction in flow velocity downstream from a fishing net. *Aquacult. Eng.* 57, 71–81. doi: 10.1016/j.aquaeng.2013.08.002

Bi, C. W., Zhao, Y. P., Dong, G. H., Xu, T. J., and Gui, F. K. (2014). Numerical simulation of the interaction between flow and flexible nets. *J. Fluids Struct.* 45, 180–201. doi: 10.1016/j.jfluidstructs.2013.11.015

Chen, T.-H., Pan, Y., Feng, D.-J., Meng, A., and Gui, F.-K. (2018). Effect on hydrodynamics of unit net of a column-type net enclosure aquaculture engineering in current by fixations. *J. Fish. China.* 42, 452–460.

Chu, Y. I., Wang, C. M., Park, J. C., and Lader, P. F. (2020). Review of cage and containment tank designs for offshore fish farming. *Aquaculture* 519, 73492. doi: 10.1016/j.aquaculture.2020.734928

Cifuentes, C., and Kim, M.-H. (2017). Hydrodynamic response of a cage system under waves and currents using a morison-force model. *Ocean Eng.* 141, 283–294. doi: 10.1016/j.oceaneng.2017.06.055

Cui, Y., Guan, C.-T., Wan, R., Huang, B., and Li, J. (2013). Numerical simulation of a flatfish cage system in waves and currents. *Aquacult. Eng.* 56, 26–33. doi: 10.1016/j.aquaeng.2013.04.001

Cui, Y., Guan, C.-T., Wan, R., Huang, B., and Li, J. (2014). Dynamic analysis of hydrodynamic behavior of a flatfish cage system under wave conditions. *China Ocean Eng.* 28, 215–226. doi: 10.1007/s13344-014-0017-4

Gharechae, A., and Ketabdari, M. J. (2020). Semi-analytical study on regular sea wave interaction with circular elastic floaters of aquaculture fish cages. *Aquacult. Eng.* 91, 102125. doi: 10.1016/j.aquaeng.2020.102125

Gui, F.-K., Zhang, B.-B., Qu, X.-Y., Wang, P., Shao, Z.-Y., and Feng, D.-J. (2020). Force analysis of piles in net enclosure aquaculture engineering subjected to waves and current. *Trans. Chin. Soc Agric. Eng.* 36, 31–38.

He, Z., Faltinsen, O. M., Fredheim, A., and Kristiansen, T. (2018). The influence of fish on the mooring loads of a floating net cage. *J. Fluids Struct.* 76, 384–395. doi: 10.1016/j.jfluidstructs.2017.10.016

Huang, X.-H., Guo, G.-X., Tao, Q.-Y., Hu, Y., Liu, H.-Y., Wang, S.-M., et al. (2018). Dynamic deformation of the floating collar of a net cage under the combined effect of waves and current. *Aquacult. Eng.* 83, 47–56. doi: 10.1016/j.aquaeng.2018.08.002

Huang, L., Li, Y., Ni, Y., Cheng, H., Wang, X., Wang, G., et al. (2019). "Study on the influence of mesh grouping on numerical simulation results of fish cages," in *Proceedings of the ASME 2019 38th International Conference on Ocean, Offshore and Arctic Engineering.* volume 9: Rodney Eatock Taylor Honoring Symposium on Marine and Offshore Hydrodynamics; Takeshi Kinoshita Honoring Symposium on Offshore Technology. Glasgow, UK. V009T13A040. doi: 10.1115/OMAE2019-95706

Liu, H.-F., Bi, C.-W., and Zhao, Y.-P. (2020). Experimental and numerical study of the hydrodynamic characteristics of a semisubmersible aquaculture facility in waves. *Ocean Eng.* 214, 107714. doi: 10.1016/j.oceaneng.2020.107714

Mohapatra, S. C., Bernardo, T. A., and Soares, G. (2021). Dynamic wave induced loads on a moored flexible cylindrical net cage with analytical and numerical model simulations. *Appl. Ocean Res.* 110, 102591. doi: 10.1016/j.apor.2021.102591

Tsukrov, I., Eroshkin, O., Fredriksson, D., Swift, M.R., and Celikkol, B. (2003). Finite element modeling of net panels using a consistent net element. *Ocean Eng.* 30, 251–270. doi: 10.1016/S0029-8018(02)00021-5

Wan, R., He, X., Wang, X.-X., and Liu, L.-L. (2007). A method of mesh group for fish cage anti-current characteristics by means of finite element analysis. *J. Ocean Univ. China.* 37, 885–888.

Xia, T., Yang, P., Li, C., and Hu, K. (2019). Numerical research on residual ultimate strength of ship hull plates under uniaxial cyclic loads. *Ocean Eng.* 172, 385–395. doi: 10.1016/j.oceaneng.2018.12.017

Xu, P.-X. (2019). Dynamic response analysis and reliability study of deep-water jacket platform structure (Chengdu, China: Southwest Petroleum University).

Yang, H., Bi, C.-W., Zhao, Y.-P., and Cui, Y. (2020). Numerical study on hydrodynamic responses of floating rope enclosure in waves and currents. *J. Mar. Sci. Eng.* 8, 82. doi: 10.3390/jmse8020082

Zhao, Y.-P., Bi, C.-W., Chen, C.-P., Li, Y.-C., and Dong, G.-H. (2015). Experimental study on flow velocity and mooring loads for multiple net cages in steady current. *Aquacult. Eng.* 67, 24–31. doi: 10.1016/j.aquaeng.2015.05.005

Zhao, Y.-P., Chen, Q.-P., and Bi, C.-W. (2022). Numerical investigation of nonlinear wave loads on a trestle-netting enclosure aquaculture facility. *Ocean Eng.* 257, 111610. doi: 10.1016/j.oceaneng.2022.111610

Zhao, M.-H., Wu, L.-G., and Liu, J.-H. (2007). Inner-force and displacement analyses of load-bearing and anti-slide piles by p-y curve method. *Chin. J. Rock Mech. Eng.* 26, 1220–1225.

frontiers | Frontiers in Marine Science

TYPE Original Research
PUBLISHED 17 May 2023
DOI 10.3389/fmars.2023.1177037

OPEN ACCESS

EDITED BY
Zhao Yunpeng,
Dalian University of Technology, China

REVIEWED BY
Kohji Iida,
Hokkaido University, Japan
Xinliang Wang,
(CAFS), China

*CORRESPONDENCE
Yong Tang
y-tang@shou.edu.cn
Leiming Yin
yinleiming@dlou.edu.cn

†These authors share first authorship

RECEIVED 01 March 2023
ACCEPTED 26 April 2023
PUBLISHED 17 May 2023

CITATION
Gong D, Cui X, Song M, Xing B, Xu P, Tang Y and Yin L (2023) Behavior of large yellow croaker (*Larimichthys crocea*) in pen aquaculture as measured by meter-scale telemetry.
Front. Mar. Sci. 10:1177037.
doi: 10.3389/fmars.2023.1177037

Behavior of large yellow croaker (*Larimichthys crocea*) in pen aquaculture as measured by meter-scale telemetry

Dehua Gong[1†], Xiaojie Cui[1†], Mingyuan Song[1], Binbin Xing[1], Pengxiang Xu[1], Yong Tang[1,2*] and Leiming Yin[1*]

[1]Center for Marine Ranching Engineering Science Research of Liaoning, Dalian Ocean University, Dalian, China, [2]Collage of Marine Sciences, Shanghai Ocean University, Shanghai, China

To understand the behavior of the large yellow croaker (*Larimichthys crocea*) in a pen aquaculture setting, three individuals in each of two experimental groups were telemetered in meter scale by four cable-synchronized hydrophones. The ultrasound pinger system was applied to track the motion of six *L. crocea* for 24 h using two fixation methods, i.e., implanting tags in the abdomen (the *in vivo* implantation group) and hanging tags on the dorsal fin (the dorsal fin suspension group). Pingers repeated unique 62.5 kHz coded signals at 5 s intervals along with a pressure signal. The results showed that fish tagged with internal pingers took approximately 3 h longer than externally tagged fish to stabilize in their behavior, as measured by depth utilization; the horizontal movements of the test fish were mostly found outside of the fence, where the test fish performed round-trip swimming, with the least probability of appearing near the production platform and more frequent activities in the feeding areas.

KEYWORDS

***Larimichthys crocea*, ultrasound pinger, long baseline (LBL), fish behavior, pen aquaculture**

1 Introduction

The large yellow croaker (*Larimichthys crocea*) belongs to the order of Osteicthys, Perciformes, Sciaenidae, and is a warm–temperate offshore pelagic migratory fish. Being one of the most important economic fishes in China (Wang et al., 2020), it is distributed in the South and the East China Sea, as well as southern Yellow Sea. Shallow-sea fenced farming is an emerging aquaculture method for *L. crocea*. This culture facility is more resistant to wind and waves, and the culture site is generally located in the outer sea area, which shares features of the natural environment, including a deep water level, high current speed, frequent water exchange, less pollution, a wide source of bait, large culture area, and plenty of space for fish activities. The *L. crocea* farmed in this area usually have a larger size, better color, and enhanced meat quality, and thus are more commercially welcomed than traditional net-cultured fish. There have been few studies on the activities of *L. crocea* in the artificial culture area. The use of ultrasonic pingers can better understand the behavioral changes of *L. crocea* in cages and provide data support for the optimization and improvement of artificial breeding modes.

In recent years, with the continuous optimization and improvement of cage structure and material, the techniques of deep-sea cage culture, shallow-sea cage culture, and lake cage culture have developed rapidly in practical production and application (Calado et al., 2021; Fu et al., 2021; Zhao and Dai, 2021); for example, Nile tilapia (*Oreochromis niloticus*), striped bass (*Morone saxatilis*) (Del Rio-Zaragoza et al., 2021), rainbow trout (*Oncorhynchus mykiss*) (Liu et al., 2021), and large yellow croaker (Han et al., 2022) can all be produced on a large scale through cage culture technology. There has been little research on the behavior tracking of *L. crocea* in cage culture in the shallow sea, and ultrasonic bio-telemetry technology is one method that can be used to study fish behavior, including migration, reproduction, habitat selection, seasonal movement patterns, and the relationship between fish and nets (Poddubnyi et al., 1966; Young et al., 1972; Biesinger et al., 2013).

Fish were monitored by fixing ultrasonic pingers to the fish body. Fixation methods include insertion into the stomach *via* injection, dorsal fin suspension, and *in vivo* implantation; the choice of implantation method mainly depends on the size and species of the fish and the objectives of the study (Bridger and Booth, 2003; Hussey et al., 2015). Once the ultrasonic marker has been fixed, the ultrasonic signal from the marked fish can be received by the receiver. The acquired data are processed to obtain changes in the underwater behavior of the marker fish, including swimming speed and horizontal and vertical movement positions (Juell and Westerberg, 1993). Synchronizing the time between the hydrophone and the 3D positioning of the ultrasonic landmarks to an accuracy of 2-5 m enables the more accurate determination of fish movements (Hou et al., 2019). The effects of different methods of fixing ultrasonic pingers on fish have been studied extensively (Adams et al., 1998; Anglea et al., 2003; Makiguchi and Ueda, 2009), external fixed ultrasonic markers may affect the swimming speed of some fish (Brown et al., 1999), and are more likely to be lost in the wild in complex conditions (Haynes, 1978). Immobilizing ultrasound pingers *in vivo* is more stable, but minimally invasive surgery increases the risk of infection and mortality in fish (Mellas and Haynes, 1985; Panther et al., 2011; Miller et al., 2014). In addition, standardized implantation techniques can improve fish survival and the retention of ultrasound pingers, and the use of sterile instruments for surgical suturing can effectively reduce the rate of infection in fish and speed up wound healing in fish implanted with ultrasound pingers (Wagner et al., 2011).

Since 2000, ultrasonic biotelemetry has developed rapidly, with improved accuracy for biolocation, increased species range, enlarged tracking range, and extended tracking durations (Wang et al., 2012; Cooke et al., 2013; Roy et al., 2014). At the same time, ultrasonic telemetry can be applied to different environmental conditions, and more and more experts and scholars have conducted detailed studies on biological and behavioral changes through ultrasonic biotelemetry. In order to determine the behavior change characteristics of *L. crocea* in a shallow-water culture environment, this experiment filled this gap based on the ultrasonic pinger method and calculated the swimming distance changes of *L. crocea* by measuring their movement depth and position, thus providing a theoretical basis for the management of *L. crocea* under shallow sea fences and their design optimization.

2 Materials and methods

2.1 The selection of experiment site and subjects

The experiment was carried out in a fenced area in shallow water off Da Chen Island, Taizhou, Zhejiang Province, China, with the size of the fenced area being around 80 m × 60 m × 12 m (length × width × depth) (Figure 1). In total, six *L. crocea* were tested, three with pingers implanted in the abdomen and the other three with pingers suspended on the dorsal fin; ultrasonic pinger could perform 24-hour diurnal tracking. At the same time, the animal-borne underwater sound recorder (AUSOMS-mini, AQUA co., Ltd., Japan, bandwidth 100 Hz to 20 kHz, sensitivity: -202 dB re $1V\text{-}\mu Pa^{-1}$) was applied in the culture enclosure for simultaneous monitoring of underwater environmental noise. In order to study the diurnal movement patterns of *L. crocea* in the enclosures, the results of this experiment were analyzed in four time periods: 18:00-0:00; 0:00-6:00; 6:00-12:00; 12:00-18:00.

Three *L. crocea* with sound health conditions were randomly selected for the surgical implantation of ultrasonic pingers in the abdomen (Figure 2A). The mass of the ultrasonic pinger was 5 g in air and almost 0 in water. The average body length of the test fish was 31.43 ± 0.74 cm, and the average body weight was 465.20 ± 13.24 g (Table 1). Before the implantation, the surgical equipment was sterilized, and the pingers were cleaned and disinfected by soaking in 75% alcohol before rinsing with distilled water to reduce adverse post-implantation irritation to the body wall. MS-222 anesthetic was added to the bucket to anesthetize the test fish, and an oxygenation pump was used to oxygenate the water during the anesthesia process. Then, minimally invasive surgery was performed to implant the ultrasonic pinger into the abdominal cavity of the *L. crocea*; the entire surgical suture time had to be completed within 45 s. After the ultrasonic pinger was fixed, the fish was housed in a temporary water tank to be oxygenated and resuscitated. When the normal swimming ability had recovered, they were put into the test area for experimentation. Another three *L. crocea* with similar health conditions to the implantation group were selected randomly, and the ultrasonic pingers were suspended around their first dorsal fin by minimally invasive surgery (Figure 2B). The average body length of the test fish was 31.47 ± 0.69 cm, and the average weight was 468.10 ± 11.68 g. The two groups of experimental fish were anesthetized with the same concentration of MS-222 during the operation, and then put into the fence after a 2-hour rest. The placement positions of the two groups of experimental fish were the same.

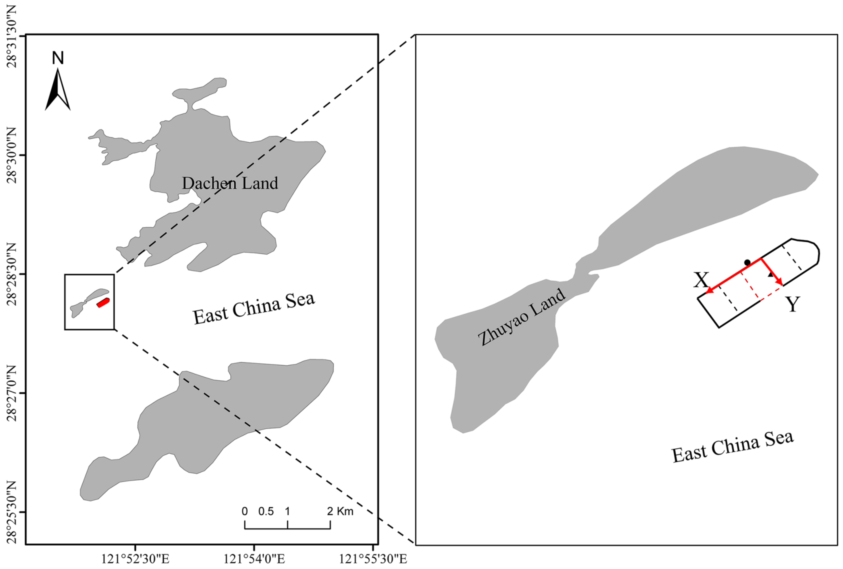

FIGURE 1
Large shallow sea fencing facilities in the sea near Dachen Island, Taizhou City, Zhejiang Province, China (X-axis is the production platform; Y-axis is the feeding platform; the red box indicates the ultrasonic mark coordinate setting; ● is the working position; ▲ is the feeding position).

2.2 Ultrasonic pinger tracking system

In this test, a wired four-channel ultrasonic pinger tracking system (FRX-4002 type, FUSION, Japan) was used to track *L. crocea*. The pinger in the system (FPX-1030 type) was from the same company as the whole system, with external dimensions of about 35 mm in length and 10 mm in diameter. Its emitting frequency was 62.5 kHz, and the sound pressure level was 155 dB (re 1μPa at 1m) (Figure 3). At an emission interval of 5 s, its battery life would be 5 days. Phase modulation coding of the emitted acoustic wave was performed using 31-bit M-sequence pseudo-random coding; the interval for the pinger to emit the pulse acoustic wave could be adjusted using magnet switch counting (Miyamoto et al., 2011). The pulse emission interval set for this experiment was 5 s.

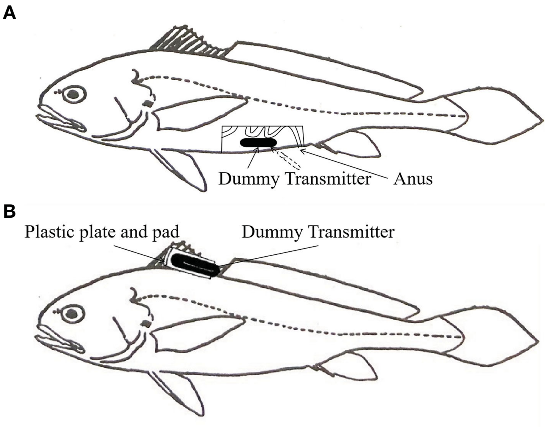

FIGURE 2
1/3 Schematic diagram of ultrasonic pinger fixation in *L. crocea*: **(A)** Ultrasonic pinger implantation. This fixation method uses a scalpel to scrape off the abdominal scales from the test fish and then cut open the abdominal cavity of the test fish to implant the ultrasonic pinger without destroying the abdominal organ tissues of the fish; **(B)** Dorsal fin suspension of the ultrasonic pinger. This fixation method uses a surgical suture to fix the ultrasonic marker near the first dorsal fin of the test fish. The plastic plate and pad have a mass of about 1 g, which weighs almost nothing in water and has a negligible effect on the swimming ability of the test fish.

The pinger tracking receiving system consisted of an array of four hydrophones and a receiver (Figure 4). The hydrophones were connected to the receiver through a data line, and the receiver could receive data from the four hydrophones in real time through a computer. The four hydrophones were set at each of the corners of the fence at 2 m under water, forming a rectangular array with a length of 75.50 m (Y-axis) and a width of 48.64 m (X-axis); the time-resolved accuracy of the system was 0.05s.

The underwater acoustic noise signal was collected by AQH hydrophones (sensitivity: -193 dB re 1 V μ Pa^{-1}, Institute of Information, Kyoto University, Japan). The bandwidth of the hydrophone was 20 Hz ~ 20 kHz. The sampling frequency of 192 kHz was stored in.wav format, and American iZotope RX 8 audio analysis software was used for human ear discrimination and time domain spectrum analysis. Finally, the frequency characteristics were obtained by fast Fourier transform (FFT) through the system's own analysis software.

2.3 Data process and analyses

The depth was measured by the mark's own pressure (depth) sensor and was transmitted to the receiving system through a double pulse. The model for depth (d) was calculated by the formula:

$$d = a \ast t - b \tag{1}$$

TABLE 1 The body length, weight, and beacon-to-body weight ratio of the tested *L. crocea*.

Group	No.	Body length/cm	Body weight/g	Beacon-to-body weight ratio/%
The dorsal fin suspension group	1	31.8	462.2	1.1%
	2	32.1	450.7	1.1%
	3	30.4	482.7	1.0%
The *in vivo* implantation group	4	32.3	483.6	1.0%
	5	31.5	465.3	1.1%
	6	30.6	455.4	1.1%

Where a and b are the fitting coefficients of the pressure sensor's depth model. These coefficients were given by the actual pressure measurements performed by the manufacturer; *t* represents the time interval between the actual double pulses measured in the data file.

The horizontal position was measured according to the long baseline (LBL) method combined with the least squares method (Madsen et al., 2004). The calculation is based on the time difference between ultrasonic pulse signals emitted by the ultrasonic markers reaching one hydrophone and reaching the rest of the three

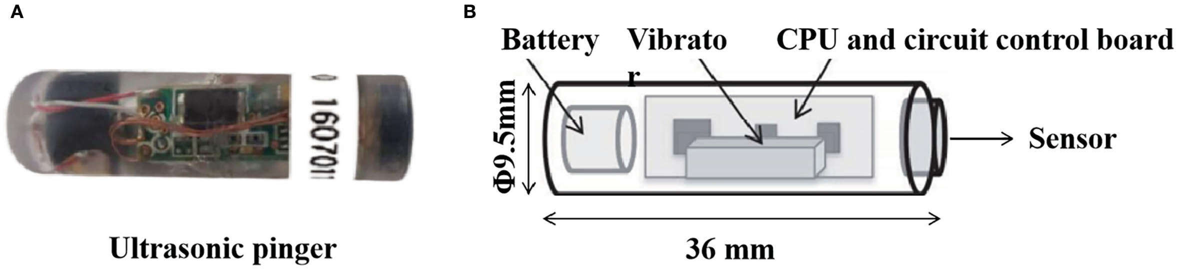

FIGURE 3
The FPX-1030 type of ultrasonic pinger with 62.5 kHz. **(A)** Actual appearance; **(B)** Schematic of 60 kHz FPX-1030 ultrasonic ping.

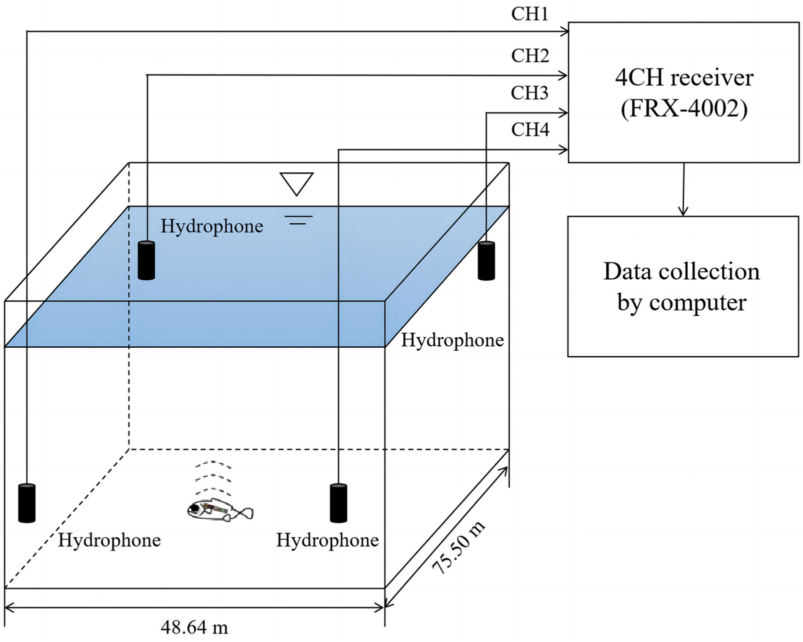

FIGURE 4
The FRX-4002 type of the ultrasonic pinger tracking system (4 receivers).

hydrophones (Figure 5). The calculation formula for the horizontal position is as follows:

$$\Delta t_j = \frac{1}{c}(\sqrt{(x_j - x_p)^2 + (y_j - y_p)^2} - \sqrt{(x_1 - x_p)^2 + (y_1 - y_p)^2}) \quad (2)$$

Where *c* is the sound velocity.

In the actual measurement, the coordinates of the speculative point P_1 are (x_{P1}, y_{P1}), and the time difference between the arrival of P_1 at receivers TD_2, TD_3, and TD_4 and the time of arrival at TD_1 can be calculated using the following formula:

$$\Delta T_j = \frac{1}{c}(\sqrt{(x_j - X_p)^2 + (y_j - X_p)^2} - \sqrt{(x_1 - X_p)^2 + (y_1 - Y_p)^2}) \quad (3)$$

where Δt_j is the slant distance time difference and ΔT_j is the projection of Δt_j on the xy plane. The difference between Δt_j and ΔT_j is greater than the given value δ.

$$\delta = \Delta t_j - \Delta T_j < \epsilon \quad (4)$$

In Equation (4), δ is the time difference and ϵ is the fixed value assigned to the location accuracy. The regression calculation using the Newton–Gaussian method was performed to solve for x_{P1} and y_{P1}.

The swimming speed is calculated according to the relation between the change of beacon position and time (V=S/t). The test results were processed in the form of mean ± S.D., the data were analyzed by one-way ANOVA with SPSS23 software, and the significance level was set as 0.05.

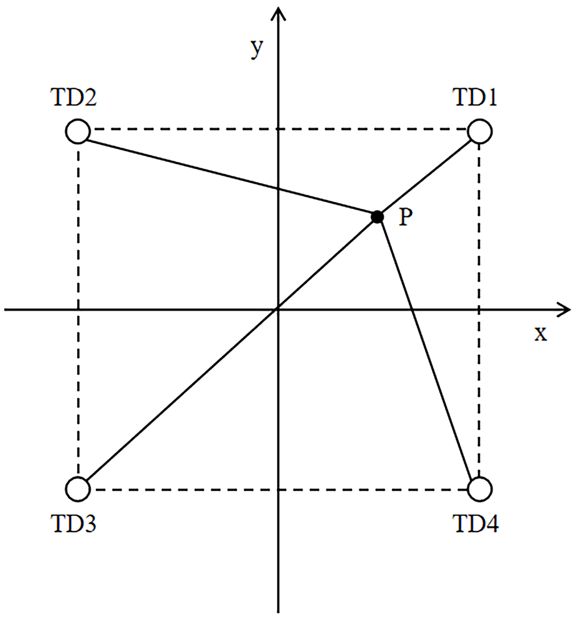

FIGURE 5
Position measurement system: TD1–TD4 are acoustic receivers; point P is the pinger for tracking.

3 Results and analysis

3.1 Distribution of two groups of *L. crocea* in the fenced area

In this experiment, the detection rate of ultrasonic signs in this test was 100%. The implantation method and the dorsal fin suspension pinger method were used for 24 h ultrasonic pinger tracking tests of *L. crocea* in the fenced area, and the vertical movement data of *L. crocea* under different fixation methods were obtained. After being placed into the fenced area, both groups of *L. crocea* showed substantial upward and downward behaviors in the beginning. The movement trajectories of the two groups were divided into four stages based on four time periods—18:00-24:00, 00:00-06:00, 06:00-12:00, and 12:00-18:00—which were analyzed as follows.

The 24 h vertical movement trajectory of the implantation group (Figure 6). After approximately 6 h (18:00-24:00) of release, the fish gradually stabilized. From 18:00 to 21:00, the fish moved substantially up and down at a depth of 0 m~6 m; from 21:00 to 24:00, the fish started to descend until stabilizing at a depth of 6 m~10 m under water. On the next day, from 00:00 to 04:00, the fish mainly moved around the depth of 6 m~10 m under water; from 04:00 to 11:00, the fish again showed substantial up and down snorkeling movements at a depth of 0 m~8 m under water; from 11:00 to 14:00, the fish descended to the depth of 6 m-10 m under water; from 14:00 to 18:00, the fish were moving at a depth of 2 m~10 m, with most of them moving up and down at depths of 4 m~8 m.

The 24 h vertical movement trajectory of the suspension group (Figure 7). After about 3 h of release, the test fish first stabilized then began to dive (18:00-21:00); from 21:00 to 22:00, the fish descended to a depth of 6-8 m. After 22:00, the test fish continued to move downward until becoming stable at a depth of 8-10 m. After 00:00 the following morning, the fish moved upward and then dived back to a depth of 8 m-10 m; from 01:00-05:00, the fish mainly moved at a depth of 4-8 m. During 05:00-09:00, the fish moved up and down significantly at a depth of 0-10 m. During 09:00-12:00, the fish moved at a depth of 2-10 m, mainly concentrating at 4-8 m for up and down snorkeling movements. From 12:00 to 15:00, the test fish continued the snorkeling movements at 2 m to 10 m under water. After 15:00, the fish stabilized again and mainly moved at 6-8 m.

There was a difference in the time to stabilization between the two groups, with the suspension group taking less time to stabilize than the implantation group ($p<0.05$) and remaining stable at depths of 4-8 m for a longer time. For the implantation group, the primary time periods for the up and down movements were between 18:00 and 24:00 at a depth of 0-6m, and between 04:00 and 11:00 at a depth of 0-8 m the following day. In contrast, for the suspension group, the main time periods for similar movements were 05:00-09:00 at a depth of 0-10 m and 12:00-15:00 at a depth of 2-10 m. The suspension group swam up and down more frequently

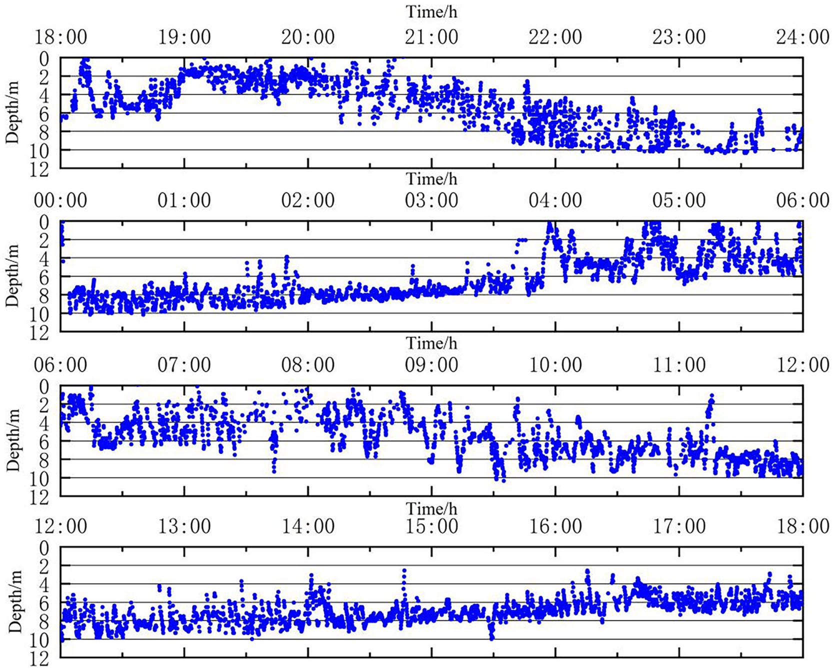

FIGURE 6
The 24 h vertical movement trajectory of the *in vivo* implantation group.

than the implanted group (P<0.05). The implantation group swam mainly at depths between 4 m and 10 m, while the fish in the dorsal fin suspension group swam mainly at water depths between 2 m and 10 m. Overall, both groups of *L. crocea* were more concentrated around 6 m.

The position data during tracking were obtained by calculating the horizontal position. The density of the scattered points reflected the emergence frequency of *L. crocea*, and the denser the points, the more frequent the emergence (Figure 8). From the horizontal position scatter distribution, it can be seen that when the

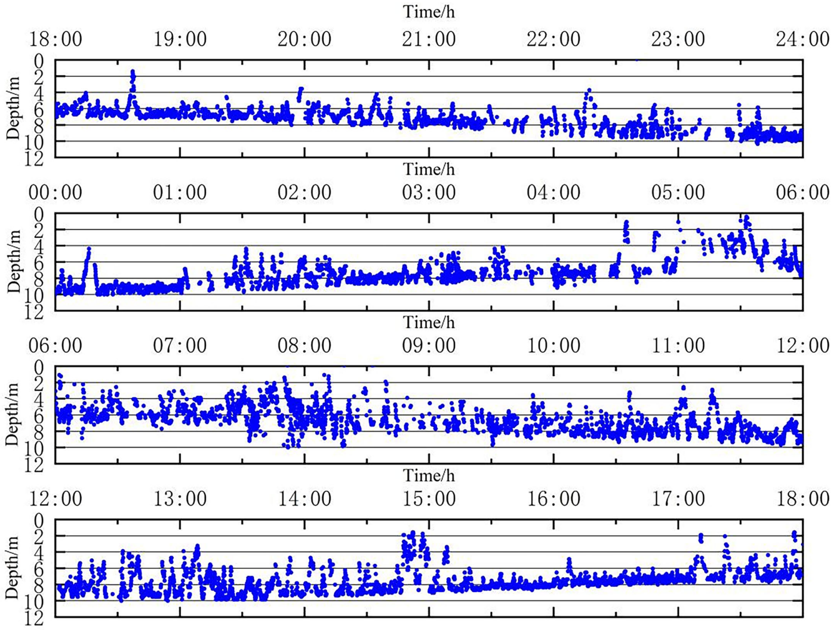

FIGURE 7
The 24 h vertical movement trajectory of the dorsal fin suspension group.

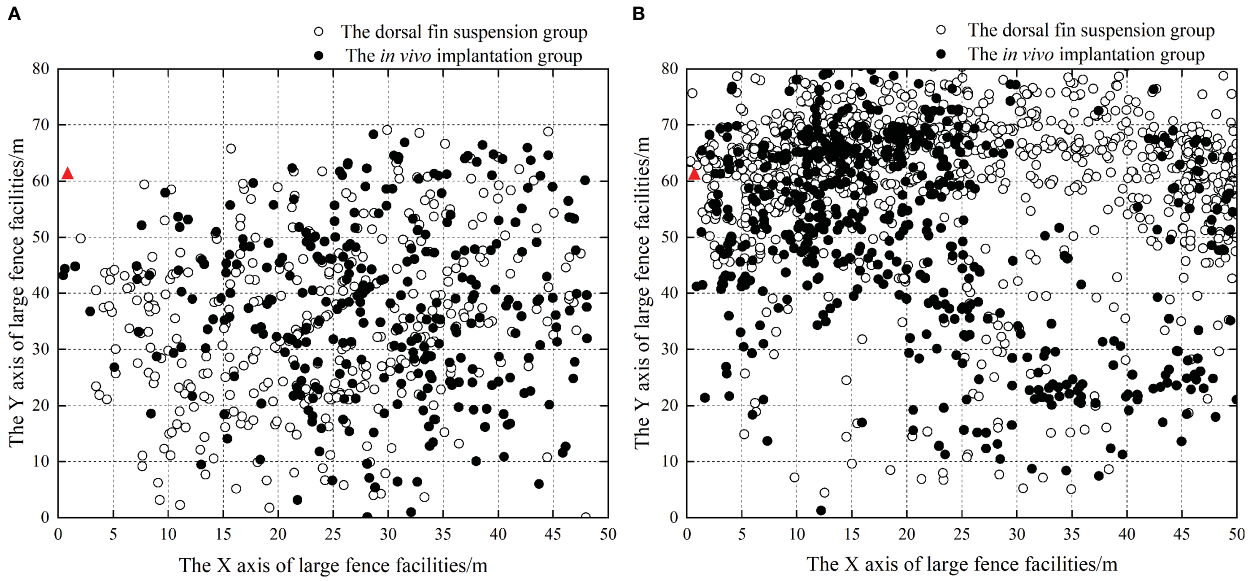

FIGURE 8
Horizontal distribution of L. crocea within the fenced area. **(A)** Schematic diagram of the horizontal distribution of two groups of experimental fish when bait was not cast in the bait casting area; **(B)** Schematic diagram of horizontal distribution of two groups of test fish when feeding in the feeding area; ▲ indicates the feeding position.

production platform and feeding area were not in operation, the test fish in both groups exhibited irregular swimming movements inside the fenced area; when the production platform and feeding area started working, both groups appeared more frequently outside of the fenced area than inside the area ($P<0.01$), and they swam back and forth along the outside for a long time. The test fish were least likely to be found near the working platform and moved more frequently in the feeding area ($P<0.01$).

3.2 The average swimming speed of the *L. crocea* with different fixation method

The mean swimming speed of the test fish under different fixation methods was calculated based on the 24 h three-dimensional position (Figure 9). The blue and black lines represent the mean swimming speeds of the dorsal fin suspension group and the implantation group, respectively. During the first 4 h of release into the fenced area (18:00-22:00), the mean swimming speed varied within a small range between the two groups: for the suspension group, the mean speed was 24.35 ± 6.54 cm·s^{-1} (about 0.88 LB·s^{-1}), and their speeds in each hour were 26.1 cm·s^{-1}, 22.9 cm·s^{-1}, 31.4 cm·s^{-1}, and 17.0 cm·s^{-1}, respectively. In contrast, in the implantation group, the mean speed was 27.78 ± 5.91 cm·s^{-1} (about 0.77 LB·s^{-1}), and their speeds in each hour were 52.1 cm·s^{-1}, 11.5 cm·s^{-1}, 20.0 cm·s^{-1}, and 27.5 cm·s^{-1}, respectively. In the first 4 h, the fish in both groups freely swam in the fenced area with an average speed of less than 1 LB·s^{-1}.

The mean swimming speed increased significantly in both groups during the time period 22:00-02:00. At 23:00, the speed increased by 39.6 cm·s^{-1} (about 1.26 LB·s^{-1}) in the suspension group and by 47.1 cm·s^{-1} (about 1.50 LB·s^{-1}) in the implantation group. During 06:00-08:00, when the *L. crocea* foraged, the suspension group increased their mean swimming speed by 101.0 cm·s^{-1} (about 3.21 LB·s^{-1}) and the implantation group increased their mean swimming speed by 81.2 cm·s^{-1} (about 2.58 LB·s^{-1}), indicating significant increases for both test groups. After 08:00, the average speed of both groups began to decrease after the end of the feeding, and the two test groups were again exercising free cruising in the fenced area. The results of the 24 h tracking test on both test groups showed that the mean swimming speed was 45.5 ± 26.1 cm·s^{-1} (about 1.45 LB·s^{-1}) in the implantation group and 45.5 ± 26.1 cm·s^{-1} (about 1.45 LB·s^{-1}) in the suspension group, with no significant effect of the different fixation methods on the swimming speed ($P>0.05$).

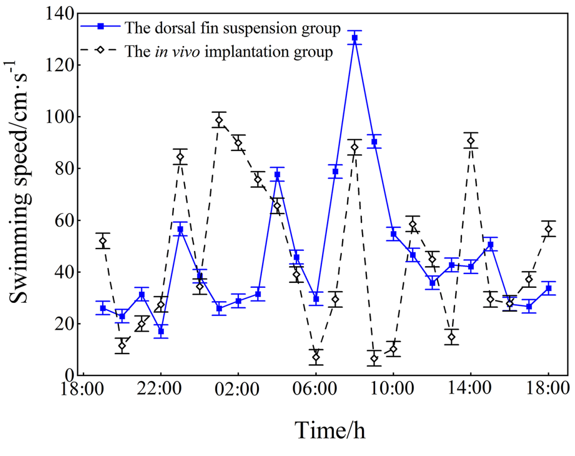

FIGURE 9
The mean swimming speed (mean ± SD) of the test fish under different fixation methods. The blue line represents the speed of the suspension group; the black line represents that of the implantation group.

3.3 The impact of vessel noise on the behavior of the *L. crocea*

The use of ultrasonic beacons could better determine the behavioral changes of *L. crocea* in cages and provide data support for the optimization and improvement of artificial culture mode. The analysis results of the simultaneous monitoring spectrum of underwater environmental noise in the fenced area are shown in Figure 10. Based on the actual situation around the fence, the analysis of the WENZ spectrum showed that the underwater background noise in the fence mainly comprised: the swimming noise (100~400 Hz); biological sounding (500~800 Hz); the accompanying biological noise generated during feeding (50~2100 Hz); and equipment noise of the artificial operation platform in the culture area (3000~5500 Hz). When small vessels passed the fenced area, the underwater environmental noise showed changes in sound pressure level at a bandwidth of 100~2500 Hz, which might include: swimming noise (100~400 Hz) generated by the test fish after being disturbed; vessel noise with the main frequency peak at 300~500 Hz; and water surface wave noise (1000-1200 Hz) from passing ships. The sound pressure level of the underwater ambient noise increased significantly, with a real-time increase in sound pressure level of approximately 14 dB.

The fish in both groups moved irregularly within the fence before the small vessels passed by. When the vessels passed by the side of the production platform, the suspension group moved back and forth, trying to swim away from the platform, with those the furthest from the noise source being the most active. For the implantation group, the fish moved towards the outer side of the fence and away from the vessel noise. They continued to move to the edge away from the fence (Figure 11). The results showed that when the vessel passed by the fence, the effect of the vessel noise on the *L. crocea* was significant (P<0.01), and the horizontal movement of the fish in both groups changed significantly after being exposed to vessel noise.

4 Discussion

4.1 Effect of suturing on the body of *L. crocea*

In this experiment, the *in vivo* implantation method and the dorsal fin suspension method were used for the fixation of ultrasonic pingers. The results showed that the time required for the suspension group to enter a stable state was about 3 h less than that for the implantation group. This is because the implantation method requires a series of complex operations that may exert a greater impact on the fish including dissection, pinger implantation, and ventral suturing. Although the dorsal fin suspension method is simpler, the implantation method is still required for long-term behavioral tracking because the pingers are easily dislodged outside the fish, which is consistent with the results of Moore et al. who studied the effects of ultrasonic pinger implantation on the behavior (Moore et al., 1990) and physiology of Atlantic salmon, concluding that the surgical implantation method is most suitable for long-term studies of the target species.

Makiguchi and Ueda (2009), in comparing the effects of the *in vivo* implantation method and the dorsal fin suspension method on the ability of the cherry salmon (*Oncorhynchus masou*), noted that the test fish required 2 h of respite recovery after the *in vivo* implantation procedure before the test could be conducted, which is consistent with the results of this study. Therefore, in future studies, the proficiency of pinger *in vivo* implantation needs to be improved and a certain time needs to be allocated for post-implantation observation, so as to ensure the success of the

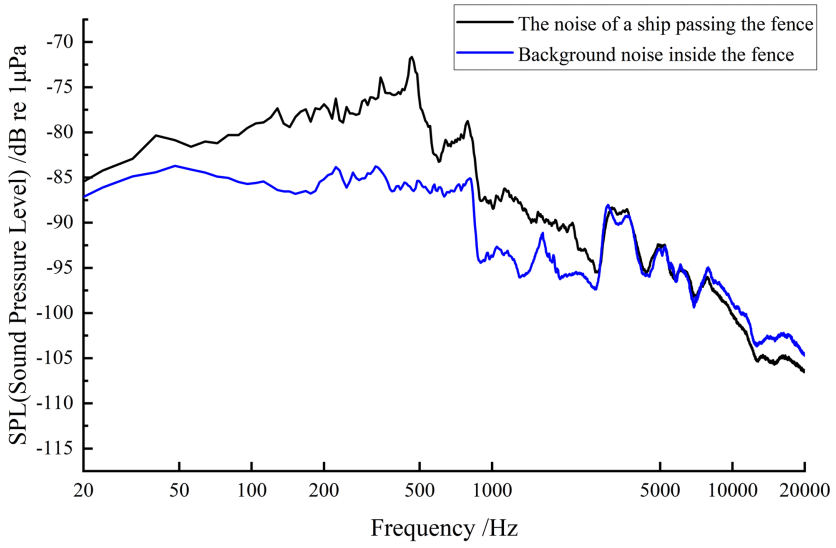

FIGURE 10
The noise power spectra of environmental noise within the fence and the noise when vessels passed by. The blue line is the noise power spectrum of environmental noise within the fence; the black line represents the noise power spectrum when vessels pass by.

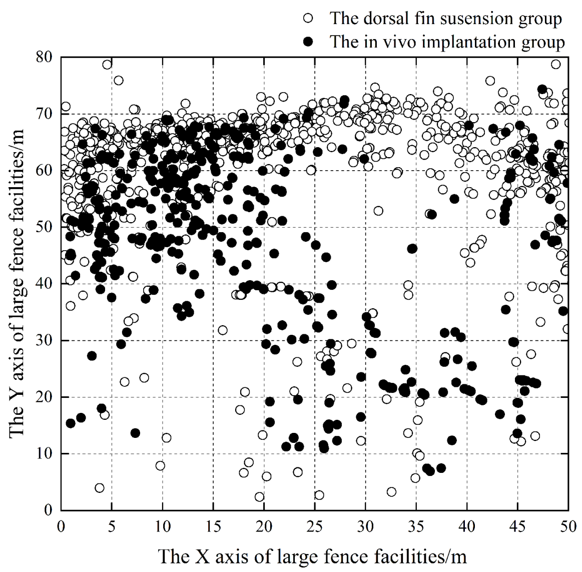

FIGURE 11
Horizontal distributions of *L. crocea* in the implantation group and the suspension group after the vessel docked. The X and Y axes of the fence facility correspond to those depicted in Figure 1, with the X-axis being the production platform and the Y-axis being the feeding platform.

implantation. This helps to extend the time that fish carry the pinger and to reduce the mortality of test fish due to improper test operations. Bridger and Booth (2003) used three methods for ultrasonic pinger fixation in fish: stomach implantation, dorsal fin suspension, and *in vivo* implantation. Their study proved that stomach implantation had the minimum negative impact on fish. In this study, only two methods, dorsal fin suspension and *in vivo* implantation, were used for 24 h tracking of the *L. crocea*. Therefore, the methods and the duration of tracking need to be improved in future studies.

The results showed that the test fish needed some time to recover after surgery, and the different methods of ultrasonic pinger implantation had no significant effect on the swimming speed. When conducting ultrasonic telemetry tests on target subjects, it is necessary to select the appropriate pinger method according to the morphological characteristics of the target subject in order to mitigate the negative effects. In order to minimize the negative effects of ultrasonic beacon on fish body, it is necessary to select appropriate ultrasonic pingers and marking method according to the morphological characteristics of target fish species in ultrasonic telemetry test (Summerfelt and Mosier, 1984; Jepsen et al., 2005; Zale et al., 2005; Panther et al., 2011; Lee et al., 2013). Implantation proficiency on the part of the experimenter is also critical, as reducing operational errors during the procedure will effectively reduce the post-operative recovery time of the experimental fish, reduce the risk of wound infection, and improve the survival rate of the fish (Cooke et al., 2003; Wagner et al., 2011).

In the future work, it is also necessary to observe the postoperative test fish, record the postoperative behavior changes of the test fish, optimize the operation plan through in-depth research, gradually improve the time of fish carrying pingers, and reduce the death of the test fish caused by improper operation of the test fish.

4.2 Behavioral changes of the *L. crocea* in the fenced area

Instead of moving around randomly and horizontally within the fence, the test fish tended to gather around the feeding area outside the fence; they may have been attracted by the bait in this area. In this experiment, the 24 h vertical movements of the fish in the implantation group and the dorsal fin suspension group were tracked. The findings that the implantation group mainly moved in the 4-10 m water layer, while the dorsal fin suspension group mainly moved in the 2-10 m water layer. In general, both groups mainly moved around 6 m under water, but their up and down floating frequencies differed, with the suspension group exhibiting a higher frequency from 6:00 to 12:00. During the period of 18:00-21:00, the implantation group mainly moved at 4-8 m and the suspension group mainly moved at 2-6 m. In addition, the two groups were found to move upward at both dusk and dawn, which is consistent with the biological behavior of the *L. crocea*. The results showed that the two fixation methods did not affect their vertical movement ability. However, there were differences in the stability of the movement.

4.3 The impact of underwater noise on *L. Crocea*

No matter which fixation method was adopted, the *L. crocea* tended to move outside of the fence when the ship passed. This is because, on the one hand, the fish have an auditory sensitivity frequency of 300~800 Hz, which makes them sensitive to low-frequency noise (Yin, 2017). The underwater noise generated by ships induced a startled escape response, and the *L. crocea* mainly moved to keep away from the noise. The main noise sources in this test area included equipment noise (3000~5500 Hz) from the artificial operation platform in the fenced culture area, ship noise with a main frequency peak at 300~500 Hz, and surface wave noise (1000~1200 Hz) generated by the vessels. All of these noises were within the hearing sensitive frequency range of the *L. crocea*, thus inducing a negative response and causing them to leave the noisy area. On the other hand, the distribution of bait attracted *L. crocea* to gather in the feeding area, where bait was fed at regular intervals for quite a long time.

Long-term exposure to high-intensity, low-frequency noise can affect the hearing, behavior, growth, stress response, feeding conversion efficiency, and immunity of fish to a certain extent. This experiment studied underwater noise, mainly because ship noise was common in the fenced culture area, and this kind of noise may impact *L. crocea*. Therefore, studying the behavior changes of *L. crocea* before and after a ship passes can better determine the behavioral characteristics of *L. crocea* in the fence. During this experiment, the two groups of test fish mainly moved within the enclosure randomly before the vessel passed. When the vessel passed the production platform, both groups escaped and moved back and forth, trying to swim away from the platform, and they moved most frequently around the edge of the fence farther from the noise. Fay and Popper (2009) studied the hearing sensitivity of teleost in 50-1000 Hz and pointed out that *L. crocea* belongs to the family of *Sciaenidae* and has a wide hearing spectrum and low hearing threshold. Shi et al. (2010) simulated the effect of ship noise on the cortisol secretion of *L. crocea*, and found that the cortisol content in the blood was significantly increased under the stimulation of ship noise, which was considered to be a stress response. Smith et al. (2004) studied the effect of white noise on goldfish (*Carassius auratus*); the results showed that both the cortisol and glucose levels in the blood of goldfish increased significantly after 10 min of exposure to white noise at 160-170 dB:re 1μpa. Yin Leiming's study adopted the ABR method to measure the hearing sensitivity of *L. crocea*; the results showed that the range was 500~800 Hz (Yin, 2017). Neo et al. (2016) used ultrasonic biotelemetry to study the behavioral changes of the European bass (*Dicentrarchus labrax*) under the noise stimulation of a large underwater horn. The results showed that continuous stimulation resulted in a rapid dive and movement away from the noise source compared with pulsed stimulation, a finding that was also consistent with the results of the current experiment.

The main frequency peaks of noise in the fenced area were 300-600 Hz. When ships passed the fenced production platform, the sound pressure level of underwater ambient noise in the 300-500 Hz bandwidth increased significantly by approximately 14 dB, and the peak of the ship noise spectrum completely obscured the biological sound of *L. crocea*. It was clear from the test results that both groups moved towards the side of the fence farther away from the production platform. *L. crocea* appeared to respond negatively to the ship noise, i.e., they appeared to flee from the noise source; it can be concluded that the ship noise startled the *L. crocea*. Wysocki et al. studied the effect of ship noise on the immunity of carp (*Cyprinus carpio*), gudgeon (*Gobio gobio*), and European perch (*Perca fluviatilis*) through playback of these noise recordings. The results showed an increase in cortisol secretion and stress levels in all three species (Wysocki et al., 2006). Codarin et al. (2009) found that ship noise affected the auditory sensitivity of several fish species. In addition, their acoustic-communication-dependent behaviors, such as mate finding, foraging, and individual fighting, were undermined. Sarà et al. (2007) studied the effects of ship noise on the migratory behavior of the Atlantic bluefin tuna (*Thunnus thynnus*) in waters off the Egadi Archipelago, Sicily, Italy. The results showed that ship noise affected the accuracy of these tunas' baiting and spawning migrations.

In conclusion, this experiment used the long baseline (LBL) method to track the *L. crocea* and monitored the data concerning their movement within the fence. An underwater acoustic measurement system was adopted to spectrally analyze noise sources in the farming environment of *L. crocea*. This study is the first to obtain the 24 h behavioral data of *L. crocea* in the fence using two ultrasonic pinger fixation methods. It was observed that the swimming range of *L. crocea* was mainly 2 to 10 m under water. In addition, the underwater ambient noise was matched with the time domain to understand the sound environment of the fenced area. The impacts of the farming environment and noise sources on the behavior and spatial distribution of *L. crocea* were analyzed to clarify the optimal underwater sound environment parameters for culturing *L. crocea*. This experiment provides preliminary understanding of the movement patterns of *L. crocea* within the fence, and can provide a scientific theoretical basis and data support for the management and optimization of shallow sea fences for *L. crocea* culture in the future. In addition, this study has implications for studies on other fish species regarding the selection of ultrasonic pinger fixation methods.

Data availability statement

The original contributions presented in the study are included in the article/supplementary material. Further inquiries can be directed to the corresponding authors.

Ethics statement

The animal study was reviewed and approved by Dalian Ocean University.

Author contributions

DG conceived and designed the experiment. YT and LY conducted the experiment. DG, XC and MS are involved in data analysis. BX and PX collected and maintained the research data. DG wrote the manuscript. DG and XC contributed equally to this work and share first authorship. All authors contributed to the article and approved the submitted version.

Funding

This research was funded by the National Key Research and Development Program of China (2019YFD0901303) and the Science and Technology Innovation Fund of Dalian, China (2021JJ11CG001).

Acknowledgments

We are grateful to the experts who helped us complete the ultrasonic pinger implantation operations and the people who helped us collect data in the field. Special thanks to Researcher Wei Song for providing venue support and assistance for this experiment.

Conflict of interest

The authors declare that the research was conducted in the absence of any commercial or financial relationships that could be construed as a potential conflict of interest.

Publisher's note

References

Adams, N. S., Rondorf, D. W., Evans, S. D., Kelly, J. E., and Perry, R. W. (1998). Effects of surgically and gastrically implanted radio transmitters on swimming performance and predator avoidance of juvenile chinook salmon (Oncorhynchus tshawytscha). *Can. J. Fisheries Aquat. Sci.* 55 (4), 781–787. doi: 10.1139/f97-285

Anglea, S., Geist, D., Brown, R., and Deters, K. (2003). Evaluation of surgically implanted acoustic transmitters on the swimming performance, predator avoidance, and buoyancy compensation of juvenile Chinook salmon. 2003. *Rep. Prepared Public Utility District.*

Biesinger, Z., Bolker, B. M., Marcinek, D., Grothues, T. M., Dobarro, J. A., and Lindberg, W. J. (2013). Testing an autonomous acoustic telemetry positioning system for fine-scale space use in marine animals. *J. Exp. Mar. Biol. Ecol.* 448, 46–56. doi: 10.1016/J.JEMBE.2013.06.007

Bridger, C. J., and Booth, R. K. (2003). The effects of biotelemetry transmitter presence and attachment procedures on fish physiology and behavior. *Rev. Fisheries Sci.* 11 (1), 13–34. doi: 10.1080/16226510390856510

Brown, R. S., Cooke, S. J., Anderson, W. G., and McKinley, R. S. (1999). Evidence to challenge the "2% rule" for biotelemetry. *North Am. J. Fisheries Manage.* 19 (3), 867–871. doi: 10.1577/1548-8675(1999)019<0867:ETCTRF>2.0.CO;2

Calado, R., Mota, V. C., Madeira, D., and Leal, M. C. (2021). Summer is coming! Tackling ocean warming in Atlantic salmon cage farming. *Animals* 11 (6), 1800. doi: 10.3390/ANI11061800

Codarin, A., Wysocki, L. E., Ladich, F., and Picciulin, M. (2009). Effects of ambient and boat noise on hearing and communication in three fish species living in a marine protected area (Miramare, Italy). *Mar. Pollut. Bull.* 58 (12), 1880–1887. doi: 10.1016/j.marpolbul.2009.07.011

Cooke, S. J., Graeb, B., Suski, C., and Ostrand, K. (2003). Effects of suture material on incision healing, growth and survival of juvenile largemouth bass implanted with miniature radio transmitters: case study of a novice and experienced fish surgeon. *J. Fish Biol.* 62 (6), 1366–1380. doi: 10.1046/j.1095-8649.2003.00119.x

Cooke, S. J., Midwood, J. D., Thiem, J. D., Klimley, P., Lucas, M. C., Thorstad, E. B., et al. (2013). Tracking animals in freshwater with electronic tags: Past, present and future. *Anim. Biotelemetry* 1 (1), 1–19. doi: 10.1186/2050-3385-1-5

Del Rio-Zaragoza, O. B., Cavalheiro Araujo, B., and Viana, M. T. (2021). Health status evaluation of striped bass (Morone saxatilis) exposed to low temperature in sea cage culture during the grow-out. *Aquaculture Res.* 52 (6), 2435–2445. doi: 10.1111/are.15093

Fay, R., and Popper, A. (2009). Fish hearing and bioacoustics since 1973. *J. Acoustical Soc. America* 125 (4), 2485–2485. doi: 10.1121/1.4808776

Fu, X., Huang, D., Xu, H., and Ma, S. (2021). Overview of the development of cage aquaculture in deep Sea. *J. Aquaculture* 42 (10), 23–26. doi: 10.3969/j.issn.1004-2091.2021.10.006

Han, X., Song, W., Gui, F., and Wang, L. (2022). Large-Scale enclosure culture technology of pseudosciaena crocea with ecological imitation and shore connection. *China Fisheries* 11), 79–81.

Haynes, J. (1978). *Movement and habitat studies of chinook salmon and white sturgeon.[Oncorhynchus tshawytscha, acipenser transmontanus]* (Richland, WA (USA: Battelle Pacific Northwest Labs.). doi: 10.2172/6632297

Hou, Y., Zou, X., Tang, W., Jiang, W., Zhu, J., Deng, C., et al. (2019). Precise capture of fish movement trajectories in complex environments *via* ultrasonic signal tag tracking. *Fisheries Res.* 219, 105307. doi: 10.1016/j.fishres.2019.105307

Hussey, N. E., Kessel, S. T., Aarestrup, K., Cooke, S. J., Cowley, P. D., Fisk, A. T., et al. (2015). Aquatic animal telemetry: A panoramic window into the underwater world. *Science* 348 (6240), 1255642. doi: 10.1126/science.1255642

Jepsen, N., Schreck, C., Clements, S., and Thorstad, E. (2005). A brief discussion on the 2% tag/bodymass rule of thumb. *Aquat. Telemetry: Adv. Appl.*, 255–259.

Juell, J.-E., and Westerberg, H. (1993). An ultrasonic telemetric system for automatic positioning of individual fish used to track Atlantic salmon (Salmo salar l.) in a sea cage. *Aquacultural Eng.* 12 (1), 1–18. doi: 10.1016/0144-8609(93)90023-5

Lee, J., Tezak, E., and Berejikian, B. (2013). Telemetry tag effects on juvenile lingcod ophiodon elongatus movement: A laboratory and field study. *J. Fish Biol.* 82 (6), 1848–1857. doi: 10.1111/jfb.12111

Liu, Z., Zhao, W., Hu, W., Zhu, B., Xie, J., Liu, Y., et al. (2021). Lipid metabolism, growth performance, antioxidant ability and intestinal morphology of rainbow trout (Oncorhynchus mykiss) under cage culture with flowing water were affected by dietary lipid levels. *Aquaculture Rep.* 19, 100593. doi: 10.1016/J.AQREP.2021.100593

Madsen, K., Nielsen, H. B., and Tingleff, O. (2004). Methods for non-linear least squares problems.

Makiguchi, Y., and Ueda, H. (2009). Effects of external and surgically implanted dummy radio transmitters on mortality, swimming performance and physiological status of juvenile masu salmon oncorhynchus masou. *J. Fish Biol.* 74 (1), 304–311. doi: 10.1111/j.1095-8649.2008.02131.x

Mellas, E. J., and Haynes, J. M. (1985). Swimming performance and behavior of rainbow trout (Salmo gairdneri) and white perch (Morone americana): Effects of attaching telemetry transmitters. *Can. J. Fisheries Aquat. Sci.* 42 (3), 488–493. doi: 10.1139/f85-066

Miller, E. A., Froehlich, H. E., Cocherell, D. E., Thomas, M. J., Cech, J. J., Klimley, A. P., et al. (2014). Effects of acoustic tagging on juvenile green sturgeon incision healing, swimming performance, and growth. *Environ. Biol. Fishes* 97, 647–658. doi: 10.1007/s10641-013-0167-x

Miyamoto, Y., Uchida, K., Takao, Y., and Sasakura, T. (2011). Development of a new ultrasonic biotelemetry system using a maximum length sequence signal. *J. Mar. Acoust Soc. Jpn* 38 (3), 119–127. doi: 10.3135/JMASJ.38.119

Moore, A., Russell, I., and Potter, E. (1990). The effects of intraperitoneally implanted dummy acoustic transmitters on the behaviour and physiology of juvenile Atlantic salmon, salmo salar l. *J. Fish Biol.* 37 (5), 713–721. doi: 10.1111/j.1095-8649.1990.tb02535.x

Neo, Y., Hubert, J., Bolle, L., Winter, H. V., Ten Cate, C., and Slabbekoorn, H. (2016). Sound exposure changes European seabass behaviour in a large outdoor floating pen: Effects of temporal structure and a ramp-up procedure. *Environ. Pollut.* 214, 26–34. doi: 10.1016/j.envpol.2016.03.075

Panther, J. L., Brown, R. S., Gaulke, G. L., Deters, K. A., Woodley, C. M., and Eppard, M. B. (2011). Influence of incision location on transmitter loss, healing, survival, growth, and suture retention of juvenile Chinook salmon. *Trans. Am. Fisheries Soc.* 140 (6), 1492–1503. doi: 10.1080/00028487.2011.637003

Poddubnyi, A., Spiktor, Y. I., and Kidiun, S. (1966). The results of preliminary experiments in tracking sturgeon carrying electronic tracer tags. *Vop. Ikhtiol.* 6, 725–734.

Roy, R., Beguin, J., Argillier, C., Tissot, L., Smith, F., Smedbol, S., et al. (2014). Testing the VEMCO positioning system: Spatial distribution of the probability of location and the positioning error in a reservoir. *Anim. Biotelemetry* 2 (1), 1–7. doi: 10.1186/2050-3385-2-1

Sarà, G., Dean, J., d'Amato, D., Buscaino, G., Oliveri, A., Genovese, S., et al. (2007). Effect of boat noise on the behaviour of bluefin tuna thunnus thynnus in the Mediterranean Sea. *Mar. Ecol. Prog. Ser.* 331, 243–253. doi: 10.3354/meps331243

Shi, H., Jiao, H., You, Z., Wang, Y., Li, S., Xu, J., et al. (2010). Effect of ship noise on plasma cortisol level of bass and yellow croaker. *Acta Ecologica Sin.* 30 (14), 3760–3765.

Smith, M. E., Kane, A. S., and Popper, A. N. (2004). Noise-induced stress response and hearing loss in goldfish (Carassius auratus). *J. Exp. Biol.* 207 (3), 427–435. doi: 10.1242/jeb.00755

Summerfelt, R. C., and Mosier, D. (1984). Transintestinal expulsion of surgically implanted dummy transmitters by channel catfish. *Trans. Am. Fisheries Soc.* 113 (6), 760–766. doi: 10.1577/1548-8659(1984)113<760:TEOSID>2.0.CO;2

Wagner, G. N., Cooke, S. J., Brown, R. S., and Deters, K. A. (2011). Surgical implantation techniques for electronic tags in fish. *Rev. Fish Biol. Fisheries* 21, 71–81. doi: 10.1007/s11160-010-9191-5

Wang, X., Lu, G., Zhao, L., Yang, Q., and Gao, T. (2020). Assessment of fishery resources using environmental DNA: Small yellow croaker (Larimichthys polyactis) in East China Sea. *PloS One* 15 (12), e0244495. doi: 10.1371/journal.pone.0244495

Wang, C., Wei, Q., Kynard, B., Du, H., and Zhang, H. (2012). Migrations and movements of adult Chinese sturgeon acipenser sinensis in the Yangtze river, China. *J. Fish Biol.* 81 (2), 696–713. doi: 10.1111/j.1095-8649.2012.03365.x

Wysocki, L. E., Dittami, J. P., and Ladich, F. (2006). Ship noise and cortisol secretion in European freshwater fishes. *Biol. Conserv.* 128 (4), 501–508. doi: 10.1016/j.biocon.2005.10.020

Yin, L. (2017). *Study on the response and mechanism of acoustic attraction behavior of pseudosciaena crocea* (Shanghai Ocean University).

Young, A., Tytler, P., Holliday, F., and MacFarlane, A. (1972). A small sonic tag for measurement of locomotor behaviour in fish. *J. Fish Biol.* 4 (1), 57–65. doi: 10.1111/j.1095-8649.1972.tb05652.x

Zale, A. V., Brooke, C., and Fraser, W. C. (2005). Effects of surgically implanted transmitter weights on growth and swimming stamina of small adult westslope cutthroat trout. *Trans. Am. Fisheries Soc.* 134 (3), 653–660. doi: 10.1577/T04-050.1

Zhao, L., and Dai, H. (2021). The experiment of domestication of tilapia in seawater and marine cage culture. *Hebei Fisheries* 11), 21–23.

frontiers | Frontiers in Marine Science

TYPE Original Research
PUBLISHED 17 May 2023
DOI 10.3389/fmars.2023.1178548

OPEN ACCESS

EDITED BY
Zhao Yunpeng,
Dalian University of Technology, China

REVIEWED BY
Hung-Jie Tang,
National Cheng Kung University, Taiwan
Peter M. J. Herman,
Delft University of Technology,
Netherlands

*CORRESPONDENCE
David W. Fredriksson
✉ David.Fredriksson@unh.edu

RECEIVED 02 March 2023
ACCEPTED 24 April 2023
PUBLISHED 17 May 2023

CITATION
Fredriksson DW, St. Gelais AT, Dewhurst T, Coleman S, Brady DC and Costa-Pierce BA (2023) Mooring tension assessment of a single line kelp farm with quantified biomass, waves, and currents.
Front. Mar. Sci. 10:1178548.
doi: 10.3389/fmars.2023.1178548

Mooring tension assessment of a single line kelp farm with quantified biomass, waves, and currents

David W. Fredriksson[1]*, Adam T. St. Gelais[2], Tobias Dewhurst[3], Struan Coleman[4], Damian C. Brady[2,4] and Barry Antonio Costa-Pierce[5,6]

[1]School of Marine Science and Ocean Engineering, University of New Hampshire, Durham, NH, United States, [2]Aquaculture Research Institute, University of Maine, Darling Marine Center, Walpole, ME, United States, [3]Kelson Marine Co., Portland, ME, United States, [4]School of Marine Sciences, Darling Marine Center, University of Maine, Walpole, ME, United States, [5]Faculty of Biosciences and Aquaculture, Nord University, Bodø, Norway, [6]Ecological Aquaculture Foundation, LLC, Biddeford, ME, United States

While the number of kelp farms have steadily increased, few have been deployed with sensors to measure mooring tensions with substantial biomass. During the kelp farming season of 2018–2019 in Saco Bay, Maine USA, a field study was conducted to assess mooring loads due to environmental conditions and kelp growth. The effort included the deployment of a farm with a 122 m cultivation line and spread mooring with rope, chain, and anchors in 15.2 m of water. The system was deployed with seeded twine in late November and harvested in May. In April, with kelp biomass estimated at 7.8 kg m^{-1}, two load cells were installed to measure mooring tensions in response to currents and waves. The currents and waves were measured with two Acoustic Doppler Current Profilers deployed adjacent to the load cells. From these measurements, we characterized the maximum loading case in response to a complex hydrodynamic environment. The maximum tension occurred on the landward side of the farm even though wave exposure was seaward. The tension in the landward side mooring was dominated by steady drag from the currents going to the east southeast. During this event, the two profilers were positioned on the leading and trailing edges of the farm relative to the prevailing current direction. Velocities measured at 0.5 m bins showed a 26.7% reduction at the depths where the kelp was located. To analyze the dynamic portion of the load cell datasets, the oscillatory components were processed into energy density spectra. Results showed that mooring tensions were not affected by waves at frequencies greater than 0.175 Hz, with most of the energy occurring near 0.12 Hz. The tension spectra did reveal energy at frequencies between 0.0075 and 0.01 Hz, indicating a low frequency response, possibly due to nonuniform velocity profiles inducing vertical motion of the cultivation line. It was also observed that the landward mooring, subjected to higher currents, was more sensitive to oscillating loads than the slack seaward side. The high-fidelity dataset will be useful for numerical modeling validation to further understand these dynamics and to optimize kelp farm designs.

KEYWORDS

ocean measurements, aquaculture engineering, macroalgae farms, *Saccharina latissima*, anchor lines

1 Introduction

The farming of brown macroalgae of order *Laminariales* (kelp) in temperate oceans has grown in recent years (Grebe et al., 2019). In the northeast of the United States (US), especially in the Gulf of Maine, the kelp industry has expanded by nearly 3,000% from 2015 to 2020, characterized by mostly small owner-operators (St-Gelais et al., 2022). This sector of the traditional working waterfront utilizes existing fishing industry infrastructure, including lobster fishing vessels, often with just 2–3 individuals as crew (Piconi et al., 2020). At this infrastructure scale, gear cannot be oversized even though more exposed sites are being considered. These factors influence both capital and equipment replacement costs that represent a significant portion of the cost of production (Coleman et al., 2022).

The evaluation and design of kelp farming systems is challenging because kelp can grow densely (Kim et al., 2015; Augyte et al., 2017), is compliant (Buck and Buchholz, 2005; Henry, 2014; Rominger and Nepf, 2014), and is often close to being neutrally buoyant (Vettori and Nikora, 2017). Because of these qualities, Fredriksson et al. (2020) examined the steady flow hydrodynamics of a full-scale physical model representing 1 m aggregates of *Saccharina latissima* grown on an ocean-deployed farm in a series of tow tank experiments. The intent was to produce normal and tangential drag coefficients to be utilized in time domain numerical models, based on the empirical approach using a modified Morison equation (Morison et al., 1950), and using the finite element method (FEM). One set of FEM approaches stem from the work of Gosz et al. (1996); Tsukrov et al. (2003), and Fredriksson et al. (2003) focusing on net systems. Many others have also developed numerical modeling techniques for containment net structures. Examples include Li et al. (2006), Zhao et al. (2007), Zhao et al. (2015), Lee et al. (2008), Lee et al. (2015), Huang and Pan (2010), Reite et al. (2014), Cifuentes and Kim, (2017), Tsarau and Kristiansen (2019), and Martin et al. (2021). Commercial codes are also available such as OrcaFlex (https://www.orcina.com/), ProteusDS (https://dsa-ltd.ca/proteusds/overview/), and AquaSim (Berstad et al., 2012; Berstad and Heimstad, 2019). Considerable work has also been done modeling single line aquaculture systems such as mussel farms (e.g., Raman-Nair and Colbourne, 2003 and Raman-Nair et al., 2008; Pribadi et al., 2019; Knysh et al., 2020). Many of these net and mussel farm modeling techniques can be modified for kelp farming applications, such as Knysh et al. (2022). As with any engineering approach, however, these computational methods are only as valuable as they are accurate. Thus, the predictions must be validated with measurements of the behavior of *in-situ* macroalgae cultivation structures.

Understanding *in-situ* physical properties of these aquaculture systems requires field instrumentation with specific sampling strategies. A body of work has been established focusing on field measurement of engineering parameters for aquaculture systems. For example, Colbourne and Allen (2001); Fredriksson et al. (2003), and Fredriksson et al. (2007a, b), developed techniques to measure loadings on fish cage systems, while Stevens et al. (2007); Stevens et al. (2008), and Nguyen et al. (2019) deployed engineering instrumentation on shellfish farms. A need also exists to establish a similar understanding of the *in-situ* characteristics of kelp farms. Specifically, this information will guide the application of numerical models and associated design procedures, especially as larger scale farms are designed for exposed ocean areas to meet demand for non-food end uses of biomass (biofuel, animal feed, bio-composite materials, carbon, and nutrient removal).

The objective of this study was to assess mooring load characteristics due to biomass and environmental conditions for an exposed kelp farm. The engineering study was conducted during the kelp farming season from November 2018 to May 2019 in Saco Bay, Maine USA. Submersible load cell instruments were custom designed and deployed on farm mooring lines to measure the tension response to directional waves and currents recorded with two bottom-mounted Acoustic Doppler Current Profilers (ADCPs). Tension datasets with wave and current information were examined along with the amount of kelp biomass growing at the time of measurement. We then examined the current velocity profile and directional wave details associated with the highest tension event. The goal is to use this high-fidelity dataset in the future to improve numerical modeling approaches, filling a critical research and development need for kelp aquaculture in emerging production regions.

2 Methodology

2.1 The kelp farm site and system

The field study was conducted at an aquaculture lease (St-Gelais et al., 2022) where a kelp farm was deployed at an exposed site in Saco Bay, Maine, USA (Figure 1). The site was permitted with a Limited Purpose Aquaculture (LPA) license, having surface dimensions of 0.3 x 122 m, a nominal mean sea level of 15.2 m, and bottom substrate composed mostly of sand. The intent of the LPA license in Maine is to provide opportunity for entry into aquaculture with a yearly lease of a single grow line. The Saco Bay LPA site was chosen for its exposure to the east, but still accessible for farm operation with only a 3.5 km transit from a pier in the Saco River.

As described in St-Gelais et al. (2022), the mooring system designed for the LPA site was based on an extreme condition that occurred in April 2007, called the Patriot's Day storm. Offshore wave characteristics of the storm were obtained at station 44007 operated by the National Data Buoy Center (NDBC) with a maximum zero-order moment wave height (H_{m0}) value equal to equal to 9.64 m with a dominant period of 11.43 s. Even though station 44007 is located approximately 19 km from the LPA site in a depth of 49 m, return period analysis was performed using 35 years of 44007 historical datasets to characterize storm severity. The analysis applied the annual maxima method (for every month) with a Weibull distribution and least squares fitting as described in Goda (2010). This produced an offshore 50-year storm condition with waves having an H_{m0} equal to 9.51 m.

To relate offshore conditions to the nearshore LPA site, wave hindcast simulations from Zou and Xie (2016) were examined for the same Patriot's Day storm that included the LPA site within the

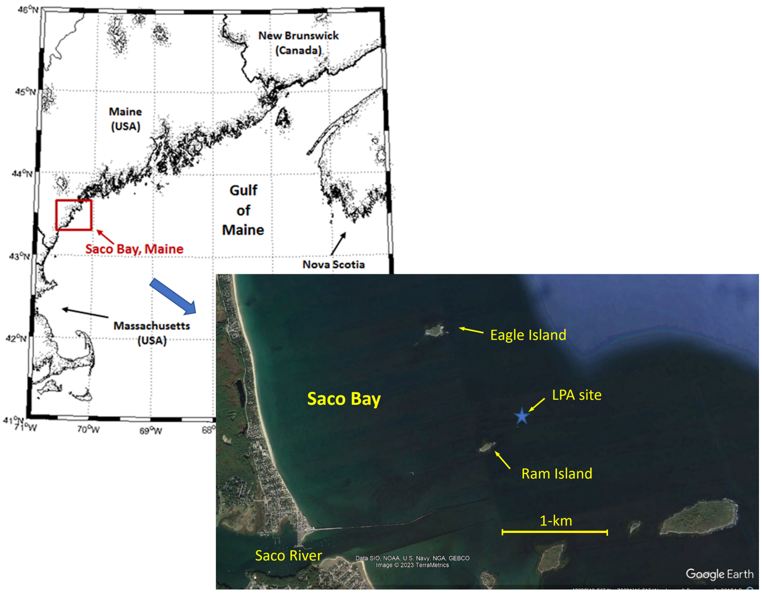

FIGURE 1
The kelp farm site in Saco Bay, ME was exposed to storms coming from the east. Access to the site was about 3.5 km from a pier in the Saco River (Google Earth Pro 7.3.6.9345, 2022).

computational domain. The dataset yielded an H_{m0} value approximately 4.5 m with peak periods on the order of 11 s. We used these parameters to develop our nominal 50-year storm wave condition for the design of the kelp farm. The design condition also included an estimated 50-year current equal to 0.56 m s^{-1}. This value was based on a set of ADCP measurements obtained at the site from 2018 that yielded a major axis tidal current (M_2) in an east–west orientation equal to 0.3 m s^{-1}. This value was multiplied by a factor 1.85 according to the Norwegian Standard NS 9415. The design condition assumed both waves and current coming from the east as a potential worst-case orientation.

2.2 Kelp growth at the Saco Bay site

During the 2018–2019 growing season, kelp was seeded on October 30, 2018, on the 122 m horizontal cultivation line secured to the pretensioned mooring system deployed on the same day. The seed slowly grew over the following months. Accelerated growth occurred in March and April before being harvested in May. During this time, biomass samples were taken from the eastern, middle, and western sections of the farm throughout the growing season. Each sample consisted of 0.5 meter of biomass from the cultivation line with holdfasts included. The number of blades were recorded along with individual length and width values. The width was measured at 3 locations along the blade. The samples were weighed at sea while suspended out of the water using a spring scale. Logistic growth curves were fitted to the time series of biomass per meter using the curve-fitting methodology described in St-Gelais et al. (2022). While St-Gelais et al. (2022) was focused on biomass for harvest and thus fit a single time series to the total biomass, the present analysis focused on quantifying biomass on the farm while the instrumentation was deployed, including the distribution of the biomass within the farm. Therefore, a separate logistic fit was applied for each of the three locations, and a composite average was derived.

2.3 Engineering instrumentation and deployment strategy

The strategy for deploying instrumentation was to measure mooring line tension in response to waves and currents from spring storm events to coincide with near harvest levels of biomass. Mooring tension measurements were obtained with two custom made load cells with data acquisition systems designed for submersible applications. The submersible load cell, data logger, and power supply components were mounted as an assembly to a stainless steel strongback that was shackled in line with each of the moorings, one of which is shown on Figure 2A. Inline tensions were measured with a pancake type load cell attached with a spacer to the flange of the strongback. A custom threaded eye was inserted through the center of the load cell to engage the instrument upon loading. The spacer was needed to allow the attachment of a thin bolt and cotter pin securing the eye to the load cell. Small gaps were maintained on either side of the spacer with washers to allow some water exchange to prevent crevice corrosion. The pancake load cell shown in Figure 2A was specified with a capacity of 8.9 kN with the strongback having a limit of 35.6 kN. The data logger and power supply were developed as part of a series of ocean observatories described in Comeau et al. (2007). For this application, the data logger was modified with two analog ports for load cell input with

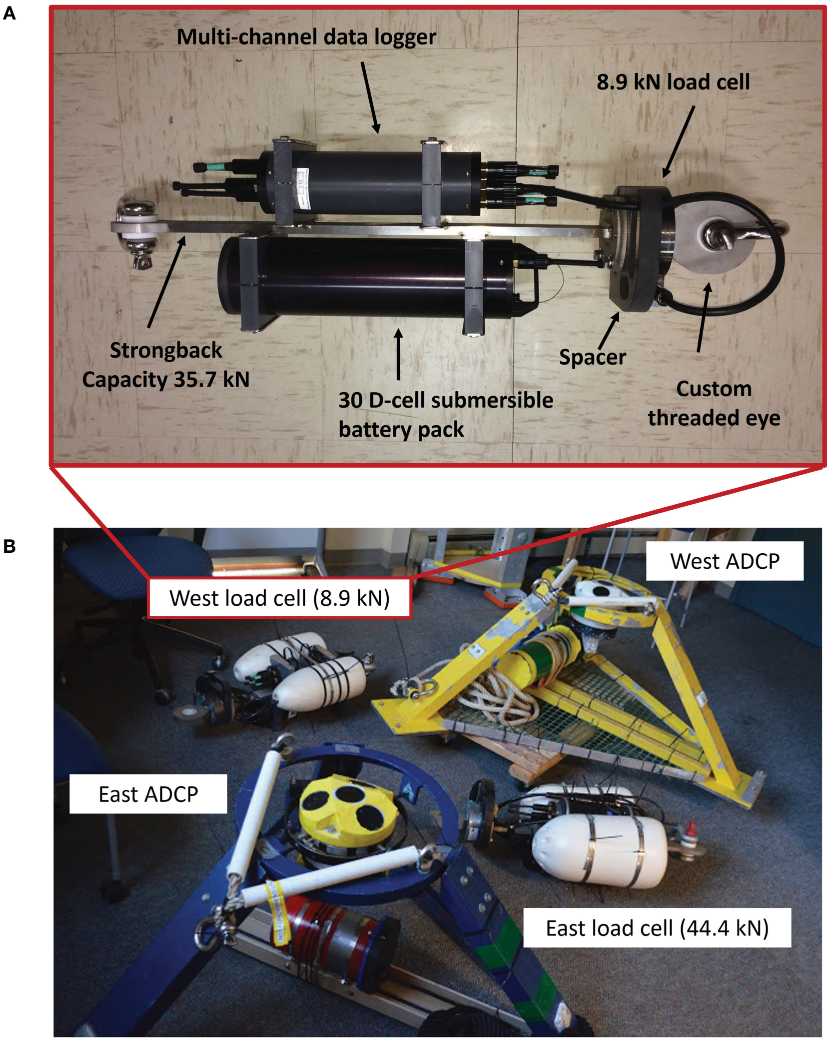

FIGURE 2
(A) The component details of the 8.9 kN capacity load cell instrumentation package deployed on the west mooring line. **(B)** Lobster floats were used to make the load cells instrumentation neutrally buoyant. The suite of instruments deployed on the kelp farm included two ADCPs and two load cell instruments.

16-bit, analog to digital conversion. The assembly weighed about 222 N. To make it neutrally buoyant, lobster floats were attached to both sides of the data logger above the heavier battery pack. The 8.9 kN load cell system was deployed on the west mooring line (landside) since it was not expected to carry the primary load of exposure. A similar load cell system was deployed on the east mooring line (oceanside), but with a higher capacity of 44.4 kN and a strongback designed for a load of 80 kN (Figure 2B). The higher capacity instrument was installed on the east due to expected higher exposure levels. Both load cells were set to measure for 30 minutes each hour at a rate of 4 Hz.

Current profile and directional wave datasets were obtained with two, 1 MHz ADCPs manufactured by Nortek (Figure 2B). The load cell and ADCP deployment positions, with respect to the kelp farm, are shown in Figure 3, and were deployed from April 24 to May 1. The ADCPs were configured to alternate between sampling velocity profiles and directional waves. East- and north-going velocities were obtained at thirty-four, 0.5 m bins above the instrument. The configuration considers the estimated depth of the water (15.2 m), height of the transducers above the bottom (0.5 m), the instrument blanking distance (0.4 m) and a 3 m tidal range. Profiles were measured every 15 min as 3 min averages (from 7 Hz sampling) from 0–3, 15–18, 30–33 and 45–48 minutes past each hour.

Both east and west ADCPs were also utilized in wave measuring mode. In this mode, velocities, pressures, and acoustic surface tracking (AST) parameters were acquired in time series bursts. The time series were processed into statistical, spectral, and directional wave information (Krogstad, 1988; Pedersen et al., 2002; Pedersen and Siegel, 2008). Bursts were set to begin following each current profile measurement. Wave orbital velocities and dynamic pressures were sampled at 2 Hz for 1024 counts, while the AST data were measured at 4 Hz for 2048 counts, each for a duration of 8 min and 32 s to fit between velocity profile acquisition.

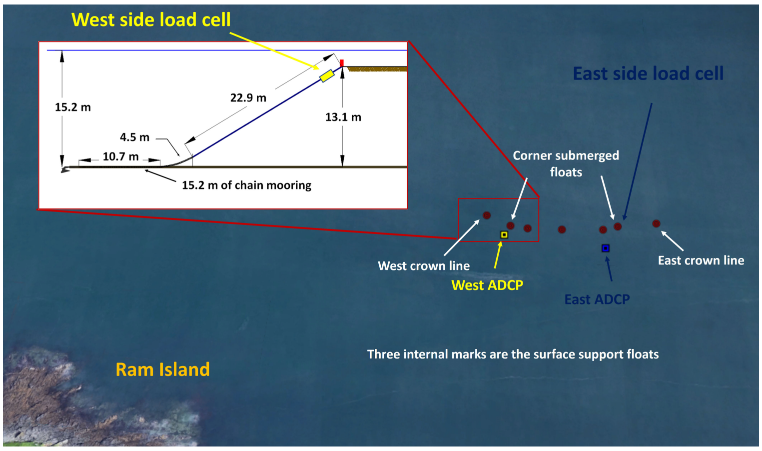

FIGURE 3
The spatial configuration of the kelp farm with the ADCPs and the load cells at the Saco Bay site (Google Earth, 2018).

3 Results

3.1 Kelp biomass

The general kelp biomass dataset as described in St-Gelais et al. (2022) was revisited to focus on the time frame for which the instruments were deployed. Kelp biomass was assessed at three regions along the cultivation line. Samples were taken at 8 locations on the west, 7 locations on the middle and 9 locations on the east sections between February 2 and May 22 (Figure 4). We then developed logistic models of kelp biomass production (Masters and Ela, 2007) for each of the regions on the cultivation line combining them into an average. The average logistic fit is also shown in Figure 4. The resulting fit had an initial value of 0.1 kg m^{-1} and an environmental limit of nearly 15 kg m^{-1}. The resulting biomass on April 25, was calculated from the data derived fit to be 7.8 kg m^{-1}. In addition to the biomass assessment, specific samples were obtained on April 24. On this day, 5 replicate samples were acquired from east, middle, and west locations along 0.5 m sections of the cultivation line for a total of 15 bundles of kelp. An average of 175 blades were counted from each 0.5 m bundle. The length of each blade collected was measured along with the width at three locations, near the stipe, in the middle and near the tip. The average length was 0.99 m with a standard deviation of 0.32 m. The average width was 0.095 m with a standard deviation of 0.034 m.

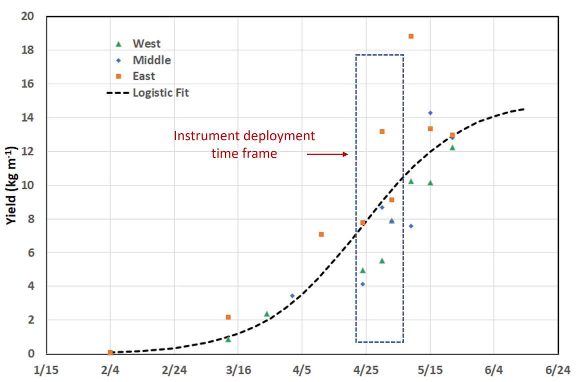

FIGURE 4
The measured and logistic curve fit biomass from the 2019 kelp growing season.

3.2 General dataset results

3.2.1 Mooring line tensions

Data from the east and west mooring load cells from April 25 to May 1 were first processed to remove offset values associated with a no-load condition. Zero values were recorded for 30 minutes before and after the deployment from each unit while unloaded on the deck of the vessel. The mean and ± the standard deviation values for the no-load condition are provided in Table 1. The west load cell zero values showed less variation than those from the east load cell due to capacity and amplifier design. In all cases, the offsets were within 0.6% of the total capacity of each respective unit and thus we were confident that the tension value margin of uncertainty was at most 100 N.

The before and after deployment zero values were averaged, then subtracted from the deployed portion of the dataset to create a time series for each instrument (Figures 5A, B). The most prominent event occurred on the west mooring line at 1:21 UTC on April 27 with the maximum tension equal to 2843 N. The corresponding highest tension on the east mooring line during this burst was considerably less at 1515 N. Averaged over the length of the deployment, tensions on the east mooring line (628 N), however, were higher than those on the west side (482 N). The east mooring line also had more frequent events as shown by the peaks greater than the mean values. Mean values for both moorings were not much greater than the calculated static pretension (418 N) created by the submerged floats at each corner.

3.2.2 ADCP datasets

Water level, velocity profiles, and directional waves were measured from the east and west ADCPs deployed just south of the load cells (Figure 3). Mean sensor depth was 15.51 m on the east

TABLE 1 Mean and ± standard deviation for the no load conditions for the east and west load cells.

Instrument	East load cell	West load cell
Capacity	44,400 N	8,900 N
Before deployment	49.9 ± 6.65 N	57.6 ± 7.00 N
After deployment	96.7 ± 3.05 N	58.5 ± 1.80 N

(seaward) and 14.72 m on the west side (landward) as shown in Figure 6A. The water level datasets also show the tides are dominated by the M_2 constituent with a period of 12.42 hours with an average range of 2.2 m. Depth averaged velocity profile results are shown on Figures 6B, C for the east- and north-going components. A vertical dashed line is included on the three plots for the time of the maximum tension on the west mooring. The line corresponds with a point between the high and low water marks on (Figure 6A) indicating an ebb tidal current. The vertical dashed line also correlates with the maximum current velocity measured from both the ADCPs.

With the ADCPs configured to calculate 3 minute averages every 15 minutes, east and west datasets were obtained from 1:15–1:18 and 1:30–1:33, before and after the time of maximum tension at 1:21 UTC. The east- and north-going components with speed and direction are provided in Table 2 for these time periods, bracketing the maximum tension event. The speed values on the west side were greater than those on the east side. Because the prevailing currents in the region were in the ESE direction, the west ADCP was likely on the unobstructed, leading edge of the farm, with the east ADCP in the lee, with a potential reduction of velocity through the farm.

Wave AST bursts measured by the ADCPs for the April 25 to May 1 deployment were used to identify the maximum wave height (H_{max}) from each instrument. The time series were also processed into a spectral energy density form. With the spectral energy density, the significant wave heights, based on the zero-order moment about the spectral curve (H_{m0}), were calculated and paired with the dominant period (T_p). The directions associated with the dominant period (T_p-direction) were also determined from the ADCPs by processing the wave orbital velocity components. The H_{max}, H_{m0}, T_p and T_p-direction results from each burst are shown on Figures 7A through D, respectively. The maximum tension event occurred between 1:18:00 and 1:26:32 UTC on April 27.

4 Maximum tension load case

4.1 West and east mooring line load cells

The 30 minute burst for the maximum tension load case is shown on Figure 8A for both the west and east side instruments. In additional to the peak value of 2843 N occurring at 1:21:53, it was clear that the west mooring line was bearing more of the load than the east with higher mean and oscillatory components. The maximum tension event coincided with the AST wave bursts obtained from 1:18:00 to 1:26:32 and between two sets of ADCP velocity profiles from 1:15–1:18 and 1:30–1:33.

Maximum, mean and standard deviation calculations were performed for both the west and east load cells from the section of tension data on Figure 8B. The results are provided in Table 3 with the static pretension. A value of significant tension (T_s) was then calculated as four times the standard deviation and is also included in Table 3. T_s can be interpreted as a measure of wave influence, comparable to the H_{m0} of the waves during this burst. The basic

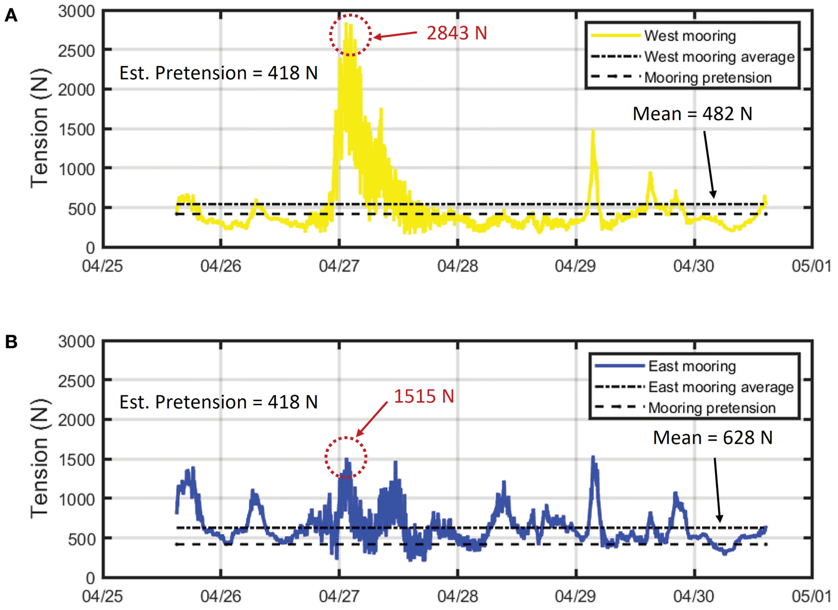

FIGURE 5
The tension results from the load cell deployment from April 25 to 30 for the **(A)** east and **(B)** west mooring lines. The largest tension value occurred on April 27 at 1:21 UTC on the west mooring line.

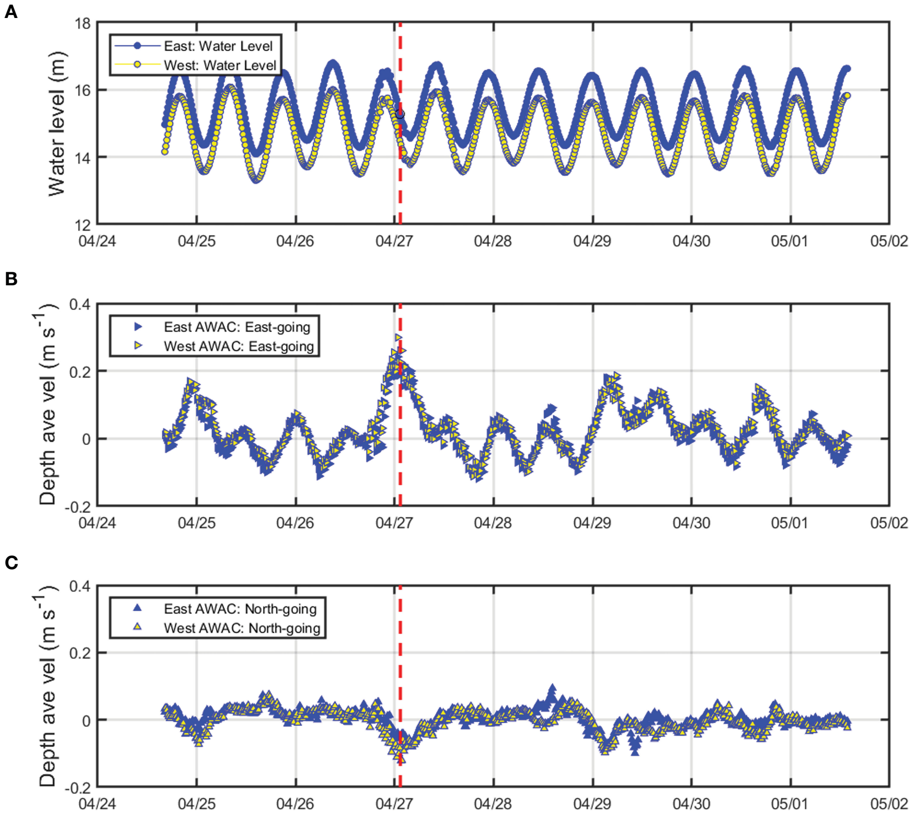

FIGURE 6
Datasets from the east and west ADCPs including the water levels **(A)**, and the east- **(B)** and north-going **(C)** depth averaged velocity components for the deployment in 2019.

statistics show that, for this event, the steady tension values induced by fluid drag and characterized by the mean have more influence on the kelp farm structure than the oscillatory components.

4.2 West and east ADCP velocity profiles

To further investigate the depth averaged current velocity results summarized in Table 2, the 1:15–1:18 and 1:30–1:33 profiles from each ADCP were examined as a function of 0.5 m depth bins (Figures 9A, B). The profile results show small differences over time within each site. However, when comparing the spatial results, a distinct velocity reduction was evident between 2 and 6 m at the east ADCP in the lee of the farm. At these bin locations, it seemed that the kelp induced work on the fluid to decrease average speed from 0.45 to 0.33 m s^{-1} (26.7%), thus creating drag on the system and contributing to the mean tension values shown in Table 3.

TABLE 2 Depth averaged velocity characteristics during the maximum tension event. Current velocity directions are described as “going-to”.

Time	Component	West ADCP	East ADCP	Speed reduction
1:15–1:18	East-going (m s^{-1})	0.261	0.221	
	North-going (m s^{-1})	−0.084	−0.049	
	Speed (m s^{-1})	0.273	0.227	17.2%
	Direction (degT)	108	102	
1:30–1:33	East-going (m s^{-1})	0.225	0.19	
	North-going (m s^{-1})	−0.122	−0.053	
	Speed (m s^{-1})	0.256	0.197	22.3%
	Direction (degT)	118	106	

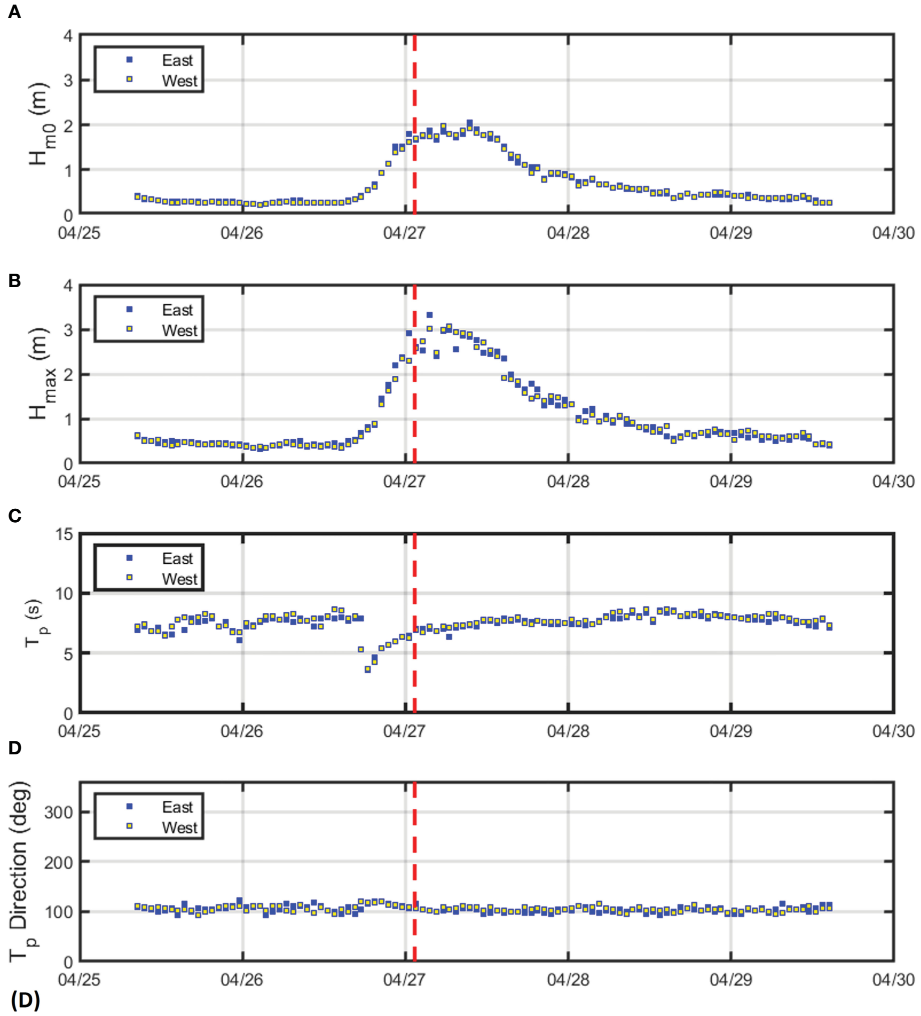

FIGURE 7
(A) The H_{m0} values from the east and west ADCPs. **(B)** The H_{max} values obtained with the zero-crossing method from the acoustic surface tracking (AST) datasets. **(C)** The T_p time series from the east and west ADCPs. **(D)** The direction of the T_p from the ADCPs. The vertical dashed line was included to identify the maximum tension event from the west mooring line.

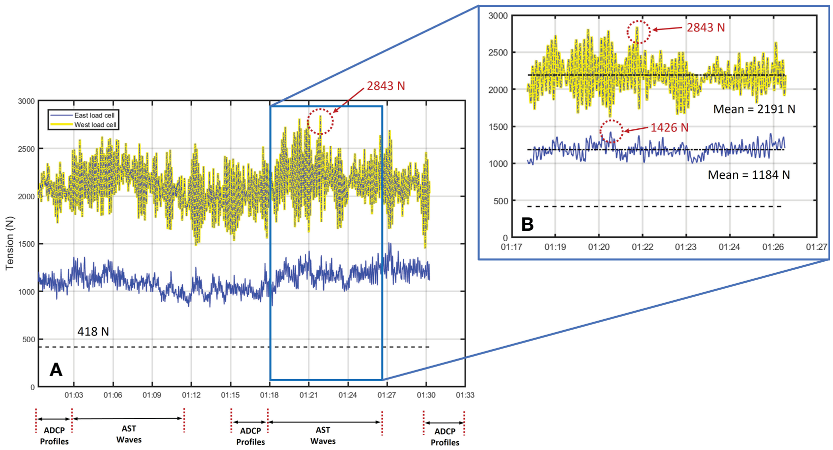

FIGURE 8
(A) The maximum tension occurred during the 30 minute load cell bursts obtained on April 27 at 1:21:53 on the west mooring. **(B)** The maximum tension value associated with the acoustic surface tracking (AST) wave burst from 1:18:00 to 1:26:32. Both mooring tension time series showed a clear wave component, though the signal was stronger on the west.

TABLE 3 Load cell statistics for the west and east mooring lines from 1:18 to 1:26:32.

Values (N)	West	East
Maximum	2843	1426
Mean	2191	1184
Pretension	418	418
Standard Deviation[1]	215	83.3
T_s[1]	860	333

[1]Calculated with the mean removed.

4.3 West and east ADCP acoustic surface track

We also investigated if steady wave conditions existed during the maximum tension event. Three sets of AST time series, representing bursts from 1:03:00 to 1:11:32, 1:18:00 to 1:26:32 and 1:33:00 to 1:41:32, were plotted from each ADCP (Figure 10). Figure 10 shows how the load cell sampling coincided with the wave burst measurements to assess potential steady state conditions. The box on Figure 10 includes the wave bursts (1:18:00–1:26:32) that were acquired when the maximum tension value was measured at 1:21:53.

Wave characteristics including the H_{max}, H_{m0}, T_p and wave direction were calculated for each of the bursts and are provided in Table 4. The values were consistent between the two west and east ADCPs with slightly larger values from 1:18:00 to 1:26:32. With this dataset, we made a general assessment that for the maximum tension case, that steady waves with an H_{m0} of 1.77 m created oscillatory tensions of T_s = 860 and 333 N for the west and east mooring line, respectively. By comparing the six wave datasets, we identified the sea as a weak stationary, and ergodic process during the 40 minutes. Therefore, oscillations in the tension time series are less likely the result of "transient effects" due to changing wave and current conditions and thus provide a better situation to assess the mooring system dynamics.

5 Discussion

5.1 Interpretation of the field study datasets

The results of this field study produced a suite of high-fidelity datasets to investigate mooring line tension of a kelp farm in response to quantified wave and current conditions with known levels of biomass. The sampling scheme developed proved effective in identifying a maximum tension event with steady state conditions for both currents and waves by profile sampling before and after wave bursts at 15 minute intervals.

The maximum tension value measured (2.8 kN) on the west mooring occurred during a mild spring storm with an H_{m0} = 1.7 m, H_{max} = 2.7 m, and T_p = 7 s. The storm produced a unique, localized hydrodynamic environment with peak profile current speeds of 0.5 m s^{-1}. It was unique in the sense that the current direction was to the ESE, nearly opposite that of the wave direction. Based on the direction of the waves and the geometric configuration of Saco Bay, it is hypothesized that waves from the east, pile up on the shore, then formed a "rip" like current out between Eagle and Ram Islands (Figure 1) to the ESE. It was this steady current that generated most

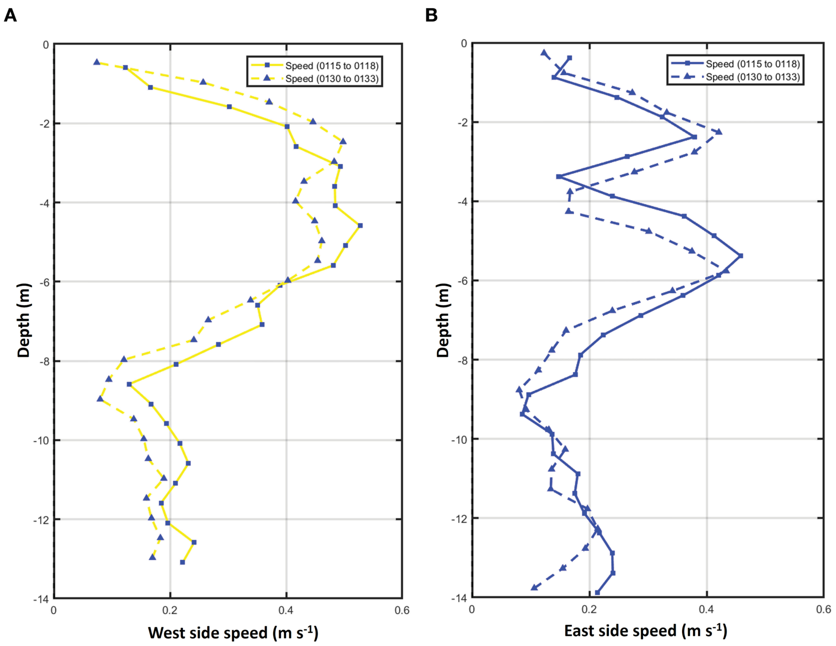

FIGURE 9
(A) The west side speed profile upstream of the farm from 1:15 to 1:18 and 1:30 to 1:33. **(B)** The east side speed profile in the lee of the farm from 01:15 to 01:18 and 01:30 to 01:33.

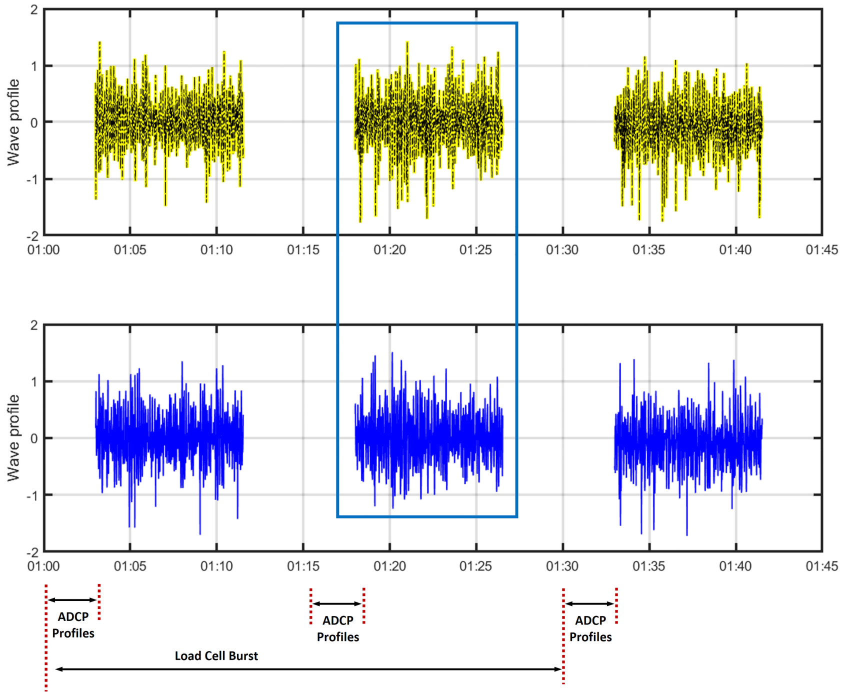

FIGURE 10
Acoustic surface tracking wave bursts obtained before, during and after the point of maximum tension (21:53 minutes) at 1:03–1:11:32, 1:18–1:26:32 and 1:33–1:41.32 minutes past the hour.

of the load on the west side mooring line. This same effect was illustrated in the wave/current/surge model simulations done for the Patriot's Day storm in Zou and Xie (2016). The ADCP results also quantified velocity reduction from the west to the east side even on this relatively small, single line farm.

The maximum tension event was further examined using a 1st order, superposition approach by removing the mean tension from each 30-minute burst to obtain the oscillatory components. We used a Fast Fourier Transform (FFT) on the zero-mean time series to isolate these frequency components of tension on the farm structure. Then, we multiplied the FFT by its complex conjugate and by normalizing per frequency bin, produced energy density spectra in units of kN^2 Hz^{-1}. The curves were smoothed by performing an 8-point frequency bin average. This technique was chosen in lieu of ensemble averaging sections to obtain potential low frequency components that could be resolved from the 30 minute burst (Figure 11A).

Each spectral curve was characterized by two distinct peaks. For the west mooring line, the largest peak occurred at 0.13 Hz, or a period of about 7.7 seconds. This was consistent with the dominant wave periods measured with the ADCPs (Table 4 and Figure 11B). In the nominal frequency band between 0.05 and 0.5 Hz, the east mooring line showed less wave energy influence, with a peak frequency of 0.12 Hz (T_p = 8.33 s), despite being oriented toward the incoming waves. This indicates a strong nonlinear interaction between current-induced and wave-induced forces: The amplitudes of the wave-induced oscillations were significantly larger on the west end of the farm. We hypothesize that since this mooring line was under a higher mean tension, it was more sensitive to oscillatory load in this complex current and wave condition. Another set of dominant peaks occurred in the range between 0.0075 and 0.01 Hz (1.6–2.2 min) indicating a substantial low frequency oscillation in the mooring system tension response. Notably, while the mean tensions and tension amplitudes in the

TABLE 4 Wave characteristics from the west and east mooring lines during the hour that the maximum tension was measured.

		H_{max} (m)	H_{m0} (m)	T_p (s)	Direction (deg)
1:03:00–1:11:32	West	2.48	1.61	6.86	109
	East	2.32	1.67	6.98	107
1:18:00–1:26:32	West	2.72	1.77	6.93	105
	East	2.75	1.76	6.90	114
1:33:00–1:41:32	West	2.42	1.61	6.99	110
	East	2.43	1.59	7.10	115

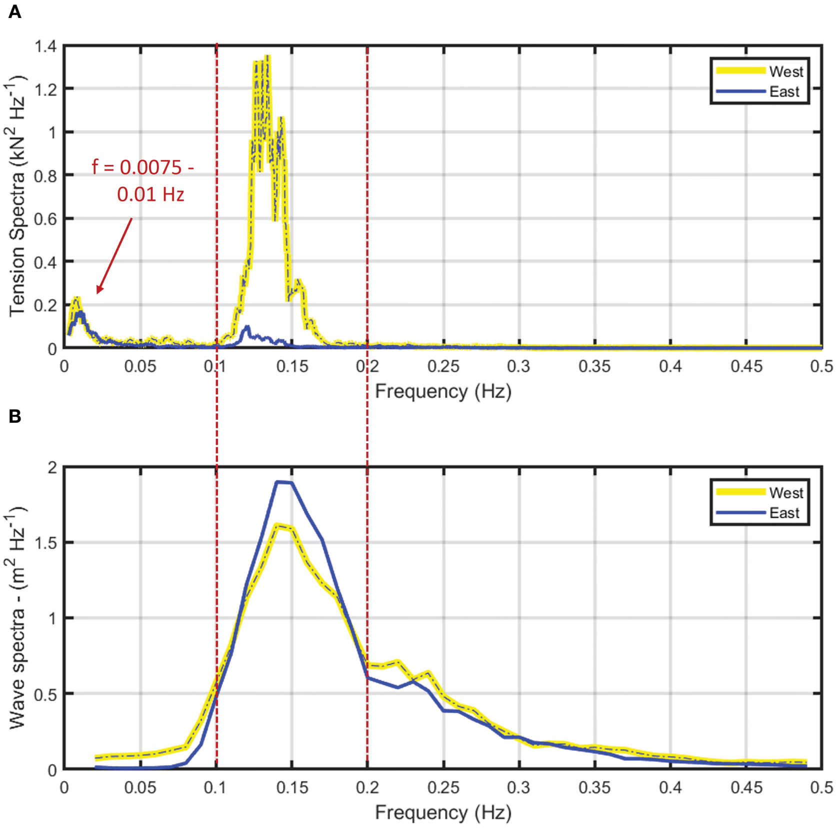

FIGURE 11

(A) Tension spectra from the west and east load cells calculated from the zero-mean, 30 minute burst of the maximum tension case. **(B)** Wave spectra from the west and east ADCPs calculated from the 1:18:00 to 1:26:32 AST bursts.

wave frequency range were substantially higher on the west side, the amplitudes of the low-frequency tension oscillations were approximately equal between the west and east mooring lines. These low-frequency oscillations are outside of the range of wave frequencies associated with highest wave energy. The wave spectral plots from the ADCPs (Figure 11B) have peak frequencies of 0.14 Hz, with seas having a broad range incorporating both swell and local wind components. It was also evident that the higher frequency wind waves (> 0.2 Hz) have little direct influence on the tension measurements.

5.2 Implications for numerical modeling approaches

The detailed load cell and ADCP datasets for the maximum tension case provided substantial insight regarding the load dynamics of the small kelp farm. The measurements quantified loading on the system as mostly from the steady currents, but with some wave influence. The farm biomass (≈7.8 kg m^{-1}) induced a 26.7% reduction in flow at the depth between 2–6 m. The tension datasets also identified low frequency oscillations. This is likely a farm dynamic response to velocity shear in the water column. It is possible that the farm is vertically oscillating, first by being pushed deeper by the stronger velocities near the surface (overcoming buoyancy) and then while in the deeper, lower velocity zone, relaxing as it floats back up to the depths of higher velocities. This process then repeats every 1–2 min.

The field measurements describe the combination of ocean processes that induce load on the kelp farm, which are transmitted to the anchors through the mooring lines. This oceanographic-structure interaction is complicated with waves and currents propagating in different directions. The waves and currents also interact producing nonlinear components. In addition, wave forcing incorporates both drag and inertia, which are 90 degrees out-of-phase. These complexities are difficult to resolve with just *in-situ* datasets.

Advanced modeling techniques such as those described in Knysh et al. (2020) and Knysh et al. (2022), however, have been applied specifically for such compliant aquaculture applications. One model platform (called HydroFE) applies the Morison et al. (1950) approach with relative velocities and accelerations. The velocities include both waves and currents with the nonlinear interaction components and the phase relationships between drag and inertia (Fredriksson et al, 2005). HydroFE and other models can use high-fidelity input to include waves and currents from different directions. For instance, our velocity profiles at 0.5 m bin resolution can be used directly as input, with waves propagating in the opposite direction and with values identical to those measured. Clear evidence exists that kelp biomass induces work on the fluid, impacting downstream circulation and current speeds. Changing the horizontal velocity field by incorporating reduction values (Knysh et al., 2022) may also be useful for systems with multiple cultivation lines such as those described in (Kite-Powell et al., 2022). Farms with multiple cultivation lines are becoming more common as kelp systems scale (e.g., DeAngelo et al., 2023). Velocity reduction schemes will also become more important to have optimized numerical modeling approaches. With the information presented here as potential validation, one possible next step would be to develop a numerical velocity reduction approach based on spatial momentum changes, potentially using normal and tangential empirical drag information (e.g., Fredriksson et al., 2020).

6 Conclusion

As macroalgae farms move into exposed areas and scale to accommodate high volume end uses, detailed and accurate modeling approaches will be needed. This high-fidelity dataset focusing on engineering parameters will improve numerical model modeling techniques that include velocity reduction caused by kelp biomass, especially as multiline kelp farms are designed. These model improvements will be crucial because steady drag effects dominate the tension values, at least during conditions with mild storms. Mooring system response as a function of current and wave forcing magnitudes and directionality is an area that needs substantial attention to reduce uncertainty during the design process. The detailed datasets presented here represent multiple potential load cases that could be used to evaluate model performance for a suite of distinct conditions. This will enable us to verify that the pertinent physical processes are adequately represented so that future designs are specified as optimized kelp farming systems.

Data availability statement

The raw data supporting the conclusions of this article will be made available by the authors, without undue reservation.

Author contributions

DF, BC-P, and AS contributed to the conceptualization of the work. DF, AS, TD, and BC-P collaborated to design the kelp farm system. AS led the field operations including deployment of gear and recovery of datasets. Data processing was done by DF with input from TD. DF worked on the initial draft of the manuscript. AS, BC-P, TD, SC, and DB provided manuscript edits. All authors contributed to the article and approved the submitted version.

Funding

Funding for this research was received in part from the United States Department of Energy Macroalgae Research Inspiring Novel Energy Resources (MARINER) program award #DEAR0000917 to the University of New England. From the same MARINER program, funds were allocated to the U.S. Naval Academy (DF's previous affiliation) as an ARPA-E Interagency Agreement No. 89703018SAR000002. Initial load cell design work was funded from the National Science Foundation Established Program to Stimulate Competitive Research (EPSCoR) award #IIA-1355457 to Maine EPSCoR at the University of Maine subaward to the University of New England (UNE), and by the UNE School of Marine & Environmental Programs. Funds for the University of Maine were received from Conscience Bay Research, LLC/Conscience Bay Company. Funding was also provided by the Aquaculture Research Institute in partnership with the University of Maine and the United States Department of Agriculture Aquaculture Experimental Station. The funders were not involved in the study design, collection, analysis, interpretation of data, the writing of this article or the decision to submit it for publication.

Acknowledgments

The authors would like to thank Liz Johndrow, Tim Arienti, Zach Miller-Hope and Addie Waters at the University of New England for field work, vessel operation and project coordination. Load cell design work was conducted at the U.S. Naval Academy with work done by Michael Stanbro. The authors also thank Dan Chadbourne for assisting in permitting, liaising with the local marine community, and vessel support.

Conflict of interest

Author BC-P was partially employed by the Ecological Aquaculture Foundation, LLC. Author TD was employed by Kelson Marine Co.

The remaining authors declare that the research was conducted in the absence of any commercial or financial relationships that could be construed as a potential conflict of interest.

Publisher's note

References

Augyte, S., Yarish, C., Redmond, S., and Kim, J. K. (2017). Cultivation of a morphological distinct strain of the sugar kelp, *Saccharina latissima* forma *angustissima*, from coastal Maine, USA, with implications for ecosystem services. *J. Appl. Phycol.* 29 (4), 1967–1976. doi: 10.1007/s10811-017-1102-x

Berstad, A. J., and Heimstad, L. F. (2019). Analysis of flexible net structures in marine environment. *Proceedings of the VIII International Conference on Computational Methods in Marine Engineering: CIMNE*, R. Bensow and J. Ringsberg (Eds). 259-270

Berstad, A. J., Walaunet, J., and Heimstad, L. F. (2012). Loads from currents and waves on net structures. *Proceedings of the ASME 2012 31st International Conference on Ocean, Offshore and Arctic Engineering. Volume 7: Ocean Space Utilization; Ocean Renewable Energy* (Rio de Janeiro, Brazil), 95–104. doi: 10.1115/omae2012-83757

Buck, B. H., and Buchholz, C. M. (2005). Response of offshore cultivated *Laminaria saccharina* to hydrodynamic forcing in the North Sea. *Aqua.* 250, 674–691. doi: 10.1016/j.aquaculture.2005.04.062

Cifuentes, C., and Kim, M. (2017). Hydrodynamic response of a cage system under waves and currents using a Morison-force model. *Ocean Eng.* 141, 283–294. doi: 10.1016/j.oceaneng.2017.06.055

Colbourne, D. B., and Allen, J. H. (2001). Observations on motions and loads in aquaculture cages from full scale and model scale measurements. *Aquacult. Eng.* 24 (2), 129–148. doi: 10.1016/S0144-8609(00)00069-8

Coleman, S., Dewhurst, T., Fredriksson, D. W., Gelais, A. T. S., Cole, K. L., MacNicoll, M., et al. (2022). Quantifying baseline costs and cataloging potential optimization strategies for kelp aquaculture carbon dioxide removal. *Front. Mar. Sci. Sec. Mar. Fish Aquacult. Living Res* 9. doi: 10.3389/fmars.2022.966304

Comeau, A. J., Lewis, M., Cullen, J., Adams, R. S., Andrea, J., Feener, S., et al. (2007). *Monitoring the spring bloom in an ice covered fjord with the Land/Ocean Biogeochemical Observatory (LOBO)*. Vancouver, BC, Canada: OCEANS 2007, 1–7. doi: 10.1109/OCEANS.2007.4449185

DeAngelo, J., Saenz, B. T., and Arzeno-Soltero, I. B. (2023). Economic and biophysical limits to seaweed farming for climate change mitigation. *Nat. Plants* 9, 45–57. doi: 10.1038/s41477-022-01305-9

Fredriksson, D. W., Dewhurst, T., Drach, A., Beaver, W. M., St. Gelais, A. T., and Johndrow, K. (2020). Hydrodynamic characteristics of a full-scale kelp model for aquaculture applications. *Aquacult. Eng.* 90. doi: 10.1016/j.aquaeng.2020.102086

Fredriksson, D. W., Swift, M. R., Eroshkin, O., Tsukrov, I., Irish, J. D., and Celikkol, B. (2005). Moored fish cage dynamics in waves and currents. Special issue on open ocean aquaculture engineering. *IEEE J. Oceanic Eng.* 30 (1), 28–36. doi: 10.1109/JOE.2004.841412

Fredriksson, D. W., Swift, M. R., Tsukrov, I., Irish, J. D., and Celikkol, B. (2003). Fish cage and mooring system dynamics using physical and numerical models with field measurements. *Aquacult. Eng.* 27 (2), 117–270. doi: 10.1016/S0144-8609(02)00043-2

Fredriksson, D. W., DeCew, J. C., and Tsukrov, I. (2007b). Development of structural modeling techniques for evaluating HDPE plastic net pens used in marine aquaculture. *Ocean Eng.* 34, 2124–2137. doi: 10.1016/j.oceaneng.2007.04.007

Fredriksson, D. W., DeCew, J. C., Tsukrov, I., Swift, M. R., and Irish, J. D. (2007a). Development of large fish farm numerical modeling techniques with in-situ mooring tension comparisons. *Aquacult. Eng.* 36, 137–148. doi: 10.1016/j.aquaeng.2006.10.001

Goda, Y. (2010). *Random seas and design of maritime structures, 3rd edition* (Advanced Series on Ocean Engineering: World Scientific) 33, 732 p. doi: 10.1142/7425

Gosz, M., Kestler, K., Swift, M. R., and Celikkol, B. (1996). Finite element modeling of submerged aquaculture net-pen systems. *Proceedings of the ASME 1997 International Mechanical Engineering Congress and Exposition* (Dallas, Texas, USA: Ocean Engineering), 8–10. doi: 10.1115/IMECE1997-1262

Google Earth (2018). *Ram Island site. 43.4697°N 70.35 °W, Elevation 954M* Data SIO, NOAA, U.S. Navy, NGA, GEBCO. Available at: https://www.google.com/earth/index.html

Google Earth Pro 7.3.6.9345 (2022). *Ram Island site. 43.4697°N 70.35°W, Elevation 5195 m* Data SIO, U.S. Navy, NGA, GEBCO. TetraMetrics 2023

Grebe, G. S., Byron, C. J., Gelais, A. S., Kotowicz, D. M., and Olsond, T. K. (2019). An ecosystem approach to kelp aquaculture in the Americas and Europe. *Aquacult. Rep.* 15, 100215. doi: 10.1016/j.aqrep.2019.100215

Henry, P. T. (2014). Bending properties of a macroalga: adaptation of peirce's cantilever test for *in-situ* measurements of *Laminaria digitate* (Laminariaceae). *Brief Commun. Amer. J. Bot.* 101 (6), 1050–1055. doi: 10.3732/ajb.1400163

Huang, C.-C., and Pan, J.-Y. (2010). Mooring line fatigue: a risk analysis for an SPM cage system. *Aquacult. Eng.* 42, 8–16. doi: 10.1016/j.aquaeng.2009.09.002

Kim, J. K., Kraemer, G. P., and Yarish, C. (2015). Use of sugar kelp aquaculture in Long Island Sounds and the Bronx River Estuary for nutrient extraction. *Mar. Ecol. Prog. Series.* 531, 155–166. doi: 10.3354/meps11331

Kite-Powell, H. L., Ask, E., Augyte, S., Bailey, D., Decker, J., Goudey, C. A., et al. (2022). Estimating production cost for large-scale seaweed farms. *Appl. Phycol.* 3 (1), 435–445. doi: 10.1080/26388081.2022.2111271

Knysh, A., Drach, A., Fredriksson, D., Dewhurst, T., and Tsukrov, I. (2022). Methodology for multidimensional approximation of current velocity fields around offshore aquaculture installations. *Aquacult. Eng.* 99. doi: 10.1016/j.aquaeng.2022.102284

Knysh, A., Tsukrov, I., Chambers, M., Swift, M. R., Sullivan, C., and Drach., A. (2020). Numerical modeling of submerged mussel longlines with protective sleeves. *Aquacult. Eng.* 88. doi: 10.1016/j.aquaeng.2019.102027

Krogstad, H. E. (1988). Maximum likelihood estimation of ocean wave spectra from general arrays of wave gauges. *Model. Ident. Control* 9 (2), 81–97. doi: 10.4173/mic.1988.2.3

Lee, C. W., Kim, Y. B., Lee, G. H., Choe, M. Y., Lee, M. K., and Koo, K. Y. (2008). Dynamic simulation of a fish cage system subjected to currents and waves. *Ocean Eng.* 35 (14-15),1521-1532. doi: 10.1016/j.oceaneng.2008.06.009

Lee, C. W., Lee, J., and Park, S. (2015). Dynamic behavior and deformation analysis of the fish cage system using mass-spring model. *China Ocean Eng* 29, 311-324. doi: 10.1007/s13344-015-0022-2

Li, Y. C., Zhao, Y. P., Gui, F. K., and Teng, B. (2006). Numerical simulation of the hydrodynamic behaviour of submerged plane nets in current. *Ocean Eng.* 33 (17–18), 2352-2368. doi: 10.1016/j.oceaneng.2005.11.013

Martin, T., Tsarau, A., and Bihs, H. (2021). A numerical framework for modelling the dynamics of open ocean aquaculture structures in viscous fluids. *Appl. Ocean. Res.* 106, 102410. doi: 10.1016/j.apor.2020.102410

Masters, G. M., and Ela, W. (2007). *Introduction to environmental engineering and science. 3rd Edn* (Hoboken, NJ: Prentice Hall) 189, 720.

Morison, J. R., Johnson, J. W., O'Brien, M. P., and Schaaf, S. A. (1950). The forces exerted by surface waves on piles. *Petrol. Trans. Am. Inst. Min. Eng.*, 149–157. doi: 10.2118/950149-G

Nguyen, N. G., Thiagarajan, K., and Auger, J. (2019). Integrity assessment of an oyster farm mooring system through *in-situ* measurements and extreme environment modeling. *Ocean. Eng.* 172, 641–659. doi: 10.1016/j.oceaneng.2018.11.023

Pedersen, T., Nylund, S., and Dolle, A. (2002). "Wave height measurements using acoustic surface tracking," in *Oceans '02 MTS/IEEE Conference, 29–31 October 2002* 3, 1747–1754. doi: 10.1109/OCEANS.2002.1191898

Pedersen, T., and Siegel, E. (2008). Wave measurements from a subsurface buoy. *Sea Technol.* 49 (2), 17–20. doi: 10.1109/CCM.2008.4480872

Piconi, P., Veidenheimer, R., and Chase, B. (2020) *Edible seaweed market analysis*. Available at: https://www.islandinstitute.org/edible-seaweed-market-analysis/.

Pribadi, A. B. K., Donatini, L., and Lataire, E. (2019). Numerical modelling of a mussel line system by means of lumped-mass approach. *J. Mar. Sci. Eng.* 7 (9), 309. doi: 10.3390/jmse7090309

Raman-Nair, W., and Colbourne, B. (2003). Dynamics of a mussel longline system. *Aquac. Eng.* 27, 191–212. doi: 10.1016/S0144-8609(02)00083-3

Raman-Nair, W., Colbourne, B., Gagnon, M., and Bergeron, P. (2008). Numerical model of a mussel longline system: coupled dynamics. *Ocean Eng.* 35, 1372–1380. doi: 10.1016/j.oceaneng.2008.05.008

Reite, K.-J., Føre, M., Aarsæther, K. G., Jensen, J., Rundtop, P., Kyllingstad, L. T., et al. (2014). FHSIM – Time Domain Simulation of Marine Systems. *Proceedings of the ASME 2014 33rd International Conference on Ocean, Offshore and Arctic Engineering* (San Francisco, California, USA: Ocean Engineering), 8A. doi: 10.1115/omae2014-23165

Rominger, J. T., and Nepf, H. M. (2014). Effects of blade flexural rigidity on drag force and mass transfer rates in model blades. *Limnol. Oceanogr.* 59 (6), 2028–2014. doi: 10.4319/lo.2014.59.6.2028

Stevens, C., Plew, D., Hartstein, N., and Fredriksson, D. W. (2008). The physics of open-water shellfish aquaculture. *Aquacult. Eng.* 38 (3), 145–160. doi: 10.1016/j.aquaeng.2008.01.006

Stevens, C., Plew, D., Smith, M. R., and Fredriksson, D. W. (2007). Hydrodynamic forcing of long-line mussel farms. *J. Waterway Port Coast. Ocean Eng.* 133 (3), 192–199. doi: 10.1061/(ASCE)0733-950X(2007)133:3(192)

St-Gelais, A. T., Fredriksson, D. W., Dewhurst, T., Miller-Hope, Z. S., Barry Costa-Pierce, B.-A., and Johndrow, K. (2022). Engineering a low-cost kelp aquaculture system for community-scale seaweed farming at nearshore exposed sites *via* user-focused design process. *Front. Sustain. Food Syst.* 6. doi: 10.3389/fsufs.2022.848035

Tsarau, A., and Kristiansen, D. (2019). Application of FhSim for the analysis of environmental loads on a complete fish-farm system. *MARINE VIII : Proceedings of the VIII International Conference on Computational Methods in Marine Engineering* (CIMNE) 2019, 271–284.

Tsukrov, I., Eroshkin, O., Fredriksson, D. W., Swift, M. R., and Celikkol, B. (2003). Finite element modeling of net panels using consistent net element. *Ocean Eng.* 30, 251–270. doi: 10.1016/S0029-8018(02)00021-5

Vettori, D., and Nikora, V. (2017). Morphological and mechanical properties of blades of *Saccharina latissima. Estuar. Coast. Shelf Sci.* 196, 1–9. doi: 10.1016/j.ecss.2017.06.033

Zhao, Y. P., Li, Y. C., Dong, G. H., Gui, F. K., and Teng, B. (2007). A numerical study on dynamic properties of the gravity cage in combined wave-current flow. *Ocean Eng.* 34 (17–18), 2350-2363. doi: 10.1016/j.oceaneng.2007.05.003

Zhao, Y. P., Wang, X. X., Decew, J., Tsukrov, I., Bai, X. D., and Bi, C. W. (2015). Comparative study of two approaches to model the offshore fish cages. *China Ocean Eng.* 29, 459–472. doi: 10.1007/s13344-015-0032-0

Zou, Q., and Xie, D. (2016). *Tide-surge and wave interaction in the gulf of Maine during an extratropical storm* Vol. 66 (Heidelberg: Ocean Dynamics), 1715–1732. doi: 10.1007/s10236-016-1002-7

Frontiers in Marine Science

TYPE Original Research
PUBLISHED 21 June 2023
DOI 10.3389/fmars.2023.1185898

EDITED BY
Edgar Mendoza,
National Autonomous University
of Mexico, Mexico

REVIEWED BY
Hung-Jie Tang,
National Cheng Kung University, Taiwan
Chuanxin Qin,
Chinese Academy of Fishery Sciences
(CAFS), China

*CORRESPONDENCE
Jiao Li
lijiao@ysfri.ac.cn

RECEIVED 14 March 2023
ACCEPTED 06 June 2023
PUBLISHED 21 June 2023

CITATION
Gong P, Li J, Wang G, Guan C, Meng Z and Jia Y (2023) Influence of reef structure and its flow field effect on the spatial behavior of *Sebastes schlegelii* adults.
Front. Mar. Sci. 10:1185898.
doi: 10.3389/fmars.2023.1185898

Influence of reef structure and its flow field effect on the spatial behavior of *Sebastes schlegelii* adults

Pihai Gong[1,2], Jiao Li[1,2]*, Gang Wang[1,2], Changtao Guan[1,2], Zhen Meng[1,2] and Yudong Jia[1,2]

[1]Yellow Sea Fisheries Research Institute, Chinese Academy of Fishery Sciences, Key Laboratory of Sustainable Development of Marine Fisheries, Qingdao, China, [2]Laboratory for Marine Fisheries Science and Food Production Process, Pilot National Laboratory for Marine Science and Technology, Qingdao, China

Sebases schlegelii is an important economic reef fish in northern China. Its distribution in the reef area is affected by the reef structure and flow field. To evaluate the effects of differently shaped artificial reefs with distinct flow field properties on the distribution of adult *S. schlegelii*, four types of artificial reefs (cubic (CAR), pyramidal (PAR), star-shaped (SAR) and tubular (TAR) artificial reef) and the related flow regimes were experimentally examined. The mean gathering rate (MGR) and wavelet analysis were adopted to analyze the distribution patterns of *S. schlegelii* adults around reef bodies in three representative environmental conditions (static water (FE1), 40 Hz water flow environment (FE2), and 50 Hz water flow environment (FE3)). The significant gathering behaviors around the artificial reefs were depicted through the MGR of adult fish during physical observations. For FE1, the MGR of adult fish showed a decrease in the order PAR > CAR > SAR > TAR. With increasing incoming velocities, the MGR changed such that the quantity of adult fish in the CAR gradually increased more than that in the PAR, but no significant differences were observed between them ($P>0.05$). Wavelet analysis showed that the fluctuations in the gathering behaviors of adults decreased with increasing flow velocities. Based on the two-factor analysis of variance, the reef structural characteristics had a more significant impact than the flow velocities on the gathering behavior of adult fish. In summary, the PAR and CAR are recommended to restore the habitats of *S. schlegelii* in marine ranches given their dominant aggregation effects on *S. schlegelii*.

KEYWORDS

flow field environment, artificial reef, Sebastes schlegelii, adult fish, behavioral response, habitat selection

1 Introduction

Marine life habitats have been destroyed by the negative effects of anthropogenic pressures, such as pollutant emissions and overfishing, leading to massive declines in natural fisheries (Wilson et al., 2010). Fish are the single most important source of high-quality protein for humans, providing 16% of the animal protein consumed by the world's population (Tidwell and Allan, 2001). Therefore, marine habitat restoration is receiving increasing attention. Artificial reefs are widely used in the United States, Australia, Europe and Asia and are regarded as effective measures for marine habitat restoration and fishery resource conservation (Lima et al., 2019). Differently shaped artificial reefs released into the sea can provide shelter, refuge and additional ecosystem services for organisms in open environments and have been shown to be of great value to many fish and invertebrate species (Komyakova et al, 2013; Lima et al., 2019). Recent studies have shown that artificial reefs can create productive habitats in certain systems (Claisse et al., 2014; Layman et al., 2016; Smith et al., 2016). They can be effective at adding fish rather than just attracting nearby fish from rocky reefs (Folpp et al., 2020). However, Baine (2001) reports that only approximately 50% of studies have found evidence of successful outcomes after deployment of artificial reefs. This may be related to the coverage area of artificial reefs and the complexity of artificial reef structures (Lemoine et al., 2019). Studies have shown that artificial reefs have a larger number of sheltering holes and more abundance and diversity of fish (Hixon and Beets, 1989; Hackradt et al., 2011). The design of artificial reefs has a significant impact on their effectiveness (Vivier et al., 2021). Fully understanding the influence of artificial reef structure on the behavioral distribution of fish can help improve artificial reef design and marine ranch construction.

To design artificial reef structures that can provide better habitats for fish, extensive research has been conducted on flow field effects (Zheng et al., 2015; Jiao et al., 2017; Ma et al., 2022). The materials (Brown, 2005; Sempere-Valverde et al., 2018), shapes (Vivier et al., 2021) and distances (Froehlich et al., 2021) of artificial reefs have also been investigated aiming to improve their ecological effects. Fish behavior is a direct response to the environment (Martins et al., 2012), and by observing fish distribution around artificial reefs, understanding the positive and negative behaviors of fish in reef selection can help develop better artificial reef design and conservation strategies. Underwater camera observation is a common method to study the biological benefits of reefs, as it allows to collect data over long time scales while avoiding human disturbance factors. It is useful for collecting valuable information regarding the distribution, relative abundance, and species–habitat associations of various fish species (Easton et al., 2015). Parsons et al. (2016) used drop cameras to study the effects of temperate rocky reef habitats on fish abundance and species composition. Li et al. (2021) studied the effects of artificial reefs and the flow field environment on the habitat selection behavior of juvenile scorpionfish *Sebastes schlegelii* with an underwater camera system, and the results showed that there were significant differences in fish aggregation around different reef structures.

Sebastes schlegelii is an economically important rocky reef fish that is mainly distributed in China, Japan and the eastern and western coasts of the Korean Peninsula (Xi et al., 2017). artificial reefs have considerable effects on the aggregation of rocky reef fishes (Folpp et al., 2020). Adult *S. schlegelii* are sexually mature individuals in the population, with reproductive functions. In industrial fishing, a large number of adult fish will be caught, resulting in a sharp decrease in their numbers in the population. Stock enhancement is an effective way to protect fish biodiversity. In China, millions of juvenile fish are released every year to restore and increase the population. Releasing populations will cause a series of negative effects on wild populations (Lorenzen et al., 2010), which is not conducive to the sustainable development of fisheries. A comprehensive understanding of the influence of reef structure on the spatial behavior of *S. schlegelii* will indeed maximize the positive consequence of the conservation of *S. schlegelii.*

The goal of our study was to determine the attraction of artificial reefs with different structures to adult *S. schlegelii* and the influence of flow field environment on this attraction. This was achieved by placing artificial reefs with different structures in indoor deep concrete pools that can create different flow field environments and using underwater cameras to observe the distribution of adult *S. schlegelii*. These observed data were used to calculate the mean gathering rate and perform wavelet analysis. Furthermore, two-way ANOVA was used to analyze the influence of reef structure and flow field environment on *S. schlegelii* distribution. Our results may contribute to the design of artificial reefs for the conservation of specific fishes and the selection of reef types for marine ranch construction.

2 Materials and methods

2.1 Fish materials

Adults *S. schlegelii* were obtained from a local commercial aquaculture farm and kept in a holding tank for 48 h. After temporary rearing, 48 adult fish with no apparent deformities or injuries and strong constitution were selected for the experiment. The average body length was 30 ± 0.5 cm, and the average weight was 565 ± 28 g. To reduce the influence of the external environment on fish behavior, no oxygenation and no baiting were used during the experiment or resting period.

2.2 Experimental artificial reefs

In this experiment, four types of reefs were selected according to their structures from the commonly used reef types in the construction of marine ranches in China. They were cube-shaped artificial reef (CAR), pyramid-shaped artificial reef (PAR), star-shaped artificial reef (SAR) and tube-shaped artificial reef (TAR). The outer dimensions of the CAR was 50 cm×50 cm×50 cm (length×width×height), and the diameter of the surface hole was 30 cm (Figure 1A). The outer dimensions of the PAR was 63 cm×63 cm×58 cm (length×width×height), and the height of the pyramid

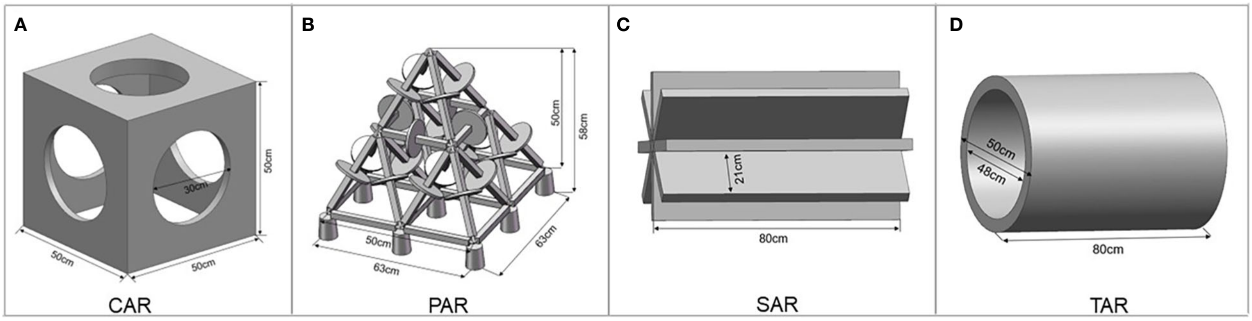

FIGURE 1
Detailed parameters for the artificial reef models tested in this study. **(A)** The cube-shaped artificial reef; **(B)** The pyramid-shaped artificial reef; **(C)** The star-shaped artificial reef; **(D)** The tube-shaped artificial reef.

structure was 50 cm (Figure 1B). The SAR had a height of 50 cm and a blade width of 21 cm (Figure 1C). The TAR was 50 cm in length and 50 cm in diameter (Figure 1D).

2.3 Experimental pool

The experiment was carried out in a disinfected indoor concrete pool. The pool size was 7 m×7 m×2 m (length×width×height), and the experimental depth was 1.2 m (Figure 2). To facilitate observation, the bottom of the pool was painted blue with environmentally friendly aquaculture paint. To facilitate statistics, the pool was divided into 196 square areas with environmentally friendly red aquaculture paint, where the side of each square area was 0.5 m, and each area was numbered as shown in Figure 2. Four submersible pumps for flow generation were installed at the bottom corners of the square pool (1-1,1-E, E-1 and E-E). The four reef placement positions are shown in Figure 2. Four floodlights were placed in the upper corner of the pool for illumination during observation. A panoramic camera was mounted on the roof beam approximately 2 m above the experimental pool, and 8 color underwater cameras were fixed near the reef fish in the pool. The video signal acquisition system comprised the camera, a router and a computer, which could monitor and record the behavior and distribution of experimental fish in the pool without interference (Figure 2).

2.4 Experimental environment parameters

2.4.1 Flow field environment design

Four submersible pumps were used to create a flow field by adjusting the electric control system outside the pool to control the flow of seawater and then adjusting the different flow rates of seawater. Three types of flow field environment were tested in the experiment. When the working frequency of the submersible pump was 0 Hz, the hydrostatic environment was named FE1; when the working frequency of the submersible pump was 40 Hz, the flow field environment was named FE2; and when the working frequency of the submersible pump was 50 Hz, the higher flow

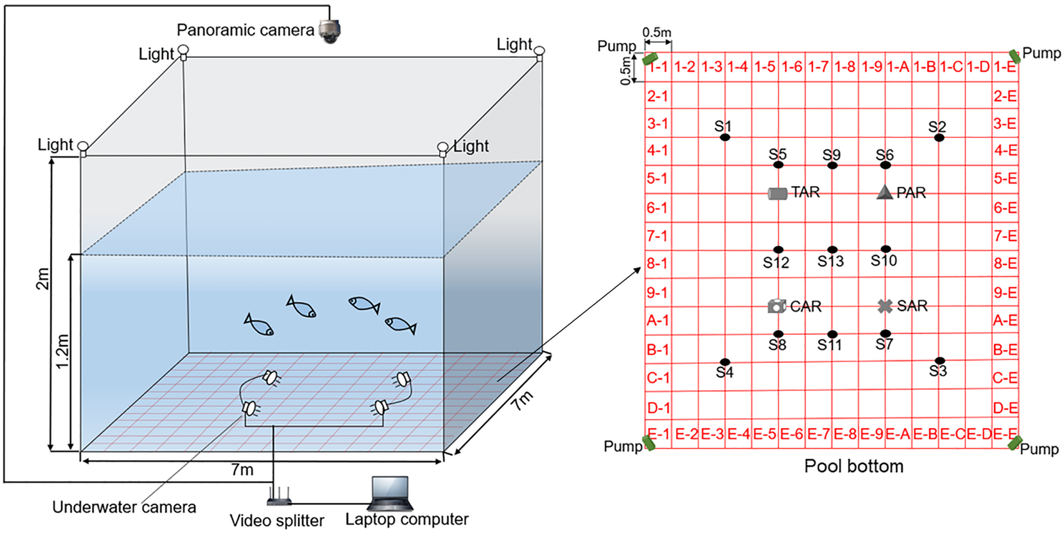

FIGURE 2
Schematic diagram showing the experimental pool, where the shaded part is the experimental area.

field environment was named FE3. Before the experiment, 14 key points were measured by an electromagnetic current meter. The S1–S13 velocity measuring points are shown in Figure 2, and key point S14 was located inside the CAR reef.

2.4.2 Water environment parameters

Before the experiment, we used a multiparameter water quality detector to measure the water environment parameters. The measured results are temperature=11°C, dissolved oxygen=8.04 mg/L, pH=7.02 and salinity=31.83‰.

2.5 Video data acquisition

Throughout the experiment, there was no feeding, oxygenation or natural light to avoid interfering with the behavior of the fish. During the experiment, four lamps with a power of 15 W were used for lighting. The experiment was divided into three experimental conditions according to different flow field environments, namely, FE1, FE2 and FE3. The observation time of each experiment was from 8:00 in the morning to 18:00 in the evening. Continuous video signals were collected throughout the experiment, and photos were taken every 10 min.

2.6 Data processing and statistical analysis

2.6.1 Mean gathering rate (MGR)

The MGR refers to the ratio between the quantity of scorpionfish gathered around a reef at a fixed time point in the experiment and the total quantity of scorpionfish in the experiment: (Li et al., 2021)

$$MGR = \frac{\sum_{i=1}^{n} M_i}{nM} \times 100\,\% \qquad (1)$$

where Mi is the quantity of fish aggregated at a fixed time point in hour i, M is the total quantity of *S. schlegelii* adults in the experiment, and n is the number of adult fish recorded.

2.6.2 Python wavelet analysis

In this study, python wavelet analysis was used to analyze the fluctuation in the quantity of adult fish attracted to the artificial reef at different times and obtain the wavelet power spectrum (Qin et al., 2016; Li et al., 2021).

2.6.3 Statistical analysis

All statistical analyses were performed using SPSS 20.0 for Windows. One-way analysis of variance (ANOVA) was used to distinguish significant differences among different structures and flow field environments, and differences were considered statistically significant at P<0.05. Two-way ANOVA was used to evaluate reef structure and flow field environment, which were the key environmental factors affecting habitat selection of adult *S. schlegelii*, and extremely significant factors were considered statistically significant at P<0.001.

3 Results

3.1 Behavior description of *S. schlegelii* adults around artificial reefs

According to the video observations, under the static water environment (FE1), adult fish swam quickly to the wall after being placed in the experimental pool. At this time, no adult fish entered the reef area, and they are all distributed near the wall and in the dark area. After 8 min, a few adult fish tentatively swam around the reef. After approximately 1 h of adaptation, the adult fish around the reef were frequently active, and most of the adult fish freely shuttled around the four types of reefs (Figure 3A). After 2 h, most of the adults began to swim freely in the boundary area between the four reefs and the pool and chased each other (Figure 3B). At the same time, the quantity of adults in the interior of the reef and the shaded area gradually tended to be stable.

In the flow field environments FE2 and FE3, due to the influence of the flow generating equipment and flow field, the adult fish showed a significant stress response when the flow generating equipment was started, swimming rapidly from the pool wall to the vicinity of the reef and gathering in large numbers in the middle blank area enclosed by the four reefs (Figure 3C). After 1 h of adaptation, some adult fish began to frequently move around the four reefs and near the pool wall.

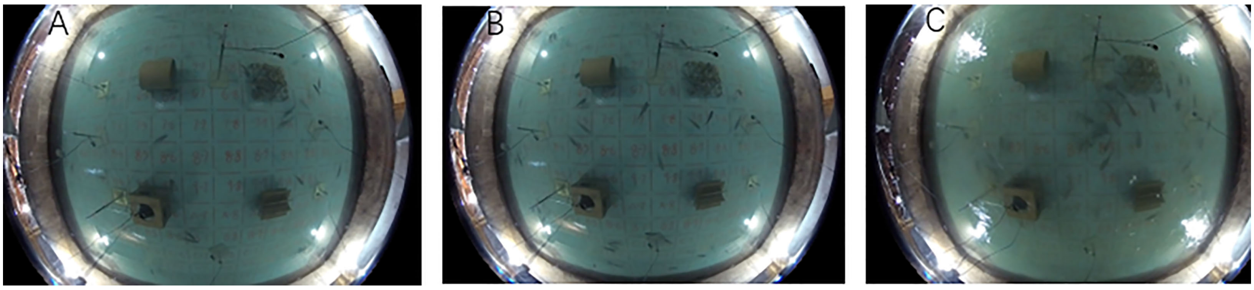

FIGURE 3
Fish behavior captured by panoramic camera in experimental pool. **(A)** The state of the fish after 1h in the experimental pool under FE1; **(B)** The state of the fish after 2h in the experimental pool under FE1; **(C)** The fish gather in the middle blank area enclosed by the four reefs under FE3.

3.2 Differences in the gathering behaviors of *S. schlegelii*

According to one-way ANOVA, in the static water environment (FE1), the MGR of adult *S. schlegelii* showed a decreasing trend in the order PAR (MGR=38.31 ± 6.02%) > CAR (MGR=35.03 ± 6.66%) > SAR (MGR=15.14 ± 4.60%) > TAR (MGR=11.52 ± 4.68%). Under the FE2 condition, the MGR showed the same trend as FE1. The MGR in the PAR was the highest at 42.53 ± 6.86% and it was the lowest in the SAR at 11.54 ± 5.35%. There was a significant difference between the MGR of adult fish of the PAR and CAR (P<0.05), while the MGR was not significantly different between the TAR and SAR (P>0.05). In the FE3 flow environment, there was no significant difference in MGR between the PAR and CAR (P>0.05), and there was a significant difference in MGR between the TAR and SAR (P<0.05). The MGRs of reefs with the same structure in the three different flow environments were also different (Figure 4). While the PAR showed no significant difference in MGR among the three flow environments (P>0.05), there were significant differences in MGR in the other three reef types between the standing water and flowing water environments (P<0.05). This indicates that the PAR has a significant advantage in attracting adult fish and has the strongest stability, while the attraction degree of the other reefs to adult fish is greatly affected by the flow field environment.

By comparing the MGR of adult fish inside and outside the four types of reefs, it was found that the aggregation of adult fish inside and outside the reefs was different in the three types of flow field environments. In the static water environment (FE1), there were significant differences in the MGR of adult fish in and out of all reefs except the CAR (P<0.05). The MGR outside the PAR was higher than that inside the PAR, while the opposite was true for the TAR and SAR. Compared with the static water environment (FE1), in the flow environments (FE2 and FE3), the MGR inside the CAR gradually decreased and that outside of it gradually increased, while the MGR inside the PAR increased significantly and that outside of it decreased. The MGRs of the adult fish inside and outside the reefs were significantly different (P<0.05). The MGRs inside the TAR and SAR decreased significantly, but there was no significant difference in the distribution of adult fish in and out of the TAR and SAR in FE3 (P>0.05). Overall, as the flow rate increased, the adults tended to cluster outside the CAR and inside the PAR (Figure 5).

3.3 Wavelet analysis of adult fish aggregation

The amount of aggregation of *S. schlegelii* adults in different reef structures was analyzed by wavelet analysis, and the variation characteristics of aggregation were studied (Figure 6). The results of the wavelet analysis show that in FE1, the number of adult fish in the CAR had three significant periods, from 8:00 to 12:00, 12:00 to 14:00 and 16:00 to 18:00. At 12:00, the continuity of the small wave spectrum was the strongest and fluctuated greatly. During 16:00~18:00, the continuity of the small wave spectrum was poor; that is, the number of adult fish changed little and tended to be stable during this period. The population of adults around the PAR showed the strongest continuity at 12:00, and the population of adult fish changed significantly. From 14:00 to 18:00, the continuity of the small wave spectrum was the worst; that is, the distribution of adult fish in the reef area fluctuated the least. In the TAR, the continuity of the wavelet spectrum was relatively strong at 12:00, and it was poor at the rest time, so the stability of adult fish aggregation was the strongest throughout the day. The continuity of the SAR wavelet spectrum was weak throughout the day, and the population of adult fish changed most stably during 8:00~10:00 and 14:00~18:00. In FE2, the CAR had the strongest wavelet continuity at 14:00. The PAR had poor continuity of the wavelet spectrum throughout the day. The TAR had the worst spectral continuity throughout the day, with little change. In FE3, the spectral continuity of the CAR was strong and fluctuated significantly from 14:00 to 16:00, and it was the worst from 12:00 to 14:00; that is, the population of adult fish fluctuated the least during this

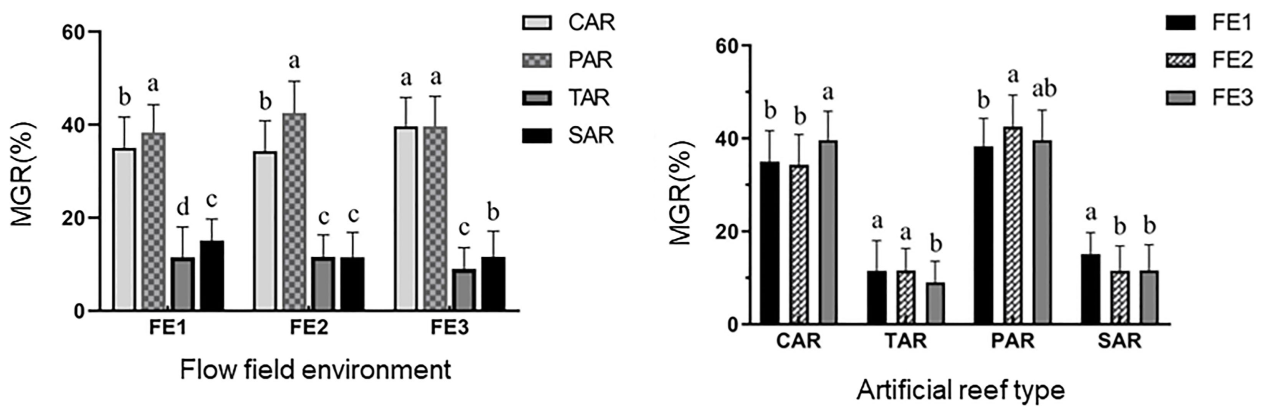

FIGURE 4
Significant difference analysis of *Sebastes schlegelii* adults attracted by four different ARs under the same flow field environment. *Different letters (a, b, c & ab) over the bar for the same reef type indicate significant differences among flow field environments (P<0.05).

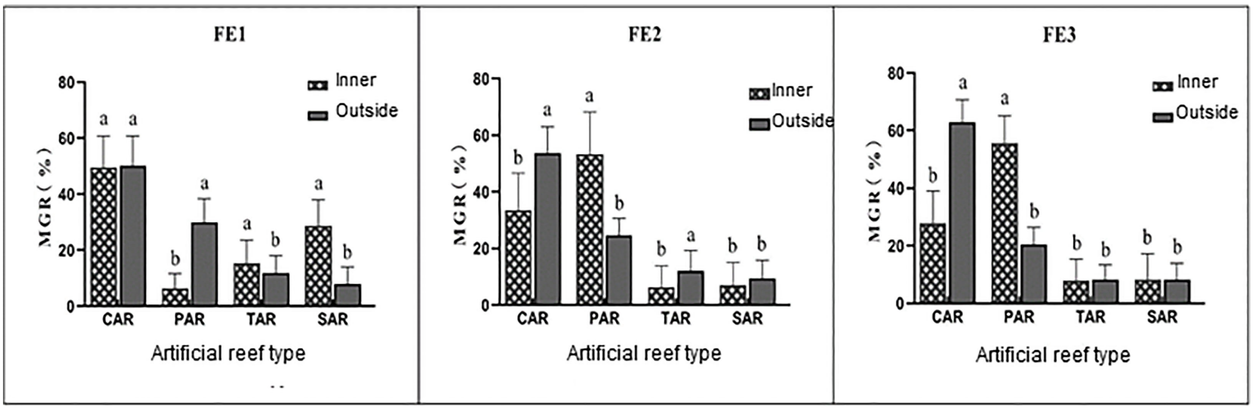

FIGURE 5
Comparison of differences in the distribution of *Sebastes schlegelii* adults inside and outside the reefs. *Different letters (a, b, c & ab) over the bars for the same reef type indicate significant differences in the mean gathering rate (MGR) inside and outside the reef (P<0.05).

period. In the PAR, the spectrum continuity was good during 14:00~16:00, that is, the fluctuation was relatively large. The distribution of adult fish in the TAR was the least and the most stable. The continuity of the SAR wavelet spectrum was strong during 12:00~16:00. The wavelet spectrum analysis showed that the continuity of the adult fish spectrum in different reef areas in the flow field environment was weaker than that in the standing water environment, and the aggregation of adult fish was more stable compared to the standing water environment.

3.4 Effect of the flow field and reef structure on the aggregation of adult fish

The effects of reef structure and flow field environment on the attraction of *S. schlegelii* adults were studied by two-factor ANOVA (Table 1). The effects of the reef structure and flow field environment factors and their interaction were all extremely significant (P<0.001). These results indicate that the two factors have significant effects on the MGR of *S. schlegelii* adults, and the

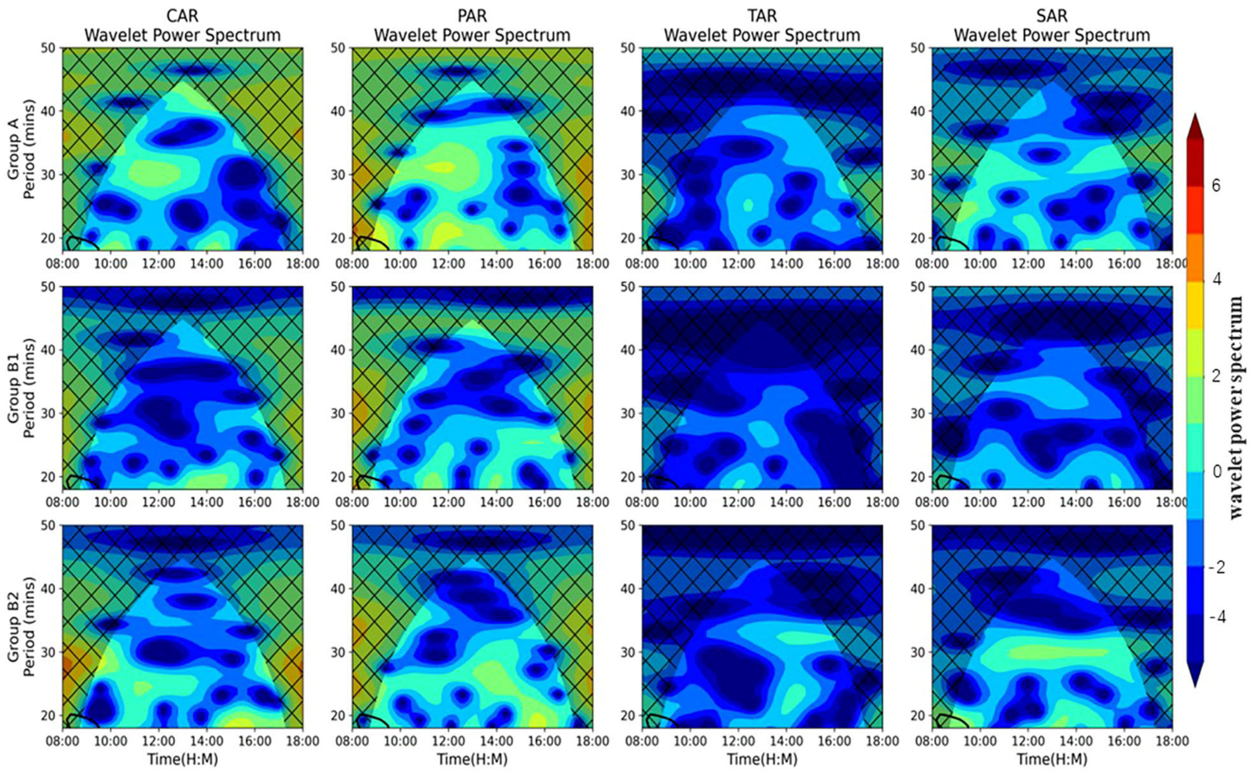

FIGURE 6
Time-frequency and frequency-domain change periods in the quantity of *Sebastes schlegelii* adults in different artificial reefs *: The conical range represents the effective value; the closed region of the black solid line is the power spectrum value tested by the standard background spectrum with 95% confidence; the color bar on the right represents the wavelet power spectrum; the larger the value, the stronger the continuity of the wavelet spectrum.

reef structure had a stronger effect than the flow field environment, indicating that reef structure has the strongest effect on the aggregation of *S. schlegelii* adults.

4 Discussion

The main results of this study show that (1) all four types of artificial reef can attract *S. schlegelii* adults, but there are significant differences in their effects. The PAR and CAR, with relatively complex structures and more holes, have stronger attracting effects on fish, while the SAR and TAR, with relatively simple structures and fewer holes, have poor attracting effects. (2) The flow field has a significant influence on the fish-attracting effect of the four reef types. The MGR trend of the four reef types in the standing water environment (FE1) was PAR > CAR > SAR > TAR. The MGRs of the CAR and PAR increased, while the MGRs of the SAR and TAR decreased with increasing incoming flow velocity. Affected by the flow field, the adult fish aggregated around the SAR and TAR were driven to the PAR and CAR. (3) The flow field also has a significant effect on the MGRs inside and outside of the reefs. In FE1, there was no significant difference in the MGRs inside and outside of the CAR, and the MGR outside of the PAR was higher than that inside of it. Due to the influence of the flow field, the MGR inside of the CAR decreased and that outside increased, while the PAR showed the opposite trend, that is, the MGR inside increased while that outside MGR decreased. (4) In contrast with the SAR and TAR, the quantity of adult fish in the PAR and CAR showed higher wavelet spectrum continuity and more considerable fluctuations, and their diurnal variation trend was higher. Wavelet analysis showed that the fluctuations in the gathering behaviors of adults decreased with increasing flow velocities. (5) Based on the two-factor ANOVA, reef structure and flow field environment have significant effects on the MGR, and the reef structure had a more significant impact than the flow field environment on the gathering behavior of adult fish. Since fish behavior around artificial reefs can be affected by dissolved oxygen levels, light conditions, unsuitable temperatures, forced proximity to humans and feeding opportunities (Martins et al., 2012), to ensure the reliability of our results, we did not provide food, oxygenation, or natural light throughout the experiment to avoid disturbing fish behavior.

Countershading refers to a type of body color with a dark back and light belly, which can prevent biological detection by predators or bait to achieve camouflage and stealth (Ruxton et al., 2004). *Sebastes schlegelii* have a blackish brown back, irregular dark black patches and a grayish white belly. This coloration is conducive to enemy avoidance and feeding. Through video observation, we noticed an interesting phenomenon in which *S. schlegelii* adults were mainly distributed at the bottom of the PAR, inside and outside of the CAR and SAR, and inside and on both sides of the TAR, which are all shaded areas, because the shadows match the body color, allowing them to hide. Many marine organisms exhibit behaviors in which they actively select backgrounds that match their species, morphology, or individual horizontal appearance (Ryer et al., 2008; Stevens and Merilaita, 2009; Morgans and Ord, 2013), and some even change their body color and brightness to quickly match the background (Johnsen et al., 2004; Smithers et al., 2018). *Sebastes schlegelii* cannot quickly change its color to match the background environment (Leclercq et al., 2010), so it can only achieve shading by actively selecting the shaded area, which is more conducive to hiding. In the experiment, we also found that *S. schlegelii* moved rapidly to the shaded area of the pool wall when transferred to the experimental pool. This behavior is also observed in juvenile fish (Li et al., 2021). Therefore, the shaded area is an important factor affecting the distribution behavior of *S. schlegelii*. Both juvenile (Li et al., 2021) and adult *S. schlegelii* exhibit background matching behavior, and appropriate shading and material color should be considered in reef design.

All four reef types had aggregation effects on adult and juvenile *S. Schlegelii* (Table 2), but the aggregation effects are quite different in standing water environments. The PAR had the best aggregation effect on adults but a poor aggregation effect on juveniles, while the CAR had a good aggregation effect on both adults and juveniles. This is related to the area of the artificial reef, the number of holes, the size of the holes and fish living habits. Species richness and H' diversity are higher in large-area artificial reefs, and the number of holes is the most important factor for reef fish (Hackradt et al., 2011). In addition, the size of the hole is related to the shelter effect provided, and relatively large holes are less effective in protecting small fish from predators (Jordan et al, 2005). Juvenile scorpionfish tend to be social, large in number and occupy a large space, while adult scorpionfish tend to be solitary, but the individuals are large, so the CAR, with a good shelter effect and large internal holes, had a good aggregation effect on both juvenile and adult scorpionfish. Compared with the other reefs, the PAR has more holes but less space, which is not conducive to the movement of young fish but can provide a individual shelter for adult fish. Although the TAR also has large holes, it had a poor aggregate effect on adults and juveniles (Table 2) because its holes are a straight-through structure with easy penetration, which is not conducive to hiding and shading *S. schlegelii*. Moreover, *S. schlegelii* will mark their territories and attack other fish entering their field of view (Xu et al., 2021). Visual barriers provided by artificial reefs can reduce aggressive behavior (Zhang et al., 2023). A simple structure such as the TAR cannot provide visual shelter, while a complex structure such as the PAR can provide more shelter space. *Sebastes schlegelii* adults preferred this structure, which is relatively enclosed and has enough room to fit their bodies.

Water flow will affect the distribution of fish around artificial reefs by increasing their swimming energy consumption and feeding patterns (Clarke et al., 2009). The biological responses of fish to water flow and turbulence are species-specific (Wang et al., 2021). This is related to the size, swimming ability and swimming pattern of the fish (Finelli et al., 2009). Bottom-dwelling fish will move closer to the sidewall to reduce energy costs when velocity increases (Wiegleb et al., 2020). In this study, increased flow rates were found to drive adults aggregating in the SAR and TAR to the PAR and CAR. This is due to the low flow rate around the PAR and CAR (Table 3), which is conducive to lower swimming energy

TABLE 1 Analysis results of the influence of flow field environment and reef structure on MGR of *S. schlegelii* adults.

Factor	Degree of freedom	Quadratic sum	F	P
Flow field environment	2	1851.64	191.53	2.00×10^{-67}
Reef structure	3	13250.89	913.79	6.17×10^{-245}
Flow field environment & Reef structure	6	359.58	12.39	2.56×10^{-13}

expenditure. The current not only affects the MGR of adult fish among reef types but also has a significant effect on the MGR inside and outside the reefs. Upwelling and eddies will occur outside the CAR (Ma et al., 2022), and the flow field characteristics inside the PAR are more complex due to the presence of disks. It is possible that the flow field characteristics in these ARs are more conducive to attracting *S. schlegelii* adults. Although studies have shown that the wake regions generated by artificial reefs may have a positive impact on fish aggregation (Song et al., 2022). However, it is necessary to further study which flow field characteristics are more favorable to *S. schlegelii*. Some studies have found that fish reefs with complex structures are more attractive to fish aggregation (Lemoine et al., 2019), which is consistent with our research results. The PAR and CAR, with relatively complex structures, showed better aggregation effects on *S. schlegelii*. This may be because reefs with complex structures can provide more holes and habitat space and have more complex flow field environment.

In conclusion, there are differences in reef type selection between juvenile and adult *S. schlegelii*, but the PAR and CAR have good aggregation effects and flow field environment, which makes them suitable for placing in northern coastal areas of China. The shaded area, number and size of holes, flow field environment

TABLE 2 Average MGR of *Sebastes schlegelii* adults and juveniles (Li et al, 2021) in different reef areas under three flow rates.

Artificial reef	FE1		FE2		FE3	
	Adult	Juvenile	Adult	Juvenile	Adult	Juvenile
PAR	38.31 ± 6.02	18.48 ± 3.24	42.53 ± 6.86	33.38 ± 5.76	39.60 ± 6.52	34.61 ± 4.67
CAR	35.03 ± 6.66	47.54 ± 5.68	34.31 ± 6.58	46.64 ± 7.67	39.69 ± 6.20	47.45 ± 4.72
SAR	15.14 ± 4.60	19.47 ± 3.94	11.54 ± 5.35	13.54 ± 7.71	11.57 ± 5.56	11.83 ± 3.14
TAR	11.52 ± 4.68	14.51 ± 3.86	11.62 ± 4.96	6.44 ± 2.69	8.96 ± 4.61	6.11 ± 2.46

TABLE 3 Average velocities at key points in the experimental pool under different flow field rates.

Point	Velocity of no reef (m/s)			Velocity of reef placement (m/s)		
	FE1	FE2	FE3	FE1	FE2	FE3
S1	0.00	0.51	0.53	0.00	0.43	0.50
S2	0.00	0.30	0.31	0.00	0.10	0.12
S3	0.00	0.45	0.51	0.00	0.42	0.46
S4	0.00	0.25	0.32	0.00	0.12	0.18
S5	0.00	0.37	0.38	0.00	0.35	0.37
S6	0.00	0.20	0.26	0.00	0.11	0.13
S7	0.00	0.29	0.34	0.00	0.21	0.25
S8	0.00	0.21	0.26	0.00	0.09	0.11
S9	0.00	0.19	0.25	0.00	0.06	0.17
S10	0.00	0.23	0.24	0.00	0.14	0.15
S11	0.00	0.22	0.23	0.00	0.15	0.20
S12	0.00	0.19	0.22	0.00	0.08	0.10
S13	0.00	0.13	0.15	0.00	0.06	0.08
S14	0.00	0.20	0.23	0.00	0.09	0.10

and complexity of the artificial reef structure are important factors determining the distribution of *S. schlegelii*, which should be taken into account in the design of reefs. The results of our study can provide guidance for managers and conservation planners for reef type selection when installing artificial reefs to restore natural habitats and protect reef fish.

Data availability statement

The raw data supporting the conclusions of this article will be made available by the authors, without undue reservation.

Ethics statement

The animal study was reviewed and approved by Institutional Animal Care and Use Committee of the Yellow Sea Fisheries Research Institute (Qingdao, China).

Author contributions

PG participated in the experimental design, data processing and manuscript writing. JL participated in the experimental design, project administration and funding acquisition. GW and CG contributed to subsequent revisions. ZM and YJ contributed to the experiment and data analysis. All authors contributed to the article and approved the submitted version.

Funding

This study is supported by the National Natural Science Foundation of China (32002442) and the National Key R&D Program (2019YFD0902101).

Conflict of interest

The authors declare that the study was conducted in the absence of any commercial or financial relationships that could be construed as a potential conflict of interest.

Publisher's note

References

Baine, M. (2001). Artificial reefs: a review of their design, application, management and performance. *Ocean Coast. Manage.* 44 (3-4), 241–259. doi: 10.1016/s0964-5691(01)00048-5

Brown, C. J. (2005). Epifaunal colonization of the loch linnhe artificial reef: influence of substratum on epifaunal assemblage structure. *Biofouling* 21 (2), 73–85. doi: 10.1080/08927010512331344197

Claisse, J.T., Pondella, D.J., II, Love, M., Zahn, L.A., Williams,, C.M., et al. (2014). Oil platforms off California are among the most productive marine fish habitats globallyle. *Proc. Natl. Acad. Sci. USA* 111(43), 15462-15467. doi: 10.1073/pnas.1411477111

Clarke, R. D., Finelli, C. M., and Buskey, E. J. (2009). Water flow controls distribution and feeding behavior of two co-occurring coral reef fishes: II. laboratory experiments. *Coral Reefs* 28 (2), 475–488. doi: 10.1007/s00338-009-0479-7

Easton, R. R., Heppell, S. S., and Hannah, R. W. (2015). Quantification of habitat and community relationships among nearshore temperate fishes through analysis of drop camera video. *Mar. Coast. Fisheries* 7 (1), 87–102. doi: 10.1080/19425120.2015.1007184

Finelli, C. M., Clarke, R. D., Robinson, H. E., and Buskey, E. J. (2009). Water flow controls distribution and feeding behavior of two co-occurring coral reef fishes: i. field measurements. *Coral Reefs* 28 (2), 461–473. doi: 10.1007/s00338-009-0481-0

Folpp, H. R., Schilling, H. T., Clark, G. F., Lowry, M. B., Maslen, B., Gregson, M., et al. (2020). Artificial reefs increase fish abundance in habitat-limited estuaries. *J. Appl. Ecol.* 57 (9), 1752–1761. doi: 10.1111/1365-2664.13666

Froehlich, C. Y. M., Garcia, A., Cintra-Buenrostro, C. E., Hicks, D. W., and Kline, R. J. (2021). Structural differences alter residency and depth activity of red snapper (Lutjanus campechanus) at two artificial reefs. *Fisheries Res.* 242, 106043. doi: 10.1016/j.fishres.2021.106043

Hackradt, C. W., Felix-Hackradt, F. C., and Garcia-Charton, J. A. (2011). Influence of habitat structure on fish assemblage of an artificial reef in southern Brazil. *Mar. Environ. Res.* 72 (5), 235–247. doi: 10.1016/j.marenvres.2011.09.006

Hixon,, M. A., and Beets,, J. P. (1989). Shelter characteristics and Caribbean fish assemblages: experiments with artificial reefs. *Bull. Mar. Sci.* 44(2), 666-680.

Jiao, L., Yan-Xuan, Z., Pi-Hai, G., and Chang-Tao, G. (2017). Numerical simulation and PIV experimental study of the effect of flow fields around tube artificial reefs. *Ocean Eng.* 134, 96–104. doi: 10.1016/j.oceaneng.2017.02.016

Johnsen, S., Widder, E. A., and Mobley, C. D. (2004). Propagation and perception of bioluminescence: factors affecting counterillumination as a cryptic strategy. *Biol. Bull.* 207 (1), 1–16. doi: 10.2307/1543624

Jordan, L. K. B., Gilliam, D. S., and Spieler, R. E. (2005). Reef fish assemblage structure affected by small-scale spacing and size variations of artificial patch reefs. *J. Exp. Mar. Biol. Ecol.* 326 (2), 170–186. doi: 10.1016/j.jembe.2005.05.023

Komyakova, V., Munday, P. L., and Jones, G. P. (2013). Relative importance of coral cover, habitat complexity and diversity in determining the structure of reef fish communities. *PloS One* 8 (12), e83178. doi: 10.1371/journal.pone.0083178

Layman, C. A., Allgeier, J. E., and Montaña, C. G. (2016). Mechanistic evidence of enhanced production on artificial reefs: a case study in a Bahamian seagrass ecosystem. *Ecol. Eng.* 95, 574–579. doi: 10.1016/j.ecoleng.2016.06.109

Leclercq, E., Taylor, J. F., and Migaud, H. (2010). Morphological skin colour changes in teleosts. *Fish Fisheries* 11 (2), 159–193. doi: 10.1111/j.1467-2979.2009.00346.x

Lemoine, H. R., Paxton, A. B., Anisfeld, S. C., Rosemond, R. C., and Peterson, C. H. (2019). Selecting the optimal artificial reefs to achieve fish habitat enhancement goals. *Biol. Conserv.* 238, 108200. doi: 10.1016/j.biocon.2019.108200

Li, J., Li, J., Gong, P., and Guan, C. (2021). Effects of the artificial reef and flow field environment on the habitat selection behavior of sebastes schlegelii juveniles. *Appl. Anim. Behav. Sci.* 245. doi: 10.1016/j.applanim.2021.105492

Lima, J. S., Zalmon, I. R., and Love, M. (2019). Overview and trends of ecological and socioeconomic research on artificial reefs. *Mar. Environ. Res.* 145, 81–96. doi: 10.1016/j.marenvres.2019.01.010

Lorenzen, K., Leber, K. M., and Blankenship, H. L. (2010). Responsible approach to marine stock enhancement: an update. *Rev. Fisheries Sci.* 18 (2), 189–210. doi: 10.1080/10641262.2010.491564

Ma, Q., Ding, J., Xi, Y., Song, J., Liang, S., and Zhang, R. (2022). An evaluation method for determining the optimal structure of artificial reefs based on their flow field effects. *Front. Mar. Sci.* 9, 962821. doi: 10.3389/fmars.2022.962821

Martins, C. I., Galhardo, L., Noble, C., Damsgard, B., Spedicato, M. T., Zupa, W., et al. (2012). Behavioural indicators of welfare in farmed fish. *Fish Physiol. Biochem.* 38 (1), 17–41. doi: 10.1007/s10695-011-9518-8

Morgans, C. L., and Ord, T. J. (2013). Natural selection in novel environments: predation selects for background matching in the body colour of a land fish. *Anim. Behav.* 86 (6), 1241–1249. doi: 10.1016/j.anbehav.2013.09.027

Parsons, D. F., Suthers, I. M., Cruz, D. O., and Smith, J. A. (2016). Effects of habitat on fish abundance and species composition on temperate rocky reefs. *Mar. Ecol. Prog. Ser.* 561, 155–171. doi: 10.3354/meps11927

Qin, Y., Xing, J., and Mao, Y. (2016). Weak transient fault feature extraction based on an optimized morlet wavelet and kurtosis. *Measurement Sci. Technol.* 27 (8), 085003. doi: 10.1088/0957-0233/27/8/085003

Ruxton, G. D., Speed, M. P., and Kelly, D. J. (2004). What, if anything, is the adaptive function of countershading? *Anim. Behav.* 68 (3), 445–451. doi: 10.1016/j.anbehav.2003.12.009

Ryer, C. H., Lemke, J. L., Boersma, K., and Levas, S. (2008). Adaptive coloration, behavior and predation vulnerability in three juvenile north pacific flatfishes. *J. Exp. Mar. Biol. Ecol.* 359 (1), 62–66. doi: 10.1016/j.jembe.2008.02.017

Sempere-Valverde, J., Ostale-Valriberas, E., Farfan, G. M., and Espinosa, F. (2018). Substratum type affects recruitment and development of marine assemblages over artificial substrata: a case study in the alboran Sea. *Estuar. Coast. Shelf Sci.* 204, 56–65. doi: 10.1016/j.ecss.2018.02.017

Smith, J. A., Lowry, M. B., Champion, C., and Suthers, I. M. (2016). A designed artificial reef is among the most productive marine fish habitats: new metrics to address 'production versus attraction'. *Mar. Biol.* 163, 1–8. doi: 10.1007/s00227-016-2967-y

Smithers, S. P., Rooney, R., Wilson, A., and Stevens, M. (2018). Rock pool fish use a combination of colour change and substrate choice to improve camouflage. *Anim. Behav.* 144, 53–65. doi: 10.1016/j.anbehav.2018.08.004

Song, M., Wang, J., Nie, Z., Wang, L., Wang, J., Zhang, J., et al. (2022). Evaluation of artificial reef habitats as reconstruction or enhancement tools of benthic fish communities in northern yellow Sea. *Mar. pollut. Bull.* 182, 113968. doi: 10.1016/j.marpolbul.2022.113968

Stevens, M., and Merilaita, S. (2009). Animal camouflage: current issues and new perspectives. *Philos. Trans. R. Soc. B-Biological Sci.* 364 (1516), 423–427. doi: 10.1098/rstb.2008.0217

Tidwell, J. H., and Allan, G. L. (2001). Fish as food: aquaculture's contribution - ecological and economic impacts and contributions of fish farming and capture fisheries. *EMBO Rep.* 2 (11), 958–963. doi: 10.1093/embo-reports/kve236

Vivier, B., Dauvin, J.-C., Navon, M., Rusig, A.-M., Mussio, I., Orvain, F., et al. (2021). Marine artificial reefs, a meta-analysis of their design, objectives and effectiveness. *Global Ecol. Conserv.* 27, e01538. doi: 10.1016/j.gecco.2021.e01538

Wang, Y., Wai, O. W. H., and Chen, Q. (2021). Laboratory study on fish behavioral response to meandering flow and riffle-pool sequence driven by deflectors in straight concrete flood channels. *J. Hydrology* 598, 125736. doi: 10.1016/j.jhydrol.2020.125736

Wiegleb, J., Hirsch, P. E., Egger, B., Seidel, F., and Burkhardt-Holm, P. (2020). Flow field-induced drag forces and swimming behavior of three benthic fish species. *Limnologica* 84, 125812. doi: 10.1016/j.limno.2020.125812

Wilson, S. K., Fisher, R., Pratchett, M. S., Graham, N. A., Dulvy, N. K., Turner, R. A., et al. (2010). Habitat degradation and fishing effects on the size structure of coral reef fish communities. *Ecol. Appl.* 20 (2), 442–451. doi: 10.1890/08-2205.1

Xi, D., Zhang, X., Lü, H., and Zhang, Z. (2017). Cannibalism in juvenile black rockfish, sebastes schlegelii (Hilgendor), reared under controlled conditions. *Aquaculture* 479, 682–689. doi: 10.1016/j.aquaculture.2017.07.007

Xu, X., Guo, H., Zhang, Z., Wang, Y., Qin, J., and Zhang, X. (2021). Impact of pre-aggressive experience on behavior and physiology of black rockfish (Sebastes schlegelii). *Aquaculture* 536, 736416. doi: 10.1016/j.aquaculture.2021.736416

Zhang, Z., Chen, Q., Guan, X., Gong, M., Zhang, J., Cheng, F., et al. (2023). Physical and social enrichment influences the adaptability-related behaviors of black rockfish sebastes schlegelii: an effect mediated by social behaviors, HPI axis and neurogenesis. *Aquaculture* 564, 739056 doi: 10.1016/j.aquaculture.2022.739056

Zheng, Y.-x., Liang, Z.-l., Guan, C.-t., Song, X.-f., Li, J., Cui, Y., et al. (2015). Numerical simulation and experimental study of the effects of disposal space on the flow field around the combined three-tube reefs. *China Ocean Eng.* 29 (3), 445–458. doi: 10.1007/s13344-015-0031-1

Frontiers in Marine Science

TYPE Original Research
PUBLISHED 05 July 2023
DOI 10.3389/fmars.2023.1178370

Check for updates

OPEN ACCESS

EDITED BY
Zhao Yunpeng,
Dalian University of Technology, China

REVIEWED BY
Ray-Yeng Yang,
National Cheng Kung University, Taiwan
Tao Tian,
Dalian Ocean University, China

*CORRESPONDENCE
Yanli Tang
tangyanli@ouc.edu.cn
Fenfang Zhao
zhaoff@ouc.edu.cn

RECEIVED 02 March 2023
ACCEPTED 16 May 2023
PUBLISHED 05 July 2023

CITATION
Yang M, Tang Y, Zhao F and Xu S (2023) Numerical simulation of offshore wind power pile foundation scour with different arrangements of artificial reefs.
Front. Mar. Sci. 10:1178370.
doi: 10.3389/fmars.2023.1178370

Numerical simulation of offshore wind power pile foundation scour with different arrangements of artificial reefs

Mingda Yang, Yanli Tang*, Fenfang Zhao* and Shiji Xu

Fisheries College, Ocean University of China, Qingdao, China

The industrial integration of offshore wind power and marine ranches has been actively explored and developed in many countries. This emerging industrial synergy can significantly improve the ecological friendliness of offshore wind power and contribute to the development of the marine economy in the region. This industrial synergy is an important development direction for future offshore engineering. Artificial reefs (ARs) are critical components of marine ranches and are widely placed around offshore wind foundations (OWFs). The ARs can block the water flow and form a complex wake region behind it, which changes the original turbulence structure and reduces scour around the OWF. Therefore, determining the arrangement of ARs for scour protection around an OWF is of great engineering significance. In this study, a three-dimensional numerical model is established using a prototype of the first offshore wind power-marine ranch demonstration project in China. The turbulent change and sediment movement between the OWF and ARs are solved using the Reynolds-averaged Navier-Stokes (RANS) and sediment transport equations. Moreover, the variations in the maximum scour depth and scour volume around the OWF at different arrangements of ARs are explored. The results demonstrate that the arrangement of ARs weakens the horseshoe vortices in front of the OWF and destroys the vortex shedding behind the OWF, thereby producing a beneficial scour protection effect. Various arrangements of ARs have different effects on scour results around the OWF. Increasing the height of the AR could significantly reduce the scour results around the OWF and play an effective role in scour protection, followed by the tandem arrangement of ARs, whereas the parallel arrangement of ARs will produce negative scour effects. This study will serve a vital guiding role in the arrangement of ARs and practical significance for scouring protection around the OWF.

KEYWORDS

offshore wind turbine, artificial reef, numerical simulation, scour depth, arrangement method

1 Introduction

The sustainable development of marine fisheries has emerged as a major global concern because of the increasing degradation of the marine environment and the global reduction of fishing resources. In many sea regions, a novel fisheries development model known as “marine ranching” is used to increase marine fisheries resources, restore ecosystem functions, and ultimately achieve sustainable use of fisheries resources (Fang et al., 2021). Alternatively, many nations are actively pursuing the development of renewable energy sources to address climate change and the increase in electricity consumption. Since wind energy has great potential as a renewable and clean energy source, offshore wind power has rapidly expanded globally over the past 20 years (Bilgili et al., 2011; Chen and Lin, 2022). However, the widespread expansion of offshore wind power and marine ranching will result in sea space overlap, which will eventually generate issues such as conflicting sea usage (Chu et al., 2022). To address this problem, Europe was the first to propose an integrated development of offshore wind facilities and marine ranching facilities. An emerging industrial synergy that significantly improves the ecological friendliness of offshore wind power and contributes to the development of the marine economy in the region is a crucial new development direction for the future (Yang et al., 2019), as shown in Figure 1A. Preliminary research has been conducted on the integrated design of offshore wind foundation (OWF) and aquaculture cages in marine ranching (Lei et al., 2021; Huang et al., 2022; Zhang et al., 2022). Artificial reefs (ARs) are vital fishery facilities in marine ranches. ARs can produce significant flow-field effects through their structures, which play a pivotal role in protecting and increasing fishery resources (Komyakova et al., 2019). Simultaneously, the change in flow around the ARs will impact the sediment movement around the OWF and ultimately affect the stability of the OWF. In order to reasonably arrange ARs to avoid aggravating the scour around the OWF, it is necessary to explore the challenges of ARs arrangement around the OWF. Therefore, scientifically arranging ARs around the OWF is of great engineering significance.

The scour around marine structures is an established engineering problem that results from interactions between currents, structures, and sediments. Large-diameter monopile foundations (abbreviated as “pile”) are the most commonly used foundation form of OWFs. However, their embedded depth is reduced by sediment scour, which can significantly affect OWF safety and service life (Dai et al., 2021). When the fluid flows through the pile, a horseshoe vortex is formed in front of the pile, fluid compression acceleration occurs on both sides of the pile, and vortex shedding occurs behind the pile. These vortex structures with high turbulent kinetic energy enhance the sediment transport capacity and eventually produce scour and deposition around the pile. In the past decades, many experimental and theoretical studies have been conducted on the scour phenomenon around piles under various conditions. They include (1) the scour mechanism due to diverse vortex systems (Sumer et al., 1992; Sumer and Fredsøe, 2001; Roulund et al., 2005; Jenkins et al., 2007; Baykal et al., 2015), (2) the scour development process over time and prediction of the scour balance time (McGovern et al., 2014; Ma et al., 2018; Schendel

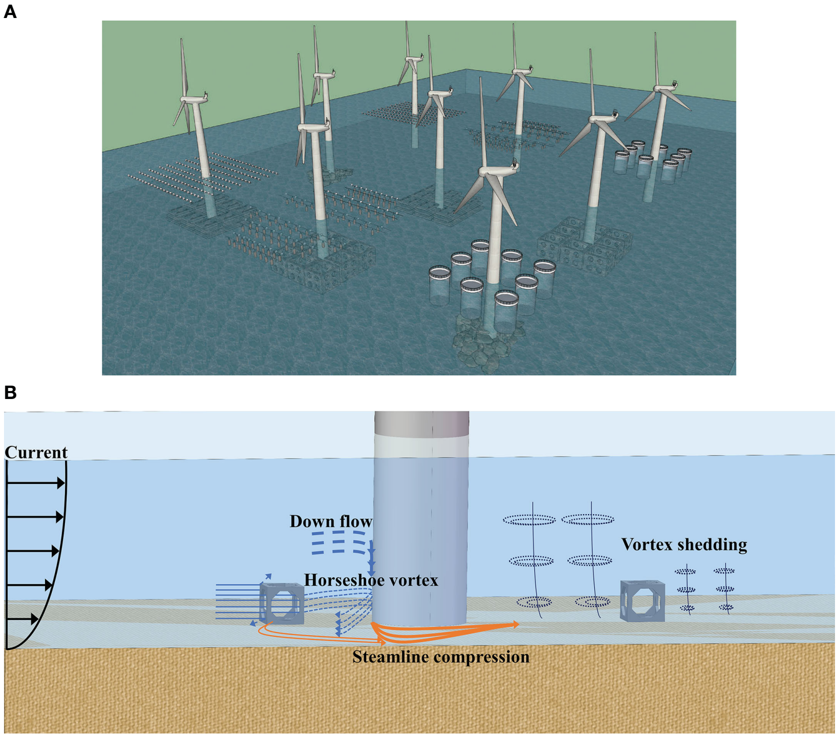

FIGURE 1
Combination of marine ranching and offshore wind power: **(A)** combination of OWFs and ARs (Yang et al., 2019) **(B)** characteristics of turbulent motion around an OWF and ARs.

et al., 2018; Lu et al., 2022), and (3) the main factors affecting the scour results and characteristics (Zhao et al., 2010; Yao et al., 2018; Gautam et al., 2021; Chen et al., 2022; Yang Q. et al., 2022).

The focus of research has shifted to effectively protecting the seabed around the OWF from scouring as the basic theory of scour has been gradually refined. The scour protection measures of OWF are classified into active and passive protection methods. Active scour protection involves the addition of structures at the bottom of the OWF, such as collars and anchor branches (Pandey et al., 2020; Yu et al., 2020; Zhang et al., 2021). These methods can change the flow pattern at the bottom of the OWF and strengthen the ability to protect the seabed, thereby further reducing sediment transport at the junction (Yang et al., 2020; Yang F. et al., 2021; Deng et al., 2022). Active scour protection structures, such as skirted mudmat foundations, multi-bucket jacket foundations, composite bucket foundations, and skirted caisson foundations, have also been designed to solve scour damage under various complex conditions (Yu et al., 2019; Yao et al., 2020; Li et al., 2022; Lian et al., 2022; Wei et al., 2022). Passive scour protection changes the flow movement mode and seabed composition without changing the structure of the OWF, such as by placing a stone protection layer covering the sediments. This is the most widely used scour protection measure in practical engineering applications. It was found that the number of stone layers is a critical factor affecting scour results (Yang Q. et al., 2021). The scour depth decreases with an increasing number of stone layers because more layers will generate more pores to consume turbulence. Therefore, determining the size of the stone and the scope and thickness of the stone protection layer are key to achieving effective scour protection (Nielsen et al., 2013; Ma and Chen, 2021). However, some field surveys of offshore wind power around the world found that the arrangement range and thickness of stone layers are difficult to implement due to the uneven size of stones in practical engineering applications. These conditions lead to the second scour around the stone protection layer, and scours at the stone's edge result in stone deformation, subsidence, and scour protection failure (Raaijmakers et al., 2010; Whitehouse et al., 2011). Another type of passive scour protection is the installation of several smaller diameter piles around the OWF, known as sacrificial piles, to reduce the flow velocity and shear stress around the OWFs. Research has found that the protective effect of sacrificial piles depends mainly on their number and arrangement (Wang et al., 2017; Nazari-Sharabian et al., 2020; Li et al., 2022). In the context of integration of marine ranching and offshore wind power, ARs play a similar role to sacrificial piles when placed around the OWF. Compared to other passive scour protection, using ARs as passive scour protection has significant advantages. Firstly, Each AR can be accurately placed around the OWF based on coordinates, quantitative research on the arrangement of multiple ARs can identify the optimal flow field effect to significantly protect from scour around the OWF (Liu and Su, 2013). Secondly, optimizing the structure of ARs can avoid their own scour and increase efficiency (Tang et al., 2022; Yang M. et al., 2022; Zhao et al., 2022). Besides, ARs are not "sacrificial" because they can improve the marine ecosystem around the OWF through the generated flow field effects and promote ecological benefits, such as sustainable use of species and habitats.

Combining OWFs with ARs to mitigate sediment scour is a pressing issue for future engineering endeavors (Pan et al., 2022), and no existing literature addresses this specific issue. There are two main theoretical justifications for using ARs as passive scour-protection structures for OWF. First, previous research demonstrated that ARs could effectively reduce wave and current energy, block sediment, and prevent erosion when used in conjunction with traditional breakwaters. These properties make ARs well-suited for addressing local scour and erosion issues in traditional underwater breakwaters (Srisuwan and Rattanamanee, 2015; López et al., 2016; Almeida, 2017; Kim et al., 2020; Ghiasian et al., 2021; Marin-Diaz et al., 2021; Kim et al., 2022). It is evident that ARs can attenuate waves and mitigate sediment transport. Second, the interaction of water with ARs creates a wake region that generates vortexes and contributes to the development of a recirculating water flow (Jung et al., 2022). The wake region behind ARs is widely regarded as an important habitat for fish, as it provides opportunities for shelter, feeding, spawning, and inhabitation. The ability of ARs to create these habitat areas is an essential aspect of their ecological functions. Previous research has used both experimental and numerical simulation techniques to quantify the size and range of wake regions behind ARs (Kim et al., 2016; Kim et al., 2019; Kim et al., 2021). These studies examined the relationship between the wake region range and various reef structure characteristics, including opening design, roughness, complexity, arrangement, and combination of ARs (Liu and Su, 2013; Jiang et al., 2016; Wang et al., 2018; Jiang et al., 2020; Wang et al., 2021; Jung et al., 2022; Zhou et al., 2022; Kim et al., 2022). When ARs are arranged around the OWF, the wake region can converge with the horseshoe vortex at the bottom of the OWF and disrupt the turbulent structure, reducing the transport capacity of the horseshoe vortex for sediment and providing scour protection, as shown in Figure 1B. However, no published literature has studied the interaction between ARs and the OWF, such as hydrodynamic interactions, sediment transport processes, and other engineering issues. Therefore, several issues require further investigation and analysis, such as the optimal spacing between ARs and the OWF for maximum scour protection effectiveness and the relationship between scour protection efficacy and the combination mode of multiple ARs.

It is essential to examine the impact of ARs on sediment scour in the vicinity of an OWF. In this study, a numerical model based on the first demonstration project of marine ranching and offshore wind power integration in China was developed using the computation fluid dynamics (CFD) method was used to investigate the effect of AR arrangement spacing and combination under steady flow on the turbulent structure, and sediment scours around the OWF. Section 2 presents the construction of the numerical model and related control equations, and verifies the accuracy of the numerical model. Section 3 discusses the results of simulation cases involving different parameter settings and describes the hydrodynamic characteristics and sediment transport processes between the AR and the OWF. The conclusions are given in Section 4. This research aims to fill a gap in the literature on the combination of ARs and OWF, provide valuable engineering guidance for arranging ARs around OWF, and suggest new approaches for scour protection in marine engineering.

2 Material and methods

2.1 Numerical methods

In the present study, a numerical analysis of the local scour between the OWF and ARs is conducted using the commercial CFD code FLOW-3D. The CFD code fully solved the three-dimensional transient Navier-Stokes governing equations using the Finite Difference Method (FDM) in a fixed Eulerian mesh. Automatic time-step adjustment is used to ensure the stability and convergence of the simulation. A first-order numerical scheme is used to discretize each term in the momentum equation. The Generalized Minimal Residual (GMRES) algorithm is selected to iteratively solve the linear system of pressure equations, which effectively improved the convergence of the simulation and significantly reduced the calculation time. A brief introduction to the theoretical model is provided, as described by some scholars (Nielsen et al., 2013; Zhang et al., 2017).

2.1.1 Governing equations of the flow

The Reynolds-averaged Navier-Stokes (RANS) equations closed with the renormalization group (RNG) turbulence model are regarded as the governing equations for the incompressible viscous fluid motion around the OWF and ARs. The governing equations of the flow can be divided into continuous and motion equations as follows:

$$\frac{\partial(uA_X)}{\partial x}+\frac{\partial(vA_y)}{\partial y}+\frac{\partial(wA_z)}{\partial z}=0; \tag{1}$$

$$\frac{\partial u}{\partial t}+\frac{1}{V_F}\left(uA_x\frac{\partial u}{\partial x}+vA_y\frac{\partial u}{\partial y}+wA_z\frac{\partial u}{\partial z}\right)=-\frac{1}{\rho}\frac{\partial p}{\partial x}+G_x+f_x; \tag{2}$$

$$\frac{\partial v}{\partial t}+\frac{1}{V_F}\left(uA_x\frac{\partial v}{\partial x}+vA_y\frac{\partial v}{\partial y}+wA_z\frac{\partial v}{\partial z}\right)=-\frac{1}{\rho}\frac{\partial p}{\partial y}+G_y+f_y;$$

$$\frac{\partial w}{\partial t}+\frac{1}{V_F}\left(uA_x\frac{\partial w}{\partial x}+vA_y\frac{\partial w}{\partial y}+wA_z\frac{\partial w}{\partial z}\right)=-\frac{1}{\rho}\frac{\partial p}{\partial z}+G_z+f_z.$$

where u, v, and w are the velocity components in x, y, and z directions, respectively. A_x, A_y and A_z represent the area fractions open to the flow in x, y and z directions, respectively. G_x, G_y, and G_z denote the body accelerations, whereas f_x, f_y, and f_z are the viscous accelerations in the respective directions x, y, and z. V_F denotes the fractional volume open to flow, p is the average hydrodynamic pressure, and ρ is the fluid density.

2.1.2 Turbulence model

The RNG k-ϵ turbulent model is adopted in this study to investigate the local scour around the OWF and ARs because the RNG model is capable of accurately capturing the flow field recirculation and is widely used to predict turbulent motion around various offshore structures. The k and ϵ equations in the RNG model are expressed as follows:

$$\frac{\partial k_T}{\partial t}+\frac{1}{V_F}\left(uA_x\frac{\partial k_T}{\partial x}+vA_y\frac{\partial k_T}{\partial y}+wA_z\frac{\partial k_T}{\partial z}\right)=P_T+G_T+Diff_{k_T}-\epsilon_T; \tag{3}$$

$$\frac{\partial \epsilon_T}{\partial t}+\frac{1}{V_F}\left(uA_x\frac{\partial \epsilon_T}{\partial x}+vA_y\frac{\partial \epsilon_T}{\partial y}+wA_z\frac{\partial \epsilon_T}{\partial z}\right)$$
$$=\frac{CDIS1\cdot\epsilon_T}{k_T}(P_T+CDIS3\cdot G_T)+Diff_\epsilon-CDIS2\frac{\epsilon_T^2}{k_T}, \tag{4}$$

where P_T denotes the turbulent kinetic energy production, k_T represents the specific kinetic energy associated with turbulent velocity fluctuations, G_T is the turbulent energy generated by buoyancy, ϵ_T is the dissipation rate of the turbulent energy, $Diff_\epsilon$ and $Diff_{kT}$ are terms related to diffusion, and *CDIS1*, *CDIS2* and *CDIS3* are dimensionless parameters.

2.1.3 Sediment transport model

The sediment scour model involves two parts: setting up sediment types and their related properties, including the grain size, mass density, and angle of repose. The other is to estimate the motion of sediment (suspended sediment transport, settling, entrainment, and bed load transport) by predicting sediment erosion, advection, and deposition.

(1) Sediment starting

The entrainment lift velocity of sediment is computed as:

$$u_{lift,i}=\alpha_i n_s d_*^{0.3}(\theta_i-\theta_{cr,i})^{1.5}\sqrt{||g||d_i\frac{(\rho_i-\rho_f)}{\rho_f},} \tag{5}$$

where α_i represents the entrainment parameter, d^* is a dimensionless parameter, and d_i is the diameter of the sediment. n_s is the outward pointing normal to the packed-bed interface. ρ_i is the density of the sediment, ρ_f is the fluid density, and $|g|$ is the magnitude of the acceleration of gravity g. θ_i indicates the local Shields parameter, $\theta_{cr,i}$ is the critical Shields parameter and computed by

$$\theta_{cr,i}=\frac{0.3}{1+1.2d_*}+0.055[1-\exp(-0.02d_*)]. \tag{6}$$

(2) Entrainment and deposition

The equation of the settling velocity ($u_{setting,i}$) and the bedload transport model proposed by Soulsby (1997) are used in the present study:

$$u_{settling,i}=\frac{v_f}{d_i}[(10.36^2+1.049d_*^3)^{0.5}-10.36], \tag{7}$$

where v_f is the kinematic viscosity of the fluid. The model introduced by Meyer-Peter (1948) is used to calculate bedload motion.

$$\Phi_i=\beta_m(\theta_i-\theta'_{cr,i})^{1.5}c_{b,i}, \tag{8}$$

where Φ_i denotes the dimensionless bedload transport rate, whileβ_m is a coefficient generally set to 8.0.

(3) Suspended sediment concentration

The suspended sediment concentration is calculated by solving its own transport equation:

$$\frac{\partial C_{s,i}}{\partial t}+\nabla\cdot(u_{s,i}C_{s,i})=\nabla\cdot\nabla(D_f C_{s,i}), \tag{9}$$

Here, $C_{s,i}$ denotes the suspended sediment mass concentration, which is defined as the sediment mass per volume of the fluid-sediment mixture; D_f is the diffusivity; and $u_{s,i}$ indicates the velocity of suspended sediment.

(4) Sea bed deformation tracking

The fractional area-volume obstacle representation (FAVOR) method is used in the CFD code, which uses the volume fraction of solids within each grid to determine the surface of the solids. In the computational domain, the sand content in each grid is calculated using Equations (5)-(9). FAVOR method is used in the sediment transport model to accurately describe the shape of the seabed by calculating the area and volume fraction parameters of accumulated sediment in each grid throughout the entire scouring process.

2.2 Computational domain and meshing

This research is based on the first demonstration project on integrating offshore wind power and marine ranches in China. The offshore wind power plant is located in Laizhou Bay, Shandong Province, China, where the water depth is approximately 10 m. The sea area is a tidal current with a maximum flow velocity of approximately 0.6 m/s. A constant flow velocity of 0.6 m/s is used as the simulated flow condition, as the scour results obtained under this flow condition can be approximated as the results of tidal current (Schendel et al., 2018). The seabed sediment mainly consisted of silty clay with a median diameter (d_{50}) of approximately 0.5 mm. The diameter of the OWF (D) is 5 m. The type of AR selected for the arrangement is shown in Figure 2A, which is widely used in the marine ranch of China, with a side length (L) of 2 m and a positive octagonal opening. The flow characteristics and scour process of this AR are fully investigated in our previous study, and the ideal design of this AR is derived and applied in this study.

The dimensions of the computational domain are 70 m in length, 20 m in width, and 10 m in height Figure 2A, including the OWF located in the center of the domain, and a 70 m×20 m×2 m sandy seabed composed of sediment with a median diameter of 0.5 mm. The parameter settings for the simulations are listed in Table 1.

An appropriate mesh size is crucial to the accuracy and efficiency of numerical simulations. The independence of the mesh is investigated to find a mesh strategy with reasonable accuracy and high efficiency. As shown in Figure 3, the computational domain is discretized using a uniformly spaced structured mesh system. A nested mesh is created around the OWF and ARs to encrypt the mesh size. According to the relevant literature, the size of the nested cell is usually set between 0.03 D and 0.05 D of the OWFs, and the external cell size is usually twice the size of the nested cell. Therefore, three mesh sizes (the global mesh/nested mesh) are set to analyze the mesh independent test as follows: 0.3 m/0.15 m, 0.24 m/0.12 m, and 0.22 m/0.11 m, respectively Figure 2B. Numerical calculations of the OWF scour process are performed for the model divided by three mesh sizes at a water depth of 10 m and a flow velocity of 0.6 m/s. The calculation time is 7000 s.

Figure 3A shows the flow velocity distribution around the OWF for three mesh sizes. It can be observed that the acceleration of the fluid on both sides of the OWF and the shedding of the vortex street behind the OWF are almost identical for the three mesh sizes.

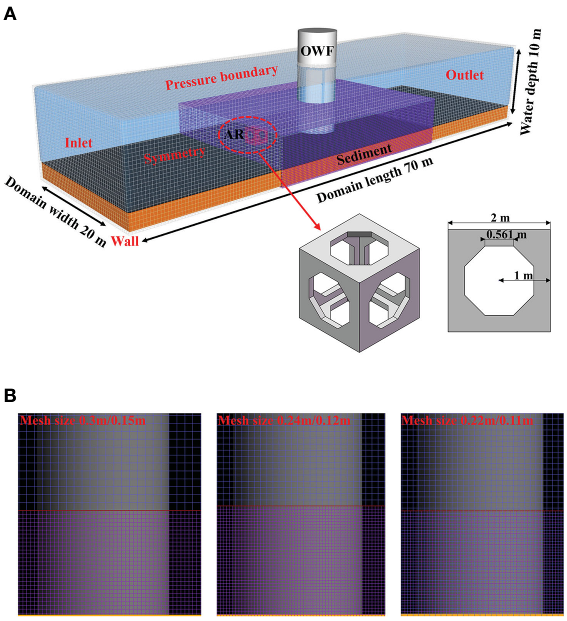

FIGURE 2
Mesh independence analysis: **(A)** distribution of the flow velocity contour near the seabed around the OWFs **(B)** distribution of scour depth on both sides of OWFs.

TABLE 1 Numerical calculation of scouring conditions.

Group	Case number	Number of AR	*G/D*	*P/L*	*T/L*	*H/L*
Control	1	0	–	–	–	–
I	2	1	-1	–	–	–
	3		-0.5			
	4		0.5			
	5		1			
	6		2			
	7		4			
II	8	2	–	0	–	–
	9			1		
	10			2		
	11			3		
	12			4		
	13			5		
III	14		–	–	0	–
	15				0.5	
	16				1	
	17				2	
IV	18	1.5	–	–	–	1.5
	19	2				2

However, a smaller mesh size will produce a more detailed description of the flow separation. The scour depth distribution of the cross-section of the OWF central axis for the three mesh sizes is shown in Figure 3B. It can be seen that the scour depth generated by mesh 0.22 m/0.11 m on both sides away from the OWF is slightly greater than the other two mesh sizes. However, the scour depths generated by the three mesh sizes are nearly identical near both sides of the OWF. These three mesh sizes can precisely simulate the turbulence characteristics and sediment scours around the OWF because they are within the range of the optimal mesh size settings. Therefore, to ensure the accuracy of the calculation results and the calculation efficiency, the subsequent research and discussion will select the middle size mesh (0.24 m/0.12 m) as the mesh parameter for the calculation.

2.3 Boundary condition

First, a velocity vector of 0.6 m/s is specified at the inlet boundary. The scour model is not active, and a sufficiently long numerical channel is used to develop the flow field fully. When the boundary layer of the seabed is fully formed, it can be regarded as a fluid that has completely developed on a rough seabed. The velocity profile is intercepted as the Neumann boundary condition at the velocity inlet of the calculation domain.

At the top, the pressure is specified as standard atmospheric pressure and zero gradients. The symmetry boundary condition is adopted on the sides of the model, where the normal velocity and all gradients in the normal direction are zero. A pressure boundary condition is adopted at the outlet, where the fluid level is specified during the entire calculation period. The surfaces of the OWF and ARs are treated as no-slip wall boundaries Figure 2A.

2.4 Validation of numerical models

In the present study, the effect of the flow field changes between the ARs and OWF on the scour results is investigated. To validate the CFD models, the velocity distribution around the AR and the scour of the pile between the present simulation results and the published data are compared.

2.4.1 Validation of velocity distribution around AR

Wang et al. (2021) conducted particle image velocimetry (PIV) experiments on a symmetrical cubic porous AR model in a tank to explore the changes of flow characteristics around the AR. The

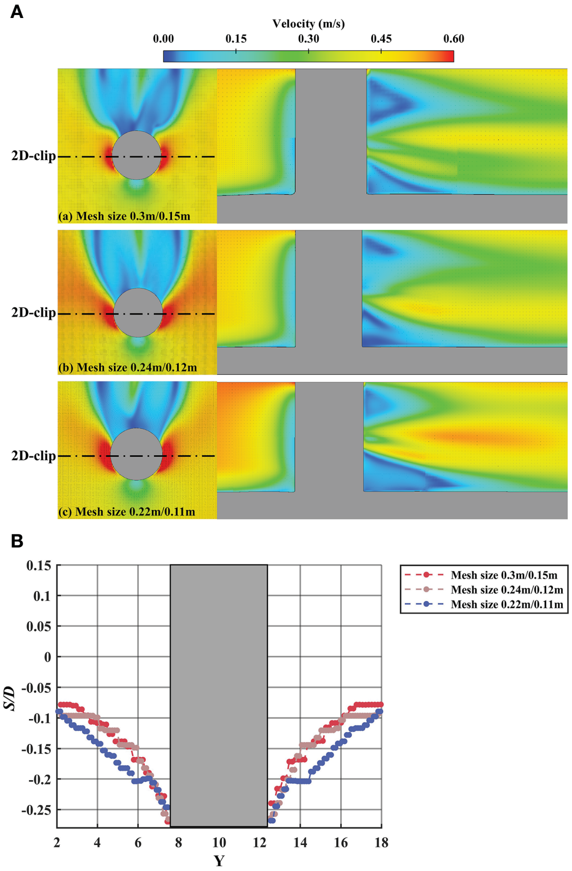

FIGURE 3
Calculation model and mesh strategy **(A)** calculation domain settings and boundary conditions **(B)** three different mesh sizes.

velocity distribution around the AR is validated by comparing the experimental data and the present simulation results.

Figure 4A shows the velocity vector distribution of fluid flow around the AR. It can be seen that the present simulation results are in good agreement with the experimental data, and a large wake region is formed behind the AR, which is crucial for present studies. The velocity distribution along y = 0.06 m, 0.1 m, and 0.15 m are represented in Figure 4B. Slight deviations arise because of turbulent motion at locations close to the AR. In general, the comparison between the PIV experimental data and the simulated results shows good agreement, and the present numerical model can accurately simulate the flow characteristics around the AR.

2.4.2 Validation of scour around pile

Further validation is performed by comparing the scour around a pile between the numerical results of the present study and published experimental data (Zhao et al., 2010). For comparison, the present simulations are conducted at a water depth of 0.5 m and a velocity of 0.441 m/s. The diameter of the pile is 0.1m, and the median particle size of the sediment is 0.4 mm.

A comparison of the scour depth between the present numerical simulations and the measured data is shown in Figure 5A, and the three-dimensional morphology is shown in Figure 5B. It can be seen that the numerical model can predict the maximum scour depth around the pile. The maximum scour depth generated is at the 45° side of the pile, where the flow compression acceleration causes the increase of seabed shear stress. Subsequently, the scour area starts to develop towards the front and both sides of the pile, forming a spoon-shaped scour hole. The simulated scour depths on both sides and in front of the pile are in excellent agreement with the measured data but slightly underestimated the scour range behind the pile. The variation in the maximum scour depth with time is illustrated in Figure 5C. It can be seen that a rapid scour phase occurred first for about 2000 s, then the scour rate decreases and reaches the scouring equilibrium phase at about 7000 s, with almost constant scour depth. The process produced by the numerical simulation is almost identical to the published experimental data. Although the scour depths calculated numerically in the early stages are slightly underestimated, they yield almost identical maximum scour depths, with an error of no more than 5%. As this study mainly investigates the impact of different layout parameters of ARs on the development of scour around the OWF, the present deviation value is within the acceptable range. Therefore, it is feasible and accurate to establish a three-dimensional numerical scour model to study scour around an OWF.

After validating the velocity distribution around the AR and the scour around a pile, it can be concluded that this numerical model can capture the flow characteristics around the AR structure and

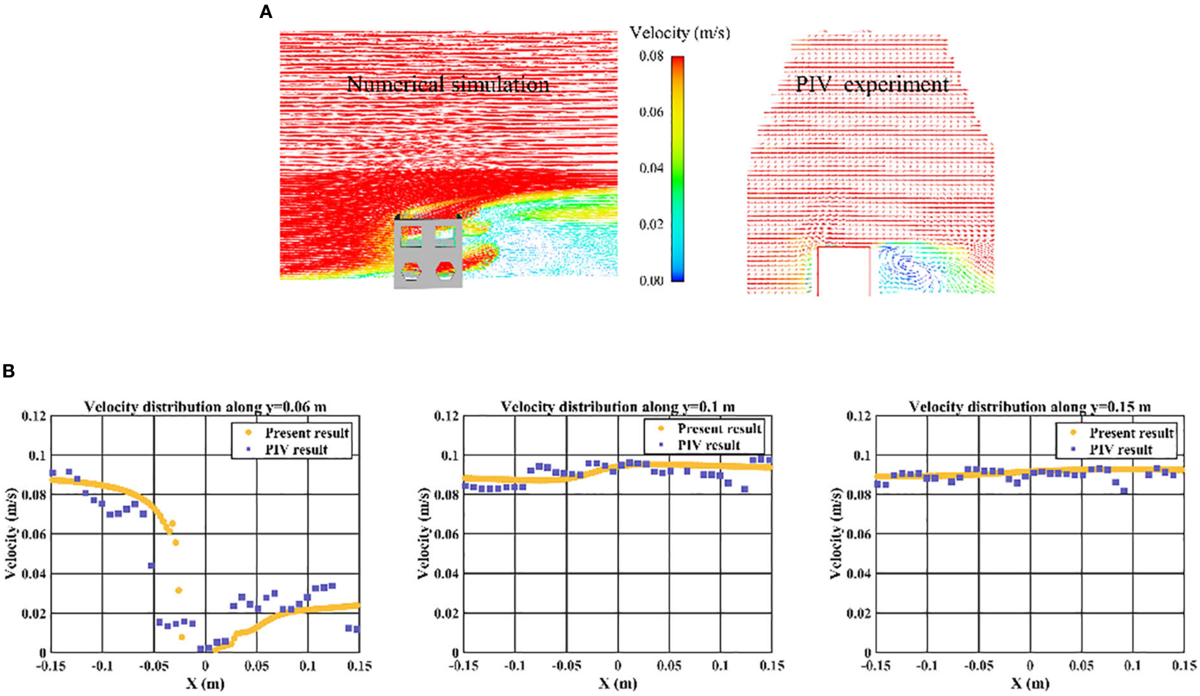

FIGURE 4
Numerical model calculation and verification about the flow of an AR: **(A)** streamline distribution around the AR **(B)** the velocity curve along y = 0.06 m, y = 0.1 m and y = 0.15 m respectively.

accurately predict the pile scour process. The present CFD model can be applied for later investigations.

2.5 Numerical simulation group setting

The numerical simulations are divided into four groups to investigate the effects of the AR arrangement on the maximum scour depth and scour volume around the OWF, in addition to flow characteristics and scour mechanism between the ARs and OWF. First, the scouring process of a single OWF (control) is simulated, and its results are compared and analyzed with the results of subsequent studies. As shown in Figure 6, in Group I, the AR is placed at different locations on the central axis of the OWF, and the normalized distances of the ARs from the OWF (G/D) are – -1.0, -0.5, 0.5, 1.0, 2.0, and 4.0, respectively. In Groups II and III, two ARs are set in front of the OWF, and the distance between the OWF center cross section and ARs is fixed at 1.0 D. In Group II, the spacing direction of two ARs is perpendicular to the flow direction, and the normalized distance between the ARs (P/L) is set from 0 to 5.0, with an interval of 1.0. In Group III, the spacing direction of two ARs are along the flow direction with normalized spaces (T/L) of 0, 0.5, 1.0, and 2.0. In Group IV, the distance between the AR and OWF is fixed at 1.0 D, and the normalized heights of the ARs (H/L) are 1.0, 1.5, and 2.0. The specific numerical case conditions and parameter settings are shown in Figure 6 and Table 2, where G is the distance between the AR and OWF, and P and T are the horizontal and vertical spacing between the two ARs, respectively.

The scour depth S and scour volume V_s are two important indicators for determining the scour results around the OWF, and are dimensionless using the diameter D and volume V_c of the OWF, respectively. S is obtained by extracting the maximum scour depth around the OWF. V_s is obtained by using MATLAB programming to fit all scour points around the OWF to a surface (Figure 7) The calculation range is 7.5 m × 20.0 m × 2.0 m, which almost contains the main scour area. The simulation time of the scour process selected is 7000 s because the purpose of this study is to examine the influence of the arrangement distance and method of ARs on scour characteristics around an OWF. This means that there may be a state where the scour equilibrium condition is not reached in some simulation cases. Further research is needed on the scour phenomenon after reaching the equilibrium conditions.

3 Numerical results and discussion

3.1 Influence of *G*/*D*

Figure 8A depicts the seabed surface elevation around the OWF for different distances between the AR and the OWF at the last moment. In the control case, it can be seen from the figure that the scour started at 45° on both sides of the OWF and gradually developed towards the front of the OWF. The main deposition area is located behind the scour hole and OWF and gradually expanded downstream. At G/D = -0.5, it can be observed that there is no impact on the scour results in front of and on both sides of the

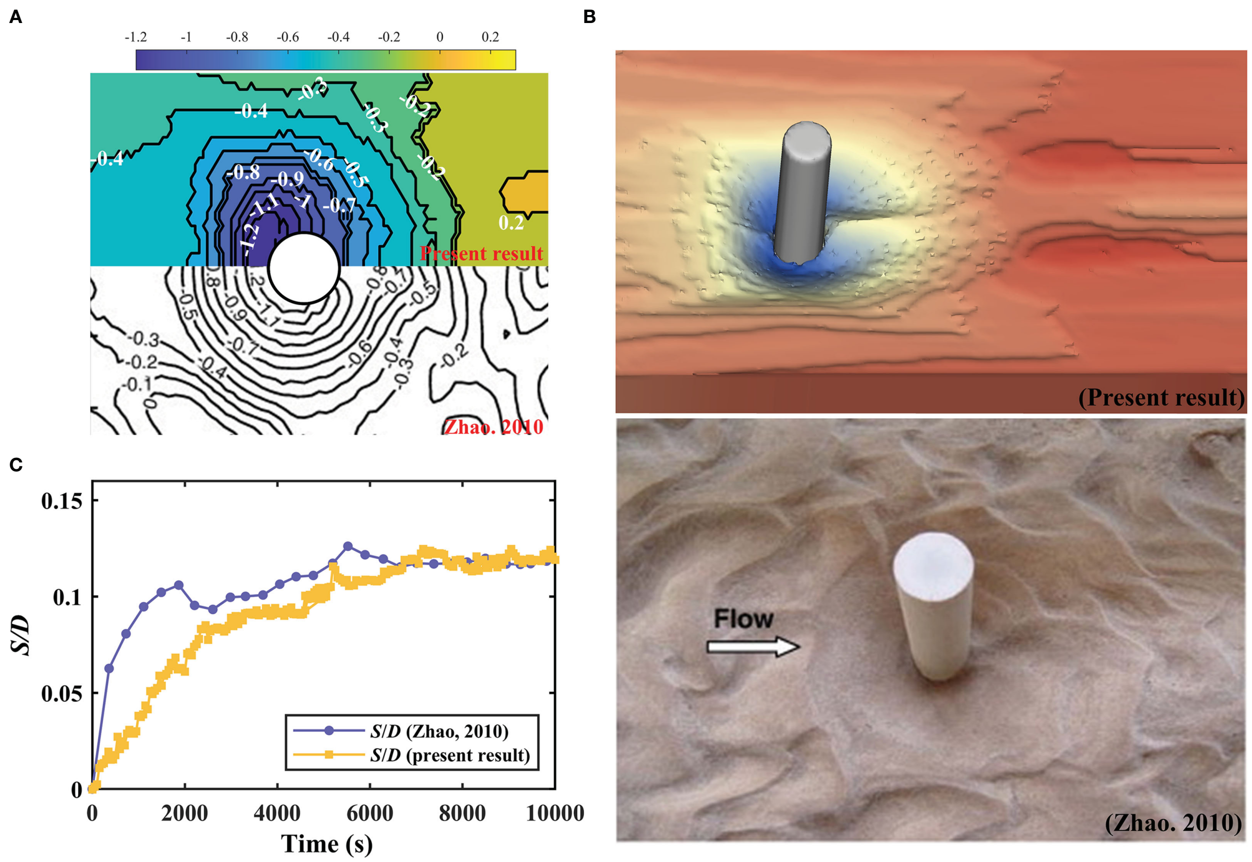

FIGURE 5

Comparison of the present results and experimental data from (Zhao et al., 2010): **(A)** contour of *S/D* at 10000 s **(B)** scour shapes at 10000 s **(C)** time development of the maximum scour depth.

OWF, and only the deposition area behind the OWF extends backward. However, it can be observed that the sediment movement in front of the OWF becomes stable, and the scour pit does not extend downstream with *G/D* = -1.0. When the AR is located in front of the OWF (*G/D* = 0.5, 1.0, 2.0, and 4.0), an obvious fault phenomenon of the scour depth occurred in the scour area. The scour depth on both sides near the OWF is relatively larger than that on both sides far away from the OWF, and an obvious spoon-shaped scour hole is finally formed around the OWF. In addition, the fault phenomenon of the scour depth becomes increasingly serious as the distance between the OWF and AR increases.

The time evolutions of the scour depth and scour volume around the OWF in the control case and Group I are shown in Figures 8B, C. It can be seen from the figure that the existence of AR can effectively reduce the scour depth and scour volume around the OWF, and the change of scour depth has the following rules: *G/D* = 0.5< *G/D* = -1.0< *G/D* = 1.0< *G/D* = 2.0 = *G/D* = 4.0< *G/D* = -0.5< control. Compared with the control case, *G/D* = 0.5 provides the most effective scour protection, which results in a 27% reduction in scour depth. The change of scour volume around the OWF has the following rules: *G/D* = -1.0< *G/D* = 0.5< *G/D* = 2.0< *G/D* = 1.0< *G/D* = 4.0< *G/D* = -0.5< control. It can be found that the scour volume around the OWF decreases by 26% when the AR is arranged at a distance of 1.0 D directly behind the OWF. Moreover, the scour depth around the OWF changes with time owing to the AR arrangement.

The scouring process of traditional pile structure can be divided into three processes: fast scouring, slow scouring, and scour balance, similar to the scouring process of the control case in Figure 8B. However, it can be observed in Figure 8B that only *G/D* = 0.5 followed this process, and the other cases reached a transient scour balance at approximately 3000s, and then the scour depth began to increase gradually. However, the physical mechanism of this phenomenon requires further investigation. It can be seen from Figure 8C that the scour volume increases rapidly in the 0–2000s, and then slowly increases. The equilibrium stage is not reached because the scour volume is the calculation of the large-scale scour area around the OWF and the scour range and scour depth are always changing. Figure 8D illustrates the variation in the normalized scour depth (S/S_C) and normalized scour volume (V/V_C) around the OWF with the distance from the AR, where S_C and V_C are the scour depth and scour volume of the control case, respectively. It can be seen that the variations in the scour depth and scour volume with distance change slightly. When *G/D* is -1.0, the effect of the AR on reducing the scour volume around the OWF is significantly greater than the effect on the scour depth. After *G/D* > 1.0, the effect of AR on the scour results around the OWF became

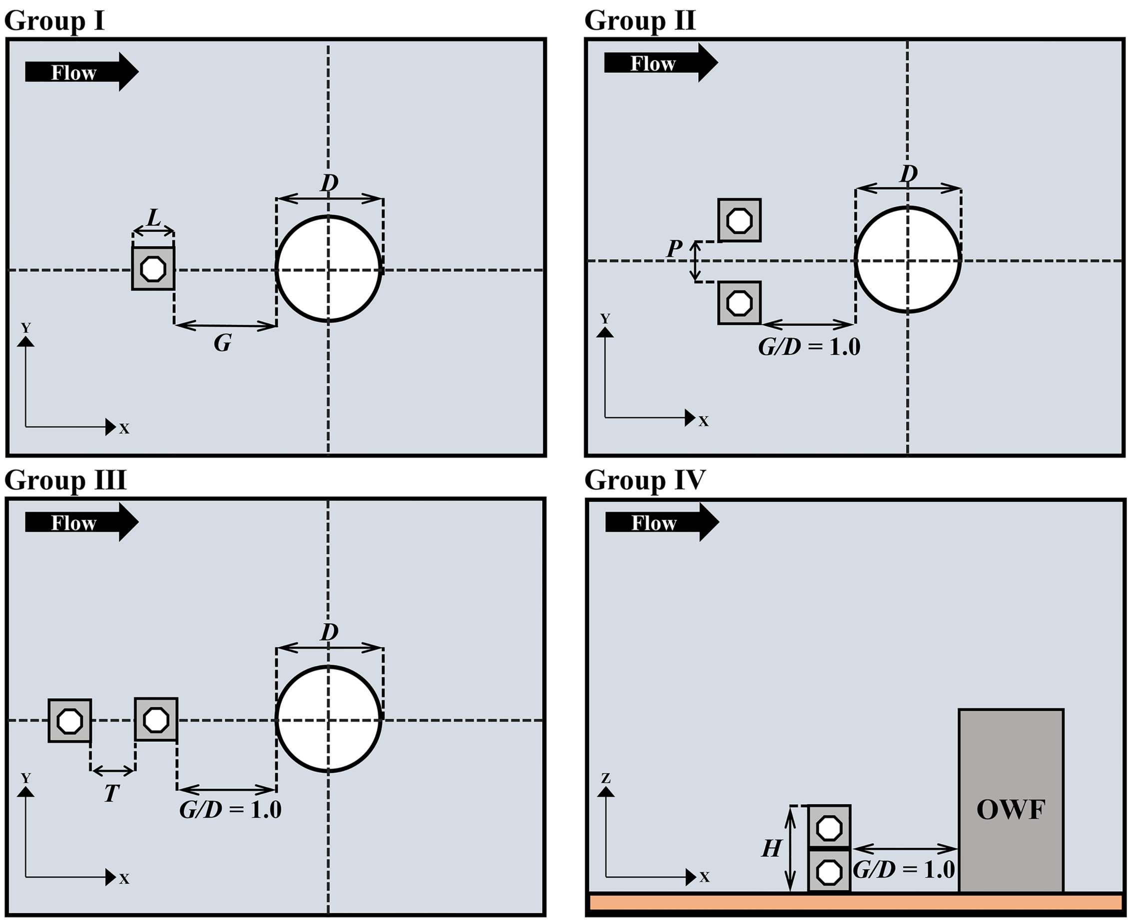

FIGURE 6
Group of numerical calculation.

stable. In general, placing a single AR directly in front of or behind an OWF provides effective scour protection. Different distances provide different scour protection, which requires further analysis and discussion.

To clarify the physical mechanism by which the presence of the AR can reduce the scour depth and scour volume around the OWF. The reasons for the different scour results caused by the different distances between the AR and the OWF are obtained. The flow velocity variation, streamline motion, turbulence intensity, vortex shedding, and shear stress distribution of the fluid around the OWF are visualized and analyzed.

Figure 9 compares the distribution of the flow velocity contour near the seabed around the OWF for the control case and Group I at the beginning of the scour. The figure shows that the flow velocity in front of the OWF decreases owing to the blocking effect of the OWF, and then the flow accelerates around the two sides of the OWF. The two sides of the OWF formed an arc-shaped fluid acceleration area. At the same time, a large slow-flow area is formed behind the OWF, and a vortex is formed in this area. However, when the AR is arranged at $G/D > 0$, it produces a wake region with a slower flow velocity at the interval between the OWF and AR. The wake region expands the scope of the slow flow area in front of the OWF, which eventually affects the scope of the acceleration area and the acceleration magnitude of the fluid on both sides of the OWF. The magnitude and range of fluid acceleration on both sides of the OWF are significantly reduced due to the presence of AR at $G/D = 0.5$, $G/D = 1.0$, and $G/D = 2.0$. However, this effect gradually decreased with increasing distance. When $G/D = 4.0$, the range of the acceleration region on both sides of the OWF is almost the same as that of the control case. It can be considered that under this distance condition, the effect of AR on the flow field around the OWF is not obvious. However, when $G/D < 0$, the effect of AR on the flow field around the OWF cannot be observed in the current view, and a more comprehensive analysis is needed in these two cases.

Bed shear stress refers to the shear drag force of the bottom flow on the bed, which is the main factor affecting the scour and deposition of the bed. The greater the shear stress, the stronger the scour capacity of the fluid on the bed surface (Yang M. et al., 2022). The shear stress distribution on both sides of the axial plane in the OWF is shown in Figure 10 for scour times of 3000 s and 7000 s. The bed shear stress on both sides of the OWF is significantly lower than that of the control case when $G/D = 1.0$, which indicates that AR can effectively reduce the bed shear stress around the OWF and reduce

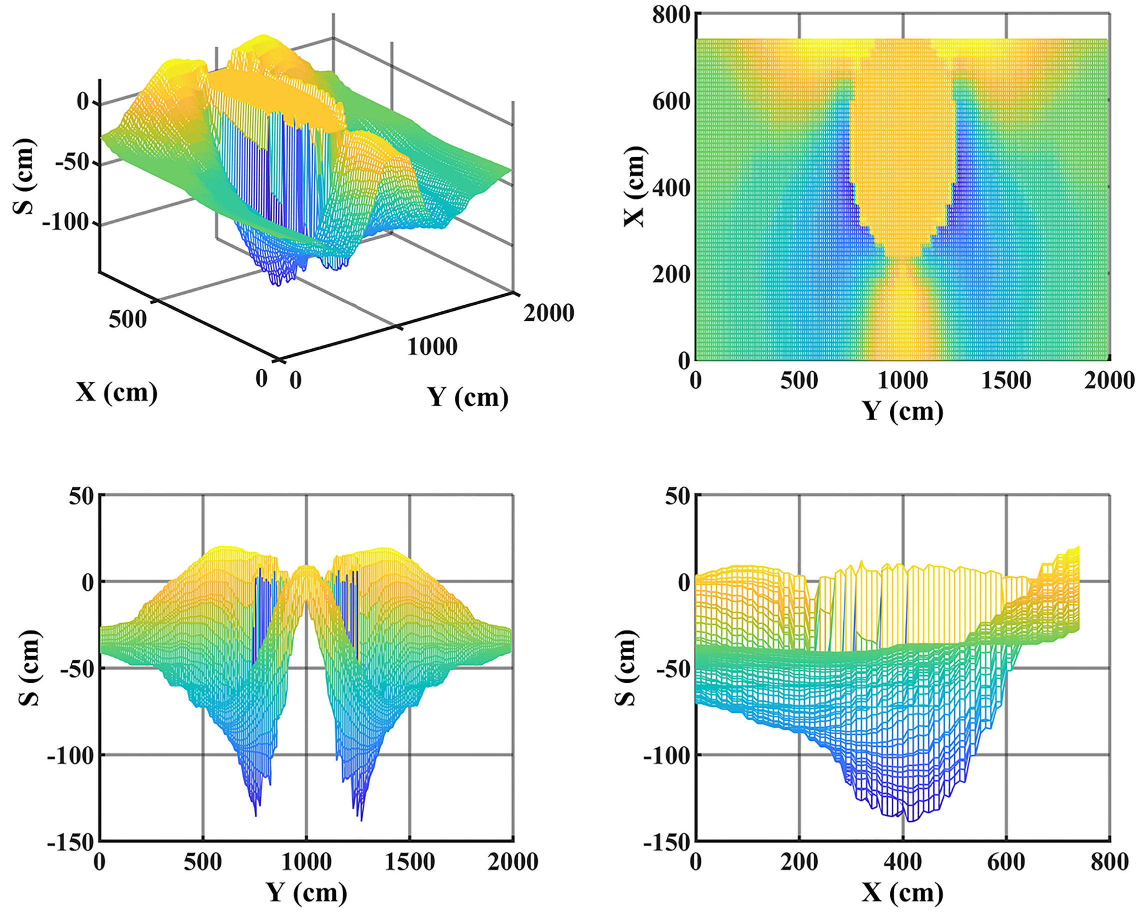

FIGURE 7
Scour volume calculation process.

the scour depth at this distance. The shear stress on both sides of the OWF is mainly influenced by the accelerating flow that bypassed the OWF. As analyzed in the previous section, when *G*/*D*< 0, AR cannot affect the flow acceleration on either side of the OWF. Therefore, at the initial time of scour, the shear stress on both sides of the OWF at *G*/*D* = -1.0 and in the control case is almost the same. However, at the end of the scour, the shear stress and scour depths on both sides of the OWF at *G*/*D* = -1.0 are significantly less than those in the control case, which indicates that at *G*/*D*= -1.0 and *G*/*D*= 1.0, indicating the mechanism of the reduction of the scour depth is different. Therefore, the mechanism of scour protection is analyzed separately for *G*/*D* > 0 and *G*/*D*< 0 in the following section. Finally, when *G*/*D* = 4.0, the shear stress on both sides of the OWF decreased only slightly compared with the control case. This also confirms the previous conclusion that the effect of the AR on the flow field around the OWF gradually decreases with increasing distance.

TABLE 2 Parameters used in the numerical calculations.

Parameter	Value
Diameter of OWF (m)	5
Side length of AR (m)	2
Water depth (m)	10
Velocity (m/s)	0.6
Diameter of the sediment d_i (mm)	0.5
Density of the sediment ρ_s (kg/m^3)	2650

The streamline distribution around the OWF at *G*/*D* = 0.5, *G*/*D* = 1.0, and *G*/*D* = 2.0 compared to the control case are shown in Figure 11. It can be clearly seen from the figure that the horseshoe vortex in front of the OWF and a streamlined compression at the OWF side lead to an increase in the bed shear stress, which is the main reason for the sediment scour around the OWF. In addition, the wake vortex behind the OWF developed rapidly and moved downstream, which is also the cause of scour. Significantly, the AR disrupted the horseshoe vortex system in front of the OWF, and a wake region is formed behind the ARs. This reduces the strength and size of the horseshoe vortex. This reduces the bed area controlled by the horseshoe vortex, and the AR eventually acts as scour protection for the sediments around the OWF.

Moreover, it can also be found that as the AR gradually moves farther away from the OWF, the strength of the horseshoe vortex becomes the dominant effect. Therefore, the scour depth and

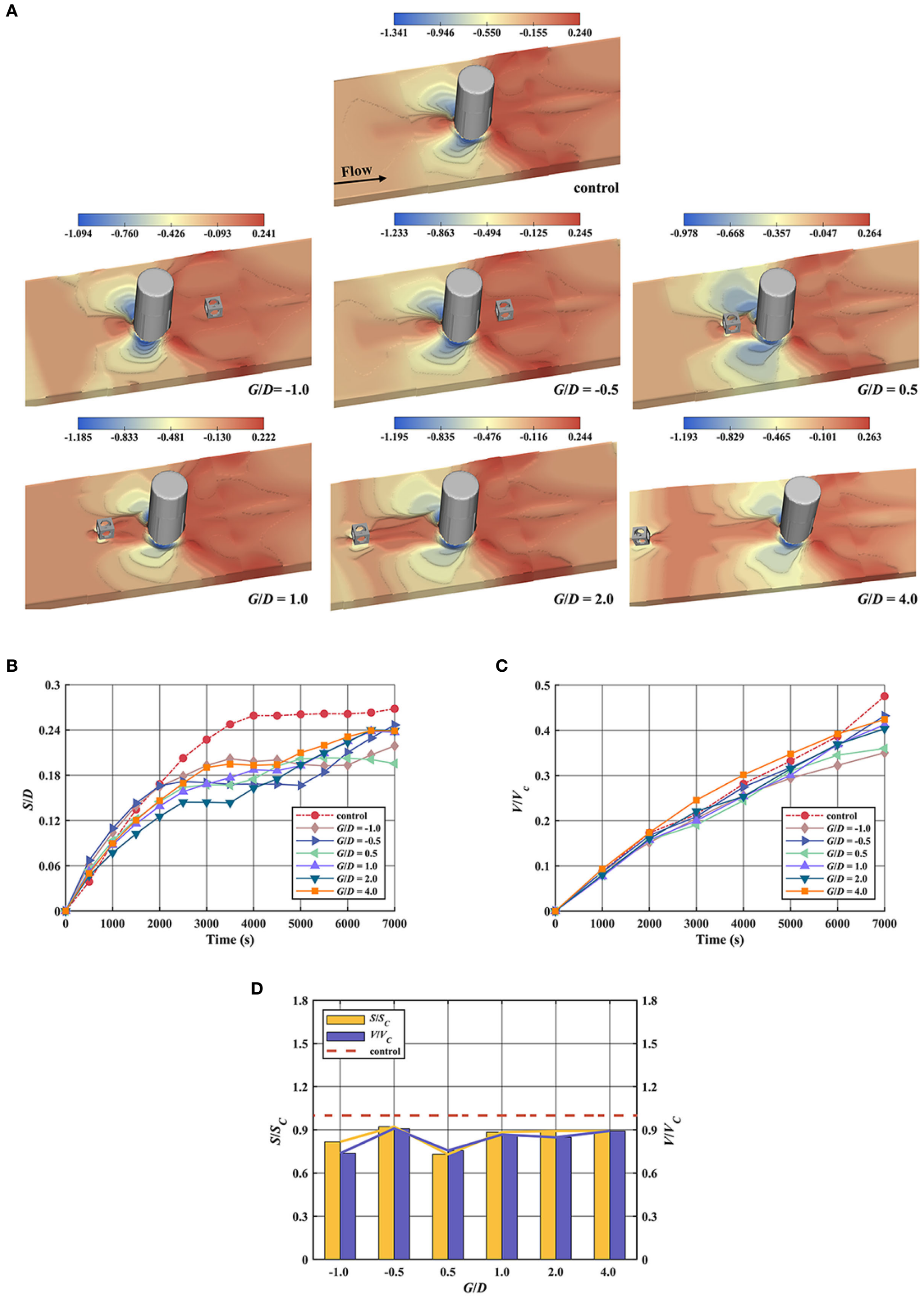

FIGURE 8
Scour calculation results of the Group I: **(A)** seabed surface elevation change around the OWF **(B)** time evolution of the scour depth around the OWF **(C)** time evolution of the scour volume around the OWF **(D)** standardization of scour depth and scour volume.

volume around the OWF increase with an increase in *G*/*D*. The turbulence intensity is a dimensionless physical quantity that represents the ratio of turbulent fluctuating velocity to the average velocity. Typically, turbulence intensities greater than 10 are considered high turbulence intensity, and the high turbulence intensities around the OWF and ARs are shown in Figure 12A. The turbulence intensity on both sides of the OWF gradually increased with *G*/*D*; therefore, the scour is more violent.

A comparison of the vortex fields of the control and $G/D< 0$ cases are shown in Figure 12B. The vortex alternately forms near the bed behind the OWF and sheds downstream. The vortex is broken by the AR but continued to shed when the AR is located at $G/D =$

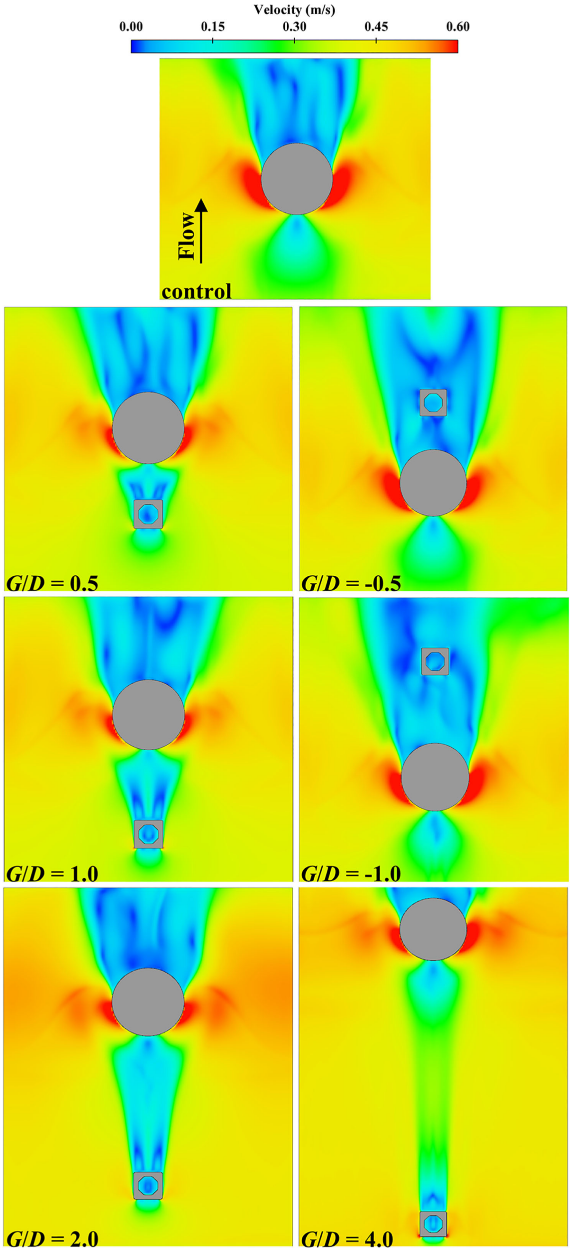

FIGURE 9
Distribution of the flow velocity contour near the seabed around the OWF in Group I.

-0.5. However, the vortex is almost completely broken after passing through AR. When AR is located at *G*/*D* = -1.0, it does not continue to be shed due to the broken vortex, thus causing the flow behind the OWF to become more stable and the scour intensity to be reduced, which eventually has a significant scour protection effect. This phenomenon not only explains the mechanism by which ARs can effectively reduce scour depth and scour volume when *G*/*D*< 0 but also clarifies why the AR at *G*/*D* = -1.0 are more effective in reducing scour intensity than at *G*/*D* = -0.5. The streamlined distribution of the rear of the OWF in the three cases are shown in Figure 12C. The top and bottom behind the OWF formed large-scale vortex shedding in the control case. Large-scale vortex shedding causes more sediment to roll up and be transported, resulting in serious scour. The AR significantly reduced the vortex formation with the OWF and broke the vortex behind, successfully destroying the original vortex system behind the OWF and playing a significant role in scour protection.

3.2 Influence of *P*/*L*

Figure 13A shows the seabed surface elevation around the OWF under different *P*/*L* values at the last moment. Regular semicircular scour holes formed on each side of the OWF and developed in front of and behind the OWF when *P*/*L* = 0. From a previous study (Yang M. et al., 2022), it is known that the sides of the AR in the flow field form a fluid compression and accelerate the movement to the rear. At this time, the width of the AR in the present case is slightly less

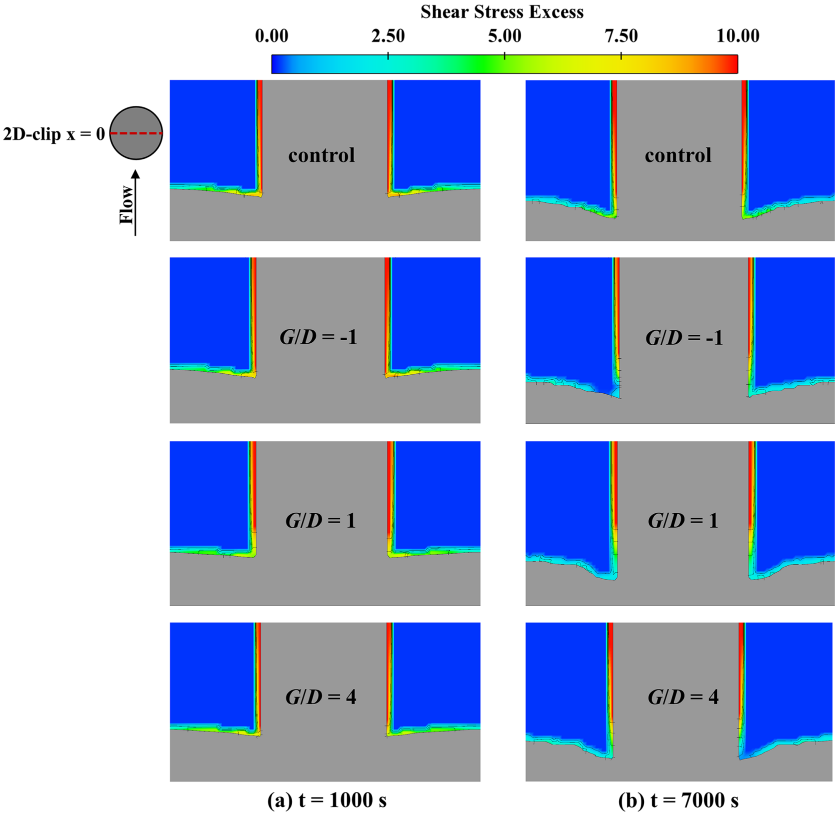

FIGURE 10
Shear stress distribution on both sides of the OWF in Group I.

than the D of the OWF, which accelerates from the outer side of the AR to the two sides of the OWF. Thus, it mixes with the flow on both sides of the OWF, and accelerates the flow, resulting in the flow and scour around the two sides of the OWF being more intense. In addition, the extent of the scour hole cannot develop to the rear of the OWF with a gradual increase in P/L, but to the inner side of the two ARs, and finally form an M-shaped scour hole. The reason for this phenomenon is that with an increase in P/L, the fluid acceleration area on the inner side of the ARs starts to form gradually and converges with the acceleration area on both sides

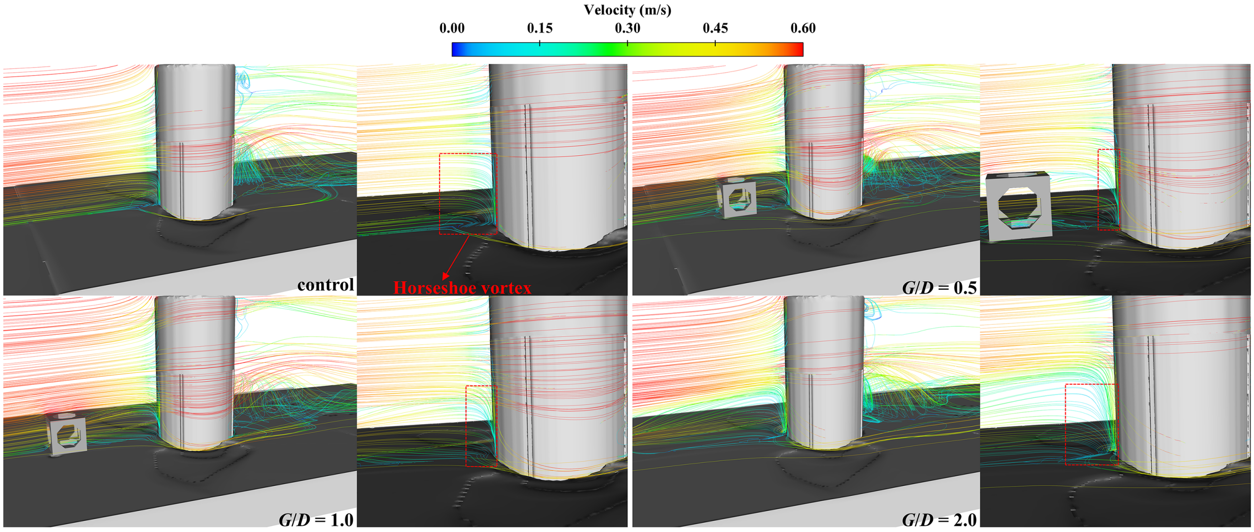

FIGURE 11
Streamline distribution around the OWF in Group I.

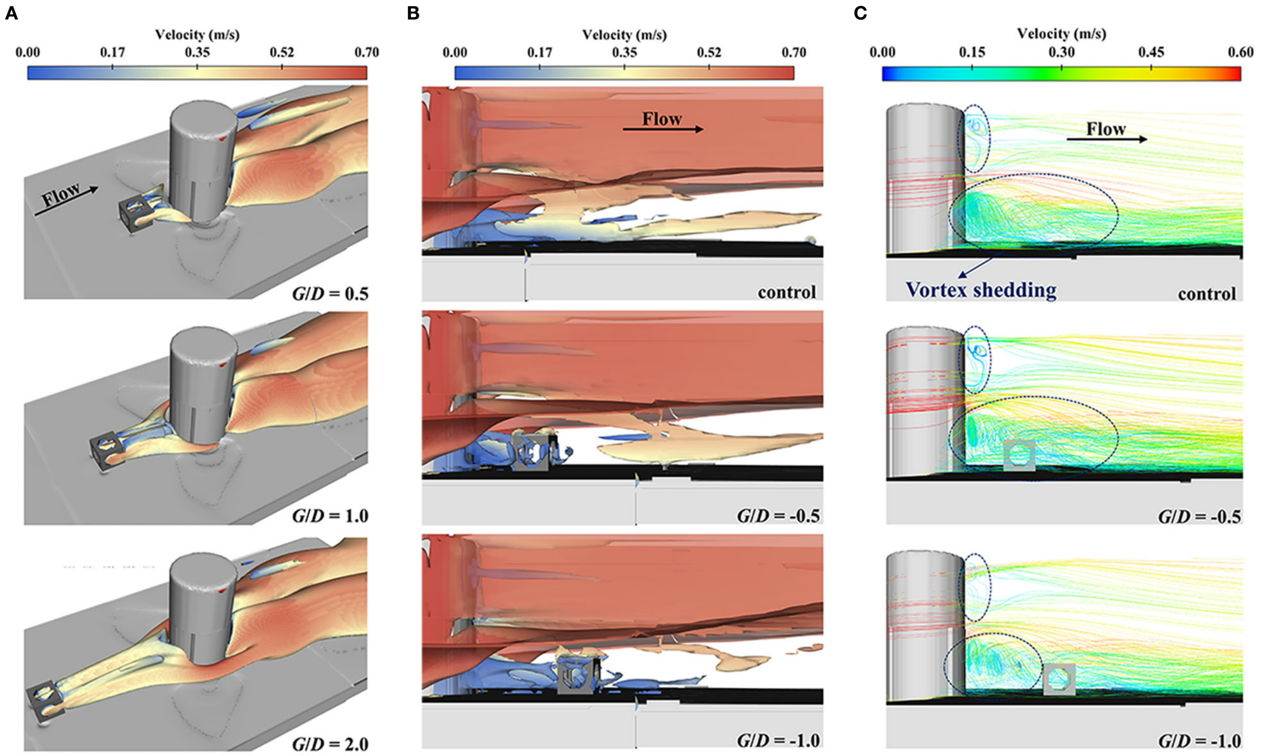

FIGURE 12
Turbulence structure and streamline distribution around the OWF: **(A)** turbulence intensity around the OWF **(B)** vorticity around the OWF (under Q-Criterion) **(C)** streamline distribution behind the OWF.

of the OWF. This causes turbulence fluctuations between the inner side of the ARs and the OWF, which eventually leads to a larger scour area.

The time evolutions of the scour depth and scour volume around the OWF in the control case and Group II are shown in Figures 13B, C. For the scour depth, it can be clearly found that the scour depth gradually decreases with the increase of P/L. When $P/L< 4.0$, the scour depth around OWF is greater than that of the Control case. This indicates that, within this arrangement, ARs have a negative effect on the scour depth around the OWF. The maximum scour depth occurred at $P/L = 0$, which is approximately 28% greater than that of the control case. When $P/L = 4.0$ or $P/L = 5.0$, the scour depth around the OWF is almost the same as that of the control case, with a difference of no more than 3%. From the development process of scour depth with time, the time to reach scour equilibrium is longer than that of the control case when $P/L = 0$ and $P/L = 1.0$. The development of the scour depth around the OWF is similar at $P/L = 2.0$ and $P/L = 3.0$. After 5000s, the scour rate decreased and gradually equilibrated. The scour development process is almost identical when $P/L = 4.0$ and $P/L = 5.0$. The difference in the final scour depth between them and the control case is no more than 3%, which indicates that when $P/L > 3.0$, the negative impact of ARs on the scour depth around the OWF disappears. However, the scour volume also decreased gradually with an increase in P/L. It is worth noting that except for the scour volume when $P/L = 0$, which is the same as that of the control case, the scour volume of the remaining five cases is less than that of the control case. The lowest scour volume is reduced by 31% compared with the control case when $P/L = 5.0$. This result indicates that, although the parallel arrangement of the ARs will have a negative effect on increasing the maximum scour depth around the OWF, it will positively affect the overall volume of scour occurring around the OWF. Figure 13D illustrates the variation in scour depth and scour volume around the OWF in Group II, where the scour depth and scour volume are normalized by the control case. It can be seen from the figure that the change rate of scour depth and scour volume gradually approaches 0 with the increase in P/L, indicating that at $G/D = 1.0$. Moreover, the P/L between the two ARs should be greater than 3.0 to avoid aggravating the maximum scour depth around the OWF.

The streamlined distribution around the OWF in Group II compared to the control case are shown in Figure 14. It can be seen that an accelerated upwelling is formed above the contact surface of the two ARs. When $P/L = 0$, the upwelling causes turbulent fluctuations in front of the OWF. The streamlines are compressed and accelerated on both sides of the OWF, which are the flow motion characteristics that cause severe scour. It can also be observed that with an increase in P/L, the turbulent fluctuations in front of the OWF gradually stabilize and disappear. The streamline distribution on both sides is gradually uniform, which is the reason why the scour depth decreases with an increase in P/L. In addition, the flow velocity behind the AR is low because the wake region is formed at the rear of each AR, and the bed shear stress is lower than the critical shear stress of the sediment. Therefore, it can

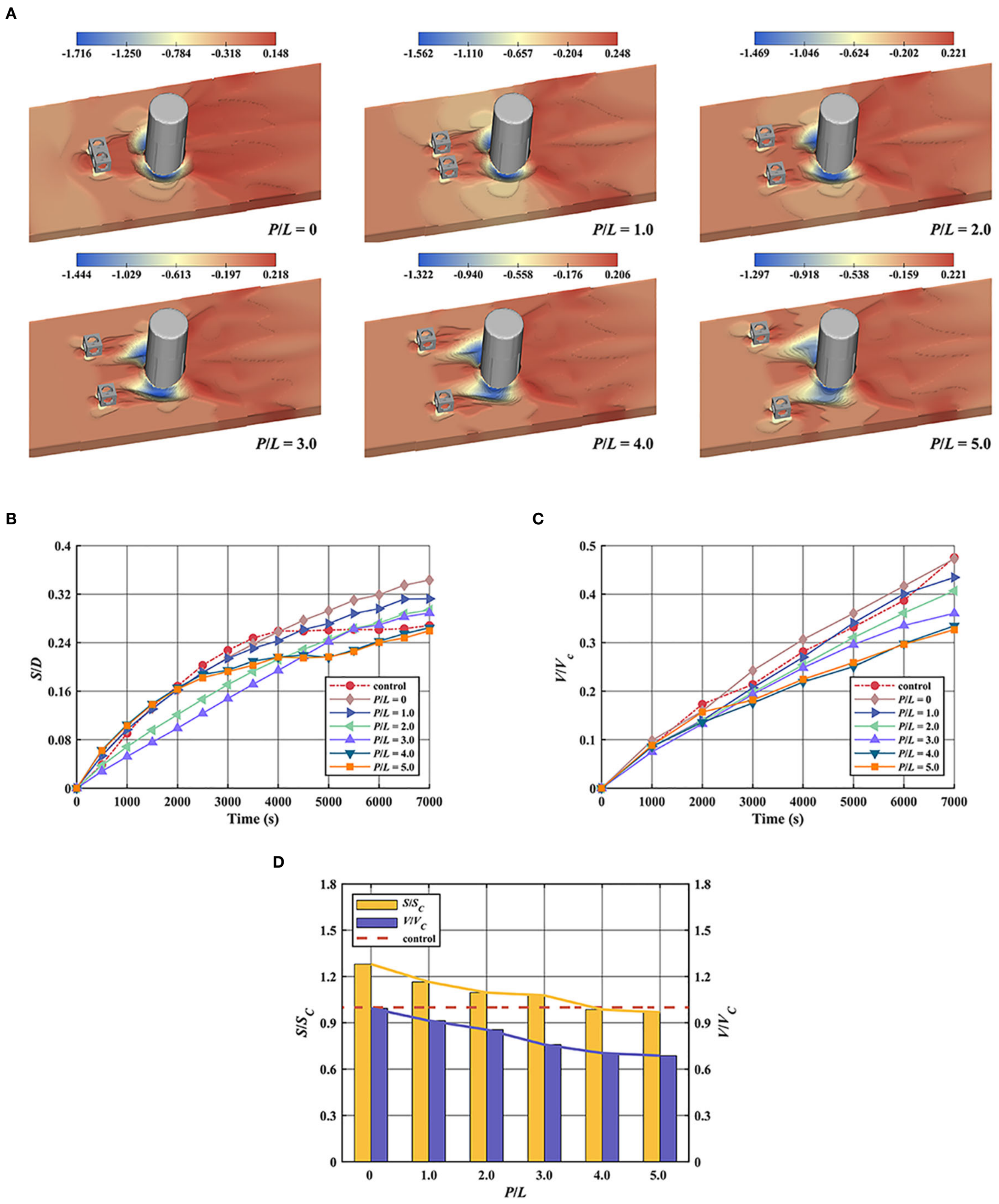

FIGURE 13
Scour calculation results of Group II: **(A)** seabed surface elevation change around the OWF **(B)** time evolution of the scour depth **(C)** time evolution of the scour volume **(D)** standardization of scour depth and scour volume.

be clearly seen that AR effectively prevents the expansion of the scour hole. However, the vortex shedding behind the OWF gradually becomes regular with an increase in *P*/*L*. These two physical phenomena led to a gradual decrease in scour volume with an increase in *P*/*L*.

3.3 Influence of the *T*/*L*

Figure 15A depicts the seabed surface elevation around the OWF under different *T*/*L* values between the AR values at the last moment. As the wake region of the ARs increases with increasing *T*/

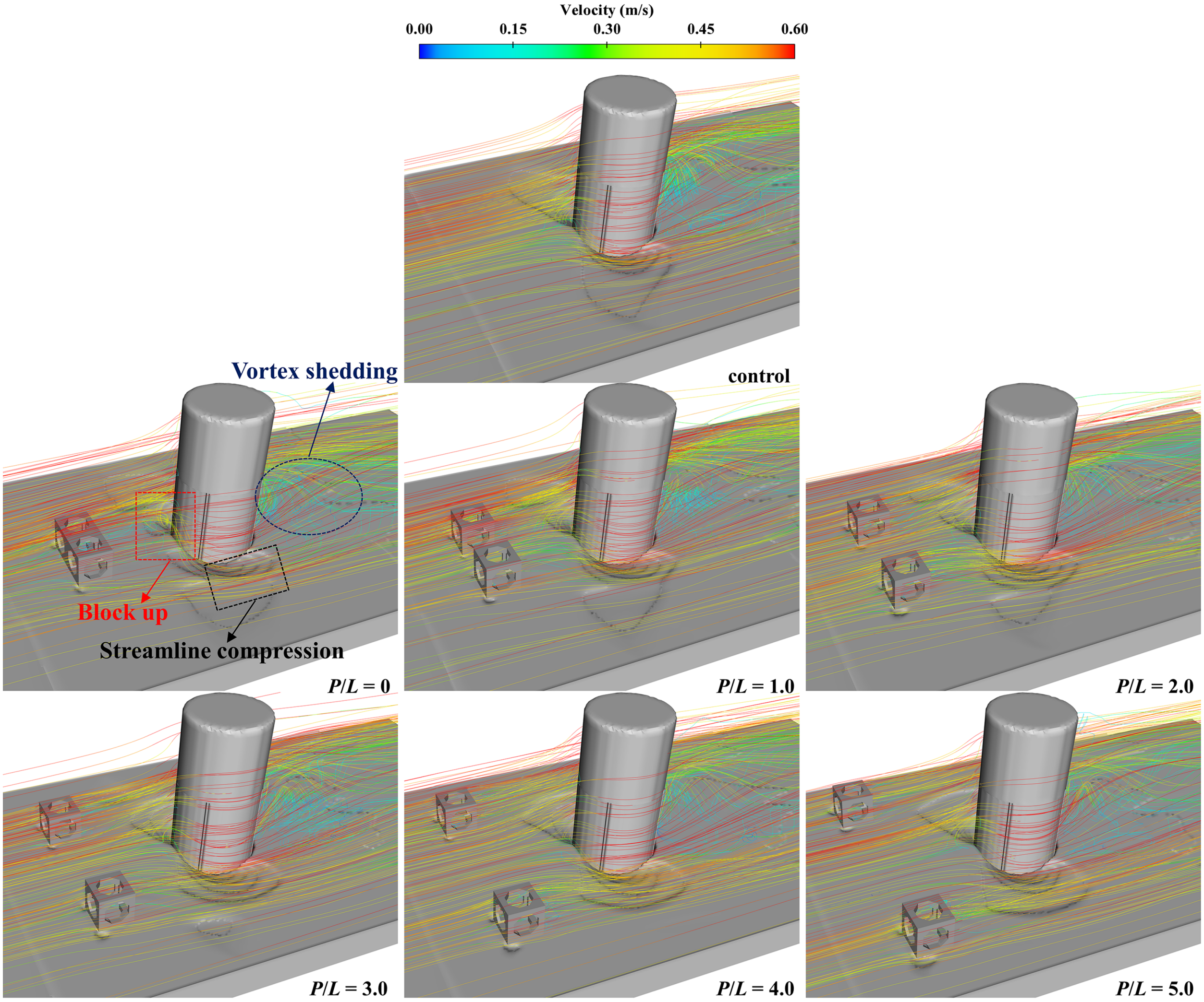

FIGURE 14
Streamline distribution around the OWF in Group II.

L (Liu and Su, 2013), the scope of the slow-flow area between the OWF and ARs also increases. This finally leads to an expansion of the extent of sediment deposition in front of the OWF with an increase in T/L. The sediment scour pattern around the OWF is almost identical in these four cases. However, it can be found that the scour depth in the outer area of the scour hole decreases with increasing T/L.

The time evolution of the scour depth and scour volume around the OWF in the control case and Group III are shown in Figures 15B, C. In this Group, ARs reduce the maximum scour depth and volume around the OWF and play an effective role in scour protection. It has the following rules for scour depth: $T/L = 0 < T/L = 0.5 \approx T/L = 2.0 < T/L = 1.0 <$ control. Compared with the Control case, the minimum scour depth occurred at $T/L = 0$, which is approximately 21% less than the control case and reached the scour equilibrium stage at 5000s. The scour development process and final scour depth of $T/L = 0.5$, and $T/L = 2.0$ are almost the same, approximately 10% more than the control case. The maximum scour depth occurred when $T/L = 1.0$, which is approximately 2% less than that of the control case. However, the scour volume in Group III is noteworthy. In these four cases of Group III, the change process of the scour volume and the value at the last moment are almost the same, and the maximum difference is no more than 3%. Compared with the Control case, the scour volume around the OWF decreased by 24% ($T/L = 0$), 22% ($T/L = 0.5$), 21% ($T/L = 1.0$), and 23% ($T/L = 2.0$). However, under the condition of $G/D = 1$ in Group I, the scour volume is only 13% less than that in the control case. The present results show that the tandem arrangement of the ARs can significantly reduce the scour volume around the OWF, but changes in the spacing between the ARs have little effect on the scour volume, as shown in Figure 15D.

The streamlined distribution around the OWF in Group III are shown in Figure 16A. The area controlled by the horseshoe vortex in front of the OWF is similar when $T/L = 0$ and $T/L = 0.5$. The horseshoe range in front of the OWF is significantly expanded when $T/L = 1.0$ and

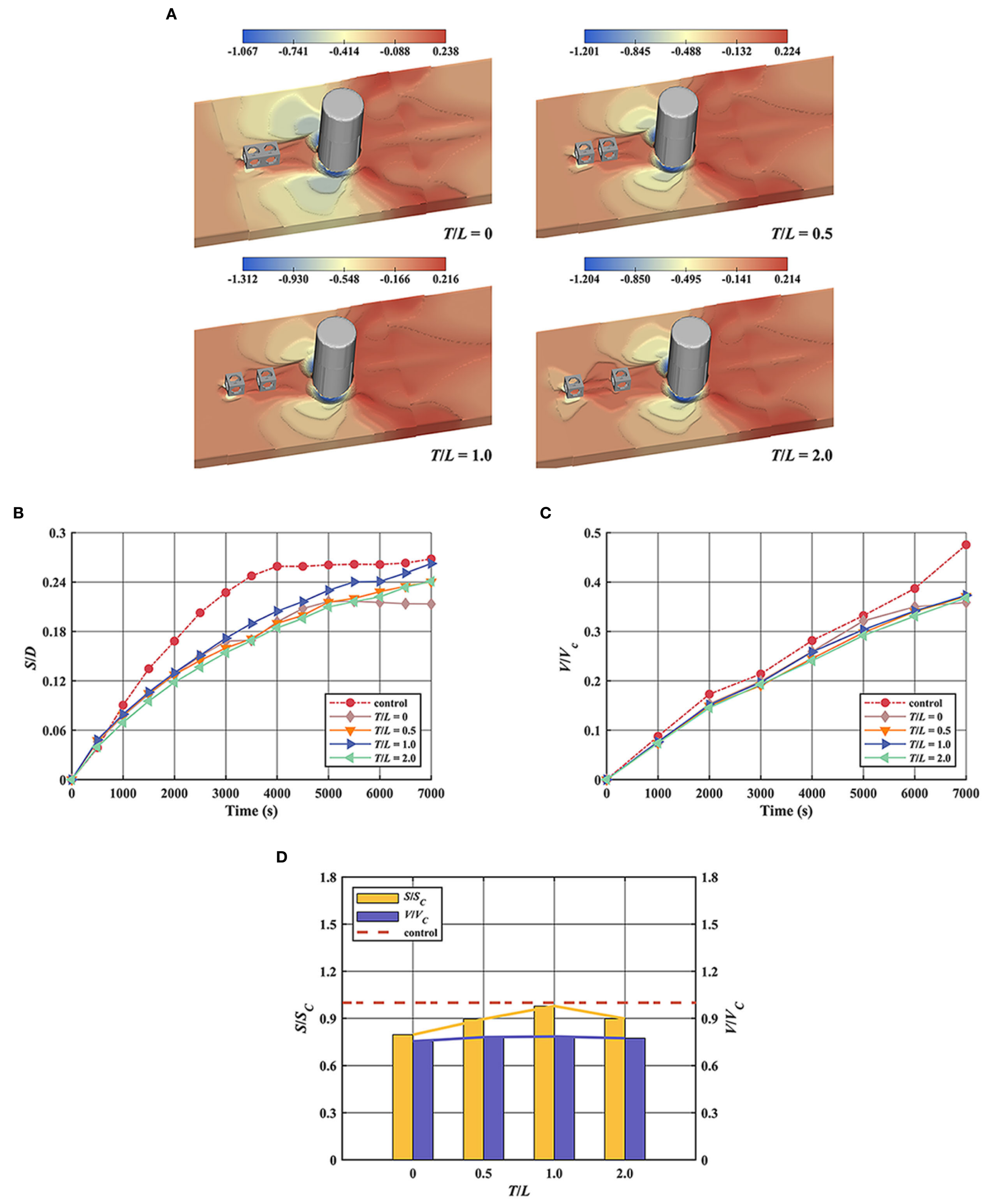

FIGURE 15
Scour calculation results of the Group III: **(A)** seabed surface elevation change around the OWF **(B)** time evolution of the scour depth around the OWF **(C)** time evolution of the scour volume around the OWF **(D)** standardization of scour depth and scour volume.

T/*L* = 2.0. However, the scour depth around the OWF at *T*/*L* = 2.0 is lower than that at *T*/*L* = 1.0. To explore the reasons for this result, the high turbulence intensity around the OWF and Ars, when *T*/*L* = 1.0 and *T*/*L* = 2.0, are shown in Figure 16B. From the figure, it can be seen that the momentum transfer of intense turbulence occurs between the two ARs when *T*/*L* = 1.0, resulting in a higher turbulent kinetic energy of the fluids around the OWF, and ultimately, more sediment is scoured away. However, when *T*/*L* = 2.0, it can be clearly seen that the momentum transfer of turbulence between the two ARs is reduced. This also affects the kinetic energy of turbulence moving from the AR to the OWF and finally results in a lower turbulence kinetic energy around the OWF at *T*/*L* = 2.0 and a lower scour depth compared to *T*/*L* = 1.0.

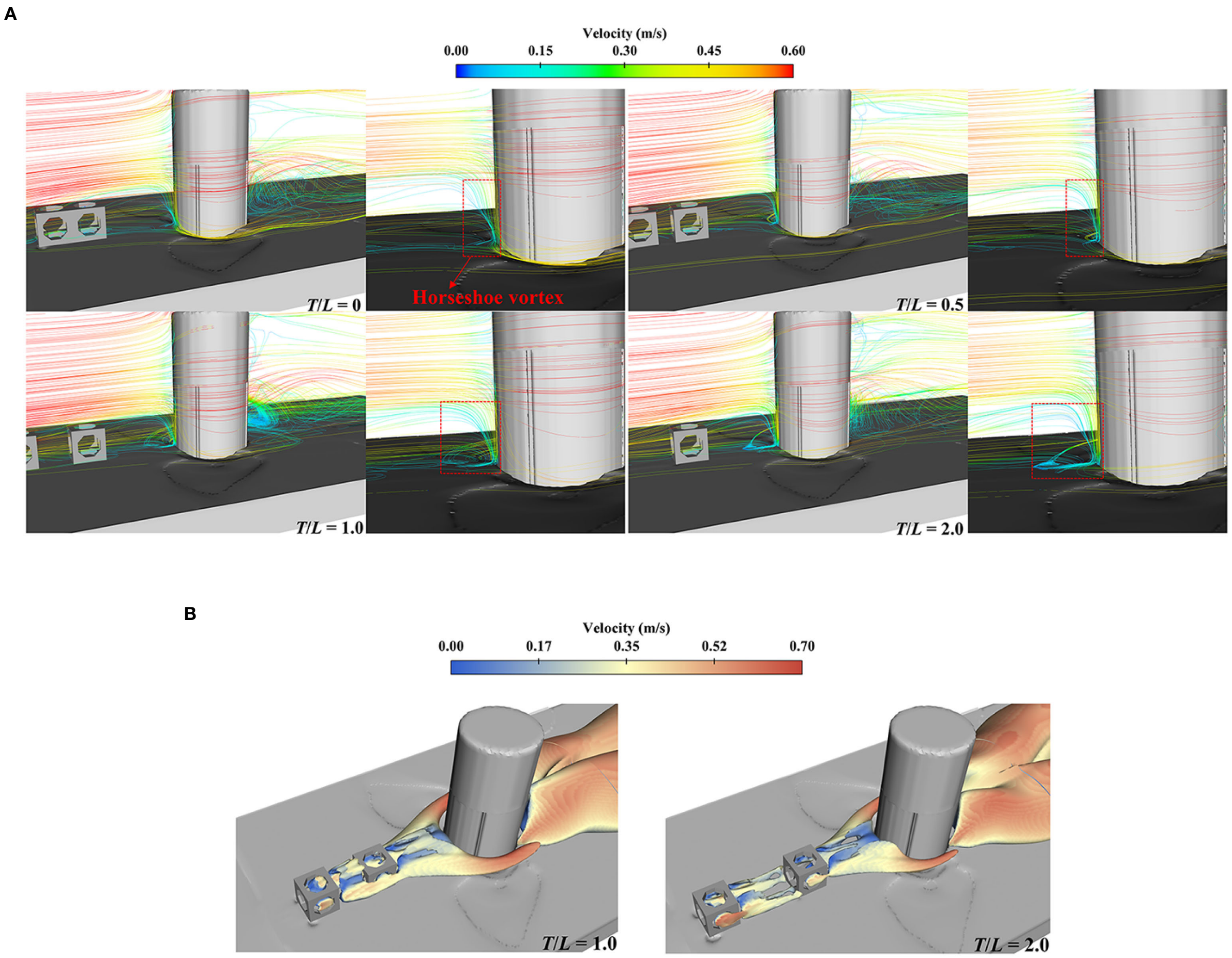

FIGURE 16
Flow velocity characteristics around the OWF in the Group III: **(A)** streamline distribution around the OWF **(B)** turbulence intensity around the OWF.

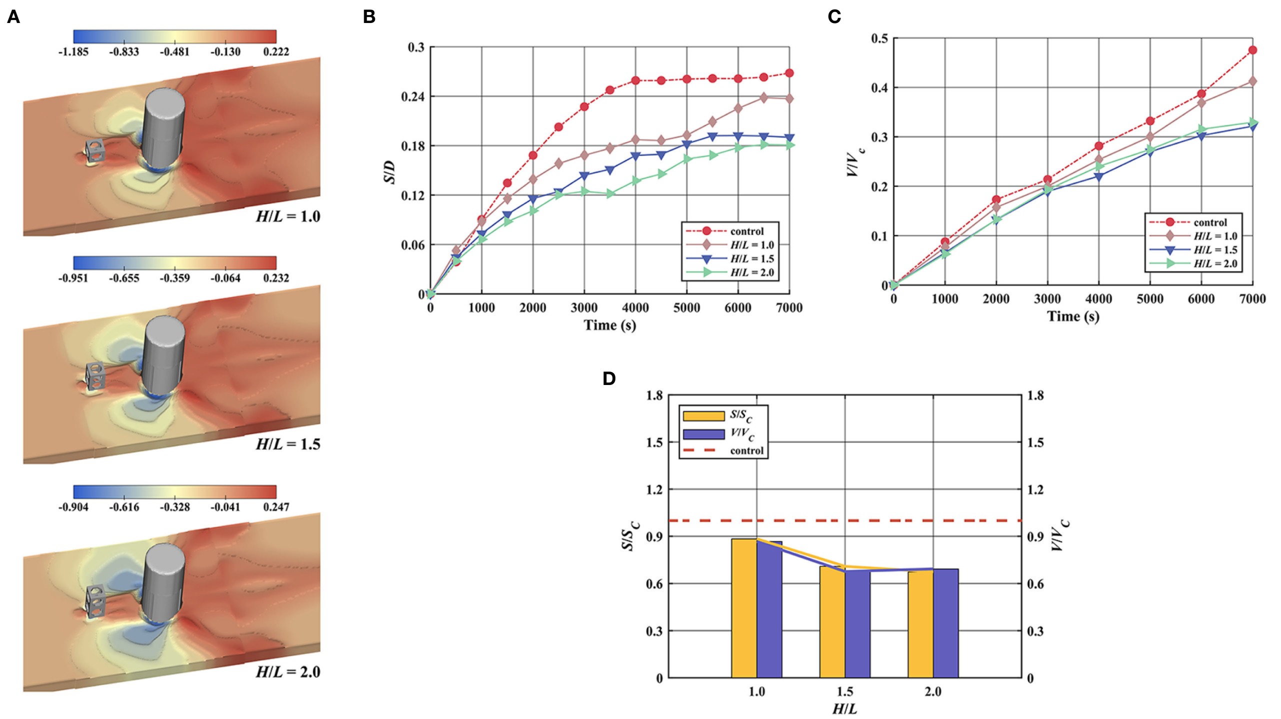

FIGURE 17
Scour calculation results of the Group IV: **(A)** seabed surface elevation change around the OWF **(B)** time evolution of the scour depth around the OWF **(C)** time evolution of the scour volume around the OWF **(D)** standardization of scour depth and scour volume.

3.4 Influence of the *H*/*L*

Figure 17A depicts the seabed surface elevation around the OWF under different *H*/*L* values between the AR values at the last moment. The depth of the scour holes on both sides of the OWF decreased with an increase in the AR height. The higher the height of the AR, the lower the slope of the scour holes. In addition, the scour range in front of the OWF also increased with an increase in the height of the AR, as can be seen from the figure that the scour depth of the scour area outside the scour pit gradually deepened with increasing height.

The time evolutions of the scour depth and scour volume around the OWF in the control case and Group IV are shown in Figures 17B, C. The maximum scour depth around the OWF decreased gradually with increasing AR height. The minimum scour depth occurred at *H*/*L* = 2.0, which is 33% less than that of the control case.

An increase in AR height could improve the scour protection ability around the OWF. It is found that the scour depth reached the equilibrium stage at *H*/*L* = 1.5 and *H*/*L* = 2.0. In terms of scour volume, all three cases significantly reduced the scour volume of the terrain surrounding the OWF, and the results for *H*/*L* = 1.5 and *H*/*L* = 2.0 are comparable, with reductions of 32% and 31%, respectively, compared to the control case. Furthermore, no more calculation cases for the height of the AR have been set to study because of the limitation of calculation resources. However, it is still possible to find a significant decrease in the rate of change of scour depth and scour volume with height change Figure 17D. The scour depth and scour volume of *H*/*L* = 1.5 are 20% and 22% less than those of *H*/*L* = 1.0, respectively. However, the difference in scour results between *H*/*L* = 1.5 and *H*/*L* = 2.0 did not exceed 5%. In contrast, the differences in scour depth and scour volume between *H*/*L* = 1.5 and *H*/*L* = 2.0 are only 5% and 2%, respectively. The results demonstrate that although the increase in height effectively reduces scour around the OWF, there is a threshold value for the height of the AR beyond which the gain in scour protection from an increase in height is less.

Figure 18 compares the distribution of the flow velocity near the seabed around the OWF for the control case and Group IV at the beginning of the scour. The figure shows that the extent of the high-flow area on both sides of the OWF regularly decreases with an increase in the AR height. The increase in the height of the ARs will increase the height range of the wake region, and the change in the height of the wake region will affect the interaction with the horseshoe vortex (Li X. et al., 2022). The wake vortex behind the higher AR is at a higher elevation, merging with the horseshoe vortex and weakening it (Figure 19). This eventually leads to a slower flow around the OWF, lower bed shear stress, and weaker scour around the OWF as the height of the ARs increases. In the future, more cases need to be simulated to explore and obtain the optimal AR height considering both the construction cost and the effectiveness of scour protection.

4 Conclusion

In this study, the potential of scour protection for OWF using ARs inspired by the mechanism of passive scour protection is evaluated numerically. A numerical model using the RANS

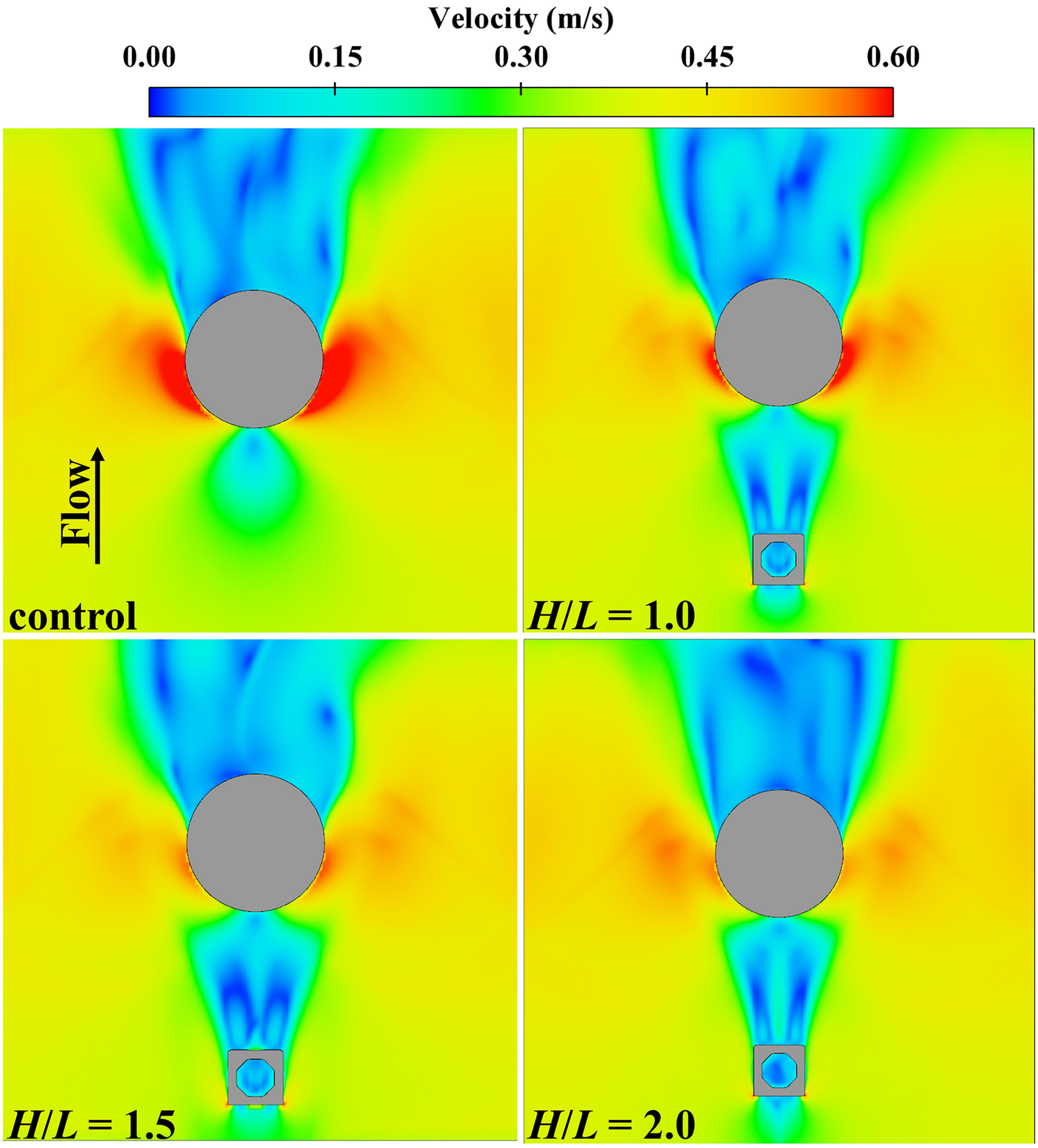

FIGURE 18
Distribution of the flow velocity contour near the seabed around the OWF in Group IV.

method with the RNG *k*-ϵ turbulence model and sediment transport model is conducted to investigate the effects of various distances between individual AR and the OWF on flow characteristics and sediment scour changes around the OWF. Based on this, the impact of various AR arrangements on the scour process around the OWF is also analyzed. Based on the numerical results, the following conclusions are drawn.

1. AR significantly reduced the scour depth and scour volume around the OWF and played a role in scour protection. The horseshoe vortex in front of the OWF is weakened by the AR and the range of fluid acceleration areas on both sides of the OWF. The shear stress on the seabed is reduced due to the effect of AR, which is the mechanism for the AR to provide a scour protection when $G/D > 0$. Finally, the scour depth and scour volume are reduced. $G/D = 0.5$ provided the most effective scour protection, which resulted in a 27.0% reduction in scour depth. The wake vortex shedding after the OWF is destroyed by the AR, which is the mechanism by which the AR provided scour protection

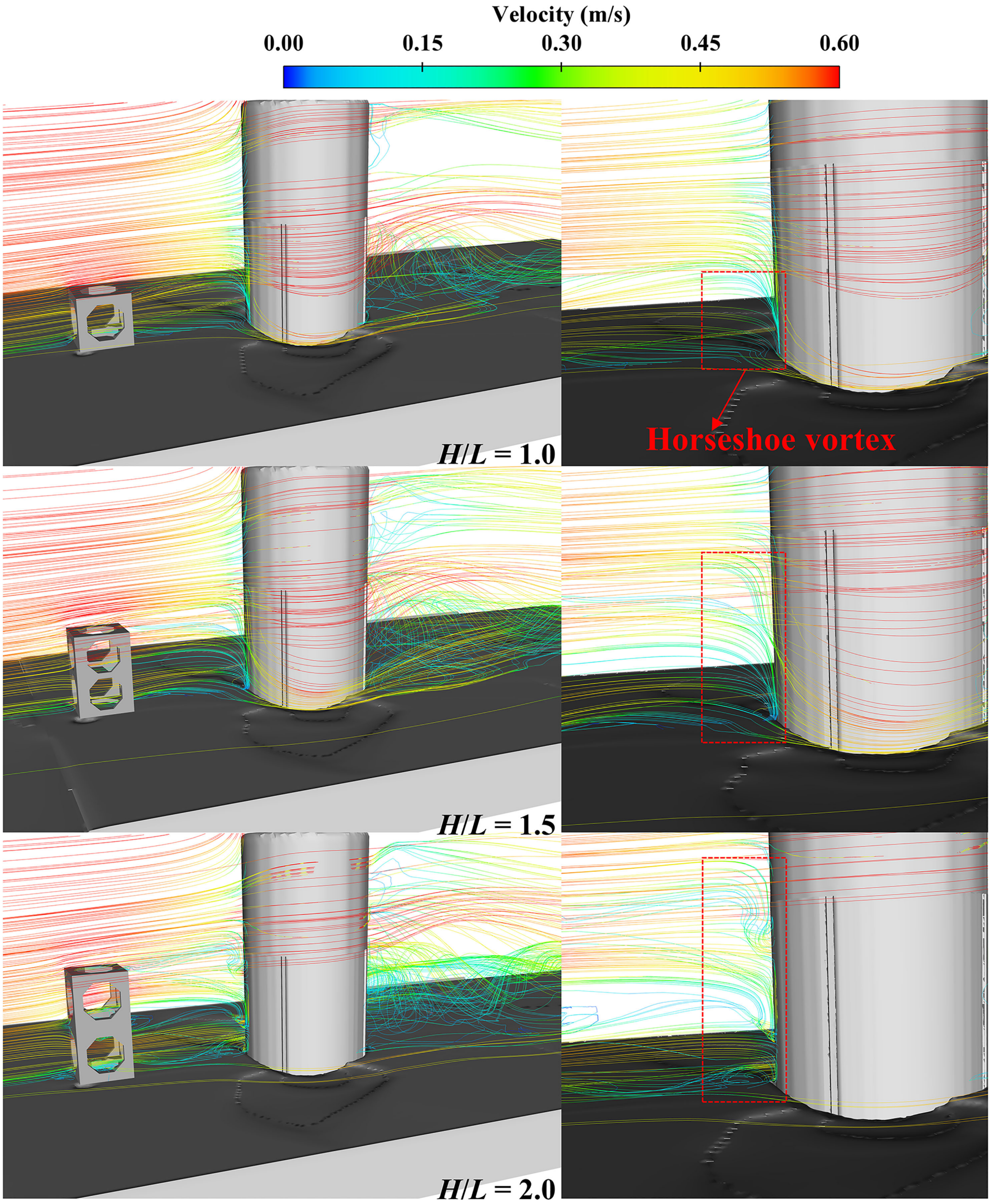

FIGURE 19
Streamline distribution around the OWF in Group IV.

when $G/D < 0$. $G/D = -1.0$ provided the most effective scour protection, which resulted in a 26% reduction in scour volume.

2. The parallel arrangement of the ARs had a negative impact on the maximum scour depth around the OWF due to the momentum transfer and acceleration of the fluid on the inner sides of the ARs and both sides of the OWF. However, this negative effect gradually decreased with increasing P/L, and when $P/L > 3.0$, the negative effects completely disappeared. The parallel arrangement of ARs had a positive role in the maximum scour volume around the OWF because the range of the wake region generated by ARs increased with an increase in the P/L. $P/L = 5.0$ provided the most effective scour protection, which resulted in a 31% reduction in scour volume.
3. The tandem arrangement of ARs effectively reduced the scour depth and scour volume around the OWF, because this arrangement affected the horseshoe vortex and reduced the turbulence intensity on both sides of the OWF. $T/L = 0$ provided the most effective scour protection, resulting in a 21% reduction in the scour depth. In addition, the tandem arrangement of ARs significantly reduced the scour volume

around the OWF compared with a single AR. However, the change in T/L had almost no effect on the reduction in scour volume. The four current T/L cases had almost the same scour protection effect, which resulted in approximately 21%–24% of the scour volume.

4. The increase in the height of the AR provided the most significant scour protection at a fixed distance from the OWF, as a higher AR produced a higher wake region and interacted more intensely with the horseshoe vortex in height. H/L = 2.0 provided the most effective scour protection, which resulted in a 33% reduction in the scour depth. There is a limit for the effect of scour protection by increasing the height of the AR, beyond which the effect of scour protection did not change.

The scour results obtained in this study can provide guidance not only for the arrangement method of ARs with OWFs, but also be applied to the arrangement method of ARs with other offshore pile structures such as submerged cage and marine ranching platforms. It also provides an innovative and more ecologically effective passive scour protection method for the traditional pile scour problem.

Data availability statement

The raw data supporting the conclusions of this article will be made available by the authors, without undue reservation.

Author contributions

MY performed the simulation and wrote the manuscript. YT and FZ helped design the study, and critically revised the manuscript. SX edited the manuscript. All authors listed have made a direct and substantial contribution to this work, gave final approval for publication, and agreed to be held accountable for the work performed therein.

Funding

The study is supported by National Natural Science Foundation of China (NSFC: 32073025).

Conflict of interest

The authors declare that the research was conducted in the absence of any commercial or financial relationships that could be construed as a potential conflict of interest.

Publisher's note

References

Almeida, L. (2017). REEFS: an artificial reef for wave energy harnessing and shore protection – a new concept towards multipurpose sustainable solutions. *Renewable Energy* 114, 817–829. doi: 10.1016/j.renene.2017.07.076

Baykal, C., Sumer, B., Fuhrman, D., Jacobsen, N., and Fredsøe, J. (2015). Numerical investigation of flow and scour around a vertical circular cylinder. *Philos. Trans. R. Society Mathematical Physical Eng. Sci.* 373, 20140104. doi: 10.1098/rsta.2014.0104

Bilgili, M., Yasar, A., and Simsek, E. (2011). Offshore wind power development in Europe and its comparison with onshore counterpart. *Renewable Sustain. Energy Rev.* 15, 905–915. doi: 10.1016/j.rser.2010.11.006

Chen, Y., and Lin, H. (2022). Overview of the development of offshore wind power generation in China. *Sustain. Energy Technol. Assessments* 53, 102766. doi: 10.1016/j.seta.2022.102766

Chen, X., Zhang, X., Liu, X., Zhang, F., Yan, J., and Wang, H. (2022). Experimental study of scour characteristics and scour hole dimensions in consolidated silt sediment under a current. *Ocean Eng.* 266, 112801. doi: 10.1016/j.oceaneng.2022.112801

Chu, Y. I., Wang, C. M., and Zhang, H. (2022). A frequency domain approach for analyzing motion responses of integrated offshore fish cage and wind turbine under wind and wave actions. *Aquacultural Eng.* 97, 102241. doi: 10.1016/j.aquaeng.2022.102241

Dai, S., Han, B., Wang, B., Luo, J., and He, B. (2021). Influence of soil scour on lateral behavior of large-diameter offshore wind-turbine monopile and corresponding scour monitoring method. *Ocean Eng.* 239, 109809. doi: 10.1016/j.oceaneng.2021.109809

Deng, X., He, S., and Cao, Z. (2022). Numerical investigation of the local scour around a coconut tree root foundation under wave-current joint actions. *Ocean Eng.* 245, 110563. doi: 10.1016/j.oceaneng.2022.110563

Fang, G., Yu, H., Sheng, H., Tang, Y., and Liang, Z. (2021). Comparative analysis of microbial communities between water and sediment in laoshan bay marine ranching with varied aquaculture activities. *Mar. Pollut. Bull.* 173, 112990. doi: 10.1016/j.marpolbul.2021.112990

Gautam, S., Dutta, D., Bihs, H., and Afzal, M. (2021). Three-dimensional computational fluid dynamics modelling of scour around a single pile due to combined action of the waves and current using level-set method. *Coast. Eng.* 170, 104002. doi: 10.1016/j.coastaleng.2021.104002

Ghiasian, M., Carrick, J., Rhode-Barbarigos, L., Haus, B., Baker, A., and Lirman, D. (2021). Dissipation of wave energy by a hybrid artificial reef in a wave simulator: implications for coastal resilience and shoreline protection. *Limnol. Oceanogr. Methods* 19, 1–7. doi: 10.1002/lom3.10400

Huang, C., Afero, F., Hung, C., Chen, B., Nan, F., Chiang, W., et al. (2022). Economic feasibility assessment of cage aquaculture in offshore wind power generation areas in changhua county, Taiwan. *Aquaculture* 548, 737611. doi: 10.1016/j.aquaculture.2021.737611

Jenkins, S., Inman, D., Richardson, M., Wever, T., and Wasyl, J. (2007). Scour and burial mechanics of objects in the nearshore. *IEEE J. Oceanic Eng.* 32, 78–90. doi: 10.1109/JOE.2007.890946

Jiang, Z., Liang, Z., Zhu, L., Guo, Z., and Tang, Y. (2020). Effect of hole diameter of rotary-shaped artificial reef on flow field. *Ocean Eng.* 197, 106917. doi: 10.1016/j.oceaneng.2020.106917

Jiang, Z., Liang, Z., Zhu, L., and Liu, Y. (2016). Numerical simulation of effect of guide plate on flow field of artificial reef. *Ocean Eng.* 116, 236–241. doi: 10.1016/j.oceaneng.2016.03.005

Jung, S., Na, W., and Kim, D. (2022). Rugosity and blocking indices of artificial reefs and their correlations with wake volume. *Ocean Eng.* 261, 112204. doi: 10.1016/j.oceaneng.2022.112204

Kim, T., Baek, S., Kwon, Y., Lee, J., Cha, S., and Kwon, S. (2020). Improved coastal erosion prevention using a hybrid method with an artificial coral reef: large-scale 3D hydraulic experiment. *Water* 12, 2801. doi: 10.3390/w12102801

Kim, D., Jung, S., Kim, J., and Na, W. (2019). Efficiency and unit propagation indices to characterize wake volumes of marine forest artificial reefs established by flatly distributed placement models. *Ocean Eng.* 175, 138–148. doi: 10.1016/j.oceaneng.2019.02.020

Kim, D., Jung, S., and Na, W. (2021). Evaluation of turbulence models for estimating the wake region of artificial reefs using particle image velocimetry and computational fluid dynamics. *Ocean Eng.* 223, 108673. doi: 10.1016/j.oceaneng.2021.108673

Kim, T., Kwon, Y., Lee, J., Lee, E., and Kwon, S. (2022). Wave attenuation prediction of artificial coral reef using machine-learning integrated with hydraulic experiment. *Ocean Eng.* 248, 110324. doi: 10.1016/j.oceaneng.2021.110324

Kim, D., Woo, J., Yoon, H., and Na, W. (2016). Efficiency, tranquillity and stability indices to evaluate performance in the artificial reef wake region. *Ocean Eng.* 122, 253–261. doi: 10.1016/j.oceaneng.2016.06.030

Komyakova, V., Chamberlain, D., Jones, G., and Swearer, S. (2019). Assessing the performance of artificial reefs as substitute habitat for temperate reef fishes: implications for reef design and placement. *Sci. Total Environ.* 668, 139–152. doi: 10.1016/j.scitotenv.2019.02.357

Lei, Y., Zheng, X., Li, W., Zheng, H., Zhang, Q., Zhao, S., et al. (2021). Experimental study of the state-of-the-art offshore system integrating a floating offshore wind turbine with a steel fish farming cage. *Mar. Structures* 80, 103076. doi: 10.1016/j.marstruc.2021.103076

Li, J., Guo, Y., Lian, J., and Wang, H. (2022). Scour effects on the bearing capacity of multi-bucket jacket foundation for offshore wind turbines. *Ocean Eng.* 259, 111848. doi: 10.1016/j.oceaneng.2022.111848

Li, X., Paassen, L., and Tao, J. (2022). Investigation of using mangrove-inspired skirt pile group as a scour countermeasure. *Ocean Eng.* 266, 113133. doi: 10.1016/j.oceaneng.2022.113133

Lian, J., Li, J., Guo, Y., Wang, H., and Yang, X. (2022). Numerical study on local scour characteristics of multi-bucket jacket foundation considering exposed height. *Appl. Ocean Res.* 121, 103092. doi: 10.1016/j.apor.2022.103092

Liu, T., and Su, D. (2013). Numerical analysis of the influence of reef arrangements on artificial reef flow fields. *Ocean Eng.* 74, 81–89. doi: 10.1016/j.oceaneng.2013.09.006

López, I., Tinoco, H., Aragonés, L., and García-Barba, J. (2016). The multifunctional artificial reef and its role in the defence of the Mediterranean coast. *Sci. Total Environ.* 550, 910–923. doi: 10.1016/j.scitotenv.2016.01.180

Lu, Y., Liang, B., Yin, Z., Pan, X., Wang, J., and Du, S. (2022). Experimental study on time factor of scour around pile groups. *Ocean Eng.* 261, 112125. doi: 10.1016/j.oceaneng.2022.112125

Ma, H., and Chen, C. (2021). Scour protection assessment of monopile foundation design for offshore wind turbines. *Ocean Eng.* 231, 109083. doi: 10.1016/j.oceaneng.2021.109083

Ma, L., Wang, L., Guo, Z., Jiang, H., and Gao, Y. (2018). Time development of scour around pile groups in tidal currents. *Ocean Eng.* 163, 400–418. doi: 10.1016/j.oceaneng.2018.06.035

Marin-Diaz, B., Fivash, G., Nauta, J., Temmink, R., Hijner, N., Reijers, V., et al. (2021). On the use of large-scale biodegradable artificial reefs for intertidal foreshore stabilization. *Ecol. Eng.* 170, 106354. doi: 10.1016/j.ecoleng.2021.106354

McGovern, D., Ilic, S., Folkard, A., McLelland, S., and Murphy, B. (2014). Time development of scour around a cylinder in simulated tidal currents. *J. Hydraulic Eng.* 140, 04014014. doi: 10.1061/(ASCE)HY.1943-7900.0000857

Meyer-Peter, E. (1948). Formulas for bed-load transport. *Proceedings of the 2nd Meeting of the International Association for Hydraulic Structures Research*, 39–64.

Nazari-Sharabian, M., Nazari-Sharabian, A., Karakouzian, M., and Karami, M. (2020). Sacrificial piles as scour countermeasures in river bridges a numerical study using FLOW-3D. *Civil Eng. J.* 6, 1091–1103. doi: 10.28991/cej-2020-03091531

Nielsen, A., Liu, X., Sumer, B., and Fredsøe, J. (2013). Flow and bed shear stresses in scour protections around a pile in a current. *Coast. Eng.* 72, 20–38. doi: 10.1016/j.coastaleng.2012.09.001

Pan, Y., Tong, H., Wei, D., Xiao, W., and Xue, D. (2022). Review of structure types and new development prospects of artificial reefs in china. *Front. Mar. Sci.* 9. doi: 10.3389/fmars.2022.853452

Pandey, M., Azamathulla, H., Chaudhuri, S., Pu, J., and Pourshahbaz, H. (2020). Reduction of time-dependent scour around piers using collars. *Ocean Eng.* 213, 107692. doi: 10.1016/j.oceaneng.2020.107692

Raaijmakers, T., Oeveren, M., Rudolph, D., Leenders, V., and Sinjou, W. (2010). Field performance of scour protection around offshore monopiles. *Int. Conf. Scour. Erosion*, 428–339. doi: 10.1061/41147(392)41

Roulund, A., Sumer, B., Fredsøe, J., and Michelsen, J. (2005). Numerical and experimental investigation of flow and scour around a circular pile. *J. Fluid Mechanics* 534, 351–401. doi: 10.1017/S0022112005004507

Schendel, A., Hildebrandt, A., Goseberg, N., and Schlurmann, T. (2018). Processes and evolution of scour around a monopile induced by tidal currents. *Coast. Eng.* 139, 65–84. doi: 10.1016/j.coastaleng.2018.05.004

Soulsby, R. (1997). *Dynamics of Marine Sands*. Thomas Telford Publishing.

Srisuwan, C., and Rattanamanee, P. (2015). Modeling of seadome as artificial reefs for coastal wave attenuation. *Ocean Eng.* 103, 198–210. doi: 10.1016/j.oceaneng.2015.04.069

Sumer, B., and Fredsøe, J. (2001). Wave scour around a large vertical circular cylinder. *J. Waterway Port Coast. Ocean Eng.* 127, 125–134. doi: 10.1061/(ASCE)0733-950X(2001)127:3(125

Sumer, B., Fredsøe, J., and Christiansen, N. (1992). Scour around vertical pile in waves. *J. Waterway Port Coast. Ocean Eng.* 118, 15–31. doi: 10.1061/(ASCE)0733-950X(1992)118:1(15

Tang, Y., Wei, S., Yang, M., Wang, X., and Zhao, F. (2022). Experimental investigation of local scour around artificial reefs in steady currents. *J. Ocean Univ. China* 21, 445–456. doi: 10.1007/s11802-022-4883-8

Wang, C., Liang, F., and Yu, X. (2017). Experimental and numerical investigations on the performance of sacrificial piles in reducing local scour around pile groups. *Nat. Hazards* 85, 1417–1435. doi: 10.1007/s11069-016-2634-0

Wang, X., Liu, X., Tang, Y., Zhao, F., and Luo, Y. (2021). Numerical analysis of the flow effect of the menger-type artificial reefs with different void space complexity indices. *Symmetry* 13, 1040. doi: 10.3390/sym13061040

Wang, G., Wan, R., Wang, X., Zhao, F., Lan, X., Cheng, H., et al. (2018). Study on the influence of cut-opening ratio, cut-opening shape, and cut-opening number on the flow field of a cubic artificial reef. *Ocean Eng.* 162, 341–352. doi: 10.1016/j.oceaneng.2018.05.007

Wei, K., Qiu, F., and Qin, S. (2022). Experimental and numerical investigation into effect of skirted caisson on local scour around the large-scale bridge foundation. *Ocean Eng.* 250, 111052. doi: 10.1016/j.oceaneng.2022.111052

Whitehouse, R., Harris, J., Sutherland, J., and Rees, J. (2011). The nature of scour development and scour protection at offshore windfarm foundations. *Mar. pollut. Bull.* 62, 73–88. doi: 10.1016/j.marpolbul.2010.09.007

Yang, F., Qu, L., Tang, G., and Lu, L. (2021). Local scour around a porous surface-piercing square monopile in steady current. *Ocean Eng.* 223, 108716. doi: 10.1016/j.oceaneng.2021.108716

Yang, M., Tang, Y., Zhao, F., Xu, S., and Fang, G. (2022). "Numerical simulation of local scour around square artificial reef," in *Proceedings of the ASME2022 41st International Conference on Ocean, Offshore and Arctic Engineering*. 13. doi: 10.1115/OMAE2022-78941

Yang, Q., Yu, P., and Liu, H. (2021). CFD modelling of local scour around tri-USAF in sand with different arrangements under steady current. *Ocean Eng.* 235, 109359. doi: 10.1016/j.oceaneng.2021.109359

Yang, Q., Yu, P., and Liu, H. (2022). Computational investigation of scour characteristics of USAF in multi-specie sand under steady current. *Ocean Eng.* 262, 112141. doi: 10.1016/j.oceaneng.2022.112141

Yang, Q., Yu, P., Liu, Y., Liu, H., Zhang, P., and Wang, Q. (2020). Scour characteristics of an offshore umbrella suction anchor foundation under the combined actions of waves and currents. *Ocean Eng.* 202, 106701. doi: 10.1016/j.oceaneng.2019.106701

Yang, H., Ru, X., Zhang, L., and Lin, C. (2019). Industrial convergence of marine ranching and offshore wind power: concept and prospect. *Bull. Chinese Acad. Sci.* 34, 6. doi: 10.16418/j.issn.1000-3045.2019.06.011

Yao, W., An, H., Draper, S., Cheng, L., and Harris, J. (2018). Experimental investigation of local scour around submerged piles in steady current. *Coast. Eng.* 142, 27–41. doi: 10.1016/j.coastaleng.2018.08.015

Yao, W., Draper, S., An, H., Cheng, L., Harris, J., and Whitehouse, R. (2020). Effect of a skirted mudmat foundation on local scour around a submerged structure. *Ocean Eng.* 218, 108127. doi: 10.1016/j.oceaneng.2020.108127

Yu, P., Hu, R., Yang, J., and Liu, H. (2020). Numerical investigation of local scour around USAF with different hydraulic conditions under currents and waves. *Ocean Eng.* 213, 107696. doi: 10.1016/j.oceaneng.2020.107696

Yu, T., Zhang, Y., Zhang, S., Shi, Z., Chen, X., Xu, Y., et al. (2019). Experimental study on scour around a composite bucket foundation due to waves and current. *Ocean Eng.* 189, 106302. doi: 10.1016/j.oceaneng.2019.106302

Zhang, Q., Tang, G., Lu, L., and Yang, F. (2021). Scour protections of collar around a monopile foundation in steady current. *Appl. Ocean Res.* 112, 102718. doi: 10.1016/j.apor.2021.102718

Zhang, C., Wang, S., Cui, M., Liu, H., Liu, A., Xu, J., et al. (2022). Modeling and dynamic response analysis of a submersible floating offshore wind turbine integrated with an aquaculture cage. *Ocean Eng.* 263, 112338. doi: 10.1016/j.oceaneng.2022.112338

Zhang, Q., Zhou, X., and Wang, J. (2017). Numerical investigation of local scour around three adjacent piles with different arrangements under current. *Ocean Eng.* 142, 625–638. doi: 10.1016/j.oceaneng.2017.07.045

Zhao, M., Cheng, L., and Zang, Z. (2010). Experimental and numerical investigation of local scour around a submerged vertical circular cylinder in steady currents. *Coast. Eng.* 57, 709–721. doi: 10.1016/j.coastaleng.2010.03.002

Zhao, F., Xu, S., Yang, M., Tang, Y., Huang, L., and Fang, G. (2022). "Experimental study on local scour of triangular artificial reef," in *Proceedings of the ASME2022 41st International Conference on Ocean, Offshore and Arctic Engineering*. 9. doi: 10.1115/OMAE2022-78936

Zhou, P., Gao, Y., and Zheng, S. (2022). Three-dimensional numerical simulation on flow behavior behind trapezoidal artificial reefs. *Ocean Eng.* 266, 112899. doi: 10.1016/j.oceaneng.2022.112899

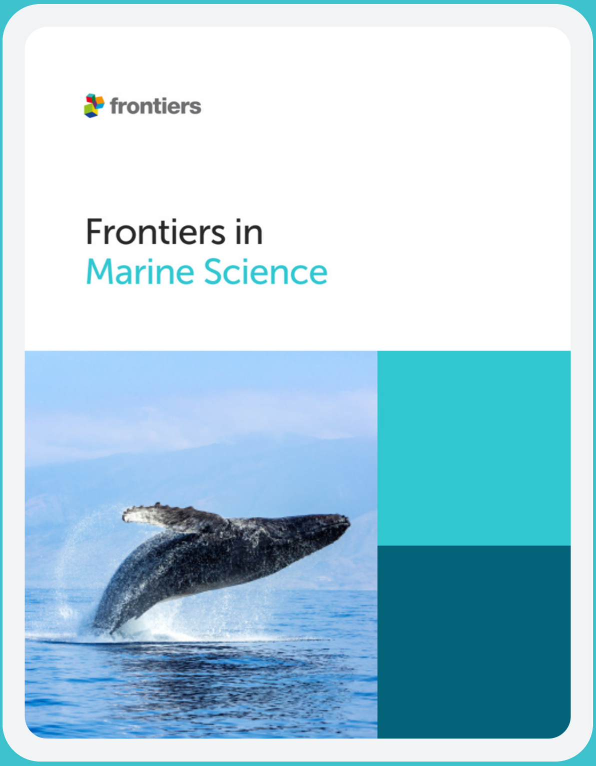

frontiers

Frontiers in
Marine Science

Frontiers

Avenue du Tribunal-Fédéral 34
1005 Lausanne, Switzerland
frontiersin.org

Contact us

+41 (0)21 510 17 00
frontiersin.org/about/contact